frontiers | Research Topics

Systemic regulation of organ homeostasis and implications of hormones and immunity, Volume II

Edited by
Vijaya Kumar Pidugu, Tatjana S. Kostic, Silvana A. Andric, Taka-aki Koshimizu and Anil Mathew Tharappel

Published in
Frontiers in Endocrinology

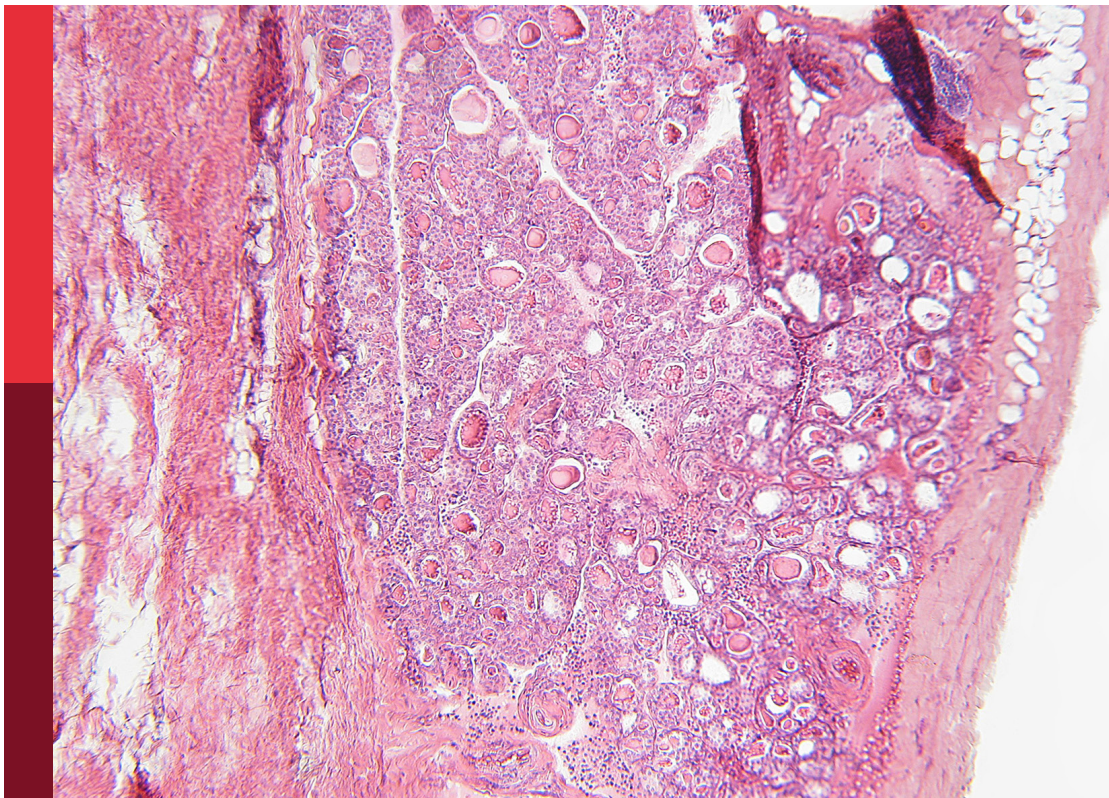

ISSN 1664-8714
ISBN 978-2-8325-2967-6
DOI 10.3389/978-2-8325-2967-6

About Frontiers

Frontiers is more than just an open access publisher of scholarly articles: it is a pioneering approach to the world of academia, radically improving the way scholarly research is managed. The grand vision of Frontiers is a world where all people have an equal opportunity to seek, share and generate knowledge. Frontiers provides immediate and permanent online open access to all its publications, but this alone is not enough to realize our grand goals.

Frontiers journal series

The Frontiers journal series is a multi-tier and interdisciplinary set of open-access, online journals, promising a paradigm shift from the current review, selection and dissemination processes in academic publishing. All Frontiers journals are driven by researchers for researchers; therefore, they constitute a service to the scholarly community. At the same time, the *Frontiers journal series* operates on a revolutionary invention, the tiered publishing system, initially addressing specific communities of scholars, and gradually climbing up to broader public understanding, thus serving the interests of the lay society, too.

Dedication to quality

Each Frontiers article is a landmark of the highest quality, thanks to genuinely collaborative interactions between authors and review editors, who include some of the world's best academicians. Research must be certified by peers before entering a stream of knowledge that may eventually reach the public - and shape society; therefore, Frontiers only applies the most rigorous and unbiased reviews. Frontiers revolutionizes research publishing by freely delivering the most outstanding research, evaluated with no bias from both the academic and social point of view. By applying the most advanced information technologies, Frontiers is catapulting scholarly publishing into a new generation.

What are Frontiers Research Topics?

Frontiers Research Topics are very popular trademarks of the *Frontiers journals series*: they are collections of at least ten articles, all centered on a particular subject. With their unique mix of varied contributions from Original Research to Review Articles, Frontiers Research Topics unify the most influential researchers, the latest key findings and historical advances in a hot research area.

Find out more on how to host your own Frontiers Research Topic or contribute to one as an author by contacting the Frontiers editorial office: frontiersin.org/about/contact

Systemic regulation of organ homeostasis and implications of hormones and immunity, volume II

Topic editors

Vijaya Kumar Pidugu — National Cancer Institute (NIH), United States
Tatjana S. Kostic — University of Novi Sad, Serbia
Silvana A. Andric — University of Novi Sad, Serbia
Taka-aki Koshimizu — Jichi Medical University, Japan
Anil Mathew Tharappel — University of Arizona, United States

Citation

Pidugu, V. K., Kostic, T. S., Andric, S. A., Koshimizu, T.-A., Tharappel, A. M., eds. (2023). *Systemic regulation of organ homeostasis and implications of hormones and immunity, volume II*. Lausanne: Frontiers Media SA.
doi: 10.3389/978-2-8325-2967-6

Table of contents

05 Editorial: Systemic regulation of organ homeostasis and implications of hormones and immunity, Volume II
Vijaya Kumar Pidugu, Tatjana S. Kostic, Silvana A. Andric, Anil M. Tharappel and Taka-Aki Koshimizu

08 Influence of arginine vasopressin on the ultradian dynamics of Hypothalamic-Pituitary-Adrenal axis
Aleksandra S. Stojiljković, Željko Čupić, Stevan Maćešić, Ana Ivanović-Šašić and Ljiljana Kolar-Anić

24 Identification and characterization of novel compound heterozygous variants in *FSHR* causing primary ovarian insufficiency with resistant ovary syndrome
Xiaopan Chen, Linjie Chen, Yang Wang, Chongyi Shu, Yier Zhou, Ruifang Wu, Bihui Jin, Leixiang Yang, Junhui Sun, Ming Qi and Jing Shu

34 The effects of three different low-volume aerobic training protocols on cardiometabolic parameters of type 2 diabetes patients: A randomized clinical trial
Paulo Gentil, Lucas Raphael Bento e Silva, Daniela Espíndola Antunes, Luciana Barbosa Carneiro, Claudio Andre Barbosa de Lira, Gislene Batista, Jordana Campos Martins de Oliveira, John Sebastião Cardoso, Daniel CostaCosta Souza and Ana Cristina Silva Rebelo

43 Low glomerular number at birth can lead to the development of chronic kidney disease
Shohei Fukunaga and Yuki Fujita

51 Low oxytocin levels are broadly associated with more pronounced psychopathology in anorexia nervosa with primarily restricting but not binge/purge eating behavior
Franziska Plessow, Francesca Galbiati, Kamryn T. Eddy, Madhusmita Misra, Karen K. Miller, Anne Klibanski, Anna Aulinas and Elizabeth A. Lawson

61 The *isl2a* transcription factor regulates pituitary development in zebrafish
Chen-Yan Yan, Feng-Yao Wu, Feng Sun, Ya Fang, Rui-Jia Zhang, Chang-Run Zhang, Cao-Xu Zhang, Zheng Wang, Rui-Meng Yang, Liu Yang, Mei Dong, Qian-Yue Zhang, Xiao-Ping Ye, Huai-Dong Song and Shuang-Xia Zhao

71 Circulating follistatin concentrations in adolescent PCOS: Divergent effects of randomized treatments
Marta Díaz, Francis de Zegher and Lourdes Ibáñezu

77 Association between serum total testosterone levels and metabolic syndrome among adult women in the United States, NHANES 2011–2016
Chenning Liu, Meiduo Zhao, Yonghua Zhao and Yuanjia Hu

86 The homeostasis model assessment of insulin resistance is a judgment criterion for metformin pre-treatment before IVF/ICSI and embryo transfer cycles in patients with polycystic ovarian syndrome
Rui Gao, Lang Qin, Zhengyu Li and Wenjiao Min

94 Different sleep pattern in over-weight/obese women with polycystic ovary syndrome
Emma Oberg, Liselotte Blomberg, Torbjörn Åkerstedt and Angelica Lindén Hirschberg

104 An insight into brown/beige adipose tissue whitening, a metabolic complication of obesity with the multifactorial origin
Khanyisani Ziqubu, Phiwayinkosi V. Dludla, Sinenhlanhla X. H. Mthembu, Bongani B. Nkambule, Sihle E. Mabhida, Babalwa U. Jack, Tawanda M. Nyambuya and Sithandiwe E. Mazibuko-Mbeje

124 Inadequate detection of the FSHR complicates future research on extragonadal FSHR localization
Victoria N. Tedjawirja, Gerrit K. J. Hooijer, C. Dilara Savci-Heijink, Kristina Kovac, Ron Balm and Vivian de Waard

129 APOC1 as a novel diagnostic biomarker for DN based on machine learning algorithms and experiment
Kuipeng Yu, Shan Li, Chunjie Wang, Yimeng Zhang, Luyao Li, Xin Fan, Lin Fang, Haiyun Li, Huimin Yang, Jintang Sun and Xiangdong Yang

140 Comparison of biochemical markers and technetium 99m methoxyisobutylisonitrile imaging in primary and secondary hyperparathyroidism
Yuhua Wang, Ye Liu, Na Li and Wanchun Zhang

148 Profiling estrogen, progesterone, and androgen receptors in colorectal cancer in relation to gender, menopausal status, clinical stage, and tumour sidedness
Bassem Refaat, Akhmed Aslam, Shakir Idris, Ahmed H. Almalki, Mofareh Y. Alkhaldi, Hassan A. Asiri, Riyad A. Almaimani, Abdulrahman Mujalli, Faisal Minshawi, Sara A. Alamri, Mona I. AlHussain, Badee A. Baltow, Mansour H. Alqasmi, Ghaiyda T. Basfar, Ohoud M. Alosaimi and Ibrahim A. Muhayya

166 ZIP9 mediates the effects of DHT on learning, memory and hippocampal synaptic plasticity of male Tfm and APP/PS1 mice
Leigang Song, Huan Chen, Dan Qiao, Bohan Zhang, Fangzhen Guo, Yizhou Zhang, Chang Wang, Sha Li and Huixian Cui

frontiers | Frontiers in Endocrinology

TYPE Editorial
PUBLISHED 26 June 2023
DOI 10.3389/fendo.2023.1235274

OPEN ACCESS

EDITED AND REVIEWED BY
Hubert Vaudry,
Université de Rouen, France

*CORRESPONDENCE
Vijaya Kumar Pidugu
Vijaya.pidugu@nih.gov

RECEIVED 06 June 2023
ACCEPTED 13 June 2023
PUBLISHED 26 June 2023

CITATION
Pidugu VK, Kostic TS, Andric SA, Tharappel AM and Koshimizu T-A (2023) Editorial: Systemic regulation of organ homeostasis and implications of hormones and immunity, Volume II. *Front. Endocrinol.* 14:1235274. doi: 10.3389/fendo.2023.1235274

Editorial: Systemic regulation of organ homeostasis and implications of hormones and immunity, Volume II

Vijaya Kumar Pidugu[1]*, Tatjana S. Kostic[2], Silvana A. Andric[2], Anil M. Tharappel[3] and Taka-Aki Koshimizu[4]

[1]Laboratory of Cancer Biology and Genetics, Center for Cancer Research, National Cancer Institute, Bethesda, MD, United States, [2]Laboratory for Reproductive Endocrinology and Signaling, Laboratory for Chronobiology and Aging, Center of Excellence for Reproductive Endocrinology and Signaling, Faculty of Sciences, University of Novi Sad, Novi Sad, Serbia, [3]Department of Pharmacology and Toxicology, R. Ken Coit College of Pharmacy, The University of Arizona, Tucson, AZ, United States, [4]Department of Pharmacology, Division of Molecular Pharmacology, Jichi Medical University, Tochigi, Japan

KEYWORDS

homeostasis, hormones, endocrine system, hypothyroidism, ISL2A, FSHR, PCOS, colorectal cancer

Editorial on the Research Topic
Systemic regulation of organ homeostasis and implications of hormones and immunity, Volume II

The multicellularity of an organism enables cells in the body to make complex tissues and organ systems that orchestrate their complex functions. The coordination of specialized functions of some of these cells is to assure the maintenance of basic metabolic functions and requirements of all other surrounding cells for the survival of organs and organ systems of the body. The endocrine system plays a critical role in regulation of homeostasis by executing a vastly complex network of molecular signaling mechanisms that communicate information in the form of hormones released by the cells. The hormone signals, in turn, stimulate organ systems to restore homeostasis. Although endocrine and immune systems regulate distinct functions, the coordinated response of these systems is needed for the maintenance of homeostasis. The altered endocrine system in the body affects the balance between pro-and anti-inflammatory immune responses. If homeostasis is not restored, the imbalance may lead to various diseases.

During the evolution process, multiple positive and negative feedback loops have developed between endocrine and immune systems to coordinate the normal body function of an organism. It is important to study these immune-endocrine interactions to understand the underlying molecular mechanisms that regulate systemic metabolism and disease progression. This could allow us to explore optimal disease management and treatment strategies for patients. In this context, the present Research Topic was intended to study the critical biological interactions of endocrine and immune systems to understand the pathophysiology of diseases and possible treatment options. Individually and

collectively, the research and review articles collected on this Research Topic make a significant addition to our understanding of immune-endocrine interactions in the context of endocrine related diseases.

The ISL LIM homeobox 2a protein (ISL2A), a novel transcription factor has been shown as a regulator of early angiogenesis, exocrine pancreas development, and neuron differentiation. However, the functional role of ISL2A in the hypothalamus-pituitary thyroid axis is elusive. Yan et al. have established homozygous *isl2a* knockout zebrafish using CRISPR/Cas9 system. Molecular characterization of isl*2a* mutant zebrafish revealed a novel transcriptional regulatory role of *isl2a* in pituitary cell differentiation. This study should facilitate future studies to unravel the molecular mechanism of hypothyroidism and possible drug development in this zebrafish model. Stojiljković et al. developed an extended, stoichiometric model of the hypothalamic-pituitary-adrenal (HPA) axis for better understanding individual or combined effect of corticotrophin-releasing hormone (CRH) and arginine vasopressin (AVP) on the secretion of adrenocorticotropic hormone (ACTH) by corticotropic cells in the human pituitary gland. The extended HPA model is associated with previous experimental findings and highlights possible implication for future studies related to homeostasis dynamic crisis, autoimmune inflammation, and exogenous administered AVP treatment. Gentil et al. conducted a randomized clinical trial on type 2 diabetes mellitus (T2DM) patients to evaluate the beneficial effect of three different aerobic exercise protocols such as moderate-intensity continuous training (MICT), short-interval high-intensity training (S-HIIT), and long interval high-intensity training (L-HIIT). Parallel comparison of cardiometabolic variables showed fundamental differences among T2DM patients undergoing different training protocols. Although all training protocols improved at least one cardiometabolic parameter, the L-HIIT training protocol showed a significant impact on maximum oxygen consumption (VO2 max). This study suggests that the L-HIIT training protocol may potentially be a cost-effective means for T2DM patients to improve their quality of life. Likewise, Oberg et al. designed a randomized trial to evaluate the correlation between sleep patterns and endocrine parameters in over-weigh/obese women with polycystic ovary syndrome (PCOS). This study found that women with PCOS had poor sleep quality compared to the control group, suggesting the implementation of standard care with better sleep cycles to improve the endocrine and psychological well-being of women with PCOS. In addition, Gao et al. investigated homeostasis model assessment of insulin resistance (HOMA-IR) as a determining factor for metformin pre-treatment before *in vitro* fertilization/intracellular sperm injection (IVF/ICSI) and embryo transfer for patients with PCOS. This retrospective study found that metformin pre-treatment could improve pregnancy rates in women with PCOS with HOMA-IR during frozen IVF/ICSI-ET cycles. Díaz et al. delineated the influence of oral contraceptives (OCs) on endocrine-metabolic markers after 6 months of use of OCs in females with PCOS. This study showed that higher levels of circulating follistatin concentration correlated with insulin resistance and increased liver fat accumulation in females with PCOS compared to the control group. This indicates OCs treatment in females with PCOS may potentially cause adverse metabolic effects. Plessow et al. assessed the relationship between oxytocin levels and eating disorder in women with anorexia nervosa or atypical anorexia nervosa with primary food restriction (AN/AtypAN-R) and AN/AtypAN with restriction plus binge purge behaviors (AN/AtypAN-BP). This trial implies that both AN/AtypAN-R and AN/AtypAN-BP may be composed of fundamentally different neurobiology as they show distinct associations with eating, depressive, and anxiety parameters. Liu et al. analyze the association between serum total testosterone (TT) levels and metabolic syndrome (MetS) in women by logistic regression models. This study concludes that total TT levels in women are inversely correlated with MetS. However, future studies are needed to determine cut-off values for abnormal TT levels in women and their association with MetS at different scales. Wang et al. compared the difference in biochemical markers and degree of lesion visualization between primary hyperparathyroidism (PHPT) and secondary hyperparathyroidism (SHPT) by technetium 99m methoxyisobutylisonitrile (^{99m}Tc-MIBI) imaging. This study revealed that the percentage of patients with positive dual-phase planar imaging on ^{99m}Tc-MIBI was higher in the PHPT group compared to the SHPT group. The range of parathyroid lesions in SHPT was smaller than in PHPT. This study also suggests that a combination of other imaging technologies is needed if ^{99m}Tc-MIBI imaging shows negative results in patents with SHPT for accurate lesion detection.

The inactivating follicle-stimulating hormone receptor (FSHR) genetic variants causes a wide spectrum of inconsistent clinical manifestations. Therefore, identification and molecular characterization of pathogenetic variants that disrupt FSHR protein function are important for the better diagnosis of primary ovarian insufficiency (POI) and resistant ovary syndrome (ROS). Using next-generation sequencing and traditional Sanger sequencing, Chen et al. identified rare compound heterozygous variants c.1384G>C/p.A462P and c.1862C>T/p.A621V in FSHR. Furthermore, *in vitro* characterization of these variants revealed a loss of intracellular signaling and receptor activation, respectively. This study expands our knowledge of understanding pathogenic variants of FSHR in connection to POI. Besides that, Tedjawirja et al. tested both monoclonal and polyclonal anti-FSHR antibodies on human premenopausal ovary, testis and skin samples and demonstrated that polyclonal anti-FSHR antibody non-specifically stained skin tissue, which is not known to express FSHR. This study points out the need for validated methods for better detection of FSH/FSHR in postmenopausal disease to avoid future challenges in the research field. Yu et al. characterized apolipoprotein C1 (APOC1) in diabetic nephropathy (DN) patients using functional gene enrichment analysis combined with mouse models and clinical samples. This study demonstrates that elevated serum and glomerular expression levels of APOC1 might be a novel biomarker for the diagnosis of DN. However, further research studies are needed to evaluate its diagnostic value. Refaat et al. investigated the prognostic value of simultaneous expression levels of estrogen receptor, progesterone receptor, and androgen receptors within the same cohort of colorectal cancer (CRC) patients in terms of gender, menopausal status, clinical stage, and tumor sidedness. The accurate determination of expression levels of sex steroid hormone receptors could significantly benefit the precise use of

steroid blockers and hormonal therapy in CRC patients. Song et al. investigated the role of dihydrotestosterone (DHT) induced zinc transporter ZIP9 and its impact on learning, memory, and hippocampal synaptic plasticity of Tfm, APP/PS1 mice. This study revealed that ZIP9 facilitates the effects of DHT on hippocampal synaptic plasticity and dendritic spine density in Tfm mice via the ERK1/2-eIF4E pathway. Moreover, the same mechanism mediated by DHT can also affect learning and memory in APP/PS1 mice. Ziqubu et al. reviewed the influence of different parameters including diet, age, genetics, chemical exposure, and thermoneutrality on Brown adipose tissue/beige adipose tissue whitening and its relation to multiple metabolic complications including mitochondrial degeneration, mitochondrial dysfunction, autophagy, inflammation, devascularization and collapsed thermogenic capacity. Similarly, Fukunaga and Fujita reviewed the low glomerular number at birth and its relationship with the development of chronic kidney disease (CKD). This review expands our understanding of the significance of low glomerular number at birth increasing the risk of CKD and preventive prenatal nutritional management.

Conclusion

Regulation of organ homeostasis is a complex process that involves the coordination of various biological mechanisms to maintain a stable internal environment within the body. The challenges lie in maintaining the delicate balance required for optimal organ function and preventing dysregulation that can lead to diseases. The knowledge gained from the Research Topic could be a steppingstone for future research to shed light on unresolved scientific problems and develop innovative treatment strategies for the life-threatening diseases.

Future perspectives

The future perspectives in the regulation of organ homeostasis and the implications of hormones and immunity are exciting and hold tremendous potential for advancements in medicine. Precision medicine, immunomodulatory therapies, hormonal interventions for organ regeneration, modulation of signaling pathways, research on hormones and aging, innovative therapeutic delivery systems, and the integration of artificial intelligence based complex data analytics are among the areas that may shape the future of this field. Continued research and technological innovations will pave the way for more targeted and effective approaches to maintaining organ homeostasis and treating a wide range of life-threatening diseases.

Author contributions

VKP wrote the original draft. All authors contributed to the editing equally and approved the submitted version.

Conflict of interest

The authors declare that the research was conducted in the absence of any commercial or financial relationships that could be constructed as a potential conflict of interest.

Publisher's note

Author disclaimer

The content is solely the responsibility of the authors and does not necessarily represent the official views or policies of the National Institutes of Health and the Department of Health and Human Services. The mention of trade names, commercial products or organizations does not imply endorsement from the US Government.

frontiers | Frontiers in Endocrinology

TYPE Original Research
PUBLISHED 05 October 2022
DOI 10.3389/fendo.2022.976323

OPEN ACCESS

EDITED BY
Giuseppe Reimondo,
University of Turin, Italy

REVIEWED BY
Nicola Romano,
University of Edinburgh,
United Kingdom
Mara Carsote,
Carol Davila University of Medicine and Pharmacy, Romania

*CORRESPONDENCE
Aleksandra S. Stojiljković
alek.stoj@gmail.com
Željko Čupić
zcupic@ihtm.bg.ac.rs

SPECIALTY SECTION
This article was submitted to Adrenal Endocrinology, a section of the journal Frontiers in Endocrinology

RECEIVED 23 June 2022
ACCEPTED 09 September 2022
PUBLISHED 05 October 2022

CITATION
Stojiljković AS, Čupić Ž, Maćešić S, Ivanović-Šašić A and Kolar-Anić Lj (2022) Influence of arginine vasopressin on the ultradian dynamics of Hypothalamic-Pituitary-Adrenal axis. *Front. Endocrinol.* 13:976323. doi: 10.3389/fendo.2022.976323

Influence of arginine vasopressin on the ultradian dynamics of Hypothalamic-Pituitary-Adrenal axis

Aleksandra S. Stojiljković[1*], Željko Čupić[2*], Stevan Maćešić[3], Ana Ivanović-Šašić[2] and Ljiljana Kolar-Anić[2,3]

[1]Institute of General and Physical Chemistry, University of Belgrade, Belgrade, Serbia, [2]Institute of Chemistry, Technology and Metallurgy, National Institute of the Republic of Serbia, University of Belgrade, Belgrade, Serbia, [3]Faculty of Physical Chemistry, University of Belgrade, Belgrade, Serbia

Numerous studies on humans and animals have indicated that the corticotrophin-releasing hormone (CRH) and arginine vasopressin (AVP) stimulate both individually and synergistically secretion of adrenocorticotropic hormone (ACTH) by corticotropic cells in anterior pituitary. With aim to characterize and better comprehend the mechanisms underlying the effects of AVP on Hypothalamic-Pituitary-Adrenal (HPA) axis ultradian dynamics, AVP is here incorporated into our previously proposed stoichiometric model of HPA axis in humans. This extended nonlinear network reaction model took into account AVP by: reaction steps associated with two separate inflows of AVP into pituitary portal system, that is synthesized and released from hypothalamic parvocellular and magnocellular neuronal populations, as well as summarized reaction steps related to its individual and synergistic action with CRH on corticotropic cells. To explore the properties of extended model and its capacity to emulate the effects of AVP, nonlinear dynamical systems theory and bifurcation analyses based on numerical simulations were utilized to determine the dependence of ultradian oscillations on rate constants of the inflows of CRH and AVP from parvocellular neuronal populations, the conditions under which dynamical transitions occur due to their synergistic action and, moreover, the types of these transitions. The results show that under certain conditions, HPA system could enter into oscillatory dynamic states from stable steady state and vice versa under the influence of synergy reaction rate constant. Transitions between these dynamical states were always through supercritical Andronov-Hopf bifurcation point. Also, results revealed the conditions under which amplitudes of ultradian oscillations could increase several-fold due to CRH and AVP synergistic stimulation of ACTH secretion in accordance with results reported in the literature. Moreover, results showed experimentally observed superiority of CRH as a stimulator of ACTH secretion compared to AVP in humans. The proposed model can be very useful in studies related to the

role of AVP and its synergistic action with CRH in life-threatening circumstances such as acute homeostasis dynamic crisis, autoimmune inflammations or severe hypovolemia requiring instant or several-days sustained corticosteroid excess levels. Moreover, the model can be helpful for investigations of indirect AVP-induced HPA activity by exogenously administered AVP used in therapeutic treatment.

KEYWORDS

Hypothalamic-Pituitary-Adrenal (HPA) axis, arginine vasopressin, AVP and CRH synergy, HPA ultradian dynamics, stoichiometric modeling, numerical simulations

Introduction

The interplay between the functions of hypothalamus, pituitary and adrenal glands creates a complex nonlinear neuroendocrine system known as the hypothalamic-pituitary-adrenal (HPA) axis. The HPA axis activity is necessary for maintaining homeostasis under physiologically normal and various stressful conditions through the action of its main hormones. Their actions are expressed through complex biochemical transformations that are intertwined *via* positive and negative feedback loops. Complex interplay between these feedback mechanisms and coupling of the HPA axis with circadian clock system give rise to daily rhythm of the main HPA axis hormones characterized by ultradian oscillations (caused by internal feedbacks) superimposed on circadian oscillations (greatly influenced by external cycles) (1–3). In humans, periods of ultradian oscillations of the HPA axis hormones altogether range between 20 minutes to 2 hours, while periods of their circadian oscillations are around 24 hours (1, 2, 4–9). Disruption in regulation of HPA axis oscillatory dynamics can lead to the development of many psychiatric and metabolic diseases (2, 10). Thus, additional experimental and theoretical investigations have been conducted to examine all constituents and detailed dynamic regulatory mechanisms underlying the HPA axis function under basal physiological and pathophysiological conditions. Effects of acute and chronic exposure to various endogenous/exogenous stressors on the HPA axis dynamics and its impairment in disease states have been also largely studied.

Beside corticotropin-releasing hormone (CRH), as one of main HPA hormones, many other neuroactive substances have been found to enter the pituitary portal circulation. This includes somatostatin, neurotensin, angiotensin II, enkephalin, arginine vasopressin (AVP), dopamine and others (11–27). However, AVP has received the most attention among them so far, due to its relevant role and effects on corticotrope cells' function and HPA axis activity. Namely, it has been indicated that both CRH and AVP act on their own receptors (28–32) on corticotrope cells in anterior pituitary to stimulate adrenocorticotropic hormone (ACTH) production and release with different (26, 33–41) or even similar potencies (42). Moreover, CRH and AVP are also capable of potentiating each other's activity (37, 38). Their synergistic stimulation of ACTH production and secretion by corticotrope cells could yield a several-fold higher output than due to the action of either one individually (26, 34–41, 43–47). However, the exact mechanism underlying their individual and synergistic action is yet to be clarified. In essence, CRH and AVP are both required as stimulatory inputs to corticotrope cells for a complete ACTH response in physiologically normal as well as in various stressful conditions (32, 38, 48–51). The ACTH stimulates the steroidogenesis from cholesterol in adrenal gland and secretion of steroid hormones. Principal representative of steroid hormones in humans is cortisol (CORT), which exerts its effect on most tissues in the body and largely regulates the activity of the HPA system through its feedback mechanisms (2, 3).

Theoretical studies of effects of AVP alone and in synergy with CRH on HPA axis activity and dynamics are very scarce. To our best knowledge, in only two theoretical studies (52, 53), impacts of AVP and/or CRH on corticotrope cells' activity are encompassed in mathematical models. These models are non-stoichiometric and describe: synthesis, accumulations, secretions and concentrations time series of CRH and AVP, ACTH and CORT as well as nonlinear feedback mechanisms with time delays considerations and effects of CRH and AVP on corticotrope cells, each by suitable mathematical function. These functions known as the ones that formally can produce oscillatory dynamics cannot be obtained as results of any real reaction mechanism comprised of a set of chemical reactions. On the other hand, if stoichiometric network approach is applied, complex biochemical transformations can be concisely described by a simplified network of interactions between the considered biochemical species. The rates of these transformations strictly follow the law of mass action. Using this approach, HPA axis oscillatory dynamics in model would emerge due to the nonlinearity of underlying biochemical

interactions of considered species through positive and negative feedback mechanisms. Moreover, its global behavior would be tractable to mathematical analysis.

In this study, our previously proposed stoichiometric model of HPA axis in humans (54) has been extended to emulate the influence of AVP on ACTH production and secretion. Using such extended HPA axis model, we investigated the AVP and CRH effects and synergistic influence on ultradian dynamics. For that purpose, numerical simulations and bifurcation analysis have been employed.

Model description

Stoichiometric model of HPA axis activity in humans developed in our earlier work (54) has been used as the basis to incorporate influence of arginine vasopressin (AVP) into the HPA mechanism described by the initial model. The AVP was introduced into this initial model of HPA axis activity by five new reaction steps ((R2.2), (R4), (R5.2), (R5.3) and (R12)), which are highlighted in bold in the Table 1. Reaction steps presented in Table 1 describe net reactions of a series of complex biochemical processes. Accordingly, reaction steps (R2.2) and (R4) describe appropriate inflows of AVP into the pituitary portal circulation as net reactions of a series of processes of AVP biosynthesis and release from the parvocellular part of the paraventricular nucleus (PVN), and from the magnocellular neurosecretory system of the hypothalamus, respectively (32, 48–51, 55). In essence, reaction steps (R2.1) and (R2.2) depict inflows of CRH and AVP, respectively, from neuronal populations of the same part of PVN. On the other hand, inflow of AVP from the magnocellular neurons (R4) can be much more abundant (up to 10-fold) than from parvocellular neurons under normal condition (51). Furthermore, these neurons are not under prominent negative feedback control by adrenal corticosteroids (51). The AVP originating from both of these parvocellular and magnocellular neuronal populations enter the pituitary portal circulation and regulate the pituitary production and secretion of ACTH, as it is summarized by reaction step (R5.2) (32, 48–51, 55). Reaction step (R5.3) describes net reaction of a series of complex biochemical processes of ACTH production and secretion by corticotrope cells that is also stimulated by CRH and AVP acting synergistically (32, 48–51, 55). End-result of complex biochemical processes leading to the elimination of AVP is described by reaction step (R12). The remaining reaction steps in Table 1 are related to the initial model of HPA axis in humans and are described in ref. (54).

The extended model given in Table 1 is now comprised of 18 reaction steps and six independent dynamic variables representing concentrations of cholesterol ([CHOL]), CRH ([CRH]), AVP ([AVP]), ACTH ([ACTH]), CORT ([CORT])

TABLE 1 The extended model of the HPA axis activity in humans with incorporated arginine vasopressin (AVP) as an additional dynamic variable; reaction steps associated with AVP are given in bold.

$\xrightarrow{k_1} CHOL$	$k_1 = 1.38 \times 10^{-4}$ mol dm^{-3} min^{-1}	(R1)
$\xrightarrow{k_{2.1}} CRH$	$k_{2.1} = 1.83 \times 10^{-8}$ mol dm^{-3} min^{-1}	(R2.1)
$\mathbf{\xrightarrow{k_{2.2}} AVP}$	$k_{2.2} = 1.83 \times 10^{-8}$ mol dm^{-3} min^{-1}	**(R2.2)**
$\xrightarrow{k_3} ALDO$	$k_3 = 6.09 \times 10^{-11}$ mol dm^{-3} min^{-1}	(R3)
$\mathbf{\xrightarrow{k_4} AVP}$	$k_4 = 1.537 \times 10^{-9}$ mol dm^{-3} min^{-1}	**(R4)**
$CRH \xrightarrow{k_{5.1}} ACTH$	$k_{5.1} = 1.83 \times 10^{4}$ min^{-1}	(R5.1)
$\mathbf{AVP \xrightarrow{k_{5.2}} ACTH}$	$k_{5.2} = 7.79 \times 10^{-3}$ min^{-1}	**(R5.2)**
$\mathbf{CRH + AVP \xrightarrow{k_{5.3}} ACTH}$	$k_{5.3} = 3.66 \times 10^{2}$ mol^{-1} dm^{3} min^{-1}	**(R5.3)**
$CHOL + ACTH \xrightarrow{k_6} CORT$	$k_6 = 11.94$ mol^{-1} dm^{3} min^{-1}	(R6)
$CHOL + ACTH \xrightarrow{k_7} ALDO$	$k_7 = 9.552 \times 10^{-2}$ mol^{-1} dm^{3} min^{-1}	(R7)
$ACTH + 2CORT \xrightarrow{k_8} 3CORT$	$k_8 = 1.26 \times 10^{14}$ mol^{-2} dm^{6} min^{-1}	(R8)
$ALDO + 2CORT \xrightarrow{k_9} CORT$	$k_9 = 7.05 \times 10^{12}$ mol^{-2} dm^{6} min^{-1}	(R9)
$CHOL \xrightarrow{k_{10}} P_1$	$k_{10} = 4.5 \times 10^{-2}$ min^{-1}	(R10)
$CRH \xrightarrow{k_{11}} P_2$	$k_{11} = 1.1 \times 10^{-1}$ min^{-1}	(R11)
$\mathbf{AVP \xrightarrow{k_{12}} P_3}$	$k_{12} = 1.386 \times 10^{-1}$ min^{-1}	**(R12)**
$ACTH \xrightarrow{k_{13}} P_4$	$k_{13} = 5.35 \times 10^{-2}$ min^{-1}	(R13)
$CORT \xrightarrow{k_{14}} P_5$	$k_{14} = 4.1 \times 10^{-1}$ min^{-1}	(R14)
$ALDO \xrightarrow{k_{15}} P_6$	$k_{15} = 1.35 \times 10^{-1}$ min^{-1}	(R15)

and ALDO ([ALDO])). Corresponding kinetic rate constants are labeled by k_a, a = 1 - 15.

Temporal concentration evolutions of all species are described by a system of ordinary differential equations (ODE) obtained by applying the law of mass action on reaction steps shown in Table 1:

$$\frac{d[CHOL]}{dt} = k_1 - (k_6 + k_7)[CHOL][ACTH] - k_{10}[CHOL] \quad (1)$$

$$\frac{d[CRH]}{dt} = k_{2.1} - (k_{5.1} + k_{11})[CRH] - k_{5.3}[CRH][AVP] \quad (2)$$

$$\frac{d[AVP]}{dt} = k_{2.2} + k_4 - k_{5.2}[AVP] - k_{5.3}[CRH][AVP] - k_{12}[AVP] \quad (3)$$

$$\frac{d[ACTH]}{dt} = k_{5.1}[CRH] + k_{5.2}[AVP] + k_{5.3}[CRH][AVP] - (k_6 + k_7)[CHOL][ACTH] - k_8[ACTH][CORT]^2 - k_{13}[ACTH] \quad (4)$$

$$\frac{d[CORT]}{dt} = k_6[CHOL][ACTH] + k_8[ACTH][CORT]^2 - k_9[ALDO][CORT]^2 - k_{14}[CORT] \quad (5)$$

$$\frac{d[ALDO]}{dt} = k_3 + k_7[CHOL][ACTH] - k_9[ALDO][CORT]^2 - k_{15}[ALDO] \quad (6)$$

Methods

Numerical method

In order to solve ODE describing the temporal evolution of extended model (Table 1), numerical simulations were conducted in the Matlab software package. Ode15s solver routine based on the Gear algorithm (56) for integration of stiff differential equations was used. In all simulations, the absolute and relative tolerance errors were 1×10^{-20} and 3×10^{-12}, respectively. Integrations of the model with 1×10^{-14}, 5×10^{-14} and 1×10^{-15} absolute tolerance levels were also tested. It was noticed that only with absolute tolerance error of 1×10^{-15}, numerical simulations were stable. Yet, in some investigated cases, 1×10^{-20} absolute tolerance level was necessary and therefore chosen as the final value. The initial concentrations in numerical simulations were: $[CHOL]_0 = 3.4 \times 10^{-4}$ mol dm^{-3}, $[CRH]_0 = 1 \times 10^{-12}$ mol dm^{-3}, $[AVP]_0 = 1 \times 10^{-12}$ mol dm^{-3}, $[ACTH]_0 = 8 \times 10^{-8}$ mol dm^{-3}, $[CORT]_0 = 4 \times 10^{-8}$ mol dm^{-3} and $[ALDO]_0 = 1.5 \times 10^{-9}$ mol dm^{-3}. If not otherwise stated, rate constants (k_a, a = 1 - 15) used in the numerical simulations were the same as in Table 1. Whenever possible, values of rate constant of reaction steps related to the initial model (not in bold in Table 1) were the same as in our previous papers (57, 58). Values of the rate constants of reaction steps (R2.2), (R4), (R5.2), (R5.3) and (R12), associated with AVP effects were derived from (39, 54, 59, 60) unless otherwise specified.

Bifurcation analysis

To determine boundaries of oscillatory domain as a function of reaction rate constants of the reactions associated with CRH (R2.1) and AVP inflows (R2.2) (Table 1), the bifurcation analysis based on numerical continuation method was applied. Namely, during each numerical continuation, selected value of $k_{2.1}$ in the range between 1×10^{-9} and 2×10^{-8} mol dm^{-3} min^{-1} was kept constant while the value of $k_{2.2}$ was varied to find the region where ultradian oscillatory dynamics can be obtained. For each value of $k_{2.2}$ steady-state concentrations were evaluated together with stability of considered steady state. All other rate constants had values as indicated in Table 1. By this method of bifurcation analysis (Method 1a, Supplementary material), the boundaries of the oscillatory domain were obtained as a function of $k_{2.1}$ and $k_{2.2}$ for one fixed $k_{5.3}$ value given in Table 1. Afterwards, the impact of CRH and AVP acting synergistically on HPA oscillatory dynamics (R5.3) (Table 1) was investigated by another method of bifurcation analysis (Method 1b, Supplementary material). This was achieved by applying numerical continuation with reaction rate constant $k_{5.3}$ as continuation parameter, for couple of $k_{2.1}$ and $k_{2.2}$ values that are selected to be very close to boundaries of oscillatory domain identified by Method 1a. By this method, for each $k_{5.3}$ value the steady-state concentrations were evaluated together with stability of the considered steady-state. Once more, all other rate constants had values as indicated in Table 1 unless otherwise specified.

The ultradian dynamics of HPA system for various combinations of $k_{2.1}$ and $k_{2.2}$ values, including the ones around oscillatory domain boundaries, was also examined by bifurcation analysis based on numerical simulations of dynamic states obtained by the above defined differential equations (1) - (6) (Method 2, Supplementary material). Namely, for a given couple of $k_{2.1}$ and $k_{2.2}$ values, set of numerical simulations were performed as a function of various values of rate constant $k_{5.3}$. By this method, bifurcation diagrams with $k_{5.3}$ as the control parameter were formed. The stable steady state of the system was denoted by one point in the [CORT] - $k_{5.3}$ bifurcation diagram whereas the oscillatory state was denoted by two points corresponding to [CORT] values in oscillation minimum and maximum. In the latter case, the steady state is unstable, and hence, unattainable to numerical simulations. These bifurcation diagrams were obtained by varying $k_{5.3}$ values in the range between 1.098×10^3 and 1.098×10^{20} mol^{-1} dm^3 min^{-1}. If values of $k_{5.3} < 1.098 \times 10^3$ mol^{-1} dm^3 min^{-1} or values of $k_{5.3} > 1.098 \times$

10^{20} mol^{-1} dm^3 min^{-1} were applied, no significant dynamic changes were observed. Furthermore, by the same method, the diagrams of amplitudes of [CORT] oscillations as a function of $k_{5.3}$ were also analyzed. All other rate constants had values as indicated in Table 1 unless otherwise specified.

Results

Using the above explained methods, the oscillatory dynamics as an essential characteristic of the HPA axis is particularly examined. Therefore, selection of the conditions that lead to its emergence is of great importance for model optimization. Since the goal of our investigations was to examine how AVP alone and in synergy with CRH can modify ultradian dynamics of HPA axis, the starting point in our analysis was to determine the dependence of boundaries of the oscillatory domain on the inflows of CRH and AVP from the parvocellular neuronal populations of PVN. These inflows represented by reactions (R2.1) and (R2.2) in Table 1, are initial steps of two parallel reaction pathways guided by signaling through CRH and AVP, respectively. They are interconnected through a complex feedback loops and capable to compensate each other. Therefore, the bifurcation analysis could provide new insights into how various levels of these two hormones' concentrations originating from the same inflow source affect ultradian dynamics of HPA model. This was achieved, here, by utilizing Method 1a of bifurcation analysis for $k_{5.3}$ = 3.66 × 10^2 mol^{-1} dm^3 min^{-1} (Table 1). Results in Figure 1 show that oscillatory domain is confined between two straight lines which represent dependence of supercritical Andronov-Hopf (AH) bifurcation on $k_{2.1}$ and $k_{2.2}$. It could also be noticed that a small decrease in the value of $k_{2.1}$ requires a much larger (circa by an order of magnitude) increase in the values of $k_{2.2}$ in order to keep HPA model in the oscillatory regime. This suggests the inferiority of AVP compared to CRH as stimulator of ACTH secretion. However, if with increasing $k_{2.2}$ at the same time $k_{2.1}$ decreases so that the system approaches the left end of the oscillatory domain intersecting the y-axis in Figure 1, the values of $k_{2.2}$ might become large enough to retain the system in oscillatory dynamic states, even though the value of $k_{2.1} \rightarrow 0$ and so does its impact. Also, in this part of Figure 1, the value of k_4, which was kept constant in this analysis (Table 1), has weak to no-significant influence compared to $k_{2.2}$. In other words, in the vicinity of y-axis, the AVP reaction pathway governed by reaction (R2.2) (Table 1) tends to predominate over the CRH reaction pathway. On the other hand, with decrease of $k_{2.2}$ and increase of $k_{2.1}$ towards the right end of the oscillatory domain intersecting the x-axis, the impact of $k_{2.2}$ may become

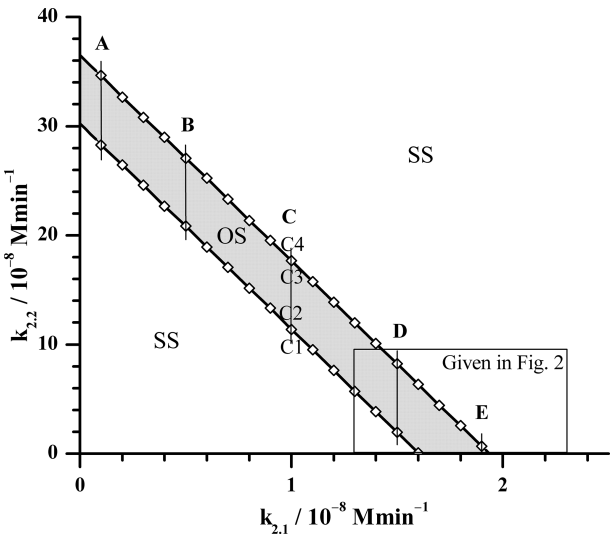

FIGURE 1
Position of supercritical AH bifurcation as a function of rate constants $k_{2.1}$ and $k_{2.2}$, obtained by Method 1a of bifurcation analysis for $k_{5.3}$ = 3.66 × 10^2 mol^{-1} dm^3 min^{-1} (the value given in Table 1). The calculated AH bifurcations, depicted by open rhombuses (◊) are interconnected by solid lines for better visualization of the oscillatory domain. OS - oscillatory domain; SS - stable steady states. Five fixed $k_{2.1}$ values denoted as cases: A ($k_{2.1}$ = 0.1 × 10^{-8} mol dm^{-3} min^{-1}), B ($k_{2.1}$ = 0.5 × 10^{-8} mol dm^{-3} min^{-1}), C ($k_{2.1}$ = 1.0 × 10^{-8} mol dm^{-3} min^{-1}), D ($k_{2.1}$ = 1.5 × 10^{-8} mol dm^{-3} min^{-1}) and E ($k_{2.1}$ = 1.9 × 10^{-8} mol dm^{-3} min^{-1}) for which Method 1b was applied near bifurcation points. In the case C, Method 1b was applied in points where values of rate constant $k_{2.2}$ are: C1 ($k_{2.2}$ = 11.2 × 10^{-8} mol dm^{-3} min^{-1}), C2 ($k_{2.2}$ = 11.4 × 10^{-8} mol dm^{-3} min^{-1}), C3 ($k_{2.2}$ = 17.6 × 10^{-8} mol dm^{-3} min^{-1}) and C4 ($k_{2.2}$ = 18.6 × 10^{-8} mol dm^{-3} min^{-1}) (More details will be shown in Figure 3). All other rate constants used in both Method 1a and 1b analysis had values as presented in Table 1, except in Method 1b where $k_{5.3}$ was varied.

comparable with k_4 (1.537×10^{-9} mol dm^{-3} min^{-1}, Table 1) and with its further decreases, more and more inferior and finally non-significant. In this part of Figure 1, also given at the bottom of Figure 2, the influence of k_4 is generally the highest possible, but lower than the influence of $k_{2.1}$ though. In essence, in the vicinity of x-axis as $k_{2.2} \rightarrow 0$, CRH reaction pathway governed by reaction (R2.1) tends to prevail over the AVP reaction pathway, in contrast to the left end of oscillatory domain.

With aim to compare the behavior of the here extended model with the initial model behavior (54, 61), the additional bifurcation analysis was done in some specific parts of bifurcation diagram depicted in Figure 1. First, detailed analysis of dynamic states was performed within the rectangle area shown in the bottom right part of Figure 1. The obtained results are given in Figure 2; Tables 2, 3. Second, more general behavior of the extended model was analyzed for selected values of $k_{2.1}$, marked by vertical lines A, B, C, D and E in Figure 1. More precisely, for each given $k_{2.1}$ value two $k_{2.2}$ values very close to each AH point were examined. Corresponding results are summarized in Figure 3 for the case of C line (points C1 – C4), although similar behavior was detected for other values of $k_{2.1}$ (A, B, D and E in Figure 1). Moreover, for three selected points in Figure 2 (P, Q and R) yielding the particularly convenient forms of bifurcation diagrams, the two models of HPA axis activity (the initial and here extended ones) were compared to each other in order to further correlate the results of simulations obtained by Method 2 with experimental findings (39, 44–47). Results are given in Figure 4. Finally, the extended model predictive potential was additionally validated by *in silico* perturbation experiments with repetitive single-pulse changes in CRH and AVP concentrations both separately and conjointly. Appropriate results are presented in Figure 5.

Moreover, let us know that the initial model described in (54) can be considered as the limiting case of the here considered model when the values of $k_{2.2}$, k_4 and initial concentration of AVP are all zero. In addition, in that case the value of the CRH inflow rate constant $k_{2.1}$ in extended model ought to be the same as k_2 value in the initial model, i.e. 1.83×10^{-8} mol dm^{-3} min^{-1}. However, in order to get better insight in local behavior of the extended model, the value of $k_{2.1}$ was varied in the range ($1.3725 - 2.1960$) $\times 10^{-8}$ mol dm^{-3} min^{-1} and $k_{2.2}$ in the range ($0.0183 - 6.4050$) $\times 10^{-8}$ mol dm^{-3} min^{-1}. Besides, for selected values of $k_{2.1}$ and $k_{2.2}$, the bifurcation diagrams with synergy constant ($k_{5.3}$) as control parameter were analyzed using Method 2.

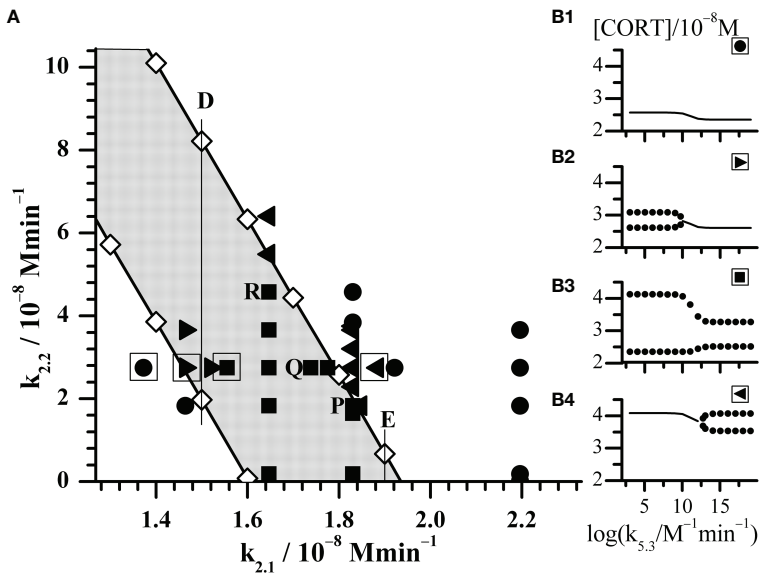

FIGURE 2
Enlarged part of the bifurcation diagram framed by rectangle in Figure 1. **(A)** Black symbols represent dynamic states identified by Method 2 with increasing $k_{5.3}$ as control parameter. Circles (●) depict points where only stable steady states were found; right triangles (►) depict points where transition from oscillatory states into stable steady states was observed; squares (■) depict points where only oscillatory states were observed; left triangles (◄) depict points where transition from stable steady states into oscillatory states was observed. **(B1–B4)** the outlooks of bifurcation diagrams depicted by corresponding black symbols in the square-bordered examples. The selected points P, Q and R will be discussed in Figure 4.

TABLE 2 Oscillation amplitudes of cortisol (Ampl.) in 10^{-8} mol dm^{-3} for two fixed values of $k_{2.2}$ and varied values of $k_{2.1}$.

$k_{2.1}$(10^{-8} mol dm^{-3} min^{-1})	$k_{2.2}$ (10^{-8} mol dm^{-3} min^{-1})		
	0*	2.745	
	Ampl. for all $k_{5.3}$	Ampl. for low $k_{5.3}$	Ampl. for high $k_{5.3}$
1.3725	0	0	0
1.4640	0	0.2400	0
1.5189	0	0.7340	0
1.5555	0	0.8845	0.3765
1.6470	0.5695	1.0100	0.8965
1.7385	0.9590	0.7645	1.0100
1.7751	1.0070	0.4400	0.9725
1.8300	0.9810	0	0.7970
1.8849	0.8075	0	0.2665
1.9215	0.5370	0	0
2.1960	0	0	0

*If $k_4 = 0$, and $[AVP]_0 = 0$, it corresponds to the initial HPA axis activity model (54).
Values of $k_{5.3} < 10^8$ mol^{-1} dm^3 min^{-1} are considered as low $k_{5.3}$, while $k_{5.3} > 10^{13}$ mol^{-1} dm^3 min^{-1} as high $k_{5.3}$. A zero-amplitude value indicates the absence of oscillatory states, i.e. the presence of stable steady states in a denoted case.

Overall, positions of points with all types of dynamics identified by Method 2 are given in Figure 2A. Their actual nature qualitatively corresponds to one of the four forms of bifurcation diagrams presented in Figure 2 B1 – B4. Results in Figure 2 show that in points which lay far enough outside of the oscillatory domain (Figure 1), only stable steady states were obtained for all applied $k_{5.3}$ values (Figure 2, B1 and all such cases are designated by ●). In the case of points lying deep enough within the oscillatory domain in Figure 1, only oscillatory states exist for all applied $k_{5.3}$ (Figure 2, B3 and all

TABLE 3 Oscillation amplitudes of cortisol concentrations (Ampl.) in 10^{-8} mol dm^{-3} for two fixed values of $k_{2.1}$ and varied $k_{2.2}$.

$k_{2.2}$ (10^{-8} mol dm^{-3} min^{-1})	$k_{2.1}$ (10^{-8} mol dm^{-3} min^{-1})			
	1.83		1.00	
	Ampl. for low $k_{5.3}$	Ampl. for high $k_{5.3}$	Ampl. for low $k_{5.3}$	Ampl. for high $k_{5.3}$
0*	0.9810	0.9810	0	0
0.0183	0.9645	0.9810	0	0
0.1830	0.9440	0.9810	0	0
1.6470	0.4865	0.9810	0	0
1.7385	0.4205	0.9755	0	0
1.8300	0.3385	0.9660	0	0
2.2875	0	0.9010	0	0
2.7450	0	0.7970	0	0
3.2025	0	0.6350	0	0
3.6600	0	0.3385	0	0
3.7515	0	0.2230	0	0
3.8430	0	0	0	0
11.2000 (C1)	0	0	0	0
11.4000 (C2)	0	0	0.1550	0
17.6000 (C3)	0	0	0	0.7715
18.6000 (C4)	0	0	0	0
Higher	0	0	0	0

*If $k_4 = 0$ and $[AVP]_0 = 0$, it corresponds to the initial HPA axis activity model (54).
Values of $k_{5.3} < 10^8$ mol^{-1} dm^3 min^{-1} are considered as low $k_{5.3}$, while $k_{5.3} > 10^{13}$ mol^{-1} dm^3 min^{-1} as high $k_{5.3}$. A zero-amplitude value indicates the absence of oscillatory states, i.e. the presence of stable steady states in a denoted case.

10.3389/fendo.2022.976323

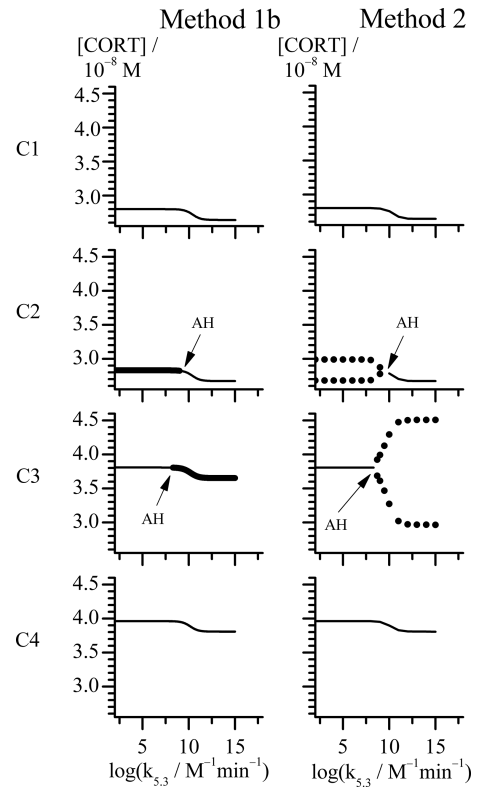

FIGURE 3
Bifurcation diagrams obtained with rate constant $k_{5.3}$ as control parameter by Methods 1b and 2 (see points C1-C4 in Figure 1). All points in case C share the same value of $k_{2.1} = 1 \times 10^{-8}$ mol dm^{-3} min^{-1}, while for each point: C1 ($k_{2.2} = 11.2 \times 10^{-8}$ mol dm^{-3} min^{-1}), C2 ($k_{2.2} = 11.4 \times 10^{-8}$ mol dm^{-3} min^{-1}), C3 ($k_{2.2} = 17.6 \times 10^{-8}$ mol dm^{-3} min^{-1}) and C4 ($k_{2.2} = 18.6 \times 10^{-8}$ mol dm^{-3} min^{-1}). Thin line represents stable steady state (Method 1b and 2). Unstable steady states are represented by thick line (Method 1b). Minimums and maximums in oscillations of cortisol concentrations are represented by circles (Method 2). All other rate constants used in analysis had values as presented in Table 1.

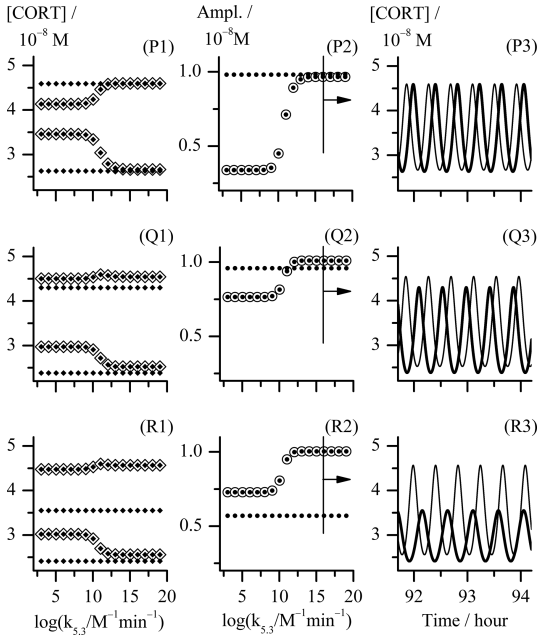

FIGURE 4
Analysis of three cases of combination of $k_{2.1}$ and $k_{2.2}$ reaction rate constants values corresponding to the points P, Q and R in Figure 2. Point P, $k_{2.1} = k_{2.2} = 1.830 \times 10^{-8}$ mol dm^{-3} min^{-1}; point Q, ($k_{2.1}$ and $k_{2.2}$) = (1.738 and 2.745) $\times 10^{-8}$ mol dm^{-3} min^{-1}, respectively; point R, ($k_{2.1}$ and $k_{2.2}$) = (1.647 and 4.575) $\times 10^{-8}$ mol dm^{-3} min^{-1}, respectively; (P1) - (R1) bifurcation diagrams and (P2) - (R2) diagrams of change of [CORT] oscillation amplitudes each obtained with $k_{5.3}$ as control parameter using Method 2; (P3) - (R3) temporal evolutions of [CORT] for $k_{5.3} = 1.098 \times 10^{16}$ mol^{-1} dm^3 min^{-1}, for the arbitrarily chosen time interval between around 92 and 94 hours. All results referring to the extended HPA model are depicted by ◈, ⊙ and thinner curves in diagrams (P1) - (R1), (P2) - (R2) and (P3) - (R3), respectively. All results referring to the initial HPA axis model (54) in diagrams (P1) - (R1), (P2) - (R2) and (P3) - (R3) are depicted by ♦, ● and thicker curves, respectively. In (P1) - (R1) bifurcation diagrams, [CORT] maximum and [CORT] minimum are denoted as pair of ◈ and pair of ♦ related to corresponding extended and initial HPA model, respectively. All other rate constants had values as given in Table 1.

such cases are designated by ■). It was observed that in this area, amplitude of oscillations depends on the value of $k_{5.3}$ and this dependence was subjected to additional analysis. On the other hand, in points found in vicinity of both lower and upper borders of oscillatory domain in Figure 1, transitions from oscillatory dynamics into stable steady states and vice versa, respectively, were induced by varying the value of $k_{5.3}$ (Figure 2, B2 and B4 and all such cases designated by ► and ◄, respectively).

A more detailed analysis of the influence of two inflow reaction constants $k_{2.1}$, $k_{2.2}$ and the synergy reaction constant $k_{5.3}$ on the global behavior of the extended HPA model was done by comparing dynamic states between the bifurcation diagrams obtained for several fixed values of each of the inflow rate constant. In the cases where oscillatory dynamic states were identified, amplitudes and their periods were of particular interest for mutual diagrams comparison. In the whole range of applied changes obtained by varying all three constants, the oscillation periods varied in very narrow range between 20 min and 30 min. This variation of periods is even lower within one bifurcation diagram where oscillatory states occurred; in these cases, periods were rather constant or nearly constant, although $k_{5.3}$ values were applied in extremely wide extent (from 1.098×10^3 to 1.098×10^{20} mol^{-1} dm^3 min^{-1}) (data not shown).

On the other hand, the amplitude changes were much more diverse and interesting. Selected results are presented in Tables 2, 3. Results in Table 2 show variations of dynamic states and amplitude values of cortisol oscillations if $k_{2.1}$ is varied for fixed $k_{2.2}$ value. Two typical cases of $k_{2.2}$ are given. In the first case $k_{2.2}$, k_4 and initial concentration of AVP are all equal to

10.3389/fendo.2022.976323

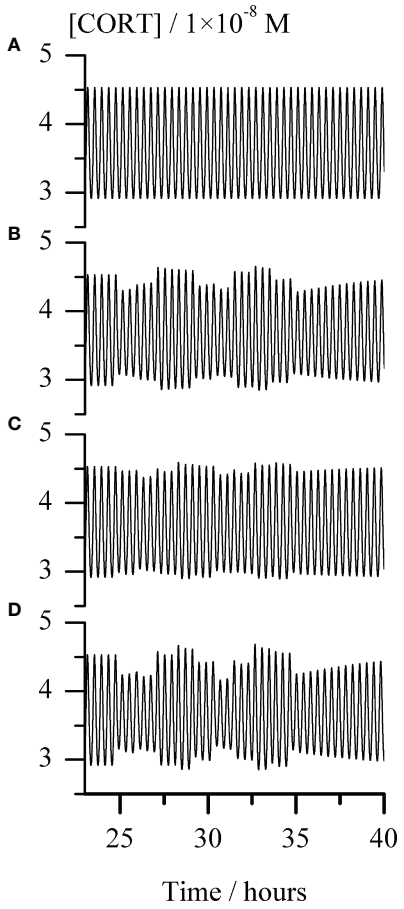

FIGURE 5
Temporal evolution of cortisol concentration ([CORT]) for repeating single-pulse perturbations with each stimulator of ACTH release alone and in combination, for the arbitrarily chosen time interval between around 23 and 40 hours. Graph **(A)** - the unperturbed extended model of HPA axis; Graphs **(B–D)** responses of the HPA axis to repeating pulse perturbations with: **(B)** CRH **(C)** AVP and **(D)** conjoint CRH and AVP. The perturbation intensities of each stimulator of ACTH secretion were the same in all corresponding cases, [CRH] = 2.5 × 10^{-9} M and AVP [AVP] = 50.0 × 10^{-9} M. In all Graphs **(B–D)**, the first pulse perturbations were applied in the maximum-to-minimum inflection point of a selected ultradian cortisol oscillation starting from the one at 1490th minute (circa 24.8 h) and repeated every 66 minutes, giving a total of 10 pulses perturbations. In all cases presented in Graphs **(A–D)**, rate constants ($k_{2.1}$ and $k_{2.2}$) = (1.647 and 4.575) × 10^{-8} mol dm^{-3} min^{-1} and $k_{5.3}$ = 1.098 × 10^{10} mol^{-1} dm^3 min^{-1}, while all other rate constants had values as given in Table 1.

zero. This corresponds to the initial model (54). Under these conditions, amplitudes do not depend on $k_{5.3}$ and hence only one value of amplitude is given for each $k_{2.1}$ value. In this case, for lower values of $k_{2.1}$ (such as for $k_{2.1} < 1.6470 \times 10^{-8}$ mol dm^{-3} min^{-1}) stable steady states were observed first. With $k_{2.1}$ increase, HPA system passes to another stable steady state transiting through oscillatory region confined between two supercritical AH bifurcation points. It was also observed that the amplitudes reach their maximum at a certain $k_{2.1}$ value within oscillatory region, which gradually decreases with approach to the AH points. In the second case, where $k_{2.2}$ is non-zero, for 2.745 × 10^{-8} mol dm^{-3} min^{-1} (Figure 2), the dynamics is much more complex since dynamic state depends strongly on values of both $k_{5.3}$ and $k_{2.1}$. Namely, for low values of $k_{2.1}$, only stable steady states were found as in the first case (Figure 2, ●). With slightly increased $k_{2.1}$ (such as for $k_{2.1}$ = 1.4640 × 10^{-8} mol dm^{-3} min^{-1} in Table 2 and Figure 2, ►) oscillatory dynamic states were found in region of low $k_{5.3}$ values but stable steady states in the region of high $k_{5.3}$ values. With further increase of $k_{2.1}$, only oscillatory dynamic states are present for all $k_{5.3}$ values. This refers to four values of $k_{2.1}$ in Table 2, which correspond to four adjacent points denoted by ■ in Figure 2. Moreover, the values of amplitude were found to be influenced by $k_{5.3}$. At modestly low values of $k_{2.1}$, oscillations

with higher amplitudes were observed in the region of low $k_{5.3}$ values, while smaller amplitudes were observed in the region of high $k_{5.3}$ values (Table 2, for $k_{2.1}$ = (1.5555 and 1.6470) × 10^{-8} mol dm^{-3} min^{-1}). On the other hand, if values of $k_{2.1}$ are modestly high (Table 2, for $k_{2.1}$ = (1.7385 and 1.7751) × 10^{-8} mol dm^{-3} min^{-1}), the $k_{5.3}$ influence is reversed so that amplitudes are then positively correlated to $k_{5.3}$. It could be noticed that in this middle $k_{2.1}$ range, for the values of $k_{2.1}$ such as (1.6470 or 1.7385) × 10^{-8} mol dm^{-3} min^{-1}, the amplitudes are higher than the ones corresponding to the same values of $k_{2.1}$ in the initial model (Table 2, $k_{2.2}$ = 0), for all applied $k_{5.3}$ values or for high $k_{5.3}$, respectively. Further increase in $k_{2.1}$, leads to the value of 1.83 × 10^{-8} mol dm^{-3} min^{-1} which corresponds exactly to k_2 value in initial model published in previous paper (54). In this case, stable steady states and oscillatory states were found for low and for high $k_{5.3}$ values, respectively (Figure 2, ◄). Finally, for the highest used values of $k_{2.1}$, such as (1.9215 and 2.1960) × 10^{-8} mol dm^{-3} min^{-1} in Table 2, only stable steady states were observed in the whole $k_{5.3}$ range. This corresponds to two adjacent points in Figure 2, depicted by ●.

The observed changes in cortisol oscillation amplitudes when $k_{5.3}$ is used as control parameter are localized in range of $k_{5.3}$ values lying roughly between 10^8 and 10^{13} mol^{-1} dm^3 min^{-1} (See, for example, cases B1 – B4 in Figure 2), although this rate constant was varied in wide interval of values between 1.098 × 10^3 and 1.098 × 10^{20} mol^{-1} dm^3 min^{-1}.

Relationships between dynamic states and amplitude values of cortisol oscillations when $k_{2.2}$ is varied for fixed $k_{2.1}$ value are shown in Table 3. Two typical cases of $k_{2.1}$ were considered in the extended model. For the first case, $k_{2.1}$ was chosen to be equal to 1.83 × 10^{-8} mol dm^{-3} min^{-1} so that the extended model could be appropriately compared with the initial model (54). The other case corresponding to $k_{2.1}$ = 1.00 × 10^{-8} mol dm^{-3} min^{-1} is more general, providing conditions for a complete set of dynamic states similar to the ones obtained in bifurcation diagrams B1 – B4 (Figure 2). This case also corresponds to line C in Figure 1 and is used as a representative example to explain the HPA system behavior near the bifurcation points (Figure 3).

Namely, the first case, where $k_{2.1}$ is equal to 1.83 × 10^{-8} mol dm^{-3} min^{-1}, shares the same rate constant value of the CRH inflow as the initial HPA model (54), for which the system is in the oscillatory state with amplitude of 0.981 × 10^{-8} mol dm^{-3} (as for $k_{2.2}$ = 0, k_4 = 0 and $[AVP]_0$ = 0 in Table 3 and point depicted by ■ laying on the x-axis itself in Figure 2). For very low value of $k_{2.2}$ such as 0.0183 × 10^{-8} mol dm^{-3} min^{-1}, there is a weak to non-existent influence of $k_{5.3}$. Oscillations are observed (Figure 2, ■) and almost unchanged in the whole range of $k_{5.3}$ values (Table 3). The contribution of AVP to system's dynamics (if any) would probably originate predominantly from the magnocellular inflow source, since k_4 has greater influence than $k_{2.2}$ in the vicinity of x-axis (where $k_{2.2} \rightarrow 0$). Yet, for the value of k_4 equal to 1.537 × 10^{-9} mol dm^{-3} min^{-1} (Table 1), k_4 is inferior to the impact of the rate constant of CRH inflow. Therefore, with $k_{5.3}$ increase, system exhibit behavior similar to the behavior of the initial model. However, by increasing $k_{2.2}$, the effect of $k_{5.3}$ becomes noticeable. First, increasing the value of $k_{2.2}$ leads to faster oscillation amplitudes decrease for low $k_{5.3}$ compared to the high $k_{5.3}$ values. With further $k_{2.2}$ increase, system transits through AH bifurcation point and oscillatory states are replaced by stable steady states for low $k_{5.3}$, while oscillations for high $k_{5.3}$ continue to decrease (Table 3 and Figure 2, five adjacent ◄). Finally, for sufficiently large $k_{2.2}$, oscillatory states completely disappear for high $k_{5.3}$ values. With any further $k_{2.2}$ increase, $k_{5.3}$ does not have any significant influence on HPA dynamics and only stable steady states could be observed for all $k_{5.3}$ values. This corresponds to two adjacent points denoted by ● in Figure 2.

In the other case, where $k_{2.1}$ is equal to 1.00 × 10^{-8} mol dm^{-3} min^{-1}, the HPA system is in stable steady states for the lowest $k_{2.2}$ values, unlike in the first case. By increasing the $k_{2.2}$, the system passes through the oscillatory domain *via* two AH bifurcations and finally enters to other stable steady states for higher $k_{2.2}$ values (Figure 1). This value of $k_{2.1}$ belongs to the points C1 - C4 region in Figure 1. The global behavior of the system in the vicinity of these two AH bifurcations was examined in these four points on line C which are listed in Table 3. Two of them (C1 and C2) are very close to the first (lower) AH bifurcation and the other two (C3 and C4) are very close to the second one (upper). Obviously, the points were chosen to cover both sides of bifurcation points. Namely, for the lowest $k_{2.2}$ value (11.20 × 10^{-8} mol dm^{-3} min^{-1}), corresponding to the point found below the first (lower) AH bifurcation (Figure 1, C1), only stable steady states were detected for all $k_{5.3}$ values. For the nearby value of the $k_{2.2}$ which is on the opposite side of this AH bifurcation (Figure 1, C2), oscillations were detected for low $k_{5.3}$ values, but only stable steady states for high $k_{5.3}$ values. On the other hand, by increasing the $k_{2.2}$ to the value slightly below the second (upper) AH bifurcation (Figure 1, C3), dynamic states were inversed so that oscillatory states were then observed only for high $k_{5.3}$ values, while for low $k_{5.3}$ values, only stable steady states were present. For the nearby value of $k_{2.2}$ (18.60 × 10^{-8} mol dm^{-3} min^{-1}) which is a bit above this AH bifurcation (Figure 1, C4), stable steady states were detected in the whole range of applied $k_{5.3}$ values. Described four bifurcation diagrams for points C1-C4 obtained by Method 1b and Method 2 are shown in Figure 3.

Both Method 1b and Method 2, provide mutually consistent results in a sense that oscillations are obtained when steady state is unstable and oscillations are absent if steady state is stable. From Figure 3, it may be noticed that change of cortisol concentrations during the transition from one steady state to another in points C1 and C4, is localized within relatively narrow and middle interval of $k_{5.3}$ values close to the positions of the AH bifurcation points observed in points C2 and C3. At the same time, in vicinity of AH bifurcation points, cortisol steady-state concentrations are gradually changed. The above

described behavior presented in Figure 3 can also be found in bifurcation diagrams B1 – B4 presented in Figure 2 with the similar $k_{5.3}$ interval. Additionally, change of amplitude of cortisol oscillations in bifurcation diagram B3 in Figure 2 is confined within the same range of $k_{5.3}$ values. Out of this range, for $k_{5.3} < 10^8$ mol^{-1} dm^3 min^{-1} and $k_{5.3} > 10^{13}$ mol^{-1} dm^3 min^{-1}, that correspond to low and high $k_{5.3}$ values, respectively, dynamic states are almost independent on $k_{5.3}$. Described global behavior of the system is the result of investigations in points on line C very close to the boundaries of the oscillatory domain obtained by Method 1a for $k_{5.3} = 3.66 \times 10^2$ mol^{-1} dm^3 min^{-1} (Table 1). If oscillatory domain is obtained for different $k_{5.3}$ value, some of these points, if not all, (including the ones on A, B, D and E lines) may be positioned differently relative to the new borders of oscillatory domain. This could provide an additional insight into the interpretation of corresponding bifurcation diagrams in Figures 3, 2.

In order to further correlate obtained results with experimental findings in the literature, the examinations of mutual combinations of $k_{2.1}$ and $k_{2.2}$ values for which system transits into oscillatory states of higher amplitudes with increase of control parameter ($k_{5.3}$) were of particular interest. Three types of distinct changes were found by comparing how amplitude of oscillations increases with control parameter in the initial and extended model when their CRH inflow is the same. They will be discussed in more details using the examples of points P, Q and R in Figure 2: point P ($k_{2.1} = k_{2.2} = 1.830 \times 10^{-8}$ mol dm^{-3} min^{-1}), point Q ($k_{2.1} = 1.738 \times 10^{-8}$ mol dm^{-3} min^{-1}, $k_{2.2} = 2.745 \times 10^{-8}$ mol dm^{-3} min^{-1}) and point R ($k_{2.1} = 1.647 \times 10^{-8}$ mol dm^{-3} min^{-1}, $k_{2.2} = 4.575 \times 10^{-8}$ mol dm^{-3} min^{-1}). In Figure 4, the bifurcation diagrams ((P1) - (R1), ◈), and diagrams of variation of [CORT] oscillation amplitudes ((P2) - (R2), ⊙) in all three points, together with the samples of temporal evolutions of [CORT] for $k_{5.3} = 1.098 \times 10^{16}$ mol^{-1} dm^3 min^{-1} ((P3) - (R3), thinner curves) in an arbitrarily selected time interval are presented. Results referring to the initial model (54) for the same values of the rate constant of CRH inflow as in cases P, Q and R, are incorporated into corresponding diagrams in Figure 4 and depicted by symbols ⬥, ● and thicker curves. Namely, the increase of [CORT] amplitudes with $k_{5.3}$ increase can be clearly seen in all three cases P, Q and R in diagrams (P1) - (R1) (◈) and (P2) - (R2) (⊙). However, it could be noticed that in the case P, oscillation amplitudes of [CORT] in extended model are lower than the ones in the initial model in the whole range of applied $k_{5.3}$ [Figure 4, (P2)]. Inversely, in the case R, oscillation amplitudes of [CORT] are higher in the extended model than the one in initial model for all applied $k_{5.3}$ [Figure 4, (R2)] and could be about 1.3- to 2-fold greater. On the other hand, for a certain combination of $k_{2.1}$ and $k_{2.2}$ values, [CORT] amplitudes in extended model could exceed the one corresponding to the initial model, but only for high $k_{5.3}$ values, as indicated in the case Q [Figure 4, (Q2)]. The described [CORT] amplitude differences between two models in all three cases could also be directly observed in Figure 4, (P3) – (R3) for $k_{5.3} = 1.098 \times 10^{16}$ mol^{-1} dm^3 min^{-1}. Due to the indications of conditions in the extended model under which amplitude of [CORT] ultradian oscillations may increase due to synergistic effect of CRH and AVP on stimulating ACTH secretion by corticotrope cells, the extended model for point R was subjected to further analysis.

Hence, *in silico* perturbation experiments were performed to additionally assess the predictive potential of the extended model in the conditions corresponding to point R (Figure 2) and $k_{5.3} = 1.098 \times 10^{10}$ mol^{-1} dm^3 min^{-1} (a value around the middle in Figure 4, (R1) and (R2)). The perturbations were induced by repeating single-pulse changes in CRH and AVP concentrations applied both separately and conjointly, and which were consistent in intensity and time of application. Results are presented in Figure 5 and show the apparent influence of acute changes in CRH or/and AVP levels on global ultradian dynamics of the HPA axis model.

As expected, separate perturbations with CRH and AVP elicited a quantitatively similar response of the HPA axis extended model, only if applied concentration (perturbation intensity) of AVP was order of magnitude higher compared to CRH (Figures 5B, C). Also, a synergistic effect is observed in the changes of the cortisol oscillation amplitudes in response to their concurrent perturbations (Figure 5D). The pattern of the system response to this perturbation is qualitatively similar to the one induced by perturbations with CRH solely. Moreover, as expected from our previous experience (54, 62), perturbations caused a highly variable response depending on the phase angle of the selected ultradian oscillation at which the first perturbation was applied. Therefore, even uniform periodic perturbations with small intensities induced strongly irregular (stochastic) appearances of [ACTH] (not shown) and [CORT] oscillations.

Discussions

According to presented results, various ultradian oscillatory dynamics can be achieved, depending on the individual values of CRH and AVP inflows, as well as the rate constant of their synergistic reaction. For a particular combination of the values of inflows rate constants used in this study, there are values of synergy rate constant $k_{5.3}$ that could influence the HPA system to enter into the oscillatory dynamic states from stable steady state and vice versa. It has been found that transitions between these dynamic states were always through supercritical AH bifurcation point.

Due to the features of the supercritical AH bifurcation, some of the well-documented properties of the HPA axis activity could be more plausibly reproduced. For instance, elasticity of HPA axis in adjusting its dynamics in order to maintain homeostasis under the action of stressful stimuli can be simulated by reversible transitions between stable steady and oscillatory

dynamic states in the vicinity of supercritical AH bifurcation. These dynamic transitions are characterized by gradual decrease in ultradian oscillation amplitudes as the system approaches supercritical AH bifurcation, causing the system to exhibit growing response to the same perturbation intensity.

It should be pointed out that above described qualitative dynamic transitions in HPA axis activity under the influence of synergy rate constant are related to the system's global behavior in points close to the boundaries of the oscillatory domain obtained by Method 1a for the value of $k_{5.3}$ in Table 1 (Figure 1). For oscillatory domain obtained for different $k_{5.3}$ value, some of these points, if not all, may be positioned differently relative to the new borders of oscillatory domain. This could provide rather additional insight into the interpretation of their bifurcation diagrams in Figure 3, but in Figure 2 as well.

On the other hand, for examined points lying deep enough within the oscillatory domain, much more diverse quantitative changes in HPA activity were identified in corresponding bifurcation diagrams. Comparison of the results of bifurcation analyses for points in which amplitude of cortisol oscillations increases with $k_{5.3}$ in the initial and extended model for the same CRH inflow constant, revealed that extended model is capable to provide potential conditions under which ultradian amplitudes of cortisol concentrations could increase several-fold due to CRH and AVP synergistic action on corticotrope cells. This is in agreement with experimental observations in studies conducted on humans during stress (39, 44–47).

The potential of the extended model under selected conditions to anticipate a synergistic effect in the HPA axis ultradian dynamics response was verified in *in silico* experiments with perturbations induced by repeating single-pulse changes in CRH and AVP concentrations applied both separately and simultaneously (Figure 5). The observed qualitative similarity between response patterns of the HPA axis to perturbation with CRH solely and conjointly with AVP (Figures 5B, D) can be also found between the results of experiments in humans with 10-hour infusions of CRH and of both peptides simultaneously (39). Although cortisol oscillations obtained by the proposed model are extremely regular (both in period and amplitude) (Figure 5A), the ones obtained after series of single-pulse perturbations that were regular in intensity and time of application, are irregular (chaotic) (Figures 5B–D). They actually more resemble experimentally measured cortisol level fluctuations frequently encountered in literature (4, 8, 9, 18, 21–23, 38, 55, 63–65), while cortisol oscillations obtained by the extended model under conditions that may be regarded as ideal for the HPA axis (i.e. without any perturbation over the time whatsoever). Moreover, the sensitivity of an oscillatory dynamics depends strongly on the phase angle of the selected ultradian oscillation at which the first perturbation was applied and thus cortisol oscillations amplitude may decrease, increase or remain unaltered. Nevertheless, further *in silico* examinations of the proposed extended model under these and similar conditions are required to fully address stress-related effects of AVP and CRH on HPA ultradian dynamics reported in the literature.

Furthermore, the extended model simulated the experimentally observed inferiority of AVP as an ACTH secretion stimulator compared to CRH in humans. Namely, both in human (39, 43–47, 55) and in rat (26, 36–38, 40, 41), CRH reaction pathway is considered to be dominant in pituitary-adrenal regulation. There are results in several studies *in vitro* in rat anterior pituitary cells and *in vivo* in rats, indicating the necessity for much higher concentrations of exogenously administered AVP in order to induce similar effects on ACTH secretion as certain injected CRH concentrations (37, 38, 40, 41). In line with above mentioned experimental findings, results in Figure 1 show that a much larger (circa by an order of magnitude) increase in the values of parvocellular AVP inflow source ($k_{2.2}$) is required to retain HPA model in the oscillatory regime after a small decrease in the value of parvocellular CRH inflow source ($k_{2.1}$). Additionally, an order of magnitude higher AVP perturbation intensity (AVP concentration) was needed to induce quantitatively similar response of HPA axis model to the one elicited by perturbation with CRH solely (Figures 5B, C). Moreover, the extended model predicted the CRH reaction pathway to almost completely prevail over the AVP reaction pathway under certain condition (Figures 1, 2). However, for some other conditions given in Figure 1, the extended model also predicted the feasibility of AVP reaction pathway governed by parvocellular AVP inflow source to take over the CRH supremacy (Figure 1). In similar conditions, the possibility for the HPA axis to exhibit oscillatory dynamics for negligible amounts of CRH was shown as well.

Additionally, during stress, particularly chronic stress and after adrenalectomy, the number of parvocellular CRH neurosecretory cells that co-produce AVP was found to increase considerably as do the amounts of synthesized AVP compared to CRH *per* cell (66, 67). Very good agreement with these experimental findings was obtained in simulations using the extended model proposed here, where by increasing the $k_{2.2}$ value much more than the value of $k_{2.1}$, higher AVP to CRH concentration ratios could be yielded (Figure 1).

At the same time, during all the analyses conducted in this study, oscillating nature of dynamic state, and even frequency of cortisol ultradian oscillations has been found relatively sustained under all investigated conditions. This is in line with experimental findings indicating preserved endogenous HPA pulsing system in humans under various conditions (6, 9, 39).

Although, the HPA axis activity model proposed here is capable to provide good results, it however also inherited several limitations. The most notable limitation stems from the conciseness of the model where many complex processes were represented by summarized and simplified reaction steps (R1) - (R15) in Table 1. Thereby, since the peptide precursors of ACTH and other steroid hormones were not included in the initial

model, nor in the current extended model, concentration of ACTH was several orders beyond its reference range values. This discrepancy may be corrected by further model augmentation with introduction of lacking reaction species and their relations, in a similar way as it was done with preceding models (54, 68, 69, for instance) that were developed from our core model (58). The same "strategy" would be applied if a certain process or the influence of a certain bioactive substance ought to be examined in more details in regard to its role in HPA axis activity, such as: cAMP/PKA, PLC/IP(3), DAG/PKC signal transduction pathways, gene transcription and translation, epinephrine (adrenalin), angiotensin II, etc. On the other hand, the low-dimensional models can be more easily manipulated mathematically with aim to define desirable dynamic states, before being extended for different applications. This is usually not the case with more detailed non-stoichiometric models.

Based on the results presented in this study, stoichiometric modeling approach, bifurcation analyses and numerical simulations have proven to be very helpful in comprehending the complex involvement of AVP in HPA axis ultradian dynamics. The proposed model provides a good basis for further investigation of conditions in which the particularly amplified effect of CRH on corticotrope cells by magnocellular AVP can be of vital importance. These conditions are associated with life-threatening circumstances such as the risk of hyponatremia due to severe hypovolemia that can occur during arduous physical work or those requiring long-term sustained rise of adrenal corticosteroids due to their known immunosuppressant and anti-inflammatory effects. Furthermore, since it is known that "AVP regulates ACTH release under certain conditions, and exogenously administered AVP is used clinically to stimulate ACTH secretion" (70) as well as that considered process is very complex for experimental investigations, the proposed model with related numerical simulations can be obviously useful for determining the appropriate drug dose for therapeutic purposes.

Conclusions

The proposed extended HPA model is positively correlated with several experimental findings in the literature and offers the potential to proceed *in silico* investigations of the influence of AVP and its synergistic action with CRH on the HPA axis dynamics. Expanding the pre-existing initial HPA model with AVP contributes to the enhancement of the model's comprehensiveness and biological plausibility, while still being sufficiently tractable to mathematical analysis and numerical simulation, despite the increased number of dynamic variables. Moreover, the presented model provides a good basis for its further development and adjustments to align with experimental finding under physiologically normal as well as various stressful conditions. Further refinement of the present model seems to be necessary if hormone levels should be quantitatively compared with experimental measurements and if apparently stochastic form of oscillations would be the aim of some future study.

Data availability statement

The original contributions presented in the study are included in the article/Supplementary Material. Further inquiries can be directed to the corresponding authors.

Author contributions

ASS contributed to conception of the study, extended model development and adjustments, conducting the analysis, results processing and interpretation, manuscript writing. ŽČ wrote the first manuscript draft, contributed to extended model development and adjustments, study design, organizing the results and interpretation. SM contributed to conducting the analysis and results processing. AI-Š also contributed to conducting the analysis, the results processing and interpretation. LjK-A contributed to study design, extended model development and adjustments, to results organization and interpretation. All authors listed have made a substantial, direct and intellectual contribution to the work, manuscript revision and approved submitted version.

Funding

We are thankful for the financial support from the Ministry of Sciences and Technology of Republic of Serbia (Grant Numbers 172015 and 45001, and Contract numbers: 451-03-68/2022-14/200026, 451-03-68/2022-14/200146 and 451-03-68/2022-14/200051. This research was also supported by Science Fund of Republic of Serbia #Grant Number. 7743504, *Physicochemical aspects of rhythmicity in NeuroEndocrine Systems: Dynamic and kinetic investigations of underlying reaction networks and their main compounds*, NES.

Acknowledgments

We are grateful to Dr. Ana Stanojević, a formerly employee of the Faculty of Physical Chemistry, University of Belgrade, who was working with us at the beginning of these investigations.

Conflict of interest

The authors declare that the research was conducted in the absence of any commercial or financial relationships that could be construed as a potential conflict of interest.

Publisher's note

All claims expressed in this article are solely those of the authors and do not necessarily represent those of their affiliated organizations, or those of the publisher, the editors and the reviewers. Any product that may be evaluated in this article, or claim that may be made by its manufacturer, is not guaranteed or endorsed by the publisher.

Supplementary material

The Supplementary Material for this article can be found online at: https://www.frontiersin.org/articles/10.3389/fendo.2022.976323/full#supplementary-material

References

1. Tsigos C, Chrousos GP. Hypothalamic–pituitary–adrenal axis, neuroendocrine factors and stress. *J Psychosom Res* (2002) 53(4):865–71. doi: 10.1016/s0022–3999(02)00429–4

2. Miller WL, Chrousos GP. "The adrenal cortex ". In: Felig P, Frohman L, editors. *endocrinology and metabolism*. New York, NY: McGraw–Hill (2001). p. 387–524.

3. Lightman SL, Windle RJ, Ma XM, Harbuz MS, Shanks NM, Julian MD, et al. Hypothalamic–pituitary–adrenal function. *Arch Physiol Biochem* (2002) 110(1–2):90–3. doi: 10.1076/apab.110.1.90.899

4. Hartmann A, Veldhuis JD, Deuschle M, Standhardt H, Heuser I. Twenty–four hour cortisol release profiles in patients with alzheimer's and parkinson's disease compared to normal controls: ultradian secretory pulsatility and diurnal variation. *Neurobiol Aging* (1997) 18(3):285–9. doi: 10.1016/s0197–4580(97)80309–0

5. Gavrila A, Peng CK, Chan JL, Mietus JE, Goldberger AL, Mantzoros CS. Diurnal and ultradian dynamics of serum adiponectin in healthy men: comparison with leptin, circulating soluble leptin receptor, and cortisol patterns. *J Clin Endocrinol Metab* (2003) 88(6):2838–43. doi: 10.1210/jc.2002–021721

6. Veldhuis JD, Iranmanesh A, Johnson ML, Lizarralde G. Amplitude, but not frequency, modulation of adrenocorticotropin secretory bursts gives rise to the nyctohemeral rhythm of the corticotropic axis in man. *J Clin Endocrinol Metab* (1990) 71(2):452–63. doi: 10.1210/jcem–71–2–452

7. Charloux A, Gronfier C, Lonsdorfer–Wolf E, Piquard F, Brandenberger G. Aldosterone release during the sleep–wake cycle in humans. *Am J Physiol* (1999) 276(1):e43–9. doi: 10.1152/ajpendo.1999.276.1.E43

8. Engler D, Pham T, Fullerton MJ, Ooi G, Funder JW, Clarke IJ. Studies of the secretion of corticotropin–releasing factor and arginine vasopressin into the hypophysial–portal circulation of the conscious sheep. i. effect of an audiovisual stimulus and insulin–induced hypoglycemia. *Neuroendocrinology* (1989) 49(4):367–81. doi: 10.1159/000125141

9. Calogero AE, Norton JA, Sheppard BC, Listwak SJ, Cromack DT, Wall R, et al. Pulsatile activation of the hypothalamic–pituitary–adrenal axis during major surgery. *Metabolism* (1992) 41(8):839–45. doi: 10.1016/0026–0495(92)90164–6

10. Vanitallie TB. Stress: a risk factor for serious illness. *Metabolism* (2002) 51(6 Suppl 1):40–5. doi: 10.1053/meta.2002.33191

11. Frohman LA, Downs TR, Clarke IJ, Thomas GB. Measurement of growth hormone–releasing hormone and somatostatin in hypothalamic–portal plasma of unanesthetized sheep. spontaneous secretion and response to insulin–induced hypoglycemia. *J Clin Invest* (1990) 86(1):17–24. doi: 10.1172/JCI114681

12. Chihara K, Arimura A, Schally AV. Immunoreactive somatostatin in rat hypophyseal portal blood: effects of anesthetics. *Endocrinology* (1979) 104(5):1434–41. doi: 10.1210/endo–104–5–1434

13. Stafford PJ, Kopelman PG, Davidson K, McLoughlin L, White A, Rees LH, et al. The pituitary–adrenal response to CRF–41 is unaltered by intravenous somatostatin in normal subjects. *Clin Endocrinol (Oxf)* (1989) 30(6):661–6. doi: 10.1111/j.1365–2265.1989.tb00272.x

14. Petraglia F, Facchinetti F, D'Ambrogio G, Volpe A, Genazzani AR. Somatostatin and oxytocin infusion inhibits the rise of plasma beta–endorphin, beta–lipotrophin and cortisol induced by insulin hypoglycemia. *Clin Endocrinol (Oxf)* (1986) 24(6):609–16. doi: 10.1111/j.1365–2265.1986.tb01656.x

15. Kiss JZ. Dynamism of chemoarchitecture in the hypothalamic paraventricular nucleus. *Brain Res Bull* (1988) 20(6):699–708. doi: 10.1016/0361–9230(88)90080–9

16. Swanson LW, Sawchenko PE, Lind RW, Rho JH. The CRH motoneuron: differential peptide regulation in neurons with possible synaptic, paracrine, and endocrine outputs. *Ann N Y Acad Sci* (1987) 512(1):12–23. doi: 10.1111/j.1749–6632.1987.tb24948.x

17. Swanson LW, Simmons DM. Differential steroid hormone and neural influences on peptide mRNA levels in CRH cells of the paraventricular nucleus: a hybridization histochemical study in the rat. *J Comp Neurol* (1989) 285(4):413–35. doi: 10.1002/cne.902850402

18. Caraty A, Grino M, Locatelli A, Oliver C. Secretion of corticotrophin releasing factor (CRF) and vasopressin (AVP) into the hypophysial portal blood of conscious, unrestrained rams. *Biochem Biophys Res Commun* (1988) 155(2):841–9. doi: 10.1016/s0006–291x(88)80572–2

19. Plotsky PM, Bruhn TO, Vale W. Evidence for multifactor regulation of the adrenocorticotropin secretory response to hemodynamic stimuli. *Endocrinology* (1985) 116(2):633–9. doi: 10.1210/endo–116–2–633

20. Plotsky PM, Bruhn TO, Vale W. Central modulation of immunoreactive corticotropin–releasing factor secretion by arginine vasopressin. *Endocrinology* (1984) 115(4):1639–41. doi: 10.1210/endo–115–4–1639

21. Redekopp C, Irvine CH, Donald RA, Livesey JH, Sadler W, Nicholls MG, et al. Spontaneous and stimulated adrenocorticotropin and vasopressin pulsatile secretion in the pituitary venous effluent of the horse. *Endocrinology* (1986) 118(4):1410–6. doi: 10.1210/endo–118–4–1410

22. Livesey JH, Donald RA, Irvine CH, Redekopp C, Alexander SL. The effects of cortisol, vasopressin (AVP), and corticotropin–releasing factor administration on pulsatile adrenocorticotropin, alpha–melanocyte–stimulating hormone, and AVP secretion in the pituitary venous effluent of the horse. *Endocrinology* (1988) 123(2):713–20. doi: 10.1210/endo–123–2–713

23. Liu J–P, Clarke IJ, Funder JW, Engler D. Studies of the secretion of corticotropin–releasing factor and arginine vasopressin into the hypophysial–portal circulation of the conscious sheep. II. the central noradrenergic and neuropeptide y pathways cause immediate and prolonged hypothalamic–pituitary–adrenal activation. potential involvement in the pseudo–cushing's syndrome of endogenous depression and anorexia nervosa. *J Clin Invest* (1994) 93(4):1439–50. doi: 10.1172/JCI117121

24. Gudelsky GA, Porter JC. Release of newly synthesized dopamine into the hypophysial portal vasculature of the rat. *Endocrinology* (1979) 104(3):583–7. doi: 10.1210/endo–104–3–583

25. Ishibashi M, Yamaji T. Direct effects of thyrotropin–releasing hormone, cyproheptadine, and dopamine on adrenocorticotropin secretion from human corticotroph adenoma cells *in vitro*. *J Clin Invest* (1981) 68(4):1018–27. doi: 10.1172/jci110324

26. Vale W, Vaughan J, Smith M, Yamamoto G, Rivier J, Rivier C. Effects of synthetic ovine corticotropin–releasing factor, glucocorticoids, catecholamines, neurohypophysial peptides, and other substances on cultured corticotropic cells. *Endocrinology* (1983) 113(3):1121–31. doi: 10.1210/endo–113–3–1121

27. Lim AT, Sheward WJ, Copolov D, Windmill D, Fink G. Atrial natriuretic factor is released into hypophysial portal blood: direct evidence that atrial natriuretic factor may be a neurohormone involved in hypothalamic pituitary

control. *J Neuroendocrinol* (1990) 2(1):15–8. doi: 10.1111/j.1365–2826.1990.tb00386.x

28. Grammatopoulos DK, Chrousos GP. Functional characteristics of CRH receptors and potential clinical applications of CRH–receptor antagonists. *Trends Endocrinol Metab* (2002) 13(10):436–44. doi: 10.1016/s1043–2760(02)00670–7

29. De Souza EB, Perrin MH, Whitehouse PJ, Rivier J, Vale W, Kuhar MJ. Corticotropin–releasing factor receptors in human pituitary gland: autoradiographic localization. *Neuroendocrinology* (1985) 40(5):419–22. doi: 10.1159/000124107

30. Smith SM, Vale WW. The role of the hypothalamic–pituitary–adrenal axis in neuroendocrine responses to stress. *Dialogues Clin Neurosci* (2006) 8(4):383–95. doi: 10.31887/DCNS.2006.8.4/ssmith

31. Benarroch EE. Oxytocin and vasopressin: social neuropeptides with complex neuromodulatory functions. *Neurology* (2013) 80(16):1521–8. doi: 10.1212/WNL.0b013e31828cfb15

32. Volpi S, Rabadan–Diehl C, Aguilera G. Vasopressinergic regulation of the hypothalamic pituitary adrenal axis and stress adaptation. *Stress* (2004) 7(2):75–83. doi: 10.1080/10253890410001733535

33. van de Pavert SA, Clarke IJ, Rao A, Vrana KE, Schwartz J. Effects of vasopressin and elimination of corticotropin–releasing hormone–target cells on pro–opiomelanocortin mRNA levels and adrenocorticotropin secretion in ovine anterior pituitary cells. *J Endocrinol* (1997) 154(1):139–47. doi: 10.1677/joe.0.1540139

34. Liu J–P, Robinson PJ, Funder JW, Engler D. The biosynthesis and secretion of adrenocorticotropin by the ovine anterior pituitary is predominantly regulated by arginine vasopressin (AVP). evidence that protein kinase c mediates the action of AVP. *J Biol Chem* (1990) 265(24):14136–42. doi: 10.1016/s0021–9258(18)77278–5

35. Kemppainen RJ, Clark TP, Sartin JL, Zerbe CA. Hypothalamic peptide regulation of ACTH secretion from sheep pituitary. *Am J Physiol* (1993) 265(4 Pt 2):R840–845. doi: 10.1152/ajpregu.1993.265.4.R840

36. Gillies GE, Linton EA, Lowry PJ. Corticotropin releasing activity of the new CRF is potentiated several times by vasopressin. *Nature* (1982) 299(5881):355–7. doi: 10.1038/299355a0

37. Familari M, Smith AI, Smith R, Funder JW. Arginine vasopressin is a much more potent stimulus to ACTH release from ovine anterior pituitary cells than ovine corticotropin–releasing factor. i. *In vitro* studies. *Neuroendocrinology* (1989) 50(2):152–7. doi: 10.1159/000125214

38. Deng Q, Zhang Z, Wu Y. The pulsatility of ACTH secretion in the rat anterior pituitary cell perifusion system. *Cell Physiol Biochem* (2017) 41(1):154–62. doi: 10.1159/000455984

39. Roelfsema F, Aoun P, Takahashi PY, Erickson D, Yang R, Veldhuis JD. Regulation of pulsatile and entropic ACTH secretion under fixed exogenous secretagogue clamps. *J Clin Endocrinol Metab* (2017) 102(7):2611–9. doi: 10.1210/jc.2017–00115

40. Watanabe T, Orth DN. Detailed kinetic analysis of adrenocorticotropin secretion by dispersed rat anterior pituitary cells in a microperifusion system: effects of ovine corticotropin–releasing factor and arginine vasopressin. *Endocrinology* (1987) 121(3):1133–45. doi: 10.1210/endo–121–3–1133

41. Rivier C, Vale W. Interaction of corticotropin–releasing factor and arginine vasopressin on adrenocorticotropin secretion *in vivo*. *Endocrinology* (1983) 113(3):939–42. doi: 10.1210/endo–113–3–939

42. Schwartz J, Vale W. Dissociation of the adrenocorticotropin secretory responses to corticotropin–releasing factor (CRF) and vasopressin or oxytocin by using a specific cytotoxic analog of CRF. *Endocrinology* (1988) 122(4):1695–700. doi: 10.1210/endo–122–4–1695

43. Milsom SR, Conaglen JV, Donald RA, Espiner EA, Nicholls MG, Livesey JH. Augmentation of the response to CRF in man: relative contributions of endogenous angiotensin and vasopressin. *Clin Endocrinol (Oxf)* (1985) 22(5):623–9. doi: 10.1111/j.1365–2265.1985.tb02998.x

44. Salata RA, Jarrett DB, Verbalis JG, Robinson AG. Vasopressin stimulation of adrenocorticotropin hormone (ACTH) in humans. *In vivo* bioassay of corticotropin–releasing factor (CRF) which provides evidence for CRF mediation of the diurnal rhythm of ACTH. *J Clin Invest* (1988) 81(3):766–74. doi: 10.1172/JCI113382

45. DeBold CR, Sheldon WR, DeCherney GS, Jackson RV, Alexander AN, Vale W, et al. Arginine vasopressin potentiates adrenocorticotropin release induced by ovine corticotropin–releasing factor. *J Clin Invest* (1984) 73(2):533–8. doi: 10.1172/JCI111240

46. Liu JH, Muse K, Contreras P, Gibbs D, Vale W, Rivier J, et al. Augmentation of ACTH–releasing activity of synthetic corticotropin releasing factor (CRF) by vasopressin in women. *J Clin Endocrinol Metab* (1983) 57(5):1087–9. doi: 10.1210/jcem–57–5–1087

47. Lamberts SW, Verleun T, Oosterom R, de Jong F, Hackeng WH. Corticotropin–releasing factor (ovine) and vasopressin exert a synergistic effect on adrenocorticotropin release in man. *J Clin Endocrinol Metab* (1984) 58(2):298–303. doi: 10.1210/jcem–58–2–298

48. Antoni FA. Vasopressinergic control of pituitary adrenocorticotropin secretion comes of age. *Front Neuroendocrinol* (1993) 14(2):76–122. doi: 10.1006/frne.1993.1004

49. Aguilera G. Regulation of pituitary ACTH secretion during chronic stress. *Front Neuroendocrinol* (1994) 15(4):321–50. doi: 10.1006/frne.1994.1013

50. Chrousos GP. Editorial: Ultradian, circadian, and stress–related hypothalamic–pituitary–adrenal axis activity–a dynamic *digital–to–analog* Modulation. *Endocrinology* (1998) 139(2):437–40. doi: 10.1210/endo.139.2.5857

51. Antoni FA. Magnocellular vasopressin and the mechanism of "Glucocorticoid escape". *Front Endocrinol (Lausanne)* (2019) 10:422. doi: 10.3389/fendo.2019.00422

52. Keenan DM, Licinio J, Veldhuis JD. A feedback–controlled ensemble model of the stress–responsive hypothalamo–pituitary–adrenal axis. *Proc Natl Acad Sci U S A* (2001) 98(7):4028–33. doi: 10.1073/pnas.051624198

53. Keenan DM, Wang X, Pincus SM, Veldhuis JD. Modelling the nonlinear time dynamics of multidimensional hormonal systems. *J Time Ser Anal* (2012) 33(5):779–96. doi: 10.1111/j.1467–9892.2012.00795.x

54. Marković VM, Čupić Ž, Maćešić S, Stanojević A, Vukojević V, Kolar–Anić Lj. Modelling cholesterol effects on the dynamics of the hypothalamic–pituitary–adrenal (HPA) axis. *Math Med Biol* (2016) 33(1):1–28. doi: 10.1093/imammb/dqu020

55. Engler D, Redei E, Kola I. The corticotropin–release inhibitory factor hypothesis: a review of the evidence for the existence of inhibitory as well as stimulatory hypophysiotropic regulation of adrenocorticotropin secretion and biosynthesis. *Endocr Rev* (1999) 20(4):460–500. doi: 10.1210/edrv.20.4.0376

56. Gear CW. Numerical initial value problems in ordinary differential equations. *Englewood Cliffs NJ: Prentice–Hall Inc* (1971).

57. Marković VM, Čupić Ž, Ivanović A, Kolar–Anić Lj. The stability of the extended model of hypothalamic–pituitary–adrenal (HPA) axis examined by stoichiometric network analysis. *Russ J Phys Chem A* (2011) 85(13):2327–35. doi: 10.1134/S0036024411130115

58. Jelić S, Čupić Ž, Kolar–Anić Lj. Mathematical modeling of the hypothalamic–pituitary–adrenal system activity. *Math Biosci* (2005) 197(2):173–87. doi: 10.1016/j.mbs.2005.06.006

59. Leng G, Onaka T, Caquineau C, Sabatier N, Tobin VA, Takayanagi Y. Oxytocin and appetite. *Prog Brain Res* (2008) 170:137–51. doi: 10.1016/S0079–6123(08)00413–5

60. Robertson GL. The regulation of vasopressin function in health and disease. *Recent Prog Horm Res* (1976) 33:333–85. doi: 10.1016/b978–0–12–571133–3.50015–5

61. Čupić Ž, Marković VM, Maćešić S, Stanojević A, Damjanović S, Vukojević V, et al. Dynamic transitions in a model of the hypothalamic–pituitary–adrenal axis. *Chaos* (2016) 26(3):033111–1–9. doi: 10.1063/1.4944040

62. Marković VM, Čupić Ž, Vukojević V, Kolar–Anić Lj. Predictive modeling of the hypothalamic–pituitary–adrenal (HPA) axis response to acute and chronic stress. *Endocr J* (2011) 58(10):889–904. doi: 10.1507/endocrj.ej11–0037

63. Ixart G, Barbanel G, Nouguier–Soulé J, Assenmacher I. A quantitative study of the pulsatile parameters of CRH–41 secretion in unanesthetized free–moving rats. *Exp Brain Res* (1991) 87(1):153–8. doi: 10.1007/BF00228516

64. Gallagher TF, Yoshida K, Roffwarg HD, Fukushima DK, Weitzman ED, Hellman L. ACTH and cortisol secretory patterns in man. *J Clin Endocrinol Metab* (1973) 36(6):1058–68. doi: 10.1210/jcem–36–6–1058

65. Horrocks PM, Jones AF, Ratcliffe WA, Holder G, White A, Holder R, et al. Patterns of ACTH and cortisol pulsatility over twenty–four hours in normal males and females. *Clin Endocrinol (Oxf)* (1990) 32(1):127–34. doi: 10.1111/j.1365–2265.1990.tb03758.x

66. Whitnall MH. Regulation of the hypothalamic corticotropin–releasing hormone neurosecretory system. *Prog Neurobiol* (1993) 40(5):573–629. doi: 10.1016/0301–0082(93)90035–q

67. de Goeij DC, Kvetnansky R, Whitnall MH, Jezova D, Berkenbosch F, Tilders FJ. Repeated stress–induced activation of corticotropin–releasing factor neurons enhances vasopressin stores and colocalization with corticotropin–releasing factor in the median eminence of rats. *Neuroendocrinology* (1991) 53(2):150–9. doi: 10.1159/000125712

68. Jelić S, Čupić Ž, Kolar–Anić Lj, Vukojević V. Predictive modeling of the hypothalamic–pituitary–adrenal (HPA) function. dynamic system theory approach by stochiometric network analysis and quenching of small amplitude oscillations. *Int J Nonolinear Sci Numer Simul* (2009) 10(11–12):1451–72. doi: 10.1515/ijnsns.2009.10.11–12.1451

69. Čupić Ž, Stanojević A, Marković VM, Kolar–Anić Lj, Terenius L, Vukojević V. The HPA axis and ethanol: a synthesis of mathematical modelling and experimental observations. *Addict Biol* (2017) 22(6):1486–500. doi: 10.1111/adb.12409

70. Hensen J, Hader O, Bähr V, Oelkers W. Effects of incremental infusions of arginine vasopressin on adrenocorticotropin and cortisol secretion in man. *J Clin Endocrinol Metab* (1988) 66(4):668–71. doi: 10.1210/jcem–66–4–668

frontiers | Frontiers in Endocrinology

TYPE Original Research
PUBLISHED 10 January 2023
DOI 10.3389/fendo.2022.1013894

OPEN ACCESS

EDITED BY
Bianca Bianco,
Faculdade de Medicina do ABC, Brazil

REVIEWED BY
Alfredo Ulloa-Aguirre,
National Autonomous University of Mexico, Mexico
Livio Casarini,
University of Modena and Reggio Emilia, Italy
Fatma Abdelhedi,
University of Sfax, Tunisia
Micheline Misrahi,
Faculté de Médecine Université Paris Saclay, France

*CORRESPONDENCE
Jing Shu
Shujing@hmc.edu.cn
Xiaopan Chen
Chenxiaopan@hmc.edu.cn

†These authors share first authorship

SPECIALTY SECTION
This article was submitted to Reproduction, a section of the journal Frontiers in Endocrinology

RECEIVED 08 August 2022
ACCEPTED 20 December 2022
PUBLISHED 10 January 2023

CITATION
Chen X, Chen L, Wang Y, Shu C, Zhou Y, Wu R, Jin B, Yang L, Sun J, Qi M and Shu J (2023) Identification and characterization of novel compound heterozygous variants in *FSHR* causing primary ovarian insufficiency with resistant ovary syndrome. *Front. Endocrinol.* 13:1013894. doi: 10.3389/fendo.2022.1013894

Identification and characterization of novel compound heterozygous variants in *FSHR* causing primary ovarian insufficiency with resistant ovary syndrome

Xiaopan Chen[1,2*†], Linjie Chen[3†], Yang Wang[2,4†], Chongyi Shu[1], Yier Zhou[1], Ruifang Wu[1], Bihui Jin[1], Leixiang Yang[2], Junhui Sun[5], Ming Qi[6] and Jing Shu[1,4*]

[1]Reproductive Medicine Center, Department of Reproductive Endocrinology, Zhejiang Provincial People's Hospital, Affiliated People's Hospital, Hangzhou Medical College, Hangzhou, China, [2]Department of Genetic and Genomic Medicine, Zhejiang Provincial People's Hospital, Affiliated People's Hospital, Hangzhou Medical College, Hangzhou, China, [3]School of Laboratory Medicine and Bioengineering, Hangzhou Medical College, Hangzhou, China, [4]The Second Clinical Medical School of Wenzhou Medical University, Wenzhou, China, [5]Reproductive Medicine Center, The First Affiliated Hospital of Wenzhou Medical University, Wenzhou, China, [6]Department of Cell Biology and Medical Genetics, School of Medicine, Zhejiang University, Hangzhou, Zhejiang, China

Primary ovarian insufficiency (POI) is among the foremost causes of women infertility due to premature partial or total loss of ovarian function. Resistant ovary syndrome (ROS) is a subtype of POI manifested as normal ovarian reserve but insensitive to gonadotropin stimulation. Inactivating variants of follicle-stimulating hormone receptor (FSHR), a class A G-protein coupled receptor, have been associated with POI and are inherited *via* an autosomal recessive pattern. In this study, we investigated the genetic causes of a primary infertility patient manifested as POI with ROS, and elucidated the structural and functional impact of variants of uncertain significance. Next-generation sequencing (NGS) combined with Sanger sequencing revealed novel compound heterozygous *FSHR* variants: c.1384G>C/p.Ala462Pro and c.1862C>T/p.Ala621Val, inherited from her father and mother, respectively. The two altered amino acid sequences, localized in the third and seventh transmembrane helix of FSHR, were predicted as deleterious by *in silico* prediction. *In vitro* experiments revealed that the p.Ala462Pro variant resulted in barely detectable levels of intracellular signaling both in cAMP-dependent CRE-reporter activity and ERK activation and displayed a severely reduced plasma membrane receptor expression. In contrast, the p.Ala621Val variant

resulted in partial loss of receptor activation without disruption of cell surface expression. In conclusion, two unreported inactivating *FSHR* variants potentially responsible for POI with ROS were first identified. This study expands the current phenotypic and genotypic spectrum of POI.

KEYWORDS

primary ovarian insufficiency, resistant ovary syndrome, follicle-stimulating hormone receptor, compound heterozygous variant, transmembrane helix

Introduction

Primary ovarian insufficiency (POI) is an etiologically and clinically heterogeneous condition caused by the early loss or complete absence of ovarian activity (1, 2). POI affects roughly 1%–2% of females <40 years old (3), making it among the foremost causes of women infertility. Resistant ovary syndrome (ROS) is a special form of POI characterized by the presence of normal ovarian reserve and resistance to gonadotropin (GN) stimulation (4–6). The etiopathogenesis of POI is multifactorial, including genetic alterations, autoimmune and metabolic disorders, viral infections, and environmental or iatrogenic factors (7). Genetic factors represent the most commonly identified causes; however, the current understanding of its hereditary basis is incomplete (8, 9).

The follicle-stimulating hormone receptor (FSHR) is expressed in granulosa cells from the primary follicle stage onwards (10, 11) and rigidly controls follicle development in response to cyclic pituitary FSH discharge (11, 12). FSHR belongs to a highly conserved subfamily of G protein-coupled receptors with a remarkably long amino-terminal extracellular domain (ECD), an intracellular carboxyl-terminal tail (C-tail), and a typical structural architecture comprising seven transmembrane helixes (TMH) interconnected by three extracellular loops (ECL) and three intracellular loops (ICL) (13, 14). Upon FSH binding, the receptor adopts a conformational change and subsequently couples to Gαs protein, which in turn activates the adenylyl cyclase, resulting in increased cAMP signaling (15, 16). Variations in any of these domains by alterations in primary DNA sequences may potentially lead to receptor dysfunction and eventually to disease (17).

Genetic variants that inactivate protein-coding genes, collectively known as loss-of-function variants, are often single-nucleotide variants that disrupt the structure and function of the protein. *FSHR* inactivating variants, one of the rare causes of POI, are inherited recessively and require homozygous or compound heterozygous status to develop the clinical phenotype (18). After the first POI-causative FSHR variant-p.Ala189Val in the ECD was reported (19), diverse inactivating variants have been identified in different FSHR domains, including the ECD (20–29); the second, fourth, and sixth TMH (26, 29–34); the first, second, and third ECL (22, 28, 35, 36); second and third ICL (21, 37); and the C-tail (27). However, pathogenic inactivating variants in the third and seventh TMH of FSHR have not been reported so far in patients with POI.

Numerous evidence indicates that the clinical manifestations of *FSHR* variants are not uniform, ranging from primary amenorrhea with puberty disorders to secondary amenorrhea, oligomenorrhea, and premature menopause, depending on the specific domain and type of variant and the degree of inactivation. Thus, expanding the POI-causing variant spectrum of *FSHR* is crucial to understand the etiopathogenesis of POI and for better clinical diagnosis that involves patients and their offspring. Herein, we reported two novel *FSHR* variants (c.1862C>T/p.Ala621Val and c.1384G>C/p.Ala462Pro) in a compound heterozygous state in a Chinese infertile woman who manifests hypergonadotropic hypogonadism (HH) with oligomenorrhea, presence of normal ovarian reserve, and resistance to exogenous GNs: three clinical characteristics of POI with ROS. Using *in vitro* functional experiments, we characterized the molecular features underlying this disease phenotype, thereby providing new insights into POI with ROS. To our knowledge, this is the first study identifying pathogenic variants in the TMH3 and TMH7 of FSHR as causative variants for POI.

Materials and methods

Ethical compliance and informed consent

The study procedures were reviewed and approved by the Institutional Ethics Committee of Zhejiang provincial People's Hospital (Approval number: 2019KY205). Written informed consent was obtained from all participants. All genetic

materials were handled in accordance with the National Regulation on Human Genetic Resources.

Case presentation and medical history

A 29-year-old Chinese female was referred to our outpatient center for 5 years of primary infertility. The female patient reached menarche at age 15 and had experienced irregular menstrual cycles (15 - 180 days) in a progressively prolonged manner. At the age of 21 years, she consulted a local hospital for irregular periods, and after sex hormonal evaluation, she was diagnosed with ovarian dysfunction and began to intermittently take exogenous hormone replacement therapy to induce artificial menstrual cycles. After the age of 21 years, her menstrual cycle never appeared again without hormone therapy. A dominant follicle was detected during an occasional ultrasound examination when she was 26-year-old. She was otherwise healthy and had an unexceptional past clinical history. No family history of consanguinity, reproductive anomaly or infertility was documented.

Fertility investigations and ROS diagnosis

Upon examination, the patient's height and weight were found to be 160 cm and 62.5 kg, respectively. Physical examination of secondary sex characteristics revealed normal breast development, normal appearance of female external genitalia, and normal armpit and pubic hair. Hormonal assays were carried out in the presence of low doses of estrogen (Estradiol Valerate Tablets 1-2mg/d, Delpharm Lille S.A.S., Lys-lez-Lannoy, France). The repeated basal hormonal evaluations in our department revealed elevated serum FSH (35.98 and 37.73 IU/L) and luteinizing hormone (LH) (21.23 and 21 IU/L) (Table 1). The patient's thyroid stimulating hormone (TSH) level was normal (2.34 mIU/L), as was her prolactin (PRL) (10.03 ng/mL) (Table 1). Despite the increase in GNs, the patient's anti-Müllerian hormone (AMH) level was 2.89 ng/mL (Table 1), suggesting a normal ovarian reserve. Transvaginal ultrasonography examination displayed a normal-sized uterus and normal-sized bilateral ovaries, consisting of 3–5 small antral follicles 3–5 mm in diameter (Supplemental Figure). The patient had no autoimmune condition, including absence of anti-nuclear and anti-cardiolipin antibodies. Immunoglobulin and natural killer cell levels were within normal ranges. Chromosome analysis and Fragile X DNA test were normal. No other relevant clinical features were observed.

After failing to observe follicle development in the natural cycle, an initial attempt of controlled ovarian stimulation (COS) was performed by a daily combination of 50 mg clomiphene and 150 IU human menopausal gonadotropins (hMG). However, the stimulation was cancelled after 8 days of treatment with a total dose of 1,200 IU FSH, as no ovarian follicle development was observed (peak serum estradiol level, 39 pg/mL). To exclude the possibility that the ovarian unresponsiveness to exogenous GNs was due to stimulation insufficiency, another COS cycle with increased daily hMG dose and prolonged stimulation was conducted. Despite increasing the daily dose of exogenous GNs up to 375 IU per day, growth of immature follicles remained unresponsive even after 15 days of stimulation with total FSH dose of 4,350 IU. Thus, the patient was clinically diagnosed with ROS according to previously described criteria (6, 38).

Endocrine assays and follicular monitoring

The FSH, LH, estrogen (E_2), PRL, and TSH concentrations were tested by a set of commercial enzyme immunoassay kits (7K72-78 & 2P13-40, Abbott, Chicago, USA). The ovarian reserve was measured by an AMH detection kit (C86002, YHLO, Shenzhen, China). Monitoring of follicle growth and development was conducted by transvaginal ultrasonography (Hitachi, Tokyo, Japan).

Massively parallel sequencing

Whole-exome sequencing was conducted on DNA samples isolated from the patient's peripheral blood leukocytes, according to the manufacturer's manual (Agilent Technologies, Santa Clara, USA; Illumina, San Diego, USA). In brief, genomic DNA was fragmented, barcoded, purified, and hybridized with capture probes during library preparation for massively parallel sequencing. The captured sequences were

TABLE 1 Clinical characteristics of the proband.

Age at presentation (years)	Age at menarche (years)	Second sex characteristics	Ovary size	Follicle count a	Follicle size (mm) a	FSH (IU/L) a	LH (IU/L) a	E2 (pg/ml) a	PRL (ng/ml) a	TSH (mIU/L) a	AMH (ng/m 1)	Autoimmune screening	Karyotype and Fragile X screening
29	15	Normal	Normal	3-5 each	Up to 5	35.98 and 37.73b	21.23 and 21.0b	45.0 and 41.9b	10.03	2.34	2.89	Normal	Normal

a, Measurements were conducted at follicle stage; b, Repeated test with 4 weeks apart; Reference values for follicle phase: FSH: 3.03-8.08 IU/L; LH: 1.80-11.78 IU/L; E: 21.00-251.00 pg/ml; PRL: 5.18-26.53 ng/ml; TSH: 0.4-4 mIU/L.

then enriched with streptavidin-conjugated paramagnetic beads and further amplified before being subjected to NGS. Clusters were generated and sequenced on the Illumina NextSeq 550 system using the Illumina Nextseq High Output Kit (20024908) to obtain approximately 90 million reads per sample (2 × 151 cycles). After quality assessment, the resulting paired-end reads were mapped to the GRCh37 assembly (hg19) of the human genome. All called variants were annotated based on public databases, including the 1KGB (39), ExAC (39), gnomAD (40), dbSNP (41), OMIM (42), ClinVar (43), and LOVD (44). Major focus of the analysis was on the 4 relevant disease-causing genes (*FSHB, FSHR, LHB and LHCGR*). Variant interpretation was based on the gene clinical and pathogenic relevance according to ACMG guidelines (45).

Sanger sequencing

Validation of NGS results was conducted by Sanger sequencing. The primers used to amplify target region of the human *FSHR* gene were designed as follows: 5′-CAAACTGGGGCAGGCTGTGATG-3′ and 5′-CTTGCATTTCATAGCAGCCACAC-3′. All the PCRs were carried out at 50 µl reaction volume using 100 ng genomic DNA on an ABI GeneAmp 9700 PCR system (Applied Biosystems, Bedford, USA), and the amplified fragments were subsequently extracted from the agarose gel, purified, and directly sequenced by Big Dye Direct Cycle Sequencing (4458688, ThermoFisher Scientific, Waltham, USA) on an ABI 3730 Genetic Analyzer (Applied Biosystems, Bedford, USA). The nucleotide sequences were blasted with the published sequence of human *FSHR* gene (http://www.ncbi.nlm.nih.gov).

Protein topology and function prediction

Protein topology prediction of *FSHR* variants was conducted using the TMHMM architecture (46). Variant pathogenicity prediction was performed using three online tools: PolyPhen-2 (47), SIFT (48), and MutationTaster (49). Evolutionary conservation analysis was performed based on multiple-alignment of the amino acids across multispecies from the HomoloGene database.

Construction of plasmid vectors

The wild-type (WT) FSHR plasmid was constructed by subcloning human FSHR cDNA from pCR-BluntII-TOPO-FSHR (P19532, Miaolingbio, Wuhan, China). The obtained polymerase chain reaction products were then cloned into pcDNA3.1 and pEGFP-N1 with the Seamless Cloning Kit (D7010, Beyotime, Shanghai, China). Point mutations were performed by using the QuickMutation Kit (Beyotime, Shanghai, China). The sequences of primers used for plasmid construction were provided in Supplemental Table. The pCRE-luciferase vector was kindly provided by Dr. Naiming Zhou (50). All vectors were thoroughly sequenced to confirm sequence integrity.

Cell maintenance and transfection

The HEK293 cell line was routinely cultured in Dulbecco's modified Eagle's medium (Gibco, Waltham, USA) containing 10% heat-inactivated fetal bovine serum (SV30087, Hyclone, Logan, China) as described previously (51). Transfection of plasmid constructs into cells was conducted using lipofectamine 3000 reagent (L3000-015, Invitrogen, Carlsbad, USA). Variants were transfected alone (3 µg) to mimic the homozygous state, or together in equimolar concentration (1.5 µg each) to mimic the compound heterozygous state.

cAMP-dependent CRE-reporter assay

Cells pre-seeded in a 96-well plate were co-transfected with either an expression vector (pWT-cDNA or variants) and reporter vector (pCRE-Luc). At 48 h after transfection, cells were incubated with the DMEM containing various concentrations of recombinant FSH (S20150007, Jinsai, Changchun, China) for 4 h at 37°C. cAMP-dependent CRE-luciferase activity was measured using the firefly luciferase assay system (RG042S, Beyotime, Shanghai, China) with a multiple function microplate reader (Tecan, Männedorf, Switzerland). Briefly, the culture medium in the plate was removed, and 50 µL per well reporter lysis buffer was added immediately. The plate was then placed on a horizontal shaker for complete lysis. The cell lysate was collected and centrifuged in 10,000 × g for 5 min. Then, 20 µl supernatant was mixed with 100 µl luciferase substrate and incubated for 5 min. Finally, the mixture was transferred into a 96-well plate, and luminance was read on Tecan luminometer 1 s/per well at the 470 nM. Efficacy and potency were determined by a three-parameter nonlinear logistic regression using GraphPad Prism 7.0 (Graph Pad Software, San Diego, USA).

Western blot analysis of ERK activation

Cells transiently expressing wild-type receptor or variants were stimulated with the FSHR agonist (S20150007, Jinsai, Changchun, China) for the indicated durations. Drug incubation was terminated by washing the cells with ice-cold phosphate buffered saline followed by the addition of lysis buffer containing complete protease inhibitor (P1010, Beyotime,

Shanghai, China) and phosphatase inhibitors cocktail (P1082, Beyotime, Shanghai, China). Equal protein amounts from cell lysates were electrophoresed on a 10% SDS-polyacrylamide gel, and then transferred to a PVDF membrane and incubated with rabbit monoclonal anti-phospho-ERK1/2 antibody (4370, Cell Signaling, Danvers, USA) followed by stripping and reprobing with anti-total ERK antibody (4695, Cell Signaling, Danvers, USA) according to manufacturers' protocols. Chemiluminescence was detected using an ECL substrate (FD8000, Fdbio science, Hangzhou, China) with ChemiDoc Touch Imaging System (Bio-Rad, Hercules). All immunoblots were semi-quantified using the Adobe Photoshop CC software, and ERK1/2 activation was calculated as the level of phosphor-ERK1/2 normalized by the total-ERK.

Cell-surface receptor expression

Cells pre-seeded in a coverslip-covered 12-well plate were transiently transfected with pWT-EGFP, pA462P-EGFP, or pA621V-EGFP. At 48 h after transfection, the coverslip seeded with transfected cells was invertedly placed on a microscope slide and observed immediately under a confocal laser-scanning microscope (Leica, Wetzlar, Germany). The transfection efficiency was determined by counting number of cells that express fluorescence divided by the total number of observed cells. Quantification of the FSHR level on cell membrane by their mean fluorescent signal intensity was measured using ImageJ (NIH, Bethesda, USA); moreover, the plugin of MorphoLibJ in ImageJ was used to create segmentation borders. Furthermore, a region of interest area was created for a final measure.

Statistical analyses

Statistical analysis of *in vitro* experimentation was performed with GraphPad Prism software using data derived from ≥3 different biological replicates. Collected data were examined for normality of distribution using Shapiro–Wilk normality test. Comparisons between groups were carried out using one-way analysis of variance followed by Tukey's multiple comparisons tests for *post-hoc* analysis. Differences between groups were considered statistically significant at $P < 0.05$.

Results

Genetic analysis and functional prediction of *FSHR* variants

Bioinformatics analysis following NGS revealed two missense variants. The first variant was a transition of guanine to cytosine at nucleotide position 1384 in Exon 10 producing an Alanine to Proline replacement at position 462 (*FSHR*_ex10 c.1384G>C/p.Ala462Pro). The second variant was a transition of cytosine to thymine at nucleotide position 1862 in Exon 10 of *FSHR* gene resulting in an amino acid substitution of Alanine to Valine at position 621 (*FSHR*_ex10 c.1862C>T/p.Ala621Val). Sanger sequencing confirmed the suspected variants and showed that the patient's parents were heterozygous carriers; the father and mother being a heterozygous carrier of c.1384G>C/p.Ala462Pro and c.1862C>T/p.Ala621Val variants, respectively (Figures 1A-C). Both variants were neither found in public population databases (1KGB, ExAC, gnomAD, and dbSNP) nor in disease databases

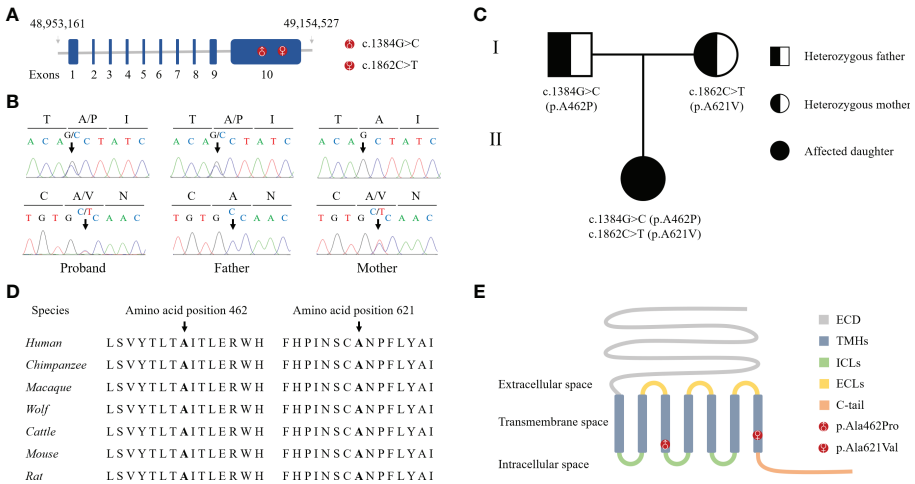

FIGURE 1
Identification of novel compound heterozygous variants in *FSHR*. **(A)** Schematic representation of the *hFSHR* gene and localization of newly identified variants. Size of exons is drawn to scale. **(B)** Validation of NGS by Sanger sequencing. **(C)** Pedigree of the family examined in the present study. **(D)** Multiple amino acid sequences alignment of FSHR target sites and their two flanks across different species. **(E)** Schematic representation of *hFSHR* and localization of newly identified variants.

(OMIM, ClinVar, and LOVD) (Table 2). Multiple sequence alignments were performed for FSHR proteins form different species; both A462 and A621 were highly evolutionarily conserved over multiple species (Figure 1D and Table 2). Protein topology prediction of the variants revealed that p.Ala462Pro and p.Ala621Val were localized in the third and seventh TMH of FSHR, respectively (Figure 1E). Furthermore, the two variants were predicted to be "Probably damaging" by PolyPhen-2, "Disease causing" by MutationTaster, and "Intolerated" by SIFT, indicating potential pathogenic effects of these two variants (Table 2). Thus, both p.Ala621Val and p.Ala462Pro were ranked as variants of uncertain significance according to ACMG pathogenicity assessing criteria (Table 2).

A462P and A621V variants were significantly impaired in cAMP-dependent CRE-luciferase activity

Examination of FSHR-mediated cAMP-dependent CRE-promoter transcription activity was conducted by co-transfection of HEK293 cells with the variants and CRE-luciferase reporter. In the presence of FSH, a dose-dependent increase in luciferase activity (EC_{50} = 11.98 IU) was recorded in cells harboring WT *FSHR* (Figure 2A). However, both FSH efficacy and potency to elicit cAMP-dependent CRE-reporter activity were significantly impaired in cells transfected with p.A621V variant as demonstrated by decreased maximal

TABLE 2 Bioinformatic prediction of the *FSHR* variants.

Variant	1KGB	ExAC	gnomAD	dbSNP	ClinVar	OMIM	LOVD	PolyPhen-2	SIFT	Mutation Taster	Conservation	ACMG classification
c.1384G>C (p.Ala462Pro)	N/F	N/F	N/F	N/F	N/F	N/F	N/F	D/C	D/C	D/C	H/C	VUS
c.1862C>T (p.Ala621Val)	N/F	N/F	N/F	N/F	N/F	N/F	N/F	D/C	D/C	D/C	H/C	VUS

N/F, Not found; D/C, Disease causing; H/C, Highly conserved; VUS, Variants of uncertain significance.

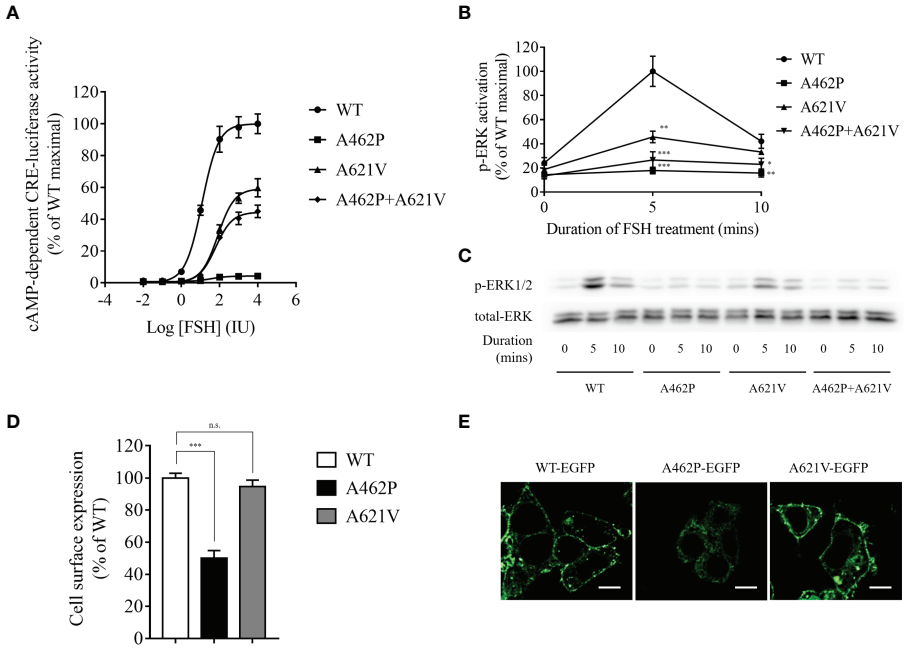

FIGURE 2
Functional evaluation of variants. **(A)** Dose-dependent curve of cAMP-dependent CRE-luciferase activity for *FSHR* variants upon FSH treatment. Variant transfected HEK293 cells were incubated with various FSH concentrations for 4 h. Data are expressed as percentage of WT maximal stimulation and represent the mean ± SEM of six independent experiments. **(B)** Time course of FSH-stimulated phosphorylation of ERK1/2 in cells expressing variants. Data are expressed as percentage of WT maximal stimulation and represent the mean ± SEM of three independent experiments. * $P < 0.05$, ** $P < 0.01$, *** $P < 0.001$ *vs.* WT *FSHR*. **(C)** Representative images of immunoblots using antibody against phosphorylated ERK1/2. Transfected cells were incubated with 500 IU FSH for the indicated time. **(D)** Bar plots showing quantitative fluorescence microscopy analysis of cell surface expression for all variants. Data are expressed as percentage of WT FSHR and represent the mean ± SEM of six independent experiments. *** P < 0.001 vs. WT *FSHR*, n.s. not significant. **(E)** Representative fluorescence microscopy images of the receptor cellular localization. Bar = 20 μm.

stimulation (59.72% of WT) and increased EC_{50} (81 IU) (Figure 2A). The most deteriorating impact in cAMP-dependent CRE-promoter activity was observed in cells expressing the p.A462P variant, whose luciferase activity was barely detectable (maximal stimulation = 4.24% of WT FSHR; EC_{50} = 32.3 IU) even in the presence 10,000 IU FSH, the highest concentration in our study (Figure 2A). When a blend of A462P and A621V was transfected together in equimolar concentration to mimic the compound heterozygous state found in the proband, there was a significant reduction either in the potency (EC_{50} = 62.16 IU) or in the efficacy (maximal stimulation = 44.95% of WT) as compared to those observed with the wild-type receptor.

A462P and A621V variants were significantly impaired in ERK activation

To further explore whether ERK activation is altered by the variants, we performed Western immunoblot using a monoclonal antibody against phosphorylated ERK1/2. As shown in Figures 2B, C, FSHR-related ERK activation was time-dependent with a maximal activation at 5 min and a subsequent reduction to 42.14% of maximal levels at 10 min in WT receptor transfected HEK293 cells after stimulation with 500 IU FSH. We found that receptors homozygous for either variant exhibited significantly reduced ERK activation compared to the WT receptor (Figures 2B, C). The homozygous A462P variant receptor almost completely abolished ERK activation at both treatment periods, whereas homozygous A621V variant receptors carried 45.79% and 33.21% of maximal ERK activation at 5 and 10 min, respectively. When both A462P and A621V variants were expressed together to mimic the compound heterozygous state of the patient, the magnitude of ERK activation in response to 5 and 10 min of FSH stimulation was severely impaired compared with the WT FSHR (Figures 2B, C).

Cell surface expression of the A462P variant was significantly impaired

Examination of the cell surface expression of p.A462P and p.A621V was conducted by transfection of HEK293 cells with these variants fused with EGFP. As shown in Figures 2D, E, the p.A621V variant and WT receptor exhibited comparable cell surface expression levels, but the p.A462P variant lost 50% of cell surface expression and was trapped intracellularly, suggesting that the nearly total loss of function in this variant might be due to reduced membrane receptor expression.

Discussion

In this study, we investigated a case of primary infertility in a woman previously diagnosed with ovarian dysfunction who in fact had POI with ROS; we identified two novel missense variants in the *FSHR* gene, c.1384G>C/p.Ala462Pro and c.1862C>T/p.Ala621Val, inherited from her father and mother, respectively. These two variants were predicted to be disease causing by bioinformatics analysis. *In vitro* functional studies confirmed that these two variants are both pathogenic inactivating variants

FSHR variants are functionally distinct with respect to their ligand binding, membrane expression, cAMP production, and other intracellular signaling characteristics (17, 52). The complexity of these variants is further amplified by the fact that causative variant of POI can be either homozygous or compound heterozygous (19, 21, 30, 53, 54). As a consequence, in a single *FSHR* gene, genetic alteration can result in various clinical manifestations, leading to the broad phenotypic spectrum of conditions arising from these variants. Thus, correlation of novel *FSHR* variants with a new case of POI characterized by endogenous HH, normal ovarian reserve, and hypo-responsiveness to hyper-physiological exogenous GN stimulation testifies to the phenotypic and etiological complexity of POI.

Patients with partially inactivating *FSHR* variants have displayed a range of clinical manifestations such as primary amenorrhea, secondary amenorrhea, and oligomenorrhea, which is in contrast to completely inactivating *FSHR* variants that cause fully absence of sexual development (55). The patient in our study displayed normal puberty and secondary sex characteristics, and presented with secondary amenorrhea and normal-sized bilateral ovaries, in which developing follicles were detected by ultrasonography. This phenotype is notably differed from patients with severe variants (19, 36, 56). The term ROS has been used to describe this special form of POI, which is caused by FSH resistance rather than follicular depletion (21, 22, 26, 27, 33, 54). Although most ROS patients presented with developing antral follicles (2-8 mm) on ultrasonography and follicular arrest at the early antral stage on ovarian biopsies, further maturation of follicle is usually blocked in these patients (21, 22, 24–27). The patient's follicles seemed incapable of proceeding through the later stages of follicular maturation, but likely produced adequate sex hormones at puberty to drive development of comparable secondary sex characteristics which accords with other studies with less severe variants (21, 22, 26, 27). The above surmise was supported by the normal AMH level detected in our case, which is consistent with previous studies

that ROS patients have age-matched AMH values while patients with common POI have low or undetectable levels of AMH (25–27, 31, 54). These observations suggest that POI caused by inactivating *FSHR* variants could have wide-range effects on clinical manifestations, with disturbance severity likely varying with the severity of inactivation and the resultant stage of follicular block.

The FSHR protein is encoded by the *FSHR* gene positioned at chromosome 2p21 (57). The two variants herein are both positioned at exon 10, which is the largest exon, mainly responsible for encoding the non-ECD domains. The p.A462P and p.A621V variants are positioned at the TMH3 and TMH7 of the receptor, respectively, where no mutation had formerly been observed in patients. Our *in vitro* functional study demonstrated that the p.A462P variant causes the intracellular retention of the receptor, leading to impaired FSHR cell membrane expression. Several previous studies have reported the association of lower membrane expression of FSHR variants with impaired intracellular signaling of the receptor (19, 21, 22, 25, 29, 31, 54, 56). In our study, the lower membrane expression of the p.A462P variant was linked with an approximately 96% reduction in the maximal response elicited by the FSH. However, FSHR cell surface localization was not affected by the p.A621V variant, but its intracellular signaling was significantly impaired. Consistent with these results, three previously identified inactivating variants of *FSHR* showing intact cell surface expression displayed a dramatic reduction in cAMP signaling (21, 22, 27). Partially functional impaired FSHR caused by variants affects the further development of follicular growth (21, 28, 31, 55), indicating that the partial functional impairment of FSHR mediated by these two novel variants might explain the follicles advanced to the small antral phase and normal AMH levels found in this patient.

Even after receiving a maximal daily FSH dose (375 IU), the patient's ovaries still remained unresponsive, which was consistent with several previous studies where partial or complete inactivating *FSHR* variants could not respond to intense and continual FSH stimulation (21, 22, 27, 28, 34, 36, 54, 58). It is worth noting that only one study has reported successful FSH treatment for ovarian stimulation in patient with ROS (24). The patient with successful treatment carried one heterozygous variant and two heterozygous SNPs. These clinical findings demonstrate that the differences in the ovarian responses to FSH stimulation noted between the successful and failed cases likely depend on the *FSHR* genotype. Patients who failed to react to follicular stimulation following an *in vitro* fertilization cycle could consider *in vitro* maturation (IVM) of the oocytes isolated from the blocked follicles. Successful IVM of oocytes was found in a primary infertility patient who carried compound heterozygous *FSHR* variants and had no response to FSH stimulation (54). Recently, Benammar et al. also reported a successful case of IVM live birth in a woman with primary infertility and ovarian resistance to FSH cause by compound heterozygous *FSHR* variants (58).

The lack of ovarian response to excessive FSH stimulation seems contradictory with the residual intracellular signaling observed *in vitro*. However, although *in vitro* functional data can be used as reference for *in vivo* scenarios, the selection of functional assay model may affect *in vitro* FSHR functionality (28). Moreover, receptor expression levels resulting from *in vitro* overexpression are far higher than in *in vivo* physiological environments, indicating that the real intracellular signaling of these variants in response to FSH stimulation would be probably poor *in vivo*. This observation suggests that in the presence of adequate FSH stimulation, partially functional but impaired FSHR might be critical for follicular growth.

In conclusion, we uncovered two novel *FSHR* variants, c.1384G>C/p.A462P and c.1862C>T/p.A621V, in a primary infertility patient affected by POI with ROS. To the best of our knowledge, these variants represent the first pathogenic inactivating variants found in the third and seventh TMH of FSHR. This study offers novel insights into the molecular basis of POI, expands the current knowledge of genotype–phenotype correlations and genetic variant spectrum of POI, and promotes the clinical diagnosis of patients with POI.

Data availability statement

The datasets presented in this study can be found in online repositories. The names of the repository/repositories and accession number(s) can be found below: https://www.ncbi.nlm.nih.gov/, PRJNA687912; https://www.ncbi.nlm.nih.gov/, SCV001478347; https://www.ncbi.nlm.nih.gov/, SCV001478348.

Ethics statement

The studies involving human participants were reviewed and approved by The Institutional Ethics Committee of Zhejiang provincial People' Hospital. The patients/participants provided their written informed consent to participate in this study.

Author contributions

XC was responsible for the experimental design, critical data analysis, interpretation, article writing and editing, and participated in conducting experimental procedures and coordination. LC, YW, CS, YZ, and LY conducted the main experimental procedures, and participated in experimental protocol design, data analysis and interpretation. BJ and RW contributed to the clinical data collection and interpretation. JHS and MQ contributed to the genetic counseling and data

interpretation. JS conceived the study, participated in experimental design and coordination, and was responsible for the project supervision and final approval of the article. All authors contributed to the article and approved the submission version.

Funding

This work was supported by grants from National Natural Science Foundation of China (81701460 to XC), General Research Program for Medicine and Health of Zhejiang Province (2020KY414 to JS, 2019KY021 to RW, and 2020KY448 to XC), Natural Science Foundation of Zhejiang Province (LY20H160046 to LY, LQ19H040005 to BJ), and Key Laboratory of Reproductive Genetics (Zhejiang University), Ministry of Education, P. R. China (ZDFY2020-RG-0006 to XC).

Acknowledgments

We would like to thank the patient and her parents for their participation in this study.

Conflict of interest

The authors declare that the research was conducted in the absence of any commercial or financial relationships that could be construed as a potential conflict of interest.

Publisher's note

Supplementary material

The Supplementary Material for this article can be found online at: https://www.frontiersin.org/articles/10.3389/fendo.2022.1013894/full#supplementary-material

References

1. Nelson LM. Clinical practice. primary ovarian insufficiency. *N Engl J Med* (2009) 360(6):606–14. doi: 10.1056/NEJMcp0808697

2. Welt CK. Primary ovarian insufficiency: A more accurate term for premature ovarian failure. *Clin Endocrinol (Oxf)* (2008) 68(4):499–509. doi: 10.1111/j.1365-2265.2007.03073.x

3. Coulam CB, Adamson SC, Annegers JF. Incidence of premature ovarian failure. *Obstet Gynecol* (1986) 67(4):604–6.

4. Jones GS, De Moraes-Ruehsen M. A new syndrome of amenorrhae in association with hypergonadotropism and apparently normal ovarian follicular apparatus. *Am J Obstet Gynecol* (1969) 104(4):597–600. doi: 10.1016/S0002-9378(16)34255-7

5. Koninckx PR, Brosens IA. The "gonadotropin-resistant ovary" syndrome as a cause of secondary amenorrhea and infertility. *Fertil Steril* (1977) 28(9):926–31. doi: 10.1016/S0015-0282(16)42792-5

6. Shangold MM, Turksoy RN, Bashford RA, Hammond CB. Pregnancy following the "insensitive ovary syndrome". *Fertil Steril* (1977) 28(11):1179–81. doi: 10.1016/S0015-0282(16)42914-6

7. Huhtaniemi I, Hovatta O, La Marca A, Livera G, Monniaux D, Persani L, et al. Advances in the molecular pathophysiology, genetics, and treatment of primary ovarian insufficiency. *Trends Endocrinol Metab* (2018) 29(6):400–19. doi: 10.1016/j.tem.2018.03.010

8. Qin Y, Jiao X, Simpson JL, Chen ZJ. Genetics of primary ovarian insufficiency: new developments and opportunities. *Hum Reprod Update* (2015) 21(6):787–808. doi: 10.1093/humupd/dmv036

9. Jaillard S, Bell K, Akloul L, Walton K, McElreavy K, Stocker WA, et al. New insights into the genetic basis of premature ovarian insufficiency: Novel causative variants and candidate genes revealed by genomic sequencing. *Maturitas* (2020) 141:9–19. doi: 10.1016/j.maturitas.2020.06.004

10. Oktay K, Briggs D, Gosden RG. Ontogeny of follicle-stimulating hormone receptor gene expression in isolated human ovarian follicles. *J Clin Endocrinol Metab* (1997) 82(11):3748–51. doi: 10.1210/jc.82.11.3748

11. Simoni M, Gromoll J, Nieschlag E. The follicle-stimulating hormone receptor: Biochemistry, molecular biology, physiology, and pathophysiology. *Endocr Rev* (1997) 18(6):739–73. doi: 10.1210/edrv.18.6.0320

12. Richards JS, Pangas SA. The ovary: Basic biology and clinical implications. *J Clin Invest* (2010) 120(4):963–72. doi: 10.1172/JCI41350

13. Jiang X, Liu H, Chen X, Chen PH, Fischer D, Sriraman V, et al. Structure of follicle-stimulating hormone in complex with the entire ectodomain of its receptor. *Proc Natl Acad Sci USA* (2012) 109(31):12491–6. doi: 10.1073/pnas.1206643109

14. Fredriksson R, Lagerstrom MC, Lundin LG, Schioth HB. The G-protein-coupled receptors in the human genome form five main families. phylogenetic analysis, paralogon groups, and fingerprints. *Mol Pharmacol* (2003) 63(6):1256–72. doi: 10.1124/mol.63.6.1256

15. Jiang X, Dias JA, He X. Structural biology of glycoprotein hormones and their receptors: Insights to signaling. *Mol Cell Endocrinol* (2014) 382(1):424–51. doi: 10.1016/j.mce.2013.08.021

16. Casarini L, Crepieux P. Molecular mechanisms of action of FSH. *Front Endocrinol (Lausanne)* (2019) 10:305. doi: 10.3389/fendo.2019.00305

17. Ulloa-Aguirre A, Zarinan T, Jardon-Valadez E, Gutierrez-Sagal R, Dias JA. Structure-function relationships of the follicle-stimulating hormone receptor. *Front Endocrinol (Lausanne)* (2018) 9:707. doi: 10.3389/fendo.2018.00707

18. Desai SS, Roy BS, Mahale SD. Mutations and polymorphisms in FSH receptor: functional implications in human reproduction. *Reproduction* (2013) 146(6):R235–48. doi: 10.1530/REP-13-0351

19. Aittomaki K, Lucena JL, Pakarinen P, Sistonen P, Tapanainen J, Gromoll J, et al. Mutation in the follicle-stimulating hormone receptor gene causes hereditary hypergonadotropic ovarian failure. *Cell* (1995) 82(6):959–68. doi: 10.1016/0092-8674(95)90275-9

20. Gromoll J, Simoni M, Nordhoff V, Behre HM, De Geyter C, Nieschlag E. Functional and clinical consequences of mutations in the FSH receptor. *Mol Cell Endocrinol* (1996) 125(1-2):177–82. doi: 10.1016/S0303-7207(96)03949-4

21. Beau I, Touraine P, Meduri G, Gougeon A, Desroches A, Matuchansky C, et al. A novel phenotype related to partial loss of function mutations of the follicle stimulating hormone receptor. *J Clin Invest* (1998) 102(7):1352–9. doi: 10.1172/JCI3795

22. Touraine P, Beau I, Gougeon A, Meduri G, Desroches A, Pichard C, et al. New natural inactivating mutations of the follicle-stimulating hormone receptor:

Correlations between receptor function and phenotype. *Mol Endocrinol* (1999) 13 (11):1844–54. doi: 10.1210/mend.13.11.0370

23. Allen LA, Achermann JC, Pakarinen P, Kotlar TJ, Huhtaniemi IT, Jameson JL, et al. A novel loss of function mutation in exon 10 of the FSH receptor gene causing hypergonadotrophic hypogonadism: Clinical and molecular characteristics. *Hum Reprod* (2003) 18(2):251–6. doi: 10.1093/humrep/deg046

24. Nakamura Y, Maekawa R, Yamagata Y, Tamura I, Sugino N. A novel mutation in exon8 of the follicle-stimulating hormone receptor in a woman with primary amenorrhea. *Gynecol Endocrinol* (2008) 24(12):708–12. doi: 10.1080/09513590802454927

25. Liu H, Xu X, Han T, Yan L, Cheng L, Qin Y, et al. A novel homozygous mutation in the FSHR gene is causative for primary ovarian insufficiency. *Fertil Steril* (2017) 108(6):1050–5 e2. doi: 10.1016/j.fertnstert.2017.09.010

26. He WB, Du J, Yang XW, Li W, Tang WL, Dai C, et al. Novel inactivating mutations in the FSH receptor cause premature ovarian insufficiency with resistant ovary syndrome. *Reprod BioMed Online* (2019) 38(3):397–406. doi: 10.1016/j.rbmo.2018.11.011

27. Khor S, Lyu Q, Kuang Y, Lu X. Novel FSHR variants causing female resistant ovary syndrome. *Mol Genet Genomic Med* (2020) 8(2):e1082. doi: 10.1002/mgg3.1082

28. Sassi A, Désir J, Janssens Véronique, Marangoni M, Daneels D, Gheldof A, et al. Novel inactivating follicle-stimulating hormone receptor (FSHR) mutations in a patient with premature ovarian insufficiency identified by next generation sequencing gene panel analysis. *F&S Rep* (2020) 1(3):193–201. doi: 10.1016/j.xfre.2020.08.008

29. Liu H, Guo T, Gong Z, Yu Y, Zhang Y, Zhao S, et al. Novel FSHR mutations in han Chinese women with sporadic premature ovarian insufficiency. *Mol Cell Endocrinol* (2019) 492:110446. doi: 10.1016/j.mce.2019.05.005

30. Doherty E, Pakarinen P, Tiitinen A, Kiilavuori A, Huhtaniemi I, Forrest S, et al. A novel mutation in the FSH receptor inhibiting signal transduction and causing primary ovarian failure. *J Clin Endocrinol Metab* (2002) 87(3):1151–5. doi: 10.1210/jcem.87.3.8319

31. Bramble MS, Goldstein EH, Lipson A, Ngun T, Eskin A, Gosschalk JE, et al. A novel follicle-stimulating hormone receptor mutation causing primary ovarian failure: A fertility application of whole exome sequencing. *Hum Reprod* (2016) 31 (4):905–14. doi: 10.1093/humrep/dew025

32. Katari S, Wood-Trageser MA, Jiang H, Kalynchuk E, Muzumdar R, Yatsenko SA, et al. Novel inactivating mutation of the FSH receptor in two siblings of Indian origin with premature ovarian failure. *J Clin Endocrinol Metab* (2015) 100(6):2154–7. doi: 10.1210/jc.2015-1401

33. Kuechler A, Hauffa BP, Koninger A, Kleinau G, Albrecht B, Horsthemke B, et al. An unbalanced translocation unmasks a recessive mutation in the follicle-stimulating hormone receptor (FSHR) gene and causes FSH resistance. *Eur J Hum Genet* (2010) 18(6):656–61. doi: 10.1038/ejhg.2009.244

34. Zarinan T, Mayorga J, Jardon-Valadez E, Gutierrez-Sagal R, Maravillas-Montero JL, Mejia-Dominguez NR, et al. A novel mutation in the FSH receptor (I423T) affecting receptor activation and leading to primary ovarian failure. *J Clin Endocrinol Metab* (2021) 106(2):e534–e50. doi: 10.1210/clinem/dgaa782

35. Franca MM, Lerario AM, Funari MFA, Nishi MY, Narcizo AM, de Mello MP, et al. A novel homozygous missense FSHR variant associated with hypergonadotropic hypogonadism in two siblings from a Brazilian family. *Sex Dev* (2017) 11(3):137–42. doi: 10.1159/000477193

36. Meduri G, Touraine P, Beau I, Lahuna O, Desroches A, Vacher-Lavenu MC, et al. Delayed puberty and primary amenorrhea associated with a novel mutation of the human follicle-stimulating hormone receptor: Clinical, histological, and molecular studies. *J Clin Endocrinol Metab* (2003) 88(8):3491–8. doi: 10.1210/jc.2003-030217

37. Woad KJ, Prendergast D, Winship IM, Shelling AN. FSH receptor gene variants are rarely associated with premature ovarian failure. *Reprod BioMed Online* (2013) 26(4):396–9. doi: 10.1016/j.rbmo.2013.01.004

38. European Society for Human R and Embryology Guideline Group on POI, Webber L, Davies M, Anderson R, Bartlett J, et al. ESHRE guideline: Management of women with premature ovarian insufficiency. *Hum Reprod* (2016) 31(5):926–37. doi: 10.1093/humrep/dew027

39. Genomes Project C, Auton A, Brooks LD, Durbin RM, Garrison EP, Kang HM, et al. A global reference for human genetic variation. *Nature* (2015) 526 (7571):68–74. doi: 10.1038/nature15393

40. Karczewski KJ, Francioli LC, Tiao G, Cummings BB, Alfoldi J, Wang Q, et al. The mutational constraint spectrum quantified from variation in 141,456 humans. *Nature* (2020) 581(7809):434–43. doi: 10.1038/s41586-020-2308-7

41. Sherry ST, Ward MH, Kholodov M, Baker J, Phan L, Smigielski EM, et al. dbSNP: The NCBI database of genetic variation. *Nucleic Acids Res* (2001) 29 (1):308–11. doi: 10.1093/nar/29.1.308

42. Amberger JS, Bocchini CA, Schiettecatte F, Scott AF, Hamosh A. OMIM.org: Online mendelian inheritance in man (OMIM(R)), an online catalog of human genes and genetic disorders. *Nucleic Acids Res* (2015) 43(Database issue): D789–98. doi: 10.1093/nar/gku1205

43. Landrum MJ, Lee JM, Riley GR, Jang W, Rubinstein WS, Church DM, et al. ClinVar: public archive of relationships among sequence variation and human phenotype. *Nucleic Acids Res* (2014) 42(Database issue):D980–5. doi: 10.1093/nar/gkt1113

44. Fokkema IF, Taschner PE, Schaafsma GC, Celli J, Laros JF, den Dunnen JT. LOVD v.2.0: The next generation in gene variant databases. *Hum Mutat* (2011) 32 (5):557–63. doi: 10.1002/humu.21438

45. Richards S, Aziz N, Bale S, Bick D, Das S, Gastier-Foster J, et al. Standards and guidelines for the interpretation of sequence variants: A joint consensus recommendation of the American college of medical genetics and genomics and the association for molecular pathology. *Genet Med* (2015) 17(5):405–24. doi: 10.1038/gim.2015.30

46. Krogh A, Larsson B, von Heijne G, Sonnhammer EL. Predicting transmembrane protein topology with a hidden Markov model: Application to complete genomes. *J Mol Biol* (2001) 305(3):567–80. doi: 10.1006/jmbi.2000.4315

47. Adzhubei IA, Schmidt S, Peshkin L, Ramensky VE, Gerasimova A, Bork P, et al. A method and server for predicting damaging missense mutations. *Nat Methods* (2010) 7(4):248–9. doi: 10.1038/nmeth0410-248

48. Ng PC, Henikoff S. SIFT: Predicting amino acid changes that affect protein function. *Nucleic Acids Res* (2003) 31(13):3812–4. doi: 10.1093/nar/gkg509

49. Schwarz JM, Cooper DN, Schuelke M, Seelow D. MutationTaster2: mutation prediction for the deep-sequencing age. *Nat Methods* (2014) 11 (4):361–2. doi: 10.1038/nmeth.2890

50. Zhu C, Huang H, Hua R, Li G, Yang D, Luo J, et al. Molecular and functional characterization of adipokinetic hormone receptor and its peptide ligands in bombyx mori. *FEBS Lett* (2009) 583(9):1463–8. doi: 10.1016/j.febslet.2009.03.060

51. Chen XP, Yang W, Fan Y, Luo JS, Hong K, Wang Z, et al. Structural determinants in the second intracellular loop of the human cannabinoid CB1 receptor mediate selective coupling to g(s) and g(i). *Br J Pharmacol* (2010) 161 (8):1817–34. doi: 10.1111/j.1476-5381.2010.01006.x

52. Ulloa-Aguirre A, Reiter E, Crepieux P. FSH receptor signaling: Complexity of interactions and signal diversity. *Endocrinology* (2018) 159(8):3020–35. doi: 10.1210/en.2018-00452

53. Latronico AC, Arnhold IJ. Gonadotropin resistance. *Endocr Dev* (2013) 24:25–32. doi: 10.1159/000342496

54. Flageole C, Toufaily C, Bernard DJ, Ates S, Blais V, Chenier S, et al. Successful *in vitro* maturation of oocytes in a woman with gonadotropin-resistant ovary syndrome associated with a novel combination of FSH receptor gene variants: A case report. *J Assist Reprod Genet* (2019) 36(3):425–32. doi: 10.1007/s10815-018-1394-z

55. Oduwole OO, Huhtaniemi IT, Misrahi M. The roles of luteinizing hormone, follicle-stimulating hormone and testosterone in spermatogenesis and folliculogenesis revisited. *Int J Mol Sci* (2021) 22(23):12735. doi: 10.3390/ijms222312735

56. Desai SS, Achrekar SK, Sahasrabuddhe KA, Meharji PK, Desai SK, Mangoli VS, et al. Functional characterization of two naturally occurring mutations (Val514Ala and Ala575Val) in follicle-stimulating hormone receptor. *J Clin Endocrinol Metab* (2015) 100(4):E638–45. doi: 10.1210/jc.2014-3662

57. Gromoll J, Pekel E, Nieschlag E. The structure and organization of the human follicle-stimulating hormone receptor (FSHR) gene. *Genomics* (1996) 35 (2):308–11. doi: 10.1006/geno.1996.0361

58. Benammar A, Fanchin R, Filali-Baba M, Vialard F, Fossard C, Vandame J, et al. Utilization of *in vitro* maturation in cases with a FSH receptor mutation. *J Assist Reprod Genet* (2021) 38(6):1311–21. doi: 10.1007/s10815-021-02249-3

frontiers | Frontiers in Endocrinology

TYPE Original Research
PUBLISHED 23 January 2023
DOI 10.3389/fendo.2023.985404

OPEN ACCESS

EDITED BY
João P. Magalhães,
University of Lisbon, Portugal

REVIEWED BY
Megan Hetherington-Rauth,
Universidade de Lisboa, Portugal
Romeu Mendes,
University Porto, Portugal

*CORRESPONDENCE
Paulo Gentil
paulogentil@hotmail.com

SPECIALTY SECTION
This article was submitted to Cardiovascular Endocrinology, a section of the journal Frontiers in Endocrinology

RECEIVED 03 July 2022
ACCEPTED 03 January 2023
PUBLISHED 23 January 2023

CITATION
Gentil P, Silva LRBe, Antunes DE, Carneiro LB, de Lira CAB, Batista G, Oliveira JCMd, Cardoso JS, Souza DC and Rebelo ACS (2023) The effects of three different low-volume aerobic training protocols on cardiometabolic parameters of type 2 diabetes patients: A randomized clinical trial.
Front. Endocrinol. 14:985404.
doi: 10.3389/fendo.2023.985404

The effects of three different low-volume aerobic training protocols on cardiometabolic parameters of type 2 diabetes patients: A randomized clinical trial

Paulo Gentil[1,2,3]*, Lucas Raphael Bento e Silva[1,4,5], Daniela Espíndola Antunes[5], Luciana Barbosa Carneiro[6], Claudio Andre Barbosa de Lira[1,4], Gislene Batista[7], Jordana Campos Martins de Oliveira[7], John Sebastião Cardoso[7], Daniel Costa Souza[1] and Ana Cristina Silva Rebelo[1,4,5]

[1]College of Physical Education and Dance, Federal University of Goiás, Goiânia, Brazil, [2]Hypertension League, Federal University of Goiás, Goiânia, Brazil, [3]Instituto VIDA, Brasilia, Brazil, [4]Faculty of Medicine, Federal University of Goiás, Goiânia, Brazil, [5]Hospital das Clínicas, Federal University of Goiás, Goiânia, Brazil, [6]Banco de Olhos Foundation, Goiânia, Brazil, [7]Faculty of Nutrition, Federal University of Goiás, Goiânia, Brazil

Objective: To compare the effects of different aerobic training protocols on cardiometabolic variables in patients with type 2 diabetes mellitus (T2DM).

Methods: This study was a parallel clinical trial. Fifty-two men and women with T2DM (>40 years) were randomly allocated into three groups, and 44 (22 males/22 females) were included in the final analysis. Exercise intensity was based on the speed corresponding to the maximum oxygen consumption ($v\dot{V}O_2max$). Moderate intensity continuous training (MICT) involved 14 minutes at 70% of $v\dot{V}O_2max$; short interval high-intensity interval training (S-HIIT) consisted of 20 bouts of 30 seconds at 100% of $V\dot{O}_2max$ with 30 seconds passive recovery; long interval high-intensity training (L-HIIT) consisted of 5 bouts of 2 minutes at 100% of $v\dot{V}O_2max$ with 2 minutes passive recovery. Training protocols were performed on a motorized treadmill two times per week for eight weeks. Glycated hemoglobin (Hb1Ac), total cholesterol, triglycerides, resting systolic blood pressure (SBP), resting diastolic blood pressure (DBP), resting heart rate (resting HR) and maximum oxygen consumption ($V\dot{O}_2max$) were measured before and after the exercise intervention. The study was registered on the Brazilian clinical trial records (ID: RBR45 4RJGC3).

Results: There was a significant difference between groups for changes on $\dot{V}O_2max$. Greater increases on $\dot{V}O_2max$ were achieved for L-HIIT ($p = 0.04$) and S-HIIT ($p = 0.01$) in comparison to MICT group, with no significant difference between L-HIIT and S-HIIT ($p = 0.9$). Regarding comparison within groups, there were significant reductions on HbA1c and triglycerides levels only for L-HIIT ($p< 0.05$). $\dot{V}O_2max$ significantly increased for both L-HIIT (MD = 3.2 ± 1.7 ml/kg/min, $p< 0.001$) and S-HIIT (MD = 3.4 ± 1.7, $p< 0.001$). There was a significant reduction on resting SBP for L-HIIT group (MD = -12.07 ± 15.3 mmHg, $p< 0.01$), but not for S-

HIIT and MICT. There were no significant changes from pre- to post-training on fasting glycemia, total cholesterol, HDL, LDL, resting HR and resting DBP for any group ($p > 0.05$).

Conclusion: Low-volume HIIT promoted greater improvements in cardiorespiratory capacity in comparison with low-volume MICT, independent of the protocols used. There were no other differences between groups. All protocols improved at least one of the variables analyzed; however, the most evident benefits were after the high-intensity protocols, especially L-HIIT.

KEYWORDS

diabetes mellitus, high-intensity interval training (HIIT), aerobic exercise (AE), glucose control, exercise is medicine

1 Introduction

Type 2 diabetes mellitus (T2DM) is one of the leading causes of disability worldwide (1). T2DM is associated with increased mortality and reduced quality of life and might have serious complications, such as retinopathy, cardiovascular diseases and limb amputations (2). Therapeutic recommendations for T2DM aim to control glycemia, lipidemia, blood pressure (BP), body mass and promote lifestyle changes, such as increase physical activity levels (3). In this sense, aerobic training is considered an effective strategy for T2DM prevention and treatment (4, 5). Traditionally, performing at least 150 min/week of moderate (MICT) to vigorous intensity continuous training distributed at a minimum of three non-consecutive day during the week has been recommended to manage T2DM (6). However, there is evidence that high-intensity interval training (HIIT) might provide superior benefits on a variety of cardiometabolic risk factors in comparison to MICT (7, 8), leading physical activity guidelines to suggested the use of HIIT for managing T2DM (9).

HIIT is a type of aerobic training that consists of performing high intensity exercise bouts alternated with passive or active recovery periods (10). There are many different types HIIT, which might result in different physiological and perceptual responses (10–12). Among them, we can highlight the protocols involving shorter intervals (S-HIIT) and longer intervals (L-HIIT) (13).

Kilpatrick et al., (14) compared three work-matched HIIT protocols performed at the same intensity, but with different interval durations (120 s vs. 60 s vs. 30 s) in healthy young people. According to the results, longer intervals were associated with greater cardiovascular stress and higher discomfort (14). Similarly, Naves et al., (11) and Silva et al., (15) found that L-HIIT promoted greater cardiovascular stress in comparison with S-HIIT in healthy young men, and women with metabolic syndrome, respectively. Interestingly, most studies involving HIIT in T2DM used long intervals (≥2 minutes), which could be potentially dangerous due to the greater cardiovascular stress, especially if we consider that most T2DM patients have increased cardiovascular risks (16). However, while L-HIIT protocols may lead to increased cardiovascular stress, it also results in higher work performed, higher oxygen consumption and higher heart rate (HR), which can make them more efficient for promoting cardiometabolic adaptations (7, 17, 18).

In this context, it is important to determine whether the use of different HIIT protocols could affect cardiometabolic adaptations in T2DM in order to allow an adequate cost benefit analysis. Therefore, the aim of the present study was to investigate the effects of three different types of aerobic training protocols on cardiometabolic parameters in people with T2DM.

2 Material and methods

2.1 Study design

This study is a parallel randomized clinical trial that involved individuals with T2DM of both sex that performed different aerobic training protocols, two times per week for eight weeks. The study was performed at the Hospital of the Federal University of Goias (Goiania, Brazil), approved by the relevant Human Research Ethics Committee (Protocol No. 2,667,732, CAAE No. 54522016.6.0000.5083) and registered on the Brazilian clinical trial records (ID: RBR-4RJGC3). All participants gave written informed consent in accordance with the Declaration of Helsinki. Participants were assigned by randomization to one of three groups using a specialized website (www.random.org): L-HIIT, S-HIIT, or MICT.

Before and after the training period, participants were evaluated for anthropometric measures, resting BP, cardiopulmonary exercise test and blood markers. Anthropometric measures included weight and height for calculating body mass index (BMI), as well as waist and hip circumference. Weight was measured using a digital scale (BC 553, Tanita®, USA), and height was measured using a portable stadiometer (Personal Caprice Portatil, Sanny®, Brazil). BMI was calculated using the following formula [BMI = weight (kg)/height $(m)^2$]. BP and HR were measured at sitting position after 10 minutes of rest according with Seventh Brazilian Arterial Hypertension Guideline using oscilometric method (Omron HEM-705) (19). Complementary results of the current experiment have been published previously (20).

All experimental procedures were carried out in the morning, with relative humidity between 40 and 60%, and temperature between 22 and 24°C, according to American College of Sports Medicine guidelines (ACSM) (21). Participants received orientation to not drink or eat

products containing alcohol or caffeine 24 hours before and on the day of the tests, to not perform physical exercises or strenuous activities on the day before exercise, to have a light meal at least 2 hours before the tests, to wear clothes suitable for physical activity practice and to keep their usual diets habits during the intervention period.

2.2 Participants

Sixty participants with T2DM were recruited from 3rd Diabetes Task Force promoted by the Eye Bank Foundation of Goiás. To be included in the study, participants had to be 40 years old or more, diagnosed with T2DM, have a fasting glycemia above 126 mg/dL and/or glycated hemoglobin greater than 6.4%, and to not participate in other physical training program. Patients were excluded if they were active smokers or had myocardial revascularization, arrhythmias and frequent extrasystoles at rest or during physical exertion, unstable angina, obstructive pulmonary disease, neoplasm, renal or liver failure, orthopedic limitations, and uncontrolled hypothyroidism and cardiovascular diseases at moderate and high risk (classes C and D), according to the criteria American Heart Association (22). To be included in the final analyses, participants had to perform more than 85% of all training sessions.

After cardiopulmonary exercise tests, eight patients were excluded, including three with an exercise capacity<6 METS, two with uncontrolled arrhythmias during physical exertion, one with unstable angina, and two with a reduction in SBP during exercise to lower levels than resting SBP. Two patients were excluded from the final analyses because they presented irregular data for determined variables. The enrolment process until participant's inclusion in final analyses is describe in Figure 1.

The was no *a priori* definition of sample size. However, the total number of 60 participants was considered adequate because it provided a power > 0.9 to detect an effect size of 0.5 (G*Power 3.1, Germany).

2.3 Medication record

Medication use was self-reported according to Table 1 and there was no change in the medications of the patients during the intervention period.

2.4 Biochemical analyses

At the first visit to the laboratory, 4 mL of whole blood was collected by the vacuum method into EDTA tubes (Plastilab, Brazil) from the antecubital vein after approximately 12 h overnight fasting. Homogenized whole blood was used for preparation and processing of samples.

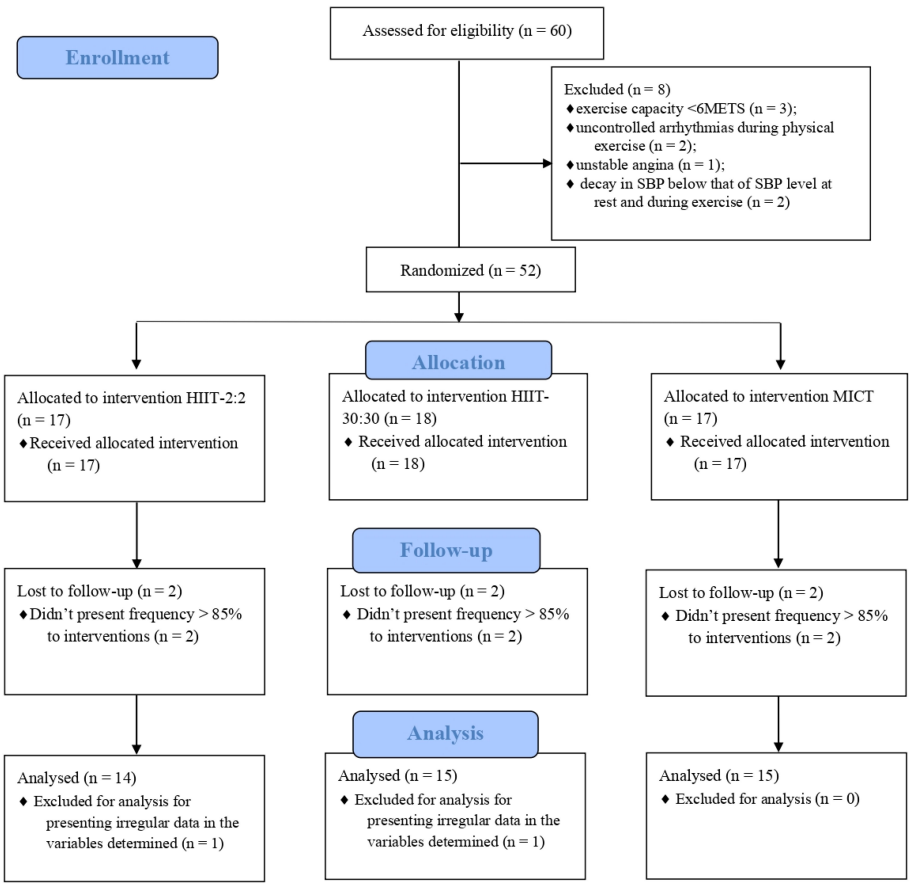

FIGURE 1
Study flow according to CONSORT recommendations. MICT, moderate intensity continuous training; HIIT, high-intensity interval training; SBP, systolic blood pressure.

10.3389/fendo.2023.985404

TABLE 1 Class of medicines used by patients.

Medication	Long HIIT (n =15)	Short HIIT (n =15)	MICT (n =14)
Biguanides	11	12	10
Sulfonylureas	1	–	3
SGLT2 inhibitors	2	–	1
DPP-4 inhibitors	1	1	1
GLP-1 analogue	–	1	2
Pioglitazones	–	1	1
Insulin	8	7	5
Anti-Hypertensive	15	15	14
Anticholesterolemic	13	12	11

HIIT, high-intensity interval training; MICT, moderate intensity continuous training; SGLT2, Sodium glucose cotransporter 2; DPP-4, Dipeptidyl peptidase-4; GLP-1, Glucagon-like peptide-1.

The following analyzes were performed for glucose metabolism: fasting glucose by enzymatic method using commercial kits (Labtest, Brazil), fasting insulin by chemiluminescence and HbA1c by immunoassay. This method is certified by the National Glycohemoglobin Standardization Program (23).

Lipid profile analysis involved total cholesterol by enzymatic system (reaction of the endpoint), HDL by System for direct homogeneous determination of HDL cholesterol in serum, and triglycerides by enzymatic system, by end point reaction, all using commercial kits (Labtest, Brazil).

2.5 Cardiopulmonary exercise test (CPET)

CPET involved an incremental ramp type protocol performed on a treadmill (Micromed®, Centurion 200, Brasília, Brazil) coupled to a computer. The test started with a two-minute warm-up with no inclination and speed correspondent to 50% of the initial values predicted for age and sex. Every 15 seconds of warm-up, speed increased by 0.5 km/h.

After warm-up, treadmill speed was set according to age and gender, following the recommendations of the Brazilian Society of Cardiology. The speed was then increased by 0.1 km/h every 10, 20 or 30 seconds until voluntary exhaustion, and participants were verbally encouraged to give their maximum effort. The test lasted between 8 to 12 minutes and ended when participants met the criteria for test interruption according to ACSM guideline (21).

Volunteers were instructed to wear comfortable clothes and avoid vigorous physical exercise (24 hours before the test), alcohol consumption (12 hours before the test) and caffeine (3 hours before the test). CPET was performed in the morning, to avoid the influence of the circadian rhythm. Ambient temperature (22°C - 24°C), relative humidity (40% - 60%) and lighting were controlled according to the preliminary conditions (23). Gas analysis was performed using a Cortex® analyzer (Metalyser II, Rome, Italy). Equipment calibration was performed for barometric pressure, ambient gas, gas mixture, flow and volume, as per the manufacturer's recommendations.

HR, BP, rating of perceived exertion (RPE) and ventilatory parameters (peak, carbon dioxide production, respiratory oxygen equivalent, respiratory equivalent of the ventilatory threshold) were monitored and registered during the test. RPE was evaluated according to the Borg 0-10 (27). The instrument presents numerical classification from "0" to "10", indicating low and maximum intensity effort, respectively. The values indicated by the volunteers were recorded at the end of each minute of the test (5th to 16th minute). Heart rate (HR) was measured by a cardiac monitor (Polar v800, Finland) during the test and up to 10 minutes of rest after its end, with the volunteer in the sitting position. Cardiac monitor was fixed in the chest and with simultaneous transmission to a watch. Data were later transferred and recorded in a specific software (Polar Flow, Finland) for proper analysis.

2.6 Exercise protocols

The protocols were customized with individualized monitored of HR, BP and v $\dot{V}O_2$max achieved in the (CPET). Their respective exercise intensities were adapted from previous studies (11, 15), and were matched by the product (time * % v $\dot{V}O_2$max).

Exercise session started with a 2 min warm-up and ended with a 2 min cooldown at 50% of v $\dot{V}O_2$max. MICT consisted of continuous walking/running at 70% of v $\dot{V}O_2$max for 14 minutes. L-HIIT consisted of 5 bouts of 2 minutes walking/running at 100% of v $\dot{V}O_2$max interspersed by a passive recovery of 2 minutes. S-HIIT consisted of 20 bouts of 30 seconds walking/running at 100% of v $\dot{V}O_2$max interspersed by a passive recovery for 30 seconds. All protocols were performed on a motorized treadmill (Micromed®, *Centurion 200*, Brasília, Brazil).

Exercise intensity was adjusted using perceived of exertion as previously suggested (24, 25).

2.7 Statistical analyses

Data normality and homogeneity were tested using the Shapiro-Wilk and Levene test, respectively. Post-training values were compared between groups using analysis of covariance (ANCOVA) with pre-training values as covariates. When a significant effect was identified, *Bonferroni's post hoc* was used to identify were differences occurred. Paired T-test was used to compare within groups differences for HbA1c, fasting glycemia, total cholesterol, triglycerides, HDL, LDL, resting SBP, resting DBP, resting HR and $\dot{V}_{O2}$max using pre- and post-training values.

All analyses were performed using SPSS statistical package (Statistical Package for Social Sciences Chicago, IL, USA) version 20.0 for Windows. Results are expressed as mean and standard deviation, and the accepted level of significance was ($p< 0.05$).

3 Results

The characteristics of participants are described in Table 2.

There were significant difference between groups for changes on $\dot{V}O_2$max, with greater increases on $\dot{V}O_2$max for L-HIIT ($p = 0.04$)

TABLE 2 Characteristics of participants.

	MICT (n = 9M;5F)	L-HIIT (n = 6M;9F)	S-HIIT (n = 7M;8F)	p-value
Age (years)	54.6 ± 8.9	57.3 ± 8.9	55.7 ± 7.4	0.69
Weight (kg)	80.7 ± 14.5	76.3 ± 16.9	79.5 ± 11.0	0.69
Height (cm)	165.4 ± 11.0	163.1 ± 8.3	165.5 ± 6.7	0.68
BMI	29.4 ± 4.9	28.5 ± 4.9	28.9 ± 3.6	0.85

BMI, body mass index; training; S-HIIT, short high-intensity interval training; L-HIIT, long high-intensity interval training; MICT, moderate intensity continuous; M, Male; F, Female. Data presented as mean ± standard deviation.

and S-HIIT (p = 0.01) in comparison with MICT group. There was no significant difference between L-HIIT and S-HIIT (p = 0.9). Pre- and post-training values and comparisons between and within groups are presented in Table 3.

In comparison with pre-training values, there was a significant reduction on HbA1c levels for L-HIIT (mean difference [MD] = -1.8 ± 1.8%, p< 0.01), while no significant change was achieved for S-HIIT (MD = -0.92 ± 2.0%, p = 0.09) and MICT (MD = -0.59 ± 1.7%, p = 0.2). Triglycerides levels significantly reduced after L-HIIT (MD = -23.80 ± 39.6 mg/dL, p = 0.04), with no changes for S-HIIT (MD = -23.19 ± 49.0 mg/dL, p = 0.09) and MICT (MD = 5.36 ± 31.9 mg/dL, p = 0.5). There were no significant changes from pre- to post-training on fasting glycemia, total cholesterol, HDL, and LDL (p > 0.05).

There was a significant reduction on resting SBP for L-HIIT group (MD = -12.07 ± 15.3 mmHg, p< 0.01), but not for S-HIIT (MD = -7.33 ± 17.1 mmHg, p = 0.1) and MICT (MD = 4.43 ± 13.1 mmHg, p = 0.2). $\dot{V}O_2$max significantly increased for both L-HIIT (MD = 3.2 ± 1.7 ml/kg/min, p< 0.001) and S-HIIT (MD = 3.4 ± 1.7, p< 0.001), but not for MICT (MD = 0.86 ± 3.8, p = 0.4). There were no significant changes from pre- to post-training for resting HR and resting DBP for any group (p > 0.05).

4 Discussion

The present study investigated the effects of three aerobic training protocols (L- HIIT, S-HIIT, and MICT) on cardiometabolic parameters of patients with T2DM. The recommendation of a minimum of 150 min per week of moderate intensity physical activities for blood glucose control and cardiovascular health is still predominant (26). However, our study demonstrated that the performance of 20 min high intensity exercise per week was sufficient to improve cardiorespiratory and metabolic fitness in patients with T2DM. These findings are particularly important since time-efficient exercise strategies emerge as promising alternatives to improve exercise adherence. Moreover, this is one of the first studies to compare HIIT protocols involving different interval lengths on metabolic parameters in T2DM patients. The present study found a significant reduction in HbA1c with large effect after L-HIIT, corroborating the idea that exercise intensity can play an important role in managing T2DM (27). Moreover, the use of HIIT protocols involving longer intervals might be preferred for blood glucose control in this population. These improvements in Hb1Ac can be explained by the increase in GLUT4 protein due to a higher concentration of calcium led by increased exercise intensity, resulting in protein translocation to the cell membrane and increasing glucose uptake by muscle cells (28–30). L-HIIT might also have led to a higher glycogen depletion, which is associated with improved glucose uptake (31, 32). A previous study demonstrated that PGC-1α increase (important protein for metabolic gene activation necessary for the use of substrate and mitochondrial biogenesis) occurs after HIIT, but not after MICT (33).

Previous studies have shown 15 to 20% reductions in cardiovascular events when HbA1c is reduced by 1% (34, 35). In addition, this reduction on HbA1c for L-HIIT group observed after 8 weeks of training is apparently higher than the observed after long-term (> 12 weeks) hypoglycemic drug treatment and insulin use (ranging from 0.6-0.8%) (45). In agreement with the current study, Winding et al., (36) found greater reductions on Hb1Ac after 11 weeks of HIIT (i.e., 10 bouts of 1 minute at 95% of peak workload interspersed by 1 minute of active rest) when compared to endurance training in individuals with T2DM. Moreover, HIIT has been shown to promote a rapid increase in skeletal muscle oxidative capacity, insulin sensitivity and glycemic control in adults with T2DM (7, 37, 38). When compared to MICT, HIIT programs have promoted greater improvements in HbA1c, fasting glycemia and other risk factors for T2DM (34, 35).

Although no significant difference was found for lipid profile between groups, there was a trend to decrease triglycerides and a large effect was found between pre and post intervention for both HIIT protocols [L-HIIT [-0.57 (wide)]; S-HIIT [-0.53 (wide)]. It is important to acknowledge that improvements in triglyceride and HDL levels are important due to the associations between dyslipidemia and cardiovascular diseases (39). The effects of HIIT on lipid profile in patients with T2DM have been inconsistent in the literature. There are studies showing improvements only in LDL cholesterol (40), only in HDL (41), or absence of alteration (42). The same studies also showed no effect of HIIT on triglycerides in patients with T2DM (40–42).

L-HIIT showed a greater reduction in resting SBP when compared to MICT (p = 0.018; d = 1.56 [large effect]). Although several studies have shown BP reductions through exercises (43), the reduction only in L-HIIT can be explained by the difference in baseline values (MICT 125 [25]mm/Hg; L-HIIT 147 [45]mm/Hg; S-HIIT 135 [20]mm/Hg), since greater reductions are seen in people with higher BP levels (44). Although there seems to be an agreement on the effectiveness of exercise to reduce BP (45), the effectiveness of aerobic exercise to reduce systolic and diastolic arterial pressure in patients with T2DM is still debated, with previous studies showing contradictory results (6, 46). Previous studies showed reductions in SBP after HIIT (~ 13 mmHg) (41) compatible with our results, revealing a potential for HIIT for controlling cardiovascular risks (47). $\dot{V}O_2$max increases after HIIT is in accordance with the results of previous studies (48–50). Between group comparisons showed that the increases in $\dot{V}O_2$max were larger in the L-HIIT and S-HIIT than MICT. This is in accordance with the suggestion that HIIT are more beneficial for the cardiorespiratory system. The absence of an increase $\dot{V}O_2$max in the MICT was unexpected but could be associated with the changes in HbA1c since there are studies showing an association between $\dot{V}O_2$max increase and in HbA1c reduction (R = −0.52, p<0.01). According to these findings, approximately 25% of the

10.3389/fendo.2023.985404

TABLE 3 Comparison between and within groups for dependent variables.

Variables	Pre	Post	Mean difference	p-value within groups	p-value between groups
	mean ± SD	mean ± SD			
HbA1c (%)					
MICT (n=14)	8.5 ± 2.4	7.9 ± 1.2	-0.59 ± 1.7	0.21	0.28
L-HIIT (n=15)	9.9 ± 2.8	8.1 ± 2.1	-1.80 ± 1.8	**<0.01**	
S-HIIT (n=15)	9.6 ± 1.9	8.7 ± 1.6	-0.92 ± 2.0	0.09	
Fasting glycemia (mg/dL)					
MICT	129.8 ± 57.1	126.7 ± 54.6	-3.07 ± 28.0	0.69	0.10
L-HIIT	145.5 ± 66.0	140.1 ± 69.0	-5.33 ± 36.3	0.58	
S-HIIT	142.7 ± 63.0	136.9 ± 57.9	-5.83 ± 29.6	0.46	
Triglycerides (mg/dL)					
MICT	159.6 ± 33.2	164.9 ± 40.3	5.36 ± 31.9	0.54	0.06
L-HIIT	164.9 ± 84.1	141.1 ± 48.1	-23.80 ± 39.6	**0.04**	
S-HIIT	185.5 ± 75.9	162.3 ± 58.3	-23.19 ± 49.0	0.09	
Total cholesterol (mg/dL)					
MICT	172.9 ± 44.7	75.1 ± 36.2	2.21 ± 43.7	0.85	0.94
L-HIIT	199.5 ± 65.2	190.9 ± 53.6	-8.60 ± 46.7	0.49	
S-HIIT	188.3 ± 38.6	180.2 ± 42.5	-8.05 ± 32.1	0.35	
HDL (mg/dL)					
MICT	44.4 ± 8.9	43.5 ± 9.2	-4.45 ± 1.2	0.49	0.16
L-HIIT	43.1 ± 10.1	47.1 ± 13.3	3.93 ± 8.9	0.11	
S-HIIT	46.4 ± 8.0	45.9 ± 7.5	-0.62 ± 6.8	0.72	
LDL (mg/dL)					
MICT	98.3 ± 40.7	98.6 ± 32.1	0.29 ± 38.9	0.98	0.27
L-HIIT	107.7 ± 43.4	113.9 ± 34.2	6.21 ± 23.2	0.32	
S-HIIT	116.7 ± 38.1	104.3 ± 35.1	-12.39 ± 27.0	0.10	
Resting SBP (mmHg)					
MICT	126.1 ± 19.8	130.5 ± 13.4	4.43 ± 13.1	0.23	0.27
L-HIIT	145.5 ± 25.5	133.5 ± 17.6	-12.07 ± 15.3	**<0.01**	
S-HIIT	138.6 ± 15.8	131.3 ± 17.6	-7.33 ± 17.1	0.12	
Resting PAD (mmHg)					
MICT	82.6 ± 7.0	86.3 ± 6.2	3.64 ± 7.6	0.10	0.21
L-HIIT	86.6 ± 10.1	84.3 ± 6.0	-2.33 ± 9.7	0.37	
S-HIIT	84.3 ± 9.7	87.7 ± 10.2	3.33 ± 8.6	0.16	
Resting HR (bpm)					
MICT	75.9 ± 11.3	68.2 ± 9.5	-7.71 ± 10.9	0.02	0.07
L-HIIT	77.5 ± 10.3	75.1 ± 8.5	-2.40 ± 6.7	0.19	
S-HIIT	71.7 ± 12.0	72.3 ± 15.0	0.6 ± 0.1	0.80	
$\dot{V}O_2$max (ml/kg/min)					
MICT	22.6 ± 8.9	23.4 ± 10.7	0.86 ± 3.8	0.41	**0.01**$^{*,\#}$

(Continued)

TABLE 3 Continued

Variables	Pre	Post	Mean difference	p-value within groups	p-value between groups
	mean ± SD	mean ± SD			
L-HIIT	22.4 ± 5.6	25.6 ± 6.3	3.2 ± 1.7	**<0.001**	
S-HIIT	19.7 ± 3.1	23.1 ± 3.7	3.4 ± 1.7	**<0.001**	

MICT, moderate intensity continuous training; L-HIIT, long high intensity interval training; S-HIIT, short high intensity interval training; HbA1c, glycated hemoglobin; HDL, high-density lipoprotein; LDL, low-density lipoprotein; SBP, systolic blood pressure; DBP, diastolic blood pressure; HR, heart rate; $\dot{V}O_2$max, maximum oxygen consumption.
* L-HIIT > MICT.
# S-HIIT > MICT.
Bold values mean p<0.05.

reductions in HbA1c may be related to the increase in $\dot{V}O_2$max (51). $\dot{V}O_2$max is an objective and independent indicator of cardiovascular risk and considered the most important physical conditioning variable (52, 53). Cardiorespiratory fitness is inversely associated with all-cause mortality and an increase of 1-2 METs (MET = 3.5ml O2/Kg/min) reduces 10% to 30% the risk of cardiovascular events (54). Although evidence for an optimal exercise intensity is still uncertain, it has been suggested that only exercise with intensity close to $\dot{V}O_2$max allows the recruitment of large motor units (i.e., type II muscle fibers) (55, 56) and induces high cardiac output, which might be important for long term VO2max improvements (57).

One important limitation of the present study is the absence of dietary control. However, participants were oriented to not change their diet. We believe that these limitations do not prevent the conclusions of the study from being elaborated. In addition, due the lack of control group, it was not possible to know whether changes observed for exercising groups were different when compared to non-exercise conditions.

5 Conclusion

Low-volume HIIT promoted greater improvements in cardiorespiratory capacity in comparison with low-volume MICT, independent of the protocols used. There were no other difference between groups. All protocols improved at least one of the variables analyzed; however, the most evident benefits were after the high-intensity protocols, especially L-HIIT. Therefore, it will be up to the professional to analyze their patients individually to propose the best intervention for each case, within an appropriate cost-benefit perspective.

Data availability statement

The raw data supporting the conclusions of this article will be made available by the authors, under reasonable request.

Ethics statement

The studies involving human participants were reviewed and approved by Federal University of Goias Ethics Committee. The patients/participants provided their written informed consent to participate in this study.

Author contributions

PG conceived and designed the research. LS, JC, and JSC performed experiments. DS and PG analyzed data, interpreted results of experiments, and drafted manuscript. DS and AR edited and revised manuscript. All authors contributed to the article and approved the submitted version.

Acknowledgments

We would like to thank all participants who volunteered their time to participate in the study.

Conflict of interest

The authors declare that the research was conducted in the absence of any commercial or financial relationships that could be construed as a potential conflict of interest.

Publisher's note

All claims expressed in this article are solely those of the authors and do not necessarily represent those of their affiliated organizations, or those of the publisher, the editors and the reviewers. Any product that may be evaluated in this article, or claim that may be made by its manufacturer, is not guaranteed or endorsed by the publisher.

References

1. Ogurtsova K, Guariguata L, Barengo NC, Ruiz PLD, Sacre JW, Karuranga S, et al. IDF diabetes atlas: Global estimates of undiagnosed diabetes in adults for 2021. *Diabetes Res Clin Pract* (2022) 183. doi: 10.1016/j.diabres.2021.109118

2. Cho NH, Shaw JE, Karuranga S, Huang Y, da Rocha Fernandes JD, Ohlrogge AW, et al. IDF diabetes atlas: Global estimates of diabetes prevalence for 2017 and projections for 2045. *Diabetes Res Clin Pract* (2018) 138:271–81. doi: 10.1016/j.diabres.2018.02.023

3. Lee I-M, Shiroma EJ, Lobelo F, Puska P, Blair SN, Katzmarzyk PT. Impact of physical inactivity on the world's major non-communicable diseases. *Lancet* (2012) 380 (9838):219–29. doi: 10.1016/S0140-6736(12)61031-9.Impact

4. Jeon CY, Lokken RP, Hu FB, van Dam RM. Physical activity of moderate intensity and risk of type 2 diabetes: a systematic review. *Diabetes Care* (2007) 30:744–52. doi: 10.2337/dc06-1842

5. De Rezende LFM, Rabacow FM, Viscondi JY, Luiz Odo C, Matsudo VK, Lee IM, et al. Effect of physical inactivity on major noncommunicable diseases and life expectancy in Brazil. *J Phys Act. Heal* (2015) 12:299–306. doi: 10.1123/jpah.2013-0241

6. Colberg SR, Sigal RJ, Fernhall B, Regensteiner JG, Blissmer BJ, Rubin RR. American College of sports medicine; American diabetes association. exercise and type 2 diabetes: the American college of sports medicine and the American diabetes association: joint position statement. *Diabetes Care* (2010) 33:147–67. doi: 10.2337/dc10-9990

7. Jelleyman C, Yates T, Donovan GO, Gray LJ, King JA, Khunti K, et al. Physical activity / metabolic effects the effects of high-intensity interval training on glucose regulation and insulin resistance : a meta-analysis. *Obes Rev* (2015) 16:942–61. doi: 10.1111/obr.12317

8. Liu J, Zhu L, Li P, and Xu N, Bing Y. Effectiveness of high-intensity interval training on glycemic control and cardiorespiratory fitness in patients with type 2 diabetes: a systematic review and meta-analysis. *Aging Clin Exp Res* (2019) 31(5):575–93. doi: 10.1007/s40520-018-1012-z

9. Colberg SR, Sigal RJ, Yardley JE, Riddell MC, Dunstan DW, Dempsey PC, et al. Physical activity/exercise and diabetes: A position statement of the American diabetes association. *Diabetes Care* (2016) 39(11):2065–79. doi: 10.2337/dc16-1728

10. Viana RB, de Lira CAB, Naves JPA, Coswig VS, Del Vecchio FB, Ramirez-Campillo R, et al. Can we draw general conclusions from interval training studies? *Sport. Med* (2018) 48(9):2001–9. doi: 10.1007/s40279-018-0925-1

11. Naves JPA, Rebelo ACS, Silva LRBE, Silva MS, Ramirez-Campillo R, Ramírez-Vélez R, et al. Cardiorespiratory and perceptual responses of two interval training and a continuous training protocol in healthy young men. *Eur J Sport Sci* (2019) 19(5):653–60. doi: 10.1080/17461391.2018.1548650

12. Souza D, Coswig V, de Lira CAB, Gentil P. H″IT″ting the barriers for exercising during social isolation. *Biol (Basel).* (2020) 9(9):245. doi: 10.3390/biology9090245

13. Tucker WJ, Sawyer BJ, Jarrett CL, Bhammar DM, Gaesser GA. Physiological responses to high-intensity interval exercise differing in interval duration. *J Strength Cond. Res* (2015) 1:3326–35. doi: 10.1519/JSC.0000000000001000

14. Kilpatrick MW, Martinez N, Little JP, Jung ME, Jones AM, Price NW, et al. Impact of high-intensity interval duration on perceived exertion. *Med Sci Sport. Exerc* (2015) 47 (5):1038–45. doi: 10.1249/MSS.0000000000000495

15. Silva L.R.B.E.L.R.B.E., Zamunér ARAR, Gentil P, Alves FMFM, Leal A.G.F.A.G.F., Soares V, et al. Cardiac autonomic modulation and the kinetics of heart rate responses in the on- and off-transient during exercise in women with metabolic syndrome. *Front Physiol* (2017) 8:542(JUL). doi: 10.3389/fphys.2017.00542

16. Lehrke M, Marx N. Diabetes mellitus and heart failure. *Am J Cardiol* (2017) 120(1): S37–47. doi: 10.1016/j.amjcard.2017.05.014

17. Hwang C-L, Wu Y-T, Chou C-H. Effect of aerobic interval training on exercise capacity and metabolic risk factors in people with cardiometabolic disorders: a meta-analysis. *J Cardiopulm. Rehabil. Prev* (2011) 31(6):378–85. doi: 10.1097/HCR.0b013e31822f16cb

18. Liubaoerjijin Y, Terada T, Fletcher K, Boulé NG. Effect of aerobic exercise intensity on glycemic control in type 2 diabetes: a meta-analysis of head-to-head randomized trials. *Acta Diabetol* (2016) 53(5):769–81. doi: 10.1007/s00592-016-0870-0

19. Malachias M, Souza W, Plavnik FL, Rodrigues C, Brandão A. 7ª diretriz brasileira de hipertensão arterial. *Arq. Bras Cardiol* (2016) 107(3). doi: 10.5935/abc.2013S010

20. Silva LRB, Gentil P, Seguro CS, de Oliveira JCM, Silva MS, Marques VA, et al. High-intensity interval training improves cardiac autonomic function in patients with type 2 diabetes: A randomized controlled trial. *Biol (Basel).* (2022) 11(1):66. doi: 10.3390/biology11010066

21. ACMS. *Diretrizes do acsm para os testes de esforço e sua prescrição*. Rio de Janeiro: Guanabara Koogan (2013).

22. Fletcher GF, Balady GJ, Amsterdam EA, Chaitman B, Eckel R, Fleg J. Exercise standards for testing and training: A statement for healthcare professionals from the American heart association. *Circulation* (2001) 104(14):1694–740. doi: 10.1161/hc3901.095960

23. National Glycohemoglobin Standardization Program (NGSP). (2019).

24. Watt B, Grove R. Perceived exertion: Antecedents asd applications. *Sport. Med* (1993) 15(4):275–97. doi: 10.1016/B978-0-443-10260-8.50017-5

25. Mezzani A, Hamm LF, Jones AM, McBride PE, Moholdt T, Stone JA, et al. Aerobic exercise intensity assessment and prescription in cardiac rehabilitation: A joint position statement of the European association for cardiovascular prevention and rehabilitation, the American association of cardiovascular and pulmonary rehabilitat. *Eur J Prev Cardiol* (2013) 20(3):442–67. doi: 10.1177/2047487312460484

26. Whelton PK, Carey RM, Aronow WS, Casey DE, Collins KJ, Himmelfarb CD, et al. ACC/AHA/AAPA/ABC/ACPM/AGS/APhA/ASH/ASPC/NMA/PCNA guideline for the prevention, detection, evaluation and management of high blood pressure in adults: A report of the American college of Cardiology/American heart association task force on clinical practic. *J Am Coll Cardiol* (2018) 71(19):e127–248. doi: 10.1016/j.jacc.2017.11.006

27. Dudley GA, Abraham WM, Terjung RL. Influence of exercise intensity and duration on biochemical adaptations in skeletal muscle. *J Appl Physiol Respir Environ Exerc. Physiol* (1982) 53(4):844–50. doi: 10.1152/jappl.1982.53.4.844

28. Garvey WT, Maianu L, Huecksteadt TP, Birnbaum MJ, Molina JM, Ciaraldi TP. Pretranslational suppression of a glucose transporter protein causes insulin resistance in adipocytes from patients with non-insulin-dependent diabetes mellitus and obesity. *J Clin Invest.* (1991) 87(3):1072–81. doi: 10.1172/jci115068

29. Mavros Y, Simar D, Singh MAF. Glucose tranporter-4 expression in monocytes: A systematic review. *Diabetes Res Clin Pract* (2009) 84(2):123–31. doi: 10.1016/j.diabres.2009.02.014

30. Sticka KD, Schnurr TM, Jerome SP, Dajles A, Reynolds AJ, Duffy LK, et al. Exercise increases glucose transporter-4 levels on peripheral blood mononuclear cells. *Med Sci Sports Exerc.* (2018) 50(5):938–44. doi: 10.1249/MSS.0000000000001528

31. Kang J, Robertson RJ, Hagberg JM, Kelley DE, Goss FL, DaSilva SG, et al. Effect of exercise intensity on glucose and insulin metabolism in obese individuals and obese NIDDM patients. *Diabetes Care* (1996) 19(4):341–9. doi: 10.2337/DIACARE.19.4.341

32. Flemming D, Ingersen A, Andersen NB, Nielsen MB, Petersen HHH, Hansen CN, et al. Effects of one-legged high-intensity interval training on insulin-mediated skeletal muscle glucose homeostasis in patients with type 2 diabetes. *Acta Physiol (Oxf)* (2019) 226 (2):e12345. doi: 10.1111/APHA.13245.

33. Schjerve IE, Tyldum G, Tjønna AE, Stølen T, Loennechen JP, Hansen HEM, et al. Both aerobic endurance and strength training programmes improve cardiovascular health in obese adults. *Clin Sci (Lond).* (2008) 115(9):283–93. doi: 10.1042/CS20070332

34. Stratton IM, Adler AI, Neil HA, Matthews DR, Manley SE, Cull CA, et al. Association of glycaemia with macrovascular and microvascular complications of type 2 diabetes (UKPDS 35): prospective observational study. *B.M.J* (2000) 321(7258):405–12. doi: 10.1136/bmj.321.7258.405

35. Selvin E, Marinopoulos S, Berkenblit G, Rami T, Brancati FL, Powe NR. Meta-analysis: glycosylated hemoglobin and cardiovascular disease in diabetes mellitus. *Ann Intern Med* (2004) 141(6):421–31. doi: 10.7326/0003-4819-141-6-200409210-00007

36. Winding KM, Munch GW, Iepsen UW, Van Hall G, Pedersen BK, Mortensen SP. The effect on glycaemic control of low-volume high-intensity interval training versus endurance training in individuals with type 2 diabetes. *Diabetes Obes Metab* (2018) 20 (5):1131–9. doi: 10.1111/dom.13198

37. Umpierre D, Ribeiro PAB, Kramer CK, Leitão CB, Zucatti ATN, Azevedo MJ, et al. Physical activity advice only or structured exercise training and association with HbA1c levels in type 2 diabetes: A systematic review and meta-analysis. *JAMA* (2011) 305 (17):1790–9. doi: 10.1001/jama.2011.576

38. Umpierre D, Ribeiro PAB, Schaan BD, Ribeiro JP. Volume of supervised exercise training impacts glycaemic control in patients with type 2 diabetes: A systematic review with meta-regression analysis. *Diabetologia* (2013) 56(2):242–51. doi: 10.1007/s00125-012-2774-z

39. Dal Canto E, Ceriello A, Rydén L, Ferrini M, Hansen TB, Schnell O, et al. Diabetes as a cardiovascular risk factor: An overview of global trends of macro and micro vascular complications. *Eur J Prev Cardiol* (2019) 26(2_suppl):25–32. doi: 10.1177/2047487319878371

40. Karstoft K, Winding K, Knudsen SH, Nielsen JS, Thomsen C, Pedersen BK, et al. The effects of free-living interval-walking training on glycemic control, body composition and physical fitness in type 2 diabetic patients: a randomized, controlled trial. *Diabetes Care* (2013) 36(2):228–36. doi: 10.2337/dc12-0658

41. Mitranun W, Deerochanawong C, Tanaka H, Suksom D. Continuous vs interval training on glycemic control and macro- and microvascular reactivity in type 2 diabetic patients. *Scand J Med Sci Sports* (2014) 24(2):e69–76. doi: 10.1111/sms.12112

42. Terada T, Friesen A, Chahal BS, Bell GJ, McCargar LJ, Boulé NG. Feasibility and preliminary efficacy of high intensity interval training in type 2 diabetes. *Diabetes Res Clin Pract* (2013) 99(2):120–9. doi: 10.1016/j.diabres.2012.10.019

43. Naci H, Salcher-Konrad M, Dias S, Blum MR, Sahoo SA, Nunan D, et al. How does exercise treatment compare with antihypertensive medications? a network meta-analysis of 391 randomised controlled trials assessing exercise and medication effects on systolic blood pressure. *Br J Sports Med* (2019) 53(14):859–69. doi: 10.1136/bjsports-2018-099921

44. Pedersen BK, Saltin B. Exercise as medicine - evidence for prescribing exercise as therapy in 26 different chronic diseases. *Scand J Med Sci Sport.* (2015) 25:1–72. doi: 10.1111/sms.12581

45. Pescatello LS, Franklin BA, Fagard R, Farquhar WB, Kelley GA, Ray CA, et al. American College of sports medicine position stand. exercise and hypertension. *Med Sci Sports Exerc* (2004) 36(3):533–53. doi: 10.1249/01.MSS.0000115224.88514.3A

46. Cornelissen VA, Smart NA. Exercise training for blood pressure: a systematic review and meta-analysis. *J Am Hear. Assoc* (2013) 2(1):e004473. doi: 10.1161/JAHA.112.004732/1/e004473

47. Francois ME, Pistawka KJ, Halperin FA, Little JP. Cardiovascular benefits of combined interval training and post-exercise nutrition in type 2 diabetes. *J Diabetes Complications* (2018) 32(2):226–33. doi: 10.1016/j.jdiacomp.2017.10.002

48. Pattyn N, Coeckelberghs E, Buys R, Cornelissen VA, Vanhees L. Aerobic interval training vs. moderate continuous training in coronary artery disease patients: A systematic review and meta-analysis. *Sport. Med* (2014) 44(5):687–700. doi: 10.1007/s40279-014-0158-x

49. Ruffino JS, Songsorn P, Haggett M, Edmonds D, Robinson AM, Thompson D, et al. A comparison of the health benefits of reduced-exertion high-intensity interval training (REHIT) and moderate-intensity walking in type 2 diabetes patients. *Appl Physiol Nutr Metab* (2017) 42(2):202–8. doi: 10.1139/apnm-2016-0497

50. Storen Y, Helgerud J, Mona, Stoa EM, Bratland-Sanda S, Unhjem RJ, et al. The effect of age on the VO2max response to high-intensity interval training. *Med Sci Sport. Exerc.* (2017) 49(1):78–85. doi: 10.1249/MSS.0000000000001070

51. Stoa EM, Storen Ø. Response to comments on "High-intensity aerobic interval training improves aerobic fitness and HbA1c among persons diagnosed with type 2 diabetes." *Eur J Appl Physiol* (2017) 117(7):1521–1. doi: 10.1007/s00421-017-3633-x

52. Kodama S, Saito K, Tanaka S, Maki M, Yachi Y, Asumi M, et al. Cardiorespiratory fitness as a quantitative predictor of all-cause mortality and cardiovascular events in healthy men and women: a meta-analysis. *JAMA* (2009) 301(19):2024–35. doi: 10.1001/jama.2009.681

53. Kokkinos P, Myers J. Exercise and physical activity: Clinical outcomes and applications. *Circulation* (2010) 122(16):1637–48. doi: 10.1161/CIRCULATIONAHA.110.948349

54. Ross R, Blair SN, Arena R, Church TS, Després JP, Franklin BA, et al. Importance of assessing cardiorespiratory fitness in clinical practice: A case for fitness as a clinical vital sign: A scientific statement from the American heart association. *Circulation* (2016) 134 (24):e653–e699. doi: 10.1161/CIR.0000000000000461

55. Gollnick PD, Piehl K, Saltin B. Selective glycogen depletion pattern in human muscle fibres after exercise of varying intensity and at varying pedalling rates. *J Physiol* (1974) 241(1):45–57. doi: 10.1113/jphysiol.1974.sp010639

56. Altenburg TM, Degens H, Van Mechelen W, Sargeant AJ, De Haan A. Recruitment of single muscle fibers during submaximal cycling exercise. *J Appl Physiol* (2007) 103 (5):1752–6. doi: 10.1152/japplphysiol.00496.2007

57. Booth FW, Chakravarthy MV, Spangenburg EE. Exercise and gene expression: Physiological regulation of the human genome through physical activity. *J Physiol* (2002) 543(2):399–411. doi: 10.1113/jphysiol.2002.019265

frontiers | Frontiers in Endocrinology

TYPE Review
PUBLISHED 26 January 2023
DOI 10.3389/fendo.2023.1120801

OPEN ACCESS

EDITED BY
Vijaya Kumar Pidugu,
National Cancer Institute (NIH),
United States

REVIEWED BY
Poonam Aggarwal,
Indian Institute of Science Education and Research Mohali, India
Swetha Ramadesikan,
Nationwide Children's Hospital Columbus, United States
Kaushik Muralidharan,
Nationwide Children's Hospital, United States

*CORRESPONDENCE
Shohei Fukunaga
korocelica@gmail.com
Yuki Fujita
yuki.fujita@med.shimane-u.ac.jp

SPECIALTY SECTION
This article was submitted to Reproduction, a section of the journal Frontiers in Endocrinology

RECEIVED 10 December 2022
ACCEPTED 13 January 2023
PUBLISHED 26 January 2023

CITATION
Fukunaga S and Fujita Y (2023) Low glomerular number at birth can lead to the development of chronic kidney disease. *Front. Endocrinol.* 14:1120801. doi: 10.3389/fendo.2023.1120801

Low glomerular number at birth can lead to the development of chronic kidney disease

Shohei Fukunaga[1]* and Yuki Fujita[2]*

[1]Division of Nephrology, Shimane University Hospital, Izumo, Shimane, Japan, [2]Department of Developmental Biology, Shimane University Faculty of Medicine, Izumo, Shimane, Japan

Chronic kidney disease (CKD) prevalence is increasing worldwide, and reducing the number of patients with CKD is of utmost importance. The environment during the fetal, perinatal, and early childhood stages may influence CKD development (developmental origins of health and disease). Under conditions of maternal malnutrition, the glomerular number of infants reduces, and the risk of developing CKD may increase. Nephron progenitor cells and ureteric buds interact with each other to form glomeruli at the tip of the ureteric bud. Thus, the number of glomeruli is determined by the number of ureteric bud branches, which are reportedly decreased due to maternal malnutrition, in turn reducing the glomerular number. Four possible mechanisms can explain the low glomerular number resulting from maternal malnutrition: 1) suppression of *c-Ret* expression, 2) suppression of nephron formation by renin-angiotensin-aldosterone system inhibition, 3) exposure to excess glucocorticoids, and 4) promotion of apoptosis. Additionally, nephron formation does not continue after birth in humans. Therefore, a low glomerular number at birth is a lifelong burden on the glomeruli and increases the risk of developing CKD. Therefore, it is important to maintain the glomerular number at birth. Accurate glomerular counts are essential for conducting studies on the glomerular number. The dissector/fractionator method is the gold standard; however, it can only be performed at some institutions. Recently, methods have been developed to measure the glomerular number by combining computed tomography and pathological examination and measure the glomerular count using magnetic resonance imaging. Models of decreased and increased glomerular numbers have been developed. Moreover, research regarding the causes of decreased glomerular number and its relationship with development of lifestyle-related diseases and renal dysfunction has significantly progressed, furthering our understanding of the importance of glomerular number.

KEYWORDS

glomerular number, chronic kidney disease, maternal malnutrition, low birth weight, nephron development

Abbreviations: AngII, Angiotensin II; AT2R, AngII type 2 receptor; BOR, Branchio-oto-renal; CAKUT, causative genes for congenital anomalies of the kidney and urinary tract; CHD7, Chromodomain Helicase DNA Binding Protein 7; CKD, chronic kidney disease; CT, computed tomography; Eya1, Eyes absent homolog 1; GDNF, Glial-cell-line-derived neurotrophic factor; Gfra1, GDNF family receptor α1; Hox11, Hombox gene 11; Pax2, Paired box gene; RAAS, renin angiotensin aldosterone system; Ret, ret proto-oncogene; Sall, sal-like; SEMA3E, Semaphorin-3E; Six, Sine oculis-related homeobox; MRI, magnetic resonance imaging.

1 Introduction

Chronic kidney disease (CKD) is becoming more prevalent worldwide; a prevalence rate of 9.1% was reported in 2017, with an increase of 29.3% since 1990 (1). In addition, approximately 2.6 million patients received renal replacement therapy in 2010, with 5.4 million expected to require it by 2030 (2). To prevent this, CKD onset and progression must be controlled. Furthermore, low-birth-weight infants have low glomerular numbers (3, 4) and are at a higher risk of developing CKD (5), indicating a link between the glomerular number and CKD development risk. This review focuses on the relationship between the glomerular number and renal function, causes of glomerular number decline, and interventions currently under investigation for glomerular number maintenance.

2 Development of glomerulus

The nephrons of the kidney originate from the branching of the ureteric bud, which interacts with the nephron progenitor cells that epithelialize to form the proximal tubules. Then, capillaries are induced to form glomeruli at the ends of branched tubular buds; therefore, the glomerular number is determined by the number of ureteric bud branches. In rats, the formation of nephrons begins on embryonic day (E) 12 and continues for 8–11 postnatal days (6). In mice, it begins on E 11 and continues for 7 postnatal days (7). Nephrogenesis is ongoing at birth in rodents. In humans, nephrons form between 9 and 34–36 weeks of gestation, and glomerulogenesis ceases at birth. However, in preterm infants, nephrons continue to form until 40 postnatal days (8), after which the number of glomeruli does not increase. Therefore, if the number is low at birth, the glomeruli will be overtaxed throughout life.

3 Relationship between glomerular number and renal function

Brenner et al., in their study in 1989, proposed that "essential hypertension is caused by a decrease in the number of glomeruli and nephrons, which results from an undesirable prenatal intrauterine environment (maternal malnutrition, stress, and chemical exposure), genetic factors, and premature birth. Low glomerular number leads to renal glomerular hypertrophy, and eventually to hypertension, CKD, nephrosclerosis, and renal failure" (Brenner's hypothesis) (Figure 1) (9). Histological comparison of the glomerular number in autopsied men who died in a traffic accident in Germany showed a decrease in glomerular number in the hypertension group, thus supporting Brenner's theory (10). Birth weight is a determinant of glomerular number, and a reduction in glomerular number because of low birth weight may be a risk factor for hypertension and end-stage renal failure in adulthood (11). A study of 2.18 million people born in Norway, who were observed for an average of 21 years, conducted between 1967 and 2004, reported that 526 developed end-stage renal failure with low birth weight and intrauterine fetal growth retardation as risk factors (12). Furthermore, a birth weight <2.5 kg is associated with a higher risk of end-stage renal failure than a weight of 3–3.5 kg (13), and patients with CKD show a higher incidence of low birth weight than those without CKD (14). Thus, a low glomerular number due to low birth weight is a risk factor for end-stage renal failure, and how high the glomerular number is maintained at birth may influence the future renal reserve.

4 Causes of decreased glomerular number at birth

While nephron formation does not occur after birth in term infants, it continues until 40 days after birth in preterm infants (8), after which the glomeruli do not increase. Thus, the total glomerular number is expected to be lower after a preterm birth. In addition, juxtamedullary nephrons may predominate over cortical nephrons, are more vulnerable to ischemia, and get easily injured due to obesity, hypertension, and diabetes (15). Thus, preterm infants may have a low glomerular number, high proportion of juxtamedullary nephrons, and may be more prone to lifestyle-related diseases.

The glomerular number reportedly demonstrates racial variation: Caucasian Americans, African Americans, Aboriginals, and Japanese have a total glomerular number of approximately 900,000 (16), 950,000 (16), 680,000 (17), and 670,000 (18), respectively (Table 1).

The glomerular number varies by sex, with a 12% lower glomerular number in women than in men (17, 19, 20).

Furthermore, glomerular number is positively correlated with birth weight (3, 11). For every 1.0 kg increase in birth weight, the number of glomeruli increases by 250,000. Low-birth-weight infants have an increased glomerular size compared with normal-birth-weight infants. This may indicate glomerular over-filtration due to the low glomerular number.

The glomerular number at birth is also strongly related to the maternal nutritional status; during World War II, from 1944 to 1945, some areas of the Netherlands suffered from extreme food shortages, and daily caloric intake dropped to 400–800 kcal per person, which was known as the Dutch famine. Children born to pregnant women who experienced the Dutch famine had a 3.2-fold higher incidence of microalbuminuria and 10% reduction in creatinine clearance during adulthood (21). Additionally, in mice and rats, the glomerular number has been reported to decrease with restricted protein (22, 23), caloric (24), and vitamin A (25) intake during gestation. Both high and low salt intake decrease glomerular number (26), whereas

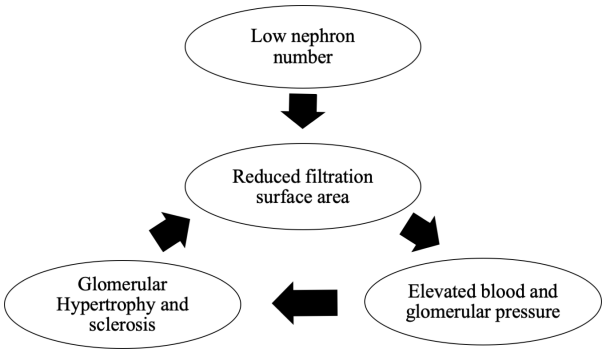

FIGURE 1
Brenner's hypothesis.

TABLE 1 Factors affecting the number of nephrons.

	Glomerular number	
	High	Low
Race (glomerular number)	Caucasian Americans (900,000), African Americans (950,000)	Aboriginals (680,000), Japanese (670,000)
Sex	Men	Women
Birth weight	>2.5 kg (normal-birth-weight)	<2.5 kg (Low-birth-weight)
Diabetes mellitus	No	Yes
Alcohol consumption	No	Yes
Smoking	No	Yes
Maternal nutritional status	No maternal malnutrition	Calories, protein, salt, vitamin A or D deficiency
Hereditary disease	No	Renal coloboma syndrome, Duane-radial ray syndrome, Axenfeld-Rieger syndrome, CHARGE syndrome, Branchio-oto-renal syndrome, Townes-Brocks syndrome, Rokitansky-Küster-Hauser syndrome

vitamin D deficiency prolongs the time taken for nephrogenesis and delays glomerular maturation (27). Animal studies have shown that nephron number decreases with deficiency of various nutrients. Among these nutrients, retinoic acid (RA), in particular, majorly influences the nephron number. In *in vitro* studies, the addition of RA to the culture medium increases the glomerular number (28). In rats, protein restriction decreases nephron number, but protein restriction and administration of RA have been reported to improve nephron number to levels comparable to those of controls (29). In contrast, postnatal administration of RA to preterm baboons does not affect nephron number (30). This may be because nephrogenesis ceases after birth in mammals. Therefore, it is important to ensure that RA is not deficient during gestation.

Four mechanisms have been postulated for the reduction of glomerular number due to low nutritional exposure:

1. Suppression of *c-Ret* expression

Glial-cell-line-derived neurotrophic factor (*GDNF*), which is secreted from the mesenchyme, acts on the Wolffian ducts to germinate and elongate ureteric buds (31) (Figure 2). The GDNF receptor molecule ret proto-oncogene (*Ret*) and its co-receptor GDNF family receptor α1 (*Gfra1*) are expressed in the ureteric bud, and *GDNF* secreted in the mesenchyme transmits signals to the ureteric bud *via Ret*. *GDNF-Ret/Gfra1* signaling is required for ureteric bud germination and elongation. Vitamin A-dependent *c-Ret* expression and nephron formation (32): Vitamin A deficiency suppresses nephron formation, and nephrons form in a vitamin A concentration-dependent manner in culture mediums, which is related to the *c-Ret* expression (33). RA increases *c-Ret* gene expression independent of the *GDNF* gene expression, suggesting that RA may have a direct effect on *c-Ret* expression.

2. Suppression of nephron formation by renin-angiotensin-aldosterone system inhibition

The renin angiotensin aldosterone system (RAAS) seems to be critically important in renal organogenesis. Hombox gene 11 (*Hox11*)/Eyes absent homolog 1 (*Eya1*)/Paired box gene 2 (*Pax2*) form a complex that directly regulates *GDNF* expression and promotes ureteric bud branching (34). Angiotensin II (AngII) upregulates *Pax2* gene expression *via* the AngII type 2 receptor (AT2R). Additionally, AT1R and AT2R expressions are strongly suppressed in a hypotrophic *in utero* environment (35). Therefore, suppression of the renin-angiotensin-aldosterone system in a low-nutritional environment suppresses renal glomerulogenesis. Furthermore, it has been reported that after glomerulogenesis, if the mother is diabetic (36) or obese (37), RAAS activation causes NF-κB activation, which enhances podocyte apoptosis, leading to a decrease in nephron number.

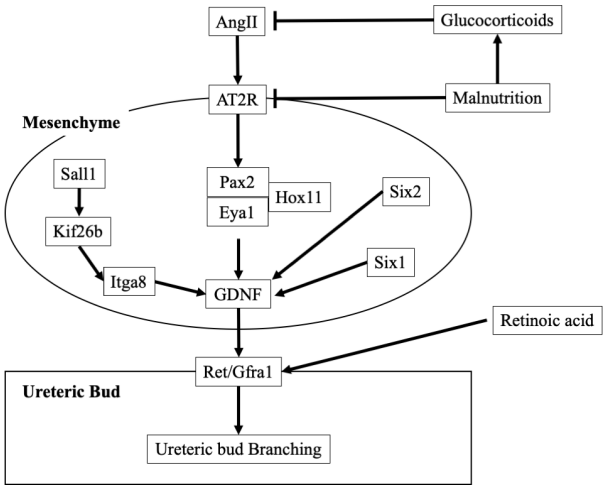

FIGURE 2
Molecular mechanisms of ureteric bud branching. AngII, Angiotensin II; AT2R, AngII type 2 receptor; Eya1, Eyes absent homolog 1; GDNF, Glial-cell-line-derived neurotrophic factor; Gfra1, GDNF family receptor α1; Hox11, Hombox gene 11; Itga, Integrin subunit aplpha; Kif, kinesin superfamily proteins; Pax2, Paired box gene; Ret, ret proto-oncogene; Sall, sal-like; Six, Sine oculis-related homeobox.

3. Exposure to excessive glucocorticoids

When pregnant women are administered high doses of glucocorticoids, infants show decreased birth weight, decreased renal weight, hypertension, proteinuria, decreased sodium excretion capacity, and increased tissue sodium content. When pregnant rats are fed a protein-restricted diet, the placenta suppresses the release of the enzyme 11β-hydroxysteroid dehydrogenase type 2, which deactivates glucocorticoids. Therefore, glucocorticoid deactivation is suppressed, and more active glucocorticoids are transferred to the fetal side. In addition, suppression of 11β-hydroxysteroid dehydrogenase type 2 expression and increased glucocorticoid receptor expression occur in the kidney (38). When the kidney is exposed to excess glucocorticoids, the expression of genes associated with the renin-angiotensin-aldosterone lineage is suppressed. In particular, AT2R-mediated *Pax2* expression is suppressed, and glomerulogenesis is inhibited (39).

4. Increased apoptosis

In low nutritional states, the glomeruli undergo apoptosis and decrease in number. Moreover, under hypotrophic conditions, the expression of DNA methyltransferases is suppressed. Hypomethylation results in *p53* overexpression, which increases the expression of apoptotic Bax and Caspase-3 and suppresses that of cell growth factors, including Bcl-2 and IGF-1. Both these phenomena are assumed to enhance apoptosis, resulting in glomerular apoptosis, thereby decreasing the glomerular number.

Recently, maternal and paternal effects on epigenetic mechanisms have been reported. A chronic high-fat diet administered to father rats caused diabetes mellitus in the next generation of female rat pups due to pancreatic beta cell dysfunction (40). Therefore, paternal lifestyle may affect the glomerular number of the offspring, and further studies are warranted.

In addition to maternal malnutrition, other complications, such as diabetes mellitus (36), alcohol consumption (41, 42), and smoking (43, 44), have also been reported to decrease the glomerular number at birth.

Hereditary disease can also cause abnormal kidney development, resulting in low nephron number. However, the identification of the causative gene is difficult, because kidney development is intricately related to a large number of genes (Figure 2). The identification rate of causative genes for congenital anomalies of the kidney and urinary tract (CAKUT) is reported to be low, with only 6.3% of CAKUT causes identified (45). Among the most frequently reported causative genes for CAKUT is an abnormality in the *Pax2* gene, which causes renal coloboma syndrome. This disease is associated with renal hypoplasia and ocular manifestation (loss of some normal ocular tissue) (46). Diseases similar to renal coloboma syndrome include Duane-radial ray syndrome (abnormal gene: sal-like (*Sall*) 4), Alagille syndrome (abnormal genes: *Jagged 1*, *NOTCH1*), Axenfeld-Rieger syndrome (abnormal gene: *Forkhead Box C1*), and CHARGE syndrome (abnormal genes: Chromodomain Helicase DNA Binding Protein 7 [*CHD7*], Semaphorin-3E [*SEMA3E*]). Branchio-oto-renal (BOR) syndrome is caused by mutation in the *EYA1*, Sine oculis-related homeobox (*Six*) *1*, *Sall1*, and *Six 5* genes (47). This disease has three main features: gill-derived malformation, such as cervical fistula, eustachian fistula, and external ear malformation; various types of hearing loss; and renal and urinary tract malformations (48). In addition, abnormalities in the *Sall 1* gene cause Townes-Brocks syndrome. The Mayer-Rokitansky-Küster-Hauser syndrome also causes renal hypoplasia. The disease is associated with vaginal and uterine defects. The causative gene has not been identified, but it is thought to be caused by an abnormality in a gene essential for the development of Müllerian and Wolffian ducts (49).

In addition, although the although the pathogenic mechanism is unclear, the frequency of CAKUT is approximately 4.5 times higher in children with Down syndrome than in those without it (50). Furthermore, children with Down syndrome potentially have mildly impaired renal function with an estimated glomerular filtration rate of approximately 80% of that of normal children (51).

In Alport syndrome, which is caused by other type 4 collagen abnormalities, the glomerular basement membrane is abnormal and glomerular structure cannot be maintained, leading to end-stage renal failure at a young age.

5 Methods to determine the glomerular count

Accurate measurement of the glomerular count is important to ascertain the glomerular number. Currently, five methods are used for glomerular counting, each with their own advantages and disadvantages (Table 2).

5.1 Acid maceration

Decapsulated kidneys are coarsely chopped and incubated in 6N hydrochloric acid at 37°C. The kidneys are disrupted *via* pipetting. Distilled water is added to the samples, which are then incubated overnight at 4°C. The sample is placed in a culture dish with a 2-mm grid, and the glomeruli are counted (52). This method is rapid, simple, and inexpensive. However, structural abnormalities of the glomeruli may make them susceptible to acid digestion, and counting errors may make assessment inaccurate.

TABLE 2 Methods of determining the glomerular count.

	Accuracy	Difficulty
Acid maceration	Somewhat low	Easy
Number of glomeruli per unit area	Low	Easy
Dissector/fractionator method	High	Difficult
Renal biopsy + CT	Somewhat high	Somewhat difficult
MRI	Somewhat high	Somewhat difficult

CT, computed tomography; MRI, magnetic resonance imaging.

5.2 Number of glomeruli per unit area

The number of glomeruli found in a tissue section is measured and presented as the number of glomeruli per unit area of the section. Although this method has been used in many studies, the number of glomeruli per unit area does not represent the total number of glomeruli in the kidney. The number of glomeruli observed in a tissue section is influenced not only by the number of glomeruli in the kidney but also by the size and shape of the glomeruli and thickness of the section. Larger glomeruli are more likely to appear in sections than smaller glomeruli. Therefore, the number of glomeruli per unit area alone cannot be used to evaluate the total number of glomeruli in the kidneys.

5.3 Dissector/fractionator method

This measurement method (53, 54) uses the Cavalieri and fractionator principles (55) and is considered the gold standard for determining the total glomerular number. The accuracy of other glomerular counting methods was validated *via* comparison with this method. However, the equipment and technology required for measurement, as well as the cost and time involved, limit the number of facilities that are equipped to use this method.

5.4 Renal biopsy + computed tomography

Glomerular count estimation using a renal biopsy specimen from a renal transplant donor and performing a contrast-enhanced CT before donation has been attempted (56). The glomerular density of the renal biopsy specimen was measured, and the kidney was reconstructed three-dimensionally from contrast-enhanced CT images to estimate the glomerular density and total renal cortical volume. The results of this method are similar to those obtained using the dissector/fractionator method. However, contrast-enhanced CT and renal biopsy need to be performed.

5.5 Magnetic resonance imaging

A method was developed to measure the glomerular count by MRI using cationic ferritin as a contrast agent. Cationized ferritin is injected intravenously to label the glomerular basement membrane of the kidney, and MRI imaging highlights the glomeruli in black. This has been reported *in vitro* in mice and rats (57) and *in vivo* in rats (58), but not in humans. An advantage of this method is that it does not require kidney specimen preparation. In addition, *in vivo* measurement may be possible; however, this method has only been reported in rats, and its safety in humans remains unclear. Furthermore, an MRI machine is required to perform this test.

6 Interventions to preserve nephron number at birth

6.1 Low-nephron number model

A low-nephron number model is necessary to examine the changes that occur in an organism when the nephron number is reduced. As aforementioned, animal models have been created with low nephron count due to maternal malnutrition. Another low-nephron number model is the hypogonadism rat model with testicular and renal hypoplasia (59). The glomerular number in this model was approximately 80% lower than the normal number. Additionally, poor ureteric bud growth, the presence of undifferentiated mesenchymal cells, and cortical non-thinning was observed, suggesting that abnormal cell proliferation results in renal hypoplasia.

Caspase-3 knockout mice also show decreased nephron numbers (60). Caspase-3 is involved in migration, proliferation, differentiation, and apoptosis. Caspase-3 knockout mice demonstrate suppressed ureteric bud branching, resulting in a low glomerular number.

The two models described above are low-nephron number models resulting from genetic abnormalities, making it difficult to control the degree of glomerular number decline.

To address that, a low-nephron number model using the Six2/iDTR model has been proposed by the author (61). This model expresses the diphtheria toxin receptor in nephron progenitor cells, which can be removed by administering diphtheria toxin to the amniotic fluid during the embryonic period. The observed kidney size and glomerular count reduction is inversely proportional to the diphtheria toxin dose, which can be employed to achieve any degree of glomerular number reduction.

6.2 High-nephron number models

High-nephron number models have also been developed. If a low nephron number increases the CKD risk, a high number may reduce it. One model of increased glomerular count involved transgenic mice expressing the truncated type II activin receptor (62). In this model, signaling through the activin receptor was attenuated, and the total glomerular number increased to approximately 180% of that in normal mice. However, the serum urea nitrogen, creatinine, and creatinine clearance rates were comparable to those of normal mice.

Another method reported by the authors was to boost the glomerular number by intraperitoneally administering RA during the embryonic period (63), which increased the total number of glomeruli in mouse pups by approximately 1.5-fold than that in the control group. No genetic modification was required, and the number of glomeruli could easily be increased. However, its effects on renal function remain unclear.

7 Clinical interventions for low nephron number

To reduce the risk of developing CKD due to low nephron number, it is important to first prevent low nephron numbers. Interventions for hereditary disease are difficult, but those for low nephron number caused by the maternal environment are possible. Pregnant women should be taught regarding proper nutrition, weight control, smoking cessation, and alcohol abstinence. In addition, management of diabetes and obesity, if present, is also important.

Once CKD progresses, it is difficult to improve renal function. Therefore, early detection of patients with low nephron numbers is crucial. Serum creatinine and cystatin C levels increase with renal

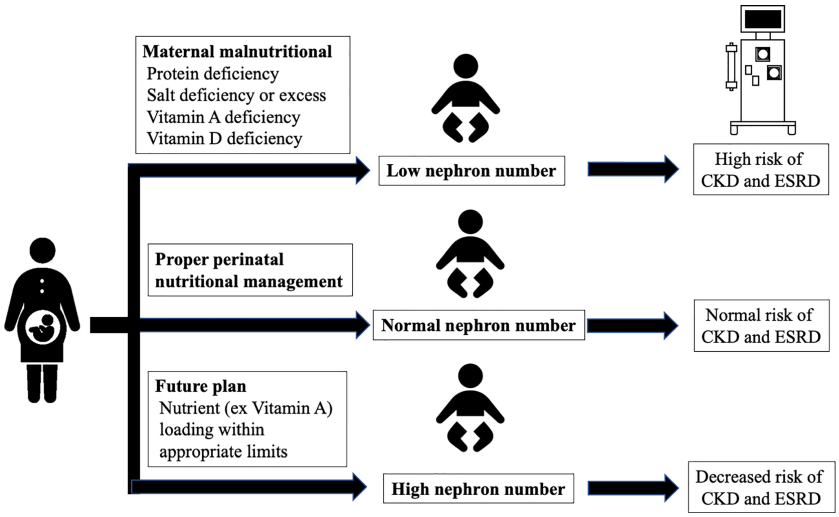

FIGURE 3
Interventions for glomerular number. CKD, chronic kidney disease; ESRD, end-stage renal disease.

dysfunction. In addition, urinary β2-microglobulin and N-acetyl-β-D-glucosaminidase are markers of tubular damage. However, all of these biomarkers are elevated after damage has occurred, and there is currently no biomarker that can detect low nephron numbers before damage has occurred.

Therefore, children at risk for low nephron numbers, such as preterm and low-birth-weight infants, should be evaluated for kidney involvement. In addition, renal evaluation is advisable, because many inherited diseases are often associated with abnormalities in renal development. Kidney size correlates with the nephron number (64), and in children, renal volume and the sum of the left and right kidney length diameters are strongly and sexually correlated with glomerular filtration rate (65). Therefore, evaluation of the kidneys should include an assessment of renal function, such as serum creatinine levels, as well as morphology using abdominal echocardiography and other techniques.

Patients with a low nephron number need to have their intraglomerular pressure lowered, as increased intraglomerular pressure causes progressive glomerulosclerosis. Renin angiotensin system inhibitors, sodium glucose cotransporter 2 inhibitors, and mineralocorticoid receptor antagonists may be effective in this regard. Dietary therapy, such as salt reduction, is also important. In addition, the first 1,000 days of life, from the fetal period to 2 years of age, are the most critical in the developmental program, and avoiding nutritional deficiencies during this period can reduce lifestyle-related diseases (CKD, hypertension, or diabetes) that may develop later in adulthood (66).

8 Conclusion

An undesirable prenatal intrauterine environment, including maternal malnutrition, decreases the fetal glomerular number and increases the risk of CKD; therefore, an appropriate environment should be maintained to prevent the decrease in fetal glomerular number. Altogether, proper perinatal nutritional management and preventing the decrease of and increasing the glomerular number at birth may greatly reduce the incidence of CKD in the future (Figure 3).

Author contributions

SF is the first author. Both authors contributed to the article and approved the submitted version.

Acknowledgments

We would like to thank Editage (www.editage.com) for the English language editing.

Conflict of interest

The authors declare that the research was conducted in the absence of any commercial or financial relationships that could be construed as a potential conflict of interest.

Publisher's note

References

1. GBD Chronic Kidney Disease Collaboration. Global, regional, and national burden of chronic kidney disease, 1990–2017: a systematic analysis for the global burden of disease study 2017. *Lancet* (2020) 395:709–33. doi: 10.1016/S0140-6736(20)30045-3

2. Liyanage T, Ninomiya T, Jha V, Neal B, Patrice HM, Okpechi I, et al. Worldwide access to treatment for end-stage kidney disease: a systematic review. *Lancet* (2015) 385:1975–82. doi: 10.1016/S0140-6736(14)61601-9

3. Mañalich R, Reyes L, Herrera M, Melendi C, Fundora I. Relationship between weight at birth and the number and size of renal glomeruli in humans: a histomorphometric study. *Kidney Int* (2000) 58:770–3. doi: 10.1046/j.1523-1755.2000.00225.x

4. Silver LE, Decamps PJ, Korst LM, Platt LD, Castro L. Intrauterine growth restriction is accompanied by decreased renal volume in the human fetus. *Am J Obstet Gynecol* (2003) 188:1320–5. doi: 10.1067/mob.2003.270

5. White SL, Perkovic V, Cass A, Chang CL, Poulter NR, Spector T, et al. Is low birth weight an antecedent of CKD in later life? a systematic review of observational studies. *Am J Kidney Dis* (2009) 54:248–61. doi: 10.1053/j.ajkd.2008.12.042

6. Cullen-McEwen LA, Armitage JA, Nyengaard JR, Moritz KM, Bertram JF. A design-based method for estimating glomerular number in the developing kidney. *Am J Physiol Renal Physiol* (2011) 300:F1448–53. doi: 10.1152/ajprenal.00055.2011

7. Sims-Lucas S, Caruana G, Dowling J, Kett MM, Bertram JF. Augmented and accelerated nephrogenesis in TGF-beta2 heterozygous mutant mice. *Pediatr Res* (2008) 63:607–12. doi: 10.1203/PDR.0b013e31816d9130

8. Rodríguez MM, Gómez AH, Abitbol CL, Chandar JJ, Duara S, Zilleruelo GE. Histomorphometric analysis of postnatal glomerulogenesis in extremely preterm infants. *Pediatr Dev Pathol* (2004) 7:17–25. doi: 10.1007/s10024-003-3029-2

9. Brenner BM, Garcia DL, Anderson S. Glomeruli and blood pressure. less of one, more the other? *Am J Hypertens* (1988) 1:335–47. doi: 10.1093/ajh/1.4.335

10. Keller G, Zimmer G, Mall G, Ritz E, Amann K. Nephron number in patients with primary hypertension. *N Engl J Med* (2003) 348:101–8. doi: 10.1056/NEJMoa020549

11. Hughson M, Farris AB3rd, Douglas-Denton R, Hoy WE, Bertram JF. Glomerular number and size in autopsy kidneys: the relationship to birth weight. *Kidney Int* (2003) 63:2113–22. doi: 10.1046/j.1523-1755.2003.00018.x

12. Vikse BE, Irgens LM, Leivestad T, Hallan S, Iversen BM. Low birth weight increases risk for end-stage renal disease. *J Am Soc Nephrol* (2008) 19:151–7. doi: 10.1681/ASN.2007020252

13. Lackland DT, Bendall HE, Osmond C, Egan BM, Barker DJ. Low birth weights contribute to high rates of early-onset chronic renal failure in the southeastern united states. *Arch Intern Med* (2000) 160:1472–6. doi: 10.1001/archinte.160.10.1472

14. Fan ZJ, Lackland DT, Lipsitz SR, Nicholas JS. The association of low birthweight and chronic renal failure among Medicaid young adults with diabetes and/or hypertension. *Public Health Rep* (2006) 121:239–44. doi: 10.1177/003335490612100304

15. Cowley AWJr, Mori T, Mattson D, Zou AP. Role of renal NO production in the regulation of medullary blood flow. *Am J Physiol Regul Integr Comp Physiol* (2003) 284: R1355–69. doi: 10.1152/ajpregu.00701.2002

16. Hughson MD, Gobe GC, Hoy WE, Manning RDJr, Douglas-Denton R, Bertram JF. Associations of glomerular number and birth weight with clinicopathological features of African americans and whites. *Am J Kidney Dis* (2008) 52:18–28. doi: 10.1053/j.ajkd.2008.03.023

17. Hoy WE, Hughson MD, Singh GR, Douglas-Denton R, Bertram JF. Reduced nephron number and glomerulomegaly in Australian aborigines: a group at high risk for renal disease and hypertension. *Kidney Int* (2006) 70:104–10. doi: 10.1038/sj.ki.5000397

18. Kanzaki G, Puelles VG, Cullen-McEwen LA, Hoy WE, Okabayashi Y, Tsuboi N, et al. New insights on glomerular hyperfiltration: a Japanese autopsy study. *JCI Insight* (2017) 2:e94334. doi: 10.1172/jci.insight.94334

19. Nyengaard JR, Bendtsen TF. Glomerular number and size in relation to age, kidney weight, and body surface in normal man. *Anat Rec* (1992) 232:194–201. doi: 10.1002/ar.1092320205

20. Hoy WE, Bertram JF, Denton RD, Zimanyi M, Samuel T, Hughson MD. Nephron number, glomerular volume, renal disease and hypertension. *Curr Opin Nephrol Hypertens* (2008) 17:258–65. doi: 10.1097/MNH.0b013e3282f9b1a5

21. Painter RC, Roseboom TJ, van Montfrans GA, Bossuyt PM, Krediet RT, Osmond C, et al. Microalbuminuria in adults after prenatal exposure to the Dutch famine. *J Am Soc Nephrol* (2005) 16:189–94. doi: 10.1681/ASN.2004060474

22. Hoppe CC, Evans RG, Moritz KM, Cullen-McEwen LA, Fitzgerald SM, Dowling J, et al. Combined prenatal and postnatal protein restriction influences adult kidney structure, function, and arterial pressure. *Am J Physiol Regul Integr Comp Physiol* (2007) 292:R462–9. doi: 10.1152/ajpregu.00079.2006

23. Hoppe CC, Evans RG, Bertram JF, Moritz KM. Effects of dietary protein restriction on nephron number in the mouse. *Am J Physiol Regul Integr Comp Physiol* (2007) 292: R1768–74. doi: 10.1152/ajpregu.00442.2006

24. Almeida JR, Mandarim-de-Lacerda CA. Maternal gestational protein-calorie restriction decreases the number of glomeruli and causes glomerular hypertrophy in adult hypertensive rats. *Am J Obstet Gynecol* (2005) 192:945–51. doi: 10.1016/j.ajog.2004.09.010

25. Lelièvre-Pégorier M, Vilar J, Ferrier ML, Moreau E, Freund N, Gilbert T, et al. Mild vitamin a deficiency leads to inborn nephron deficit in the rat. *Kidney Int* (1998) 54:1455–62. doi: 10.1046/j.1523-1755.1998.00151.x

26. Koleganova N, Piecha G, Ritz E, Becker LE, Müller A, Weckbach M, et al. Both high and low maternal salt intake in pregnancy alter kidney development in the offspring. *Am J Physiol Renal Physiol* (2011) 301:F344–54. doi: 10.1152/ajprenal.00626.2010

27. Nascimento FA, Ceciliano TC, Aguila MB, Mandarim-de-Lacerda CA. Maternal vitamin d deficiency delays glomerular maturity in F1 and F2 offspring. *PloS One* (2012) 7: e41740. doi: 10.1371/journal.pone.0041740

28. Vilar J, Gilbert T, Moreau E, Merlet-Bénichou C. Metanephros organogenesis is highly stimulated by vitamin a derivatives in organ culture. *Kidney Int* (1996) 49:1478–87. doi: 10.1038/ki.1996.208

29. Makrakis J, Zimanyi MA, Black MJ. Retinoic acid enhances nephron endowment in rats exposed to maternal protein restriction. *Pediatr Nephrol* (2007) 22:1861–7. doi: 10.1007/s00467-007-0572-5

30. Sutherland MR, Gubhaju L, Yoder BA, Stahlman MT, Black MJ. The effects of postnatal retinoic acid administration on nephron endowment in the preterm baboon kidney. *Pediatr Res* (2009) 65:397–402. doi: 10.1203/PDR.0b013e3181975f52

31. Sainio K, Suvanto P, Davies J, Wartiovaara J, Wartiovaara K, Saarma M, et al. Glial-cell-line-derived neurotrophic factor is required for bud initiation from ureteric epithelium. *Development* (1997) 124:4077–87. doi: 10.1242/dev.124.20.4077

32. Moreau E, Vilar J, Lelièvre-Pégorier M, Merlet-Bénichou C, Gilbert T. Regulation of c-ret expression by retinoic acid in rat metanephros: implication in nephron mass control. *Am J Physiol* (1998) 275:F938–45. doi: 10.1152/ajprenal.1998.275.6.F938

33. Merlet-Bénichou C. Influence of fetal environment on kidney development. *Int J Dev Biol* (1999) 43:453–6.

34. Gong KQ, Yallowitz AR, Sun H, Dressler GR, Wellik DM. A hox-Eya-Pax complex regulates early kidney developmental gene expression. *Mol Cell Biol* (2007) 27:7661–8. doi: 10.1128/MCB.00465-07

35. Zhang SL, Moini B, Ingelfinger JR. Angiotensin II increases pax-2 expression in fetal kidney cells *via* the AT2 receptor. *J Am Soc Nephrol* (2004) 15:1452–65. doi: 10.1097/01.asn.0000130567.76794.58

36. Tran S, Chen YW, Chenier I, Chan JS, Quaggin S, Hébert MJ, et al. Maternal diabetes modulates renal morphogenesis in offspring. *J Am Soc Nephrol* (2008) 19:943–52. doi: 10.1681/ASN.2007080864

37. Prior LJ, Davern PJ, Burke SL, Lim K, Armitage JA, Head GA. Exposure to a high-fat diet during development alters leptin and ghrelin sensitivity and elevates renal sympathetic nerve activity and arterial pressure in rabbits. *Hypertension* (2014) 63:338–45. doi: 10.1161/HYPERTENSIONAHA

38. Bertram C, Trowern AR, Copin N, Jackson AA, Whorwood CB. The maternal diet during pregnancy programs altered expression of the glucocorticoid receptor and type 2 11beta-hydroxysteroid dehydrogenase: potential molecular mechanisms underlying the programming of hypertension in utero. *Endocrinology* (2001) 142:2841–53. doi: 10.1210/endo.142.7.8238

39. Pham TD, MacLennan NK, Chiu CT, Laksana GS, Hsu JL, Lane RH. Uteroplacental insufficiency increases apoptosis and alters p53 gene methylation in the full-term IUGR rat kidney. *Am J Physiol Regul Integr Comp Physiol* (2003) 285:R962–70. doi: 10.1152/ajpregu.00201.2003

40. Ng SF, Lin RC, Laybutt DR, Barres R, Owens JA, Morris MJ. Chronic high-fat diet in fathers programs β-cell dysfunction in female rat offspring. *Nature* (2010) 467:963–6. doi: 10.1038/nature09491

41. Gray SP, Denton KM, Cullen-McEwen L, Bertram JF, Moritz KM. Prenatal exposure to alcohol reduces nephron number and raises blood pressure in progeny. *J Am Soc Nephrol* (2010) 21:1891–902. doi: 10.1681/ASN.2010040368

42. Gray SP, Kenna K, Bertram JF, Hoy WE, Yan EB, Bocking AD, et al. Repeated ethanol exposure during late gestation decreases nephron endowment in fetal sheep. *Am J Physiol Regul Integr Comp Physiol* (2008) 295:R568–74. doi: 10.1152/ajpregu.90316.2008

43. Al-Odat I, Chen H, Chan YL, Amgad S, Wong MG, Gill A, et al. The impact of maternal cigarette smoke exposure in a rodent model on renal development in the offspring. *PloS One* (2014) 9:e103443. doi: 10.1371/journal.pone.0103443

44. Taal HR, Geelhoed JJ, Steegers EA, Hofman A, Moll HA, Lequin M, et al. Maternal smoking during pregnancy and kidney volume in the offspring: the generation r study. *Pediatr Nephrol* (2011) 26:1275–83. doi: 10.1007/s00467-011-1848-3

45. Hwang DY, Dworschak GC, Kohl S, Saisawat P, Vivante A, Hilger AC, et al. Mutations in 12 known dominant disease-causing genes clarify many congenital anomalies of the kidney and urinary tract. *Kidney Int* (2014) 85:1429–33. doi: 10.1038/ki.2013.508

46. Sanyanusin P, Schimmenti LA, McNoe LA, Ward TA, Pierpont ME, Sullivan MJ, et al. Mutation of the PAX2 gene in a family with optic nerve colobomas, renal anomalies and vesicoureteral reflux. *Nat Genet* (1995) 9:358–64. doi: 10.1038/ng0495-358

47. Kochhar A, Fischer SM, Kimberling WJ, Smith RJ. Branchio-oto-renal syndrome. *Am J Med Genet A* (2007) 143A:1671–8. doi: 10.1002/ajmg.a.31561

48. Chen A, Francis M, Ni L, Cremers CW, Kimberling WJ, Sato Y, et al. Phenotypic manifestations of branchio-oto-renal syndrome. *Am J Med Genet* (1995) 58:365–70. doi: 10.1002/ajmg.1320580413

49. Chen N, Zhao S, Jolly A, Wang L, Pan H, Yuan J, et al. Perturbations of genes essential for müllerian duct and wölffian duct development in Mayer-Rokitansky-Küster-Hauser syndrome. *Am J Hum Genet* (2021) 108:337–45. doi: 10.1016/j.ajhg.2020

50. Kupferman JC, Druschel CM, Kupchik GS. Increased prevalence of renal and urinary tract anomalies in children with down syndrome. *Pediatrics* (2009) 124:e615–21. doi: 10.1542/peds.2009-0181

51. Yamakawa S, Nagai T, Uemura O. Down syndrome and mild kidney dysfunction. *Pediatr Int* (2018) 60:391–3. doi: 10.1111/ped.13525

52. MacKay K, Striker LJ, Pinkert CA, Brinster RL, Striker GE. Glomerulosclerosis and renal cysts in mice transgenic for the early region of SV40. *Kidney Int* (1987) 32:827–37. doi: 10.1038/ki.1987.283

53. Bertram JF. Counting in the kidney. *Kidney Int* (2001) 59:792–6. doi: 10.1046/j.1523-1755.2001.059002792.x

54. Cullen-McEwen LA, Douglas-Denton RN, Bertram JF. Estimating total nephron number in the adult kidney using the physical disector/fractionator combination. *Methods Mol Biol* (2012) 886:333–50. doi: 10.1007/978-1-61779-851-1_30

55. Hinchliffe SA, Sargent PH, Howard CV, Chan YF, van Velzen D. Human intrauterine renal growth expressed in absolute number of glomeruli assessed by the disector method and cavalieri principle. *Lab Invest* (1991) 64:777–84.

56. Sasaki T, Tsuboi N, Kanzaki G, Haruhara K, Okabayashi Y, Koike K, et al. Biopsy-based estimation of total nephron number in Japanese living kidney donors. *Clin Exp Nephrol* (2019) 23:629–37. doi: 10.1007/s10157-018-01686-2

57. Beeman SC, Cullen-McEwen LA, Puelles VG, Zhang M, Wu T, Baldelomar EJ, et al. MRI-Based glomerular morphology and pathology in whole human kidneys. *Am J Physiol Renal Physiol* (2014) 306:F1381–90. doi: 10.1152/ajprenal.00092.2014

58. Bennett KM, Baldelomar EJ, Morozov D, Chevalier RL, Charlton JR. New imaging tools to measure nephron number *in vivo*: opportunities for developmental nephrology. *J Dev Orig Health Dis* (2021) 12:179–83. doi: 10.1017/S204017442000001X

59. Suzuki H, Yagi M, Saito K, Suzuki K. Embryonic pathogenesis of hypogonadism and renal hypoplasia in hgn/hgn rats characterized by male sterility, reduced female fertility and progressive renal insufficiency. *Congenit Anom (Kyoto)* (2007) 47:34–44. doi: 10.1111/j.1741-4520.2006.00138.x

60. Araki T, Saruta T, Okano H, Miura M. Caspase activity is required for nephrogenesis in the developing mouse metanephros. *Exp Cell Res* (1999) 248:423–9. doi: 10.1006/excr.1999.4424

61. Fukunaga S, Yamanaka S, Fujimoto T, Tajiri S, Uchiyama T, Matsumoto K, et al. Optimal route of diphtheria toxin administration to eliminate native nephron progenitor cells *in vivo* for kidney regeneration. *Biochem Biophys Res Commun* (2018) 496:1176–82. doi: 10.1016/j.bbrc.2018.01.166

62. Maeshima A, Shiozaki S, Tajima T, Nakazato Y, Naruse T, Kojima I. Number of glomeruli is increased in the kidney of transgenic mice expressing the truncated type II activin receptor. *Biochem Biophys Res Commun* (2000) 268:445–9. doi: 10.1006/bbrc.2000.2171

63. Fukunaga S, Ogawa N, Matsumoto A, Ito T, Tanabe K, Otani H. Administration of retinoic acid to pregnant mice increases the number of fetal mouse glomeruli. *Biochem Biophys Rep* (2022) 30:101245. doi: 10.1016/j.bbrep.2022.101245

64. Bueters RR, van de Kar NC, Schreuder MF. Adult renal size is not a suitable marker for nephron numbers: an individual patient data meta-analysis. *Kidney Blood Press Res* (2013) 37:540–6. doi: 10.1159/000355734

65. Adibi A, Adibi I, Khosravi P. Do kidney sizes in ultrasonography correlate to glomerular filtration rate in healthy children? *Australas Radiol* (2007) 51:555–9. doi: 10.1111/j.1440-1673.2007.01864.x

66. UNICEF Nutrition report. IMPROVING CHILD NUTRITION. (2013). Available at: https://data.unicef.org/resources/improving-child-nutrition-the-achievable-imperative-for-global-progress/.

frontiers | Frontiers in Endocrinology

TYPE Original Research
PUBLISHED 31 January 2023
DOI 10.3389/fendo.2022.1049541

OPEN ACCESS

EDITED BY
Donna Toufexis,
University of Vermont, United States

REVIEWED BY
Odile Viltart,
INSERM U1266 Institut de Psychiatrie et Neurosciences de Paris, France
Joanna Spencer-Segal,
University of Michigan, United States

*CORRESPONDENCE
Elizabeth A. Lawson
ealawson@partners.org

†These authors have contributed equally to this work and share first authorship

SPECIALTY SECTION
This article was submitted to Neuroendocrine Science, a section of the journal Frontiers in Endocrinology

RECEIVED 20 September 2022
ACCEPTED 28 December 2022
PUBLISHED 31 January 2023

CITATION
Plessow F, Galbiati F, Eddy KT, Misra M, Miller KK, Klibanski A, Aulinas A and Lawson EA (2023) Low oxytocin levels are broadly associated with more pronounced psychopathology in anorexia nervosa with primarily restricting but not binge/purge eating behavior.
Front. Endocrinol. 13:1049541.
doi: 10.3389/fendo.2022.1049541

Low oxytocin levels are broadly associated with more pronounced psychopathology in anorexia nervosa with primarily restricting but not binge/purge eating behavior

Franziska Plessow[1†], Francesca Galbiati[1†], Kamryn T. Eddy[2], Madhusmita Misra[1,3], Karen K. Miller[1], Anne Klibanski[1], Anna Aulinas[1] and Elizabeth A. Lawson[1*]

[1]Neuroendocrine Unit, Department of Medicine, Massachusetts General Hospital and Harvard Medical School, Boston, MA, United States, [2]Eating Disorders Clinical and Research Program, Department of Psychiatry, Massachusetts General Hospital and Harvard Medical School, Boston, MA, United States, [3]Division of Pediatric Endocrinology, Massachusetts General Hospital for Children and Harvard Medical School, Boston, MA, United States

Objective: Anorexia nervosa (AN) is commonly associated with depression, anxiety, and deficits in socioemotional functioning. Basal levels of oxytocin, a neurohormone with antidepressant, anxiolytic, and prosocial properties, are low in women with AN. However, the relationship between oxytocin and psychopathology of AN/atypical AN has not been examined in individuals with primarily food restriction (AN/AtypAN-R) or those with restriction plus binge/purge behaviors (AN/AtypAN-BP) alone, which is important to further elucidate the neurobiology of different AN presentations. We investigated whether oxytocin levels are related to eating, affective, and socioemotional psychopathology in women with AN/AtypAN-R and separately AN/AtypAN-BP.

Methods: In a cross-sectional study of 53 women with low-weight AN or atypical AN based on DSM-5 (AN/AtypAN-R: n=21, AN/AtypAN-BP: n=32), we obtained fasting serum oxytocin levels and self-report measures of psychopathology, including the Eating Disorder Examination–Questionnaire (EDE-Q), Beck Depression Inventory-IA (BDI), State-Trait Anxiety Inventory (STAI), and Toronto Alexithymia Scale (TAS-20).

Results: In individuals with AN/AtypAN-R, oxytocin levels were negatively associated with eating psychopathology (EDE-Q Global Score: r=-0.49, p=0.024), depressive and anxiety symptoms (BDI Total Score: r=-0.55, p=0.009; STAI Trait Score: r=-0.63, p=0.002), and socioemotional symptoms (TAS-20 Difficulty Identifying Feelings Score: r=-0.49, p=0.023). In contrast, in those with AN/AtypAN-BP oxytocin levels were negatively associated with depressive symptoms only (BDI Total Score: r=-0.52, p=0.049).

Conclusions: These findings support the notion that AN/AtypAN-R and AN/AtypAN-BP might have divergent underlying neurobiology. Understanding these

10.3389/fendo.2022.1049541

differences is crucial to develop targeted treatments for a population with high levels of chronicity, for which no specific pharmacological treatments are currently available.

Clinical trial registration: https://clinicaltrials.gov, identifier: NCT01121211

KEYWORDS

anorexia nervosa, binge/purge behavior, dietary restriction, oxytocin, psychopathology

1 Introduction

Anorexia nervosa (AN), a psychiatric disorder with a prime onset period in adolescence and early adulthood, manifests with different clinical presentations, calling for treatments based on carefully developed pathophysiological models. Its core clinical features include a distorted body image, intense fear of gaining weight, and food restriction despite a low body mass index (BMI) (1). It is also characterized by the common occurrence of comorbid symptoms, including depressive and anxiety symptoms and deficits in socioemotional functioning (2–4). AN has two major clinical presentations; (i) predominantly food restriction, or (ii) food restriction combined with cycles of binge eating and/or purging behaviors. AN is often treatment-refractory, and novel treatments are needed to improve outcomes. Investigating the neurobiological mechanisms underlying restricting and binge/purge presentations could inform urgently needed individualized treatment strategies.

The neurohormone oxytocin affects food intake as well as cognitive, emotional, and social functioning and might play a role in the pathophysiology of AN spanning ED pathology and associated depressive and anxiety symptoms and impairments in socioemotional functioning (5). Prior studies of females with AN demonstrate oxytocin deficiency in the setting of chronic starvation (6–9). These findings are complemented by studies showing that weight-restored individuals with a history of AN have lower basal oxytocin levels than healthy controls, suggesting chronic alteration of oxytocin signaling (2, 10). Furthermore, our group has previously shown that in women with restored weight but persistent symptoms of disordered eating, fasting oxytocin levels were associated with greater ED pathology and more pronounced anxiety (2). Similarly, in a mixed sample of women with low-weight AN, partially recovered AN (90-120% expected body weight [EBW]), and healthy controls, we previously found an association between low fasting oxytocin levels and increased symptoms of alexithymia independent of BMI and estrogen status (11). Finally, in individuals with AN, oxytocin receptor polymorphisms were found to be associated with severity of ED pathology, and oxytocin and oxytocin receptor polymorphisms showed associations with disorder-specific decrements in emotion perception ability (12, 13), further pointing towards a potential involvement of the oxytocin system in AN psychopathology. While establishing a clinically relevant oxytocin-deficient state in AN, most investigations to date have examined oxytocin levels in AN without distinguishing between restricting and binge/purge subtypes, and the few studies that compared oxytocin levels across AN subtypes did not investigate their associations with type and severity of psychopathology within each AN presentation (2, 5, 7, 10, 11, 14, 15). One small study showed low levels of oxytocin in cerebrospinal fluid (CSF) in individuals with AN restricting type (n=5) but not those with AN binge/purge type (n=12) compared to healthy controls (n=11) (7). Other studies detected no differences in oxytocin levels between subtypes when assessed peripherally (14, 15). Of note, peripheral oxytocin levels have been shown to correlate with CSF levels, however current evidence indicates that this relationship may be context-dependent (16–19). To our knowledge, no studies have analyzed the correlation between oxytocin levels and psychopathology in different AN presentations, which could have clinical implications.

We aimed to extend our understanding of the role of oxytocin in the pathophysiology of AN and its different presentations by investigating the relationship between fasting peripheral oxytocin levels and severity of psychopathology, including eating disorder (ED) psychopathology, depressive and anxiety symptoms, and deficits in socioemotional functioning. Using a transdiagnostic approach, we recruited women with AN (BMI<18.5) and atypical AN (BMI≥18.5) who presented with active primarily restricting behaviors (AN/AtypAN-R) and those who were restricting combined with bingeing and/or purging behaviors (AN/AtypAN-BP). Based on the preliminary finding that, compared to healthy controls, CSF oxytocin levels were low in individuals with AN of the restricting type but not those with the binge/purge subtype (7), we hypothesized that lower fasting serum oxytocin levels would be associated with more pronounced ED psychopathology, depressive and anxiety symptoms, and deficits in socioemotional functioning in women with AN/AtypAN-R but not those with AN/AtypAN-BP.

Abbreviations: AN, anorexia nervosa; AN/AtypAN-BP, AN with dietary restriction plus binge/purge behavior; AN/AtypAN-R, AN with solely dietary restriction; BDI, Beck Depression Inventory-IA; BMI, body mass index; BRAC, Brigham Research Assay Core; CSF, cerebrospinal fluid; CV, coefficient of variance; DAPP-BQ, Dimensional Assessment of Personality Pathology – Basic Questionnaire; EBW, expected body weight; EDE-Q, Eating Disorder Examination – Questionnaire; GAD, generalized anxiety disorder; ISEL, Interpersonal Support Evaluation List; LSAS-SR, Liebowitz Social Anxiety Scale; MDD, major depressive disorder; OCD, obsessive compulsive disorder; OCPs, oral contraceptive pills; PTSD, posttraumatic stress disorder; STAI, State-Trait Anxiety Inventory; TAS-20, Toronto Alexithymia Scale.

2 Material and methods

2.1 Participants

Fifty-three females, 18-49 years, who met DSM-5 criteria for AN (n=31) or atypical AN (n=22) and participated in a randomized, placebo-controlled clinical trial of low-dose testosterone therapy for AN (clinicaltrials.gov identifier: NCT01121211) or an observational study of neurobiological underpinnings of illness trajectories in a sample of adolescent and young adult females with low-weight eating disorders (R01 MH103402), all of them with active AN or atypical AN at the time of data collection, were included in this study. Clinical characteristics, including endocrine parameters from partially overlapping datasets have been previously published (14, 20–23). However, the relationship between oxytocin levels and psychopathology, the focus of this paper, has not been reported. Binge/purge behaviors were defined by the occurrence of at least three behaviors over the past three months (frequency: ≥1/month). Of the 31 women with AN, 12 met criteria for AN/AtypAN-R, and 19 met criteria for AN/AtypAN-BP. Of the 22 participants with atypical AN, nine were categorized as AN/AtypAN-R and 13 as AN/AtypAN-BP. Participants were recruited from the community through advertisements and referrals from healthcare providers.

Exclusion criteria included a history of psychotic disorder, active suicidal ideation, diabetes mellitus, untreated hypothyroidism, unstable medical illness, pregnancy, breastfeeding, and low serum potassium levels. For participants of the clinical trial, further exclusion criteria (relevant to the trial) included free testosterone levels above the median for healthy women of reproductive age, use of androgens/androgen precursors over the past three months, not willing to use contraception, substance use disorder in the past six months, bipolar I disorder, severe current depressive symptoms (Hamilton Depression Rating Scale [HAM-D] (24) score >20, excluding two eating/weight loss items related to AN symptoms), investigational psychotropic drug within the past three months, dose or drug change in psychotropic treatment within the last six weeks, dose change in oral contraceptive pill or transdermal estrogen therapy within the last month, creatinine level >1.5x upper limit, or ALT >2x upper limit of normal. For participants of the observational study, the following additional exclusion criteria applied: other medical explanation for low weight, use of systemic hormones within eight weeks, use of Depo-Provera within three months, substance use disorder within the past month, hematocrit <30%, and gastrointestinal tract surgery.

2.2 Procedures

Study visits took place at the Massachusetts General Hospital Translational Clinical Research Center and the Athinoula A. Martinos Center for Biomedical Imaging. A screening visit to determine eligibility included the medical history, physical examination [with height, weight, frame size, calculation of BMI and %EBW using the Metropolitan Height and Weight Tables 1983 (25)], psychiatric interviews, questionnaires, and blood and urine collection. DSM-5 criteria for AN/Atypical AN were confirmed by the Structural Clinical Interview for DSM-IV (SCID-IV (26); clinical trial) or Eating Disorder Examination (EDE (27); observational study).

At the main study visit after an overnight fast, a urine pregnancy test and a morning blood draw for oxytocin and estradiol levels were obtained, and participants completed questionnaires to assess psychopathology. For participants of the observational study, the Toronto Alexithymia Scale (TAS-20) was completed within a week of that day. For participants enrolled in the clinical trial, all assessments were completed prior to randomization to the treatment arms and receipt of any study medication.

2.3 Self-report measures of psychopathology

2.3.1 ED psychopathology

The Eating Disorder Examination – Questionnaire (EDE-Q) is a well-validated 28-item self-report measure that assesses attitudes and behaviors related to eating patterns and body image over the past 28 days and yields a global score and four subscale scores (Dietary Restraint, Eating Concern, Shape Concern, and Weight Concern). Scale scores range from 0 to 6 with higher scores representing more severe symptoms. Internal consistency for the Global Score is (α=0.90) (28). We considered an EDE-Q Global Score >2.5 (1 SD above the healthy population mean) to indicate active ED psychopathology (29–33).

2.3.2 Depressive and anxiety symptoms

The 21-item Beck Depression Inventory-IA (BDI), a revised version of the original BDI (34), assesses severity of depressive symptoms over the previous two weeks with scores of 0-9 indicating minimal depressive symptoms, 10-16 mild depression, 17-29 moderate depression, and 30-63 severe depression (34). Internal consistency ranges from 0.73 to 0.92 (35).

The 20-item State-Trait Anxiety Inventory (STAI) Trait scale assesses trait anxiety with high internal consistency ($\alpha \geq 0.89$) (36). In a female population (19-39 years), the mean STAI Trait Score was 36.2 with a standard deviation of 9.5 (36). STAI Trait Scores 1 SD above the mean are considered to be consistent with clinically significant anxiety symptoms (37).

2.3.3 Socioemotional functioning

The 20-item TAS-20 is a well-validated measure of alexithymia with good internal consistency (α=0.81) (38, 39). Sum scores are determined for three subscales (Difficulty Identifying Feelings, Difficulty Describing Feelings, and Externally Oriented Thinking) together with a global score (≤51: nonalexithymia, 52–60: possible alexithymia, ≥61: alexithymia) (38). To capture the multifacetedness of socioemotional functioning, participants additionally completed the Liebowitz Social Anxiety Scale (LSAS-SR), the Dimensional Assessment of Personality Pathology – Basic Questionnaire (DAPP-BQ), and the Interpersonal Support Evaluation List (ISEL). The LSAS-SR assesses fear and avoidance of eleven social situations and 13 situations of public performance over the past week, which are summarized on four scales with higher scores indicating more severe psychopathology: Public Fear, Social Fear, Public Avoidance, and Social Avoidance (40). From the DAPP-BQ, participants rated 14 Suspiciousness and 16 Insecure Attachment items. Summated scores for Suspiciousness and Insecure Attachment scales were calculated

with higher scores indicating more severe psychopathology (41). The 40-item ISEL assesses the perceived availability of potential social resources yielding a summary score lower scores indicating less perceived support (42).

2.4 Biochemical analysis

Serum samples were stored at -80°C and run in a single batch. Oxytocin concentration was measured in unextracted serum by ELISA in the Brigham Research Assay Core (BRAC) Laboratory using reagents purchased from Enzo Life Sciences, Farmingdale, NY, USA. We have previously demonstrated a robust correlation between extracted and unextracted serum oxytocin levels (43). The assay had a detection limit of 15 pg/mL. In-house quality-control samples had a mean of 81 and 120 pg/mL, and a low and high quality-control pools between-assay coefficient of variation (CV) of 18 and 20%, respectively. The cross-reactivity of Lys8-vasopressin, Arg8-vasopressin, met-enkephalin, VIP, somatostatin, Ser4, Ile8-oxytocin, and alpha-ANP in the oxytocin assay is <0.02%. Serum estradiol was measured by the BRAC using liquid chromatography-tandem mass spectrometry. The assay had a lower limit of detection of 1 pg/mL and intra-assay CV <5%.

2.5 Data analysis

STATA® software (version 14.2; StataCorp LLC, College Station, TX, USA) was used for statistical analyses. Data were tested for normality using the Shapiro-Wilk test. Age, duration of illness, estradiol levels, and oxytocin levels were not normally distributed. Log-transformation prior to analysis resulted in a normal distribution for estradiol and oxytocin levels. For the other two measures, non-parametric tests were performed. Primary outcomes were EDE-Q Global, BDI Total, and STAI Trait scores for ED-specific, depressive, and anxiety symptoms, respectively. For socioemotional functioning, the TAS-20 served as the primary assessment tool. We have previously shown that among the TAS-20 scores, the Difficulty Identifying Feelings Score showed the strongest link with oxytocin levels (11). Accordingly, we chose the TAS-20 Difficulty Identifying Feelings Score as the primary outcome measure for socioemotional functioning in this study. Further TAS-20 scores and other measures of key subcomponents of socioemotional functioning (i.e., LSAS-SR, DAPP-BQ, and ISEL) were analyzed as additional exploratory outcomes.

We compared AN/AtypAN-R and AN/AtypAN-BP groups using t-tests for independent samples for continuous variables (except for age and duration of illness, for which Mann-Whitney U-tests were performed) and Fisher's exact tests for nominal data. Pearson correlations investigated the relationship between (log-transformed) oxytocin levels and measures of psychopathology. In addition, we performed multivariate linear regression analyses to determine the relationship between baseline oxytocin levels and psychopathology controlling for time since diagnosis, which differed between study groups. Individuals with AN and atypical AN were combined for all analysis due to comparable characteristics (see Table 1 for a comparison of hormone levels and key psychopathology endpoints). Statistical significance was defined as a two-tailed p-value <0.05. Data are reported as mean ± SD, median (IQR), or n (%).

3 Results

3.1 Participant characteristics

Participant characteristics are presented in Table 2. Time since diagnosis was shorter in the AN/AtypAN-R group compared to the AN/AtypAN-BP group, while age, BMI, and estrogen status did not differ between groups. Furthermore, AN/AtypAN-R and AN/AtypAN-BP groups showed no difference in frequency of key comorbidities and medication intake.

3.2 Self-report measures of psychopathology

Group means and between-group comparisons of psychopathology are summarized in Table 2. Twelve participants with AN/AtypAN-R (57.1%) and 11 participants with AN/AtypAN-BP (73.3%) had an EDE-Q Global Score in the clinical range. Eleven participants with AN/

TABLE 1 Participant characteristics of hormone levels and key psychopathology endpoints for women with anorexia nervosa (AN) versus atypical AN (AtypAN).

Characteristic	AN (n=31)	AtypAN (n=22)	p	Hedges' g
Estradiol (pg/mL)[a]	55.9 ± 61.1	65.8 ± 48.8	n/a	n/a
Ln-estradiol[a]	3.3 ± 1.4	3.7 ± 1.2	0.364	-0.30
Fasting oxytocin (pg/mL)	1,018 ± 582	872 ± 308	n/a	n/a
Ln-fasting oxytocin	6.8 ± 0.5	6.7 ± 0.4	0.554	0.17
EDE-Q Global Score[b]	3.0 ± 1.6	3.5 ± 1.3	0.358	-0.33
BDI Total Score[c]	22.1 ± 10.8	23.4 ± 3.0	0.717	-0.15
STAI Trait Score	53.7 ± 10.4	54.1 ± 13.1	0.906	-0.03
TAS-20 Difficulty Identifying Feelings Score[d]	20.0 ± 6.5	20.8 ± 6.6	0.699	-0.12

Mean ± SD. [a]Data available for 36 participants (21 with AN and 15 with AtypAN), all of whom were off oral contraceptive pill medication. [b]Data available for 35 participants (19 with AN and 16 with AtypAN). [c]Data available for 36 participants (20 with AN and 16 with AtypAN). [d]Data available for 50 participants (29 with AN and 21 with AtypAN). BDI, Beck Depression Inventory-IA; EDE-Q, Eating Disorder Examination Questionnaire; STAI, State-Trait Anxiety Inventory; TAS-20, Toronto Alexithymia Scale.

10.3389/fendo.2022.1049541

TABLE 2 Participant characteristics for women with anorexia nervosa (AN)/Atypical AN who are solely restricting (AN/AtypAN-R) versus those who restrict in combination with binge/purge behaviors (AN/AtypAN-BP).

Characteristic	AN/AtypAN-R (n=21)	AN/AtypAN-BP (n=32)	p	Effect size[a]
Age (years)	25.0 (21.0-28.0)	21.5 (19.5-33.0)	0.636	r=0.06
Duration of illness (months)[b]	8.0 (5.0-13.0)	16.5 (11.0-27.5)	**0.004**	r=-0.41
Lowest adult weight (kg)	43.8 ± 5.8	42.8 ± 5.8	0.533	g=0.17
Weight (kg)	49.9 ± 4.9	48.7 ± 5.4	0.417	g=0.23
BMI (kg/m^2)	18.5 ± 1.9	18.2 ± 1.4	0.548	g=0.18
%EBW	83.9 ± 6.9	84.7 ± 7.5	0.730	g=-0.11
Amenorrhea[c]	6 (30.0)	9 (28.1)	1.000	OR=1.10
Current MDD	10 (47.6)	17 (53.1)	0.782	OR=0.80
Current GAD	15 (71.4)	19 (59.4)	0.400	OR=1.71
Current OCD	1 (4.8)	1 (3.1)	1.000	OR=1.55
Current PTSD	6 (28.6)	7 (21.9)	0.746	OR=1.43
Antidepressant medication	14 (66.7)	20 (62.5)	1.000	OR=1.20
Anxiolytic medication	10 (47.6)	11 (34.4)	0.397	OR=1.74
Mood stabilizers	1 (4.8)	3 (9.4)	1.000	OR=0.48
Antipsychotic medication	4 (19.1)	3 (9.4)	0.415	OR=2.27
Hypnotic medication	1 (4.8)	3 (9.4)	1.000	OR=0.48
Melatonin	2 (9.5)	0 (0.0)	0.152	N/A
OCPs[c]	8 (40.0)	7 (21.9)	0.213	OR=2.38
Estradiol (pg/mL)[d]	76.6 ± 58.1	51.7 ± 53.8	n/a	n/a
Ln-estradiol[d]	3.9 ± 1.3	3.3 ± 1.3	0.229	g=0.42
Fasting oxytocin (pg/mL)	873 ± 534	1,013 ± 456	n/a	n/a
Ln-oxytocin	6.6 ± 0.5	6.8 ± 0.4	0.158	g=-0.41
EDE-Q Global Score[e]	2.8 ± 1.6	3.9 ± 1.1	**0.025**	g=-0.75
BDI Total Score[f]	19.3 ± 11.3	27.3 ± 9.5	**0.032**	g=-0.74
STAI Trait Score	51.5 ± 11.7	55.4 ± 11.2	0.231	g=-0.34
TAS-20 Difficulty Identifying Feelings Score[g]	19.0 ± 6.9	21.3 ± 6.1	0.216	g=-0.35
TAS-20 Difficulty Describing Feelings Score[g]	15.1 ± 4.9	16.9 ± 4.5	0.185	g=-0.38
TAS-20 Externally Oriented Thinking Score[g]	17.9 ± 4.9	18.6 ± 4.7	0.606	g=-0.14
TAS-20 Total Score[g]	52.0 ± 13.1	56.9 ± 11.2	0.168	g=-0.40
LSAS-SR Social Fear Score[f]	14.7 ± 6.3	16.9 ± 5.2	0.261	g=-0.37
LSAS-SR Public Fear Score[f]	15.6 ± 6.4	19.4 ± 4.9	0.064	g=-0.64
LSAS-SR Social Avoidance Score[f]	13.4 ± 7.2	16.3 ± 6.4	0.218	g=-0.41
LSAS-SR Public Avoidance Score[f]	13.0 ± 7.1	16.7 ± 6.6	0.132	g=-0.52
DAPP-BQ Suspiciousness Score[f]	27.8 ± 8.9	34.4 ± 11.7	0.061	g=-0.64
DAPP-BQ Insecure Attachment Score[f]	36.3 ± 14.1	42.9 ± 16.2	0.207	g=-0.43
ISEL Total Score[f]	82.8 ± 17.8	68.9 ± 22.1	**0.045**	g=0.69

Mean ± SD, median (IQR), or n (%). Significant values (p<0.05) are highlighted in bold. [a]Effect sizes are reported as Hedges' g for group comparisons of normally distributed continuous variables analyzed with independent-sample t-tests, r for non-normally distributed variables analyzed with Mann-Whitney U-test, and OR (exact) for nominal variables analyzed with Fisher's exact test. [b]Four participants with AN/AtypAN-BP did not provide information for duration of illness. [c]Data available for 52 participants (20 participants with AN/AtypAN-R and 32 with AN/AtypAN-BP). [d]Data available for 36 participants, all of whom were off OCP medication (12 participants with AN/AtypAN-R and 24 with AN/AtypAN-BP). [e]Data available for 35 participants (21 participants with AN/AtypAN-R and 14 with AN/AtypAN-BP). [f]Data available for 36 participants (21 participants with AN/AtypAN-R and 15 with AN/AtypAN-BP). [g]Data available for 50 participants (21 participants with AN/AtypAN-R and 29 with AN/AtypAN-BP). BDI, Beck Depression Inventory-IA; BMI, body mass index; DAPP-BQ, Dimensional Assessment of Personality Pathology – Basic Questionnaire; %EBW, percent expected body weight; EDE-Q, Eating Disorder Examination Questionnaire; GAD, generalized anxiety disorder; ISEL, Interpersonal Support Evaluation List; LSAS-SR, Liebowitz Social Anxiety Scale; MDD, major depressive disorder; OCD, obsessive-compulsive disorder; OCPs, oral contraceptive pills; PTSD, posttraumatic stress disorder; STAI, State-Trait Anxiety Inventory; TAS-20, Toronto Alexithymia Scale.

AtypAN-R (52.4%) and 13 individuals with AN/AtypAN-BP (86.7%) had a BDI Total Score consistent with moderate or severe depressive symptoms. Fifteen participants with AN/AtypAN-R (71.4%) and 26 individuals with AN/AtypAN-BP (81.3%) had a STAI Trait Score consistent with clinically significant anxiety. Nine individuals with AN/AtypAN-R (42.9%) and 19 participants with AN/AtypAN-BP (65.5%) had a TAS-20 Total Score in the range of possible or definite symptoms of alexithymia. ED psychopathology and depressive symptoms were more pronounced in individuals with AN/AtypAN-BP than in those with AN/AtypAN-R, as indicated by higher EDE-Q Global and BDI Total scores, respectively. In addition, the AN/AtypAN-BP group had a lower perception of social support than the AN/AtypAN-R group, as indicated by a lower ISEL Total Score. When controlling for illness duration, no significant group differences remained (ps≥0.094).

3.3 Oxytocin levels and relationship with psychopathology

Fasting oxytocin levels did not differ between groups (Table 2). In individuals with AN/AtypAN-R, oxytocin levels were broadly associated with symptom severity, namely, lower oxytocin levels were associated with higher EDE-Q Global, BDI Total, and STAI Trait scores, reflecting more pronounced ED, depressive, and anxiety symptoms, respectively (Table 3; Figure 1). Furthermore, in individuals with AN/AtypAN-R, oxytocin levels were related to socioemotional functioning with lower oxytocin levels being associated with higher TAS-20 Difficulty Identifying Feelings, LSAS-SR Social Fear, LSAS-SR Public Fear, LSAS-SR Social Avoidance, and DAPP-BQ Suspiciousness scores (indicating more pronounced deficits in socioemotional functioning) and decreased ISEL Total Scores (indicating a reduced perception of social support). Conversely, in individuals with AN/AtypAN-BP, the only observed association was between low oxytocin levels and higher BDI Total Scores; no other relationships reached significance in the AN/AtypAN-BP group (Table 3; Figure 1).

4 Discussion

To the best of our knowledge, this is the first study to examine relationships between fasting serum oxytocin levels and psychopathology in a broad sample of individuals with active AN and atypical AN who engage in primary restriction (AN/AtypAN-R) and, separately, in those who restrict combined with binge and/or purge behaviors (AN/AtypAN-BP). In females with AN/AtypAN-R, we observed robust negative correlations between basal oxytocin levels and severity of ED psychopathology, depressive and anxiety symptoms, and impairment of socioemotional functioning. In contrast, in women with AN/AtypAN-BP, there was only an association between lower oxytocin levels and more pronounced depressive symptoms, while no other significant relationships between oxytocin levels and psychopathology were identified in this

TABLE 3 Associations between (log-transformed) fasting oxytocin levels and psychopathology in women with anorexia nervosa (AN)/Atypical AN who are solely restricting (AN/AtypAN-R) versus those who restrict in combination with binge/purge behaviors (AN/AtypAN-BP).

Self-report measures of psychopathology	AN/AtypAN-R (n=21)		AN/AtypAN-BP (n=32)	
	r	p	r	p
Primary endpoints				
EDE-Q Global Score (eating disorder psychopathology)	-0.49	**0.024**	-0.25[a]	0.396
BDI Total Score (depressive symptoms)	-0.55	**0.009**	-0.52[b]	**0.049**
STAI Trait Score (anxiety symptoms)	-0.63	**0.002**	-0.24	0.190
TAS-20 Difficulty Identifying Feelings Score (socioemotional functioning)	-0.49	**0.023**	-0.10[c]	0.614
Exploratory endpoints (socioemotional functioning)				
TAS-20 Difficulty Describing Feelings Score	-0.29	0.205	0.04[c]	0.834
TAS-20 Externally Oriented Thinking Score	-0.09	0.684	0.34[c]	0.075
TAS-20 Total Score	-0.40	0.071	0.11[c]	0.586
LSAS-SR Social Fear Score	-0.56	**0.008**	-0.15[b]	0.582
LSAS-SR Public Fear Score	-0.44	**0.046**	-0.21[b]	0.457
LSAS-SR Social Avoidance Score	-0.57	**0.006**	-0.07[b]	0.814
LSAS-SR Public Avoidance Score	-0.41	0.063	-0.02[b]	0.932
DAPP-BQ Suspiciousness Score	-0.49	**0.024**	-0.16[b]	0.562
DAPP-BQ Insecure Attachment Score	-0.25	0.285	0.14[b]	0.618
ISEL Total Score	0.47	**0.031**	0.51[b]	0.051

Significant values (p<0.05) are highlighted in bold. [a]Based on 14 participants. [b]Based on 15 participants. [c]Based on 29 participants. BDI, Beck Depression Inventory-IA; DAPP-BQ, Dimensional Assessment of Personality Pathology – Basic Questionnaire; EDE-Q, Eating Disorder Examination – Questionnaire; ISEL, Interpersonal Support Evaluation List; LSAS-SR, Liebowitz Social Anxiety Scale; STAI, State-Trait Anxiety Inventory; TAS-20, Toronto Alexithymia Scale.

10.3389/fendo.2022.1049541

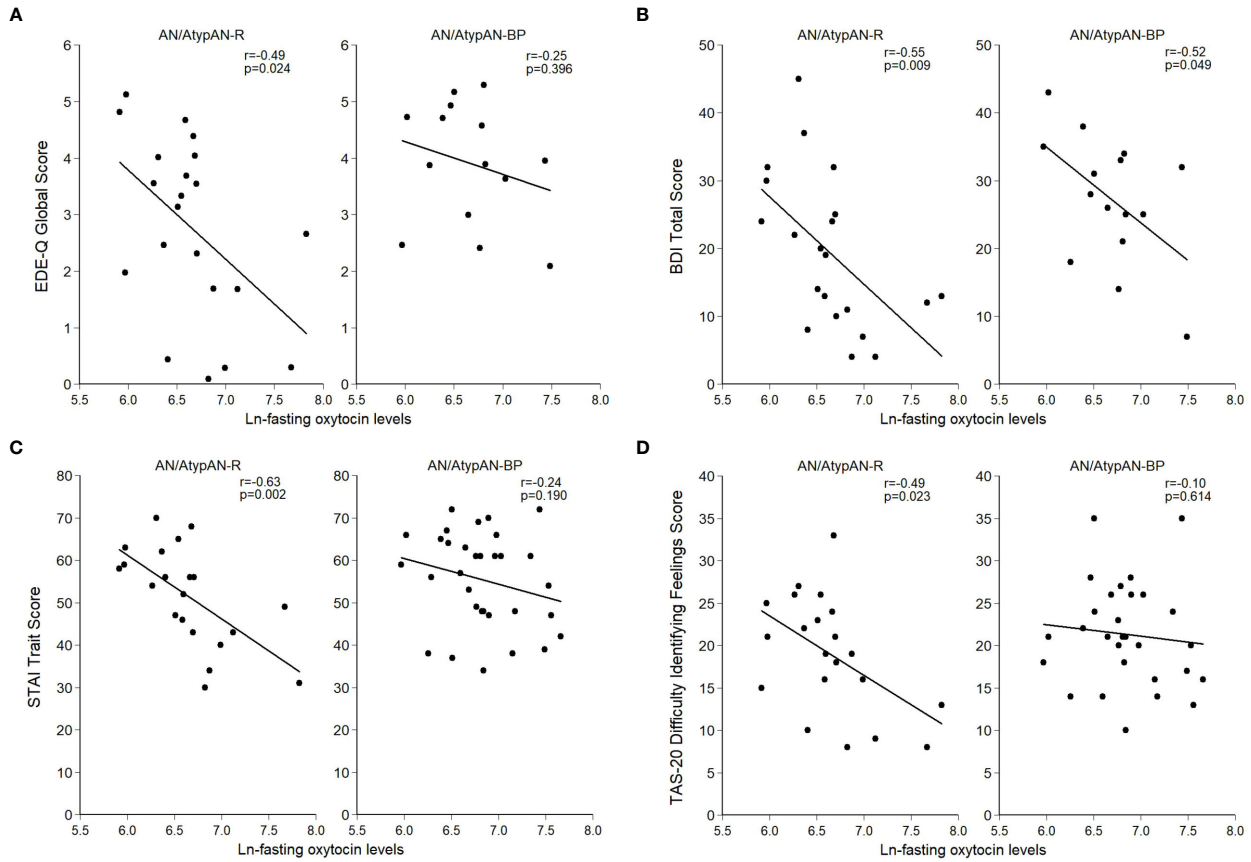

FIGURE 1
Relationship between (log-transformed) fasting oxytocin levels and psychopathology in women with anorexia nervosa (AN)/Atypical AN who are solely restricting (AN/AtypAN-R) and those who restrict in combination with binge/purge behaviors (AN/AtypAN-BP). **(A)** Eating Disorder Examination – Questionnaire (EDE-Q) Global Score (eating disorder psychopathology); **(B)** Beck Depression Inventory-IA (BDI) Total Score (depressive symptoms); **(C)** State-Trait Anxiety Inventory (STAI) Trait Score (anxiety symptoms); and **(D)** Toronto Alexithymia Scale (TAS-20) Difficulty Identifying Feelings Score (socioemotional functioning).

study. These data indicate possible differences in underlying pathophysiology across AN presentations.

Our findings suggest a role of oxytocin pathways in the ED pathology of AN/AtypAN-R. The result pattern observed in the AN/AtypAN-R group resembles findings we previously reported in individuals with AN in partial recovery, where fasting oxytocin levels were associated with greater ED pathology, and individuals with clinically significant ED pathology displayed lower oxytocin levels than those without clinically significant symptoms (2). While the previous study did not distinguish between individuals with primarily restricting and those with additional binge/purge presentation, in the present investigation in women with AN and atypical AN, despite similar levels of serum oxytocin in females with AN/AtypAN-R and AN/AtypAN-BP, we found a robust relationship between oxytocin and ED psychopathology in individuals with AN/AtypAN-R but not AN/AtypAN-BP. The lack of an observed relationship between oxytocin and psychopathology in women with AN/AtypAN-BP could be the result of binge/purge behaviors altering peripheral oxytocin, and it is still possible that central oxytocin and psychopathology are related in this AN presentation. Alternatively, it is conceivable that oxytocin plays a more substantial role in the modulation of psychopathology in AN/AtypAN-R than AN/AtypAN-BP. While future research studies are needed to understand the cause of the different observation of oxytocin levels in CSF, serum oxytocin appears to be a biomarker for severity of psychopathology specifically in AN/AtypAN-R.

The potential relevance of oxytocin in the psychopathology of AN/AtypAN-R seems to go beyond ED pathology and also spans depressive and anxiety symptoms and socioemotional functioning. Comorbid depression and anxiety are common in AN (44, 45). On average, our sample showed moderate levels of depressive symptoms and clinically significant anxiety. Preclinical and clinical studies have demonstrated that oxytocin has antidepressant and anxiolytic properties, including improving psychopathology and pathophysiology in clinical populations (46–49). For example, single-dose intranasal administration of oxytocin reduced amygdala reactivity and functional connectivity to fear-inducing stimuli in individuals with generalized social anxiety disorders (50, 51), and repeated doses of intranasal oxytocin over four weeks added to pharmacological treatment with escitalopram improved depressive symptoms in individuals with treatment-resistant major depressive disorders (52). In women with partially recovered AN, we previously reported a correlation between lower fasting serum oxytocin levels and more pronounced anxiety symptoms (2). For the first time, the present study reports a relationship between low levels of oxytocin and more pronounced depressive and anxiety symptoms in

individuals with active AN/AtypAN-R, suggesting that low oxytocin may mediate mood and anxiety symptoms in this subgroup. In individuals with active AN/AtypAN-BP, we also found a negative association between oxytocin levels and depressive symptoms, mirroring the pattern in AN/AtypAN-R, whereas there was no evidence for a linear relationship between oxytocin levels and anxiety in AN/AtypAN-BP.

In addition to a negative relationship between oxytocin levels and difficulty identifying feelings in females with AN/AtypAN-R but not AN/AtypAN-BP, our study provides a multifaceted exploratory assessment of socioemotional functioning that shows a consistent pattern of lower oxytocin levels associated with worse socioemotional functioning in women with AN/AtypAN-R but not AN/AtypAN-BP. Individuals with AN often show impaired socioemotional functioning by means of increased social anxiety (53), suspiciousness and insecure attachment (54), difficulty recognizing others' emotions (55), and alexithymia (56), which often does not resolve with weight gain (54, 57, 58). Animal research has demonstrated a prosocial role of oxytocin, including the promotion of maternal and pair bonding (59, 60), approach behavior under stress (61), and increased duration of eye contact and higher number of prosocial choices in rhesus macaques (62). In humans, oxytocin administration has been shown to improve socioemotional functioning in healthy individuals (63) and across a variety of psychiatric conditions associated with socioemotional challenges, including autism spectrum disorder, schizophrenia, and social anxiety (50, 63, 64). In the context of AN, a previous study from our group of women with low-weight AN (without distinction between presentations), partially recovered AN (90-120% EBW), and healthy controls found an association between low fasting oxytocin levels and increased symptoms of alexithymia independent of BMI and estrogen status, raising the question of whether low oxytocin levels could contribute to social emotional functioning difficulties in AN (11). However, relationships between oxytocin levels and other measures of socioemotional functioning were not identified, groups were analyzed conjointly rather than separately, and the role of AN presentations was not addressed. Some studies have suggested closer resemblance of the binge/purge presentation of AN to bulimia nervosa than primarily restricting AN (7, 15). Our study extends our prior findings by showing broad and consistent relationships between oxytocin levels and socioemotional functioning with lower oxytocin levels being associated with more pronounced socioemotional dysfunction in women with AN/AtypAN-R but not AN/AtypAN-BP. The broader sample comprising individuals with AN and atypical AN increases generalizability of the observed findings.

Limitations of this study include the relatively small sample size, which could have introduced bias. Furthermore, as a cross-sectional investigation we report associations and cannot determine causality. Longitudinal studies in larger samples of women with AN/AtypAN-R and AN/AtypAN-BP that build on the presented findings and further explore the role of additional key characteristics will be essential to further investigate the role of oxytocin in mediating psychopathology. For example, a longer duration of illness in individuals with AN/Atypical AN-BP compared to AN/Atypical AN-R represents a commonly observed difference. This difference is rooted in the fact that diagnostic crossover during prolonged illness from AN/Atypical presentations with primarily dietary restriction to eating disorders featuring binge-eating and/or purging is common (~50%), while the reverse crossover rarely occurs (65). A lack of an observed relationship between oxytocin and psychopathology in our sample of individuals with AN/AtypAN-BP could be related to a longer duration of illness, and/or it could highlight a neurobiological shift that occurs simultaneously with and/or is driving the observed behavioral changes taking place with diagnostic crossover. Future studies should examine groups of individuals with AN/Atypical AN-R and AN/Atypical AN-BP who are comparable in duration of illness to shed light on the separate and joint impact of symptom presentation and illness duration on the studied endocrine-psychopathological link. Furthermore, follow-up prospective studies in individuals undergoing diagnostic crossover from AN/AtypAN-R to AN/AtypAN-BP are needed to build on the reported findings and examine the relationship between oxytocin levels and psychopathology longitudinally to better understand its potential role in diagnostic crossover. Lastly, future studies investigating the relationship between oxytocin levels and psychopathology across AN subtypes should consider including CSF oxytocin levels to better understand the relationship between central and peripheral oxytocin levels in the context of these research questions.

In summary, the present study is the first to show consistent relationships between fasting serum oxytocin levels and psychopathology (spanning ED psychopathology, depressive and anxiety symptoms, and impairments in socioemotional functioning) in women with active AN/AtypAN-R. Our sample of individuals with active AN/AtypAN-BP only showed an association between low oxytocin levels and depressive symptoms, while no other relationships between oxytocin and psychopathology were observed. These findings are crucial to better elucidate oxytocin physiology and its role in psychopathology in AN presentations, highlighting a potentially different underlying psychopathology in AN-R and AN-BP. Additional studies are needed to further investigate the role of oxytocin in the psychopathology of AN and explore the potential of oxytocin pathways as neurohormonal treatment targets for selected AN presentations, and future randomized controlled trials could consider using the outcomes that we found to be associated with peripheral oxytocin levels as primary endpoints.

Data availability statement

Data from the randomized, placebo-controlled clinical trial of low-dose testosterone therapy for AN (clinicaltrials.gov identifier: NCT01121211) are available upon reasonable request to KM (kkmiller@mgh.harvard.edu). Data from the observational study of neurobiology of low-weight eating disorders (R01 MH103402) will be available upon request to the corresponding author and through National Institute of Mental Health.

Ethics statement

This research was approved by the Institutional Review Board of Mass General Brigham and carried out in accordance with the Declaration of Helsinki. Informed written consent was obtained from all participants.

Author contributions

FP, FG, AA, and EL conceived the study idea and designed this investigation. FP and AA performed the analysis. FP, FG, and EL wrote the manuscript. KE, MM, KM, AK, and AA provided feedback on the manuscript. All authors contributed to the article and approved the submitted version.

Funding

This work was supported by the Charles A. King Trust Postdoctoral Research Fellowship Program, Bank of America, N.A., Co-Trustees (FP), Fundación Alfonso Martín Escudero (AA), and National Institutes of Health (R01 MH083657 [AK], R01 MH103402 [KTE, MM, and EAL], K23 MH092560 [EAL], K24 MH120568 [EAL], P30 DK040561, 1 UL1 TR001102-01, and 8 ULI TR000170-05). Funding sources had no role in the design of the study, collection, analysis, and interpretation of data, writing of the manuscript, or decision to submit the article for publication.

Conflict of interest

KM has received study medication from Pfizer and an investigator-initiated research grant from Amgen. She has had equity in Bristol-Myers Squibb, General Electric, Boston Scientific, Amgen, and Becton Dickinson. EL was on the scientific advisory board and has/had a financial interest in OXT Therapeutics, a company that developed oxytocin-based therapeutics for obesity and metabolic disease. She also received an investigator-initiated grant from Tonix Pharmaceuticals.

The remaining authors declare that the research was conducted in the absence of any commercial or financial relationships that could be construed as a potential conflict of interest.

Publisher's note

References

1. American Psychiatric Association. *Diagnostic and statistical manual of mental disorders. 5th ed.* Washington, DC, USA: American Psychiatric Association (2013).

2. Afinogenova Y, Schmelkin C, Plessow F, Thomas JJ, Pulumo R, Micali N, et al. Low fasting oxytocin levels are associated with psychopathology in anorexia nervosa in partial recovery. *J Clin Psychiatry* (2016) 77(11):e1483–e90. doi: 10.4088/JCP.15m10217

3. Kaye WH, Bulik CM, Thornton L, Barbarich N, Masters K. Comorbidity of anxiety disorders with anorexia and bulimia nervosa. *Am J Psychiatry* (2004) 161(12):2215–21. doi: 10.1176/appi.ajp.161.12.2215

4. Woodside BD, Staab R. Management of psychiatric comorbidity in anorexia nervosa and bulimia nervosa. *CNS Drugs* (2006) 20(8):655–63. doi: 10.2165/00023210-200620080-00004

5. Plessow F, Eddy KT, Lawson EA. The neuropeptide hormone oxytocin in eating disorders. *Curr Psychiatry Rep* (2018) 20(10):91. doi: 10.1007/s11920-018-0957-0

6. Chiodera P, Volpi R, Capretti L, Marchesi C, d'Amato L, De Ferri A, et al. Effect of estrogen or insulin-induced hypoglycemia on plasma oxytocin levels in bulimia and anorexia nervosa. *Metabolism* (1991) 40(11):1226–30. doi: 10.1016/0026-0495(91)90220-Q

7. Demitrack MA, Lesem MD, Listwak SJ, Brandt HA, Jimerson DC, Gold PW. CSF oxytocin in anorexia nervosa and bulimia nervosa: Clinical and pathophysiologic considerations. *Am J Psychiatry* (1990) 147(7):882–6. doi: 10.1176/ajp.147.7.882

8. Lawson EA, Donoho DA, Blum JI, Meenaghan EM, Misra M, Herzog DB, et al. Decreased nocturnal oxytocin levels in anorexia nervosa are associated with low bone mineral density and fat mass. *J Clin Psychiatry* (2011) 72(11):1546–51. doi: 10.4088/JCP.10m06617

9. Schorr M, Marengi DA, Pulumo RL, Yu E, Eddy KT, Klibanski A, et al. Oxytocin and its relationship to body composition, bone mineral density, and hip geometry across the weight spectrum. *J Clin Endocrinol Metabol* (2017) 102(8):2814–24. doi: 10.1210/jc.2016-3963

10. Lawson EA, Holsen LM, Santin M, Meenaghan E, Eddy KT, Becker AE, et al. Oxytocin secretion is associated with severity of disordered eating psychopathology and insular cortex hypoactivation in anorexia nervosa. *J Clin Endocrinol Metabol* (2012) 97 (10):E1898–908. doi: 10.1210/jc.2012-1702

11. Schmelkin C, Plessow F, Thomas JJ, Gray EK, Marengi DA, Pulumo R, et al. Low oxytocin levels are related to alexithymia in anorexia nervosa. *Int J Eat Disord* (2017) 50 (11):1332–8. doi: 10.1002/eat.22784

12. Burmester V, Nicholls D, Buckle A, Stanojevic B, Crous-Bou M. Review of eating disorders and oxytocin receptor polymorphisms. *J Eat Disord* (2021) 9(1):85. doi: 10.1186/s40337-021-00438-0

13. Kucharska K, Kot E, Biernacka K, Zimowski J, Rogoza R, Rybakowski F, et al. Interaction between polymorphisms of the oxytocinergic system genes and emotion perception in inpatients with anorexia nervosa. *Eur Eat Disord Rev* (2019) 27(5):481–94. doi: 10.1002/erv.2698

14. Aulinas A, Plessow F, Pulumo RL, Asanza E, Mancuso CC, Slattery M, et al. Disrupted oxytocin-appetite signaling in females with anorexia nervosa. *J Clin Endocrinol Metabol* (2019) 104(10):4931–4940. doi: 10.1210/jc.2019-00926

15. Monteleone AM, Scognamiglio P, Volpe U, Di Maso V, Monteleone P. Investigation of oxytocin secretion in anorexia nervosa and bulimia nervosa: Relationships to temperament personality dimensions. *Eur Eat Disord Rev* (2016) 24 (1):52–6. doi: 10.1002/erv.2391

16. Carson DS, Berquist SW, Trujillo TH, Garner JP, Hannah SL, Hyde SA, et al. Cerebrospinal fluid and plasma oxytocin concentrations are positively correlated and negatively predict anxiety in children. *Mol Psychiatry* (2015) 20(9):1085–90. doi: 10.1038/mp.2014.132

17. Chen Q, Zhuang J, Zuo R, Zheng H, Dang J, Wang Z. Exploring associations between postpartum depression and oxytocin levels in cerebrospinal fluid, plasma and saliva. *J Affect Disord* (2022) 315:198–205. doi: 10.1016/j.jad.2022.07.052

18. Kagerbauer SM, Martin J, Schuster T, Blobner M, Kochs EF, Landgraf R. Plasma oxytocin and vasopressin do not predict neuropeptide concentrations in human cerebrospinal fluid. *J Neuroendocrinol* (2013) 25(7):668–73. doi: 10.1111/jne.12038

19. Martin J, Kagerbauer SM, Schuster T, Blobner M, Kochs EF, Landgraf R. Vasopressin and oxytocin in CSF and plasma of patients with aneurysmal subarachnoid haemorrhage. *Neuropeptides* (2014) 48(2):91–6. doi: 10.1016/j.npep.2013.12.004

20. Aulinas A, Marengi DA, Galbiati F, Asanza E, Slattery M, Mancuso CJ, et al. Medical comorbidities and endocrine dysfunction in low-weight females with avoidant/restrictive food intake disorder compared to anorexia nervosa and healthy controls. *Int J Eat Disord* (2020) 53(4):631–6. doi: 10.1002/eat.23261

21. Breithaupt L, Chunga-Iturry N, Lyall AE, Cetin-Karayumak S, Becker KR, Thomas JJ, et al. Developmental stage-dependent relationships between ghrelin levels and hippocampal white matter connections in low-weight anorexia nervosa and atypical anorexia nervosa. *Psychoneuroendocrinology* (2020) 119:104722. doi: 10.1016/j.psyneuen.2020.104722

22. Kimball A, Schorr M, Meenaghan E, Bachmann KN, Eddy KT, Misra M, et al. A randomized placebo-controlled trial of low-dose testosterone therapy in women with anorexia nervosa. *J Clin Endocrinol Metabol* (2019) 104(10):4347–55. doi: 10.1210/jc.2019-00828

23. Mancuso C, Izquierdo A, Slattery M, Becker KR, Plessow F, Thomas JJ, et al. Changes in appetite-regulating hormones following food intake are associated with changes in reported appetite and a measure of hedonic eating in girls and young women with anorexia nervosa. *Psychoneuroendocrinology* (2019) 113:104556. doi: 10.1016/j.psyneuen.2019.104556

24. Hamilton M. The assessment of anxiety states by rating. *Br J Med Psychol* (1959) 32 (1):50–5. doi: 10.1111/j.2044-8341.1959.tb00467.x

25. Metropolitan Life Insurance Company. Metropolitan height and weight tables. *Stat Bull* (1983) 64(1):2–9.

26. First MB, Spitzer RL, Williams JB. *Structured clinical interview for diagnostic and statistical manual of mental disorders. 4th ed.* New York, NY, USA: Biometrics Research (2002).

27. Fairburn CG, Cooper Z, O'Connor M. *Eating disorder examination edition 17.0D*. Oxford, UK: Centre for Research on Eating Disorders at Oxford (2014).

28. Peterson CB, Crosby RD, Wonderlich SA, Joiner T, Crow SJ, Mitchell JE, et al. Psychometric properties of the eating disorder examination-questionnaire: Factor structure and internal consistency. *Int J Eat Disord* (2007) 40(4):386–9. doi: 10.1002/eat.20373

29. Aardoom JJ, Dingemans AE, Slof Op't Landt MC, Van Furth EF. Norms and discriminative validity of the eating disorder examination questionnaire (EDE-q). *Eat Behav* (2012) 13(4):305–9. doi: 10.1016/j.eatbeh.2012.09.002

30. Kelly NR, Cotter EW, Mazzeo SE. Eating disorder examination questionnaire (EDE-q): Norms for black women. *Eat Behav* (2012) 13(4):429–32. doi: 10.1016/j.eatbeh.2012.09.001

31. Luce KH, Crowther JH, Pole M. Eating disorder examination questionnaire (EDE-q): Norms for undergraduate women. *Int J Eat Disord* (2008) 41(3):273–6. doi: 10.1002/eat.20504

32. Mond JM, Chen A, Kumar R. Eating-disordered behavior in Australian and Singaporean women: A comparative study. *Int J Eat Disord* (2010) 43(8):717–23. doi: 10.1002/eat.20771

33. Nakai Y, Nin K, Fukushima M, Nakamura K, Noma S, Teramukai S, et al. Eating disorder examination questionnaire (EDE-q): Norms for undergraduate Japanese women. *Eur Eat Disord Rev* (2014) 22(6):439–42. doi: 10.1002/erv.2324

34. Beck AT, Steer RA. *Manual for the beck depression inventory*. San Antonio, TX, USA: Psychological Corporation (1993).

35. Beck AT, Steer RA, Garbin MG. Psychometric properties of the beck depression inventory: Twenty-five years of evaluation. *Clin Psychol Rev* (1988) 8(1):77–100. doi: 10.1016/0272-7358(88)90050-5

36. Spielberger CD, Gorsuch RL, Lushene R, Vagg PR, Jacobs GA. *Manual for the stait-trait anxiety inventory*. Palo Alto, CA: Consulting Psychologists Press (1983).

37. Vautier S. A longitudinal SEM approach to STAI data: Two comprehensive multitrait-multistate models. *J Pers Assess* (2004) 83(2):167–79. doi: 10.1207/s15327752jpa8302_11

38. Bagby RM, Parker JD, Taylor GJ. The twenty-item Toronto alexithymia scale–i. item selection and cross-validation of the factor structure. *J Psychosom Res* (1994) 38 (1):23–32. doi: 10.1016/0022-3999(94)90005-1

39. Bagby RM, Taylor GJ, Parker JDA. The twenty-item Toronto alexithymia scale: II. convergent, discriminant, and concurrent validity. *J Psychosom Res* (1994) 38(1):33–40. doi: 10.1016/0022-3999(94)90006-x

40. Rytwinski NK, Fresco DM, Heimberg RG, Coles ME, Liebowitz MR, Cissell S, et al. Screening for social anxiety disorder with the self-report version of the liebowitz social anxiety scale. *Depress Anxiety* (2009) 26(1):34–8. doi: 10.1002/da.20503

41. Kushner SC, Quilty LC, Tackett JL, Bagby RM. The hierarchical structure of the dimensional assessment of personality pathology (DAPP-BQ). *J Pers Disord* (2011) 25 (4):504–16. doi: 10.1521/pedi.2011.25.4.504

42. Cohen S, Mermelstein R, Kamarck T, Hoberman HM. Measuring the functional components of social support. In: Sarason IG, Sarason BR, editors. *Social support: Theory, research and applications. NATO ASI series (D: Behavioural and social sciences)*. Dordrecht, NL: Springer (1985). p. 73–94.

43. Lawson EA, Holsen LM, Santin M, DeSanti R, Meenaghan E, Eddy KT, et al. Postprandial oxytocin secretion is associated with severity of anxiety and depressive symptoms in anorexia nervosa. *J Clin Psychiatry* (2013) 74(5):e451–7. doi: 10.4088/JCP.12m08154

44. Geist R, Davis R, Heinmaa M. Binge/purge symptoms and comorbidity in adolescents with eating disorders. *Can J Psychiatry* (1998) 43(5):507–12. doi: 10.1177/070674379804300510

45. McElroy SL, Kotwal R, Keck PEJr., Akiskal HS. Comorbidity of bipolar and eating disorders: Distinct or related disorders with shared dysregulations? *J Affect Disord* (2005) 86(2-3):107–27. doi: 10.1016/j.jad.2004.11.008

46. Arletti R, Bertolini A. Oxytocin acts as an antidepressant in two animal models of depression. *Life Sci* (1987) 41(14):1725–30. doi: 10.1016/0024-3205(87)90600-x

47. Kanat M, Heinrichs M, Mader I, van Elst LT, Domes G. Oxytocin modulates amygdala reactivity to masked fearful eyes. *Neuropsychopharmacology* (2015) 40 (11):2632–8. doi: 10.1038/npp.2015.111

48. Matsushita H, Tomizawa K, Okimoto N, Nishiki T, Ohmori I, Matsui H. Oxytocin mediates the antidepressant effects of mating behavior in male mice. *Neurosci Res* (2010) 68(2):151–3. doi: 10.1016/j.neures.2010.06.007

49. Ring RH, Malberg JE, Potestio L, Ping J, Boikess S, Luo B, et al. Anxiolytic-like activity of oxytocin in male mice: Behavioral and autonomic evidence, therapeutic implications. *Psychopharmacol (Berl)* (2006) 185(2):218–25. doi: 10.1007/s00213-005-0293-z

50. Gorka SM, Fitzgerald DA, Labuschagne I, Hosanagar A, Wood AG, Nathan PJ, et al. Oxytocin modulation of amygdala functional connectivity to fearful faces in generalized social anxiety disorder. *Neuropsychopharmacology* (2015) 40(2):278–86. doi: 10.1038/npp.2014.168

51. Labuschagne I, Phan KL, Wood A, Angstadt M, Chua P, Heinrichs M, et al. Oxytocin attenuates amygdala reactivity to fear in generalized social anxiety disorder. *Neuropsychopharmacology* (2010) 35(12):2403–13. doi: 10.1038/npp.2010.123

52. Scantamburlo G, Hansenne M, Geenen V, Legros JJ, Ansseau M. Additional intranasal oxytocin to escitalopram improves depressive symptoms in resistant depression: An open trial. *Eur Psychiatry* (2015) 30(1):65–8. doi: 10.1016/j.eurpsy.2014.08.007

53. Bulik CM. Family histories of bulimic women with and without comorbid alcohol abuse or dependence. *Am J Psychiatry* (1991) 148(9):1267–8. doi: 10.1176/ajp.148.9.1267

54. Holliday J, Uher Rpdel, Landau S, Collier D, Treasure J. Personality pathology among individuals with a lifetime history of anorexia nervosa. *J Pers Disord* (2006) 20 (4):417–30. doi: 10.1521/pedi.2006.20.4.417

55. Jansch C, Harmer C, Cooper MJ. Emotional processing in women with anorexia nervosa and in healthy volunteers. *Eat Behav* (2009) 10(3):184–91. doi: 10.1016/j.eatbeh.2009.06.001

56. Lule D, Schulze UM, Bauer K, Scholl F, Muller S, Fladung AK, et al. Anorexia nervosa and its relation to depression, anxiety, alexithymia and emotional processing deficits. *Eat Weight Disord* (2014) 19(2):209–16. doi: 10.1007/s40519-014-0101-z

57. Beadle JN, Paradiso S, Salerno A, McCormick LM. Alexithymia, emotional empathy, and self-regulation in anorexia nervosa. *Ann Clin Psychiatry* (2013) 25 (2):107–20.

58. Speranza M, Loas G, Wallier J, Corcos M. Predictive value of alexithymia in patients with eating disorders: A 3-year prospective study. *J Psychosom Res* (2007) 63 (4):365–71. doi: 10.1016/j.jpsychores.2007.03.008

59. Insel TR. A neurobiological basis of social attachment. *Am J Psychiatry* (1997) 154 (6):726–35. doi: 10.1176/ajp.154.6.726

60. Williams JR, Insel TR, Harbaugh CR, Carter CS. Oxytocin administered centrally facilitates formation of a partner preference in female prairie voles (Microtus ochrogaster). *J Neuroendocrinol* (1994) 6(3):247–50. doi: 10.1111/j.1365-2826.1994.tb00579.x

61. Young LJ. The neurobiology of social recognition, approach, and avoidance. *Biol Psychiatry* (2002) 51(1):18–26. doi: 10.1016/s0006-3223(01)01268-9

62. Ebitz RB, Watson KK, Platt ML. Oxytocin blunts social vigilance in the rhesus macaque. *Proc Natl Acad Sci U.S.A.* (2013) 110(28):11630–5. doi: 10.1073/pnas.1305230110

63. Guastella AJ, Ward PB, Hickie IB, Shahrestani S, Hodge MA, Scott EM, et al. A single dose of oxytocin nasal spray improves higher-order social cognition in schizophrenia. *Schizophr Res* (2015) 168(3):628–33. doi: 10.1016/j.schres.2015.06.005

64. Parker KJ, Oztan O, Libove RA, Sumiyoshi RD, Jackson LP, Karhson DS, et al. Intranasal oxytocin treatment for social deficits and biomarkers of response in children with autism. *Proc Natl Acad Sci U.S.A.* (2017) 114(30):8119–24. doi: 10.1073/pnas.1705521114

65. Plessow F, Eddy KT. Diagnostic crossover. In: Wade T, editor. *Encyclopedia of feeding and eating disorders*. New York, NY, USA: Springer (2017). p. 1–5.

frontiers | Frontiers in Endocrinology

TYPE Original Research
PUBLISHED 07 February 2023
DOI 10.3389/fendo.2023.920548

OPEN ACCESS

EDITED BY
Marco António Campinho,
University of Algarve, Portugal

REVIEWED BY
Tapas Chakraborty,
Kyushu University, Japan
Jean-Louis Charli,
UNAM Campus Morelos, National Autonomous University of Mexico, Mexico

*CORRESPONDENCE
Shuang-Xia Zhao
zhaozhao1215@126.com
Huai-Dong Song
huaidong_s1966@163.com

†These authors have contributed equally to this work

SPECIALTY SECTION
This article was submitted to Thyroid Endocrinology, a section of the journal Frontiers in Endocrinology

RECEIVED 19 April 2022
ACCEPTED 25 January 2023
PUBLISHED 07 February 2023

CITATION
Yan C-Y, Wu F-Y, Sun F, Fang Y, Zhang R-J, Zhang C-R, Zhang C-X, Wang Z, Yang R-M, Yang L, Dong M, Zhang Q-Y, Ye X-P, Song H-D and Zhao S-X (2023) The *isl2a* transcription factor regulates pituitary development in zebrafish.
Front. Endocrinol. 14:920548.
doi: 10.3389/fendo.2023.920548

The *isl2a* transcription factor regulates pituitary development in zebrafish

Chen-Yan Yan[1,2†], Feng-Yao Wu[1†], Feng Sun[1], Ya Fang[1], Rui-Jia Zhang[1], Chang-Run Zhang[1], Cao-Xu Zhang[1], Zheng Wang[1], Rui-Meng Yang[1], Liu Yang[1], Mei Dong[1], Qian-Yue Zhang[1], Xiao-Ping Ye[1], Huai-Dong Song[1*] and Shuang-Xia Zhao[1*]

[1]Department of Molecular Diagnostics and Endocrinology, The Core Laboratory in Medical Center of Clinical Research, Shanghai Ninth People's Hospital, Shanghai Jiao Tong University (SJTU) School of Medicine, Shanghai, China, [2]Geriatric Medicine Center, Department of Endocrinology, Zhejiang Provincial People's Hospital, Affiliated People's Hospital, Hangzhou Medical College, Hangzhou, Zhejiang, China

Background: ISL LIM homeobox 2, also known as insulin gene enhancer protein ISL-2 (*ISL2*), is a transcription factor gene that participates in a wide range of developmental events. However, the role of *ISL2* in the hypothalamus-pituitary-thyroid axis is largely unknown. In the present study, we characterized the expression patterns of *ISL2* and revealed its regulative role during embryogenesis using zebrafish.

Methods: We used the CRISPR/Cas9 system to successfully establish homozygous *ISL2*-orthologue (*isl2a* and *isl2b*) knockout zebrafish. Moreover, we utilized these knockout zebrafish to analyze the pituitary and thyroid phenotypes *in vivo*. For further molecular characterization, *in situ* hybridization and immunofluorescence were performed.

Results: The *isl2a* mutant zebrafish presented with thyroid hypoplasia, reduced whole-body levels of thyroid hormones, increased early mortality, gender imbalance, and morphological retardation during maturity. Additionally, thyrotropes, a pituitary cell type, was notably decreased during development. Importantly, the transcriptional levels of pituitary-thyroid axis hormones-encoding genes, such as *tshba*, *cga*, and *tg*, were significantly decreased in *isl2a* mutants. Finally, the thyroid dysplasia in *isl2a* mutant larvae may be attributed to a reduction in proliferation rather than changes in apoptosis.

Conclusions: In summary, *isl2a* regulates the transcriptional levels of marker genes in hypothalamus-pituitary-thyroid axis, and *isl2a* knockout causing low thyroid hormone levels in zebrafish. Thus, *isl2a* identified by the present study, is a novel regulator for pituitary cell differentiation in zebrafish, resulting in thyroid gland hypoplasia and phenotypes of hypothyroidism.

KEYWORDS

ISL2, pituitary development, thyroid dysgenesis, transcription factor, zebrafish

Introduction

The pituitary gland regulates growth, reproduction, and metabolism, and links the nervous and endocrine systems. The pituitary is largely conserved across vertebrates; it is divided into two major parts: the adenohypophysis, which includes the anterior and intermediate lobes, and the neurohypophysis/posterior lobe, which originates from neural ectoderm (1, 2). The adenohypophysis contains multiple glandular cells that are distinguished by the hormones they produce: thyrotropes (thyroid stimulating hormone, TSH), somatotropes (growth hormone, GH), lactotropes (prolactin, PRL), gonadotropes (luteinizing hormone, LH; and follicle-stimulating hormone, FSH), and corticotropes (adrenocorticotrophic hormone, ACTH) (2). The neurohypophysis facilitates the passage of vasopressin and oxytocin into the peripheral blood circulation, which are synthesized in the hypothalamus (2). The intermediate lobe contains melanotropes, which synthesize proopiomelanocortin (POMC), the major precursor of endorphins and melanocyte-stimulating hormone (2).

Multiple transcription factors and genes are involved in pituitary induction, cellular commitment, and cell type specification, including *shha*, *pitx3*, *pit1*, *six1b*, and *eya1* (3–7). *ISL1*, *ISL2*, *LHX3*, and *LHX4* belong to the LIM homeodomain transcription factors that have two tandem cysteine/histidine-rich, zinc-binding LIM domains (8). In particular, several studies have confirmed that *ISL1*, *LHX3*, and *LHX4* play a role in pituitary development (2). Interestingly, *Lhx3* and *Lhx4* participate in the early steps of pituitary ontogenesis in mice and have partially overlapped functions in the development of the anterior pituitary primordium called Rathke's pouch (9–11). In parallel, *ISL1* is involved in the development and function of thyrotropes as well as gonadotropes (12, 13). Moreover, *ISL1* participates in thyroid and hypothalamus development in addition to pituitary development (14–16).

The hypothalamus-pituitary-thyroid (HPT) axis regulates multiple body functions in all vertebrates *via* endocrine hormones including TSH, thyroxine (T4) and 3,5,3′-triiodothyronine (T3). Despite the fact that thyroid follicles do not form a compact gland but remain loosely dispersed along the pharyngeal midline, T4 has negative feedback effects on the release of TSH in the pituitary of zebrafish, an ideal model system in endocrine research due to its high conservation of molecular mechanisms involved in organogenesis, hormone transport and metabolism, as well as hormone action in target tissues (17, 18). Nevertheless, unlike in mammals, the role of the thyrotropin releasing hormone in the regulation of TSH release in fish is less well established (19). Due to the absence of a portal system between the hypothalamus and the pituitary, the zebrafish hypothalamus directly innervates the pituitary (20). Notably, *ISL2* and *ISL1* are both members of the Islet-1 family, and share 72% protein sequence identity in mice (21). These two genes may have similar functions given their close structural similarities. However, the role of *ISL2* in pituitary development has not been clarified yet. Thus, we investigate the role of *ISL2* in the development and function of the HPT axis.

In the current study, we utilized the zebrafish model to characterize the role of *ISL2* in the development of HPT axis. We found that *ISL2*, as a transcription factor, is a critical factor for the correct differentiation of pituitary sub-types and that it affects thyroid development through reducing proliferation rather than affecting apoptosis.

Abbreviations: HPT, hypothalamus-pituitary-thyroid; hpf, hours post-fertilization; dpf, days post-fertilization; mpf, months post-fertilization; WISH, whole-mount *in situ* hybridization; TSH, thyroid stimulating hormone; T4, thyroxine; T3, 3,5,3′-triiodothyronine; TH, thyroid hormone; FSH, follicle-stimulating hormone; LH, luteinizing hormone.

Materials and methods

Zebrafish husbandry

The Tübingen strain of zebrafish (Danio rerio) used in this study was maintained at 28.5°C with a light-dark cycle of 14 hours/10 hours and at a stocking density of 6-8 fishes/L. The zebrafish were fed twice a day with Paramecium, Brine Shrimp, and flake food. Food concentration depends on zebrafish body weight and the purpose for which the animals are kept. The embryo stages are expressed in hours post-fertilization (hpf) at a standard temperature. Fertilized eggs were collected *via* natural spawning and raised in egg water (0.06 g/L Instant Ocean Sea Salt and 22.2 ug/L methyl blue). The Tg (*tg*: egfp) transgenic line that specifically expresses green fluorescent protein (EGFP) in thyroid cells was used for this study. The Shanghai Jiao Tong University School of Medicine's Institutional Animal Care and Use Committee examined and approved all animal protocols.

Generation of the *isl2a* and *isl2b* CRISPR knockout zebrafish lines

Knockout fish lines were generated *via* the CRISPR/Cas9 technique (22, 23). CRISPOR (http://crispor.tefor.net/) was used to design an *isl2a* sgRNA targeting exon 3 near the LIM2 domain (5'-GGCGGACCACGGACTGCTAA-3'). Similarly, the *isl2b* sgRNA, targeting exon 2 in the LIM2 domain (5'-GGGAGACG CGCAGGATGTAC-3'), was synthesized in the same way as *isl2a*. Then, using the MEGA script™ T7 Transcription Kit (Ambion), sgRNAs were transcribed and purified using the mirVana™ miRNA Isolation Kit (Ambion). Cas9 mRNA was transcribed with the SP6 mMESSAGE mMACHINE™ Kit (Ambion) and purified with the AxyPrep DNA Gel Extraction Kit (Axygen). A total of 50 pg of sgRNA and 300 pg of Cas9 mRNA (2 nL volume) were injected into single-cell stage fertilized wild-type embryos.

Sanger sequencing was used to confirm the mutation at the target location. The surviving sgRNA/Cas9-injected embryos (F0 founders) were nurtured to adulthood and outcrossed with wild-type adults to produce the F1 generation. The knockout line was established using an F0 founder with germline transmission and a high rate of indels. F1 generation embryos were brought to adulthood, fin clipped, and sequenced. Individuals carrying the same variant were identified and pooled together. All experiments were carried out on embryos derived from F2 or F3 offspring.

A whole larva or fin clip was placed in a separate tube with 50 µL of lysis buffer (1M Tris-HCl, 0.5µM EDTA, 10% Tween and 10%

NP40) to extract genomic DNA in order to determine the genotype of the larvae. Lysis was initiated at 95 °C for 10 min, then the samples were incubated at 55°C overnight before being heated to 98°C for 10 min. Lysed samples were genotyped by PCR amplification of a region of interest (containing the *isl2a* 13bp insertion or *isl2b* 5bp deletion) using Taq DNA Polymerase (Lifefeng) and specific primers (Table S1). The samples were subjected to Sanger sequencing using the same primers used for amplification. All larvae were genotyped to generate lines and for all phenotypic characterizations.

Whole-mount *in situ* hybridization

WISH was undertaken as previously described (24) using digoxigenin-labeled probes (Roche). The probes were made as previously described (25, 26). The target gene's coding sequence fragment was amplified and cloned into the pGEM®-T vector (Promega) using wild-type strain cDNA. For anti-sense DIG-labeled RNA probes, cloned DNA was linearized with various endonuclease enzymes before being produced with SP6 RNA polymerase or T7 RNA polymerase using the DIG RNA labeling kit (all Roche). In zebrafish, *shha* (3), *pitx3* (4), *lhx4* and *lhx3* (27) are involved in the determination of the fate of pituitary precursor cells. *Pit1* and *six1b* are required for lineage-specific differentiation of the pituitary; the *pit1* lineage depends on *pit1* (5), while the non-*pit1* lineage depends on the *eya1*/*six1b* protein complex (6). Pituitary precursors differentiate into specific cell types with markers, including *gh* (for somatotropes), *tshba* (for thyrotropes), *cga* (for thyrotropes and gonadotropes), *prl* (for lactotropes) and *pomca* (for corticotropes and melanotropes) (28). Thus, *isl2a*, *isl2b*, pituitary cell markers (including *shha, pitx3, lhx4, lhx3, pit1, six1b, gh, prl, tshba, cga*, and *pomca*), and thyroid cell markers (including *tg*) were synthesized. All primer sequences are described in Table S2. All DNA constructs were verified by sequencing.

Embryos were fixed in 4% paraformaldehyde, rinsed in 1× phosphate-buffered saline with 0.1% Tween® 20 detergent (PBST), destained in 5% hydrogen peroxide, washed in 25-100% methanol successively and stored in 100% methanol at -20 °C until needed. Embryos were rinsed with 75-25% methanol followed by 1× PBST on the first day of the WISH procedure. Embryos were fixed again with 4% paraformaldehyde and washed with 1× PBST after being treated with proteinase K (Sigma) according to the developing stages for permeabilization. Embryos were hybridized with the RNA probes in the hybridization mix solution overnight at 68°C. On the second day, embryos were blocked with 10% fetal bovine serum (Thermo) and incubated with anti-digoxigenin-alkaline phosphatase Fab fragments (Roche) overnight at 4°C after being washed with 2× saline sodium citrate, 0.1% Tween 20 (SSCT)/50% deionized formamide, 2× SSCT and 0.2× SSCT at 68°C. Embryos were produced on the third day using 5-bromo-4-chloro-3'-indolyphosphate p-toluidine salt (BCIP)/nitro-blue tetrazolium chloride (NBP) substrate (Roche). Staining was developed and stopped before the background signals started to appear.

mRNA extraction and qRT-PCR analysis

Total RNA from 3 days post-fertilization (dpf) and 5dpf *isl2a*$^{+/+}$, *isl2a*$^{+/-}$ and *isl2a*$^{-/-}$ larvae, was extracted utilizing TRIzol (Ambion, Life Technologies). Reverse transcription of total RNA (1ug) to single-stranded cDNA was carried out using the PrimeScript™ RT reagent Kit with gDNA Eraser (Perfect Real Time, Takara) and further diluted 1:10. Next, we use the Quant Studio 12K Flex Real-Time PCR System (ABI, USA) to perform qRT-PCR. The primer sequences for real-time detection of target gene mRNA are shown in Table S3. The reaction mixture, containing diluted cDNA template, primers, and 2× TB Green Premix (Takara), was amplified under cycling conditions based on the manufacturer's protocol. Finally, we analyzed the generated data using the corresponding software. The transcripts of all genes were normalized against the housekeeping genes, such as elongation factor 1-alpha (*ef1α*) and beta-actin (*actb*). To determine the relative levels of mRNA expression between experimental samples and controls, we used the ΔΔCq method. At the same time, the data comprising the results were from at least two separate experiments run in triplicate.

Morphological studies in knockout zebrafish

Daily counts of *isl2a*$^{+/+}$, *isl2a*$^{+/-}$ and *isl2a*$^{-/-}$ larvae were made, and notable dysmorphologies such as edema, head, and eye malformations were checked for. For head, ear, eye and female vent size measurements, *isl2a*$^{+/+}$, *isl2a*$^{+/-}$, and *isl2a*$^{-/-}$ larvae were anesthetized in 160 mg/L tricaine methane sulfonate (MS222, Sigma) and positioned in 3% methylcellulose. Lateral images of the head and the whole body of 3dpf and 5dpf larvae were acquired using a Research Stereo Microscope SMZ25 equipped with a Microscope Camera DS-Ri2 (Nikon) and NIS-Elements BR 4.50.00 software. Measurements were manually performed in a blinded manner using ImageJ software. Body length from the anterior tip of the snout to the base of the posterior caudal fin was measured. Heart rate was measured using 30 second video recordings. The body lengths of 14 dpf, 41 dpf, 77 dpf and 7.5 months post-fertilization (mpf) zebrafish were measured by a vernier caliper.

Histological analysis of gonadal tissues

To prepare tissue sections, 42 dpf fishes were anesthetized with 160 mg/L tricaine methane sulfonate (MS222, Sigma), and their gonads were carefully dissected. In this study, gonads from three fish per group were used for the histological analysis. Samples fixed in paraformaldehyde were dehydrated in ethanol, cleared in xylene, embedded in paraffin, cut into 5μm sections, stained with hematoxylin-eosin and observed under a microscope. The staging of ovary and testes development was based on the cellular structure (29, 30).

TUNEL and EdU assays

For immunofluorescence staining, the embryos were fixed with 4% paraformaldehyde, permeabilized with 0.5% Triton X-100, and blocked with 5% bovine serum albumin. The embryos were then incubated with primary antibodies against EGFP (1:200; Abcam) at 4°C overnight, followed by incubation with an anti-rabbit IgG

secondary antibody/Alexa-Fluor 488 (1:500; Life Technologies). After completion of the immunofluorescence staining, proliferation and apoptosis were analyzed by EdU and TUNEL assays using a Click-iT EdU Imaging Kit (Invitrogen) and a One Step TUNEL Apoptosis Assay Kit (Beyotime) according to the manufacturer's protocol, respectively. Finally, the fluorescent signals were detected by confocal microscopy. The number of EdU- or TUNEL- positive thyroid cells was calculated by delineating the region of *tg* expression using ImageJ software. Stacks were recorded using a 20× objective plus 2× zoom (Nikon C2+ confocal system; Nikon), and the images were processed utilizing Adobe Photoshop CS2.

Measurement of hormone levels

Whole-body thyroid hormone levels (T4 and T3), gonadotropic hormone concentrations (FSH and LH) in gonads were measured using commercial ELISA kits (Cloud-Clone Corp., Wuhan, China, and ELK Biotechnology Corp., Wuhan, China, respectively) following the manufacturer's instructions (31, 32). The numbers of individuals used in thyroid hormone levels measurement for the time point of 44dpf was one fish as a sample. The whole gonadal tissues of two fish as a sample to extract gonadotropic hormone at 42dpf. Briefly, each sample was completely homogenized by continuous vortex for 1-2 min at 65 Hz on ice, and centrifuged at 5000 × g for 10 min at 4° C. Next, supernatants were collected and stored at -80 °C for the measurement. As for the levels of testosterone and estradiol in the gonads, a high-performance liquid chromatography System (LC-30A, SHIMADZU, JAPAN) coupled with a triple quadrupole mass spectrometer (QTRAP6500, SCIEX, USA) method (HPLC-MS) was used for multiple reaction monitoring (MRM) analysis (33). The detection of testosterone (289.2/97.3) was operated in positive mode and estradiol (271.2/145) in negative mode. The instrument parameters were as follows: capillary voltage: 5500 V (+)/-4500 (-). MRM declustering potential, entrance potential, collision energy, collision cell exit potential were optimized for each metabolite by flow-injection analysis mode. The sample preparation was performed as follows: the whole gonadal tissues of around 4 mpf zebrafish were completely homogenized with 0.4 ml 0.1× phosphate-buffered saline solution, then centrifugation at 15,000 rpm for 20min at 4°C. The supernatant was removed, added to a threefold precooled methanol solution, and stored at -20°C for 30 minutes. Then centrifugation again at 15,000 rpm for 10min at 4°C, the supernatant was removed and blow-dried under nitrogen, and resuspended in 100ul isopropanol/acetonitrile/water solution (30:65:5). After centrifugation, the supernatant was immediately used for hormone analysis.

Statistical analysis

The data of testosterone and estradiol is presented as the mean ± SEM, other data is presented as the mean ± SD or percentages. For data failing the normality test, the pairwise statistical significance was established using Student's unpaired t-test or Mann-Whitney test, and multiple comparisons were determined using one-way ANOVA with Tukey's test. All statistical analyses were performed using GraphPad Prism6 software (GraphPad, San Diego, CA, USA). The significant differences were shown at * $P < 0.05$, ** $P < 0.01$, *** $P < 0.001$ and **** $P < 0.0001$.

Results

Zebrafish ISL2 orthologue gene knockout using CRISPR/Cas9

The zebrafish genome encodes two single *ISL2* orthologues (*isl2a* has 90.2% identity and *isl2b* has 89.5% identity at the amino acid level compared to the human *ISL2* protein) with a highly conserved domain (Figure 1A). To examine potential functional effects of *ISL2* loss-of-function *in vivo*, we generated *isl2a* and *isl2b* knockout models using CRISPR/Cas9 technology in zebrafish. The *isl2a*-CRISPR-target site was designed in exon 3 of *isl2a*, and CRISPR/Cas9-induced insertions of 13 nucleotides were chosen for further *isl2a* mutant line generation and maintenance (Figure 1B). The target site for *isl2b* was designed in exon 2 of *the gene*, and CRISPR/Cas9-induced deletions of five nucleotides were selected for further generation and maintenance in the *isl2b* mutant line (Figure 1C). At 3 dpf, qRT-PCR analysis validated an almost complete lack of *isl2a* mRNA in $isl2a^{-/-}$ larvae and approximately half of the transcript was present in $isl2a^{+/-}$ larvae, which demonstrates the efficacy of the *isl2a* knockout. Both mutants were verified *via* Sanger sequencing and were predicted to produce truncated proteins.

Isl2a loss-of-function variant reduces subtypes of pituitary cells

As we all know, *isl2a* is expressed in a diffuse anterior area, as well as in the pineal gland and ventral hindbrain at 24 hpf (Figure 2A). However, the expression of *isl2a* was limited to the pineal gland and subsets of the retinal and otic cells at 48 hpf, with modest expression in the diencephalon at 48 hpf (Figure 2A). To investigate the potential effects of *ISL2* on HPT axis development, we performed WISH to analyze the mRNA expression levels of several cell marker genes, including *tshba* (encoding the beta subunit of TSH) and *tg* (encoding thyroglobulin). Interestingly, the thyrotropes were reduced in $isl2a^{-/-}$ embryos compared to $isl2a^{+/+}$ and $isl2a^{+/-}$ embryos with reduced expression of *tshba* and *cga* (encoding alpha subunit of TSH, LH, and FSH) at 3 dpf (Figure 2B). Somatotropes and lactotropes, on the other hand, showed no alternations in $isl2a^{-/-}$ embryos, as indicated by the expression of their corresponding markers, *gh* and *prl*, respectively (Figure 2B). In addition, no significant difference in corticotropes and melanotropes among the $isl2a^{+/+}$, $isl2a^{+/-}$ and $isl2a^{-/-}$ embryos was observed, as indicated by *pomca* expression (Figure 2B). Similarly, *tshba*, *cga*, and *tg* transcript levels in $isl2a^{-/-}$ embryos were reduced to 8.62%, 10.50%, and 71.00% of the levels in $isl2a^{+/+}$ embryos, respectively, according to qRT-PCR analyses (Figure 2C).

For *isl2b*, it is expressed in zebrafish several structures, including midbrain, hindbrain and pharyngeal arch at 24 hpf, and retinal, one endoderm primordium, and branchial arches at 48 hpf (Figure S1A). No significant differences in *tshba* or *tg* transcription levels were found among the $isl2b^{+/+}$, $isl2b^{+/-}$ and $isl2b^{-/-}$ embryos (Figure S1B). Interestingly, we found genetic compensation in the *isl2b* mutants.

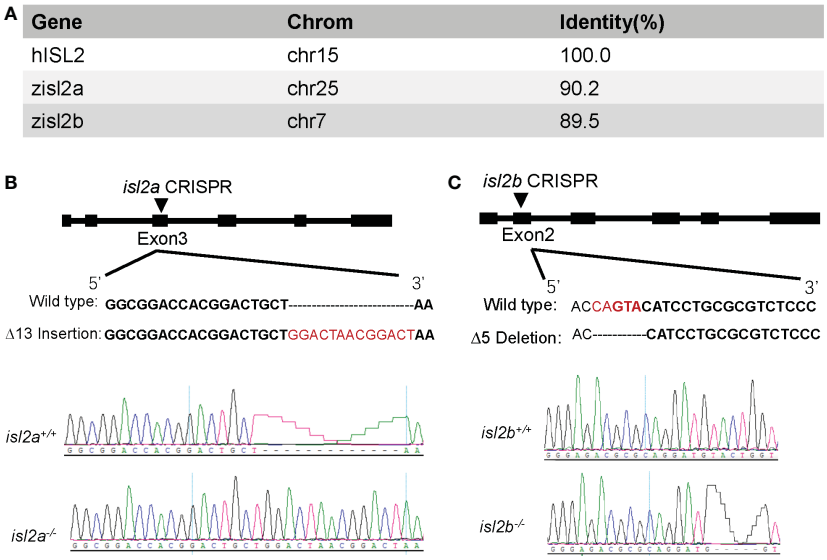

FIGURE 1
Generation of *isl2a* and *isl2b* knockout zebrafish utilizing CRISPR-Cas9 technology. **(A)** Amino acid identity between zebrafish and human *ISL2* proteins was performed using UCSC Blat software. **(B)** The *isl2a*-CRISPR-target site (black bold words) was designed in exon3 of *isl2a* and the CRISPR/Cas9-induced insertion of 13 nucleotides (red words) was selected for further investigation. **(C)** In the case of *isl2b*, the CRISPR-target site (bold words) was designed in exon2, and the induced deletion of five nucleotides (red words) was selected for further investigation. Genotypes, including wild-type and homozygotes, were analyzed and shown in the bottom panel. Both genotypes were predicted to produce truncated proteins.

Compared to $isl2b^{+/+}$ embryos, the expression of *isl2a* in $isl2b^{+/-}$ and isl2b$^{-/-}$ embryos were significantly increased by 26.81% and 51.56%, respectively (Figure S1C). Genetic compensation may contribute to the lack of differential expression of the *tshba* and *tg* transcripts. Furthermore, in the offspring of $isl2a^{+/-}isl2b^{+/-}$ mating, we found reduced *tshba* and *cga* transcripts in $isl2a^{-/-}$ zebrafish, but no phenotype in $isl2b^{-/-}$ zebrafish (Figure S1D).

We next investigated early pituitary development. As shown in Figure 2D, the overall size of the pituitary, as analyzed by *shha*, *pitx3*, *lhx3*, and *lhx4* expression, was not affected in *isl2a* mutants at 24 hpf. These results suggest that overall cell numbers in *isl2a* mutants were normal, indicating that *isl2a* is not necessary for early development of the pituitary. To investigate early cell fate specification in the pituitary of *isl2a* mutants, the expression levels of *pit1* and *six1b* were analyzed. There were no noticeable variations in *pit1* or *six1b* expression in *isl2a* mutants at 48 hpf compared to controls (Figure 2D). Thus, these findings suggest that *isl2a* wasn't essential for the early formation of the pituitary or for the specification of pit1 and non-pit1 lineages.

Effects of low TSH level on thyroid morphology and function

As shown in Figure 3A, the expression levels of *tg* were reduced in $isl2a^{-/-}$ eymbryos compared to control embryos both at 3 dpf and 5 dpf, and the trendline of change was similar to that of *tshba*. Notably, $isl2a^{-/-}$ larvae at 5dpf presented reduced mRNA expression of *tshba*, *cga*, *tg* and two other thyroid markers (*tpo* and *slc5a5*) as shown in Figure 3B. As detected by WISH, $isl2a^{-/-}$ larvae present with thyroid hypoplasia. To determine whether the thyroaplasia was due to low TSH level through the pituitary-thyroid axis, we further investigated the mRNA level of thyroid primordium markers (*nkx2.1* and *pax2a*) at 48 hpf when the activating effect of TSH has not yet been fully established. Mutants presented no significant reduction of both early development marker transcripts compared to controls (data not shown), indicating that *isl2a* knockout does not directly affect the development of thyroid primordium.

To further elucidate the involved mechanisms, we analyzed cell proliferation and apoptotic markers in thyroid cells expressing *tg*. Consistent with previously published data reporting that thyrotropin stimulates the proliferation of thyroid cells *in vivo* (34), there were significantly fewer EdU-positive cell fragments within the *tg* domain in 120 hpf $isl2a^{-/-}$ zebrafish's thyroids ($P < 0.05$, Student's t-test) compared to $isl2a^{+/+}$zebrafish, and no statistically relevant difference was observed in TUNEL-positive cell fragments in 127 hpf larvae (Figures 3C, D). Overall, these findings suggest that loss of *isl2a* expression impairs zebrafish pituitary development and that thyroaplasia may be induced by low TSH levels through reducing proliferation.

Because thyrotropes defects in *isl2a* mutants during early pituitary development should influence HPT axis function in adults, we used ELISA to compare the whole-body contents of thyroid hormones (THs) in $isl2a^{-/-}$ and $isl2a^{+/+}$ adults. Whole body contents of T4 and T3 in $isl2a^{-/-}$ zebrafish at 44 dpf were significantly lower than those in $isl2a^{+/+}$ zebrafish (Figure 3D), indicating that *isl2a* knockout affects thyroid function.

Developmental phenotype of *isl2a* mutants

The surviving F3 $isl2a^{-/-}$ embryos were brought to adulthood. In addition to development and growth, we observed a low survival ratio in $isl2a^{-/-}$ individuals. Compared to wild-type fish (86.8% at 7.5 hpf and 84.9% at 24 hpf, n = 159), the survival ratio of $isl2a^{-/-}$ embryos was

10.3389/fendo.2023.920548

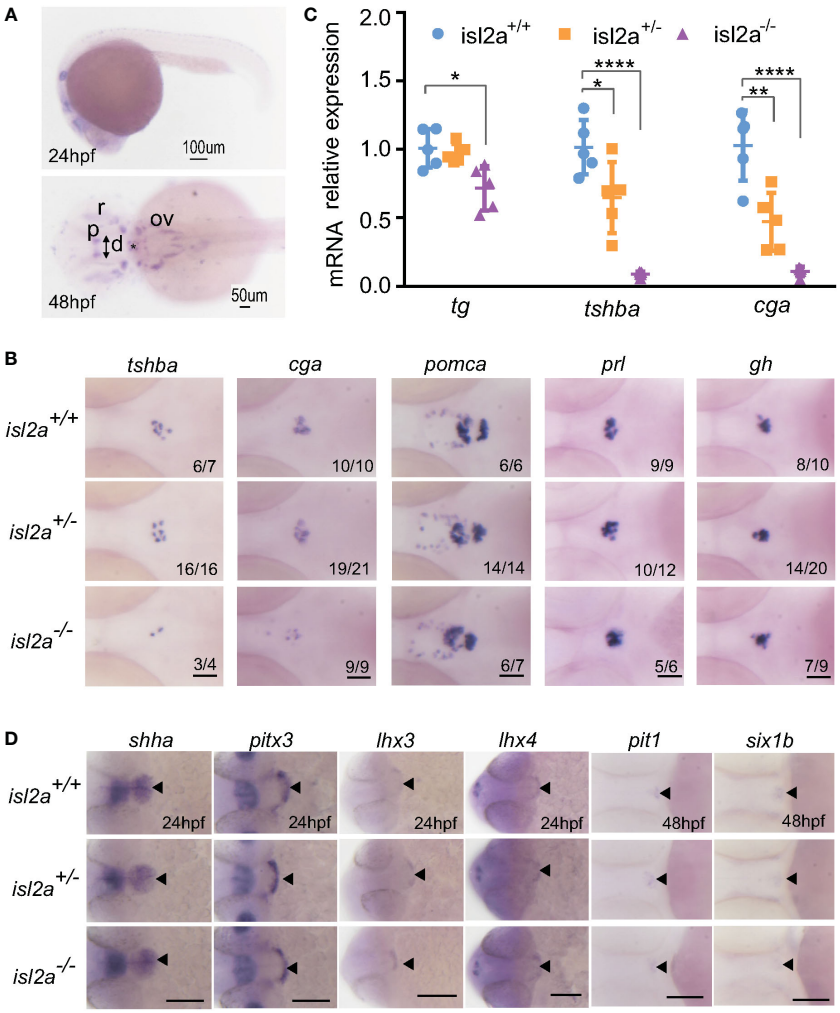

FIGURE 2
Effect of *isl2a* knockout on the expression of genes involved in pituitary development *via* whole-mount *in situ* hybridization. **(A)** Spatiotemporal expression patterns of *isl2a* by whole-mount RNA *in situ* hybridization at 24 and 48 hpf. Scale bars = 100 μm/50 μm. Asterisks (*) indicate the position of midbrain-hindbrain boundary. p, pineal gland; r, retinal; ov, otic vesicle; d, diencephalon. **(B)** Knockout of *isl2a* resulted in reduced *tshba* and *cga* expression, while the expression of *pomca*, *prl*, and *gh* was not changed in larvae at 3 dpf. Pituitary precursors differentiate into specific cell types with markers, including *gh* (for somatotropes), *tshba* (for thyrotropes), *cga* (for thyrotropes and gonadotropes), *prl* (for lactotropes), and *pomca* (for corticotropes and melanotropes). All images are dorsal views with the head pointing towards the left. Scale bar = 50 μm. Numbers indicate the ratio of embryos with the shown phenotype. **(C)** qRT-PCR analysis demonstrates the expression of total *tg*, *tshba* and *cga* in $isl2a^{+/+}$, $isl2a^{+/-}$ and $isl2a^{-/-}$ larvae at 3 dpf. Data is represented as mean ± SD (n = 5, 15 fish per tube). *P<0.05, **P<0.01, ****P<0.001. **(D)** Ventral views of embryos at 24 hpf show no differences in *shha*, *pitx3*, *lhx3* and *lhx4* expression in *isl2a* mutants. Dorsal views of embryos at 48 hpf show no difference in gene expression, indicating specification of pit-1 lineage (*pit1*, for somatotropes, thyrotropes, and lactotropes) or non-pit-1 lineage (*six1b* for corticotropes, gonadotropes, and melanotropes). Thus, pituitary induction and lineage specification were unaffected in *isl2a* mutants. Scale bar = 100 μm. The black triangle indicates gene expression in the adenohypophyseal placode.

86.9% at 7.5 hpf and 55.0% at 24 hpf (n = 253) (Figure 4A). Absence of *isl2a* led to premature death between 0 and 36 hpf, suggesting an essential role for *isl2a* in survival. The female to male ratios were 28.6%, 23.8%, and 16.7% in $isl2a^{+/+}$, $isl2a^{+/-}$, and $isl2a^{-/-}$ adults (Figure 4B).

Several development indicators, including body length, heart rate, eye size, and ear size, showed no significant difference between $isl2a^{-/-}$ zebrafish and their $isl2a^{+/+}$ and $isl2a^{+/-}$ siblings at 5 dpf (Figure 4D), whereas three diameter lines of the skull showed statistically differences between different groups at 5 dpf (Figure 4E). A severe short body length was observed in $isl2a^{-/-}$ larvae from 14 dpf onwards, which progressed during the time course. Measurements taken from different body lengths of $isl2a^{-/-}$ individuals identified significant reductions at 14 dpf, and the reductions were more apparent at 41 dpf when the body size was smaller compared to $isl2a^{+/+}$ and $isl2a^{+/-}$ siblings, with differences visible to the naked eye (Figures 4C, F). At 77 dpf, the differences in body length between groups were further enhanced, but the differences disappeared at 7.5 mpf (Figure 4F).

In order to determine the effect of low expression levels of *cga* or low thyroid hormones on gonad development between wild-type and *isl2a* mutants, gonads were dissected to extract gonadotropin and steroid hormones, and to conduct histological analyses. Surprisingly, the FSH levels in $isl2a^{-/-}$ zebrafish gonads were significantly higher than their $isl2a^{+/+}$ and $isl2a^{+/-}$ siblings at 42 dpf (Figure S2A). However, no significant difference in the LH levels between the three groups (Figure S2B). Histological sections of 42dpf $isl2a^{-/-}$ and $isl2a^{+/+}$ zebrafish both showed ovary or testis (Figure S2C). Moreover, the histological structures of the gonadal tissues were more immature

10.3389/fendo.2023.920548

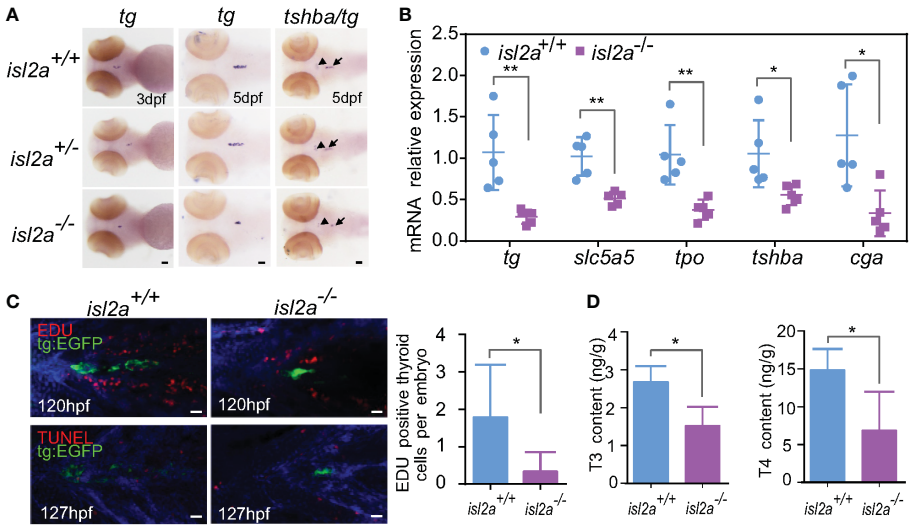

FIGURE 3
Isl2a mutants show reduced thyroid function. **(A)** The assessment of *tg* expression in *isl2a* mutants at 3 dpf and 5 dpf *via* whole-mount *in situ* hybridization. At 5 dpf, *isl2a*$^{-/-}$ zebrafish had lower expression of *tg* and *tshba* as denoted by black arrows and arrowhead, respectively. Scale bar = 50 μm. **(B)** qRT-PCR analysis of the total expression of *tg*, *slc5a5*, *tpo*, *tshba*, and *cga* in *isl2a*$^{+/+}$ and *isl2a*$^{-/-}$ larvae at 5 dpf. Error bars represent ± SD (n = 5, 15 fish per tube). **(C)** Both EGFP (green) and EdU immunoreactivity (red) were present in the thyroid of 120 hpf Tg (*tg*:egfp) wild-type (n = 7) larvae, whereas nearly no EdU-positive cells were detected within the *tg* domain in *isl2a*$^{-/-}$ larvae (n = 6). There were also no TUNEL-positive cells (red) in the *tg* domain at 127 hpf. Scale bar = 500 μm. **(D)** Thyroxine (T4) and 3,5,3′-triiodothyronine (T3) levels in the zebrafish body at 44 dpf. Error bars represent ± SD (n = 4). Asterisks indicate significant differences between *isl2a*$^{+/+}$ and *isl2a*$^{-/-}$ groups (*P < 0.05, **P < 0.01).

in the *isl2a*$^{-/-}$ zebrafish, when compared to that in wild-type zebrafish. Surprisingly, no significant difference was obtained from the levels of testosterone and estradiol between *isl2a*$^{-/-}$ and *isl2a*$^{+/+}$ zebrafish at around 4mpf (Figures S3A, S3B). As for secondary sex characteristics of the *isl2a*$^{-/-}$ zebrafish, we observed a decrease in vent size in *isl2a*$^{-/-}$ female zebrafish at 77dpf compared to that in wild-type female zebrafish (Figures S3C, S3D).

Discussion

In the present study, the expression patterns and functional roles of *ISL2* orthologues (*isl2a* and *isl2b*) in zebrafish were characterized. Using the CRISPR-Cas9 knockout strategy, we discovered that the homozygous variant of *isl2a* caused pituitary and thyroid developmental defects during embryogenesis with reduced expression

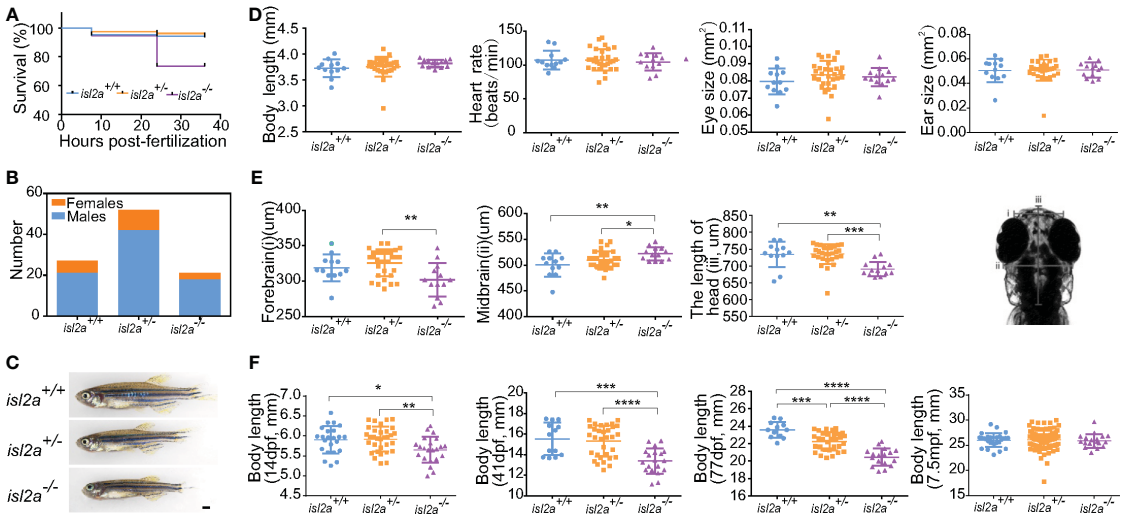

FIGURE 4
Growth retardation in *isl2a* knockout zebrafish. **(A)** The Kaplan-Meier survival curve of *isl2a*$^{+/+}$ (n = 159), *isl2a*$^{+/-}$ (n = 173), and *isl2a*$^{-/-}$ (n = 253) larvae shows differences. **(B)** Male/female ratios in *isl2a*$^{+/+}$ (male/female = 20/6), *isl2a*$^{+/-}$ (male/female = 42/10), and *isl2a*$^{-/-}$ (male/female = 18/3). **(C)** The *isl2a* variant caused significant growth defects in 41 dpf zebrafish adults. Scale bar = 1 mm. **(D)** Comparison of developmental indicators, including body length, heart rate, eye size, and ear size, among *isl2a*$^{-/-}$, *isl2a*$^{+/+}$ and *isl2a*$^{+/-}$ siblings at 5 dpf. **(E)** Comparison of three diameter lines of skull among different groups at 5 dpf. **(F)** Dynamic tracking of the body length of *isl2a*$^{-/-}$ individuals and their *isl2a*$^{+/+}$ and *isl2a*$^{+/-}$ siblings at 14 dpf, 41 dpf, 77 dpf, and 7.5 mpf. *P<0.05, **P<0.01, ***P<0.001, ****P<0.0001.

levels of *tshba*, *cga*, and *tg*. Interestingly, no significant differences in *isl2b* mutants suggested that the low rate of overt phenotypes observed in the zebrafish may be explained by genetic compensation for the effects of loss-of-function variants (35, 36). Moreover, the significantly fewer thyrotrope cells in the pituitary compared to controls as well as the low T3 and T4 levels in *isl2a* homozygous zebrafish were also consistent with central hypothyroidism.

The phenotype of *isl2a* null zebrafish indicates that *ISL2* is involved in thyrotrope development similar to *ISL1*, which is enrichment in thyrotrope lineages in human fetal pituitaries (7) as well as involved in thyrotrope development (12). We hypothesized that *ISL2* and *ISL1* may exert some redundancy in differentiating the pituitary. As we all know, *Lhx3* and *Lhx4 as well as Isl1* and *Isl2* are two such paralogous pairs (37). *Lhx3* and *Isl1* interact inside a well-characterized transcriptional complex that regulates motor neuron development. Indeed, the lack of thyrotropes in *Lhx3* null mice may be due to a delay in *Isl1* expression (12). Interestingly, there is also a *Lhx3*-binding domain in *Isl2* (38). Taken together, we suppose that *ISL2* may form a transcriptional complex with *LHX3* to participate in pituitary development. Besides *ISL1*, several transcription factors, including *POU1F1*, *GATA2*, and *PITX2*, are also required for thyrotrope differentiation (2). Whether *ISL2* acts as a novel regulatory factor or depends on these transcription factors to function in the specification of thyrotropes deserves further study.

Our results agreed with the previous studies on the role of TSH-TSH receptor (TSHR) signaling during thyroid morphogenesis in zebrafish. Knockdown of *tshr* function by morpholino microinjection into embryos causes defects in thyroid later functional differentiation rather than affects early morphogenesis (18). TSH plays an important role in thyroid development by activating the G-protein-coupled TSHR on the surface of the thyroid, but it occurs later than the thyroid primordium development process (39, 40). Taking advantage of this time lag in development, we confirmed that thyroid morphology and function in $isl2a^{-/-}$ zebrafish are impacted by low TSH levels rather than abnormal thyroid primordium development. Moreover, we found that thyroid hypoplasia is caused by defective thyrotropes through the proliferation pathway. In zebrafish, the *pomca*-expressing cells in the ventral diencephalon are hypothalamic and belong to the arcuate nucleus (41). Due to the distribution of *pomca*-expressing cells in the pituitary and hypothalamus without a significant difference among *isl2a* groups, we presume that hypothalamic development is unaffected. Moreover, the role of the thyrotropin releasing hormone in the regulation of TSH release in zebrafish is less well established. Thus, the possibility of hypothalamic defects or releasing factors secretion contributing to the phenotypes is little.

We discovered that $isl2a^{-/-}$ zebrafish showed growth retardation during the juvenile stage but reached normal size during adult stage (7.5 mpf) like their control siblings. Significantly, this phenotype is commonly observed in mutant zebrafish with defects in TH signaling, including thyroglobulin (*tg*), dual oxidase (*duox*), and thyroid-stimulating hormone subunit beta a (*tshba*) mutants (44, 42). Compared with the infertility observed in the homozygous *tshba* mutants (44), there were much less severe reproduction defects in our $isl2a^{-/-}$ fish, just with increased early mortality in embryos. This is due to residual TSH signaling left in the *isl2a* mutants being functional. Nevertheless, decreased TH or TSH signaling cannot fully account for the gender imbalance in our *isl2a* mutants. In previous studies, it was demonstrated that the levels of testosterone were critical to the secondary sex characteristics development (43). Notably, the expression of *cga*, which encodes the α- protein subunits shared by TSH and gonadotrophins, significantly decreased in *isl2a* mutants. The increased proportion of males in *isl2a* mutants is probably attributed to abnormal gonadotrope development and function. In this study, we analyzed gonadal histology and gonadotropin and steroid hormones concentrations. We observed that FSH concentrations were higher in 42 dpf $isl2a^{-/-}$ zebrafish than their $isl2a^{+/+}$ and $isl2a^{+/-}$ siblings, although the gonadal development is delayed. However, the levels of testosterone and estradiol in $isl2a^{-/-}$ were not decreased compared to that in $isl2a^{+/+}$ zebrafish at around 4 mpf. Thus, the maturation of gonads in the *tshba* mutants was not totally affected in $isl2a^{-/-}$ zebrafish, but the morphologic development of gonad was delayed due to growth retardation during the juvenile stage. Moreover, the defective development of secondary sex characteristics was observed in $isl2a^{-/-}$ zebrafish at 77dpf, caused by impaired TSH signaling in zebrafish as previously reported (32).

The present study has several limitations. First, although downregulation of *isl2a* in zebrafish embryos resulted in HPT axis developmental abnormalities, the mechanisms were not fully elucidated in this study. Further experiments are needed to better understand the molecular events linking this specific regulation of *ISL2* in the HPT axis. Second, the present study did not further explore the impact of *isl2a* on gonadotropes due to the limitation of few homozygotes. Further validations in older adult zebrafish are necessary. Due to the limited data in this study, it is crucial to evaluate the results carefully, especially because the phenotype was subtle. Third, there are inevitable species differences between knockout zebrafish models and humans. Homozygous or compound heterozygous *ISL2* mutations in central hypothyroidism patients have not been detected thus far. Finally, the possibility of the off-target effect in CRISPR-Cas9 applications has not been completely eliminated in our study, albeit we chose a high-scoring guide RNA for our intended target with the silico tool. Despite these limitations, we established the utility of this technique as a tool for human cell biology in pituitary development and disease.

In conclusion, we propose that *ISL2* is important for embryonic pituitary development. In particular, our findings provide insight into the specific regulation of *ISL2* during the terminal differentiation of the pituitary from the lineage cells to thyrotropes. Moreover, $isl2a^{-/-}$ zebrafish could be used as an alternative *in vivo* model for studying the underlying mechanisms of hypothyroidism diseases and high-throughput screening of potential drugs for treating central hypothyroidism.

Data availability statement

The original contributions presented in the study are included in the article/Supplementary Material. Further inquiries can be directed to the corresponding authors.

Ethics statement

The animal study was reviewed and approved by the Institutional Animal Care and Use Committee of Shanghai Jiao Tong University School of Medicine.

Author contributions

C-YY designed and performed the *in vivo* experiments and wrote the draft of the article. F-YW undertook some of the experiments. FS, YF, R-JZ and C-RZ established knockout zebrafish. C-XZ, ZW and LY assisted in the maintenance of zebrafish. R-MY, MD, Q-YZ and X-PYconceived the study and provided experimental guidance. S-XZ and H-DS critically reviewed the manuscript. All authors contributed to the article and approved the submitted version.

Funding

This work has been partially supported by the National Natural Science Foundation of China (82070816, 81870537, 82170802, 81770786, 81661168016, and 81870540), National Key R&D Program of China (2017YFC1001801), Shanghai Municipal Education Commission-Two-hundred Talent (20161318), Innovative Research Team of High-Level Local Universities in Shanghai (SHSMU-ZDCX20210901, SHSMU-ZDCX20212501).

Conflict of interest

The authors declare that the research was conducted in the absence of any commercial or financial relationships that could be construed as a potential conflict of interest.

Publisher's note

Supplementary material

The Supplementary Material for this article can be found online at: https://www.frontiersin.org/articles/10.3389/fendo.2023.920548/full#supplementary-material

SUPPLEMENTARY FIGURE 1
Expression patterns of *isl2b* in zebrafish and no hypothalamus-pituitary-thyroid axis phenotype in mutants. **(A)** Spatiotemporal expression patterns of *isl2b* by WISH at 24 and 48 hpf. At 24 hpf, small black arrows indicate the position of *in situ* hybridization high signals in the midbrain, hindbrain and pharyngeal arch. At 48 hpf, small black arrows indicate the position of high signals in the hindbrain, one endoderm primordium, and branchial arches. Besides, cells in retinal (r) also showed high signals. Scale bars = 200 μm/100 μm. **(B)** Compared to their wild-type and heterozygous siblings, the expression levels of *tshba* and *cga* were unchanged in the *isl2b* mutants. Scale bar = 50 μm. **(C)** Relative levels of *isl2a* transcripts in each *isl2b* genotype group according to qRT-PCR analysis. Error bars represent ± SD (n = 5). **(D)** Expression levels of *tshba* and *cga* in *isl2a* and *isl2b* knockout larvae. Scale bar = 50 μm.

SUPPLEMENTARY FIGURE 2
Gonadotropic hormone concentrations and histological analysis of gonads in *isl2a* knockout zebrafish. **(A, B)** Follicle-stimulating hormone (FSH) and Luteinizing hormone (LH) concentrations in the zebrafish gonads at 42 dpf. Error bars represent ± SD (n = 5, n= 6, n= 4 in $isl2a^{+/+}$, $isl2a^{+/-}$, and $isl2a^{-/-}$, respectively). Asterisks indicate significant differences between groups (** $P < 0.01$). **(C)** Representative histological sections of gonads from $isl2a^{-/-}$ and $isl2a^{+/+}$ zebrafish at 42 dpf by hematoxylin-eosin staining. The gonad can be identified as an ovary by the presence of cortical alveolar oocytes (indicating black arrows) and perinucleolar oocytes (indicating black asterisks). The testis was identified by the presence of lumina filled with sperm, by the clustered organisation (spermatocysts), and by the clusters of spermatogonia. Scale bar = 25 μm.

SUPPLEMENTARY FIGURE 3
The levels of gonadal hormones (testosterone and estradiol) and changes in secondary sex characteristics in $isl2a^{-/-}$ zebrafish. **(A)** Quantitative analysis of whole-gonad testosterone contents in $isl2a^{-/-}$ zebrafish (6 males and 5 females) their wild-type siblings (6 males and 6 females) at 4 mpf by HPLC-MS in positive ion mode. Error bars represent ± SEM. **(B)** Semiquantitative analysis of whole-gonad estradiol contents in $isl2a^{-/-}$ zebrafish (6 males and 5 females) and their wild-type siblings (6 males and 6 females) at 4 mpf by HPLC-MS in negative ion mode. Error bars represent ± SEM. **(C, D)** Representative female vent in $isl2a^{-/-}$ and $isl2a^{+/}$zebrafish at 77 dpf. Red asterisks indicate the vent anterior to the anal fin. Scale bar = 100 μm. * $P < 0.05$.

References

1. Pogoda HM, Hammerschmidt M. How to make a teleost adenohypophysis: Molecular pathways of pituitary development in zebrafish. *Mol Cell Endocrinol* (2009) 312(1-2):2–13. doi: 10.1016/j.mce.2009.03.012

2. Alatzoglou KS, Gregory LC, Dattani MT. Development of the pituitary gland. *Compr Physiol* (2020) 10(2):389–413. doi: 10.1002/cphy.c150043

3. Sbrogna JL, Barresi MJ, Karlstrom RO. Multiple roles for hedgehog signaling in zebrafish pituitary development. *Dev Biol* (2003) 254(1):19–35. doi: 10.1016/s0012-1606(02)00027-1

4. Dutta S, Dietrich J-E, Aspöck G, Burdine RD, Schier A, Westerfield M, et al. ≪Em<Pitx3≪/Em< defines an equivalence domain for lens and anterior pituitary placode. *Dev (Cambridge England)* (2005) 132(7):1579. doi: 10.1242/dev.01723

5. Nica G, Herzog W, Sonntag C, Hammerschmidt M. Zebrafish Pit1 mutants lack three pituitary cell types and develop severe dwarfism. *Mol Endocrinol (Baltimore Md)* (2004) 18(5):1196–209. doi: 10.1210/me.2003-0377

6. Nica G, Herzog W, Sonntag C, Nowak M, Schwarz H, Zapata AG, et al. Eya1 is required for lineage-specific differentiation, but not for cell survival in the zebrafish adenohypophysis. *Dev Biol* (2006) 292(1):189–204. doi: 10.1016/j.ydbio.2005.12.036

7. Zhang S, Cui Y, Ma X, Yong J, Yan L, Yang M, et al. Single-cell transcriptomics identifies divergent developmental lineage trajectories during human pituitary development. *Nat Commun* (2020) 11:5275. doi: 10.1038/s41467-020-19012-4

8. Hobert O, Westphal H. Functions of lim-homeobox genes. *Trends Genet TIG* (2000) 16(2):75–83. doi: 10.1016/s0168-9525(99)01883-1

9. Sheng HZ, Zhadanov AB, Mosinger BJr., Fujii T, Bertuzzi S, Grinberg A, et al. Specification of pituitary cell lineages by the lim homeobox gene Lhx3. *Sci (New York NY)* (1996) 272(5264):1004–7. doi: 10.1126/science.272.5264.1004

10. Raetzman LT, Ward R, Camper SA. Lhx4 and Prop1 are required for cell survival and expansion of the pituitary primordia. *Dev (Cambridge England)* (2002) 129(18):4229–39. doi: 10.1242/dev.129.18.4229

11. Ellsworth BS, Butts DL, Camper SA. Mechanisms underlying pituitary hypoplasia and failed cell specification in Lhx3-deficient mice. *Dev Biol* (2008) 313(1):118–29. doi: 10.1016/j.ydbio.2007.10.006

12. Castinetti F, Brinkmeier ML, Mortensen AH, Vella KR, Gergics P, Brue T, et al. Isl1 is necessary for maximal thyrotrope response to hypothyroidism. *Mol Endocrinol (Baltimore Md)* (2015) 29(10):1510–21. doi: 10.1210/me.2015-1192

13. Takuma N, Sheng HZ, Furuta Y, Ward JM, Sharma K, Hogan BL, et al. Formation of rathke's pouch requires dual induction from the diencephalon. *Dev (Cambridge England)* (1998) 125(23):4835–40. doi: 10.1242/dev.125.23.4835

14. Yuan S, Schoenwolf GC. Islet-1 marks the early heart rudiments and is asymmetrically expressed during early rotation of the foregut in the chick embryo. *Anatomical Rec* (2000) 260(2):204–7. doi: 10.1002/1097-0185(20001001)260:2<204::aid-ar90>3.0.co;2-5

15. Thor S, Ericson J, Brännström T, Edlund T. The homeodomain lim protein isl-1 is expressed in subsets of neurons and endocrine cells in the adult rat. *Neuron* (1991) 7 (6):881–9. doi: 10.1016/0896-6273(91)90334-v

16. Nasif S, de Souza FS, González LE, Yamashita M, Orquera DP, Low MJ, et al. Islet 1 specifies the identity of hypothalamic melanocortin neurons and is critical for normal food intake and adiposity in adulthood. *Proc Natl Acad Sci United States America* (2015) 112(15):E1861–70. doi: 10.1073/pnas.1500672112

17. Marelli F, Persani L. How zebrafish research has helped in understanding thyroid diseases. *F1000Research* (2017) 6:2137. doi: 10.12688/f1000research.12142.1

18. Opitz R, Maquet E, Zoenen M, Dadhich R, Costagliola S. Tsh receptor function is required for normal thyroid differentiation in zebrafish. *Mol Endocrinol (Baltimore Md)* (2011) 25(9):1579–99. doi: 10.1210/me.2011-0046

19. Schmidt F, Braunbeck T. Alterations along the hypothalamic-Pituitary-Thyroid axis of the zebrafish (Danio rerio) after exposure to propylthiouracil. *J Thyroid Res* (2011) 2011:376243. doi: 10.4061/2011/376243

20. Machluf Y, Gutnick A, Levkowitz G. Development of the zebrafish hypothalamus. *Ann New York Acad Sci* (2011) 1220:93–105. doi: 10.1111/j.1749-6632.2010.05945.x

21. Lee H, Kim M, Kim N, Macfarlan T, Pfaff SL, Mastick GS, et al. Slit and semaphorin signaling governed by islet transcription factors positions motor neuron somata within the neural tube. *Exp Neurol* (2015) 269:17–27. doi: 10.1016/j.expneurol.2015.03.024

22. Hruscha A, Krawitz P, Rechenberg A, Heinrich V, Hecht J, Haass C, et al. Efficient Crispr/Cas9 genome editing with low off-target effects in zebrafish. *Dev (Cambridge England)* (2013) 140(24):4982–7. doi: 10.1242/dev.099085

23. Hwang WY, Fu Y, Reyon D, Maeder ML, Tsai SQ, Sander JD, et al. Efficient genome editing in zebrafish using a crispr-cas system. *Nat Biotechnol* (2013) 31(3):227–9. doi: 10.1038/nbt.2501

24. Schäfer M, Rembold M, Wittbrodt J, Schartl M, Winkler C. Medial floor plate formation in zebrafish consists of two phases and requires trunk-derived midkine-a. *Genes Dev* (2005) 19(8):897–902. doi: 10.1101/gad.336305

25. Li SZ, Liu W, Li Z, Wang Y, Zhou L, Yi MS, et al. Molecular characterization and expression pattern of a germ cell marker gene dnd in gibel carp (Carassius gibelio). *Gene* (2016) 591(1):183–90. doi: 10.1016/j.gene.2016.07.027

26. Zhong JX, Zhou L, Li Z, Wang Y, Gui JF. Zebrafish noxa promotes mitosis in early embryonic development and regulates apoptosis in subsequent embryogenesis. *Cell Death differentiation* (2014) 21(6):1013–24. doi: 10.1038/cdd.2014.22

27. Herzog W, Zeng X, Lele Z, Sonntag C, Ting JW, Chang CY, et al. Adenohypophysis formation in the zebrafish and its dependence on sonic hedgehog. *Dev Biol* (2003) 254 (1):36–49. doi: 10.1016/s0012-1606(02)00124-0

28. Shi C, Lu Y, Zhai G, Huang J, Shang G, Lou Q, et al. Hyperandrogenism in pomca-deficient zebrafish enhances somatic growth without increasing adiposity. *J Mol Cell Biol* (2020) 12(4):291–304. doi: 10.1093/jmcb/mjz053

29. Selman K, Wallace RA, Sarka A, Qi X. Stages of oocyte development in the zebrafish, brachydanio rerio. *J morphology* (1993) 218(2):203–24. doi: 10.1002/jmor.1052180209

30. Leal MC, Cardoso ER, Nóbrega RH, Batlouni SR, Bogerd J, França LR, et al. Histological and stereological evaluation of zebrafish (Danio rerio) spermatogenesis with an emphasis on spermatogonial generations. *Biol Reprod* (2009) 81(1):177–87. doi: 10.1095/biolreprod.109.076299

31. Guo Y, Chen L, Wu J, Hua J, Yang L, Wang Q, et al. Parental Co-exposure to bisphenol a and nano-Tio(2) causes thyroid endocrine disruption and developmental neurotoxicity in zebrafish offspring. *Sci total Environ* (2019) 650(Pt 1):557–65. doi: 10.1016/j.scitotenv.2018.09.007

32. Song J, Lu Y, Cheng X, Shi C, Lou Q, Jin X, et al. Functions of the thyroid-stimulating hormone on key developmental features revealed in a series of zebrafish dyshormonogenesis models. *Cells* (2021) 10(8):1984. doi: 10.3390/cells10081984

33. Nouri MZ, Kroll KJ, Webb M, Denslow ND. Quantification of steroid hormones in low volume plasma and tissue homogenates of fish using lc-Ms/Ms. *Gen Comp Endocrinol* (2020) 296:113543. doi: 10.1016/j.ygcen.2020.113543

34. Ledent C, Parmentier M, Maenhaut C, Taton M, Pirson I, Lamy F, et al. The tsh cyclic amp cascade in the control of thyroid cell proliferation: The story of a concept. *Thyroidology* (1991) 3(3):97–101.

35. Rossi A, Kontarakis Z, Gerri C, Nolte H, Hölper S, Krüger M, et al. Genetic compensation induced by deleterious mutations but not gene knockdowns. *Nature* (2015) 524(7564):230–3. doi: 10.1038/nature14580

36. Kettleborough RN, Busch-Nentwich EM, Harvey SA, Dooley CM, de Bruijn E, van Eeden F, et al. A systematic genome-wide analysis of zebrafish protein-coding gene function. *Nature* (2013) 496(7446):494–7. doi: 10.1038/nature11992

37. Sharma K, Sheng HZ, Lettieri K, Li H, Karavanov A, Potter S, et al. Lim homeodomain factors Lhx3 and Lhx4 assign subtype identities for motor neurons. *Cell* (1998) 95(6):817–28. doi: 10.1016/s0092-8674(00)81704-3

38. Gadd MS, Bhati M, Jeffries CM, Langley DB, Trewhella J, Guss JM, et al. Structural basis for partial redundancy in a class of transcription factors, the lim homeodomain proteins, in neural cell type specification. *J Biol Chem* (2011) 286(50):42971–80. doi: 10.1074/jbc.M111.248559

39. Marians RC, Ng L, Blair HC, Unger P, Graves PN, Davies TF. Defining thyrotropin-dependent and -independent steps of thyroid hormone synthesis by using thyrotropin receptor-null mice. *Proc Natl Acad Sci United States America* (2002) 99 (24):15776–81. doi: 10.1073/pnas.242322099

40. Yang J, Yi N, Zhang J, He W, He D, Wu W, et al. Generation and characterization of a hypothyroidism rat model with truncated thyroid stimulating hormone receptor. *Sci Rep* (2018) 8(1):4004. doi: 10.1038/s41598-018-22405-7

41. Liu NA, Ren M, Song J, Ríos Y, Wawrowsky K, Ben-Shlomo A, et al. *In vivo* time-lapse imaging delineates the zebrafish pituitary proopiomelanocortin lineage boundary regulated by Fgf3 signal. *Dev Biol* (2008) 319(2):192–200. doi: 10.1016/j.ydbio.2008.03.039

42. Chopra K, Ishibashi S, Amaya E. Zebrafish duox mutations provide a model for human congenital hypothyroidism. *Biol Open* (2019) 8(2):bio037655. doi: 10.1242/bio.037655

43. Zhai G, Shu T, Xia Y, Lu Y, Shang G, Jin X, et al. Characterization of sexual trait development in Cyp17a1-deficient zebrafish. *Endocrinology* (2018) 159(10):3549–62. doi: 10.1210/en.2018-00551

frontiers | Frontiers in Endocrinology

TYPE Original Research
PUBLISHED 09 February 2023
DOI 10.3389/fendo.2023.1125569

OPEN ACCESS

EDITED BY
Julius Hreinsson,
Sahlgrenska University Hospital, Sweden

REVIEWED BY
Mayank Choubey,
New York University, United States
Nicolas Crisosto,
University of Chile, Chile

*CORRESPONDENCE
Lourdes Ibáñez
lourdes.ibanez@sjd.es

SPECIALTY SECTION
This article was submitted to Reproduction, a section of the journal Frontiers in Endocrinology

RECEIVED 16 December 2022
ACCEPTED 30 January 2023
PUBLISHED 09 February 2023

CITATION
Díaz M, de Zegher F and Ibáñez L (2023) Circulating follistatin concentrations in adolescent PCOS: Divergent effects of randomized treatments.
Front. Endocrinol. 14:1125569.
doi: 10.3389/fendo.2023.1125569

Circulating follistatin concentrations in adolescent PCOS: Divergent effects of randomized treatments

Marta Díaz[1,2], Francis de Zegher[3] and Lourdes Ibáñez[1,2]*

[1]Endocrinology Department, Institut de Recerca Sant Joan de Déu, University of Barcelona, Barcelona, Spain, [2]Centro de Investigación Biomédica en Red de Diabetes y Enfermedades Metabólicas Asociadas, Instituto de Salud Carlos III, Madrid, Spain, [3]University of Leuven, Leuven, Belgium

Purpose: Follistatin is a glycoprotein that represses members of the transforming growth factor-β superfamily including activin. Higher follistatin levels have been associated with an increased risk for type 2 diabetes and with polycystic ovary syndrome (PCOS). In non-obese adolescent girls with PCOS, insulin sensitization results in a healthier endocrine-metabolic outcome than oral contraception (OC); we assessed whether those differences are underscored by changes in serum follistatin concentrations.

Methods: Circulating follistatin, endocrine-metabolic markers and hepato-visceral fat were measured longitudinally in 72 girls with PCOS [age, 16 years; body mass index (BMI), 23 Kg/m^2] randomized to receive PioFluMet [pioglitazone (7.5 mg/d), metformin (850 mg/d) and flutamide (62.5 mg/d), n=17]; EE-CA [an OC containing 35 µg ethinylestradiol (EE) and 2 mg cyproterone acetate (CA), n=17]; SPIOMET [Spironolactone (50 mg/d), pioglitazone (7.5 mg/d) and metformin (850 mg/d), n=18], or EE-LNG [an OC containing 20 µg EE and 100 mg levonorgestrel (LNG), n=20]. Twenty-eight age- and BMI-matched healthy girls served as controls.

Results: Pre-treatment follistatin levels were similar in PCOS and controls. OCs raised serum follistatin after 6 months (6.8-fold vs 2.5-fold for EE-CA and EE-LNG, respectively). Neither SPIOMET nor PioFluMet changed follistatin levels. Follistatin correlated negatively with high-molecular weight adiponectin and positively with mean serum insulin concentrations during an oral glucose tolerance test at baseline, and with liver fat after 6 months.

Conclusion: In girls with PCOS, follistatin levels rise significantly after 6 months on OCs and this increase associates to a worsening of markers of insulin resistance and to changes in liver fat.

KEYWORDS

follistatin, PCOS, hepato-visceral fat, metformin, pioglitazone, spironolactone, flutamide

1 Introduction

Adolescent polycystic ovary syndrome (PCOS) is a common endocrine disorder hallmarked by clinical and biochemical androgen excess and irregular menses. PCOS appears to be driven by ectopic lipid accumulation specially in the liver that essentially originates from a mismatch between (reduced) prenatal adipogenesis and (augmented) postnatal lipogenesis, resulting in central obesity, insulin resistance, non-alcoholic fatty liver disease (NAFLD), and low-grade inflammation (1). There is no approved therapy for PCOS, but girls are commonly treated with oral contraceptives (OCs), even if not at pregnancy risk. OCs revert the signs and symptoms of androgen excess but fail to address the core problem, and upon treatment discontinuation, there is a rebound of hyperandrogenism and oligo-anovulation. An alternative approach under investigation are the low-dose combinations of insulin sensitizers and anti-androgens with additive effects that switch ectopic fat to eutopic depots, thereby normalizing ovarian function and potentially reducing the risk of long-term co-morbidities. We performed three pilot studies in non-obese girls with PCOS comparing the effects of such combinations with those of OCs. In the first clinical trial (ISRCTN45546616), girls were randomized to receive for one year a low-dose combination of two insulin sensitizers [pioglitazone (7.5 mg/d), and metformin (850 mg/d)] and one anti-androgen [flutamide (62.5 mg/d)] (PioFluMet), or an OC containing ethinylestradiol-cyproterone acetate [EE-CA; 35 μg of EE plus 2 mg of CA for 21/28 d, placebo for 7/28 d; Diane 35 Diario®, Bayer-Schering, Madrid, Spain]. Both treatments decreased similarly androgen excess, but PioFluMet had more benefits on cardiometabolic parameters and adipose tissue expression of genes related to inflammation, fat accretion and lipoprotein metabolism (2, 3). In the other two studies (ISRCTN29234515 and ISRCTN11062950), girls were randomized to receive for one year a low-dose combination of spironolactone (50 mg/d), pioglitazone (7.5 mg/d), and metformin (850 mg/d) (SPIOMET) or an OC containing EE-levonorgestrel [EE-LNG; 20 μg of EE plus 100 mg of LNG for 21/28 d, placebo for 7/28 d; Loette Diario®, Pfizer, Madrid, Spain] (4, 5). The pooled results of these two studies disclosed that SPIOMET intervention is followed by a healthier metabolic status [less insulin resistance and C-reactive protein (CRP) concentrations, less hepato-visceral fat, and higher high-molecular-weight (HMW) adiponectin], and by more ovulations than treatment with OCs (5).

Follistatin was initially identified in and isolated from follicular fluid based on its inhibition of pituitary FSH secretion (6). Later on, follistatin was characterized as a reproductive hormone inhibiting the secretion of members of the transforming growth factor (TGF)-β family of proteins, including activin and inhibin, and as an enhancer of muscle mass through the inhibition of myostatin (7). In humans, follistatin derives mainly from the liver and augmented follistatin levels have been associated with an increased risk for type 2 diabetes, independently of established risk markers (8). Recently, follistatin has been considered to play a role in the etiology of PCOS, as women diagnosed with this disorder depict increased follistatin concentrations *versus* controls, independently of body mass index (BMI) (9, 10). However, those studies were conducted in adult women with a wide age-range diagnosed with PCOS using heterogeneous criteria. Here, we assessed whether the divergent metabolic effects of OCs and low-dose PioFluMet or SPIOMET in adolescent girls with PCOS over the first 6 months of treatment associate to changes in circulating follistatin levels.

2 Materials and methods

2.1 Study design

The study population consisted of 72 non-obese adolescent girls with PCOS belonging to the above described clinical trials [n=17 and n=17 receiving PioFluMet and EE-CA respectively; n=18 and n=20 receving SPIOMET and EE-LNG respectively); mean age, 16 years; mean BMI, 23 kg/m^2; all of them were at last 2 years beyond menarche. The girls were recruited in the Adolescent Endocrinology Unit of Sant Joan de Déu University Hospital, Barcelona, Spain. Randomization was performed with the SealedEnvelop program (Sealed Envelop Ltd., London, UK) (http://www.SealedEnvelop.com), using random permuted blocks with strata for age and BMI (10).The inclusion criteria were (2–5): 1) hirsutism (score > 8 on Ferriman-Gallwey scale); 2) amenorrhea (no menses for more than 3 months) or oligomenorrhea (menstrual intervals >45 days); 3) absence of sexual activity throughout the study duration (and thus, no need for contraception). Exclusion criteria were: 21-hydroxylase deficiency; glucose intolerance or diabetes; evidence of thyroid, liver, or kidney dysfunction; hyperprolactinemia; and prior use of medications affecting gonadal/adrenal function, or carbohydrate/lipid metabolism.

Twenty-eight age- and BMI-matched healthy girls recruited from nearby schools served as controls. All had regular cycles, were non-hirsute, and had normal serum glucose, lipids and androgens.

The PioFluMet study (ISRCTN45546616) and both SPIOMET studies (ISRCTN29234515 and ISRCTN11062950) were conducted after approval by the Institutional Review Board of Sant Joan de Déu University Hospital, after written consent by parents, and assent by each of the study girls, including the healthy controls who allowed to derive indicative values.

2.2 Assessments

Height and weight were measured and BMI calculated. Blood samples were obtained-in the follicular phase or after 2 months of amenorrhea- in the morning after an overnight fast. Serum glucose was measured by the glucose oxidase method. Insulin, testosterone and sex hormone binding globulin (SHBG) were assayed by immunochemiluminiscence (DPC IMMULITE 2500, Siemens, Erlangen, Germany); intra- and inter-assay coefficients of variation (CVs) were <10%; HDL-cholesterol, LDL-cholesterol and triglycerides were assessed by an enzymatic method and C-reactive protein (CRP) was measured with a hightly sensitive method (Architect c8000 autoanalyzer, Abbott laboratories, North Chicago, IL). Homeostasis model assessment for insulin resistance (HOMA-IR) was calculated as fasting insulin (mU/L) x fasting glucose (mmol/L)/22.5.

10.3389/fendo.2023.1125569

Circulating follistatin and HMW-adiponectin were measured by specific ELISAs (R&D Systems, Minneapolis, USA) with intra- and inter-assay CVs <9% for both assays.

Abdominal fat partitioning (subcutaneous and visceral fat areas) as well as liver fat were assessed by magnetic resonance imaging (MRI) using a multiple-slice MRI 1.5 Tesla scan (Signa LX Echo Speed Plus Excite, General Electric, Milwaukee, WI), as reported (2–4).

2.3 Statistics

Statistical analysis were performed with GraphPad Prism 6.01. Results are expressed as mean ± SEM. Variables were checked for normality using the Kolmogorov–Smirnov test prior to analyses. Comparisons within groups were performed using paired t-test. For between groups differences, unpaired t-test or Man-Whitney U test were used for normally distributed or nonparametric variables, respectively.

Correlation analysis was used to study the associations between follistatin concentrations and auxological, endocrine-metabolic, and body composition parameters. Three outliers were identified by the interquartile range method; correlations are presented for n=69 out of 72 girls. The level of significance was set at $p< 0.05$.

3 Results

Both PioFluMet and SPIOMET reduced androgen excess within 6 months towards normal, similarly to EE-CA or EE-LNG. However, only treatment with PioFluMet or SPIOMET -but not with OCs- reduced both the hepatic fat excess and insulin resistance (Table 1).

Pre-treatment follistatin levels were similar in girls with PCOS and in controls (0.7 ± 0.1 ng/mL in both subgroups). OCs significantly raised serum follistatin after 6 months; this increase was higher with EE-CA than with EE-LNG (6.8-fold vs 2.5-fold *versus* baseline; $p<0.0006$ and $p<0.003$, respectively). Neither SPIOMET nor PioFluMet had effects on follistatin levels (Table 1).

At baseline, circulating follistatin correlated negatively with HMW-adiponectin ($r=-0.316$, $p=0.009$) and positively with mean insulin levels during an oral glucose tolerance test (OGTT; $r= 0.303$, $p= 0.012$) [Figures 1A, B]. Pre-treatment liver fat was not related to follistatin levels; however, after 6 months on treatment, liver fat directly and significantly associated with serum follistatin [Figures 1C, D)].

4 Discussion

To our knowledge this is the first longitudinal study comparing the effects of OCs *vs* insulin sensitization on circulating follistatin levels in non-obese adolescent girls with PCOS. Our results disclose that follistatin concentrations increase with OC therapy but remain unchanged with PioFluMet or SPIOMET combinations.

Girls with PCOS and without obesity showed similar serum follistatin concentrations as compared to age- and BMI-matched

TABLE 1 Data from adolescent girls with androgen excess who were randomized to receive ethinylestradiol-cyproteroneacetate [EE-CA (N=17)], low-dose pioglitazone-flutamide-metformin [PioFluMet (N=17)], ethinylestradiol-levonorgestrel [EE-LNG(N=20)] or low-dose spironolactone-pioglitazone-metformin [SPIOMET (N=18)] for 6 months, and from age and BMI-matched-healthy control girls (N=28).

			Ethinylestradiol-Cyproteroneacetate [EE-CA (N=17)]			Pioglitazone-Flutamide-Metformin [PioFluMet (N=17)]			Ethinylestradiol-Levonorgestrel [EE-LNG (N=20)]			Spironolactone-Pioglitazone-Metformin [SPIOMET (N=18)]		
	Controls (N=28)	PCOS (N=73)	Baseline	6 mo	Δ 0-6 mo	Baseline	6 mo	Δ 0-6 mo	Baseline	6 mo	Δ 0-6 mo	Baseline	6 mo	Δ 0-6 mo
Age (yr)	16.3 ± 0.3	15.8 ± 0.2	15.9 ± 0.3	–	–	16.5 ± 0.3	–	–	15.7 ± 0.3	–	–	15.4 ± 0.3	–	–
BMI (kg/m^2)	22.6 ± 0.4	23.5 ± 0.4	23.1 ± 0.6	23.6 ± 0.7^a	0.5 ± 0.2	23.2 ± 0.5	23.3 ± 0.5	0.1 ± 0.2	24.6 ± 0.9	25.0 ± 0.9	0.4 ± 0.3	23.1 ± 0.7	23.1 ± 0.7	0.0 ± 0.2
SHBG (nmol/L)	67 ± 9	29 ± 2***	23 ± 3	159 ± 10^c	136 ± 9	28 ± 3	35 ± 4^a	7 ± 3	32 ± 3	60 ± 5^c	28 ± 5	30 ± 3	30 ± 2	0 ± 2^f
Testosterone (ng/dL)	29 ± 2	55 ± 3***	57 ± 7	32 ± 4^c	-25 ± 5	62 ± 7	43 ± 5^b	-19 ± 6	54 ± 5	29 ± 3^c	-25 ± 5	47 ± 3	31 ± 3^c	-16 ± 4
FAI	1.5 ± 0.3	8.3 ± 0.6***	10.8 ± 1.8	1.1 ± 0.4^c	-9.7 ± 1.5	9.5 ± 1.4	4.9 ± 0.7^c	-4.6 ± 0.9^e	6.7 ± 0.8	1.9 ± 0.2^c	-4.8 ± 0.8	6.5 ± 1.0	4.3 ± 0.5^b	-2.2 ± 0.7^d
Fasting insulin (μU/mL)	4.9 ± 0.7	11.0 ± 0.8***	9.7 ± 1.1	8.1 ± 1.3	-1.6 ± 1.7	10.2 ± 1.9	5.5 ± 1.3^a	-4.7 ± 1.8	13.5 ± 1.8	15.0 ± 1.5	1.5 ± 1.1	10.1 ± 1.5	8.9 ± 1.1	-1.2 ± 1.0
HOMA-IR	1.1 ± 0.2	2.3 ± 0.2**	2.0 ± 0.3	1.7 ± 0.3	-0.3 ± 0.4	2.1 ± 0.4	1.2 ± 0.3^a	-0.9 ± 0.4	2.9 ± 0.4	3.3 ± 0.4^a	0.4 ± 0.3	2.1 ± 0.3	1.8 ± 0.2	-0.3 ± 0.2^d

(*Continued*)

TABLE 1 Continued

			Ethinylestradiol-Cyproteroneacetate [EE-CA (N=17)]			Pioglitazone-Flutamide-Metformin [PioFluMet (N=17)]			Ethinylestradiol-Levonorgestrel [EE-LNG (N=20)]			Spironolactone-Pioglitazone-Metformin [SPIOMET (N=18)]		
	Controls (N=28)	PCOS (N=73)	Baseline	6 mo	Δ 0-6 mo	Baseline	6 mo	Δ 0-6 mo	Baseline	6 mo	Δ 0-6 mo	Baseline	6 mo	Δ 0-6 mo
LDL-cholesterol (mg/dL)	83 ± 4	84 ± 2	81 ± 3	102 ± 5[c]	21 ± 5	80 ± 5	82 ± 3	2 ± 3[e]	90 ± 3	105 ± 5[c]	15 ± 4	84 ± 6	84 ± 5	0 ± 3[e]
HDL-cholesterol (mg/dL)	53 ± 2	52 ± 1	50 ± 2	61 ± 3[c]	11 ± 2	56 ± 3	57 ± 2	1 ± 2[f]	51 ± 2	52 ± 3	1 ± 2	51 ± 2	54 ± 2[a]	3 ± 1
Triglycerides (mg/dL)	53 ± 3	67 ± 6	89 ± 20	130 ± 20[b]	41 ± 21	65 ± 11	67 ± 6	1 ± 7	58 ± 5	65 ± 6	7 ± 5	59 ± 5	58 ± 4	-1 ± 5
C-Reactive Protein (mg/L)	0.7 ± 0.2	1.2 ± 0.1*	0.9 ± 0.2	1.7 ± 0.3[a]	0.8 ± 0.3	1.0 ± 0.2	0.4 ± 0.1[b]	-0.6 ± 0.2[f]	1.4 ± 0.3	2.4 ± 0.5[a]	1.0 ± 0.4	1.4 ± 0.4	0.5 ± 0.1[a]	-0.9 ± 0.4[e]
HMW adiponectin (mg/L)	10 ± 1	9 ± 1	16 ± 3	11 ± 1[a]	-5 ± 2	11 ± 2	18 ± 1[c]	7 ± 2[f]	6 ± 1	9 ± 2	3 ± 2	6 ± 1	15 ± 2[a]	9 ± 2
Follistatin (ng/mL)	0.7 ± 0.1	0.7 ± 0.1	0.6 ± 0.2	3.9 ± 0.8[c]	3.3 ± 0.8	0.4 ± 0.1	0.5 ± 0.1	0.1 ± 0.1[f]	0.8 ± 0.1	2.0 ± 0.4[b]	1.2 ± 0.4	1.1 ± 0.3	1.0 ± 0.1	-0.1 ± 0.3[e]
MRI subcutaneous Fat (cm^2)	98 ± 22	152 ± 10	130 ± 16	145 ± 18[a]	15 ± 7	127 ± 13	123 ± 14	-4 ± 6[d]	193 ± 26	195 ± 25	2 ± 8	152 ± 17	147 ± 17	-5 ± 6
Visceral Fat (cm^2)	29 ± 3	37 ± 2	32 ± 2	35 ± 2	3 ± 2	36 ± 3	31 ± 2[b]	-5 ± 2[e]	40 ± 4	41 ± 4	1 ± 2	39 ± 3	35 ± 2	-4 ± 3
Liver fat (%)	11.5 ± 2.8	16.4 ± 0.7	17.0 ± 1.6	18.9 ± 1.5	1.9 ± 1.5	15.1 ± 1.5	10.1 ± 1.2[b]	-5.0 ± 1.7[e]	16.3 ± 1.5	20.1 ± 1.6[a]	3.8 ± 1.5	17.2 ± 1.3	11.0 ± 1.1[c]	-6.2 ± 1.0[f]

Values are mean ± SEM. MRI, magnetic resonance imaging; BMI, bone mineral density; SHBG, sex hormone-binding globulin; FAI, free androgen index; HOMA-IR, homeostasis model assessment insulin resistance; HMW, high-molecular weight.
*p <0.05, **p<0.01 and ***p≤0.0001 between PCOS at start and healthy control girls.
[a]p <0.05, [b] p≤0.01 and [c]p ≤0.001 within subgroups for 0-6 mo change (Δ).
[d]p <0.05, [e] p ≤0.01, [f] p ≤0.001 between EE-CA and PioFluMet subgroup & EE-LNG and SPIOMET subgroup for 0-6 mo changes (Δ).

10.3389/fendo.2023.1125569

10.3389/fendo.2023.1125569

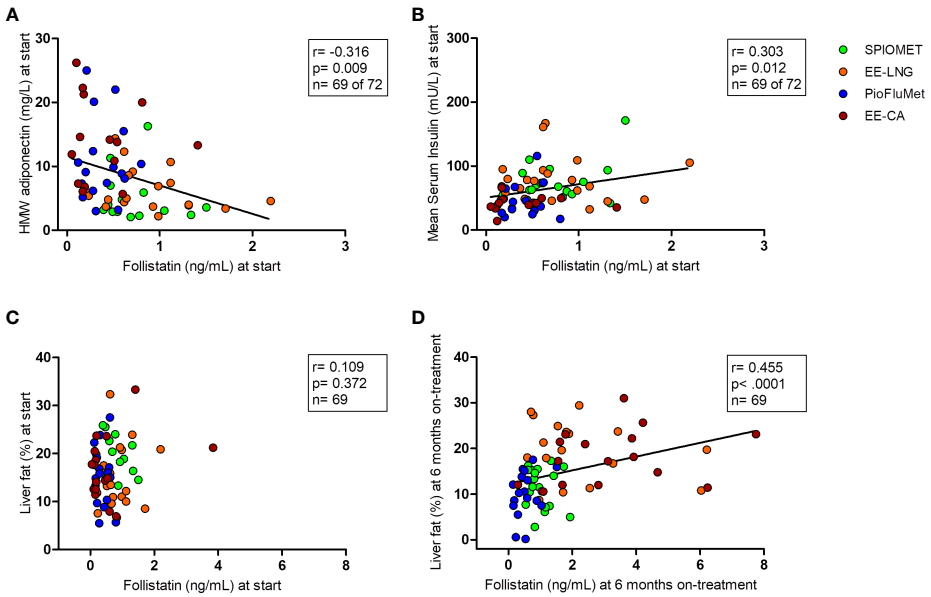

FIGURE 1
Bivariate correlations between circulating follistatin and, respectively, HMW-adiponectin and mean insulin concentration during an oral glucose tolerance test at baseline [panels **(A)** and **(B)**], and liver fat at baseline and after 6 months on treatment [panels **(C)** and **(D)**], in adolescent girls with PCOS (N=69), randomized to receive PioFluMet, SPIOMET, EE-CA or EE-LNG.

healthy girls, in contrast to previously reported data (9, 10). However, those dissimilar data should be interpreted with caution, because in the meta-analysis performed pooling the results of eight studies comparing follistatin levels in women with PCOS and in healthy controls with a wide range of age and BMI, the association between follistatin and PCOS could vary when the average age difference between PCOS patients and controls was very wide (10). Also, in patients with nonalcoholic simple steatosis – which is common in PCOS- follistatin levels were found to be comparable to those of healthy controls regardless of BMI (11).

Overall, our data agree with previous studies showing a raise in follistatin concentrations after treatment with OCs containing different combinations of estroprogestagens (12, 13). Here, we report for the first time that the increase in follistatin levels is less pronounced when the OC contains LNG as progestagen instead of CA, and that low-dose combinations of insulin sensitizers and anti-androgens such as PioFluMet and SPIOMET that improve metabolic health in adolescent PCOS, have no effects on circulating follistatin. To our knowledge, there are no other studies directly comparing the effects of different OC combinations or the effects of new progestagens like dienogest on follistatin concentrations. Although the increase in follistatin levels may be attributted to increased hepatocyte secretion, those studies might unveil the existence of additional pathways through which estro-progestagens can induce elevations of follistatin.

In our population of girls with PCOS, follistatin associated positively with mean serum insulin concentrations during an OGTT and with liver fat. These findings agree with a previous report showing that the rise in follistatin levels is capable of inducing adipose tissue insulin resistance and thus could increase the risk for type 2 diabetes (8). On the other hand, the inverse association found between circulating follistatin and HMW-adiponectin - an adipokine with insulin-sensitizing and cardio-protective properties (5), is in alignment with the inhibitory effect of HMW-adiponectin on hepatic follistatin secretion (14).

Limitations of the present study include the relative small number of patients allocated to each intervention and the lack of follistatin results during the period off intervention. The strengths include the longitudinal design, the homogenity of the study population and the assessment of two different interventions with insulin sensitizing therapies (PioFluMet and SPIOMET), and with OCs as well (EE-CA and EE-LNG); i.e., with two approaches with divergent effects on metabolic health.

In conclusion, in girls with PCOS, follistatin levels rise significantly after 6 months on OCs and this increase associates to a worsening of markers of insulin resistance and to the changes in ectopic fat depots, specifically in liver fat.

Data availability statement

The raw data supporting the conclusions of this article will be made available by the authors, without undue reservation.

Ethics statement

The studies involving human participants were reviewed and approved by Ethics Committee Pediatric Research Institute Sant Joan de Déu. Written informed consent to participate in this study was provided by the participants' legal guardian/next of kin.

Author contributions

MD contributed to literature search, design of Figures and Tables, data collection, data analysis and interpretation and wrote the manuscript. LI contributed to study design, literature search, data analysis and interpretation and reviewed/edited the manuscript. FZ contributed to data interpretation and reviewed/edited the manuscript. All authors contributed to the article and approved the submitted version.

Funding

This study was supported by grants from the Ministerio de Ciencia e Innovacion, Instituto de Salud Carlos III (PI09/90444, PI11/00049, and PI11/00085), and by the Fondo Europeo de Desarrollo Regional (FEDER) (PI15/01078).

Acknowledgments

MD and LI are clinical investigators of CIBERDEM (Centro de Investigación Biomédica en Red de Diabetes y Enfermedades Metabólicas Asociadas, Instituto de Salud Carlos III, Madrid, Spain). LI is the guarantor of this work and, as such, had full access to all the data in the study and takes responsibility for the integrity of the data and the accuracy of the data analysis.

Conflict of interest

The authors declare that the research was conducted in the absence of any commercial or financial relationships that could be construed as a potential conflict of interest.

Publisher's note

All claims expressed in this article are solely those of the authors and do not necessarily represent those of their affiliated organizations, or those of the publisher, the editors and the reviewers. Any product that may be evaluated in this article, or claim that may be made by its manufacturer, is not guaranteed or endorsed by the publisher.

References

1. de Zegher F, López-Bermejo A, Ibáñez L. Central obesity, faster maturation, and 'PCOS' in girls. *Trends Endocrinol Metab* (2018) 29(12):815–8. doi: 10.1016/j.tem.2018.09.005

2. Ibáñez L, Díaz M, Sebastiani G, Sánchez-Infantes D, Salvador C, Lopez-Bermejo A, et al. Treatment of androgen excess in adolescent girls: ethinylestradiol-cyproteroneacetate versus low-dose pioglitazone-flutamide-metformin. *J Clin Endocrinol Metab* (2011) 96(11):3361–6. doi: 10.1210/jc.2011-1671

3. Díaz M, Chacón MR, López-Bermejo A, Maymó-Masip E, Salvador C, Vendrell J, et al. Ethinyl estradiol-cyproterone acetate versus low-dose pioglitazone-flutamide-metformin for adolescent girls with androgen excess: divergent effects on CD163, TWEAK receptor, ANGPTL4, and LEPTIN expression in subcutaneous adipose tissue. *J Clin Endocrinol Metab* (2012) 97(10):3630–8. doi: 10.1210/jc.2012-1754

4. Ibáñez L, Del Río L, Díaz M, Sebastiani G, Pozo Ó. J., López-Bermejo A, et al. Normalizing ovulation rate by preferential reduction of hepato-visceral fat in adolescent girls with polycystic ovary syndrome. *J Adolesc Health* (2017) 61(4):446–53. doi: 10.1016/j.jadohealth.2017.04.010

5. Ibáñez L, Díaz M, García-Beltrán C, Malpique R, Garde E, López-Bermejo A, et al. Toward a treatment normalizing ovulation rate in adolescent girls with polycystic ovary syndrome. *J Endocr Soc* (2020) 4(5):bvaa032. doi: 10.1210/jendso/bvaa032

6. Robertson DM, Klein R, de Vos FL, McLachlan RI, Wettenhall RE, Hearn MT, et al. The isolation of polypeptides with FSH suppressing activity from bovine follicular fluid which are structurally different to inhibin. *Biochem Biophys Res Commun* (1987) 149 (2):744–9. doi: 10.1016/0006-291x(87)90430-x

7. Lee SJ, Lee YS, Zimmers TA, Soleimani A, Matzuk MM, Tsuchida K, et al. Regulation of muscle mass by follistatin and activins. *Mol Endocrinol* (2010) 24 (10):1998–2008. doi: 10.1210/me.2010-0127

8. Wu C, Borné Y, Gao R, López Rodriguez M, Roell WC, Wilson JM, et al. Elevated circulating follistatin associates with an increased risk of type 2 diabetes. *Nat Commun* (2021) 12(1):6486. doi: 10.1038/s41467-021-26536-w

9. Teede H, Ng S, Hedger M, Moran L. Follistatin and activins in polycystic ovary syndrome: relationship to metabolic and hormonal markers. *Metabolism* (2013) 62 (10):1394–400. doi: 10.1016/j.metabol.2013.05.003

10. Raeisi T, Rezaie H, Darand M, Taheri A, Garousi N, Razi B, et al. Circulating resistin and follistatin levels in obese and non-obese women with polycystic ovary syndrome: A systematic review and meta-analysis. *PloS One* (2021) 16(3):e0246200. doi: 10.1371/journal.pone.0246200

11. Polyzos SA, Kountouras J, Anastasilakis AD, Triantafyllou GA, Mantzoros CS. Activin a and follistatin in patients with nonalcoholic fatty liver disease. *Metabolism* (2016) 65(10):1550–8. doi: 10.1016/j.metabol.2016.07.009

12. Chen MJ, Yang WS, Chen HF, Kuo JJ, Ho HN, Yang YS, et al. Increased follistatin levels after oral contraceptive treatment in obese and non-obese women with polycystic ovary syndrome. *Hum Reprod* (2010) 25(3):779–85. doi: 10.1093/humrep/dep459

13. Shah A, Dodson WC, Kris-Etherton PM, Kunselman AR, Stetter CM, Gnatuk CL, et al. Effects of oral contraception and lifestyle modification on incretins and TGF-ß superfamily hormones in PCOS. *J Clin Endocrinol Metab* (2021) 106(1):108–19. doi: 10.1210/clinem/dgaa682

14. Wanninger J, Liebisch G, Eisinger K, Neumeier M, Aslanidis C, Voggenreiter L, et al. Adiponectin isoforms differentially affect gene expression and the lipidome of primary human hepatocytes. *Metabolites* (2014) 4(2):394–407. doi: 10.3390/metabo4020394

frontiers | Frontiers in Endocrinology

TYPE Original Research
PUBLISHED 09 February 2023
DOI 10.3389/fendo.2023.1053665

OPEN ACCESS

EDITED BY
Kelly Louise Walton,
Monash University, Australia

REVIEWED BY
Aafia Rashid,
Sher-I-Kashmir Institute of Medical Sciences, India
Giovanna Motta,
University Hospital of the City of Health and Science of Turin, Italy

*CORRESPONDENCE
Yuanjia Hu
yuanjiahu@um.edu.mo

SPECIALTY SECTION
This article was submitted to Reproduction, a section of the journal Frontiers in Endocrinology

RECEIVED 26 September 2022
ACCEPTED 30 January 2023
PUBLISHED 09 February 2023

CITATION
Liu C, Zhao M, Zhao Y and Hu Y (2023) Association between serum total testosterone levels and metabolic syndrome among adult women in the United States, NHANES 2011–2016. *Front. Endocrinol.* 14:1053665. doi: 10.3389/fendo.2023.1053665

Association between serum total testosterone levels and metabolic syndrome among adult women in the United States, NHANES 2011–2016

Chenning Liu[1,2], Meiduo Zhao[3], Yonghua Zhao[1] and Yuanjia Hu[1,2*]

[1]State Key Laboratory of Quality Research in Chinese Medicine, Institute of Chinese Medical Sciences, University of Macau, Macao, Macao SAR, China, [2]Department of Public Health and Medicinal Administration, Faculty of Health Sciences, University of Macau, Macao, Macao SAR, China, [3]Department of Epidemiology and Biostatistics, Institute of Basic Medical Sciences Chinese Academy of Medical Sciences, School of Basic Medicine Peking Union Medical College, Beijing, China

Objective: To investigate the association between serum total testosterone (TT) levels and metabolic syndrome (MetS) or its components among adult women.

Methods: 2,678 women from NHANES 2011-2016 were included in this cross-sectional study. MetS was determined according to the National Cholesterol Education Program Adult Treatment Panel III guidelines. The association between serum TT levels and MetS was evaluated by two logistics regression models and the adjusted restricted cubic spline (RCS). Stratified analysis and sensitive analysis were also conducted.

Results: Continuous TT levels were negatively associated with the occurrence of MetS, and the ORs associated with per SD increase in ln TT were 0.70 (95%CI: 0.58-0.85) in 2011-2014 and 0.56 (95%CI: 0.39-0.79) in 2015-2016 in Model A. High TT group were less likely to have MetS (OR=0.60, 95%CI: 0.45-0.80 in 2011-2014 and OR=0.50, 95%CI: 0.32-0.78 in 2015-2016) when compared to the low TT group. When TT levels were divided into quartiles, TT levels were negatively correlated with the incidence of MetS (p for trend < 0.001). Similar trend was observed in Model B. Multivariate-adjusted logistic regression with RCS exhibited that TT had a L-shaped dose–response association with MetS or its components. Interaction analyses revealed that women who were less than 50 years old (OR=0.37, 95%CI: 0.22, 0.63), with depression (OR=0.50, 95%CI: 0.29, 0.87) or being smokers (OR=0.37, 95%CI: 0.23, 0.54) showed lower ORs than those who were over 50 years old (OR=0.66, 95%CI: 0.40, 1.09), without depression (OR=0.59, 95%CI: 0.41, 0.85) or non-smokers (OR=0.59, 95%CI: 0.39, 0.89) when measure the association between ln TT and the occurrence of MetS.

Conclusions: Our study indicated that TT levels are negatively correlated with the occurrence of MetS, with interaction effects of age, smoke behaviors, and depressive status.

KEYWORDS

serum total testosterone levels, metabolic syndrome, women, adults, NHANES (National Health and Nutrition Examination Survey)

1 Introduction

Metabolic syndrome (MetS) represents a cluster of metabolic abnormalities. These abnormalities would increase the risk of cardiovascular disease and all-cause mortality (1–3). The prevalence of MetS among American adults has increased substantially, rising from 25.3% in 1988-1994 to 36.9% in 2015-2016 according to the National Health and Nutrition Examination Survey (NHANES) data (4, 5).

Although previous studies have reported that sex hormones are related to an increased cardiometabolic risk and mortality, including MetS, type 2 diabetes mellitus (T2DM), and hypertension (6–8), the roles of these hormones among women are poorly understood. Existing literature has indicated that testosterone deficiency or low serum total testosterone (TT) levels are correlated with an increased risk of MetS or its components in the male population (9–11), and an association between metabolic abnormalities and hyperandrogenism in young women with polycystic ovarian syndrome (PCOS) (12–14). However, the relationships between TT and MetS are inconsistent in the previous studies of women due to different research subjects under certain conditions (such as different ethnic, age group, patient-based samples, post-menopausal women, and small sample sizes) or different research types (7, 15–20).

Thus, this cross-sectional study aims to investigate the association between TT levels and MetS or its components among adult women by using the large and nationally representative survey of the US population from NHANES 2011-2016. This work may provide insightful suggestions on the impact of TT levels on women, which may further be derived to clinical evidence on the controversy of hormonal therapies for women in preventing and managing MetS.

2 Methods

2.1 Data source

NHANES (21) is a major program carried out by the National Center for Health Statistics (NCHS), which is part of the Centers for Disease Control and Prevention (CDC). It is a series of cross-sectional surveys with every two-year cycle since 1999. This survey used a complex, multistage, stratified probability sampling method to collect nationally representative health statistics on the US population. To produce more reliable and precise statistics, NHANES over-sampled certain population subgroups. Therefore, sample weights were taken into consideration during our data analyses in order to correct for differential selection probabilities, compensate for possible inadequacies in the eligible population, and adjust for non-coverage and non-response.

All NHANES data collection protocols were approved by the National Center for Health Statistics Institutional Review Board and all participants signed an informed consent. NHANES survey data, detailed survey operation manuals, consent documents, and brochures of each period are publicly available on the NHANES website (https://www.cdc.gov/nchs/nhanes).

2.2 Study participants

29,902 participants had completed the interviews and received medical and laboratory testing from the NHANES 2011-2016. We excluded men (n=14,751), women who were less than 20 years (n=6,348), pregnant (n=155) and lactating women (n=108) from our analysis. Those with missing information on TT, MetS or covariates were further excluded. Therefore, the final sample size of our analysis was 2,678 women (Figure 1). In order to observe the consistency of research results over different time periods, we divided these datasets into two parts: the data from NHANES 2011-2014 (1,828 women) and the data from NHANES 2015-2016 (850 women).

2.3 Diagnosis of MetS

The diagnosis of MetS was determined according to the National Cholesterol Education Program Adult Treatment Panel III guidelines (22). The study participants who met at least 3 of the following criteria were categorized in the MetS group: (1) Elevated waist circumference (>88 cm in women), (2) Elevated serum triglycerides (≥150 mg/dL), (3) Reduced HDL-C (<50 mg/dL in women), (4) High Blood pressure (≥130/85 mm Hg), (5) Elevated serum glucose (≥110 mg/dL).

2.4 Serum TT measurement

The serum samples were processed, stored, and transported to the Division of Environmental Health Laboratory Sciences, National Center for Environmental Health for analysis. The concentration of TT was performed by isotope dilution liquid chromatography tandem mass spectrometry (ID-LC-MS/MS) method, which was developed by the CDC. Detailed quality control and quality assurance instructions were discussed in the NHANES Laboratory/Medical Technologists Procedures Manual (LPM).

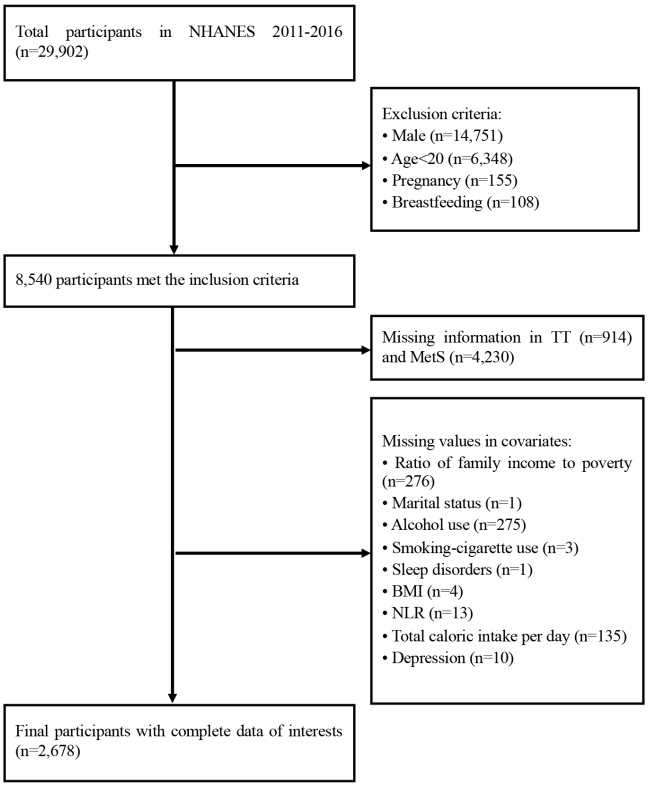

FIGURE 1
Flowchart of the study design. TT, total serum testosterone level; MetS, metabolic syndrome; BMI, body mass index; NLR, neutrophil-to-lymphocyte ratio.

2.5 Covariates assessment

Based on previous studies and clinical plausibility, the following covariates were included in our analysis to reduce potential confounding bias. Information on age, race (Mexican American, other Hispanic, non-Hispanic white, non-Hispanic black, other race-including multi-racial), education (less than high school, high school or equivalent, college or above), marital status (married, widowed, divorced, separated, never married, living with partner), and ratio of family income to poverty (≤1.00, 1.01-3.00, >3.00) were obtained through self-reports of demographic questionnaires. The body mass index (BMI; calculated as weight in kilograms divided by the square of height in meters) was categorized into 4 groups: underweight (<18.5 kg/m2), normal weight (18.5-24.9 kg/m2), overweight (25.0-29.9 kg/m2), obesity (≥30 kg/m2). Alcohol use referred to participants who had at least 12 drinks of any type of alcoholic beverage in any one year. Alcoholic beverages included liquor, beer, wine, wine coolers, and any other type of alcoholic beverage. Information about smokers was that participants who had smoked ≥100 cigarettes in their lifetimes. NHANES has incorporated the Patient Health Questionnaire (PHQ-9) since 2005, which is a self-reported assessment based on nine signs and symptoms of depression over the past two weeks. The score for each item ranged from 0 to 3, and the total score for each participant ranged from 0 to 27. A total score of ≥5 was used as the cut-off for depression. Participants were asked "Ever told doctor had trouble sleeping?", and those who answered "yes" were considered to have sleep disorders. The total caloric intake per day was estimated based on the types and amounts of foods and beverages (including all types of water) consumed during the 24-hour period prior to the interview (midnight to midnight). Lymphocyte and neutrophil counts were assessed using automated hematology analysis devices and expressed as ×1,000 cells/mm^3. The neutrophil-to-lymphocyte ratio (NLR) was measured as the ratio of neutrophil count-to-lymphocyte count.

2.6 Statistical analysis

Categorical variables were expressed as percentage (%) and compared using the chi-square test or Fisher's exact test when appropriate. Continuous data with normally distributions were expressed as mean (± standard deviation [SD]) and compared by independent samples t-test. Variables with skewed distributions were expressed as median (interquartile range [IQR]) and compared using the nonparametric Wilcoxon rank sum test. In the data analysis of NHANES 2011-2014, we used two logistics regression models to investigate the association between serum TT levels and MetS among women. Model A only adjusted for age, race, and BMI. Model B further adjusted for other demographic characteristics, lifestyle variables, and some related health indicators: education level, marital status, ratio of family income to poverty, alcohol use, smoking-cigarette use, depression, sleep disorders, total caloric intake per day, and NLR. We also evaluated the presence of nonlinear dose-response relationships between ln-transformed TT (ln TT) and MetS or its components by the adjusted restricted cubic spline (RCS) with three knots (percentile 25, 50, and 75). We

measured the interaction of TT with various clinical parameters with product interaction terms. To investigate the modified effect of age, depression, smoking status and TT on the incidence of MetS, we stratified the study population by age (less than 50 years or above), depression status (No or Yes) and smoke (No or Yes). We also performed sensitive analysis after excluding participants who were taking antidiabetic drugs, hypertension medication or lipid-lowering medication or women with ovary removed, and comparing results across samples over different time periods. For the female population from NHANES 2015-2016, we also used two logistics regression models with increasing degrees of adjustment to evaluate the association between TT levels and the odds ratio of MetS. Meanwhile, we also stratified women by age (less than 50 years or above) to determine the relationship between TT levels and MetS at different age stages. All reported p values were 2-sided, and the significance level was set at 0.05. R software (Version 4.1.2) was used for statistical analysis.

3 Results

3.1 Characteristics of the participants

The baseline characteristics of the study population with weighted estimates were presented in Table 1. Women were ranged from 20 to 80 years, with an average age of 49.52 ± 16.86 years. The weighted distribution of races was as follows: 6.9% of the participants were Mexican American, 5.4% were other Hispanic, 70.0% were non-Hispanic White, 10.5% were non-Hispanic Black, and 7.1% were others. The distribution of age, education level, marital status, ratio of family income to poverty, BMI, alcohol use, smoking-cigarette use, depression, sleep disorders, NLR, and TT levels were significantly different between the MetS group and the non-MetS group (all p<0.05). The median (IQR) of TT levels in MetS group were 17.80 [12.20, 24.01] ng/dL, which were lower than that in non-MetS group (22.20 [15.50, 30.30] ng/dL). In general, TT levels were negative correlated with age (Figure S1).

3.2 Correlation between TT and the incidence of MetS or its components

Table 2 showed the results from the multivariate regression models between TT levels and MetS in women. In Model A, continuous TT levels were negatively associated with the occurrence of MetS, and the ORs associated with per SD increase in ln TT were 0.70 (95%CI: 0.58-0.85) in 2011-2014 and 0.56 (95%CI: 0.39-0.79) in 2015-2016 after adjusting for age, race, and BMI. Similarly, women in high TT group were less likely to have MetS (OR=0.60, 95%CI: 0.45-0.80 in 2011-2014 and OR=0.50, 95%CI: 0.32-0.78 in 2015-2016) when compared to the low TT group. When TT levels were divided into quartiles, the results in 2011-2014 and 2015-2016 both suggested that TT levels were negatively correlated with the incidence of MetS (p for trend < 0.001). Women in Quartile 4 (30.10-575.00 ng/dL) in 2011-2014, Quartile 3 (20.40-28.10 ng/dL) and Quartile 4 (28.30-444.00 ng/dL) in 2015-2016 showed statistically significant lower odds of MetS. Similar trend that a statistically lower occurrence of MetS was observed among women with high TT levels were obtained in Model B: OR=0.70 (95%CI: 0.56-0.87) in 2011-2014 and OR=0.57 (95%CI: 0.33-0.99) in 2015-2016 per SD increase in ln TT; OR=0.61 (95%CI: 0.45-0.81) in 2011-2014 and OR=0.47 (95%CI: 0.24, 0.92) in 2015-2016 in high TT group. Multivariate-adjusted logistic regression with RCS exhibited that TT levels had a L-shaped dose–response association with MetS or its components, when analyzed the association between TT levels and the incidence of MetS or its components (Figure 2).

3.3 Stratified analyses by potential effect modifiers

To investigate the potential modified effect of TT levels and the other factors on the occurrence of MetS, we stratified the study population with the mentioned modifiers. Interaction analyses revealed that TT levels were significantly associated with MetS for the following factors: age, depression, and smoking behaviors (all p for interaction < 0.05). As shown in Figure 3, women who were less than 50 years old (OR=0.37, 95%CI: 0.22, 0.63), with depression (OR=0.50, 95%CI: 0.29, 0.87) or being smokers (OR=0.37, 95%CI: 0.23, 0.54) showed lower ORs than those who were over 50 years old (OR=0.66, 95%CI: 0.40, 1.09), without depression (OR=0.59, 95%CI: 0.41, 0.85) or non-smokers (OR=0.59, 95%CI: 0.39, 0.89) when we measured the association between ln TT and the occurrence of MetS. Table 3 showed different trends between the concentration of TT and the occurrence of MetS from the multivariate regression analysis when women were divided into two groups according to the average menopausal age (50 years). It suggested that TT levels were negatively associated with the occurrence of MetS among women who were less than 50 years during different time periods. Continuous TT levels were negatively associated with the occurrence of MetS, and the ORs associated with per SD increase in ln TT were both 0.54 (95%CI: 0.32-0.92) in 2011-2014 and 2015-2016. Meanwhile, women in high TT group were less likely to have MetS (OR=0.37, 95%CI: 0.22-0.63 in 2011-2014 and OR=0.28, 95%CI: 0.12-0.67 in 2015-2016). However, for women ≥50 years, there was no statistically significant difference between high TT group and low TT group (p > 0.05). In addition, when the TT levels were divided into quartiles, there was no statistical difference in the occurrence of MetS between the groups, except for women in Quartile 4 who had a decreased risk of MetS than that in Quartile 1.

3.4 Sensitive analysis

Given the observation that the concentration of TT was prognostic for women with MetS, a sensitivity analysis was investigated. We conducted sensitivity analyses after excluding the participants who were taking antidiabetic drugs, hypertension medication or lipid-lowering medication or those women with ovary removed, and comparing results across samples over different time periods, and similar results were obtained (Tables 2, 3, Figure S2, and Figure S3).

10.3389/fendo.2023.1053665

TABLE 1 Characteristics of study participants in the NHANES 2011-2016*.

Variables	Overall (n=2,678)	MetS (n=813)	Non-MetS (n=1,865)	*p*-value
Weighted sample size	78,487,974	22,829,762	55,658,212	
Age, years	49.52 ± 16.86	55.60 ± 14.52	47.02 ± 17.12	<0.001
Race, n (%)				0.150
Mexican American	344 (6.9)	123 (7.9)	221 (6.5)	
Other Hispanic	303 (5.4)	101 (4.9)	202 (5.7)	
Non-Hispanic White	1125 (70.0)	358 (71.9)	767 (69.2)	
Non-Hispanic Black	572 (10.5)	167 (9.3)	405 (11.0)	
Other Race	334 (7.1)	64 (5.9)	270 (7.6)	
Education level, n (%)				0.003
Less than high school	522 (12.4)	220 (17.1)	302 (10.5)	
High school or equivalent	533 (20.1)	178 (22.1)	355 (19.3)	
College or above	1623 (67.5)	415 (60.8)	1208 (70.2)	
Marital status, n (%)				<0.001
Married	1225 (53.3)	381 (53.4)	844 (53.3)	
Widowed	282 (8.3)	124 (13.3)	158 (6.3)	
Divorced	334 (11.7)	118 (13.7)	216 (10.9)	
Separated	106 (2.2)	39 (2.2)	67 (2.2)	
Never married	530 (16.5)	100 (9.8)	430 (19.2)	
Living with partner	201 (8.0)	51 (7.6)	150 (8.2)	
Ratio of family income to poverty, n (%)				0.003
≤1.00	662 (15.9)	227 (17.4)	435 (15.3)	
1.01-3.00	1065 (35.5)	362 (41.1)	703 (33.2)	
>3.00	951 (48.6)	224 (41.4)	727 (51.5)	
BMI (kg/m^2), n (%)				<0.001
<18.5	54 (2.1)	1 (0.1)	53 (2.9)	
18.5-24.9	731 (27.8)	49 (5.7)	682 (36.9)	
25.0-29.9	743 (28.6)	201 (24.6)	542 (30.2)	
≥30.0	1150 (41.5)	562 (69.6)	588 (30.0)	
Alcohol use, n (%)	1683 (70.6)	451 (64.2)	1232 (73.2)	<0.001
Smoking-cigarette use, n (%)	950 (39.7)	349 (48.5)	601 (36.1)	0.001
Depression, n (%)	777 (27.1)	322 (37.9)	455 (22.7)	<0.001
Sleep disorders, n (%)	839 (33.5)	328 (44.0)	511 (29.2)	<0.001
Total caloric intake per day (kcal, day), n (%)				0.729
<1550	1086 (37.0)	349 (37.4)	737 (36.8)	
1550-1972	623(25.5)	170 (23.3)	453 (26.4)	
1973-2554	580 (22.9)	184 (23.9)	396 (22.5)	
≥2555	389 (14.7)	110 (15.4)	279 (14.4)	
NLR	2.14 ± 1.11	2.34 ± 1.35	2.05 ± 0.99	<0.001
Total testosterone (ng/dL)	20.50 [14.50, 28.90]	17.80 [12.20, 24.01]	22.20 [15.50, 30.30]	<0.001

*All estimates accounted for sample weights and complex survey designs, and means and percentages were adjusted for survey weights of NHANES. MetS, metabolic syndrome; BMI, body mass index; NLR, neutrophil-to-lymphocyte ratio.

4 Discussion

We used the datasets from NHANES 2011-2016 for multi-dimensional analysis in order to obtain reliable results of the relationship between TT and Mets in the adult female population. In this large cross-sectional study of nationally representative US adult women, we found that TT levels negatively correlated with the occurrence of MetS, which was in accordance with previous observational studies in the male population (8, 9, 23, 24). In analyzing the data of NHANES 2011-2014, we used 2 models with increasing degrees of adjustment for confounding factors, and a similar trend that a statistically lower occurrence of MetS was observed among women with high TT levels was obtained. Meanwhile, these trends were in agreement with the sensitive analysis results of the participants after excluding those who were taking antidiabetic drugs, hypertension medication or lipid-lowering medication or those women with ovary removed. And similar results were obtained from the datasets of NHANES 2015-2016. However, there was no statistically significant difference between high TT group and low TT group among women ≥50 years.

In our study, median testosterone in women was 20.50 [14.50, 28.90] ng/dL, and TT levels were negative correlated with age. Our study suggested that TT had a L-shaped dose–response association with MetS and its components, and the relationships between TT levels and the outcome were not exactly the same when the concentration of TT was in different quartile range. Although these results are consistent with some previous studies, the discrepancies in different studies may be associated with different genders and ages. TT levels vary greatly in different genders, ages, or conditions. The normal physiologic range of TT in male population is 450-600 ng/dL (25, 26), and the cut-off value for the diagnosis of testosterone deficiency is 300 ng/dL, which may need testosterone replacement therapy (26). In addition, a reduction of serum TT levels is associated with aging in both men and women (27–29).

Androgen excess is one of the main characteristics of PCOS and is present in 70% of diagnosed women (30, 31). PCOS, which affects 5-20% of women of reproductive age worldwide, is associated with an increased risk of metabolic abnormalities, especially among those women who also show hyperandrogenism (32–34). Therefore, women with PCOS may interfere with the research results. These biases are found in previous studies focusing on the associations between TT and MetS. Cross-sectional relationships between endogenous androgens, sex hormone-binding globulin (SHBG), and

TABLE 2 The association between TT and MetS in women[a].

TT	Model A		Model B	
	2011-2014	2015-2016	2011-2014	2015-2016
As continuous (ln, per SD)	0.70 (0.58, 0.85)***	0.56 (0.39, 0.79)**	0.70 (0.56, 0.87)**	0.57 (0.33, 0.99)*
By cut-off				
Low	Ref.		Ref.	
High	0.60 (0.45, 0.80)***	0.50 (0.32,0.78)**	0.61 (0.45, 0.81)**	0.47 (0.24, 0.92)*
Interquartile (ng/dL) [b]				
Quartile 1	Ref.		Ref.	
Quartile 2	0.88 (0.56, 1.37)	0.62 (0.37, 1.06)	0.88 (0.54, 1.44)	0.68 (0.23, 1.99)
Quartile 3	0.68 (0.41, 1.11)	0.41 (0.20, 0.85)*	0.66 (0.38, 1.15)	0.48 (0.11, 2.10)
Quartile 4	0.55 (0.36, 0.82)**	0.36 (0.22, 0.61)**	0.55 (0.35, 0.88)**	0.39 (0.12, 1.23)

[a]The association between TT and MetS in women was presented by the ORs (95%CI). [b]Interquartile (ng/dL) for 2011-2014: Quartile 1, 1.02-13.80; Quartile 2, 13.84-20.70; Quartile 3, 20.71-30.06, Quartile 4, 30.10-575.00; Interquartile (ng/dL) for 2015-2016: Quartile 1, 1.52-14.10; Quartile 2, 14.20-20.30; Quartile 3, 20.40-28.10; Quartile 4, 28.30-444.00; Model A: Adjusted for age, race, and BMI. Model B: Adjusted for age, race, education level, marital status, ratio of family income to poverty, BMI, alcohol use, smoking-cigarette use, depression, sleep disorders, total caloric intake per day, and NLR. TT, total serum testosterone level; MetS, metabolic syndrome; BMI, body mass index; NLR, neutrophil-to-lymphocyte ratio; OR, odds ratio; CI, confidence interval. *p ≤ 0.05; **p ≤ 0.01; ***p ≤ 0.001.

MetS were summarized in a meta-analysis, which aimed to compare the relationships in terms of sex differences (15). This study comprised 13,974 men and 4,063 women on the relationship between TT and MetS, and the results showed a reduced MetS risk with higher TT levels in male population. In contrast, women who were in the highest tertile of TT had an increased risk of incident MetS compared with women in the lowest tertile (RR 1.68, 95% CI 1.15, 2.45). However, of the 15 studies which were included in this meta-analysis, 13 studies did not adjust for age and 9 studies focused on elderly women (55 years old and above). In addition, 6 studies are focused on women with PCOS, who have an increased risk of metabolic syndrome. All these biases may affect the results.

In terms of the MetS components, the relationships showed a L-shaped dose–response between TT levels and all components in our study, which was consistent with most previous results in male population (11, 35). An analysis from NHANES 2011-2012

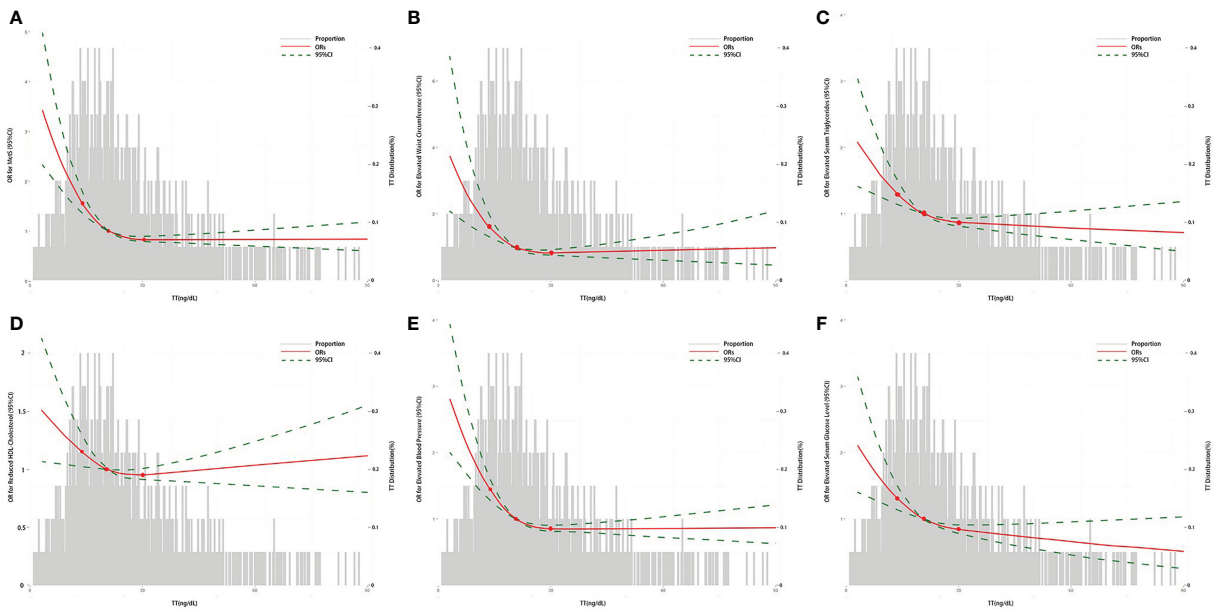

FIGURE 2
The association between TT and the ORs for MetS or its components in women by logistic regression. **(A)** The association between TT and the ORs for MetS; **(B)** The association between TT and the ORs for elevated waist circumference; **(C)** The association between TT and the ORs for elevated serum triglycerides; **(D)** The association between TT and the ORs for reduced HDL-Cholesterol; **(E)** The association between TT and the ORs for elevated blood pressure; **(F)** The association between TT and the ORs for elevated serum glucose level. The curves represent the adjusted ORs of MetS or its components by ln-transformed TT levels. The dose response association was estimated by using nonlinear dose-response relationships between ln TT and MetS or its components by the adjusted restricted cubic spline with three knots (percentile 25, 50, and 75). Model adjusted for age, race, education level, marital status, ratio of family income to poverty, BMI, alcohol use, smoking-cigarette use, depression, sleep disorders, total caloric intake per day, and NLR. TT, total serum testosterone level; MetS, metabolic syndrome; BMI, body mass index; NLR, neutrophil-to-lymphocyte ratio; OR, odds ratio.

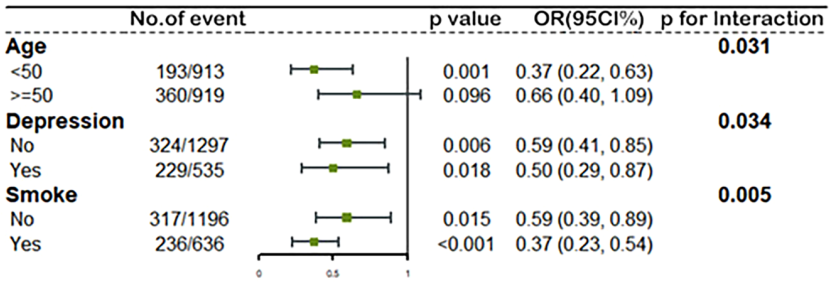

FIGURE 3
The association between ln TT and MetS stratified by age, depression status and smoke by logistic regression. All models adjusted for race, education level, marital status, ratio of family income to poverty, BMI, alcohol use, sleep disorders, total caloric intake per day, and NLR. The green spot and lines represent the odds ratios (OR) and 95% confidence interval of OR. Ln TT, ln-transformed total serum testosterone level; MetS, metabolic syndrome; BMI, body mass index; NLR, neutrophil-to-lymphocyte ratio.

reported the inverse relationship between TT levels and MetS components, and indicated that only serum triglycerides, HDL-C, and serum glucose were correlated with TT levels (17). The differential results between TT levels and MetS components may be due to the difference of the sample size.

Given that previous studies on the relationship between TT and MetS in certain conditions or different age groups had obtained different results, we expanded our study by stratified analyses to demonstrate that TT had different impacts on MetS at different ages. Globally, the mean age of natural menopause is around 50 years, with remarkably little geographic variation (36, 37). Therefore, we stratified women according to the average menopausal age, and different trends were observed. This research showed that there was no statistically significant difference between the two groups divided by serum TT levels among women aged 50 or above, which was consistent with that of some studies on postmenopausal women (38, 39). A multicenter prospective cohort study from the Netherlands Study of Depression in Older Persons suggested that there was no association between TT and MetS or its components in women aged between 60 and 93 years, regardless of whether major depressive disorder was adjusted for (40). These results may mean that the increased prevalence of the MetS after menopause may be related to estrogen deficiency caused by ovarian failure or the change of other androgens, rather than the effect of TT.

However, the research has several limitations too. In this research, we did not include evaluation of albumin and sex hormone binding globulin levels to calculate free androgen index or bioavailable TT, and did not consider other androgens, such as dehydroepiandrosterone and androstenedione. Besides, the cross-sectional nature of the survey could not determine causal inference. In addition, although we controlled for wide ranges of major potential confounders including demographics, self-reported diseases, medications, lifestyles, and dietary risk factors in the multivariable logistic models, there might be residual confounding from unmeasured factors which could have impacted the effect size estimates. Unfortunately, women with PCOS cannot be excluded from the datasets in this study, which may cause bias.

To our knowledge, this is the first large scale epidemiological study that used nationally representative US population data and examined the association between TT levels and the incidence of Mets or its components among adult women of all ages by multi-dimensional analysis which includes stratified analysis and sensitive analysis. In addition, our results are robust after adjustment for a wide spectrum of potential confounders.

TABLE 3 The association between TT and MetS in female population from different age stages (<50 years and ≥50 years) [a].

TT	<50 years		≥50 years	
	2011-2014	2015-2016	2011-2014	2015-2016
As continuous (ln, per SD)	0.54 (0.32, 0.92)*	0.54 (0.32, 0.92)*	0.74 (0.58, 0.96)*	0.71 (0.43, 1.16)
By cut-off				
Low	Ref.		Ref.	
High	0.37 (0.22, 0.63)***	0.28 (0.12, 0.67)*	0.66 (0.40, 1.09)	0.70 (0.30, 1.65)
Interquartile				
Quartile 1	Ref.		Ref.	
Quartile 2	0.84 (0.43, 1.63)	0.77 (0.12, 5.05)	0.93 (0.60, 1.44)	0.35 (0.07, 1.84)
Quartile 3	0.26 (0.12, 0.54)***	0.23 (0.22, 2.35)	0.75 (0.35, 1.58)	0.64 (0.13, 3.24)
Quartile 4	0.48 (0.23, 1.00)*	0.29 (0.03, 2.62)	0.53 (0.31, 0.93)*	0.42 (0.10, 1.71)

[a]The association between TT and MetS in women was presented by the ORs (95%CI). All models adjusted for race, education level, marital status, ratio of family income to poverty, BMI, alcohol use, smoking-cigarette use, depression, sleep disorders, total caloric intake per day, and NLR. TT, total serum testosterone level; MetS, metabolic syndrome; BMI, body mass index; NLR, neutrophil-to-lymphocyte ratio; OR, odds ratio; CI, confidence interval. *p ≤ 0.05, ***p ≤ 0.001.

5 Conclusions

The present cross-sectional study indicated that TT levels were negatively correlated with the occurrence of MetS or its components, and TT had a L-shaped dose-response association with MetS or its components. In addition, the trend of negative correlation between TT levels and the occurrence of MetS was more obvious among women who were less than 50 years old, with depression or being smokers than those who were over 50 years old, without depression or non-smokers. However, different trends were observed when we stratified women according to the average menopausal age. There was no statistically significant association between serum TT levels and the occurrence of MetS among women aged 50 or above. Future studies are necessary to determine the cut-off value for abnormal TT levels in women and the impacts of TT on Mets in different ranges.

Data availability statement

The original contributions presented in the study are included in the article/Supplementary Material. Further inquiries can be directed to the corresponding author.

Ethics statement

The studies involving human participants were reviewed and approved by National Center for Health Statistics Institutional Review Board. The patients/participants provided their written informed consent to participate in this study.

Author contributions

YH contributed to the conception and design of this study. CL and MZ organized the database and CL wrote the first draft of the manuscript. MZ performed the statistical analysis. YZ put forward academic suggestions and revised the draft. All authors contributed to the article and approved the submitted version.

Conflict of interest

The authors declare that the research was conducted in the absence of any commercial or financial relationships that could be construed as a potential conflict of interest.

Publisher's note

Supplementary material

The Supplementary Material for this article can be found online at: https://www.frontiersin.org/articles/10.3389/fendo.2023.1053665/full#supplementary-material

SUPPLEMENTARY FIGURE 1
Distribution of TT by age. The spot represents each observation, and the red line is estimated by spearman correlation.TT, total serum testosterone level.

SUPPLEMENTARY FIGURE 2
The association between TT and MetS among participants who were not taking antidiabetic drugs, hypertension medication or lipid-lowering medication with logistic regression. The green spot and lines represent the odds ratios (OR) and 95% confidence interval of OR. Model adjusted for race, education level, marital status, ratio of family income to poverty, BMI, alcohol use, smoking-cigarette use, depression, sleep disorders, total caloric intake per day, and NLR. TT, total serum testosterone level; MetS, metabolic syndrome; BMI, body mass index; NLR, neutrophil-to-lymphocyte ratio.

SUPPLEMENTARY FIGURE 3
The association between TT and MetS among participants without ovary removed by logistic regression. The green spot and lines represent the odds ratios (OR) and 95% confidence interval of OR. Model adjusted for race, education level, marital status, ratio of family income to poverty, BMI, alcohol use, smoking-cigarette use, depression, sleep disorders, total caloric intake per day, and NLR. TT, total serum testosterone level; MetS, metabolic syndrome; BMI, body mass index; NLR, neutrophil-to-lymphocyte ratio.

References

1. Grundy SM. Metabolic syndrome: a multiplex cardiovascular risk factor. *J Clin Endocrinol Metab* (2007) 92(2):399–404. doi: 10.1210/jc.2006-0513

2. Lai Y-J, Yen Y-F, Chen L-J, Hsu L-F, Ahmadi MN, Inan-Eroglu E, et al. Modification of the all-cause and cardiovascular disease related mortality risk with changes in the metabolic syndrome status: a population-based prospective cohort study in Taiwan. *Diabetes Metab* (2022) 20:101415. doi: 10.1016/j.diabet.2022.101415

3. Moore KJ, Shah R. Introduction to the obesity, metabolic syndrome, and CVD compendium. *Circ Res* (2020) 126(11):1475–6. doi: 10.1161/CIRCRESAHA.120.317240

4. Moore JX, Chaudhary N, Akinyemiju T. Metabolic syndrome prevalence by race/ethnicity and sex in the united states, national health and nutrition examination survey, 1988–2012. *Prev Chronic Dis* (2017) 14:E24. doi: 10.5888/pcd14.160287

5. Hirode G, Wong RJ. Trends in the prevalence of metabolic syndrome in the united states, 2011-2016. *JAMA* (2020) 323(24):2526–8. doi: 10.1001/jama.2020.4501

6. Sarah T, Henri W, Sebastian EB, Henry V, Marcus D, Stephan F, et al. Inverse association between total testosterone concentrations, incident hypertension and blood pressure. *Aging Male* (2011) 14(3):176–82. doi: 10.3109/13685538.2010.529194

7. Patel SM, Ratcliffe SJ, Reilly MP, Weinstein R, Bhasin S, Blackman MR, et al. Higher serum testosterone concentration in older women is associated with insulin resistance, metabolic syndrome, and cardiovascular disease. *J Clin Endocrinol Metab* (2009) 94 (12):4776–84. doi: 10.1210/jc.2009-0740

8. Kim C, Halter JB. Endogenous sex hormones, metabolic syndrome, and diabetes in men and women. *Curr Cardiol Rep* (2014) 16(4):467. doi: 10.1007/s11886-014-0467-6

9. Rao PM, Kelly DM, Jones TH. Testosterone and insulin resistance in the metabolic syndrome and T2DM in men. *Nat Rev Endocrinol* (2013) 9(8):479–93. doi: 10.1038/nrendo.2013.122

10. David EL, Leo N, Kari P, Kristiina N, Tomi-Pekka T, Veli-Pekka V, et al. Testosterone and sex hormone-binding globulin predict the metabolic syndrome and diabetes in middle-aged men. *Diabetes Care* (2004) 27(5):1036–41. doi: 10.2337/diacare.27.5.1036

11. Akishita M, Fukai S, Hashimoto M, Kameyama Y, Nomura K, Nakamura T, et al. Association of low testosterone with metabolic syndrome and its components in middle-aged Japanese men. *Hypertension Res* (2010) 33(6):587–91. doi: 10.1038/hr.2010.43

12. Kawwass JF, Sanders KM, Loucks TL, Rohan LC, Berga SL. Increased cerebrospinal fluid levels of GABA, testosterone and estradiol in women with polycystic ovary syndrome. *Hum Reprod (Oxford England)* (2017) 32(7):1450–6. doi: 10.1093/humrep/dex086

13. Dumesic DA, Oberfield SE, Stener-Victorin E, Marshall JC, Laven JS, Legro RS. Scientific statement on the diagnostic criteria, epidemiology, pathophysiology, and molecular genetics of polycystic ovary syndrome. *Endocrine Rev* (2015) 36(5):487–525. doi: 10.1210/er.2015-1018

14. Krentowska A, Kowalska I. Metabolic syndrome and its components in different phenotypes of polycystic ovary syndrome. *Diabetes/metabolism Res Rev* (2022) 38(1): e3464. doi: 10.1002/dmrr.3464

15. Brand JS, Tweel IVD, Grobbee DE, Emmelot-Vonk MH, Schouw YTVD. Testosterone, sex hormone-binding globulin and the metabolic syndrome: a systematic review and meta-analysis of observational studies. *Int J Epidemiol* (2011) 40(1):189–207. doi: 10.1093/ije/dyq158

16. Kische H, Gross S, Wallaschofski H, Völzke H, Dörr M, Nauck M, et al. Clinical correlates of sex hormones in women: The study of health in pomerania. *Metabolism: Clin Exp* (2016) 65(9):1286–96. doi: 10.1016/j.metabol.2016.05.011

17. Liang JX, Peng QH, Yang XY, Yang CB. The association between serum testosterone levels and metabolic syndrome among women. *Diabetol Metab syndrome* (2021) 13(1):26. doi: 10.1186/s13098-021-00643-6

18. Fatani SH, Abdelbasit NA, Al-Amodi HS, Mukhtar MM, Babakr AT. Testosterone, obesity, and waist circumference as determinants of metabolic syndrome in Saudi women. *Diabetes Metab Syndr Obes* (2018) 11:175–81. doi: 10.2147/DMSO.S156021

19. Polotsky AJ, Allshouse A, Crawford SL, Harlow SD, Khalil N, Santoro N, et al. Relative contributions of oligomenorrhea and hyperandrogenemia to the risk of metabolic syndrome in midlife women. *J Clin Endocrinol Metab* (2012) 97(6):E868–77. doi: 10.1210/jc.2011-3357

20. He Y, Lu Y, Zhu Q, Wang Y, Lindheim SR, Qi J, et al. Influence of metabolic syndrome on female fertility and in vitro fertilization outcomes in PCOS women. *Am J obstetrics gynecology* (2019) 221(2):138.e1–138.e12. doi: 10.1016/j.ajog.2019.03.011

21. *Centers for disease control and prevention, NCHS: about national health and nutrition examination survey (NHANES)* (2020). Available at: https://www.cdc.gov/nchs/nhanes/about_nhanes.htm.

22. Expert Panel on Detection, Evaluation, and Treatment of High Blood Cholesterol in Adults. Executive summary of the third report of the national cholesterol education program (NCEP) expert panel on detection, evaluation, and treatment of high blood cholesterol in adults (Adult treatment panel III). *JAMA* (2001) 285(19):2486–97. doi: 10.1001/jama.285.19.2486

23. Rodriguez A, Muller DC, Metter EJ, Maggio M, Harman SM, Blackman MR, et al. Aging, androgens, and the metabolic syndrome in a longitudinal study of aging. *J Clin Endocrinol Metab* (2007) 92(9):3568–72. doi: 10.1210/jc.2006-2764

24. Saad F, Gooren L. The role of testosterone in the metabolic syndrome: a review. *J Steroid Biochem Mol Biol* (2009) 114(1-2):40–3. doi: 10.1016/j.jsbmb.2008.12.022

25. Mouser JG, Loprinzi PD, Loenneke JP. The association between physiologic testosterone levels, lean mass, and fat mass in a nationally representative sample of men in the united states. *Steroids* (2016) 115:62–6. doi: 10.1016/j.steroids.2016.08.009

26. Mulhall JP, Trost LW, Brannigan RE, Kurtz EG, Redmon JB, Chiles KA, et al. Evaluation and management of testosterone deficiency: AUA guideline. *J Urol* (2018) 200 (2):423–32. doi: 10.1016/j.juro.2018.03.115

27. Henry AF, Christopher L, Carol AD, Catherine BJ, Andre BA, Andrea DC, et al. Age trends in the level of serum testosterone and other hormones in middle-aged men: longitudinal results from the Massachusetts male aging study. *J Clin Endocrinol Metab* (2002) 87(2):589–98. doi: 10.1210/jcem.87.2.8201

28. Alvin MM. Andropause: clinical implications of the decline in serum testosterone levels with aging in men. the journals of gerontology. *Ser A Biol Sci Med Sci* (2002) 57(2): M76–99. doi: 10.1093/gerona/57.2.m76

29. Skiba MA, Bell RJ, Islam RM, Handelsman DJ, Desai R, Davis SR. Androgens during the reproductive years: What is normal for women? *J Clin Endocrinol Metab* (2019) 104(11):5382–92. doi: 10.1210/jc.2019-01357

30. Winters SJ, Talbott E, Guzick DS, Zborowski J, McHugh KP. Serum testosterone levels decrease in middle age in women with the polycystic ovary syndrome. *Fertil steril* (2000) 73(4):724–9. doi: 10.1016/s0015-0282(99)00641-x

31. Gerard C, Didier D, Evanthia DK, Héctor FEM, Stephen F, Alessandra G, et al. The polycystic ovary syndrome: a position statement from the European society of endocrinology. *Eur J Endocrinol* (2014) 171(4):P1–29. doi: 10.1530/EJE-14-0253

32. Nigel KS, Samantha C, Anju EJ, Samantha KH, Cheryce LH, Rebecca FG, et al. Women with polycystic ovary syndrome have intrinsic insulin resistance on euglycaemic-hyperinsulaemic clamp. *Hum Reprod (Oxford England)* (2013) 28(3):777–84. doi: 10.1093/humrep/des463

33. Azziz R, Carmina E, Chen ZJ, Dunaif A, Laven JSE, Legro RS, et al. Polycystic ovary syndrome. *Nat Rev Dis Primers* (2016) 2:16057. doi: 10.1038/nrdp.2016.57

34. Panagiotis A, Basil CT, Robert PK. Polycystic ovarian syndrome (PCOS): Long-term metabolic consequences. *Metabolism: Clin Exp* (2018) 86:33–43. doi: 10.1016/j.metabol.2017.09.016

35. Kim M, Kyung YS, Ahn TY. Cross-sectional association of metabolic syndrome and its components with serum testosterone levels in a Korean-screened population. *World J men's Health* (2020) 38(1):85–94. doi: 10.5534/wjmh.190030

36. Susan RD, Rodney JB. Treating menopause-MHT and beyond. *Nat Rev Endocrinol* (2022) 18(8): 490–502. doi: 10.1038/s41574-022-00685-4

37. InterLACE Study Team. Variations in reproductive events across life: a pooled analysis of data from 505 147 women across 10 countries. *Hum Reprod (Oxford England)* (2019) 34(5):881–93. doi: 10.1093/humrep/dez015

38. Healy LA, Ryan AM, Carroll P, Ennis D, Crowley V, Boyle T, et al. Metabolic syndrome, central obesity and insulin resistance are associated with adverse pathological features in postmenopausal breast cancer. *Clin Oncol (Royal Coll Radiologists (Great Britain))* (2010) 22(4):281–8. doi: 10.1016/j.clon.2010.02.001

39. Golden SH, Ding JZ, Szklo M, Schmidt MI, Duncan BB, Dobs A. Glucose and insulin components of the metabolic syndrome are associated with hyperandrogenism in postmenopausal women: the atherosclerosis risk in communities study. *Am J Epidemiol* (2004) 160(6):540–8. doi: 10.1093/aje/kwh250

40. Wit AED, Giltay EJ, Boer MKD, Bosker FJ, Mast RCVD, Comijs HC, et al. Associations between testosterone and metabolic syndrome in depressed and non-depressed older men and women. *Int J geriatric Psychiatry* (2019) 34(3):463–71. doi: 10.1002/gps.5040

frontiers | Frontiers in Endocrinology

TYPE Original Research
PUBLISHED 09 February 2023
DOI 10.3389/fendo.2023.1106276

OPEN ACCESS

EDITED BY
Jiming Chen,
Changzhou No.2 People's Hospital, China

REVIEWED BY
Xia Bai Rong,
The First Affiliated Hospital of University of Science and Technology of China Anhui Provincial Hospital, China
Zhong Xingming,
Guangdong Provincial Family Planning Hospital, China
Hong Cai,
Hangzhou First People's Hospital, China
Yan Wang,
Sichuan Academy of Medical Sciences and Sichuan Provincial People's Hospital, China

*CORRESPONDENCE
Zhengyu Li
zhengyuli01@126.com
Wenjiao Min
71761715@qq.com

SPECIALTY SECTION
This article was submitted to Reproduction, a section of the journal Frontiers in Endocrinology

RECEIVED 23 November 2022
ACCEPTED 26 January 2023
PUBLISHED 09 February 2023

CITATION
Gao R, Qin L, Li Z and Min W (2023) The homeostasis model assessment of insulin resistance is a judgment criterion for metformin pre-treatment before IVF/ICSI and embryo transfer cycles in patients with polycystic ovarian syndrome.
Front. Endocrinol. 14:1106276.
doi: 10.3389/fendo.2023.1106276

The homeostasis model assessment of insulin resistance is a judgment criterion for metformin pre-treatment before IVF/ICSI and embryo transfer cycles in patients with polycystic ovarian syndrome

Rui Gao [1,2], Lang Qin[1,2], Zhengyu Li[2,3]* and Wenjiao Min[4]*

[1]The Reproductive Medical Center, Department of Gynecology and Obstetrics, West China Second University Hospital, Sichuan University, Chengdu, China, [2]Key Laboratory of Birth Defects and Related Diseases of Women and Children, Sichuan University, Ministry of Education, Chengdu, China, [3]Department of Gynecology and Obstetrics, West China Second University Hospital, Sichuan University, Chengdu, China, [4]Psychosomatic Department, Sichuan Provincial People's Hospital, University of Electronic Science and Technology of China, Chinese Academy of Sciences Sichuan Translational Medicine Research Hospital, Chengdu, China

Purpose: The aim of this study was to explore the value of the homeostasis model assessment of IR (HOMA-IR) as a judgment criterion for metformin pre-treatment before *in vitro* fertilization/intracellular sperm injection (IVF/ICSI) and embryo transfer (ET) for polycystic ovarian syndrome (PCOS) patients.

Materials and methods: The clinical and laboratory information of PCOS patients who received IVF/ICSI-ET from January 2017 to September 2021 was retrospectively analyzed. We compared the clinical pregnancy rate (primary outcome) and controlled ovarian stimulation (COS)-related parameters (secondary outcomes) between patients with and without metformin pre-treatment for all PCOS patients not grouped by HOMA-IR, PCOS patients with HOMA-IR < 2.71, and PCOS patients with HOMA-IR ≥ 2.71.

Results: A total of 969 PCOS patients who received the GnRH-antagonist protocol were included in this study. For all PCOS patients, the metformin group showed comparable clinical pregnancy rates in fresh ET cycles and frozen ET cycles compared with the control group (55.9% vs. 57.1%, p = 0.821 and 63.8% vs. 60.9%, p = 0.497). For PCOS patients with HOMA-IR < 2.71, the clinical pregnancy rates in both fresh ET cycles and frozen ET cycles were statistically similar between the two groups (61.5% vs. 57.6%, p = 0.658 and 70.6% vs. 66.7%, p = 0.535). For PCOS patients with HOMA-IR ≥ 2.71, the clinical pregnancy rate in fresh ET cycles was comparable between the two groups (51.5% vs. 56.3, p = 0.590), but it was statistically higher in the metformin group than in the control group in frozen ET cycles (57.1% vs. 40.0%, p = 0.023). The metformin group had

less oocytes retrieved, a lower cleaved oocyte rate, a lower available D3 embryo rate, a lower blastocyst formation rate, and a lower available blastocyst rate than the control group.

Conclusion: HOMA-IR is a judgment criterion for metformin pre-treatment before IVF/ICSI-ET in patients with PCOS. Metformin pre-treatment could be added for PCOS patients with HOMA-IR ≥ 2.71 during frozen IVF/ICSI-ET cycles to improve the clinical pregnancy rate.

KEYWORDS

polycystic ovary syndrome, *in vitro* fertilization, intracellular sperm injection, embryo transfer, metformin, insulin resistance, HOMA-IR, clinical pregnancy rate

1 Introduction

Polycystic ovary syndrome (PCOS) is an endocrinological problem that affects about 5%–10% of women of childbearing age all over the world (1). Oligo-anovulation, clinical and/or biochemical hyperandrogenism, and polycystic ovary morphology (PCOM) on ultrasonography are the most important clinical manifestations of PCOS (2). It was reported that approximately 80% of anovulation infertility was caused by PCOS (3). *In vitro* fertilization/intracellular sperm injection (IVF/ICSI)–embryo transfer (ET) is a third-line method that helps PCOS patients who are unable to conceive after adjusting lifestyle and medication treatment (3). However, performing IVF/ICSI-ET for PCOS patients is full of challenge because of the poorer-quality embryos, the higher risk of ovarian hyper-stimulation syndrome (OHSS), and the lower clinical pregnancy rate compared with healthy women (4).

IR is defined as reduced insulin sensitivity, and an increased amount of insulin is needed to realize its normal function; the hyperinsulinemic–euglycemic clamp (HEC) technique was considered to be the gold standard for measuring insulin sensitivity (5). As previously reported, the incidence of IR among PCOS patients varies from 50% to 70% in different regions (6). IR was reported as an important risk factor of failure of IVF/ICSI-ET for PCOS patients, because it may impair the oocyte development/maturation and reduce endometrial receptivity (7). The homeostasis model assessment of IR (HOMA-IR) is widely used to assess the degree of IR (8). Metformin is a common insulin-sensitizing agent, but the application of metformin on PCOS patients undergoing IVF/ICSI-ET is full of controversy. A systematic review and meta-analysis showed that metformin may reduce live birth rate during the GnRH-antagonist protocol, but its effect on the clinical pregnancy rate was uncertain (9). At present, the studies focusing on the association between metformin pre-treatment and IVF/ICSI-ET outcomes were heterogeneous. In particular, there are a few studies that are focused on the influence of HOMA-IR on outcomes of metformin pre-treatment in PCOS patients undergoing IVF/ICSI-ET.

We speculated that a different HOMA-IR reflects the different efficacies of metformin pre-treatment on IVF/ICSI-ET among PCOS patients. To confirm this conjecture, we performed this retrospective study to explore the value of HOMA-IR as a judgment criterion for metformin pre-treatment before IVF/ICSI-ET cycles in patients with PCOS.

2 Materials and methods

2.1 Participants and study design

A single-center retrospective cohort study was performed at West China Second University Hospital, Sichuan University from January 2017 to September 2021. The study was approved by the Ethics Committee of West China Second University Hospital. PCOS patients who received IVF/ICSI-ET because of anovulation infertility or male infertility were included in this study. Sociodemographic information, clinical manifestations, laboratory indicators, and treatment information of these PCOS patients were collected from the electronic medical record management system. The diagnosis of PCOS was based on the Rotterdam criteria, which required that at least two of the following three criteria were satisfied: oligomenorrhea or anovulation, clinical or biochemical hyperandrogenism, and polycystic ovaries on ultrasonography (defined as either an ovary with antral follicle count ≥ 12 or an ovarian volume ≥ 10 cm^3); other causes of hyperandrogenism and ovulation dysfunction were excluded (2).

The exclusion criteria were as follows: (1) incomplete sociodemographic information, clinical manifestations, laboratory indicators, or treatment information; (2) patients with other factors of infertility such as Asherman's syndrome, submucosal fibroids of the uterus, and other uterine malformations; (3) patients with other endocrine diseases such as thyroid diseases, diabetes mellitus, and hyperprolactinemia; and (4) patients with a history of recurrent spontaneous abortion. All included patients were checked again for their metformin pre-treatment protocols. Patients who received a metformin pre-treatment form at least 3 months before their IVF/ICSI-ET cycles constituted the metformin group; patients without metformin pre-treatment made up the control group, and other patients were excluded. The subgroup analyses were based on HOMA-IR < 2.71 and HOMA-IR ≥ 2.71 according to a previous study, which reported that HOMA-IR ≥ 2.71 is a significant risk factor of adverse pregnancy outcomes for women who received fresh IVF/ICSI-ET (10).

2.2 Controlled ovarian stimulation and embryo transfer

All included PCOS patients underwent a GnRH-antagonist protocol for controlled ovarian stimulation (COS); they were started on intramuscular injections of recombinant FSH (Injection Gonal-F, Merck Serono Specialties, Italy) or human menopausal gonadotropin (hMG, Lizhu Pharmaceutical Trading, China) from the second day of their menstrual cycle. The starting dose was between 150 IU/day and 225 IU/day. A GnRH antagonist (Injection Cetrotide acetate, Aeterna Zentaris, Canada) was administered at a dose of 0.25 mg/day from the sixth day of the menstrual cycle until the ovulation trigger day. The cycles were cancelled in patients with no follicle greater than 10 mm after 10 days of recombinant FSH/hMG stimulation. For all PCOS patients, when at least two follicles are ≥18 mm or three follicles ≥17 mm, the final stage of triggering ovulation was performed using human chorionic gonadotropin (hCG; Lizhu Pharmaceutical Trading, China) at doses from 8,000 IU to 10,000 IU. For patients at a high risk for ovarian hyper-stimulation syndrome (OHSS), 4,000 IU to 5,000 IU of hCG was used to trigger ovulation.

Oocyte retrieval was performed 36–38 h after triggering ovulation. Oocyte assessment was performed by the standard morphology criteria, and nuclear maturity assessment was performed. Conventional IVF or ICSI was performed depending on semen parameters. For patients who received fresh ET cycles, ET was performed 3 or 5 days after oocyte retrieval according to the type of embryo; other embryos were all frozen. For patients who received their first frozen ET cycles, artificial menstrual cycle was established by the exogenous addition of estradiol and ET was performed 3 or 5 days after the addition of progesterone. All patients were given luteal phase support *via* the intramuscular injection of progesterone (100 mg/day) or vaginal progesterone gel (90 mg/day) plus oral dydrogesterone (20 mg/day). Two weeks after ET, pregnancy was assessed by serum β-hCG levels and confirmed by transvaginal ultrasound 4 weeks after ET. Serum β-hCG levels > 50 IU/L were regarded as biochemical pregnancy and the presence of the gestational sac was regarded as clinical pregnancy.

2.3 Information collection and outcomes

Fasting plasma glucose (FPG) and fasting insulin (FINS) measured before metformin treatment were collected, and HOMA-IR was calculated with the following formula: HOMA-IR = FGP (mmol/L) FINS (mIU/L)/22.5. We summed up the basic information of patients, including their fertility history, clinical manifestations of PCOS, age, body mass index (BMI), and history of oral contraceptives (OC) treatment. BMI was calculated by the body weight in kilograms divided by the square of the height in meters (kg/m^2). Venous blood samples were taken 2–4 days during a spontaneous menstrual cycle or an independent cycle phase in the presence of amenorrhea before metformin pre-treatment to detect anti-Müllerian hormone (AMH), dehydroepiandrosterone (DHEAS), androstenedione (ASD), follicle-stimulating hormone (FSH), luteinizing hormone (LH), estradiol (E2), progesterone (P), testosterone (T), and sex hormone binding globulin (SHBG) levels. At the same time, homocysteine (HCY), high-density lipoprotein cholesterol (HDL-C), and triglycerides (TG) were also assessed after an overnight fast of at least 10 h.

COS-related parameters were also collected, including OHSS rate, the type of gonadotropin (Gn), the starting dosage of Gn, the total number of Gn days, and the total Gn dosage. Serum LH, E2, and P levels were detected and single endometrial thickness (ET) was measured by ultrasonography on the trigger day. The number of follicles ≥14 mm on the trigger day and the number of oocytes retrieved were also collected. Embryo grading was done by a standard morphology assessment according to modified Veeck's scoring. The IVF/ICSI fertilization rate, cleavage rate, available D3 embryo rate, high-quality D3 embryo rate, blastocyst formation rate, available blastocyst rate, and high-quality blastocyst rate were calculated and were selected as secondary outcomes of this study. Clinical pregnancy rate was defined as the presence of a gestational sac per ET cycle and was selected as the primary outcome of this study.

2.4 Statistical analysis

We used a Kolmogorov–Smirnov test to estimate whether data were normally distributed. Normally distributed continuous variables were presented as means ± standard deviations (SDs) and were analyzed by *t*-test. Non-normally distributed continuous variables were presented as median (25th–75th percentiles) and were analyzed by the Kruskal–Wallis test. Categorical measurements were presented as a percentage and were compared by chi-squared test; if numbers were less than 5 in at least 20% of the cells, Fisher's exact test was performed. The adjusted difference in the clinical pregnancy rate between the two groups was expressed as odds ratio (OR), 95% confidence intervals (CIs), and adjusted *p*-value. *p*-value < 0.05 was regarded as statistically different. All the statistical analyses were performed by SPSS, version 26.0 (SPSS Inc., Chicago, IL, UPL).

3 Results

3.1 Basic information of PCOS patients

PCOS patients who entered IVF/ICSI-ET cycles because of anovulation infertility or male infertility were searched in the electronic medical record management system. After exclusion, 969 PCOS patients were included in this study. Among them, 366 patients were in the metformin group and 603 patients were in the control group. There was a statistical difference in BMI and history of OC treatment between the two groups ($p < 0.05$). For patients who received metformin pre-treatment, the HOMA-IR of 171 patients (46.7%) was <2.71 and that of 195 patients (53.3%) was ≥2.71. For patients in the control group, the HOMA-IR of 435 patients (72.1%) was <2.71 and that of 168 patients (27.9%) was ≥2.71.

Compared with the control group, the metformin group had lower levels of AMH, basal P, basal FSH, basal LH, and SHBG, and higher levels of HCY and TG. In addition, the metformin group had a higher total dosage of Gn, a shorter duration of Gn, and lower E2 levels on the trigger day than the control group. A detailed information of PCOS patients in the metformin group and control

group is shown in Table 1. For PCOS patients with HOMA-IR < 2.71, the metformin group had a higher age, BMI, duration of infertility, FAI, HCY, and TG, and lower basal FSH levels than the control group. The proportion of history of OC treatment and type of Gn were significantly different between the two groups (as shown in Supplementary Table 1). For PCOS patients with HOMA-IR ≥ 2.71, the metformin group had lower basal FSH and basal LH levels, and higher basal T, FAI, and HDL-C levels than the control group. The proportion of PCOM and type of Gn were significantly different between the two groups (as shown in Supplementary Table 2).

TABLE 1 Baseline information and laboratory data between the metformin group and the control group.

	Metformin group (*n* = 366)	Control group (*n* = 603)	*p*-value
Age (year)	30 ± 4	29 ± 4	0.036
BMI (kg/m^2)	23.60 ± 3.34	22.64 ± 3.41	<0.001
Duration of infertility (years)	4 ± 3	3 ± 2	0.001
HOMA-IR [*n* (%)]			<0.001
<2.71	171 (46.7)	435 (72.1)	
≥2.71	195 (53.3)	168 (27.9)	
Type of infertility [*n* (%)]			0.285
Primary	249 (68.0)	390 (64.7)	
Secondary	117 (32.0)	213 (35.3)	
PCOM [*n* (%)]	303/366 (82.8)	519/603 (86.1)	0.167
history of OC treatment [*n* (%)]	279/366 (76.2)	171/603 (28.4)	<0.001
AMH (ng/ml)	9.81 ± 4.77	10.46 ± 5.05	0.046
Basal E2 (pg/ml)	41.4 ± 15.5	42.8 ± 17.0	0.191
Basal P (ng/ml)	0.48 ± 0.19	0.52 ± 0.24	0.009
Basal FSH (IU/L)	6.2 ± 1.8	6.8 ± 1.8	<0.001
Basal LH (IU/L)	8.6 ± 5.8	9.5 ± 5.9	0.026
Basal T (mg/dl)	0.53 ± 0.26	0.46 ± 0.66	0.070
Basal DHEAS (μg/dl)	243.8 ± 117.1	236.5 ± 117.0	0.447
Basal ASD (ng/ml)	3.72 ± 1.36	3.78 ± 1.39	0.590
Basal SHBG (nmol/L)	33.9 ± 24.0	53.0 ± 36.8	<0.001
FAI	4.7 ± 3.9	4.7 ± 3.9	<0.001
HCY (μmol/L)	9.58 ± 2.35	9.18 ± 2.40	0.014
HDL-C (mmol/L)	1.34 ± 0.36	1.32 ± 0.33	0.450
TG (mmol/L)	2.06 ± 1.94	1.67 ± 1.77	0.002
Type of Gn [*n* (%)]			<0.001
rFSH	168 (45.9)	372 (61.7)	
hMG	198 (54.1)	231 (38.3)	
Starting dosage of Gn (IU)	178.0 ± 52.8	178.7 ± 55.6	0.848
Total dosage of Gn (IU)	1,933.2 ± 803.9	1,807.1 ± 711.2	0.011
Duration of Gn (days)	11 ± 2	10 ± 2	<0.001
On the trigger day			
E2 (pg/ml)	4,468.8 ± 2,688.7	5,166.2 ± 2,977.1	<0.001
P (ng/ml)	1.08 ± 0.92	1.15 ± 0.55	0.123
LH (IU/L)	2.7 ± 2.1	2.7 ± 2.1	0.949

(Continued)

TABLE 1 Continued

	Metformin group (n = 366)	Control group (n = 603)	p-value
Single endometrium thickness (mm)	5.1 ± 1.0	5.3 ± 1.1	0.059
No. of follicles ≥ 14 mm	10 ± 4	10 ± 3	0.137
Fertility methods [n (%)]			0.002
IVF	327 (89.3)	486 (80.6)	
ICSI	9 (2.5)	30 (5.0)	
IVF+ICSI	30 (8.2)	87 (14.4)	

BMI, body mass index; HOMA-IR, the homeostasis model assessment of insulin resistance; PCOM, polycystic ovarian morphology; OC, oral contraceptives; AMH, anti-Mullerian hormone; E2, estradiol; P, progesterone; FSH, follicle-stimulating hormone; LH, luteinizing hormone; T, testosterone; DHEAS, dehydroepiandrosterone sulfate; ASD, androstenedione; SHBG, sex hormone binding globulin; FAI, free androgen index; HCY, homocysteine; HDL-C, high-density lipoprotein cholesterol; TG, triglycerides; Gn, gonadotropin; rFSH, recombinant FSH; hMG, human menopausal gonadotropin; IVF, in vitro fertilization; ICSI, intracellular sperm injection. p < 0.05 was regarded as statistical different.

3.2 Metformin pre-treatment for all PCOS patients

We compared the COS-related parameters and clinical pregnancy rates between the metformin group and the control group for all PCOS patients. The results showed that the metformin group had fewer oocytes retrieved (15 ± 7 vs. 16 ± 8, p = 0.004), a lower cleaved oocyte rate (97.9% vs. 98.5, p = 0.013), a lower available D3 embryo rate (68.9% vs. 73.4%, p < 0.001), a lower blastocyst formation rate (69.3% vs. 71.7%, p = 0.043), and a lower available blastocyst rate (85.9% vs. 90.8%, p < 0.001) than the control group. However, there was no statistical difference in IVF fertilization rate (p = 0.726), ICSI fertilization rate (p = 0.294), high-quality D3 embryo rate (p = 0.092), and high-quality blastocyst rate (p = 0.749) between the two groups. We did not find a statistical difference in severe OHSS rate between the two groups (p = 0.372).

For 345 PCOS patients who received fresh ET cycles (177 patients in the metformin group and 168 patients in the control group), the clinical pregnancy rate between the metformin group and the control group was comparable (55.9% vs. 57.1%, p = 0.821). For 552 PCOS patients who received their first frozen ET cycles (207 patients in the metformin group and 345 patients in the control group), there was no statistical difference in the clinical pregnancy rate between the two groups (63.8% vs. 60.9%, p = 0.497). The above results are shown in Table 2. After adjusting for age, BMI, duration of infertility, history of OC treatment, AMH, basal FSH, basal LH, FAI, HCY, and TG, as these factors were statistically different between the two groups and were reported to be associated with the clinical pregnancy rate in IVF/ICSI-ET before, there was no statistical difference in the clinical pregnancy rate between the two groups either (as shown in Supplementary Table 3).

3.3 Metformin pre-treatment for PCOS patients with HOMA-IR < 2.71

We did not find any statistical difference in IVF fertilization rate, ICSI fertilization rate, cleaved oocyte rate, high-quality D3 embryo rate, blastocyst formation rate, and high-quality blastocyst rate between the metformin group and the control group for PCOS patients with HOMA-IR < 2.71. However, there was a significantly lower available D3 embryo rate (66.1% vs. 72.3%, p < 0.001) and

TABLE 2 COS outcomes and clinical pregnancy outcomes between the metformin group and the control group in all PCOS patients.

	Metformin group (n = 366)	Control group (n = 603)	p-value
No. of oocytes retrieved	15 ± 7	16 ± 8	0.004
IVF fertilization rate [n (%)]	4,137/4,395 (94.1)	6,639/7,065 (94.0)	0.726
ICSI fertilization rate [n (%)]	228/255 (89.4)	984/1131 (87.0)	0.294
Cleaved oocyte rate [n (%)]	4,275/4,365 (97.9)	7,512/7,623 (98.5)	0.013
Available D3 embryo rate [n (%)]	2,946/4,275 (68.9)	5,514/7,512 (73.4)	<0.001
High-quality D3 embryo rate [n (%)]	1,530/3,219 (47.5)	2,790/5,649 (49.4)	0.092
Blastocyst formation rate [n (%)]	1,386/2,001 (69.3)	3,093/4,311 (71.7)	0.043
Available blastocyst rate [n (%)]	1,191/1,386 (85.9)	2,808/3,092 (90.8)	<0.001
High-quality blastocyst rate [n (%)]	414/1,386 (29.9)	909/3,092 (29.4)	0.749
Severe OHSS rate [n (%)]	9/366 (2.5)	21/603 (3.5)	0.372
CPR in fresh cycle [n (%)]	99/177 (55.9)	96/168 (57.1)	0.821
CPR in frozen cycle [n (%)]	132/207 (63.8)	210/345 (60.9)	0.497

IVF, in vitro fertilization; ICSI, intracytoplasmic sperm injection; OHSS, ovarian hyper-stimulation syndrome; CPR, clinical pregnancy rate. p < 0.05 was regarded as statistical different.

available blastocyst rate (84.8% vs. 91.3%, $p < 0.001$) in the metformin group compared with the control group. We found no statistical difference in severe OHSS rate between the two groups ($p = 0.836$).

The clinical pregnancy rate between the metformin group and the control group was comparable for 198 PCOS patients who received fresh ET cycles (61.5% vs. 57.6%, $p = 0.658$). There was no statistical difference in the clinical pregnancy rate between the metformin group and the control group (70.6% vs. 66.7%, $p = 0.535$) for 372 PCOS patients who received their first frozen ET cycles (102 patients in the metformin group and 270 patients in the control group). The above results are shown in Table 3. After adjusting for age, BMI, duration of infertility, history of OC treatment, basal FSH, FAI, HCY, and TG, there was no statistical difference in the clinical pregnancy rate between the two groups either (as shown in Supplementary Table 4).

3.4 Metformin pre-treatment for PCOS patients with HOMA-IR ≥ 2.71

For PCOS patients with HOMA-IR ≥ 2.71, we found no difference in IVF fertilization rate, ICSI fertilization rate, high-quality D3 embryo rate, available blastocyst rate, or high-quality blastocyst rate between the metformin group and the control group. The cleaved oocyte rate (97.5% vs. 98.7%, $p = 0.009$), available D3 embryo rate (71.6% vs. 76.1%, $p = 0.001$), and blastocyst rate (43.2% vs. 50.4%, $p < 0.001$) were statistically lower in the metformin group than in the control group (as shown in Table 3).

Among 147 fresh ET cycles (99 in the metformin group and 48 in the control group), the clinical pregnancy rate was comparable in the metformin group and the control group (51.5% vs. 56.3, $p = 0.590$). However, among 180 frozen ET cycles (105 in the metformin group and 75 in the control group), the clinical pregnancy rate in the metformin group was significantly higher than in the control group (57.1% vs. 40.0%, $p = 0.023$). After adjusting for PCOM, T, basal FSH, basal LH, and FAI, there was no statistical difference in the clinical pregnancy rate in fresh ET cycles either. The clinical pregnancy rate in frozen ET cycles was still higher in the metformin group than in the control group ($p = 0.007$) (as shown in Supplementary Table 5).

4 Discussion

PCOS is the most common endocrinopathy with complex reproductive, metabolic, and psychological manifestations (11). It is challenging for PCOS patients to receive IVF/ICSI-ET because of unsatisfactory COS-related parameters, a lower clinical pregnancy rate, and a higher risk of OHSS, miscarriage, and other pregnancy complications compared with healthy women (4). IR reflects metabolic and mitogenic disorders (12), playing crucial roles in the pathological mechanisms of PCOS, and is closely associated with obesity and hyperandrogenism (13, 14). HOMA-IR is a simple and convenient indicator to evaluate the degree of IR (15). Patients with a higher HOMA-IR were reported to have a lower implantation rate (15), a lower clinical pregnancy rate (15, 16), and a higher risk of early miscarriage (17) and late miscarriage (10) than patients with a lower HOMA-IR in IVF/ICSI-ET cycles. Metformin is a synthetically derived biguanide that is widely used in PCOS patients because it improves insulin sensitivity (18, 19), but the application of metformin is full of controversy. A cohort study indicated no positive role of metformin on the success rate of IVF/ICSI-ET for PCOS patients (20). In addition, a randomized double-blind controlled trial (RCT) exploring the efficacy of pre-treatment of metformin for all PCOS patients who received IVF/ICSI-ET treatment showed no difference in implantation rate, multiple pregnancy rate, miscarriage rate, or live

TABLE 3 COS outcomes and clinical pregnancy outcomes between the metformin group and the control group in PCOS patients of different HOMA-IR subgroups.

	HOMA-IR < 2.71			HOMA-IR ≥ 2.71		
	Metformin group (*n* = 171)	Control group (*n* = 435)	*p*-value	Metformin group (*n* = 195)	Control group (*n* = 168)	*p*-value
No. of oocytes retrieved	15 ± 8	16 ± 8	0.300	14 ± 6	16 ± 8	0.004
IVF fertilization rate [*n* (%)]	1,995/2,135 (93.4)	4,581/4,866 (94.1)	0.259	2,142/2,256 (94.9)	2,058/2,199 (93.6)	0.051
ICSI fertilization rate [*n* (%)]	111/132 (84.1)	804/930 (86.5)	0.462	117/123 (92.7)	180/201 (89.6)	0.078
Cleaved oocyte rate [*n* (%)]	2,070/2,106 (98.3)	5,304/5,385 (98.5)	0.520	2,205/2,259 (97.5)	2,208/2,238 (98.7)	0.009
Available D3 embryo rate [*n* (%)]	1,368/2,070 (66.1)	3,834/5,304 (72.3)	<0.001	1,578/2,205 (71.6)	1,680/2,208 (76.1)	0.001
High-quality D3 embryo rate [*n* (%)]	729/1,539 (47.4)	1,971/4,044 (48.7)	0.360	801/1,680 (47.7)	819/1,605 (51.0)	0.055
Blastocyst formation rate [*n* (%)]	651/930 (70.0)	2,133/2,943 (72.5)	0.143	735/1,701 (43.2)	690/1,368 (50.4)	<0.001
Available blastocyst rate [*n* (%)]	552/651 (84.8)	1,947/2,133 (91.3)	<0.001	639/735 (86.9)	861/960 (89.7)	0.079
High-quality blastocyst rate [*n* (%)]	189/651 (29.0)	615/2,133 (28.8)	0.922	225/735 (30.6)	294/960 (30.6)	0.995
Severe OHSS rate [*n* (%)]	9/171 (5.3)	21/435 (4.8)	0.836	–	–	–
CPR in fresh cycle [*n* (%)]	48/78 (61.5)	69/120 (57.6)	0.658	51/99 (51.5)	27/48 (56.3)	0.590
CPR in frozen cycle [*n* (%)]	72/102 (70.6)	180/270 (66.7)	0.535	60/105 (57.1)	30/75 (40.0)	0.023

HOMA-IR, the homeostasis model assessment of insulin resistance; IVF, in vitro fertilization; ICSI, intracytoplasmic sperm injection; OHSS, ovarian hyper-stimulation syndrome; CPR, clinical pregnancy rate. p < 0.05 was regarded as statistical different.

birth rate (21). Similarly, another systematic review and meta-analysis showed a similar clinical pregnancy rate for all PCOS patients with and without metformin pre-treatment during IVF/ICSI-ET cycles (22).

In this study, we retrospectively collected information on IVF/ICSI-ET cycles for 969 PCOS patients and investigated the value of HOMA-IR as a judgment criterion for metformin pre-treatment before IVF/ICSI-ET cycles in patients with PCOS. Clinical pregnancy rate was selected as the primary outcome of this study. For all PCOS patients not grouped according to HOMA-IR, we observed a comparable clinical pregnancy rate in both fresh ET and frozen ET cycles between the metformin group and the control group, which were in correlation with previous studies (22). For PCOS patients with HOMA-IR < 2.71, there was no statistical difference in the clinical pregnancy rate between the metformin group and the control group in both fresh and frozen ET cycles. For PCOS patients with HOMA-IR ≥ 2.71, we observed a higher clinical pregnancy rate in the metformin group than in the control group in frozen ET cycles, which was similar to a previous systematic review and meta-analysis that observed the same outcome in PCOS patients with BMI > 26 kg/m^2 (22). We can initially conclude that metformin pre-treatment increases the clinical pregnancy rate for PCOS patients with HOMA-IR ≥ 2.71 in frozen IVF/ICSI-ET cycles, which was in agreement with our knowledge that metformin can ameliorate IR and decrease the adverse effects of IR on IVF/ICSI-ET outcomes. However, the difference in the clinical pregnancy rate between the two groups was not significant in fresh ET cycles even for PCOS patients with HOMA-IR ≥ 2.71. We try to explain the results and speculate that metformin pre-treatment may affect the endometrial receptivity of PCOS patients during fresh ET cycles; therefore, the effect of metformin pre-treatment on the clinical pregnancy rate was weakened. During frozen ET cycles, artificial menstrual cycle was established; therefore, the effect of metformin pre-treatment on endometrial receptivity was not shown.

COS-related parameters were selected as secondary outcomes of this study. We have to be concerned that metformin pre-treatment seems to have an important influence on the COS-related parameters. All of the included PCOS patients received the GnRH-antagonist protocol treatment. We found that metformin not only decreased the number of oocytes retrieved, the available D3 embryo rate, the cleaved oocyte rate, and the blastocyst formation rate for all PCOS patients not grouped according to HOMA-IR and PCOS patients with HOMA-IR ≥ 2.71, but also decreased the available D3 embryo rate and the available blastocyst rate for all PCOS patients not grouped according to HOMA-IR and PCOS patients with HOMA-IR < 2.71. The above results were in agreement with a previous RCT, which found that metformin pre-treatment decreased the mean number of the retrieved oocytes and the number of fertilized oocytes (21). Interestingly, although the influence of metformin on COS-related parameters was observed in our study and a previous RCT, no adverse effect of metformin on the clinical pregnancy rate was found. The above results indicated that the influence of metformin pre-treatment on COS-related parameters should not be considered as an adverse effect in IVF/ICSI-ET because COS-related parameters are not correlated with IVF/ICSI-ET outcomes entirely.

There were some limitations preventing the generalization of the results. Firstly, this study was a single-center retrospective cohort study, the grade of clinical evidence was limited, and we did not perform a follow-up investigation on the changes in HOMA-IR, BMI, blood lipid, and other indicators in the metformin group after metformin pre-treatment, which could have been helpful for analyzing the correlation between indicator changes and pregnancy outcome. Secondly, because this is a retrospective study, we could not be involved with the patients; thus, the duration and dosage of metformin pre-treatment for included PCOS patients were different, which may affect the outcomes of this study. Thirdly, we selected 2.71 as the cutoff value of HOMA-IR according to previous reports; whether the cutoff value may affect the outcomes of this study was not clear and needs to be explored in the future, but this study indicated that HOMA-IR was a useful indicator for the guidance of metformin pre-treatment before IVF/ICSI-ET for PCOS patients. The above limitations indicated that we must interpret the results of this study with caution, and a well-designed RCT with a large sample size should be performed to obtain a more valuable conclusion.

In conclusion, metformin pre-treatment could be added for PCOS patients with HOMA-IR ≥ 2.71 during frozen IVF/ICSI-ET cycles to improve the clinical pregnancy rate, but for PCOS patients with HOMA-IR < 2.71 or PCOS patients receiving fresh IVF/ICSI-ET treatment, metformin pre-treatment was not proven to be of benefit by the present study. The influence of metformin on COS-related parameters of PCOS patients should be considered in the GnRH-antagonist protocol. The results of this study need to be proven by a well-designed RCT with and large sample size in the future.

Data availability statement

The raw data supporting the conclusions of this article will be made available by the authors, without undue reservation.

Ethics statement

The study was approved by the Ethics Committee of West China Second University Hospital.

Author contributions

ZL contributed to this study's conception and design. Material preparation, data collection, and analysis were performed by RG and WM. The first draft of the manuscript was written by RG and LQ, and all authors commented on previous versions of the manuscript. All authors contributed to the article and approved the submitted version.

Funding

This study was supported by the Medical Science and Technology Project of Sichuan Provincial Health Commission (grant number 21PJ050).

Conflict of interest

The authors declare that the research was conducted in the absence of any commercial or financial relationships that could be construed as a potential conflict of interest.

Publisher's note

All claims expressed in this article are solely those of the authors and do not necessarily represent those of their affiliated organizations, or those of the publisher, the editors and the reviewers. Any product that may be evaluated in this article, or claim that may be made by its manufacturer, is not guaranteed or endorsed by the publisher.

Supplementary material

The Supplementary Material for this article can be found online at: https://www.frontiersin.org/articles/10.3389/fendo.2023.1106276/full#supplementary-material

References

1. Goodarzi MO, Dumesic DA, Chazenbalk G, Azziz R. Polycystic ovary syndrome: Etiology, pathogenesis and diagnosis. *Nat Rev Endocrinol* (2011) 7(4):219–31. doi: 10.1038/nrendo.2010.217

2. Chang J, Azziz R, Legro R, Dewailly D, Franks R, Tarlatzis R, et al. Revised 2003 consensus on diagnostic criteria and long-term health risks related to polycystic ovary syndrome. *Fertil Steril* (2004) 81(1):19–25. doi: 10.1016/j.fertnstert.2003.10.004

3. Balen AH, Morley LC, Misso M, Franks S, Legro RS, Wijeyaratne CN, et al. The management of anovulatory infertility in women with polycystic ovary syndrome: An analysis of the evidence to support the development of global WHO guidance. *Hum Reprod Update* (2016) 22(6):687–708. doi: 10.1093/humupd/dmw025

4. Sha T, Wang X, Cheng W, Yan Y. A meta-analysis of pregnancy-related outcomes and complications in women with polycystic ovary syndrome undergoing IVF. *Reprod BioMed Online* (2019) 39(2):281–93. doi: 10.1016/j.rbmo.2019.03.203

5. Krentz AJ. Insulin resistance. *Bmj* (1996) 313(7069):1385–9. doi: 10.1136/bmj.313.7069.1385

6. Joham AE, Norman RJ, Stener-Victorin E, Legro RS, Franks S, Moran LJ, et al. Polycystic ovary syndrome. *Lancet Diabetes Endocrinol* (2022) 10(9):668–80. doi: 10.1016/S2213-8587(22)00163-2

7. Fica S, Albu A, Constantin M, Dobri GA. Insulin resistance and fertility in polycystic ovary syndrome. *J Med Life* (2008) 1(4):415–22.

8. Matli B, Schulz A, Koeck T, Falter T, Lotz J, Rossmann H, et al. Distribution of HOMA-IR in a population-based cohort and proposal for reference intervals. *Clin Chem Lab Med* (2021) 59(11):1844–51. doi: 10.1515/cclm-2021-0643

9. Tso LO, Costello MF, Albuquerque LET, Andriolo RB, Macedo CR. Metformin treatment before and during IVF or ICSI in women with polycystic ovary syndrome. *Cochrane Database Syst Rev* (2020) 12(12):Cd006105. doi: 10.1002/14651858.CD006105.pub4

10. Yang T, Yang Y, Zhang Q, Liu D, Liu N, Li Y, et al. Homeostatic model assessment for insulin resistance is associated with late miscarriage in non-dyslipidemic women undergoing fresh IVF/ICSI embryo transfer. *Front Endocrinol (Lausanne)* (2022) 13:880518. doi: 10.3389/fendo.2022.880518

11. Teede HJ, Misso ML, Costello MF, Dokras A, Laven J, Moran L, et al. Recommendations from the international evidence-based guideline for the assessment and management of polycystic ovary syndrome. *Hum Reprod* (2018) 33(9):1602–18. doi: 10.1093/humrep/dey256

12. American Diabetes Association. Standards of medical care in diabetes-2015 abridged for primary care providers. *Clin Diabetes* (2015) 33(2):97–111. doi: 10.2337/diaclin.33.2.97

13. Stepto NK, Cassar S, Joham AE, Hutchison SK, Harrison CL, Goldstein RF, et al. Women with polycystic ovary syndrome have intrinsic insulin resistance on euglycaemic-hyperinsulaemic clamp. *Hum Reprod* (2013) 28(3):777–84. doi: 10.1093/humrep/des463

14. Meyer C, McGrath BP, Teede HJ. Overweight women with polycystic ovary syndrome have evidence of subclinical cardiovascular disease. *J Clin Endocrinol Metab* (2005) 90(10):5711–6. doi: 10.1210/jc.2005-0011

15. Song H, Yu Z, Li P, Wang Y, Shi Y. HOMA-IR for predicting clinical pregnancy rate during IVF. *Gynecol Endocrinol* (2022) 38(1):33–8. doi: 10.1080/09513590.2021.1952976

16. Chang EM, Han JE, Seok HH, Lee DR, Yoon TK, Lee WS. Insulin resistance does not affect early embryo development but lowers implantation rate in *in vitro* maturation-*in vitro* fertilization-embryo transfer cycle. *Clin Endocrinol (Oxf)* (2013) 79(1):93–9. doi: 10.1111/cen.12099

17. Chen Y, Guo J, Zhang Q, Zhang C. Insulin resistance is a risk factor for early miscarriage and macrosomia in patients with polycystic ovary syndrome from the first embryo transfer cycle: A retrospective cohort study. *Front Endocrinol (Lausanne)* (2022) 13:853473. doi: 10.3389/fendo.2022.853473

18. Mastrototaro L, Roden M. Insulin resistance and insulin sensitizing agents. *Metabolism* (2021) 125:154892. doi: 10.1016/j.metabol.2021.154892

19. Morley LC, Tang T, Yasmin E, Norman RJ, Balen AH. Insulin-sensitising drugs (metformin, rosiglitazone, pioglitazone, d-chiro-inositol) for women with polycystic ovary syndrome, oligo amenorrhoea and subfertility. *Cochrane Database Syst Rev* (2017) 11(11):Cd003053. doi: 10.1002/14651858.CD003053.pub6

20. Kalem MN, Kalem Z, Gurgan T. Effect of metformin and oral contraceptives on polycystic ovary syndrome and IVF cycles. *J Endocrinol Invest* (2017) 40(7):745–52. doi: 10.1007/s40618-017-0634-x

21. Abdalmageed OS, Farghaly TA, Abdelaleem AA, Abdelmagied AE, Ali MK, Abbas AM. Impact of metformin on IVF outcomes in overweight and obese women with polycystic ovary syndrome: A randomized double-blind controlled trial. *Reprod Sci* (2019) 26(10):1336–42. doi: 10.1177/1933719118765985

22. Wu Y, Tu M, Huang Y, Liu Y, Zhang D. Association of metformin with pregnancy outcomes in women with polycystic ovarian syndrome undergoing *In vitro* fertilization: A systematic review and meta-analysis. *JAMA Netw Open* (2020) 3(8):e2011995. doi: 10.1001/jamanetworkopen.2020.11995

frontiers | Frontiers in Endocrinology

TYPE Original Research
PUBLISHED 10 February 2023
DOI 10.3389/fendo.2023.1068045

OPEN ACCESS

EDITED BY
Lisa Owens,
St. James's Hospital, Ireland

REVIEWED BY
Stephen Franks,
Imperial College London, United Kingdom
Daniel Ninello Polesel,
Federal University of São Paulo, Brazil

*CORRESPONDENCE
Emma Oberg
emma.oberg@regionstockholm.se

SPECIALTY SECTION
This article was submitted to Reproduction, a section of the journal Frontiers in Endocrinology

RECEIVED 12 October 2022
ACCEPTED 30 January 2023
PUBLISHED 10 February 2023

CITATION
Oberg E, Blomberg L, Åkerstedt T and Hirschberg AL (2023) Different sleep pattern in over-weight/obese women with polycystic ovary syndrome.
Front. Endocrinol. 14:1068045.
doi: 10.3389/fendo.2023.1068045

Different sleep pattern in over-weight/obese women with polycystic ovary syndrome

Emma Oberg[1,2]*, Liselotte Blomberg[3], Torbjörn Åkerstedt[4] and Angelica Lindén Hirschberg[1,3]

[1]Department of Women's and Children's Health, Division of Neonatology, Obstetrics and Gynecology, Karolinska Institutet, Stockholm, Sweden, [2]Department of Pelvic Cancer, Theme Cancer, Karolinska University Hospital, Stockholm, Sweden, [3]Department of Gynecology and Reproductive Medicine, Karolinska University Hospital, Stockholm, Sweden, [4]Department of Clinical Neuroscience, Karolinska Institutet, Stockholm, Sweden

Context: Sleep duration and sleep quality have important health implications although our knowledge of objectively measured sleep variables in women with Polycystic Ovary Syndrome (PCOS) is limited.

Objective: To compare sleep variables assessed by actigraphy in over-weight/obese women with PCOS and controls, and to assess sleep variables after behavioral modification intervention in comparison with minimal intervention in a randomized trial.

Design: Randomized controlled trial, and a control group.

Setting: Outpatient gynecological clinic at a university hospital in Sweden.

Participants: 39 women fulfilling all Rotterdam PCOS criteria, randomized to behavioral modification intervention or minimal intervention and 21 controls with no other metabolic disease, all aged 18-40 years with a BMI ≥ 27 kg/m^2.

Intervention: A four-month behavioral modification intervention including weekly group meetings focusing on behavioral and healthy lifestyle aspects. Minimal intervention reflecting standard care.

Main outcome measure: Sleep durations and sleep efficiency assessed by actigraphy.

Results: Compared to the control group, women with PCOS had significantly shorter time in bed (501 vs 548 min, p= 0.049), sleep time over 24 hours (448 vs 567 min, p=0.005) and sleep time at night (434 vs 511 min, p=0.002), poorer sleep efficiency (87 vs 93%, p<0.001), and longer wakefulness after sleep onset (64 vs 38 min, p<0.001). However, total sleep time at night for women with PCOS (7.2hrs) was within the normal range. Following behavioral modification intervention, the reduction from baseline in sleep over 24 hours and in the daytime sleep were significant compared to the minimal intervention group (78 min, p=0.009 and 43 min, p=0.003 respectively).

Conclusions: We found over-weight/obese women with PCOS to have normal sleep duration, but worse sleep efficiency than controls. Behavioral modification

intervention seems to reduce the amount of daytime sleep, suggesting improved sleep behavior.

Clinical trials registration: https://doi.org/10.1186/ISRCTN48947168, identifier ISRCTN48947168.

KEYWORDS

polycystic ovary syndrome (PCOS), sleep, behavior modification, lifestyle, actigraphy

Introduction

Polycystic ovary syndrome (PCOS) is the most common endocrine disorder in fertile women with a prevalence of 8-13% (1). It is characterized by oligo- or anovulation, clinical or biochemical hyperandrogenism and polycystic ovaries on ultrasound (2, 3). PCOS is a heterogenous condition and has previously been considered a disorder of infertility and clinical hyperandrogenism mainly manifested by hirsutism. Today, other aspects of PCOS are increasingly recognized including metabolic disturbances such as insulin resistance and abdominal obesity, as well as psychiatric morbidity e.g. depression and anxiety (4–8). We have recently demonstrated that psychological well-being is severely impacted in overweight women with PCOS (9).

In addition, sleep disturbances have been reported as common among women with PCOS, and the occurrence of obstructive sleep apnea (OSA) is higher than for controls (10–15). OSA is characterized by daytime sleepiness, somnolence and fatigue, restless sleep, and morning headaches (16). The most recent international PCOS clinical guidelines, recommend screening for OSA to identify and alleviate symptoms and to explore if fatigue potentially contributes to mood disorders as well as to attempt optimizing the sleep (2). Other aspects of sleep behavior than OSA in women with PCOS, such as sleep time, timings of sleep and sleep efficiency, have mainly been characterized by studies looking at self-reported parameters (10, 15, 17). Furthermore, evidence from objective measurements of sleep behavior in women with PCOS using actigraphy or polysomnography other than for diagnosing OSA is scarce (18, 19).

Studies on non-PCOS, including female only populations, have shown that short sleep duration is linked to obesity, decreased insulin sensitivity as well as increased hunger and appetite (20–22). In addition, daytime napping is positively correlated with body mass index (BMI) and waist circumference in women (23). Furthermore, sleep duration shorter than 6 hours (360 minutes) is associated with menstrual cycle disturbances (both long and short cycles) (24). There is also evidence showing that altering the timings of wakefulness and sleep, being awake at night and asleep during the day, is associated with impaired glucose tolerance and increased insulin resistance (21). Finally, both short and long sleep times are associated with increased mortality (25).

The observations in women with PCOS indicate a need for investigating if overweight/obese women with PCOS differ from body mass index (BMI)-matched controls with respect to objective indicators of sleep efficiency and awakenings, the timing of sleep, its variability, as well as sleep duration. Moreover, since lifestyle management including exercise, diet, behavioral intervention, or a combination of those, is the first line treatment for over-weight women with PCOS, it is important to assess its impact on sleep health variables in this population (2).

The primary objective of this study was therefore to assess objective sleep variables by actigraphy in over-weight/obese women with PCOS in comparison with BMI- and age-matched controls. In addition, to investigate the effect of behavioral modification intervention in comparison with minimal intervention on sleep variables in a randomized trial of women with PCOS, as well as to look for any correlations between sleep variables and anthropometric, endocrine and psychological well-being parameters.

Materials and methods

Study design

This is a secondary analysis of data from a Randomized Controlled Trial (RCT) (ISRCTN48947168), previously described in Oberg et al. (26) where 68 over-weight/obese women with PCOS where randomized to receive behavioral modification intervention or minimal intervention in a 1:1 ratio for four months with a further follow up at 12 months (26). Weight change and reproductive outcomes in relation to weight loss were the primary outcomes (26). Other previously published data include psychological well-being parameters as well as endocrine and metabolic variables (9).

In this study, we have focused on objectively measured sleep variables in the same population of over-weight/obese women with PCOS and measured the treatment effects of the four-month intervention within and between groups. Sleep-registration with actigraphy was initiated part of the way through the inclusion period resulting in 39 out of the 68 women with PCOS completing the sleep registration at baseline (22 in the behavioral modification intervention group and 17 in the minimal intervention group), and 28 women at four months (13 in the behavioral modification intervention group and 15 in the minimal intervention group). In addition, we have introduced a control group of 21 women with comparable BMI and age to the women with PCOS without any metabolic-, endocrine or other illness, and compared the baseline sleep variables from our whole population of over-weight/obese women with PCOS (n=39) with the controls. Written consent has been obtained from all study participants. The local ethics committee

in Stockholm has approved the study (2012/146-31/3, 2012/1762-32, 2014/1406-32, 2020/00653).

Women with PCOS

Study participants were recruited through adverts in a local newspaper as well as on a website for clinical studies. Inclusion criteria were BMI ≥ 27 kg/m^2, age between 18-40 years and using the PCOS Rotterdam consensus, fulfilling all three PCOS diagnostic criteria: oligo- or anovulation, clinical or biochemical hyperandrogenism and polycystic ovaries on ultrasound (3). A serum testosterone > 310 pg/mL measured by tandem mass spectrometry indicated biochemical hyperandrogenism, and a Ferriman-Gallwey score ≥ 8 was used to define hirsutism and a measure of clinical hyperandrogenism (27). Ovaries were considered polycystic if at least one had a volume ≥ 10 mL or ≥ 12 antral follicles when using transvaginal ultrasound (Sonoline SI-250, Siemens Healthcare Diagnostics) (2, 3). Criteria of exclusion were other chronic illnesses including eating disorders or ongoing medication, pregnancy or breast-feeding, smoking, or a substantial change in weight during the past year as well as working night-shifts. A washout period of three months was used for participants using a hormonal contraceptive.

Controls

The women used as controls were recruited *via* a web-site advert based on the same inclusion criteria of age (18 to 40 years old) and BMI (≥ 27 kg/m^2) as the women with PCOS. The controls also needed to have a regular menstrual cycle length of 23 to 32 days. Exclusion criteria, in addition to the ones described above for the patient group, were having oligo- or amenorrhea, clinical or biochemical hyperandrogenism or a previous diagnosis of PCOS.

Study intervention

Behavioral modification intervention

We used a behavioral modification intervention, developed as a training course with focus on achieving long-term weight control (26). The study participants were divided into small groups in which they attended weekly meetings throughout the four-month intervention period together with the course leader working through topics such as personal leadership, mindfulness, problem solving, stress management, stimulus control, techniques for avoiding instant gratification as well as more practical aspects concerning weight control, diet and physical activity. Preparation for each meeting by reading and personal reflection was encouraged (28). In addition, individual coaching sessions with the course leader were held once a month.

Minimal intervention

The minimal intervention group received standard care comprising oral and written information on healthy living including advice on diet and exercise delivered by a research midwife.

Procedures

Women with PCOS

Before and after the 4-month intervention, the women with PCOS underwent a physical examination on menstrual cycle day 6-8. In women with oligo- or amenorrhea, a bleeding was induced by taking 10 mg medroxyprogesterone for seven days. A thorough medical history was taken, anthropometric measurements were obtained, a gynecological examination including transvaginal ultrasound was completed and fasting blood sampling was carried out allowing for analysis of hormones, binding proteins and metabolic variables. The participants also filled in a questionnaire assessing the psychological general wellbeing index (PGWBI) at baseline and 4 months.

Controls

A medical history was taken from the controls to ensure they fulfilled the entry criteria and no exclusion criteria. Fasting blood sampling was carried out on cycle day 6-8 to allow for analysis of hormones and binding proteins and anthropometric measurements were obtained. The controls did not receive any intervention and were only assessed at baseline.

Actigraph assessment of sleep

Both the women with PCOS and the controls wore an actigraph, ActiSleep+ (ActiGraph) device on their non-dominant wrist or in some cases where this was not possible, around their ankle. They were encouraged to wear the device for 7 consecutive days, the whole time apart from when showering/taking a bath or undertaking other water-based activities. Patients and controls with recordings for less than three consecutive periods of 24 hours were excluded from the study. The PCOS study population carried the actigraph at baseline and at 4 months, and the control group only at baseline.

Actigraphy uses an accelerometer that measures movements and uses three-dimension acceleration data which are converted to estimated sleep parameters using the commonly used and validated Sadeh sleep algorithm (29). A recent study validating actigraphy as a method of assessing sleep variables compared to the gold standard method for sleep assessment of polysomnography, found actigraphy to give valid estimates of total sleep time, wake after sleep onset as well as sleep efficiency (30). The manufacturer's data analysis software ActiLife 6 (ActilGraph) was used to extract data from the devices and each patient's report was reviewed manually by the first author (EO). Recordings of sleep durations were: total sleep time over 24h (TST 24h, min), time in bed at night (TIB, min), total sleep time at night (TST night, min) and total sleep time during the day (TST day, min) (defined as a new episode of sleep initiated 30 minutes or later after time of rising, when occurring after 08:00). In addition, the time of rising (ToR) and the bed time were recorded. The number of wakeups (n) and wakefulness after sleep onset (WASO, min), as well as energy expenditure (kcal/day) and steps taken (n) were extracted. The sleep parameters for all recorded consecutive 24-hour periods obtained from the actigraph were averaged for each participant. Averages for weekdays (Monday to Thursday) and weekends (Friday and Saturday) were also obtained for all sleep parameters. Sleep efficiency (TST night/TIB x100) was calculated.

Biochemical measurements

The sex steroids were analyzed by liquid chromatography tandem-mass spectrometry (31, 32). The analyses of binding proteins and other hormones were carried out using electrochemiluminescence immunoassay (ECLIA) from Roche Diagnostics AG (CH 6343 Rotkreuz, Switzerland) (Cobas8000®) the Department of Clinical Chemistry, Karolinska University Hospital, Stockholm, Sweden. Free androgen index (FAI) was calculated (testosterone nmol/L divided by SHBG nmol/L x 100).

Assessment of psychological general well-being

The non-disease specific questionnaire PGWBI was used to assess the psychological well-being. The PGWBI contains 22 questions with 6 answers to choose from and it assesses the well-being during the previous month (33, 34). The questions are divided into the six dimensions of *anxiety*, *depressed mood*, *positive well-being*, *self-control*, *general health* and *vitality*. All dimensions can be added to achieve a *global score* (34). Greater well-being is always indicated by a higher score (e.g. a high score for depressed mood indicates a greater well-being) (34). We have previously shown that the well-being in this group was very low at baseline and that some aspects of well-being (anxiety, general health and depressed mood) improved following behavioral modification (9).

Statistics

Statistical analysis was carried out using SPSS software version 26 (IBM; Stockholm, Sweden). In Tables 1, 2, proportions or percentages are used to present categorical data, continuous data is presented as means ± standard error (SE). For continuous data, normal distribution was tested for using histograms, as well as calculation of skewness. Student's t-test was used to assess the difference in baseline characteristics between the groups for continuous variables, and Fisher's Exact test for categorical data. Analysis of covariance was used to compare the group of women with PCOS with the controls with respect to the sleep variables in Figure 1, adjusted for the potential confounders: being in a stable relationship, having children, BMI and waist circumference. A linear mixed model analysis was used to assess the effects of the intervention within and between the treatment groups at four months (Table 2 and Figure 2) where the factors used were treatment (behavioral modification intervention and minimal intervention), time (baseline and four months) and the interaction treatment x time. The results from the mixed model analysis are presented as means as well as SE for within group analysis and as the mean difference of the change from baseline along with the 95% confidence intervals (CI) for between group analysis. The analysis was carried out on an intention-to treat (ITT) basis. All analyses were carried out both on the mean of all 24-hour sleep periods recorded for each participant, as well as the mean of the weekday (Monday to Thursday) and weekend (Friday and Saturday) sleep. The bivariate correlation analysis of baseline demographic, anthropometric, accelerometer data and endocrine variables with sleep parameters, as well as the correlation analysis between the change of these variables following the 4-month intervention period were performed using Spearman rank correlation. Statistical significance was assumed at *P*-values < 0.05. This is a secondary analysis, where the power calculation based on weight change following intervention has previously been published (26).

Results

Baseline characteristics

Table 1 outlines the baseline demographic, anthropometric, and endocrine variables for the whole group of women with PCOS (behavioral modification intervention and minimal intervention), as well as for the control group. The whole group of women with PCOS and the controls were comparable in regard to age and BMI on a group level. The women with PCOS had a larger waist circumference and a higher WHR. Furthermore, there were expected between group differences for the endocrine variables, with the women with PCOS having higher androgen levels than the controls. The percentage of women with PCOS with biochemical hyperandrogenism was 76%. In addition, the women with PCOS were more likely to be in a stable relationship and to have children than the controls. There was no difference in education level or in the number of current students between the groups. None of the study participants was unemployed. There was no difference in baseline characteristics between the women with PCOS randomized to behavioral modification intervention and minimal intervention as previously published (9, 26).

Sleep in women with PCOS compared to controls

When looking at all days of the week, the women with PCOS had significantly shorter mean total sleep time over 24 hours (TST 24h, min), time in bed at night (TIB, min), total sleep time at night (TST night, min), total sleep time during the day (TST day, min), poorer sleep efficiency (%), and longer periods of wakefulness after sleep onset (WASO, min) than the control group as shown in Figures 1A, B. However, we found no differences between the groups in the number of awakenings per night, or in the bed-time. The mean time of rising (ToR) occurred earlier for the PCOS patients than for the controls. When adjusting for being in a relationship, having children, BMI and waist circumference, the differences between groups for TST day and ToR disappeared, but all other differences between groups remained. When looking at the sleep parameters for weekdays only (Monday to Thursday) all differences between groups remained, apart from the TIB, where the difference no longer was significant (data not shown). Regarding sleep data for weekends only (Fridays and Saturdays), the women with PCOS still had a significantly shorter TST 24h (p=0.041), TST night (p=0.015), poorer sleep efficiency (p<.001) and a longer WASO (p<0.001) compared to controls.

10.3389/fendo.2023.1068045

TABLE 1 Baseline characteristics of the PCOS population as well as the control group.

	PCOS population (n=39) #	Controls (n=21)	*p*-value
Demographics			
Age (year)	30.1 ± 5.3	29.9 ± 5.2	0.849
Education			0.197
Primary	1/39 (2.6%)	0/21 (0%)	
Secondary	13/39 (33.3%)	3/21 (14.3%)	
University	14/39 (35.9%)	10/21 (47.6%)	
Current student	8/39 (20.5%)	8/21 (38.1%)	0.220
Unemployed	0/39	0/21	
In a stable relationship	26/39 (66.7%)	8/21 (38.1%)	**0.028**
Have children	16/39 (41.0%)	3/21 (14.3%)	**0.044**
Anthropometric			
Body weight (kg)	93.2 ± 16.2	86.6 ± 10.7	0.083
BMI (kg/m^2)	34.1 ± 33.9	31.6 ± 31.6	0.064
Waist circumference (cm)	103.7 ± 11.3	94.4 ± 8.4	**0.001**
Hip circumference (cm)	116.6 ± 10.5	117.4 ± 7.9	0.813
WHR	0.89 ± 0.06	0.81 ± 0.05	< **0.001**
Endocrine Variables			
FSH (IU/L)	6.6 ± 3.5	7.1 ± 2.1	0.584
LH (IU/L)	6.7 ± 3.2	6.5 ± 2.9	0.887
Testosterone (pg/mL)	392.5 ± 137.9	270.0 ± 95.2	**0.001**
SHBG (nmol/L)	27.3 ± 15.1	54.8 ± 40.1	< **0.001**
Free Androgen Index	6.5 ± 3.9	2.3 ± 1.0	< **0.001**
Androstenedione (pg/mL)	1628 ± 525	1055 ± 251	< **0.001**
Estradiol (pg/mL)	49.9 ± 26.7	48.9 ± 32.3	0.906

• Baseline categorical data is presented as a proportion/percentage, and continuous data as means ± standard deviation.
• To determine the difference between groups, the independent sample t-test was used for continuous data and the Fisher's exact test for categorical data.
• BMI, body mass index; FSH, follicle stimulating hormone; LH, luteinizing hormone; min minutes; SHBG, sex hormone-binding globulin; WHR, waist/hip ratio.
• Free androgen index calculated as testosterone nmol/L divided by SHBG nmol/L x 100.
• # subset of a larger population where data previously has been published.
• P-values in bold indicate statistical significance.

Sleep following behavioral modification intervention in women with PCOS

For the women with PCOS, the TST 24h and the TST daytime decreased in the behavioral modification intervention group albeit not significantly, following the 4-months behavioral intervention program, and increased in the PCOS minimal intervention group during the same period, as shown in Figure 2. This resulted in a significant difference following intervention in the TST 24h and the TST daytime between the PCOS women having received behavioral modification intervention and the minimal intervention group (Figure 2). As outlined in Table 2, we found no other within or between group differences to the actigraphy recorded sleep parameters following the 4 months behavioral modification intervention. No significant within or between group differences following intervention was seen when analyzing the data separately for weekdays (Monday to Thursday) and weekend (Friday and Saturday) (data not shown).

Correlations between sleep variables and baseline characteristics

For the women with PCOS at baseline, there were no correlations between the objective sleep variables and the hormonal and anthropometric measurements respectively, nor were there any correlations between the changes in these variables following intervention. In the same study, we have previously shown that psychological well-being was severely reduced at baseline however behavioral modification intervention had a positive impact on some of the dimensions of well-being (9). In terms of correlations between sleep variables and the psychological well-being measurements at baseline, there was a positive correlation between sleep efficiency and the variables self-control (r = 0.41, p = 0.023) and a negative correlation between WASO and self-control (r = -0.38. p = 0.035).

Discussion

To our knowledge, this is the first study investigating objectively measured sleep health variables in overweight women with PCOS both compared to controls, as well as after lifestyle intervention. We found that women with PCOS had poorer sleep efficiency and longer wakefulness after sleep onset than controls. Furthermore, there was a non-significant reduction in total sleep time over 24 hours, as well as in total daytime sleep following behavioral modification intervention, although this was significant when compared to the minimal intervention group. There was no reduction in the total sleep time at night, suggesting less daytime napping after behavioral modification intervention.

In adults, the recommended sleep duration is between 6h to 8h per night, where sleep over 9h could be used to detect co-morbidity (35). The women with PCOS had a mean total sleep time at night of 7.2h, whereas the control group had a somewhat longer night sleep of 8.5h. When looking at the sleep time over the 24-hour window, we found that the control group slept two hours longer than the PCOS women. This was partly due to 47 minutes longer time in bed, largely caused by later rising, as well as 57 minutes of daytime sleep (napping). Despite the longer time in bed, which normally results in less effective sleep, the sleep efficiency was significantly higher in the control group and wakefulness after sleep onset significantly shorter. Both are key indicators of sleep quality (36). This implies that sleep quality was better in the control group, despite their total sleep time being longer.

An increased sleep duration could have been an artefact of a wider sleep window. The data for the control group was partly recorded during the beginning of the COVID-19 pandemic, when working from home was recommended, which could have permitted a larger

10.3389/fendo.2023.1068045

TABLE 2 Sleep, anthropometric, endocrine and metabolic parameters at baseline and after 4 months of intervention for the women with PCOS.

	Behavioral Modification Intervention (n=22)			Minimal Intervention (n=17)			Difference in change between groups	
Sleep parameters	Baseline	4 months	*P*-value	Baseline	4 months	*P*-value	Behavioral Modification - Minimal Intervention	*P*-value
TIB (min)	497.2 (459-535)	464.0 (416-512)	.208	502.4 (460-545)	509.7 (465-555)	.783	-40.5 (-115.7 to 34.7)	.280
Sleep efficiency (%)	86.8 (85.1-88.5)	87.0 (85.0-89.1)	.803	86.8 (84.9-88.7)	87.4 85.4-89.5)	.534	-0.40 (-3.4 to 2.5)	.786
Nb wakeups/ night	18.4 (15.6-21.1)	19.1 (6.1-32.1)	.902	17.5 (14.4-20.5)	24.6 (12.5-36.8)	.221	-6.4 (-24.0 to 11.2)	.445
WASO (min)	63.1 (54.0-72.1)	58.8 (47.4-70.2)	.483	62.9 (52.7-73.1)	62.7 (51.9-73.4)	.964	-4.0 (-21.3 to 13.4)	.646
Anthropometric #								
Body weight (kg)	91.9 (84.6-99.2)	89.4 (81.9-96.8)	**.042**	97.7 (90.1-105)	95.5 (87.8-103)	.087	-0.3 (-3.9 to 3.2)	.842
BMI (kg/m^2)	33.4 (31.2-35.5)	32.4 (30.2-34.6)	**.037**	35.6 (33.3-37.9)	34.8 (32.5-37.1)	.077	-0.1 (-1.4 to 1.1)	.841
Waist (cm)	103.5 (98.4-109)	99.9 (94.6-105)	**.023**	106.0 (101-111)	102.4 (96.9-108)	**.036**	0.003 (-4.5 to 4.5)	.999
Endocrine variables #								
Testosterone (pg/mL)	360.1 (302-418)	370.7 (301-441)	.759	434.9 (369-501)	361.8 (290-434)	.065	83.7 (-21.5 to 189.0)	.114
Free Androgen Index	5.5 (4.1-7.0)	4.8 (2.9-6.7)	.489	7.7 (6.0-9.4)	5.5 (3.5-7.3)	.060	1.5 (-1.7 to 4.8)	.349
Metabolic variables #								
Fasting Insulin (mIE/L)	13.5 (9.2-17.9)	11.3 (6.3-16.4)	.324	17.0 (12.1-21.8)	17.5 (12.3-22.7)	.819	-2.8 (-9.4 to 3.9)	.401
Fasting Glucose (mmol/L)	4.7 (4.4-5.0)	4.7 (4.3-5.0)	.751	4.9 (4.5-5.2)	5.0 (4.7-5.4)	.238	-0.2 (-0.7 to 0.2)	.280
HOMA	2.9 (1.8-4.1)	2.4 (1.0-3.7)	.291	3.8 (2.6-5.1)	4.3 (3.0-5.7)	.401	-1.0 (-2.6 to 0.6)	.185

- Data given mean and mean differences with its 95% Confidence Interval.
- BMI, body mass index; HOMA, Homeostatic Model of Assessment; min, minutes; Nb, number; TIB, time in bed; WASO, wakefulness after sleep onset.
- Free androgen index calculated as testosterone nmol/L divided by SHBG nmol/L x 100.
- # subset of a larger population where data previously has been published.
- Homeostatic Model of Assessment (HOMA) index calculated using the formula (insulin mIE/L) x (glucose mg/dL)/405.
- P-values in bold indicate statistical significance.

night time sleep window for this group as well as opportunities for daytime napping. In addition, the proportion of women with children was lower among the controls, and fewer were in a stable relationship. However, there was no difference in the proportion of students between the groups and no-one was unemployed, factors that could otherwise have permitted a wider sleep window and provided an explanation for the longer sleep times in the control group. When controlling for the potential covariates of being in a relationship, having children, BMI and waist circumference, the difference between groups in daytime sleep and time of rising disappeared, leading us to believe that being in a relationship and having children affected these variables. However, this does not alter the fact that sleep quality, in terms of sleep efficiency, was considerably higher in the control group even after adjusting for covariates.

Our findings are in agreement with two other studies that have found lower actigraphy recorded sleep efficiency in women with PCOS compared to controls; Shreeve et al. (19) looking at adults and Simon et al. (18) studying adolescents (18, 19). Another study using polysomnography (one night only in a sleep laboratory) by Sousa et al. (37), found lower sleep efficiency in a PCOS adolescent population compared to controls (37). Three other relatively small polysomnography studies based on adult PCOS populations vs healthy controls, Hachul et al. (38), Suri et al. (39) and Fogel et al. (11), also found poorer sleep efficiency in the PCOS groups but the results did not reach significance, potentially because of the small sample size (11, 38, 39). In terms of wakefulness after sleep onset, results from polysomnography studies by Sousa et al. (37), and Suri et al. (39) agree with our results of women with PCOS having a longer wakefulness after sleep onset than controls, however Simon et al. (18) and Hachul et al. (38) found no difference between the groups.

In terms of psychiatric well-being, we found a positive correlation between self-control and sleep efficiency and a negative correlation between self-control and wakefulness after sleep onset which is reasonable since the latter contributes largely to the sleep efficiency

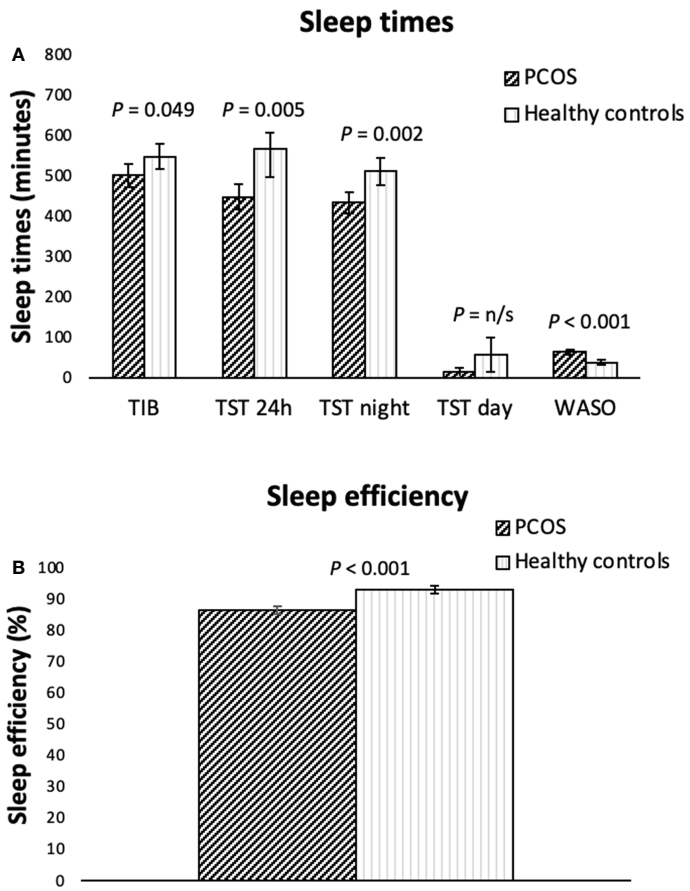

FIGURE 1
Actigraphy measured sleep variables (**A**, sleep times, **B**, sleep efficiency) for overweight/obese women with PCOS (n=39) and healthy controls (n=21) of a similar age and weight presented as means including the 95% CI. P-values are adjusted: controlling for being in a relationship, having children, BMI and waist circumference as covariates. H, hours; min, minutes; TIB, time in bed; TST, total sleep time; WASO, wakefulness after sleep onset. Sleep efficiency: total sleep time/time in bed x 100.

measure. A recent study by Yang et al. (40) found an association between self-reported sleep parameters and anxiety/depression status in Chinese women with PCOS, hypothesizing that sleep disturbances might be part of the etiology of the psychiatric co-morbidity in this patient group. However, the causality of these associations has to be investigated further (40).

In addition to comparing the objectively measured sleep variables in women with POCS with controls, we have also for the first time investigated the effects of lifestyle intervention on sleep variables in women with PCOS. We found that following behavioral modification intervention the overweight/obese women with PCOS displayed a non-significant reduction in the total sleep time over 24 hours and in daytime sleep, compared to the minimal intervention group where the total sleep time over 24 hours and daytime sleep increased, and the difference in these changes following intervention between groups was significant. As no such significant difference between groups was seen for the total sleep time at night, the reduction of total sleep time over 24hours is explained by less daytime napping following behavioral modification intervention. A meta-analysis based on a non-PCOS population by Zhong et al. (41) showed that daytime napping is associated with increased risk of death of all causes (41). Another meta-analysis found that daytime napping is associated with an increased risk of type 2 diabetes mellitus (42). This is in line with our previously published findings for the same population of women with PCOS showing improved metabolic parameters following behavioral modification intervention (26).

A strength of the study is the use of actigraphy for objectively measured sleep variables compared to the majority of studies on similar populations using subjective reporting of sleep quality. Actigraphy also allows for a non-invasive method of assessing sleep for a long period of time in a patient's normal environment. However, actigraphy cannot be used for the assessment of obstructive sleep apnea. One limitation of his study is that the collection of sleep data for the control group partly was completed during the COVID-19 pandemic, when working from home was recommended by the authorities, enabling a wider window of sleep. In addition, there were differences in the proportion of women with children, as well as those in a stable relationship between the groups, however these differences were adjusted for in the statistical analyses.

In conclusion, we found that women with PCOS had shorter sleep duration, although within the normal range, but poorer sleep-efficiency and longer periods of wakefulness after sleep onset

10.3389/fendo.2023.1068045

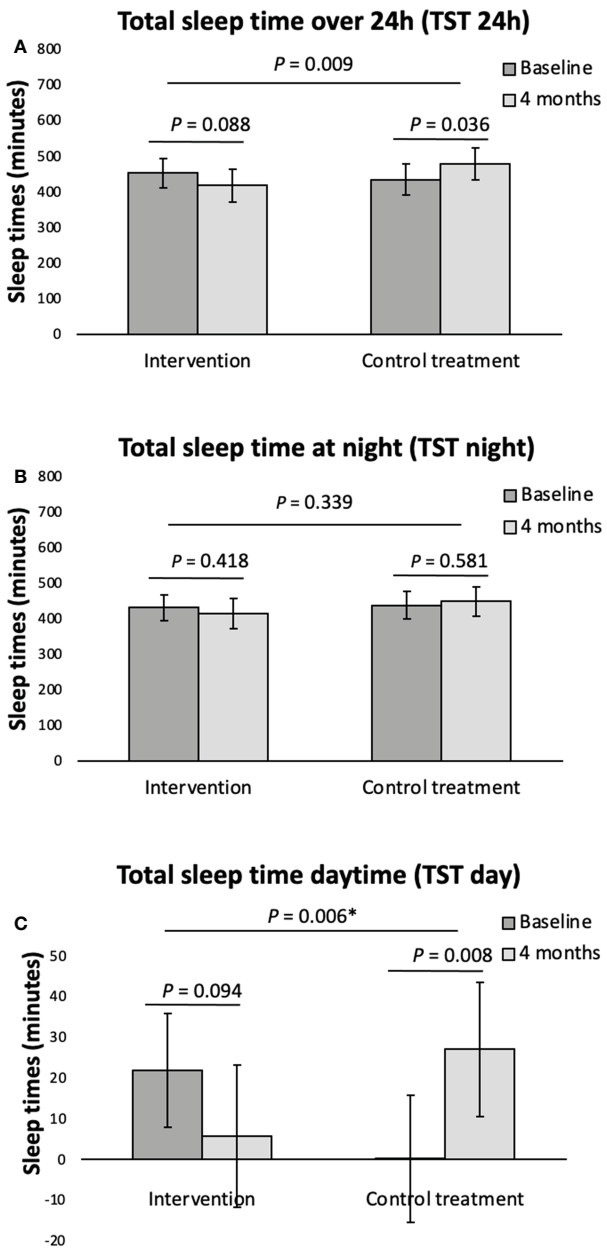

FIGURE 2
Actigraphy registered sleep variables (**A**, total sleep time over 24h, **B**, total sleep time at night, **C**, total sleep time daytime) at baseline and following 4 months intervention for the overweight women with PCOS. Data given as mean with its 95% Confidence Interval calculated using a mixed model on an ITT basis. *P-value corrected for the confounder TST day using analysis of covariance. TST, total sleep time.

compared to controls. In terms of sleep quality after lifestyle intervention in the women with PCOS, there was a non-significant reduction in the total sleep time over 24 hours, as well as total daytime sleep following behavioral modification intervention, which was significant when compared to the minimal intervention group. Behavioral modification intervention seems to reduce the amount of daytime sleep, suggesting improved sleep behavior.

Data availability statement

The raw data supporting the conclusions of this article will be made available by the authors, without undue reservation.

Ethics statement

The studies involving human participants were reviewed and approved by Regionala etikprövningsnämnden Stockholm, Avdelning 3. The patients/participants provided their written informed consent to participate in this study.

Author contributions

All authors contributed to the study conception and design. Data collection and analysis were performed by EO and ALH. The first draft of the manuscript was written by EO and all authors commented

on previous versions of the manuscript. All authors contributed to the article and approved the submitted version.

Funding

Grants supporting writing of the paper are the Swedish Research Council (ALH 2017-02051), the Stockholm County Council (ALH 2018-1157) and Karolinska Institutet (ALH).

Acknowledgments

We would like to thank Elisabeth Berg at Karolinska Institutet for advice regarding the statistical analysis as well as the research midwives Anna Cockin, Berit Legerstam and Siv Rödin Andersson at the Women's Health Research Unit at the Karolinska University Hospital for their logistical support.

Conflict of interest

The authors declare that the research was conducted in the absence of any commercial or financial relationships that could be construed as a potential conflict of interest.

Publisher's note

References

1. Bozdag G, Mumusoglu S, Zengin D, Karabulut E, Yildiz BO. The prevalence and phenotypic features of polycystic ovary syndrome: A systematic review and meta-analysis. *Hum Reprod* (2016) 31(12):2841–55. doi: 10.1093/humrep/dew218

2. Teede H, Misso ML, Costello MF, Dokras A, Laven J, Moran L, et al. International evidence-based guidelines for the assessment and managment of polycystic ovary syndrome 2018. *Melbourne Aust* (2018). doi: 10.1111/cen.13795

3. Rotterdam EA-SPCWG. Revised 2003 consensus on diagnostic criteria and long-term health risks related to polycystic ovary syndrome. *Fertil Steril* (2004) 81(1):19–25. doi: 10.1016/j.fertnstert.2003.10.004

4. Diamanti-Kandarakis E, Dunaif A. Insulin resistance and the polycystic ovary syndrome revisited: An update on mechanisms and implications. *Endocr Rev* (2012) 33 (6):981–1030. doi: 10.1210/er.2011-1034

5. Moran LJ, Misso ML, Wild RA, Norman RJ. Impaired glucose tolerance, type 2 diabetes and metabolic syndrome in polycystic ovary syndrome: A systematic review and meta-analysis. *Hum Reprod Update* (2010) 16(4):347–63. doi: 10.1093/humupd/dmq001

6. Cooney LG, Lee I, Sammel MD, Dokras A. High prevalence of moderate and severe depressive and anxiety symptoms in polycystic ovary syndrome: A systematic review and meta-analysis. *Hum Reprod* (2017) 32(5):1075–91. doi: 10.1093/humrep/dex044

7. Dokras A, Stener-Victorin E, Yildiz BO, Li R, Ottey S, Shah D, et al. Androgen excess- polycystic ovary syndrome society: Position statement on depression, anxiety, quality of life, and eating disorders in polycystic ovary syndrome. *Fertil Steril* (2018) 109 (5):888–99. doi: 10.1016/j.fertnstert.2018.01.038

8. Cesta CE, Mansson M, Palm C, Lichtenstein P, Iliadou AN, Landen M. Polycystic ovary syndrome and psychiatric disorders: Co-morbidity and heritability in a nationwide Swedish cohort. *Psychoneuroendocrinology* (2016) 73:196–203. doi: 10.1016/j.psyneuen.2016.08.005

9. Oberg E, Lundell C, Blomberg L, Gidlof SB, Egnell PT, Hirschberg AL. Psychological well-being and personality in relation to weight loss following behavioral modification intervention in obese women with polycystic ovary syndrome: A randomized controlled trial. *Eur J Endocrinol* (2020) 183(1):1–11. doi: 10.1530/EJE-20-0066

10. Moran LJ, March WA, Whitrow MJ, Giles LC, Davies MJ, Moore VM. Sleep disturbances in a community-based sample of women with polycystic ovary syndrome. *Hum Reprod* (2015) 30(2):466–72. doi: 10.1093/humrep/deu318

11. Fogel RB, Malhotra A, Pillar G, Pittman SD, Dunaif A, White DP. Increased prevalence of obstructive sleep apnea syndrome in obese women with polycystic ovary syndrome. *J Clin Endocrinol Metab* (2001) 86(3):1175–80. doi: 10.1210/jcem.86.3.7316

12. Kumarendran B, Sumilo D, O'Reilly MW, Toulis KA, Gokhale KM, Wijeyaratne CN, et al. Increased risk of obstructive sleep apnoea in women with polycystic ovary syndrome: A population-based cohort study. *Eur J Endocrinol* (2019) 180(4):265–72. doi: 10.1530/EJE-18-0693

13. Thannickal A, Brutocao C, Alsawas M, Morrow A, Zaiem F, Murad MH, et al. Eating, sleeping and sexual function disorders in women with polycystic ovary syndrome (Pcos): A systematic review and meta-analysis. *Clin Endocrinol (Oxf)* (2020) 92(4):338–49. doi: 10.1111/cen.14153

14. Vgontzas AN, Legro RS, Bixler EO, Grayev A, Kales A, Chrousos GP. Polycystic ovary syndrome is associated with obstructive sleep apnea and daytime sleepiness: Role of insulin resistance. *J Clin Endocrinol Metab* (2001) 86(2):517–20. doi: 10.1210/jcem.86.2.7185

15. Franik G, Krysta K, Madej P, Gimlewicz-Pieta B, Oslizlo B, Trukawka J, et al. Sleep disturbances in women with polycystic ovary syndrome. *Gynecol Endocrinol* (2016) 32 (12):1014–7. doi: 10.1080/09513590.2016.1196177

16. Shahveisi K, Jalali A, Moloudi MR, Moradi S, Maroufi A, Khazaie H. Sleep architecture in patients with primary snoring and obstructive sleep apnea. *Basic Clin Neurosci* (2018) 9(2):147–56. doi: 10.29252/NIRP.BCN.9.2.147

17. Mo L, Mansfield DR, Joham A, Cain SW, Bennett C, Blumfield M, et al. Sleep disturbances in women with and without polycystic ovary syndrome in an Australian national cohort. *Clin Endocrinol (Oxf)* (2019) 90(4):570–8. doi: 10.1111/cen.13922

18. Simon SL, McWhirter L, Diniz Behn C, Bubar KM, Kaar JL, Pyle L, et al. Morning circadian misalignment is associated with insulin resistance in girls with obesity and polycystic ovarian syndrome. *J Clin Endocrinol Metab* (2019) 104(8):3525–34. doi: 10.1210/jc.2018-02385

19. Shreeve N, Cagampang F, Sadek K, Tolhurst M, Houldey A, Hill CM, et al. Poor sleep in pcos; is melatonin the culprit? *Hum Reprod* (2013) 28(5):1348–53. doi: 10.1093/humrep/det013

20. Beccuti G, Pannain S. Sleep and obesity. *Curr Opin Clin Nutr Metab Care* (2011) 14 (4):402–12. doi: 10.1097/MCO.0b013e3283479109

21. Depner CM, Stothard ER, Wright KPJr. Metabolic consequences of sleep and circadian disorders. *Curr Diabetes Rep* (2014) 14(7):507. doi: 10.1007/s11892-014-0507-z

22. Bjorkelund C, Bondyr-Carlsson D, Lapidus L, Lissner L, Mansson J, Skoog I, et al. Sleep disturbances in midlife unrelated to 32-year diabetes incidence: The prospective population study of women in gothenburg. *Diabetes Care* (2005) 28(11):2739–44. doi: 10.2337/diacare.28.11.2739

23. Yazdanpanah MH, Farjam M, Naghizadeh MM, Jedi F, Mohebi K, Homayounfar R. Sleep duration and anthropometric indices in an Iranian population: The fasa Persian cohort study. *Sci Rep* (2021) 11(1):16249. doi: 10.1038/s41598-021-95796-9

24. Lim AJ, Huang Z, Chua SE, Kramer MS, Yong EL. Sleep duration, exercise, shift work and polycystic ovarian syndrome-related outcomes in a healthy population: A cross-sectional study. *PloS One* (2016) 11(11):e0167048. doi: 10.1371/journal.pone.0167048

25. Akerstedt T, Ghilotti F, Grotta A, Zhao H, Adami HO, Trolle-Lagerros Y, et al. Sleep duration and mortality - does weekend sleep matter? *J Sleep Res* (2019) 28(1): e12712. doi: 10.1111/jsr.12712

26. Oberg E, Gidlof S, Jakson I, Mitsell M, Tollet Egnell P, Hirschberg AL. Improved menstrual function in obese women with polycystic ovary syndrome after behavioural modification intervention-a randomized controlled trial. *Clin Endocrinol (Oxf)* (2019) 90 (3):468–78. doi: 10.1111/cen.13919

27. Labrie F, Cusan L, Gomez JL, Cote I, Berube R, Belanger P, et al. Effect of intravaginal dhea on serum dhea and eleven of its metabolites in postmenopausal women. *J Steroid Biochem Mol Biol* (2008) 111(3-5):178–94. doi: 10.1016/j.jsbmb.2008.06.003

28. Ingvar M, Eldh G. *Hjärnkoll på vikten*. Natur, Kultur, editors (2010), p. 203. (Stockholm, Sweden: Natur & Kultur).

29. Regalia G, Gerboni G, Migliorini M, Lai M, Pham J, Puri N, et al. Sleep assessment by means of a wrist actigraphy-based algorithm: Agreement with polysomnography in an ambulatory study on older adults. *Chronobiol Int* (2021) 38(3):400–14. doi: 10.1080/07420528.2020.1835942

30. Quante M, Kaplan ER, Cailler M, Rueschman M, Wang R, Weng J, et al. Actigraphy-based sleep estimation in adolescents and adults: A comparison with polysomnography using two scoring algorithms. *Nat Sci Sleep* (2018) 10:13–20. doi: 10.2147/NSS.S151085

31. Ke Y, Bertin J, Gonthier R, Simard JN, Sensitive LFA. Simple and robust lc-Ms/Ms method for the simultaneous quantification of seven androgen- and estrogen-related

steroids in postmenopausal serum. *J Steroid Biochem Mol Biol* (2014) 144:523–34. doi: 10.1016/j.jsbmb.2014.08.015

32. Ke Y, Gonthier R, Isabelle M, Bertin J, Simard JN, Dury AY, et al. A rapid and sensitive uplc-Ms/Ms method for the simultaneous quantification of serum androsterone glucuronide, etiocholanolone glucuronide, and androstan-3alpha, 17beta diol 17-glucuronide in postmenopausal women. *J Steroid Biochem Mol Biol* (2015) 149:146–52. doi: 10.1016/j.jsbmb.2015.02.009

33. Lundgren-Nilsson A, Jonsdottir IH, Ahlborg GJr., Tennant A. Construct validity of the psychological general well being index (Pgwbi) in a sample of patients undergoing treatment for stress-related exhaustion: A rasch analysis. *Health Qual Life Outcomes* (2013) 11:2. doi: 10.1186/1477-7525-11-2

34. Chassany O DE, Dubois D, Wu A, Dupuy H. The psychological general well-being index (Pgwbi) user manual. *Lyon France: MAPI Res Institute* (2004).

35. Cappuccio FP, D'Elia L, Strazzullo P, Miller MA. Sleep duration and all-cause mortality: A systematic review and meta-analysis of prospective studies. *Sleep* (2010) 33 (5):585–92. doi: 10.1093/sleep/33.5.585

36. Ohayon M, Wickwire EM, Hirshkowitz M, Albert SM, Avidan A, Daly FJ, et al. National sleep foundation's sleep quality recommendations: First report. *Sleep Health* (2017) 3(1):6–19. doi: 10.1016/j.sleh.2016.11.006

37. de Sousa G, Schluter B, Menke T, Trowitzsch E, Andler W, Reinehr T. Relationships between polysomnographic variables, parameters of glucose metabolism, and serum androgens in obese adolescents with polycystic ovarian syndrome. *J Sleep Res* (2011) 20(3):472–8. doi: 10.1111/j.1365-2869.2010.00902.x

38. Hachul H, Polesel DN, Tock L, Carneiro G, Pereira AZ, Zanella MT, et al. Sleep disorders in polycystic ovary syndrome: Influence of obesity and hyperandrogenism. *Rev Assoc Med Bras (1992)* (2019) 65(3):375–83. doi: 10.1590/1806-9282.65.3.375

39. Suri J, Suri JC, Chatterjee B, Mittal P, Adhikari T. Obesity may be the common pathway for sleep-disordered breathing in women with polycystic ovary syndrome. *Sleep Med* (2016) 24:32–9. doi: 10.1016/j.sleep.2016.02.014

40. Yang Y, Deng H, Li T, Xia M, Liu C, Bu XQ, et al. The mental health of Chinese women with polycystic ovary syndrome is related to sleep disorders, not disease status. *J Affect Disord* (2021) 282:51–7. doi: 10.1016/j.jad.2020.12.084

41. Zhong G, Wang Y, Tao T, Ying J, Zhao Y. Daytime napping and mortality from all causes, cardiovascular disease, and cancer: A meta-analysis of prospective cohort studies. *Sleep Med* (2015) 16(7):811–9. doi: 10.1016/j.sleep.2015.01.025

42. Chen GC, Liu MM, Chen LH, Xu JY, Hidayat K, Li FR, et al. Daytime napping and risk of type 2 diabetes: A meta-analysis of prospective studies. *Sleep Breath* (2018) 22 (3):815–24. doi: 10.1007/s11325-017-1528-z

frontiers | Frontiers in Endocrinology

TYPE Review
PUBLISHED 16 February 2023
DOI 10.3389/fendo.2023.1114767

OPEN ACCESS

EDITED BY
Magdalene K. Montgomery,
The University of Melbourne, Australia

REVIEWED BY
Endre Károly Kristóf,
University of Debrecen, Hungary
Bo Zhu,
Boston Children's Hospital and Harvard Medical School, United States

*CORRESPONDENCE
Sithandiwe E. Mazibuko-Mbeje
36588296@nwu.ac.za

SPECIALTY SECTION
This article was submitted to Obesity, a section of the journal Frontiers in Endocrinology

RECEIVED 02 December 2022
ACCEPTED 06 February 2023
PUBLISHED 16 February 2023

CITATION
Ziqubu K, Dludla PV, Mthembu SXH, Nkambule BB, Mabhida SE, Jack BU, Nyambuya TM and Mazibuko-Mbeje SE (2023) An insight into brown/beige adipose tissue whitening, a metabolic complication of obesity with the multifactorial origin. *Front. Endocrinol.* 14:1114767. doi: 10.3389/fendo.2023.1114767

An insight into brown/beige adipose tissue whitening, a metabolic complication of obesity with the multifactorial origin

Khanyisani Ziqubu[1], Phiwayinkosi V. Dludla[2,3], Sinenhlanhla X. H. Mthembu[1,2], Bongani B. Nkambule[4], Sihle E. Mabhida[2], Babalwa U. Jack[2], Tawanda M. Nyambuya[5] and Sithandiwe E. Mazibuko-Mbeje[1*]

[1]Department of Biochemistry, North-West University, Mmabatho, South Africa, [2]Biomedical Research and Innovation Platform, South African Medical Research Council, Tygerberg, South Africa, [3]Department of Biochemistry and Microbiology, Faculty of Science and Agriculture, University of Zululand, KwaDlangezwa, South Africa, [4]School of Laboratory Medicine and Medical Sciences, University of KwaZulu-Natal, Durban, South Africa, [5]Department of Health Sciences, Faculty of Health and Applied Sciences, Namibia University of Science and Technology, Windhoek, Namibia

Brown adipose tissue (BAT), a thermoregulatory organ known to promote energy expenditure, has been extensively studied as a potential avenue to combat obesity. Although BAT is the opposite of white adipose tissue (WAT) which is responsible for energy storage, BAT shares thermogenic capacity with beige adipose tissue that emerges from WAT depots. This is unsurprising as both BAT and beige adipose tissue display a huge difference from WAT in terms of their secretory profile and physiological role. In obesity, the content of BAT and beige adipose tissue declines as these tissues acquire the WAT characteristics *via* the process called "whitening". This process has been rarely explored for its implication in obesity, whether it contributes to or exacerbates obesity. Emerging research has demonstrated that BAT/beige adipose tissue whitening is a sophisticated metabolic complication of obesity that is linked to multiple factors. The current review provides clarification on the influence of various factors such as diet, age, genetics, thermoneutrality, and chemical exposure on BAT/beige adipose tissue whitening. Moreover, the defects and mechanisms that underpin the whitening are described. Notably, the BAT/beige adipose tissue whitening can be marked by the accumulation of large unilocular lipid droplets, mitochondrial degeneration, and collapsed thermogenic capacity, by the virtue of mitochondrial dysfunction, devascularization, autophagy, and inflammation.

KEYWORDS

brown adipose tissue, beige adipose tissue, whitening, obesity, metabolic complications

1 Introduction

Adipose tissue is an endocrine organ that has become the central focus in research toward a better understanding of the pathological mechanisms associated with obesity (1, 2). The latter is characterized by adipose tissue hypertrophy "adipocytes expansion" and hyperplasia "increase adipocytes number" caused by a chronic imbalance between energy intake and expenditure (1, 3). There are three distinct types of adipocytes that have been well studied in mammals (4): (i.) white adipocytes comprised of large single lipid droplet and few mitochondria, and this form of adipose is predominately useful to facilitate the storage of excess energy in a form of fats (5), and (ii.) brown adipocytes, and (iii.) beige or brite adipocytes rich in mitochondria, which are important organelles for regulating thermogenesis, mainly *via* the action of uncoupling protein 1 (UCP1) (5). Although brown and beige adipocytes share thermogenic capacity, several characteristics established that both are distinct cell types, which are different in terms of origin, anatomical location, and plasticity (6, 7). Of note, beige adipocytes emerge from white adipose tissue (WAT) depots *via* the process called "browning" (8, 9).

The (re)discovery of brown (BAT) and beige adipose tissue has garnered interest as therapeutic targets to promote energy expenditure and counteract complications linked with obesity (7). Notably, previous conversations have emphasized the importance of sufficient vasculature to improve mitochondrial function in BAT and alleviate obesity-associated complications (10). The vascular rarefaction in BAT was associated with the dysfunction and loss of BAT commonly referred to as "whitening" (11). It is well accepted that both BAT and beige adipose tissue are subjected to a whitening effect which is common in obesity, whereby they acquire unilocular cells that gradually lose all the brown characteristics and assume WAT characteristics (12). Moreover, the whitening of adipose tissue is accompanied by lipid accumulation due to reduced substrate oxidation and the loss of mitochondria through the impairment of molecular mechanisms regulating thermogenesis, as well as those involving autophagy and mitophagy (12). Others have demonstrated that brown-to-white adipose tissue conversion may activate undesirable metabolic complications such as inflammatory response and, the much-explored pyrin domain-containing protein 3 (NLRP3) inflammasome (13). Recently, BAT whitening was defined as a long-term obesity complication that displayed a progressive severity upon chronic intake of a high-fat diet (HFD) during the pathogenesis of obesity (14). Thus, with the rapidly rising prevalence of obesity (15), there is an urgent need to understand the causative and underlying factors implicated in BAT/beige adipose tissue whitening, including elucidating the molecular drivers of their plasticity. This encompasses deciphering pathophysiological mechanisms that implicate the development and aggravation of obesity, as shown by the fact that dysfunctional adipose tissue in obesity leads to a variety of secondary metabolic complications.

The current review elaborates on the prominent mechanisms involved in BAT/Beige adipose tissue whitening, while a sharp focus is placed on the impact of critical factors that contribute to obesity, such as diet, age, temperature, and various chemical substances. Importantly, an overview of BAT and beige adipose tissue, and their physiological relevance is given to highlight vital mechanisms implicated in the process of thermogenesis.

2 An overview of BAT and beige adipose tissue, and their physiological importance

As aforementioned, adipocytes are broadly classified into three distinct types: (i) brown adipocytes, (ii) white adipocytes, and (iii) beige or brite adipocytes (Figure 1) (4). These cells differ in terms of function and morphology, and their localization on various fat depots in mice and humans (16, 17). Importantly, brown adipocytes are enriched in the BAT depot, whereas both white and beige adipocytes are found within WAT depots (18). Predominantly, beige adipocytes emerge in subcutaneous WAT depots, including the anterior and inguinal subcutaneous WAT in mice (18, 19). In contrast to WAT, BAT was mainly viewed as the key site for upholding thermal homeostasis during cold adaptation in human infants (20). Despite a century of studies on neonatal BAT, the knowledge about BAT physiological features and the mechanisms by which this tissue regulates body temperature homeostasis in human neonates is scanty, mainly due to the lack of appropriate methods for such investigations. Recently, studies have utilized infrared thermography as a suitable non-invasive technique to investigate neonatal BAT activity (21, 22). It was reported that a single short-term cold exposure during the first day of life improves body temperature adaptation (21). The later rediscovered BAT and recruitable beige adipose tissue in adult humans which was initially thought to exist in newborn babies and hibernating animals only have highlighted the potential influence of this tissue in improving human health (23). This is attributable to the thermogenic and endocrine functions of these tissues to promote energy expenditure and secrete metabolic regulating molecules, called batokines, such as vascular endothelial growth factors (VEGF)-A, bone morphogenic protein 8b (BMP8b), neuregulin 4 (NRG4) and fibroblast growth factor 21 (FGF21) (24). Recent research has indicated that disease progression is consistent with impairment of gene expression levels of batokines regulating sympathetic neurite outgrowth, vascularization and glucose metabolism in animal model of T2D (25). Thus, the physiological functions of BAT and beige adipose tissue have spurred a new wave of interest in their effects on modulating metabolism. This is supported by mounting research on the health benefits of BAT, especially in combating obesity (26–28). Owing to this, several selective markers of adipose tissues have been identified and characterized as potential biomarkers in obesity, as reviewed by Pilkington et al. (29).

2.1 The development of BAT/beige adipose tissue: Implications in the pathogenesis of obesity

Although brown, white, and beige adipocytes are derived from similar mesenchymal stem cells, they originate from different

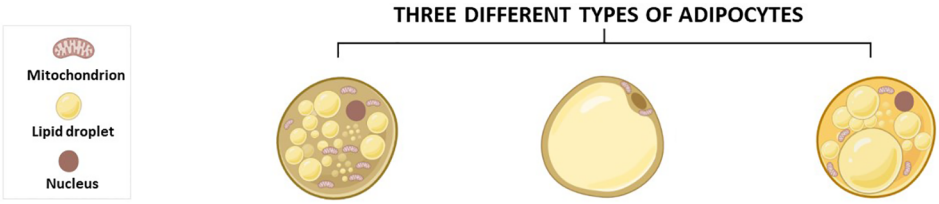

	BROWN ADIPOCYTES	WHITE ADIPOCYTES	BEIGE/BRITE ADIPOCYTES
Location	**Humans:** Anterior cervical, supraclavicular, axillary, paravertebral **Mice:** Interscapular, perirenal	**Humans:** Subcutaneous, visceral **Mice:** inguinal, gonadal, mesenteric	**Humans:** Supraclavicular, but predominantly in subcutaneous WAT depot **Mice:** Anterior and inguinal subcutaneous WAT depot
Primary function	Thermogenesis, endocrine signaling	Energy storage, endocrine signaling	Adaptive thermogenesis, endocrine signaling
Mitochondrial content	High	Low	Medium
Lipid droplets	Small multilocular	Large unilocular	Small multilocular
UCP1 expression	High	Low/undetectable	Inducible
Thermogenic capacity	High	None	Medium
Marker genes	Ucp1; Pgc1A; Cidea; Ebf2; Prdm16; Dio2; Zic1; Lhx8	Leptin; HoxC9; Tcf21; Lpl; Nrip1; Rb1; Fabp4	Ucp1; Pgc1A; CD137; Cited1; HoxC9; Tmem26

FIGURE 1
Schematic overview showing the characteristics of brown, white, and beige/brite adipocytes, including their localization, morphology, physiological function, and marker genes. In brief, the anatomical location of these adipocytes differs, except for white and beige adipocytes which are found within WAT depots. In terms of morphology and function, brown adipocytes are comprised of small multilocular lipid droplets, high mitochondrial content, and increased UCP1 expression, which can be also induced in beige adipocytes to promote thermogenesis and enhance energy expenditure, features that are important for the treatment of obesity. In sharp contrast, white adipocytes have fewer mitochondria and large unilocular lipid droplets to facilitate the storage of energy in a form of fats. Of note, these adipocytes have similar and distinct marker genes which could play an important role in tracking metabolic complications linked with obesity. Cidea, cell death-inducing DNA fragmentation factor-like effector A; CD137, tumour necrosis factor receptor superfamily, member 9; Dio2, Iodothyronine deiodinase 2; Lhx8, LIM homeobox protein 8; Pgc1A, peroxisome proliferator-activated receptor coactivator 1 alpha; Prdm16, PR domain-containing 16; Tcf21, Transcription factor 21; TMEM26, transmembrane protein 26; UCP1, uncoupling protein 1; WAT, white adipose tissue; Rb1, RB transcriptional corepressor 1; Zic1, zinc finger protein of the cerebellum.

precursor cells with unique marker genes, as shown in Figure 2 (30–33). Genetic-lineage tracing indicates that white adipocytes descend from Myf5- (PDGFRα+, CD29, CD44+) progenitors of mesenchymal stem cells (34, 35), while brown adipocytes originate from Myf5+ (CD34+/CD29, MYF5-, PAX3+) progenitors which differentiate into mature brown adipocytes (36–38). Interestingly, the existence of beige adipocytes which resemble white adipocytes in having a low basal expression of UCP1, but like classical brown adipocytes respond to thermogenic stimuli with high UCP1 expression (39). These cells are distinct types of thermogenic fat cells that originate from two distinct processes, *de novo* differentiation from Myf5- progenitor cells and transdifferentiation from white adipocytes *via* a process called "browning" (4). A study by Oguri et al. (40) showed that CD81+, Sca1+, PDGFRα+ adipocyte progenitors give rise to beige adipocytes and CD81 loss causes obesity, insulin resistance, and inflammation in mice. In addition to canonical beige adipocytes, a study of adipocyte heterogeneity has demonstrated that there is a subpopulation of thermal stress-induced glycolytic beige adipocytes that emerge from inguinal WAT (41, 42). Although cells in the MyoD1+ lineage do not typically give rise to any adipocytes, it was reported that glycolytic beige adipocytes descend from MyoD1+ progenitors that emerge within a stromal vascular fraction of inguinal WAT when beta-3 adrenergic receptor (β-AR) signaling is inhibited (41, 42). Thus, this has reignited the interest in studying and understanding the role of WAT browning in obesity (26, 28, 43). While white adipocytes transdifferentiate into beige adipocytes, both brown and beige adipocytes can transdifferentiate into white adipocytes through a process called "whitening", which is quite common in obesity (44, 45). By now, it is evident that the differentiation process constitutes an essential component for understanding the developmental fate and function of BAT, which explains the increased exploration of these transcriptional factors in preclinical models of obesity (46–48).

Of note, bone morphogenetic protein (BMP)-7, a secretory protein that acts as an autocrine/paracrine mediator, promotes the differentiation of both brown and beige adipocytes in mice (49, 50). Recently, Townsend et al. (51) demonstrated that BMP7-loaded silk hydrogels into the subcutaneous WAT of mice induced brown adipogenesis in committed and uncommitted progenitor cells, which in turn increased energy expenditure and reduced weight gain in mice. In human-neck adipose-derived stromal cells, BMP7 enhanced mitochondrial DNA content, concomitant with increased

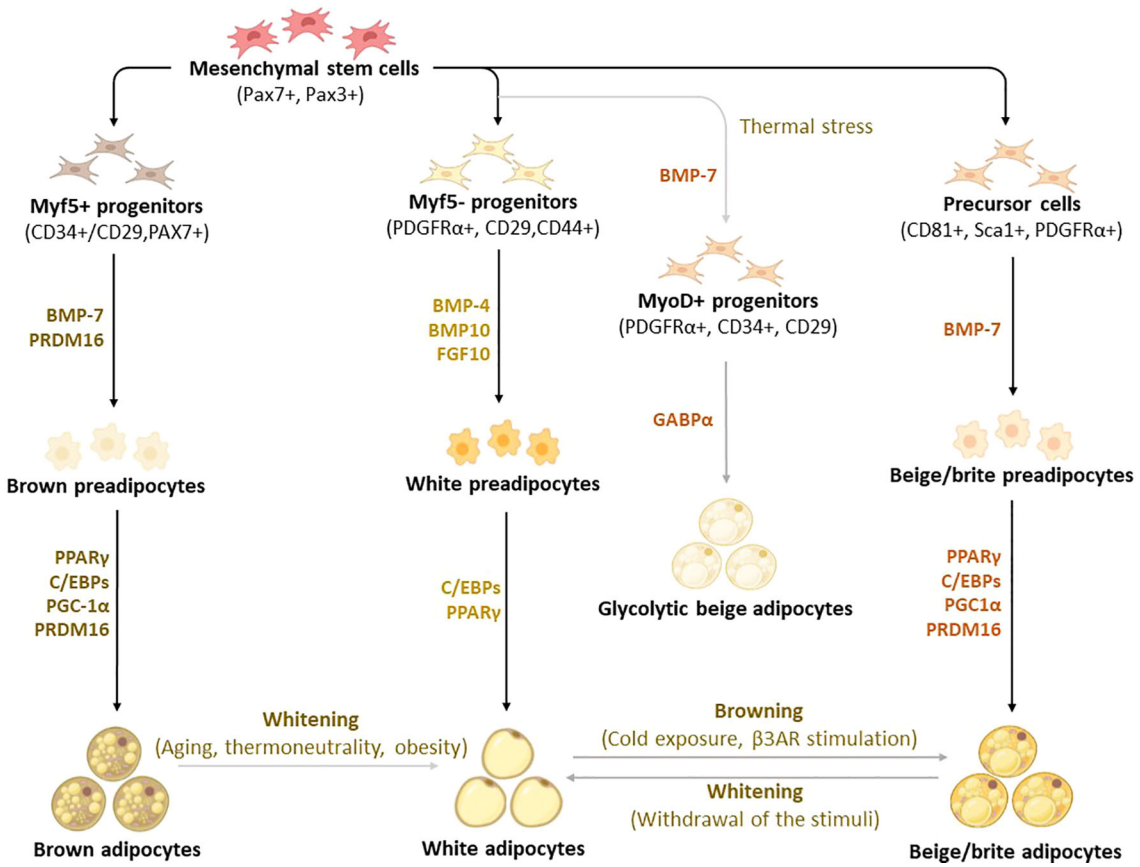

FIGURE 2
Differentiation and transdifferentiation trajectories of major adipocyte populations, including brown and white adipocytes, as well as canonical and glycolytic beige/brite adipocytes. Generally, brown adipocytes are derived from Myf5+ progenitors, whereas white and beige adipocytes originate from Myf5- progenitors that descend from mesenchymal stem cells. New advances on adipocyte origin show that there is another subpopulation of beige adipocytes known as glycolytic beige adipocytes, which are derived from MyoD+ progenitors within the stromal vascular fraction of inguinal WAT in response to thermal stress. During differentiation secretory factors BMP-7 and transcriptional factor PRDM16 induce Myf5+ cell commitment to brown preadipocytes whereas BMP-4, BMP-10, and FGF10 induce Myf5- cell commitment to white preadipocytes. On the other hand, BMP-7 induces a commitment of beige adipocyte precursors to canonical beige preadipocytes. Differentiation of all types of preadipocytes into mature adipocytes is driven by PPARγ, and C/EBPs, whereas brown and beige adipocytes require the expression of additional factors, including PRDM16 and PGC1α. Moreover, GABPα regulates the differentiation of glycolytic beige adipocytes. During transdifferentiation, white adipocytes convert to beige adipocytes following cold exposure or β3-AR stimulation. Likewise, brown and beige adipocytes can transdifferentiate into white-like adipocytes, a process termed whitening. β3-AR, beta-3 adrenergic receptor; BMP, bone morphogenetic protein; C/EBPs, CCAAT/enhancer-binding proteins; GABPα, GA-binding protein alpha; PGC1α, peroxisome proliferator-activated receptor coactivator 1 alpha; PPARγ, peroxisome proliferator-activated receptor-gamma; PRDM16, PR domain-containing 16; UCP1, Uncoupling protein 1.

gene expression of proliferator-activated receptor coactivator 1 alpha (PGC1α), a transcriptional co-regulator, responsible for mitochondrial biogenesis (52). Amongst other transcriptional factors, PR domain containing 16 (PRDM16) plays a key role in determining the fate of brown adipocyte differentiation (53). An elegant study by Seale et al. (54) has demonstrated that the loss of PRDM16 in brown adipose precursors results in the loss of brown adipocyte characteristics, which in turn promotes skeletal muscle differentiation instead of brown adipocyte differentiation. Importantly, PRDM16 is not only required for determining brown adipocyte fate but also for regulating thermogenic programming and maintenance of brown adipocyte identity (55). Adipogenic transcriptional factors, such as CCAAT enhancer-binding proteins (C/EBPs), and peroxisome proliferator-activated receptor (PPAR)-γ have long been known to play a central role in regulating adipocyte differentiation in almost all types of adipocytes (56–58). To further highlight the significance of studying adipocyte differentiation in obesity, a recently published protocol (59) compares white, beige, and brown adipocyte differentiation, further characterizing the expression of distinct transcriptional factors that are involved in thermogenesis. In fact, findings from this study indicate that differentiated pre-adipocytes from interscapular BAT has a higher thermogenic potential and expression levels of UCP1 with compared to WAT-derived cells. A comprehensive characterization of mature brown adipocyte subpopulations using single-nucleus ribonucleic acid (RNA) sequencing identified a rare subpopulation of adipocytes that increases in abundance at higher temperatures, suggesting a lower thermogenic activity (60). This subpopulation regulates the activity of neighboring adipocytes *via* acetate-mediated modulation of their thermogenic capacity (60).

2.2 Physiological functions of BAT/beige adipose tissue and their role in regulating metabolic health

2.2.1 Activation of thermogenesis and the effect of various stimuli

A consistently growing body of literature indicates that elevating the thermogenic capacity of BAT through activation, recruitment, or BAT transplant could be an ideal approach to mitigate obesity (Figure 3) (61–63). The thermogenesis in BAT and beige adipose tissue is facilitated by UCP1 or thermogenin, a mitochondrial inner membrane protein that uncouples substrate oxidation from ATP synthesis, thereby dissipating excess energy as heat (64). In addition to a well-recognized UCP1-dependent thermogenic mechanism, there is a newly identified UCP1-independent thermogenic mechanism that could potentially offer a new target for the treatment of obesity and type 2 diabetes, especially targeting UCP1-negative adipocytes in the elderly and people with obesity (65–67). The UCP1-independent thermogenic mechanism involves ATP-dependent Calcium (Ca2+) cycling by Sarco/endoplasmic reticulum Ca2+-ATPase 2b, which enhances energy expenditure and glucose oxidation in beige adipocytes (68). A study by Okamatsu-Ogura et al. (68) has discovered that cold exposure induces UCP1-independent active lipid metabolism in BAT of UCP1-knockout mice. Recently, Oeckl et al. (69) identified the futile ATP-consuming triglyceride/fatty acid cycle as a central process that contributes to thermogenesis in BAT of UCP1-knockout mice. To date, UCP1 is the most investigated mitochondrial carrier protein, involved in the modulation of oxidative phosphorylation, with its isoforms like UCP2 also found in other tissues like the heart where they protect against oxidative stress (70). By now, it is well-accepted that cold exposure is a

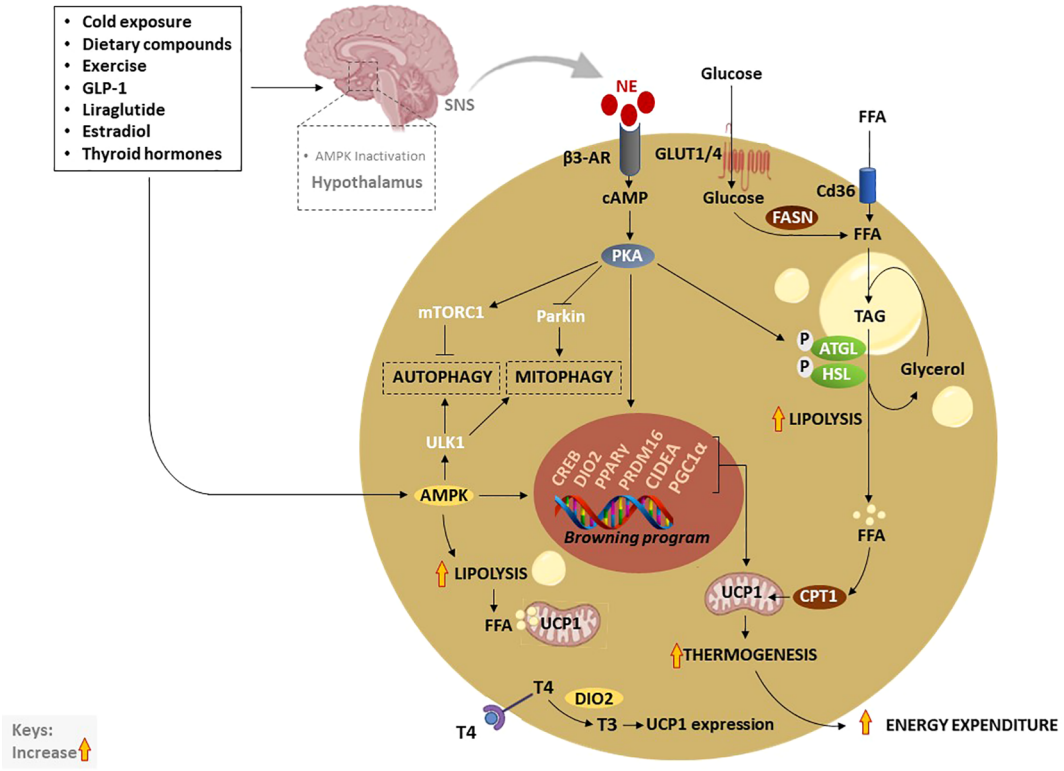

FIGURE 3
Thermogenic activation of brown and beige adipocytes by various exogeneous and endogenous stimuli. Traditionally, cold exposure and other dietary compounds activate thermogenesis *via* NE, excreted by the SNS, or through direct activation of AMPK. Inactivation of hypothalamic AMPK by thermogenic stimuli like estradiol, GLP-1, liraglutide or thyroid hormones, stimulate SNS resulting in the release of NE and stimulation of β3-AR which subsequently increase cAMP and activate PKA. Moreover, elevated cAMP activates CREB causing the transcription of thermogenic genes such as PPARγ, DIO2, PRDM16, PGC1α, and CIDEA. On the other hand, the cAMP-PKA signaling pathway promotes lipolysis just like AMPK through the phosphorylation of ATGL and HSL. Liberated FFA contributes to the upregulation of UCP1 and increases thermogenesis. In addition, enhanced TAG-derived fatty acids uptake upregulates CPT1, resulting in increased FFA transport into mitochondria. Glucose act as a substrate to generate FFA *via* FSAN, which ultimately contributes to heat production. Upon β3-AR stimulation, adenylate cyclase cAMP/PKA also activates mTORC1 and inhibits Parkin to repress autophagy/mitophagy, as a means to maintain beige adipocytes. Inversely, AMPK promotes promote autophagy/mitophagy to maintain mitochondrial health *via* the phosphorylating of ULK1 in brown adipocytes. AMPK, AMP-activated protein kinase; β3-AR, Beta-3 adrenergic receptor; PPARγ, peroxisome proliferator-activated receptor-gamma; CIDEA, cell death-inducing DNA fragmentation factor-like effector A; C/EBPs, CCAAT/enhancer-binding proteins; cAMP, cyclic adenosine monophosphate-protein kinase A; DIO2, Iodothyronine deiodinase 2; FASN, fatty acid synthase; FFA, free fatty acids; GLUTs, glucose transporters; HSL, hormone-sensitive lipase; NE, norepinephrine; PKA, protein kinase A; PRDM16, PR domain-containing 16; PGC1α, peroxisome proliferator-activated receptor coactivator 1 alpha; UCP1, Uncoupling protein 1; SNS, sympathetic nervous system; T4, thyroxine; T3, triiodothyronine; TAG, triacylglyceride.

classical stimulus that utilizes glucose and fatty acids as substrates for adaptive thermogenesis (71). In humans, cold exposure increases glucose uptake and non-esterified fatty acid turnover, suggesting that activation of thermogenesis can help to improve plasma glucose clearance (71). Apart from the cold exposure, thermogenic stimuli, such as dietary compounds, physical exercise, and other various agents, including glucagon-like peptide-1 (GLP-1), thyroid hormones (THs), liraglutide and thiazolidinediones, are known to upregulate the genes involved in thermogenesis and induce WAT browning (26).

In general, thermogenesis is modulated by stimulating the sympathetic nervous system (SNS), which is in part regulated through the release of norepinephrine (NE) to activate β3-AR signaling in response to various stimuli (72). Amongst all other well-known mechanisms that regulate thermogenesis, the cyclic adenosine monophosphate-protein kinase A (cAMP-PKA) signaling pathway, and AMP-activated protein kinase (AMPK) are classical mechanisms that have been studied in depth (72). Upon activation, PKA phosphorylates adipose triglyceride lipase (ATGL) and hormone-sensitive lipase (HSL), enzymes that promote lipolysis, leading to the breakdown of triacylglyceride (TAG) to free fatty acids (FFA), again *via* AMPK (72–74). Resultant FFA can be further broken down and oxidized in the mitochondria by carnitine palmitoyltransferase 1 (CPT1) to produce heat *via* UCP1 (75). Of note, glucose transporter (GLUT)-1 and GLUT4 are expressed in human BAT to facilitate glucose uptake by brown adipocytes (76, 77). In response to chronic cold-exposure, glucose uptake by BAT is utilized for the fatty acid synthesis and β-oxidation process (78). Alternatively, cAMP-PKA signaling modulates the phosphorylation of cAMP-response element binding protein (CREB), which in turn promotes the transcription of mitochondrial biogenic and thermogenic genes, such as PGC1α, PRDM16, PPARγ, and UCP1 (79). Lipid-droplet-associated protein also known as cell death-inducing DNA fragmentation factor-like effector A (CIDEA) regulates UCP1 transcription for browning and thermogenesis in human adipocytes (80). In specific, CIDEA inhibits liver X receptor (LXR), a repression of UCP1 enhancer activity, and strengthens the binding of PPARγ to UCP1 enhancer, promoting UCP1 transcription in CIDEA knockout primary human adipocytes (80). Another prominent mechanism that is modulated by the kinase enzymes, PKA and AMPK is the regulation of autophagy "degradation of cellular components" or mitophagy "selective degradation of mitochondria" which plays an important role in BAT/beige adipose tissue plasticity (12, 81, 82). In BAT, activation of thermogenesis is paralleled by a reduction in the autophagic degradative activity, which converges at PKA that activates the rapamycin complex 1 (mTORC1) and inhibits Parkin transcription (83, 84). Moreover, melanocyte-inducing transcription factor (MITF) and forkhead box O3 (FOXO3) were identified as downstream autophagy-related transcription factors that are downregulated by cAMP-PKA during autophagy regression in beige adipocytes (83).

Inversely, AMPK is required for the efficient removal of damaged mitochondria or mitophagy through phosphorylation of unc-51-like kinase 1 (ULK1) as a means to maintain BAT and induce browning (85). Thus, targeting AMPK might be a plausible approach for the treatment of various metabolic diseases as recently reviewed by López (86). Dietary components such as polyphenols have been reported to activate the SNS and stimulate the release of THs, which in turn increase thermogenesis and induce WAT browning *via* the AMPK-PGC1α/Sirt1 and PPAR signaling pathways (87, 88). Apart from that, dietary intake alone is known to induce thermogenesis by increasing postprandial energy expenditure, contributing 5–15% of total daily energy expenditure (89). Other data has uncovered that WAT browning is a highly dynamic physiological process, in which O-linked b-N-acetylglucosamine (O-GlcNAc) signaling in agouti-related protein (AgRP) neurons is essential for suppressing thermogenesis to conserve energy upon fasting (90). In terms of hormonal control, both insulin and leptin act on hypothalamic or proopiomelanocortin neurons to promote WAT browning (91). Interestingly, overexpression of glucose-regulated protein 78 kDa/binding immunoglobulin protein (GRP78) in the ventromedial nucleus of the hypothalamus (VMH) alleviated ER stress and obesity; however, this was not dependent on leptin but it was related to the increased thermogenic activation of BAT and WAT browning (92). GLP-1, a hormone that controls satiation and glucose metabolism *via* vagal afferent neurons was reported to stimulate BAT thermogenesis by regulating sirtuin 1 (SIRT1) (93), and hypothalamic AMPK (94). Metabolism-activating hormones thyroxine (T4) and triiodothyronine (T3) which are mainly secreted by the thyroid gland convert from T4 to T3 by type II iodothyronine deiodinase (DIO2) promoting UCP1 expression in BAT (95). Importantly, THs target the hypothalamus in the brain to modulate energy balance *via* AMPK (96, 97). Specifically, THs act on the VMH to regulate the thermogenic program in BAT (98, 99). For instance, it was reported that the central T3 promotes hepatic lipogenesis and thermogenic program in BAT through the parasympathetic nervous system and SNS, respectively (98). These effects were coordinated by distinct signaling pathways in the VMH, JNK1, and ceramides/endoplasmic reticulum stress under the control of AMPK (98). Other fundamental hormones include estradiol, a female reproductive hormone, which inhibits AMPK leading to the activation of BAT thermogenesis *via* estrogen receptor alpha selectively in the VMH (100).

2.2.2 The role of autophagy and inflammation on BAT/beige adipose tissue plasticity

Autophagy is a fundamental lysosomal catabolic process that degrades and recycles damaged cellular components such as lipids, proteins, and organelles for cellular survival in stress conditions (101–103). Although selective autophagic degradation of mitochondria termed "mitophagy" seems to be beneficial to eliminate damaged mitochondria from accumulated reactive oxygen species (ROS) in active BAT, there are some conflicting results in the literature regarding the importance of this process during the activation of BAT by cold exposure (84, 104–107). For example, Cairó et al. (107) reported that cold-induced thermogenic activation of BAT in mice was linked with autophagy repression, in part by upregulating cAMP-PKA pathway in NE-exposed brown

adipocytes. Surprisingly, chronic cold exposure promoted autophagy/mitophagy in primary brown adipocytes and BAT from mice (105, 106). Yau et al. (106) showed similar effect on the activation of autophagy in BAT from mice in response to cold exposure, and this was marked by increased mRNA expression of the autophagic genes, including, sequestosome 1 *(Sqstm1)*, autophagy-related (*Atg*)-5, *Atg7*, and *Ulk1*. This effect promoted β-oxidation, mitochondrial turnover, and thermogenesis in BAT (106). These results further indicate that autophagic processes in BAT are tightly regulated in response to cold exposure, as increasingly discussed (12, 83, 84).

Another hypothesis implementing the role of mitophagy on BAT/beige adipose tissue plasticity also prevails, and it is linked to the process of adipose tissue whitening (13, 83, 108, 109). For example, thermoneutrality reacclimatization after chronic cold exposure or withdrawal of thermogenic stimuli activate autophagic response and promotes the transition of BAT/beige adipose tissue to white-like adipose tissue in mice (83). Obviously, there are some distinct differences between BAT and beige adipose tissue whitening, such as that the brown adipocytes "disappear" from WAT depots and acquire unilocular phenotype with loss of UCP1 expression while brown adipocytes display an increased lipid accumulation, followed by protein degradation, and loss of protein synthesis without disappearance (12). Alternatively, reversal of beige-to-white adipocytes is tightly coupled with autophagy-mediated mitochondrial clearance after withdrawal of the external cues in mice (83). Notably, beige adipocytes progressively lose their morphological structure and molecular characteristics to acquire white-like characteristics bypassing an intermediate precursor stage (83). Inversely, inhibition of autophagy by UCP1+ adipocyte-specific deletion of Atg5 or Atg12 maintained functional beige adipocytes even after stimuli withdrawal (83). More evidence showed that inhibition of Parkin-mediated mitophagy underlies the maintenance of beige adipocyte in mice (108). Interestingly, physiological conditions such as aging can promote autophagy, which result to the loss of BAT activity. Indeed, upregulation of autophagy in BAT of mice is consistent with age-dependent decline of BAT activity and reduced metabolic rate (109). However, inhibition of mitophagy by BAT-specific deletion of the *Atg7* gene could improve insulin sensitivity and energy metabolism, as well as maintained higher mitochondrial content by suppressing mitochondrial clearance (109).

Beyond dysregulation of autophagy, inflammation is another instrumental process that may negatively influence BAT activity and compromise the metabolic rate of this tissue. Although the relationship between autophagy and inflammation is relatively complex, they both constitute a natural response to stress conditions. Apparently, elevated inflammatory status impairs brown adipocyte metabolic activity and promotes whitening (110). Kotzbeck et al. (13) showed that BAT whitening is coupled with a decreased mitochondrial content as whitened adipocytes become dysfunctional as they render low-grade inflammatory state that eventually leads to cell death. To further highlight the link between dysregulated autophagy and inflammation, it was demonstrated that activation of the NLRP3 inflammasome and increased expression of inflammatory markers, including F4/80, tumor necrosis factor-alpha (TNF-α), interleukin (IL)-1β, IL-10, IL-18, monocyte chemoattractant protein 1 (Mcp-1), and caspase-1 was linked with Atgl-deficiency in mice (13). Other studies showed that deletion of transcription factor nuclear factor erythroid-2, like-1 (Nfe2l1) induced ER stress, inflammation, mitochondrial dysfunction, insulin resistance, and whitening in BAT (111, 112). Altogether, mitophagic maintenance of the healthy network of mitochondria in BAT and beige adipose tissue is crucial for cell survival but requires a balanced remodeling system of mitochondrial biogenesis and degradation.

3 Factors inducing BAT/beige adipose tissue whitening or inactivation in obesity

3.1 Natural factors inducing BAT/beige adipose tissue whitening

While the browning of WAT has long been a growing area of interest in obesity research, whitening of BAT as an obesity-related complication with metabolic and health implications has been receiving less attention. Latterly, there is cumulative emerging evidence on BAT whitening, and it demonstrates that this phenomenon is multifactorial in origin. Notably, it has long been established that risk factors such as diet, age, genetics, as well as some chemicals can negatively influence the health of the general population (113). Risk factors such as excessive intake of an unhealthy diet can directly contribute to adiposity or weight gain (114), whereas aging is an undeniable major consequence that has long been linked with deteriorated health (115). Although acknowledged to significantly affect metabolic health, precise pathological mechanisms involved in this process are not completely understood. Interestingly, experimental evidence indicates that factors such as diet, thermoneutrality, age, and genetics can induce the whitening of BAT, and exacerbate obesity (Table 1).

3.1.1 High fat diet induced BAT/beige adipose tissue whitening by suppressing angiogenesis and elevating inflammation

It is acknowledged that the consumption of a diet rich in fat and cholesterol, and sugar, is the most common cause of obesity and metabolic syndrome (130, 131). In fact, animal models are a good example of the impact of such a diet, with evidence indicating that feeding rats two individual components of a western-style diet 60% HFD and 55% high fructose diet can cause fat accumulation, drive a state of insulin resistance and other metabolic complications (132–134). Based on growing experimental evidence, exposing rodents to HFD-feeding can cause several pathological abnormalities that include adipocyte hyperplasia and hypertrophy (132). The latter is linked with the state of inflammation, whereby adipose tissue expansion results in the release of proangiogenic cytokines, such as leptin, adiponectin, VEGF, TNF-α, and transforming growth factor beta (TGF-β) angiopoietin; such evidence has been extensively

TABLE 1 Summary of evidence reporting on BAT/beige adipose tissue whitening-induced by diet, thermoneutrality, age, and genetics.

Factors	Model	Intervention protocol	Main findings		Author, year
			Effect	Mechanism	
Diet	CD-1 mice	Mice fed HFD for 10 weeks	Increased fat deposition in BAT without altering triglyceride and free fatty acids levels the in blood	Not investigated	Gao et al., 2015 (116)
	C57BL/6 mice	Mice fed HFD for 10 weeks	Induced expansion of beige adipocytes residing in the WAT depot	Downregulated UCP1 gene expression	Dobner et al., 2017 (117)
	C57BL/6J mice	Mice fed HFD for 1, 3, or 7 day(s)	Increased lipid accumulation and insulin resistance in BAT	Upregulated Cd36, Hsl, Srebp1c, and downregulated pPKB; LPL; Ppargc1a mRNA expression	Kuipers et al., 2019 (118)
	C57BL/6 mice	Mice fed HFD and HFrD for 12 weeks	Increased iBAT lipid droplet, and lipid storage pattern resembling WAT	Downregulated VEGF-A, UCP1, B3-AR, Plin1 and Cidea gene expression	Miranda et al., 2020 (119)
	Wistar rats	Mice fed HCD, HFD, HFHSD from 8 weeks to 16 weeks	Increased iBAT adipocyte area more prominent in HFHSD	Downregulated FGF21, PPARγ, SIRT1, CPT1, MAPK3, Gsk3-β, IRS-2, and GLUT4 gene expression	Serdan et al., 2021 (120)
	C57Bl6/J mice	Mice dam fed HFD for 6 weeks prior to mating, and during gestation and lactation	Increased triglycerides, oxidative phosphorylation, and lipid synthesis in BAT of male offspring, while the opposite effect was observed in female	Upregulated Cd36, Cpt1, Plin2, Cidea, and Pparγ mRNA expression and downregulated Ucp1, Dio2, Pgc1α, and Prdm16	Savva et al., 2022 (121)
	C57BL/6J mice	Mice received HFD for 12-, 16- and 20- weeks	Increased large lipid droplets, impaired thermogenesis, increased inflammation, and ER stress, and decreased energy expenditure in iBAT	Upregulated Tlr4, and Nlrp3 mRNA expression, and downregulated UCP1, Bmp8b, Nrg4, Vegfa, Ampk and Sirt-1	Rangel-Azevedo et al., 2022 (14)
Thermoneutral	A/J mice	Mice raised at 22°C or 30°C and fed HFD for 20 weeks	Increased paler brown/beige adipocytes at 30°C, while decreased thermogenic program and sympathetic drive	Downregulated UCP1, PGC1α, Dio2, Elovl3, and Cox1 gene expression, as well as tymine hydroxylase, NETO, and norepinephrine content	Cui et al., 2016 (122)
	C57BL/6J mice	Mice kept at 28°C for 10 days	Increased white-like adipocyte, macrophage infiltration, crown-like structure, and mitochondrial degeneration in iBAT and mBAT	Loss or deficiency of ATGL	Kotzbeck et al., 2018 (13)
	Wild-type mice	Mice housed at 30°C for 3 days, 7 days, or 4 weeks	Induced autophagy, increased white-like unilocular adipocytes, and decreased mitochondrial density in iBAT	Upregulated TFEB gene expression and downregulated UCP1, PGC1α, Cox4i1, Cox7a, and Cox8b	Sass et al., 2021 (123)
Age	C57BL/6 mice	Mice euthanized at 3-, 6-, 9-, or 12-months of age	Increased lipid droplets size and area in classical brown adipocytes while decreased clusters of beige cells and subcutaneous and visceral WAT	Not investigated	Gonçalves et al., 2017 (124)
	Wild-Type and RAG1 KO mice	Mice were used for experiments at 3- and 18-months of age	Inhibited brown adipocyte differentiation, and increased larger unilocular lipid droplets *via* senescent T cells infiltration in iBAT of aged mice	Upregulated IFN-γ gene expression and downregulated UCP1, PPARγ, and PGC1α	Pan et al., 2021 (125)
	Stromal vascular fraction (SVF) cells	SVF cells isolated from BAT were cocultured with senescent T cells	Decreased brown adipocytes differentiation	Downregulated UCP1, PPARγ, PGC1α, PLIN1, and adiponectin gene expression	
	Tianfu Black rabbits	Rabbits were used for experiments at infant stage, 15 days, 85 days, and 2 years	Inhibited brown adipocytes diffferentiation, and increased unilocular adipocytes and decreased multilocular adipocytes in BAT	Increased lncRNAs, and downregulated CYTB, COX2, and ND1 gene expression	Du et al., 2021 (126)
	New Zealand White rabbits	Rabbits were used for experiments at the ages of 1 day and 3, 6, and 12 weeks	Increased brown adipocyte hypertrophy, and restriction of FSTL1+ progenitors adipogenic capacity	Downregulated UCP1 and DIO2 gene expression, linked with FSTL1 deficiency	Haung et al., 2022 (127)

(Continued)

TABLE 1 Continued

Factors	Model	Intervention protocol	Main findings		Author, year
			Effect	Mechanism	
	FVB mice	Mi were used for experiments at 1-, 3-, 6-, and 12- months	Increased unilocular adipocytes in beige adipose tissue while decreased multilocular adipocytes	Not investigated	Scambi et al., 2022 (128)
	Adipose-derived stromal cells	Stromal cells from inguinal WAT of 2-months-old mice	Induced switch from a brown- to white-like precursor transcriptional signature	Upregulated NFkB gene expression and downregulated E2F1	
Genetic mutation	Zucker diabetic fa/fa rats	3 weeks of intervention	Increased large unilocular lipid droplets in iBAT while decreased glucose utilization	Downregulated UCP1	Lapa et al., 2017 (129)
	Leptin receptor-deficient (*db/db*) mice	Mice were used for experiments at 13 weeks of age	Increased white-like unilocular adipocyte, macrophage infiltration, and crown-like structure in iBAT	Not investigated	Kotzbeck et al., 2018 (13)
	Goto-Kakizaki rats	Mice fed HC for 8 weeks	Increased adipocyte area in iBAT while decreased cell density and glucose uptake	Upregulated CPT1, CPT2, SIRT1, PGC1α, and leptin gene expression and downregulated UCP1 and Glut-1	Serdan et al., 2021 (120)

ATGL, adipose triglyceride lipase; AMPK, AMP-activated protein kinase; BAT, brown adipose tissue; BMP8b, bone morphogenetic protein 8 beta; Cd36, cluster of differentiation 36; Cidea, cell death-inducing DNA fragmentation factor-like effector A; CYTB, cytochrome-B; Cpt 1, carnitine palmitoyltransferase 1; Cox, cyclooxygenase; DIO2, iodothyronine deiodinase 2; E2F1, E2F transcription factor 1; ER stress, endoplasmic reticulum stress; FGF21, fibroblast growth factor-21; Fis1, mitochondrial fission 1 protein; FSTL1, follistatin-like 1; GLUT, glucose transporter; Gsk3-β, glycogen synthase kinase 3 β; MAPK3, mitogen-activated protein kinase 3; HC, high cholesterol; HFD, high fat die;, HFHSD, high fat high sugar diet; Hsl, hormone-sensitive lipase; iBAT, interscapular brown adipose tissue; IFN-γ, interferon; LncRNAs, long non-coding RNAs; mBAT, mediastinal BAT; ND1, NADH dehydrogenase 1; NETO, norepinephrine turnover; NRG4, neuregulin 4; IRS-2, insulin receptor substrates 2; Plin, perilipin; PKB, Protein kinase B; PRDM16, PR domain containing 16; PPARγ, peroxisome proliferator-activated receptor-γ; PGC1α/Ppargc1, peroxisome proliferator- activated receptor γ coactivator 1-alpha; Sirt1, Sirtuin 1; Srebp1c, sterol regulatory element-binding protein 1c; TFEB, transcription factor EB; TLR4, Toll-like receptor 4; UCP1, uncoupling protein 1; VEGFs, vascular endothelial growth factors; WAT, white adipose tissue.

reviewed elsewhere (135, 136). Amongst other cytokines, VEGF-A is a major proangiogenic factor that is commonly downregulated in obesity (137–140). In fact, adipose tissue vascularization regulates chronic inflammation and systemic insulin sensitivity (141). In obese subjects, adipose tissue displays capillary rarefaction and hypoxia, which are paralleled with the infiltration of macrophages and the release of inflammatory cytokines (137, 142, 143). Several lines of evidence showed that HFD and high-fat high-sugar diet induce BAT/beige adipocytes dysfunction and whitening through vascular rarefaction linked with the state of inflammation (116–121).

Although the whitening is less studied in beige adipose tissue compared to BAT, the whitening of beige adipocytes was observed in HFD-fed C57BL/6 mice, and it was marked by enlarged adipocyte size and reduced expression of UCP1 (117). In classical BAT, HFD-feeding progressively induced fat deposition in BAT, which resulted in the expansion and whitening of BAT in female CD-1 mice (64). Similarly, chronic HFD feeding in mice resulted in progressive BAT whitening, which was associated with low energy expenditure, and down-regulation gene expression of Bmp8b, Nrg4, Vegfa involved in regulating vascularization, as well as upregulation of inflammasome and endoplasmic reticulum stress (14). Furthermore, BAT from HFD-fed C57BL/6J mice displayed lipid accumulation and insulin resistance, which were accompanied by reduced glucose and triglyceride-derived fatty acids uptake (118). Of note, Ucp1 gene expression was unaltered, whereas the expression of PGC1α and protein kinase B (PKB) were suppressed, suggesting the impairment of mitochondrial biogenesis and insulin sensitivity (118). More insights on the mechanism showed that HFD-induced iBAT whitening in C57 BL/6 mice, which was accompanied by decreased expression of the genes promoting vascularization, thermogenesis, fatty acids oxidation including VEGF-A, Ucp1, β3-AR, Cidea, and carnitine palmitoyltransferase (CPT) (119). In the same study, they demonstrated that counteracting BAT whitening using PPARα agonists can help to ameliorate the complications associated with obesity (119). The combination of HFD and high-sugar diet impaired BAT function in Wistar rats (120). The evidence of whitening in these animals was marked by the increased adipocytes area and decreased expression of BAT markers, such as FGF21, PPARγ, SIRT1, and CPT1, as well as the genes involved in the insulin signaling including insulin receptor substrate 2 (IRS-2), and glucose transporter (GLUT)-4 (120).

Amid finding the connection between the pathogenesis of obesity and its risk factors, maternal nutrition has become a target to understand the development of obesity and beyond (144). Such nutrition has a significant contribution to the developmental origins of metabolic complications upon growth to adulthood (145). Although adipose tissue plays an utmost important role in newborns as a regulator of energy homeostasis and thermogenesis (146, 147), it is not clear how maternal nutrition affects offspring adipose tissue function. Recently, Savva et al. (121) investigated the impact of maternal HFD on adipose tissue programming in male and female C57Bl6/J mice offspring. Interestingly, only male offspring exhibited a whitening of BAT and impaired metabolic profile whereas female counterparts

presented with enhanced thermogenesis and cell differentiation in BAT (121), which can be attributed to the presence of estrogen in females (148). On the other hand, the whitening of BAT in male offspring was accompanied by the upregulation of the genes involved in lipid metabolisms such as Cd36, Cpt1, Cidea, and Pparγ, as well as the downregulation of BAT markers including DIO2, UCP1, PGC1α and PRDM16 (121).

3.1.2 Thermoneutrality-induced BAT whitening through mitophagy stimulation and SNS-derived signals reduction

Ambient temperature has a strong impact on body metabolism and energy expenditure, which in turn affects the morphology and thermogenesis function of BAT. Although the thermoneutral condition of approximately 22°C is the standard living environmental condition for humans, it is known to cause BAT involution and adiposity in rodents (149). However, the effect of seasonal changes on BAT thermogenesis and plasticity is still not well understood in humans. Apparently during winter season, human subcutaneous WAT display increased mRNA expression of UCP1, PGC1α, and transmembrane protein 26 (TMEM26), along with other genes involved in energy utilization and lipolysis, such as adiponectin, acetyl CoA carboxylase (ACC), and HSL (150). However, this effect was suppressed by excessive lipid accumulation and inflammation in obesity (150). In healthy men, whole-body energy expenditure and cold-induced thermogenesis were assessed in both summer and winter, using fluorodeoxyglucose (FDG)-positron emission tomography (PET) combined with computed tomography (CT) (151). Cold-induced thermogenesis was increased in winter compared to summer in a BAT-dependent manner, suggesting that the metabolic activity of human BAT is maximal in winter (151). In terms of glucose metabolism, it was reported that winter swimmers displayed no BAT glucose uptake at a thermal comfort zone while winter swimmers have higher cold-induced thermogenesis than control subjects in young healthy men (152).

In mice, a thermoneutral zone of 30°C is used for thermally humanizing mice BAT, which shows a remarkable resemblance to human BAT (153, 154). It has been reported that thermoneutral housing of mice in conjunction with or without a high-calorie diet, strongly reduces metabolic capacity and increases lipid accumulation in BAT, leading to a "white-like" appearance (13, 122, 123). Indeed, A/J mice housed at 30°C with HFD displayed paler and larger brown or beige adipocytes (122). This was accompanied by reduced SNS and thermogenic program which were evident by decreased tyrosine hydroxylase and norepinephrine turnover, as well as the decreased mRNA expression of UCP1, PGC1α, DIO2, elongation of very long chain fatty acids protein 3 (Elovl3) and cyclooxygenase (Cox)-1 (122). Other evidence showed that BAT whitening can be linked to the recruitment of immune cells involved in pro-inflammation and mitophagy.

An ambient temperature of 28 showed that interscapular and mediastinal BAT from C57Bl/6j mice acquired a white-like unilocular adipocyte phenotype, which involved increased macrophage infiltration, formation of crown-like structures, and degenerating mitochondria, marked by adipose triglyceride lipase (Atgl)-deficiency (13). A study by Sass et al. (123), showed that thermoneutral adaptation at 30 induced BAT whitening which was characterized by increased unilocular adipocytes and mitochondrial degradation in Wild-type mice. This was also accompanied by the decreased gene expression of thermogenic markers, including UCP1, PGC1α, cytochrome c oxidase subunit 4 isoform 1 (Cox4i1), cytochrome c oxidase subunit 7A (Cox7a), and cytochrome c oxidase subunit 8B (Cox8b), while the expression levels of the autophagy-regulating transcription factor EB (TFEB) was continuously increased (123). Moreover, the inhibition of autophagy reversed the whitening in BAT (123). This agrees with the previous evidence indicating that suppression of brown adipocyte autophagy improves energy metabolism in part by regulating mitochondrial turnover in mice (109).

3.1.3 Aging-induced BAT/beige adipose tissue whitening by elevating lncRNAs expression and interferon-γ secretion

Aging has long been implicated in adipose tissue dysfunction and increased risk of obesity (155). A considerable decline in BAT and beige adipose tissue with advancing years and increasing body fat percentage has been determined (156). Generally, aging is closely associated with low-grade systemic inflammation, and alterations in endocrine signals (157); mechanisms that are linked with BAT dysfunction upon aging (156, 158). Several mechanisms that might contribute to the age-related decline in BAT activity have been studied in animals and humans. For instance, Berry et al. (159) have demonstrated that mouse and human beige progenitor cells undergo an age-related senescence-like phenotype that accounts for age-dependent beiging failure; however, genetically or pharmacologically activation of p38/Ink4a-Arf pathway rejuvenated beige progenitors and restored beiging potential. Tajima et al. (160) identified mitochondria lipoylation as a molecular process underlying the age-related decline in BAT thermogenesis of mice, implying that a defect in mitochondrial lipoylation and fuel oxidation in BAT, leads to glucose intolerance and obesity upon aging. Conversely, α-lipoic acid supplementation enhanced mitochondrial lipoylation which in turn restored BAT function in aged mice (160).

A notable observation was made by the decline in BAT content and activity linked with the whitening during adiposity in rodents and rabbits (161). In female C57BL/6 mice aged (6-12 months old), BAT displayed a morphological change toward the fat storage phenotype with increased lipid droplet size and area (124). This was accompanied by the loss of clusters of beige adipocytes from subcutaneous and visceral WAT (124). To elucidate the underlying mechanism, a recent study by Pan et al. (125) reported an increase of unilocular lipid droplets and senescent T cells infiltration which induces BAT whitening *via* interferon (IFN)-γ secretion in 18-month-old and 3-month-old mice. Moreover, IFN-γ lead to the inhibition of brown pre-adipocyte differentiation which contributed to adipose tissue remodeling in aged mice (125). This was further verified using stromal vascular fraction cells isolated from BAT and T cells co-culture, which showed a reduction in UCP1, PPARγ,

PGC1α, Plin1, and adiponectin gene expression (125). Although subcutaneous and visceral WAT supposedly comprised of beige adipocytes were enlarged, UCP1 was poorly detected in young mice and it was not detected in old mice, suggesting that there was a complete loss of thermogenic capacity upon aging. A switch from brown/beige- to white-like adipocytes was observed in FVB mice after 12- months of age (128). Moreover, the transcriptional profile of adipose-derived stromal cells mirrors these changes both at mRNA and microRNA transcriptional levels through E2F transcription factor 1 (E2F1) and nuclear factor kappa B (NFkβ) (128).

In 2 years old (aged) rabbits, BAT presented large unilocular lipid droplets with a dramatic decrease in transcriptional copy numbers of the mitochondrial genes, including cytochrome B, COX2, and NADH dehydrogenase 1 (126). Importantly, long non-coding RNAs (lncRNAs) were highly expressed in the BAT of aged rabbits. When assessed using *in vitro* model, these lncRNAs appeared to cause impairment in brown adipocyte differentiation. Presumably, lncRNAs suppressed the expression of brown adipocyte transcriptional factors, however, this requires further investigation (126). Recently, Huang et al. (127) have demonstrated that rabbit BAT involutes in a manner similar to humans with the analogous progenitor hierarchy. A progressively whitening with adipocyte hypertrophy and loss of UCP1 expression in the interscapular, subscapular, and suprascapular BAT depots of the rabbits was readily seen from 3 weeks of age and full conversion to WAT-like tissues at 12 weeks (127). This BAT whitening was associated with the restricted adipogenic capacity of follistatin-like 1 (Fstl1+) progenitors (127). Moreover, deletion of the Fstl1 gene or ablation of Fstl1+ progenitors in mice induced BAT paucity (127). This suggested that lncRNAs can be one of the molecular drivers of BAT whitening upon aging. However, this requires confirmation in human studies.

3.1.4 Genetic models of type 2 diabetes presented BAT whitening

The concept of the genetic alteration as the cause of obesity has been progressively investigated over the past two decades (162). Based upon the years of discoveries, the genetic causes of obesity can be broadly classified into polygenic and monogenic (162). Specifically, polygenic obesity (or common obesity) is caused by multiple gene mutations or polymorphisms that promote weight gain (163). On the other hand, monogenic obesity which is inherited in a Mendelian pattern is typically rare and is characterized by early-onset, high severity, and a single gene mutation in the leptin-melanocortin pathway (162, 163). For these reasons, most people with obesity have certain mutated genes that predispose them to gain excess weight.

To gain a profound understanding of genetic obesity, animal models of obesity and type 2 diabetes such as leptin receptor-deficient *db/db* mice, and Zucker fatty *fa/fa* rats have been widely utilized (161). Over the past few years, these models have been also used to study the impact of genetic obesity on the morphology and function of BAT. However, the special focus herein is on BAT whitening. A study by Lapa et al. (129) showed that BAT from Zucker diabetic fatty *fa/fa* rats, displayed a ubiquitous white adipose-like tissue phenotype, with large unilocular lipid droplets and impaired glucose utilization at 14 weeks of age. This BAT involution was accompanied by the increased synthesis and accumulation of intracellular fatty acids, as well as the decreased expression of UCP1 (129). Although the underlying molecular mechanisms have not been elucidated so far, iBAT from db/db mice displays whitening and crown-like structure formation at 13 weeks of age (13).

In a non-obese model of T2D, which shares a susceptibility locus on chromosome 10 like in humans, lower cell density and higher adipocyte area were recorded in Goto-Kakizaki rats (120). Interestingly, glucose uptake in BAT was impaired in both baseline and even after 30 min of stimulation with 1 mg/kg CL316,243, a β3-adrenergic agonist (120). Subsequently, there was an increased expression of genes involved in fatty acid oxidation (CPT1 and CPT2), BAT metabolism (Sirt1 and PGC1α), but decreased gene expression of GLUT-1 compared to other experimental groups (120). Possibly, impairment of the β3-adrenergic response could suggest an increased expression of the above-mentioned genes, acting as a compensatory mechanism.

3.2 Chemically induced BAT/beige adipose tissue whitening

In parallel with other risk factors, chemicals such as endocrine-disrupting chemicals (EDCs) are known to significantly contribute to the high prevalence of obesity (164). These chemicals are found in a wide spectrum of consumer products, like tobacco, flame retardants, and pesticides which people are most likely to be exposed to in their daily life through ingestion, inhalation, or direct dermal contact (164). The potential targets for EDCs are the glucocorticoid and mineralocortcoid receptors, which are members of the steroid receptor subfamily that mediate the actions of glucocorticoids and mineralocorticoids, the main classes of corticosteroids (165). These chemicals can act directly on adipose tissue to induce hypertrophy and dysfunction of this tissue (166). Several lines of evidence have demonstrated that exposure to certain chemicals can negatively impact the phenotype and physiological functions of BAT and beige adipose tissue by inducing whitening (Table 2).

3.2.1 Bevacizumab impaired vascular network and induced whitening in BAT

Bevacizumab, a recombinant humanized anti-vascular endothelial growth factor (VEGF) antibody, is trailed in retinopathy of premature infants (175). Although anti-VEGF agents are the first-line treatment for various angiogenesis-related retinal diseases, it is not clear how the anti-VEGF antibody can accelerate the risks of systemic complications after intravitreal injection in premature infants (176). A study by Jo et al. (167) showed that intravitreally injection with anti-VEGF antibody (1 μg/eye) increases lipid droplet accumulation and induces the loss of vascular network in neonatal C57BL/6 mice. In addition to reduced

VEGF levels, this was accompanied by the downregulation of mitochondria-related genes PGC1α and UCP1 (167). Since BAT is a highly vascularized tissue, it is evident that anti-VEGF agents interfere with BAT vascularization, which in turn induces BAT whitening and dysfunction.

3.2.2 Nicotine exposure during the prenatal and lactation period induces BAT/beige adipose tissue whitening in offspring

Nicotine is a chemical that is widely found in tobacco, and it has been associated with many health problems (177). Accordingly, epidemiological studies have reported that maternal smoking during pregnancy might be a serious risk factor for childhood obesity (178). Of major concern, maternal nicotine exposure has become a growing risk factor for the health of the offspring and the origin of chronic diseases beyond infancy. For example, prenatal or lactation exposure to nicotine is associated with increased gonadal and inguinal subcutaneous WAT depots and dysfunction in offspring (179). However, the impact of nicotine on BAT structure and function is not well understood. Previously, it was reported that nicotine exposure in adult mice increases BAT thermogenesis and promotes weight loss *via* the inactivation of hypothalamic AMPK (180), and induces WAT browning through the hypothalamic κ opioid receptor (181). Paradoxically, maternal nicotine exposure induces BAT dysfunction and weight gain in both male offspring (168, 169).

TABLE 2 Summary of evidence reporting on BAT/beige adipose tissue whitening induced by chemicals like bevacizumab, nicotine, dechlorane plus, serotonin and glucocorticoid.

Chemical	Model	Intervention protocol	Main findings		Author, year
			Effect	Mechanism	
Bevacizumab	C57BL/6 mice	Neonatal mice injected with 1 μg/eye bevacizumab (anti-VEGF antibody) on a postnatal day 14, 17 and 21	Increased lipid droplet expansion in the iBAT while decreased vascular density	Downregulated VEGF levels, and PGC1α and Ucp1 gene expression	Jo et al., 2015 (167)
Nicotine	Wistar rat's offspring	Male offspring from Wistar rats were exposed to 1 mg/kg nicotine twice a day for 26 weeks during pregnancy or lactation	Increased lipid droplet expansion and impaired mitochondria in the iBAT	Downregulated Prdm16, PGC1α, Ucp1 and Cpt2 mRNA expression	Fan et al., 2016 (168)
	Wistar rat's offspring	Female offspring from Wistar rats were exposed to 1 mg/kg nicotine twice a day for 4- and 26 weeks during pregnancy and lactation	Increased unilocular lipid droplets, impaired angiogenesis, abnormal mitochondria in the iBAT	Downregulated PGC1α, UCP1, Prdm16, Cidea; Vegfr2, Vegf, Hgf, Npy, and Resistin gene expression	Chen et al., 2020 (169)
	C3H10T/12 cells	Differentiated C3H10T/12 cells exposed to 0.5, 5, 50 μM nicotine for 24, 36, and 48 h	Suppressed beige "Brown-like" phenotype and angiogenesis	Downregulated PGC1α, UCP1, Prdm16, Vegf, Hgf, and Ang2 gene expression	
Dechlorane plus	C57BL/6 mice	Mice fed HFD and 1000 μg/kg dechlorane plus for 28 days	Increased lipid accumulation and WAT-like phenotype in BAT	Downregulated Ucp1 mRNA expression	Peshdary et al., 2020 (170)
Serotonin	HIB1B brown adipocytes	Non-differentiated and differentiated HIB1B brown adipocytes were exposed to 10 μM serotonin with or without palmitic acid for 30 h	Increased transdifferentiation of beige adipocytes into white adipocytes while decreased brown adipocytes differentiation	Upregulated UCP2, FASN, leptin and adiponectin gene expression and downregulated BMP-7, UCP1, FGF21, pAMPK, Prdm16 and Pparγ, and Cpt1	Rozenblit-Susan et al., 2018 (171)
Glucocorticoid	CD1 mice	Mice were orchidectomized or ovariectomized prior to exposure to 250 μg/day of corticosterone for 4 weeks, with or without androgen	Increased androgens sensitized glucocorticoid-induced intracellular lipid accumulation and lipid droplet size expansion in the BAT	Downregulated UCP1 gene expression while Ppargc1a, Pparg, and Acaca remain unaltered	Gasparini et al., 2019 (172)
	C57BL/6J wild-type mice	Mice injected with 5 mg/kg dexamethasone every second day for 1 week	Increased autophagy, enlarged lipid droplets, and triglycerides in the iBAT	Upregulated ATG7, BTG1, Rb1, Nrip1, Rbl1/p107 gene expression, and downregulated UCP1	Deng et al., 2020 (173)
	Brown adipocytes precursor cells	Precursor cells were isolated from scapular fat of newborn Wild-Type mice, differentiated, and exposed to 1 μM dexamethasone for 24 h	Increased fat mass and autophagy, and decreased oxygen consumption rate	Upregulated ATG7 and BTG1 gene expression, and downregulated Ucp1, Nrip1 and Agt mRNA expression	
	C57BL/6 (C57BL/6NCrl) mice	Male mice were exposed to oral treatments of 50 μg/ml corticosterone for 4 weeks	Increased adipocyte area, insulin resistance, and weight of the iBAT, while mitochondrial content remain unchanged	Downregulated UCP1 gene expression	Bel et al., 2022 (174)

Acaca, acetyl-coa carboxylase alpha; Agt, angiotensinogen; Ang2, angiopoietin-2; AMPK, AMP-activated protein kinase; ATG7, autophagy-related 7; iBAT, interscapular brown adipose tissue; BTG1, B cell translocation gene 1; Bmp7, bone morphogenetic protein 7; Cidea, cell death-inducing DNA fragmentation factor-like effector A; Cpt 1, carnitine palmitoyltransferase 1; FGF21, fibroblast growth factor-21; Fis1, mitochondrial fission 1 protein; Hgf, hepatocyte growth factor; HFD, high fat diet; Npy, neuropeptide; Nrip1, nuclear receptor interacting protein 1; PRDM16, PR domain containing 16; PPARγ, peroxisome proliferator-activated receptor gamma; PGC1α, peroxisome proliferator-activated receptor γ coactivator 1-alpha; Rb1, RB transcriptional corepressor 1; Rbl1/p107, RB transcriptional corepressor like 1; UCP1, uncoupling protein 1; VEGFs, vascular endothelial growth factors; WAT, white adipose tissue.

In male rat offspring exposed to 1 mg/kg nicotine during pregnancy and lactation, BAT displayed a whitening phenotype characterized by lipid droplet accumulation and impaired mitochondrial structure (168). Moreover, the expression of BAT structure and function-related genes such as PRDM16, PGC1α, UCP1, and CPT2 was decreased. Similarly (169), female rat offspring exposed to 1 mg/kg nicotine during pregnancy and lactation presented white-like adipocytes, impaired angiogenesis, and abnormal mitochondrial structure in iBAT. This was accompanied by a down-regulation of brown-like genes PGC1α, UCP1, Prdm16, and Cidea, as well as a decrease in BAT secretion of pro-angiogenic factors including VEGF, VEGF receptor 2, hepatocyte growth factor (Hgf), neuropeptide (Npy), and resistin (169). This was further confirmed *in vitro* using C3H10T1/2 cells, showing a reduction of beige "brown-like" phenotype and angiogenesis, as well as brown-like gene expression of PGC1α and UCP1. Altogether, this evidence suggests that nicotine disrupts angiogenesis in the early development stage and impairs blood vessel formation to induce BAT whitening through downregulation of the PGC1α–UCP1 signals.

3.2.3 Dechlorane plus disrupted mitochondrial UCP1 and induced BAT whitening

Dechlorane plus, an endocrine-disrupting chemical found in flame retardants, is a potential obesogen (182). Apparently, dechlorane plus can induce adiposity by promoting adipogenesis in cultured adipocytes *via* PPARγ independent mechanism (183). Consistently, Peshdary et al. (170) reported that 1000 μg/kg dechlorane plus induces a WAT-like phenotype and disrupts the function of BAT in part by downregulation of UCP1 mRNA expression in C57BL/6 mice. These outcomes are in line with UCP1 gene knockout in mice suggesting that loss of UCP1 could result in the whitening of BAT (184, 185). However, more research on the impact of dechlorane plus on BAT and beige adipose tissue function is warranted to better understand its influence on obesity and other related diseases.

3.2.4 Serotonin-impaired brown adipocytes differentiation and induced beige adipocyte whitening

Endogenous chemicals such as neurotransmitters like serotonin are known to regulate adipogenesis (186). A study by Rozenblit-Susan et al. (171) demonstrated that serotonin (10 μM) induces whitening in palmitic acid-exposed HIB1B adipocytes by shifting their metabolism to lipogenesis rather than lipid oxidation in part by, suppressing brown adipocytes differentiation and inducing beige adipocytes transdifferentiation into white adipocytes. Moreover, this was confirmed by the downregulation of brown adipocyte differentiation markers, such as Prdm16, Bmp7, and Pparγ (171). Consistently, expression of BAT markers such as UCP1 and FGF21, as well as pAMPK/AMPK ratio were downregulated while genes regulating lipogenesis fatty acid synthase (FASN), leptin, and adiponectin were upregulated (171). The observed effects of serotonin require further investigations in human adipose tissue, supposedly similar effects attained in humans could have major implications on obesity reducing WAT and increasing BAT activity.

3.2.5 Glucocorticoids induced BAT whitening by stimulating autophagy

The class of steroid hormones glucocorticoids and corticosterone are known to modulate glucose homeostasis in humans and rodents, respectively (187). Hypercortisolism caused by either endogenous overproduction of glucocorticoids or exogenous administration of glucocorticoids as anti-inflammatory medication can induce the development of obesity. A study by Gasparini et al. (172) reported that corticosterone (250 μg/day) induces intracellular lipid accumulation and reduces UCP1 expression in BAT of CD1 mice. Interestingly, no significant changes were observed in PGC1α, FASN, or acetyl-coa carboxylase alpha (Acaca) expression, implying that changes in lipid accumulation did not directly involve mitochondrial biogenesis, adipogenesis, or lipogenesis in BAT (172).

Several potent synthetic glucocorticoids including dexamethasone have been developed for pharmacological use (187). For example, dexamethasone has been implicated in the study of adipogenesis (188). Here, Deng et al. (173) showed that exposing C57BL/6 mice to 5 mg/kg dexamethasone for one week induced autophagy and lipid droplet expansion in iBAT. Similar outcomes were observed *in vitro* using brown adipocytes precursor cells. Notably, dexamethasone increased ATG7 expression, in part by increasing the expression of B cell translocation gene 1 (BTG1) that stimulates the activity of CREB1 (173). Consistently, UCP1 expression was downregulated, while the expression of WAT marker genes RB transcriptional corepressor 1 (Rb1), nuclear-receptor-interacting protein 1 (Nrip1), and Rbl1/p107 (RB transcriptional corepressor like 1) were upregulated (173). Other evidence showed that chronic exposure to corticosterone can induce the whitening of BAT in C57BL/6 mice, this was evident by increased adipocyte area and elevated expressions of UCP1 in BAT (174). Of note, the whitened phenotype has not been previously associated with increased uncoupling proteins under chronic stress, however, Bel et al. (174) suggested that the increased UCP1 expression could be a compensatory mechanism under certain stress.

4 Summary and outlook

Although the remodeling of BAT and beige adipose tissue through whitening appears to be more common in obesity, it remains unclear how this maladaptive process occurs. Several lines of evidence have demonstrated that the BAT/beige adipose tissue whitening is multifactorial in origin. Indeed, various factors such as diet, age, genetics, thermoneutrality, and chemical exposure have been shown to greatly influence the whitening of adipose tissue by targeting different mechanisms (Figure 4). Apart from these factors, chronic exposure to high levels of particulate matter, a complex mixture of solid and liquid particles derived from human activities and natural sources, also promotes the whitening of BAT, as reviewed by Guardia and Shin (110). Although the activity of BAT has been strongly linked with the protection against obesity, fatty liver, and T2D (189), the dysfunction or whitening of BAT in obesity, may contribute to or exacerbate other metabolic complications (190). For instance, recent evidence has demonstrated that severe hyperprolactinemia can also promote BAT whitening and aggravates HFD-induced metabolic dysregulations (191). This suggests that the whitening could

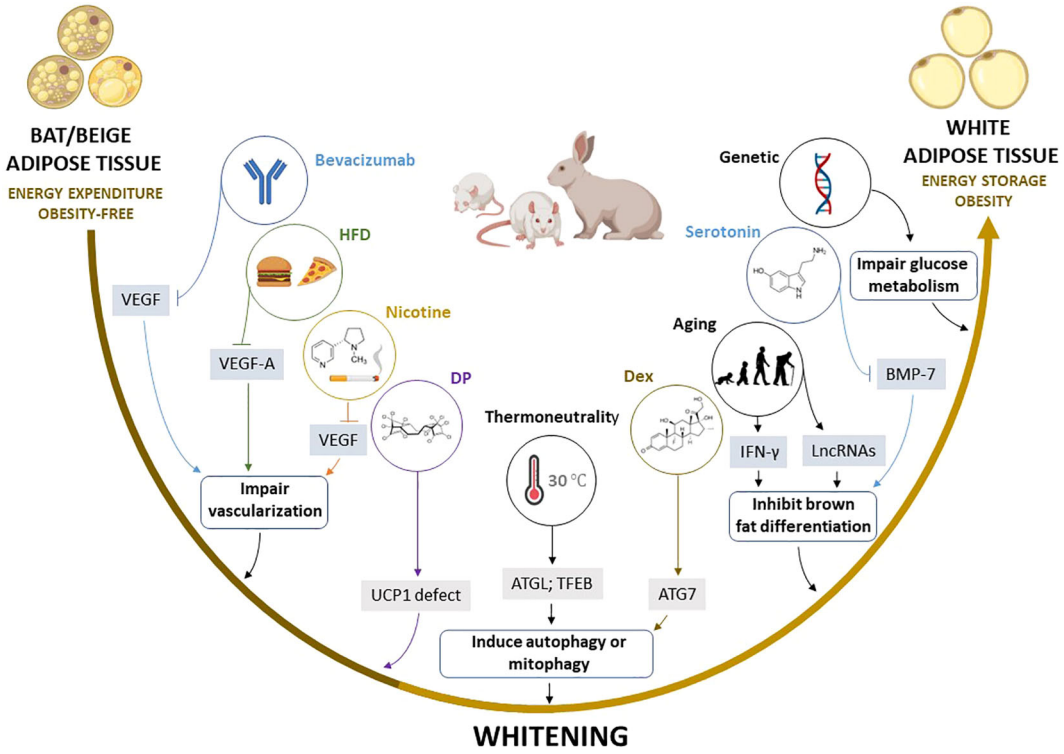

FIGURE 4
Summary of the proposed mechanisms by which multiple factors induce the whitening of brown (BAT) and beige adipose tissue. Factors such as high fat diet (HFD), bevacizumab, and nicotine induce the whitening by suppressing pro-angiogenic cytokines such as VEGF and VEGF-A, which inhibit angiogenesis and impair vascularization in BAT and beige adipose tissue, whereas thermoneutral zone and dexamethasone (Dex) exposure increase ATG7 and TFEB, which stimulate autophagy or mitophagy. Other factors such as aging, and elevated serotonin induce BAT/beige adipose tissue whitening by increasing INF-γ, and LncRNAs, and decreasing BMP-7, which in turn inhibits brown adipocyte differentiation. Moreover, dechlorane plus (DP) contributes to whitening in part by inhibiting UCP1 expression. ATG7, autophagy-related 7; LncRNAs, long non-coding RNAs; BMP-7, bone morphogenetic protein 7; BTG1, B cell translocation gene 1; IFN-γ, interferon-gamma; UCP1, uncoupling protein 1; TFEB, transcription factor EB; VEGF, vascular endothelial growth factor.

TABLE 3 An overview of the potential biomarkers of BAT/beige adipose tissue whitening.

Gene	Upregulation/Downregulation (knockout)	Association with or implication in whitening	Author, year
ATGL	Downregulation	Induce mitophagy, brown adipocyte death, and crown-like structure formation	Kotzbeck et al., 2018 (13)
ATG7	Upregulation	Induce autophagy and increase adiposity	Deng et al., 2020 (173)
BTG1	Upregulation	Induce autophagy and increase adiposity	
BMP-7	Downregulation	Inhibit brown adipocytes differentiation	Rozenblit-Susan et al., 2018 (171)
PRDM16	Downregulation	Inhibit brown adipocytes differentiation	
IFN-γ	Upregulation	Inhibit differentiation of preadipocyte brown adipocytes	Pan et al., 2021 (125)
FSTL1	Downregulation	Loss of brown adipogenic competence of progenitors	Haung et al., 2022 (127)
LncRNAs	Upregulation	Impair brown adipocyte differentiation	Du et al., 2021 (126)
TFEB	Upregulation	Induce mitophagic mitochondrial degradation *via* the autophagosomal and lysosomal machinery	Sass et al., 2021 (123)
UCP1	Downregulation	Increase glucose intolerance, large unilocular adipocytes, and inflammation markers, and decrease mitochondrial subunit protein	Winn et al., 2017 (184); Peshdary et al., 2020 (170)
VEGF	Downregulation	Suppress angiogenesis and decrease vascular density	Jo et al., 2015 (167); Chen et al., 2020 (169)
VEGF-A	Downregulation	Increase inflammation and endoplasmic reticulum stress, and decrease anti-inflammatory cytokines	Miranda et al., 2020 (119); Rangel-Azevedo et al., 2022 (14)

ATGL, adipose triglyceride lipase; ATG7, autophagy-related 7; BMP-7, bone morphogenetic protein 7; BTG1, B cell translocation gene 1; FSTL1, follistatin-like 1; IFN-γ, interferon gamma; LncRNAs, long non-coding RNAs; PRDM16, PR domain containing 16; UCP1, uncoupling protein 1; TFEB, transcription factor EB; VEGF, vascular endothelial growth factor.

represent one of the complications implicated in the pathogenesis of obesity, and it can lead to other secondary complications.

Of note, experimental evidence discussed in this review indicates that autophagy, inflammation, and impairment of angiogenesis "vascularization" are central processes implicated in BAT/beige adipose tissue whitening (83, 108, 167, 169). For example, the most prominent mechanisms implicated in adipose tissue whitening include the inhibition of VEGFs, PGC1α, and BMP-7 which impair vascularization, mitochondrial biogenesis, and brown adipocyte differentiation, respectively. This may lead to more sophisticated processes like infiltration of INF-γ secreting T cells, increased autophagy, and impaired substrate metabolism. Such evidence is in line with the finding from gene knockout models, which suggested that the whitening of BAT is under the control of β-AR (13), BMP (192), and mitochondrial transcription factor A (193), and other genes regulating BAT function (194–198), as well as miRNAs that regulate multiple processes including the differentiation and function of brown adipocytes (199, 200). Based on the current evidence, there are several potential marker genes that are involved in regulating BAT/beige adipose tissue whitening (Table 3). However, this requires further investigations in both non-clinical and clinical settings. Particular attention should be placed on identifying plausible therapeutic avenues to prevent or reverse adipose tissue whitening in obesity. This includes assessing and understanding the therapeutic effects of prominent agents like metformin in targeting the adipose tissue to manage obesity-associated complications (201).

Author contributions

KZ, PVD, and SM-M- concept and original draft. KZ and SXM performed the literature search, study selection, and data extraction. KZ, PD, SXHM, BBN, SEM, BUJ, TMN and SEM-M - manuscript writing and approval of the final draft. All authors contributed to the article and approved the submitted version.

Funding

This work was funded by the National Research Foundation (NRF) Support for NRF rated scientist 113674 to Sithandiwe E. Mazibuko-Mbeje. Funding from North-West University is also acknowledged. The work reported herein was made possible through funding by the South African Medical Research Council (SAMRC) through its Division of Research of Capacity Development under the Early Investigators Programme from the South African National Treasury (funding number: HDID8682/MB2022/EIP052). Baseline funding from the Northwest University is also acknowledged. The content hereof is the sole responsibility of the authors and do not necessarily represent the official views of the SAMRC. Also, all the content expressed in this review is the official views of the authors and do not represent that of the North-West University.

Acknowledgments

KZ and SXHM are funded by the SAMRC through its Division of Research Capacity Development under the internship scholarship programme from funding received from the South African National Treasury. Grant holders acknowledge that opinions, findings, and conclusions, or recommendations expressed in any publication generated by the SAMRC.

Conflict of interest

The authors declare that the research was conducted in the absence of any commercial or financial relationships that could be construed as a potential conflict of interest.

Publisher's note

References

1. Wang QA, Tao C, Gupta RK, Scherer PE. Tracking adipogenesis during white adipose tissue development, expansion and regeneration. *Nat Med* (2013) 19:1338–44. doi: 10.1038/nm.3324

2. Jakab J, Miškić B, Mikšić Š, Juranić B, Ćosić V, Schwarz D, et al. Adipogenesis as a potential anti-obesity target: A review of pharmacological treatment and natural products. *Diabetes Metab Syndr Obes* (2021) 14:67. doi: 10.2147/DMSO.S281186

3. Choe SS, Huh JY, Hwang IJ, Kim JI, Kim JB. Adipose tissue remodeling: Its role in energy metabolism and metabolic disorders. *Front Endocrinol (Lausanne)* (2016) 7:30. doi: 10.3389/fendo.2016.00030

4. Giralt M, Villarroya F. White, brown, beige/brite: Different adipose cells for different functions? *Endocrinology* (2013) 154:2992–3000. doi: 10.1210/en.2013-1403

5. Cedikova M, Kripnerová M, Dvorakova J, Pitule P, Grundmanova M, Babuska V, et al. Mitochondria in white, brown, and beige adipocytes. *Stem Cells Int* (2016) 2016:6067349. doi: 10.1155/2016/6067349

6. Kajimura S, Spiegelman BM, Seale P. Brown and beige fat: Physiological roles beyond heat-generation. *Cell Metab* (2015) 22:546. doi: 10.1016/J.CMET.2015.09.007

7. Cheng L, Wang J, Dai H, Duan Y, An Y, Shi L, et al. Brown and beige adipose tissue: a novel therapeutic strategy for obesity and type 2 diabetes mellitus. *Adipocyte* (2021) 10:48–65. doi: 10.1080/21623945.2020.1870060

8. Lee YH, Kim SN, Kwon HJ, Granneman JG. Metabolic heterogeneity of activated beige/brite adipocytes in inguinal adipose tissue. *Sci Rep* (2017) 7:39794. doi: 10.1038/SREP39794

9. Keipert S, Jastroch M. Brite/beige fat and UCP1 - is it thermogenesis? *Biochim Biophys Acta* (2014) 1837:1075–82. doi: 10.1016/J.BBABIO.2014.02.008

10. Bagchi M, Kim LA, Boucher J, Walshe TE, Kahn CR, D'Amore PA. Vascular endothelial growth factor is important for brown adipose tissue development and maintenance. *FASEB J* (2013) 27:3257–71. doi: 10.1096/FJ.12-221812

11. Shimizu I, Aprahamian T, Kikuchi R, Shimizu A, Papanicolaou KN, Maclauchlan S, et al. Vascular rarefaction mediates whitening of brown fat in obesity. *J Clin Invest* (2014) 124(5):2099–112. doi: 10.1172/JCI71643DS1

12. Cairó M, Villarroya J. The role of autophagy in brown and beige adipose tissue plasticity. *J Physiol Biochem* (2020) 76:213–26. doi: 10.1007/S13105-019-00708-1/FIGURES/4

13. Kotzbeck P, Giordano A, Mondini E, Murano I, Severi I, Venema W, et al. Brown adipose tissue whitening leads to brown adipocyte death and adipose tissue inflammation. *J Lipid Res* (2018) 59:784–94. doi: 10.1194/JLR.M079665

14. Rangel-Azevedo C, Santana-Oliveira DA, Miranda CS, Martins FF, Mandarim-de-Lacerda CA, Souza-Mello V. Progressive brown adipocyte dysfunction: Whitening and impaired nonshivering thermogenesis as long-term obesity complications. *J Nutr Biochem* (2022) 105:109002. doi: 10.1016/J.JNUTBIO.2022.109002

15. Agha M, Agha R. The rising prevalence of obesity: part a: impact on public health. *Int J Surg Oncol (N Y)* (2017) 2:17. doi: 10.1097/ij9.0000000000000017

16. Chernukha IM, Fedulova L v., Kotenkova EA. White, beige and brown adipose tissue: structure, function, specific features and possibility formation and divergence in pigs. *Foods Raw Materials* (2022) 10:10–8. doi: 10.21603/2308-4057-2022-1-10-18

17. Sidossis L, Kajimura S. Brown and beige fat in humans: thermogenic adipocytes that control energy and glucose homeostasis. *J Clin Invest* (2015) 125:478–86. doi: 10.1172/JCI78362

18. Ikeda K, Maretich P, Kajimura S. The common and distinct features of brown and beige adipocytes. *Trends Endocrinol Metab* (2018) 29:191. doi: 10.1016/J.TEM.2018.01.001

19. Zhang F, Hao G, Shao M, Nham K, An Y, Wang Q, et al. An adipose tissue atlas: An image-guided identification of human-like BAT and beige depots in rodents. *Cell Metab* (2018) 27:252–62.e3. doi: 10.1016/J.CMET.2017.12.004

20. Heaton JM. The distribution of brown adipose tissue in the human. *J Anat* (1972) 112:35.

21. González-García I, Urisarri A, Nogueiras R, Diéguez C, Couce ML, López M. An updated view on human neonatal thermogenesis. *Nat Rev Endocrinol* (2022) 18 (5):263–4. doi: 10.1038/s41574-022-00642-1

22. Urisarri A, González-García I, Estévez-Salguero Á, Pata MP, Milbank E, López N, et al. BMP8 and activated brown adipose tissue in human newborns. *Nat Commun* (2021) 12:1–13. doi: 10.1038/s41467-021-25456-z

23. Virtanen KA. The rediscovery of BAT in adult humans using imaging. *Best Pract Res Clin Endocrinol Metab* (2016) 30:471–7. doi: 10.1016/j.beem.2016.09.001

24. Ahmad B, Vohra MS, Saleemi MA, Serpell CJ, Fong IL, Wong EH. Brown/Beige adipose tissues and the emerging role of their secretory factors in improving metabolic health: The batokines. *Biochimie* (2021) 184:26–39. doi: 10.1016/J.BIOCHI.2021.01.015

25. Ziqubu K, Dludla PV, Moetlediwa MT, Nyawo TA, Pheiffer C, Jack BU, et al. Disease progression promotes changes in adipose tissue signatures in type 2 diabetic (db/db) mice: The potential pathophysiological role of batokines. *Life Sci* (2023) 313:121273. doi: 10.1016/J.LFS.2022.121273

26. Singh R, Barrios A, Dirakvand G, Pervin S. Human brown adipose tissue and metabolic health: Potential for therapeutic avenues. *Cells* (2021) 10(11):3030. doi: 10.3390/CELLS10113030

27. Carey AL, Kingwell BA. Brown adipose tissue in humans: Therapeutic potential to combat obesity. *Pharmacol Ther* (2013) 140:26–33. doi: 10.1016/J.PHARMTHERA.2013.05.009

28. Wang CH, Wei YH. Therapeutic perspectives of thermogenic adipocytes in obesity and related complications. *Int J Mol Sci* (2021) 22(13):7177. doi: 10.3390/ijms22137177

29. Pilkington AC, Paz HA, Wankhade UD. Beige adipose tissue identification and marker specificity–overview. *Front Endocrinol (Lausanne)* (2021) 12:599134/BIBTEX. doi: 10.3389/FENDO.2021.599134/BIBTEX

30. Carobbio S, Rosen B, Vidal-Puig A. Adipogenesis: New insights into brown adipose tissue differentiation. *J Mol Endocrinol* (2013) 51(3):T75–85. doi: 10.1530/JME-13-0158

31. Merrick D, Sakers A, Irgebay Z, Okada C, Calvert C, Morley MP, et al. Identification of a mesenchymal progenitor cell hierarchy in adipose tissue. *Science* (2019) 364(6438):eaav2501. doi: 10.1126/SCIENCE.AAV2501

32. Ladoux A, Peraldi P, Chignon-Sicard B, Dani C. Distinct shades of adipocytes control the metabolic roles of adipose tissues: From their origins to their relevance for medical applications. *Biomedicines* (2021) 9:1–17. doi: 10.3390/BIOMEDICINES9010040

33. Duerre DJ, Galmozzi A. Deconstructing adipose tissue heterogeneity one cell at a time. *Front Endocrinol (Lausanne)* (2022) 13:847291. doi: 10.3389/FENDO.2022.847291

34. Russell AP, Crisan M, Léger B, Corselli M, McAinch AJ, O'Brien PE, et al. Brown adipocyte progenitor population is modified in obese and diabetic skeletal muscle. *Int J Obes* (2012) 36(1):155–8. doi: 10.1038/ijo.2011.85

35. Crisan M, Casteilla L, Lehr L, Carmona M, Paoloni-Giacobino A, Yap S, et al. A reservoir of brown adipocyte progenitors in human skeletal muscle. *Stem Cells* (2008) 26:2425–33. doi: 10.1634/STEMCELLS.2008-0325

36. Carobbio S, Guénantin AC, Samuelson I, Bahri M, Vidal-Puig A. Brown and beige fat: From molecules to physiology and pathophysiology. *Biochim Biophys Acta Mol Cell Biol Lipids* (2019) 1864:37–50. doi: 10.1016/J.BBALIP.2018.05.013

37. Van Nguyen TT, Vu VV, Pham PV. Transcriptional factors of thermogenic adipocyte development and generation of brown and beige adipocytes from stem cells. *Stem Cell Rev Rep* (2020) 16:876–92. doi: 10.1007/S12015-020-10013-W

38. Sanchez-Gurmaches J, Guertin DA. Adipocytes arise from multiple lineages that are heterogeneously and dynamically distributed. *Nat Commun* (2014) 5:4099. doi: 10.1038/NCOMMS5099

39. Wu J, Boström P, Sparks LM, Ye L, Choi JH, Giang AH, et al. Beige adipocytes are a distinct type of thermogenic fat cell in mouse and human. *Cell* (2012) 150:366–76. doi: 10.1016/j.cell.2012.05.016

40. Oguri Y, Shinoda K, Kim H, Alba DL, Bolus WR, Wang Q, et al. CD81 controls beige fat progenitor cell growth and energy balance *via* FAK signaling. *Cell* (2020) 182:563–77.e20. doi: 10.1016/J.CELL.2020.06.021

41. Joshi J, Beaudoin GAW, Patterson JA, García-García JD, Belisle CE, Chang LY, et al. Thermogenic adipocytes: lineage, function and therapeutic potential. *Biochem J* (2020) 477:2055–69. doi: 10.1042/BCJ20200298

42. Chen Y, Ikeda K, Yoneshiro T, Scaramozza A, Tajima K, Wang Q, et al. Thermal stress induces glycolytic beige fat formation *via* a myogenic state. *Nature* (2019) 565:180–5. doi: 10.1038/S41586-018-0801-Z

43. Whittle A, Relat-Pardo J, Vidal-Puig A. Pharmacological strategies for targeting BAT thermogenesis. *Trends Pharmacol Sci* (2013) 34:347–55. doi: 10.1016/j.tips.2013.04.004

44. Cinti S. Adipocyte differentiation and transdifferentiation: Plasticity of the adipose organ. *J Endocrinol Invest* (2002) 25:823–35. doi: 10.1007/BF03344046

45. Shimizu I, Walsh K. The whitening of brown fat and its implications for weight management in obesity. *Curr Obes Rep* (2015) 4:224–9. doi: 10.1007/s13679-015-0157-8

46. Sim CK, Kim SY, Brunmeir R, Zhang Q, Li H, Dharmasegaran D, et al. Regulation of white and brown adipocyte differentiation by RhoGAP DLC1. *PloS One* (2017) 12(3):e0174761. doi: 10.1371/journal.pone.0174761

47. Pradhan RN, Bues JJ, Gardeux V, Schwalie PC, Alpern D, Chen W, et al. Dissecting the brown adipogenic regulatory network using integrative genomics. *Sci Rep* (2017) 7:42130. doi: 10.1038/srep42130

48. Mae J, Nagaya K, Okamatsu-Ogura Y, Tsubota A, Matsuoka S, Nio-Kobayashi J, et al. Adipocytes and stromal cells regulate brown adipogenesis through secretory factors during the postnatal white-to-Brown conversion of adipose tissue in Syrian hamsters. *Front Cell Dev Biol* (2021) 9:698692. doi: 10.3389/fcell.2021.698692

49. Schulz TJ, Huang P, Huang TL, Xue R, McDougall LE, Townsend KL, et al. Brown-fat paucity due to impaired BMP signalling induces compensatory browning of white fat. *Nature* (2013) 495(7441):379–83. doi: 10.1038/nature11943

50. Tseng YH, Kokkotou E, Schulz TJ, Huang TL, Winnay JN, Taniguchi CM, et al. New role of bone morphogenetic protein 7 in brown adipogenesis and energy expenditure. *Nature* (2008) 454(7207):1000–4. doi: 10.1038/nature07221

51. Townsend KL, Pritchard E, Coburn JM, Kwon YM, Blaszkiewicz M, Lynes MD, et al. Silk hydrogel-mediated delivery of bone morphogenetic protein 7 directly to subcutaneous white adipose tissue increases browning and energy expenditure. *Front Bioeng Biotechnol* (2022) 10:884601. doi: 10.3389/FBIOE.2022.884601

52. Shaw A, Tóth BB, Arianti R, Csomós I, Póliska S, Vámos A, et al. BMP7 increases UCP1-dependent and independent thermogenesis with a unique gene expression program in human neck area derived adipocytes. *Pharm (Basel)* (2021) 14(11):1078. doi: 10.3390/PH14111078

53. Jiang N, Yang M, Han Y, Zhao H, Sun L. PRDM16 regulating adipocyte transformation and thermogenesis: A promising therapeutic target for obesity and diabetes. *Front Pharmacol* (2022) 13:870250/BIBTEX. doi: 10.3389/FPHAR.2022.870250/BIBTEX

54. Seale P, Bjork B, Yang W, Kajimura S, Chin S, Kuang S, et al. PRDM16 controls a brown fat/skeletal muscle switch. *Nature* (2008) 454:961–7. doi: 10.1038/NATURE07182

55. Harms MJ, Ishibashi J, Wang W, Lim HW, Goyama S, Sato T, et al. Prdm16 is required for the maintenance of brown adipocyte identity and function in adult mice. *Cell Metab* (2014) 19:593–604. doi: 10.1016/j.cmet.2014.03.007

56. Cristancho AG, Lazar MA. Forming functional fat: a growing understanding of adipocyte differentiation. *Nat Rev Mol Cell Biol* (2011) 12:722–34. doi: 10.1038/NRM3198

57. Lefterova MI, Zhang Y, Steger DJ, Schupp M, Schug J, Cristancho A, et al. PPARgamma and C/EBP factors orchestrate adipocyte biology *via* adjacent binding on a genome-wide scale. *Genes Dev* (2008) 22:2941–52. doi: 10.1101/GAD.1709008

58. Pu Y, Veiga-Lopez A. PPARγ agonist through the terminal differentiation phase is essential for adipogenic differentiation of fetal ovine preadipocytes. *Cell Mol Biol Lett* (2017) 22:6. doi: 10.1186/S11658-017-0037-1

59. Rocha AL, Guerra BA, Boucher J, Mori MA. A method to induce Brown/Beige adipocyte differentiation from murine preadipocytes. *Bio Protoc* (2021) 11(24):e4265. doi: 10.21769/BIOPROTOC.4265

60. Sun W, Dong H, Balaz M, Slyper M, Drokhlyansky E, Colleluori G, et al. snRNA-seq reveals a subpopulation of adipocytes that regulates thermogenesis. *Nature* (2020) 587:98–102. doi: 10.1038/S41586-020-2856-X

61. Yoneshiro T, Saito M. Activation and recruitment of brown adipose tissue as anti-obesity regimens in humans. *Ann Med* (2015) 47:133–41. doi: 10.3109/07853890.2014.911595

62. Kuryłowicz A, Puzianowska-Kuźnicka M. Induction of adipose tissue browning as a strategy to combat obesity. *Int J Mol Sci* (2020) 21:1–28. doi: 10.3390/IJMS21176241

63. Payab M, Abedi M, Foroughi Heravani N, Hadavandkhani M, Arabi M, Tayanloo-Beik A, et al. Brown adipose tissue transplantation as a novel alternative to obesity treatment: a systematic review. *Int J Obes* (2020) 45(1):109–21. doi: 10.1038/s41366-020-0616-5

64. Song NJ, Chang SH, Li DY, Villanueva CJ, Park KW. Induction of thermogenic adipocytes: Molecular targets and thermogenic small molecules. *Exp Mol Med* (2017) 49(7):e353. doi: 10.1038/emm.2017.70

65. Chouchani ET, Kazak L, Spiegelman BM. New advances in adaptive thermogenesis: UCP1 and beyond. *Cell Metab* (2019) 29:27–37. doi: 10.1016/J.CMET.2018.11.002

66. Mottillo EP, Ramseyer VD, Granneman JG. SERCA2b cycles its way to UCP1-independent thermogenesis in beige fat. *Cell Metab* (2018) 27:7–9. doi: 10.1016/J.CMET.2017.12.015

67. Ikeda K, Yamada T. UCP1 dependent and independent thermogenesis in brown and beige adipocytes. *Front Endocrinol (Lausanne)* (2020) 11:498. doi: 10.3389/FENDO.2020.00498

68. Okamatsu-Ogura Y, Kuroda M, Tsutsumi R, Tsubota A, Saito M, Kimura K, et al. UCP1-dependent and UCP1-independent metabolic changes induced by acute cold exposure in brown adipose tissue of mice. *Metabolism* (2020) 113:154396. doi: 10.1016/J.METABOL.2020.154396

69. Oeckl J, Janovska P, Adamcova K, Bardova K, Brunner S, Dieckmann S, et al. Loss of UCP1 function augments recruitment of futile lipid cycling for thermogenesis in murine brown fat. *Mol Metab* (2022) 61:101499. doi: 10.1016/J.MOLMET.2022.101499

70. Dludla PV, Nkambule BB, Tiano L, Louw J, Jastroch M, Mazibuko-Mbeje SE. Uncoupling proteins as a therapeutic target to protect the diabetic heart. *Pharmacol Res* (2018) 137:11–24. doi: 10.1016/j.phrs.2018.09.013

71. Ouellet V, Labbé SM, Blondin DP, Phoenix S, Guérin B, Haman F, et al. Brown adipose tissue oxidative metabolism contributes to energy expenditure during acute cold exposure in humans. *J Clin Invest* (2012) 122:545–52. doi: 10.1172/JCI60433

72. Zhang Z, Yang D, Xiang J, Zhou J, Cao H, Che Q, et al. Non-shivering thermogenesis signalling regulation and potential therapeutic applications of brown adipose tissue. *Int J Biol Sci* (2021) 17:2853–70. doi: 10.7150/IJBS.60354

73. Kim S-J, Tang T, Abbott M, Viscarra JA, Wang Y, Sul HS. AMPK phosphorylates Desnutrin/ATGL and hormone-sensitive lipase to regulate lipolysis and fatty acid oxidation within adipose tissue. *Mol Cell Biol* (2016) 36:1961. doi: 10.1128/MCB.00244-16

74. Pagnon J, Matzaris M, Stark R, Meex RCR, Macaulay SL, Brown W, et al. Identification and functional characterization of protein kinase a phosphorylation sites in the major lipolytic protein, adipose triglyceride lipase. *Endocrinology* (2012) 153:4278–89. doi: 10.1210/EN.2012-1127

75. Calderon-Dominguez M, Sebastián D, Fucho R, Weber M, Mir JF, García-Casarrubios E, et al. Carnitine palmitoyltransferase 1 increases lipolysis, UCP1 protein expression and mitochondrial activity in brown adipocytes. *PloS One* (2016) 11(7): e0159399. doi: 10.1371/JOURNAL.PONE.0159399

76. Ramage LE, Akyol M, Fletcher AM, Forsythe J, Nixon M, Carter RN, et al. Glucocorticoids acutely increase brown adipose tissue activity in humans, revealing species-specific differences in UCP-1 regulation. *Cell Metab* (2016) 24:130–41. doi: 10.1016/J.CMET.2016.06.011

77. Orava J, Nuutila P, Lidell ME, Oikonen V, Noponen T, Viljanen T, et al. Different metabolic responses of human brown adipose tissue to activation by cold and insulin. *Cell Metab* (2011) 14:272–9. doi: 10.1016/J.CMET.2011.06.012

78. Jung SM, Doxsey WG, Le J, Haley JA, Mazuecos L, Luciano AK, et al. *In vivo* isotope tracing reveals the versatility of glucose as a brown adipose tissue substrate. *Cell Rep* (2021) 36(4):109459. doi: 10.1016/J.CELREP.2021.109459

79. Tabuchi C, Sul HS. Signaling pathways regulating thermogenesis. *Front Endocrinol (Lausanne)* (2021) 12:595020/BIBTEX. doi: 10.3389/FENDO.2021.595020/BIBTEX

80. Jash S, Banerjee S, Lee MJ, Farmer SR, Puri V. CIDEA transcriptionally regulates UCP1 for britening and thermogenesis in human fat cells. *IScience* (2019) 20:73–89. doi: 10.1016/J.ISCI.2019.09.011

81. Ferhat M, Funai K, Boudina S. Autophagy in adipose tissue physiology and pathophysiology. *Antioxid Redox Signal* (2019) 31:487–501. doi: 10.1089/ARS.2018.7626

82. Desjardins EM, Steinberg GR. Emerging role of AMPK in brown and beige adipose tissue (BAT): Implications for obesity, insulin resistance, and type 2 diabetes. *Curr Diabetes Rep* (2018) 18(10):80. doi: 10.1007/S11892-018-1049-6

83. Altshuler-Keylin S, Shinoda K, Hasegawa Y, Ikeda K, Hong H, Kang Q, et al. Beige adipocyte maintenance is regulated by autophagy-induced mitochondrial clearance. *Cell Metab* (2016) 24:402–19. doi: 10.1016/J.CMET.2016.08.002

84. Cairó M, Campderrós L, Gavaldà-Navarro A, Cereijo R, Delgado-Anglés A, Quesada-López T, et al. Parkin controls brown adipose tissue plasticity in response to adaptive thermogenesis. *EMBO Rep* (2019) 20:e46832. doi: 10.15252/EMBR.201846832

85. Mottillo EP, Desjardins EM, Crane JD, Smith BK, Green AE, Ducommun S, et al. Lack of adipocyte AMPK exacerbates insulin resistance and hepatic steatosis through brown and beige adipose tissue function. *Cell Metab* (2016) 24:118–29. doi: 10.1016/J.CMET.2016.06.006

86. López M. Hypothalamic AMPK as a possible target for energy balance-related diseases. *Trends Pharmacol Sci* (2022) 43:546–56. doi: 10.1016/J.TIPS.2022.04.007

87. Saito M, Matsushita M, Yoneshiro T, Okamatsu-Ogura Y. Brown adipose tissue, diet-induced thermogenesis, and thermogenic food ingredients: From mice to men. *Front Endocrinol (Lausanne)* (2020) 11:222. doi: 10.3389/fendo.2020.00222

88. Zhang X, Li X, Fang H, Guo F, Li F, Chen A, et al. Flavonoids as inducers of white adipose tissue browning and thermogenesis: Signalling pathways and molecular triggers. *Nutr Metab (Lond)* (2019) 16:47. doi: 10.1186/s12986-019-0370-7

89. Ho KKY. Diet-induced thermogenesis: Fake friend or foe? *J Endocrinol* (2018) 238:R185–91. doi: 10.1530/JOE-18-0240

90. Ruan HB, Dietrich MO, Liu ZW, Zimmer MR, Li MD, Singh JP, et al. O-GlcNAc transferase enables AgRP neurons to suppress browning of white fat. *Cell* (2014) 159:306–17. doi: 10.1016/J.CELL.2014.09.010

91. Dodd GT, Decherf S, Loh K, Simonds SE, Wiede F, Balland E, et al. Leptin and insulin act on POMC neurons to promote the browning of white fat. *Cell* (2015) 160:88–104. doi: 10.1016/J.CELL.2014.12.022

92. Contreras C, González-García I, Seoane-Collazo P, Martínez-Sánchez N, Liñares-Pose L, Rial-Pensado E, et al. Reduction of hypothalamic endoplasmic reticulum stress activates browning of white fat and ameliorates obesity. *Diabetes* (2017) 66:87–99. doi: 10.2337/DB15-1547

93. Xu F, Lin B, Zheng X, Chen Z, Cao H, Xu H, et al. GLP-1 receptor agonist promotes brown remodelling in mouse white adipose tissue through SIRT1. *Diabetologia* (2016) 59:1059–69. doi: 10.1007/S00125-016-3896-5

94. Beiroa D, Imbernon M, Gallego R, Senra A, Herranz D, Villarroya F, et al. GLP-1 agonism stimulates brown adipose tissue thermogenesis and browning through hypothalamic AMPK. *Diabetes* (2014) 63:3346–58. doi: 10.2337/DB14-0302

95. Solmonson A, Mills EM. Uncoupling proteins and the molecular mechanisms of thyroid thermogenesis. *Endocrinology* (2016) 157:455–62. doi: 10.1210/EN.2015-1803

96. López M, Varela L, Vázquez MJ, Rodríguez-Cuenca S, González CR, Velagapudi VR, et al. Hypothalamic AMPK and fatty acid metabolism mediate thyroid regulation of energy balance. *Nat Med* (2010) 16:1001–8. doi: 10.1038/NM.2207

97. Contreras C, González-García I, Martínez-Sánchez N, Seoane-Collazo P, Jacas J, Morgan DA, et al. Central ceramide-induced hypothalamic lipotoxicity and ER stress regulate energy balance. *Cell Rep* (2014) 9:366–77. doi: 10.1016/J.CELREP.2014.08.057

98. Martínez-Sánchez N, Seoane-Collazo P, Contreras C, Varela L, Villarroya J, Rial-Pensado E, et al. Hypothalamic AMPK-ER stress-JNK1 axis mediates the central actions of thyroid hormones on energy balance. *Cell Metab* (2017) 26:212–29.e12. doi: 10.1016/J.CMET.2017.06.014

99. Martínez-Sánchez N, Moreno-Navarrete JM, Contreras C, Rial-Pensado E, Fernø J, Nogueiras R, et al. Thyroid hormones induce browning of white fat. *J Endocrinol* (2017) 232:351–62. doi: 10.1530/JOE-16-0425

100. Martínez De Morentin PB, González-García I, Martins L, Lage R, Fernández-Mallo D, Martínez-Sánchez N, et al. Estradiol regulates brown adipose tissue thermogenesis *via* hypothalamic AMPK. *Cell Metab* (2014) 20:41–53. doi: 10.1016/J.CMET.2014.03.031

101. Levine B, Klionsky DJ. Development by self-digestion: molecular mechanisms and biological functions of autophagy. *Dev Cell* (2004) 6:463–77. doi: 10.1016/S1534-5807(04)00099-1

102. Mizushima N, Komatsu M. Autophagy: renovation of cells and tissues. *Cell* (2011) 147:728–41. doi: 10.1016/J.CELL.2011.10.026

103. Singh R, Kaushik S, Wang Y, Xiang Y, Novak I, Komatsu M, et al. Autophagy regulates lipid metabolism. *Nature* (2009) 458(7242):1131–5. doi: 10.1038/nature07976

104. Gospodarska E, Nowialis P, Kozak LP. Mitochondrial turnover: a phenotype distinguishing brown adipocytes from interscapular brown adipose tissue and white adipose tissue. *J Biol Chem* (2015) 290:8243–55. doi: 10.1074/JBC.M115.637785

105. Lu Y, Fujioka H, Joshi D, Li Q, Sangwung P, Hsieh P, et al. Mitophagy is required for brown adipose tissue mitochondrial homeostasis during cold challenge. *Sci Rep* (2018) 8(1):8251. doi: 10.1038/S41598-018-26394-5

106. Yau WW, Wong KA, Zhou J, Thimmukonda NK, Wu Y, Bay BH, et al. Chronic cold exposure induces autophagy to promote fatty acid oxidation, mitochondrial turnover, and thermogenesis in brown adipose tissue. *IScience* (2021) 24(5):102434. doi: 10.1016/J.ISCI.2021.102434

107. Cairó M, Villarroya J, Cereijo R, Campderrós L, Giralt M, Villarroya F. Thermogenic activation represses autophagy in brown adipose tissue. *Int J Obes* (2016) 40(10):1591–9. doi: 10.1038/ijo.2016.115

108. Lu X, Altshuler-Keylin S, Wang Q, Chen Y, Sponton CH, Ikeda K, et al. Mitophagy controls beige adipocyte maintenance through a parkin-dependent and UCP1-independent mechanism. *Sci Signal* (2018) 11(527):eaap8526. doi: 10.1126/SCISIGNAL.AAP8526

109. Kim D, Kim JH, Kang YH, Kim JS, Yun SC, Kang SW, et al. Suppression of brown adipocyte autophagy improves energy metabolism by regulating mitochondrial turnover. *Int J Mol Sci* (2019) 20(14):3520. doi: 10.3390/ijms20143520

110. della Guardia L, Shin AC. White and brown adipose tissue functionality is impaired by fine particulate matter (PM 2.5) exposure. *J Mol Med (Berl)* (2022) 100:665–76. doi: 10.1007/S00109-022-02183-6

111. Bartelt A, Widenmaier SB, Schlein C, Johann K, Goncalves RLS, Eguchi K, et al. Brown adipose tissue thermogenic adaptation requires Nrf1-mediated proteasomal activity. *Nat Med* (2018) 24(3):292–303. doi: 10.1038/nm.4481

112. Hou Y, Liu Z, Zuo Z, Gao T, Fu J, Wang H, et al. Adipocyte-specific deficiency of Nfe2l1 disrupts plasticity of white adipose tissues and metabolic homeostasis in mice. *Biochem Biophys Res Commun* (2018) 503:264–70. doi: 10.1016/J.BBRC.2018.06.013

113. Pillon NJ, Loos RJF, Marshall SM, Zierath JR. Metabolic consequences of obesity and type 2 diabetes: Balancing genes and environment for personalized care. *Cell* (2021) 184:1530–44. doi: 10.1016/j.cell.2021.02.012

114. Nascimento GG, Peres MA, Mittinty MN, Peres KG, Do LG, Horta BL, et al. Diet-induced overweight and obesity and periodontitis risk: An application of the parametric g-formula in the 1982 pelotas birth cohort. *Am J Epidemiol* (2017) 185:442–51. doi: 10.1093/aje/kww187

115. Fabbri E, Zoli M, Gonzalez-Freire M, Salive ME, Studenski SA, Ferrucci L. Aging and multimorbidity: New tasks, priorities, and frontiers for integrated gerontological and clinical research. *J Am Med Dir Assoc* (2015) 16:640–7. doi: 10.1016/J.JAMDA.2015.03.013

116. Gao M, Ma Y, Liu D. High-fat diet-induced adiposity, adipose inflammation, hepatic steatosis and hyperinsulinemia in outbred CD-1 mice. *PloS One* (2015) 10(3): e0119784. doi: 10.1371/journal.pone.0119784

117. Dobner J, Ress C, Rufinatscha K, Salzmann K, Salvenmoser W, Folie S, et al. Fat-enriched rather than high-fructose diets promote whitening of adipose tissue in a sex-dependent manner. *J Nutr Biochem* (2017) 49:22–9. doi: 10.1016/j.jnutbio.2017.07.009

118. Kuipers EN, Held NM, In het Panhuis W, Modder M, Ruppert PMM, Kersten S, et al. A single day of high-fat diet feeding induces lipid accumulation and insulin resistance in brown adipose tissue in mice. *Am J Physiol Endocrinol Metab* (2019) 317: E820–30. doi: 10.1152/ajpendo.00123.2019

119. Miranda CS, Silva-Veiga F, Martins FF, Rachid TL, Mandarim-De-Lacerda CA, Souza-Mello V. PPAR-α activation counters brown adipose tissue whitening: a comparative study between high-fat– and high-fructose–fed mice. *Nutrition* (2020) 78:110791. doi: 10.1016/j.nut.2020.110791

120. Serdan TDA, Masi LN, Pereira JNB, Rodrigues LE, Alecrim AL, Scervino MVM, et al. Impaired brown adipose tissue is differentially modulated in insulin-resistant obese wistar and type 2 diabetic goto-kakizaki rats. *Biomedicine Pharmacotherapy* (2021) 142:112019. doi: 10.1016/j.biopha.2021.112019

121. Savva C, Helguero LA, González-Granillo M, Melo T, Couto D, Buyandelger B, et al. Maternal high-fat diet programs white and brown adipose tissue lipidome and transcriptome in offspring in a sex- and tissue-dependent manner in mice. *Int J Obes* (2022) 46:831–42. doi: 10.1038/s41366-021-01060-5

122. Cui X, Nguyen NLT, Zarebidaki E, Cao Q, Li F, Zha L, et al. Thermoneutrality decreases thermogenic program and promotes adiposity in high-fat diet-fed mice. *Physiol Rep* (2016) 4(10):e12799. doi: 10.14814/phy2.12799

123. Sass F, Schlein C, Jaeckstein MY, Pertzborn P, Schweizer M, Schinke T, et al. TFEB deficiency attenuates mitochondrial degradation upon brown adipose tissue whitening at thermoneutrality. *Mol Metab* (2021) 47:101173. doi: 10.1016/j.molmet.2021.101173

124. Gonçalves LF, Machado TQ, Castro-Pinheiro C, de Souza NG, Oliveira KJ, Fernandes-Santos C. Ageing is associated with brown adipose tissue remodelling and loss of white fat browning in female C57BL/6 mice. *Int J Exp Pathol* (2017) 98:100–8. doi: 10.1111/IEP.12228

125. Pan XX, Yao KL, Yang YF, Ge Q, Zhang R, Gao PJ, et al. Senescent T cell induces brown adipose tissue "Whitening" via secreting IFN-γ. *Front Cell Dev Biol* (2021) 9:637424. doi: 10.3389/fcell.2021.637424

126. Du K, Bai X, Yang L, Shi Y, Chen L, Wang H, et al. *De novo* reconstruction of transcriptome identified long non-coding RNA regulator of aging-related brown adipose tissue whitening in rabbits. *Biol (Basel)* (2021) 10(11):1176. doi: 10.3390/biology10111176

127. Huang Z, Zhang Z, Moazzami Z, Heck R, Hu P, Nanda H, et al. Brown adipose tissue involution associated with progressive restriction in progenitor competence. *Cell Rep* (2022) 39(2):110575. doi: 10.1016/J.CELREP.2022.110575

128. Scambi I, Peroni D, Nodari A, Merigo F, Benati D, Boschi F, et al. The transcriptional profile of adipose-derived stromal cells (ASC) mirrors the whitening of adipose tissue with age. *Eur J Cell Biol* (2022) 101(2):151206. doi: 10.1016/J.EJCB.2022.151206

129. Lapa C, Arias-Loza P, Hayakawa N, Wakabayashi H, Werner RA, Chen X, et al. Whitening and impaired glucose utilization of brown adipose tissue in a rat model of type 2 diabetes mellitus. *Sci Rep* (2017) 7(1):16795. doi: 10.1038/s41598-017-17148-w

130. Konda PY, Poondla V, Jaiswal KK, Dasari S, Uyyala R, Surtineni VP, et al. Pathophysiology of high fat diet induced obesity: impact of probiotic banana juice on obesity associated complications and hepatosteatosis. *Sci Rep* (2020) 10(1):1–17. doi: 10.1038/s41598-020-73670-4

131. Kayode OO. Diet and obesity. In: *Psychology and pathophysiological outcomes of eating* IntechOpen (2021). doi: 10.5772/INTECHOPEN.98326

132. de Moura e Dias M, dos Reis SA, da Conceição LL, de Oliveira Sediyama CMN, Pereira SS, de Oliveira LL, et al. Diet-induced obesity in animal models: points to consider and influence on metabolic markers. *Diabetol Metab Syndr* (2021) 13:1–14. doi: 10.1186/S13098-021-00647-2/TABLES/3

133. Lang P, Hasselwander S, Li H, Xia N. Effects of different diets used in diet-induced obesity models on insulin resistance and vascular dysfunction in C57BL/6 mice. *Sci Rep* (2019) 9(1):19556. doi: 10.1038/s41598-019-55987-x

134. Hariri N, Thibault L. High-fat diet-induced obesity in animal models. *Nutr Res Rev* (2010) 23:270–99. doi: 10.1017/S0954422410000168

135. Herold J, Kalucka J. Angiogenesis in adipose tissue: The interplay between adipose and endothelial cells. *Front Physiol* (2021) 11:624903. doi: 10.3389/FPHYS.2020.624903

136. Corvera S, Gealekman O. Adipose tissue angiogenesis: impact on obesity and type-2 diabetes. *Biochim Biophys Acta* (2014) 1842:463–72. doi: 10.1016/J.BBADIS.2013.06.003

137. Paavonsalo S, Hariharan S, Lackman MH, Karaman S. Capillary rarefaction in obesity and metabolic diseases–Organ-Specificity and possible mechanisms. *Cells* (2020) 9:2683. doi: 10.3390/CELLS9122683

138. Miranda M, Escoté X, Ceperuelo-Mallafré V, Megía A, Caubet E, Näf S, et al. Relation between human LPIN1, hypoxia and endoplasmic reticulum stress genes in subcutaneous and visceral adipose tissue. *Int J Obes (Lond)* (2010) 34:679–86. doi: 10.1038/IJO.2009.290

139. Elias I, Franckhauser S, Bosch F. New insights into adipose tissue VEGF-a actions in the control of obesity and insulin resistance. *Adipocyte* (2013) 2:109. doi: 10.4161/ADIP.22880

140. Pellegata NS, Berriel Diaz M, Rohm M, Herzig S. Obesity and cancer–extracellular matrix, angiogenesis, and adrenergic signaling as unusual suspects linking the two diseases. *Cancer Metastasis Rev* (2022) 41:517–47. doi: 10.1007/S10555-022-10058-Y

141. Ye J. Adipose tissue vascularization: its role in chronic inflammation. *Curr Diabetes Rep* (2011) 11:203–10. doi: 10.1007/S11892-011-0183-1

142. O'Rourke RW, White AE, Metcalf MD, Olivas AS, Mitra P, Larison WG, et al. Hypoxia-induced inflammatory cytokine secretion in human adipose tissue stromovascular cells. *Diabetologia* (2011) 54:1480. doi: 10.1007/S00125-011-2103-Y

143. Fujisaka S, Usui I, Ikutani M, Aminuddin A, Takikawa A, Tsuneyama K, et al. Adipose tissue hypoxia induces inflammatory M1 polarity of macrophages in an HIF-1α-dependent and HIF-1α-independent manner in obese mice. *Diabetologia* (2013) 56:1403–12. doi: 10.1007/S00125-013-2885-1/FIGURES/4

144. Parlee SD, MacDougald OA. Maternal nutrition and risk of obesity in offspring: The Trojan horse of developmental plasticity. *Biochim Biophys Acta Mol Basis Dis* (2014) 1842:495–506. doi: 10.1016/j.bbadis.2013.07.007

145. Sarker G, Litwan K, Kastli R, Peleg-Raibstein D. Maternal overnutrition during critical developmental periods leads to different health adversities in the offspring: relevance of obesity, addiction and schizophrenia. *Sci Rep* (2019) 9(1):17322. doi: 10.1038/s41598-019-53652-x

146. Lidell ME. Brown adipose tissue in human infants. *Handb Exp Pharmacol* (2019) 251:107–23. doi: 10.1007/164_2018_118

147. Quesada-López T, Gavaldà-Navarro A, Morón-Ros S, Campderrós L, Iglesias R, Giralt M, et al. GPR120 controls neonatal brown adipose tissue thermogenic induction. *Am J Physiol Endocrinol Metab* (2019) 317:742–50. doi: 10.1152/ajpendo.00081.2019.-Adaptive

148. González-García I, Contreras C, Estévez-Salguero Á, Ruíz-Pino F, Colsh B, Pensado I, et al. Estradiol regulates energy balance by ameliorating hypothalamic ceramide-induced ER stress. *Cell Rep* (2018) 25:413–23.e5. doi: 10.1016/J.CELREP.2018.09.038

149. Johnson F, Mavrogianni A, Ucci M, Vidal-Puig A, Wardle J. Could increased time spent in a thermal comfort zone contribute to population increases in obesity? *Obes Rev* (2011) 12:543–51. doi: 10.1111/j.1467-789X.2010.00851.x

150. Kern PA, Finlin BS, Zhu B, Rasouli N, McGehee RE, Westgate PM, et al. The effects of temperature and seasons on subcutaneous white adipose tissue in humans: evidence for thermogenic gene induction. *J Clin Endocrinol Metab* (2014) 99:E2772–9. doi: 10.1210/JC.2014-2440

151. Yoneshiro T, Matsushita M, Nakae S, Kameya T, Sugie H, Tanaka S, et al. Brown adipose tissue is involved in the seasonal variation of cold-induced thermogenesis in humans. *Am J Physiol Regul Integr Comp Physiol* (2016) 310:R999–1009. doi: 10.1152/AJPREGU.00057.2015

152. Søberg S, Löfgren J, Philipsen FE, Jensen M, Hansen AE, Ahrens E, et al. Altered brown fat thermoregulation and enhanced cold-induced thermogenesis in young, healthy, winter-swimming men. *Cell Rep Med* (2021) 2(10):100408. doi: 10.1016/J.XCRM.2021.100408

153. Fischer AW, Cannon B, Nedergaard J. Optimal housing temperatures for mice to mimic the thermal environment of humans: An experimental study. *Mol Metab* (2018) 7:161–70. doi: 10.1016/j.molmet.2017.10.009

154. Speakman JR, Keijer J. Not so hot: Optimal housing temperatures for mice to mimic the thermal environment of humans. *Mol Metab* (2013) 2:5–9. doi: 10.1016/j.molmet.2012.10.002

155. Mancuso P, Bouchard B. The impact of aging on adipose function and adipokine synthesis. *Front Endocrinol (Lausanne)* (2019) 10:137. doi: 10.3389/fendo.2019.00137

156. Zoico E, Rubele S, de Caro A, Nori N, Mazzali G, Fantin F, et al. Brown and beige adipose tissue and aging. *Front Endocrinol (Lausanne)* (2019) 10:368. doi: 10.3389/fendo.2019.00368

157. Mogilenko DA, Shchukina I, Artyomov MN. Immune ageing at single-cell resolution. *Nat Rev Immunol* (2021) 22(8):484–98. doi: 10.1038/s41577-021-00646-4

158. Bahler L, Verberne HJ, Admiraal WM, Stok WJ, Soeters MR, Hoekstra JB, et al. Differences in sympathetic nervous stimulation of brown adipose tissue between the young and old, and the lean and obese. *J Nucl Med* (2016) 57:372–7. doi: 10.2967/jnumed.115.165829

159. Berry DC, Jiang Y, Arpke RW, Close EL, Uchida A, Reading D, et al. Cellular aging contributes to failure of cold-induced beige adipocyte formation in old mice and humans. *Cell Metab* (2017) 25:166–81. doi: 10.1016/J.CMET.2016.10.023

160. Tajima K, Ikeda K, Chang HY, Chang CH, Yoneshiro T, Oguri Y, et al. Mitochondrial lipoylation integrates age-associated decline in brown fat thermogenesis. *Nat Metab* (2019) 1:886–98. doi: 10.1038/S42255-019-0106-Z

161. Lutz TA, Woods SC. Overview of animal models of obesity. *Curr Protoc Pharmacol* (2012) 58:5.61.1–5.61.18. doi: 10.1002/0471141755.ph0561s58

162. Loos RJF, Yeo GSH. The genetics of obesity: from discovery to biology. *Nat Rev Genet* (2022) 23:120–33. doi: 10.1038/s41576-021-00414-z

163. Thaker V v. *Genetic and Epigenetic Causes of Obesity. n.d. Adolesc Med State Art Rev*. (2017) 28(2):379–405.

164. Amato AA, Wheeler HB, Blumberg B. Obesity and endocrine-disrupting chemicals. *Endocr Connect* (2021) 10:R87–105. doi: 10.1530/EC-20-0578

165. Zhang J, Yang Y, Liu W, Schlenk D, Liu J. Glucocorticoid and mineralocorticoid receptors and corticosteroid homeostasis are potential targets for endocrine-disrupting chemicals. *Environ Int* (2019) 133(Pt A):105133. doi: 10.1016/j.envint.2019.105133

166. Pestana D, Teixeira D, Meireles M, Marques C, Norberto S, Sá C, et al. Adipose tissue dysfunction as a central mechanism leading to dysmetabolic obesity triggered by chronic exposure to p,p'-DDE. *Sci Rep* (2017) 7(1):2738. doi: 10.1038/s41598-017-02885-9

167. Jo DH, Park SW, Cho CS, Powner MB, Kim JH, Fruttiger M, et al. Intravitreally injected anti-VEGF antibody reduces brown fat in neonatal mice. *PloS One* (2015) 10 (7):e0134308. doi: 10.1371/journal.pone.0134308

168. Fan J, Ping J, Zhang Wx, Rao Ys, Liu Hx, Zhang J, et al. Prenatal and lactation nicotine exposure affects morphology and function of brown adipose tissue in male rat offspring. *Ultrastruct Pathol* (2016) 40:288–95. doi: 10.1080/01913123.2016.1223243

169. Chen Hj, Li Gl, Zhang Wx, Fan J, Hu L, Zhang L, et al. Maternal nicotine exposure during pregnancy and lactation induces brown adipose tissue whitening in female offspring. *Toxicol Appl Pharmacol* (2020) 409:115298. doi: 10.1016/J.TAAP.2020.115298

170. Peshdary V, Styles G, Rigden M, Caldwell D, Kawata A, Sorisky A, et al. Exposure to low doses of dechlorane plus promotes adipose tissue dysfunction and glucose intolerance in male mice. *Endocrinol (United States)* (2021) 161:1–15. doi: 10.1210/ENDOCR/BQAA096

171. Rozenblit-Susan S, Chapnik N, Froy O. Serotonin prevents differentiation into brown adipocytes and induces transdifferentiation into white adipocytes. *Int J Obes* (2018) 42:704–10. doi: 10.1038/ijo.2017.261

172. Gasparini SJ, Swarbrick MM, Kim S, Thai LJ, Henneicke H, Cavanagh LL, et al. Androgens sensitise mice to glucocorticoid-induced insulin resistance and fat accumulation. *Diabetologia* (2019) 62:1463–77. doi: 10.1007/s00125-019-4887-0

173. Deng J, Guo Y, Yuan F, Chen S, Yin H, Jiang X, et al. Autophagy inhibition prevents glucocorticoid-increased adiposity *via* suppressing BAT whitening. *Autophagy* (2020) 16:451–65. doi: 10.1080/15548627.2019.1628537

174. Bel JS, Tai TC, Khaper N, Lees SJ. Chronic glucocorticoid exposure causes brown adipose tissue whitening, alters whole-body glucose metabolism and increases tissue uncoupling protein-1. *Physiol Rep* (2022) 10(9):e15292. doi: 10.14814/PHY2.15292

175. Jin H, Li D, Wang X, Jia J, Chen Y, Yao Y, et al. VEGF and VEGFB play balancing roles in adipose differentiation, gene expression, and function. *Endocrinology* (2018) 159:2036–49. doi: 10.1210/en.2017-03246

176. Zayek M, Parker K, Rydzewska M, Rifai A, Bhat R, Eyal F. Bevacizumab for retinopathy of prematurity: 2-year neurodevelopmental follow-up. *Am J Perinatol* (2021) 38:1158–66. doi: 10.1055/s-0040-1710556

177. Mishra A, Chaturvedi P, Datta S, Sinukumar S, Joshi P, Garg A. Harmful effects of nicotine. *Indian J Med Paediatric Oncol* (2015) 36:24–31. doi: 10.4103/0971-5851.151771

178. Riedel C, Schönberger K, Yang S, Koshy G, Chen YC, Gopinath B, et al. Parental smoking and childhood obesity: Higher effect estimates for maternal smoking in pregnancy compared with paternal smoking-a meta-analysis. *Int J Epidemiol* (2014) 43:1593–606. doi: 10.1093/ije/dyu150

179. Zhang Wx, Chen Hj, Fan J, Li Gl, Sun A, Lan L, et al. The association between maternal nicotine exposure and adipose angiogenesis in female rat offspring: A mechanism of adipose tissue function changes. *Toxicol Lett* (2020) 318:12–21. doi: 10.1016/J.TOXLET.2019.10.007

180. Martínez De Morentin PB, Whittle AJ, Fernø J, Nogueiras R, Diéguez C, Vidal-Puig A, et al. Nicotine induces negative energy balance through hypothalamic AMP-activated protein kinase. *Diabetes* (2012) 61:807–17. doi: 10.2337/DB11-1079

181. Seoane-Collazo P, Liñares-Pose L, Rial-Pensado E, Romero-Picó A, Moreno-Navarrete JM, Martínez-Sánchez N, et al. Central nicotine induces browning through hypothalamic κ opioid receptor. *Nat Commun* (2019) 10(1):4037. doi: 10.1038/S41467-019-12004-Z

182. Mohajer N, Du CY, Checkcinco C, Blumberg B. Obesogens: How they are identified and molecular mechanisms underlying their action. *Front Endocrinol (Lausanne)* (2021) 12:780888. doi: 10.3389/fendo.2021.780888

183. Peshdary V, Calzadilla G, Landry A, Sorisky A, Atlas E. Dechlorane plus increases adipogenesis in 3T3-L1 and human primary preadipocytes independent of peroxisome proliferator-activated receptor γ transcriptional activity. *Int J Obes* (2019) 43:545–55. doi: 10.1038/s41366-018-0072-7

184. Winn NC, Vieira-Potter VJ, Gastecki ML, Welly RJ, Scroggins RJ, Zidon TM, et al. Loss of UCP1 exacerbates Western diet-induced glycemic dysregulation independent of changes in body weight in female mice downloaded from. *Am J Physiol Regul Integr Comp Physiol* (2017) 312:74–84. doi: 10.1152/ajpregu.00425.2016.-We

185. Winn NC, Grunewald ZI, Gastecki ML, Woodford ML, Welly RJ, Clookey SL, et al. Deletion of UCP1 enhances ex vivo aortic vasomotor function in female but not male mice despite similar susceptibility to metabolic dysfunction. *Am J Physiol Endocrinol Metab* (2017) 313:E402–12. doi: 10.1152/AJPENDO.00096.2017

186. Oh CM, Namkung J, Go Y, Shong KE, Kim K, Kim H, et al. Regulation of systemic energy homeostasis by serotonin in adipose tissues. *Nat Commun* (2015) 6:6794. doi: 10.1038/ncomms7794

187. Luijten IHN, Cannon B, Nedergaard J. Glucocorticoids and brown adipose tissue: Do glucocorticoids really inhibit thermogenesis? *Mol Aspects Med* (2019) 68:42–59. doi: 10.1016/j.mam.2019.07.002

188. Zilberfarb V, Siquier K, Strosberg AD, Issad T. Effect of dexamethasone on adipocyte differentiation markers and tumour necrosis factor-alpha expression in human PAZ6 cells. *Diabetologia* (2001) 44:377–86. doi: 10.1007/S001250051630

189. Wibmer AG, Becher T, Eljalby M, Crane A, Andrieu PC, Jiang CS, et al. Brown adipose tissue is associated with healthier body fat distribution and metabolic benefits independent of regional adiposity. *Cell Rep Med* (2021) 2(7):100332. doi: 10.1016/j.xcrm.2021.100332

190. Alcalá M, Calderon-Dominguez M, Serra D, Herrero L, Viana M. Mechanisms of impaired brown adipose tissue recruitment in obesity. *Front Physiol* (2019) 10:94. doi: 10.3389/fphys.2019.00094

191. Lopez-Vicchi F, de Winne C, Ornstein AM, Sorianello E, Toneatto J, Becu-Villalobos D. Severe hyperprolactinemia promotes brown adipose tissue whitening and aggravates high fat diet induced metabolic imbalance. *Front Endocrinol (Lausanne)* (2022) 13:883092. doi: 10.3389/FENDO.2022.883092

192. Blázquez-Medela AM, Jumabay M, Rajbhandari P, Sallam T, Guo Y, Yao J, et al. Noggin depletion in adipocytes promotes obesity in mice. *Mol Metab* (2019) 25:50–63. doi: 10.1016/J.MOLMET.2019.04.004

193. Vernochet C, Damilano F, Mourier A, Bezy O, Mori MA, Smyth G, et al. Adipose tissue mitochondrial dysfunction triggers a lipodystrophic syndrome with insulin resistance, hepatosteatosis, and cardiovascular complications. *FASEB J* (2014) 28:4408–19. doi: 10.1096/FJ.14-253971

194. Cannavino J, Shao M, An YA, Bezprozvannaya S, Chen S, Kim J, et al. Regulation of cold-induced thermogenesis by the RNA binding protein FAM195A. *Proc Natl Acad Sci U.S.A.* (2021) 118(23):e2104650118. doi: 10.1073/PNAS.2104650118/SUPPL_FILE/PNAS.2104650118.SD04.XLSX

195. Ahmadian M, Liu S, Reilly SM, Hah N, Fan W, Yoshihara E, et al. ERRγ preserves brown fat innate thermogenic activity. *Cell Rep* (2018) 22:2849–59. doi: 10.1016/J.CELREP.2018.02.061

196. Cui J, Pang J, Lin YJ, Gong H, Wang ZH, Li YX, et al. Adipose-specific deletion of Kif5b exacerbates obesity and insulin resistance in a mouse model of diet-induced obesity. *FASEB J* (2017) 31:2533–47. doi: 10.1096/FJ.201601103R

197. Silvester AJ, Aseer KR, Yun JW. Ablation of DJ-1 impairs brown fat function in diet-induced obese mice. *Biochimie* (2018) 154:107–18. doi: 10.1016/J.BIOCHI.2018.08.005

198. Ahmadian M, Abbott MJ, Tang T, Hudak CSS, Kim Y, Bruss M, et al. Desnutrin/ATGL is regulated by AMPK and is required for a brown adipose phenotype. *Cell Metab* (2011) 13:739–48. doi: 10.1016/J.CMET.2011.05.002

199. Mori MA, Thomou T, Boucher J, Lee KY, Lallukka S, Kim JK, et al. Altered miRNA processing disrupts brown/white adipocyte determination and associates with lipodystrophy. *J Clin Invest* (2014) 124:3339–51. doi: 10.1172/JCI73468

200. Lou P, Bi X, Tian Y, Li G, Kang Q, Lv C, et al. MiR-22 modulates brown adipocyte thermogenesis by synergistically activating the glycolytic and mTORC1 signaling pathways. *Theranostics* (2021) 11:3607–23. doi: 10.7150/THNO.50900

201. Ziqubu K, Mazibuko-Mbeje SE, Mthembu SXH, Mabhida S, Jack BU, Nyambuya TM. Anti-obesity effects of metformin: A scoping review evaluating the feasibility of brown adipose tissue as a therapeutic target. *Int J Mol Sci* (2023) 24:2227. doi: 10.3390/ijms24032227

10.3389/fendo.2023.1114767

Glossary

Acaca	acetyl-coa carboxylase alpha
AMPK	AMP-activated protein kinase
ATG7	autophagy related 7
BAT	brown adipose tissue
β3-AR	Beta-3 adrenegic receptor
BTG1	B cell translocation gene 1
Bmp7	bone morphogenetic protein 7
BMP8b	bone morphogenetic protein 8 beta
Cd36	cluster of differentiation 36
Cidea	cell death-inducing DNA fragmentation factor-like effector A
CPTs	carnitine palmitoyltransferases
Cox	cyclooxygenase
Dex	dexamethasone
Dio2	iodothyronine deiodinase 2
DP	dechlorane plus
EPDR1	ependymin-related protein 1
EDCs	endocrine-disrupting chemical
Elovl3	Elongation of very long chain fatty acids protein 3
FGF21	fibroblast growth factor-21
Fis1	mitochondrial fission 1 protein
GLUT	Glucose transporter
Gsk3-β	glycogen synthase kinase 3 β
Hgf	hepatocyte growth factor
HFD	high fat diet
HFHSD	high fat high sugar diet
HSL	hormone-sensitive lipase
IL-6	interleukin-6
IGF-1	insulin-like growth Factor-1
IGFBP-2	Insulin-like growth factor-binding protein 2
IFN-γ	interferon
lncRNAs	long non-coding RNAs
IRS-2	insulin receptor substrates 2
MAPK3	mitogen-activated protein kinase 3
NGF	nerve-growth factor
NRG4	neuregulin 4
Npy	neuropeptide
Nrip1	nuclear receptor interacting protein 1
NETO	norepinephrine turnover
Plin	perilipin
PKB	Protein kinase B
PRDM16	PR domain containing 16
PPARγ	peroxisome proliferator-activated receptor-γ
PGC1α	peroxisome proliferator- activated receptor γ coactivator 1-alpha
Rb1	RB transcriptional corepressor 1
Rbl1/ p107	RB transcriptional corepressor like 1
Sirt1	Sirtuin 1
Srebp1c	sterol regulatory element-binding protein 1c
TFEB	transcription factor EB
UCP1	uncoupling protein 1
VEGFs	vascular endothelial growth factors; 12,13-dihydroxy-9Z-octadecenoic acid

frontiers | Frontiers in Endocrinology

TYPE Original Research
PUBLISHED 16 February 2023
DOI 10.3389/fendo.2023.1095031

OPEN ACCESS

EDITED BY
Marcello Pinti,
University of Modena and Reggio Emilia, Italy

REVIEWED BY
Indrashis Bhattacharya,
Central University of Kerala, India
Deepa Bhartiya,
Indian Council of Medical Research (ICMR), India

*CORRESPONDENCE
Victoria N. Tedjawirja
v.n.tedjawirja@amsterdamumc.nl

SPECIALTY SECTION
This article was submitted to Endocrinology of Aging, a section of the journal Frontiers in Endocrinology

RECEIVED 10 November 2022
ACCEPTED 30 January 2023
PUBLISHED 16 February 2023

CITATION
Tedjawirja VN, Hooijer GKJ, Savci-Heijink CD, Kovac K, Balm R and de Waard V (2023) Inadequate detection of the FSHR complicates future research on extragonadal FSHR localization. *Front. Endocrinol.* 14:1095031. doi: 10.3389/fendo.2023.1095031

Inadequate detection of the FSHR complicates future research on extragonadal FSHR localization

Victoria N. Tedjawirja[1]*, Gerrit K. J. Hooijer[2], C. Dilara Savci-Heijink[2], Kristina Kovac[3], Ron Balm[1] and Vivian de Waard[3]

[1]Department of Surgery, Amsterdam Cardiovascular Sciences, Amsterdam University Medical Centre (UMC), University of Amsterdam, Amsterdam, Netherlands, [2]Department of Pathology, Amsterdam University Medical Centre (UMC), University of Amsterdam, Amsterdam, Netherlands, [3]Department of Medical Biochemistry, Amsterdam Cardiovascular Sciences, Amsterdam University Medical Centre (UMC), University of Amsterdam, Amsterdam, Netherlands

Introduction: Recently, follicle stimulating hormone (FSH) through interaction with its receptor (FSHR) has been proposed to play a role in postmenopausal osteoporosis and cardiovascular disease, rather than the loss of estrogen. To explore this hypothesis, unravelling which cells express extragonadal FSHR on protein level is key.

Methods: We used two commercial anti-FSHR antibodies and validated them by performing immunohistochemistry on positive (ovary, testis) and negative controls (skin).

Results: The monoclonal anti-FSHR antibody could not identify the FSHR in ovary or testis. The polyclonal anti-FSHR antibody stained the granulosa cells (ovary) and Sertoli cells (testis), yet there was equally intense staining of other cells/extracellular matrix. Furthermore, the polyclonal anti-FSHR antibody also stained skin tissue extensively, suggesting that the antibody stains more than just FSHR.

Discussion: The findings in this study may add accuracy to literature on extragonadal FSHR localization and warrants attention to the use of inadequate anti-FSHR antibodies to value the potential role of FSH/FSHR in postmenopausal disease.

KEYWORDS

follicle stimulating hormone receptor, extragonadal cells, antibodies, immunohistochemistry, control

Introduction

Extragonadal sites with a functional FSH receptor (FSHR) were identified in hepatocytes, adipocytes, vascular endothelial cells (EC), monocytes/macrophages, and osteoclasts (1–4). This provoked the hypothesis that the elevated follicle-stimulating hormone (FSH) levels across the menopausal transition, rather than the decline in estrogen levels, could play a role in the development of postmenopausal osteoporosis and cardiovascular disease (CVD) for which encouraging data have been published (1–4). Similarly, the enhanced development of abdominal aortic aneurysm (AAA), a dilatation of the aorta which can be life-threatening

upon rupture (5), in postmenopausal women has been attributed to the decrease of serum estrogen (6, 7). However, the effect of hormonal replacement therapy on AAA in postmenopausal women was inconclusive (8–10) and perhaps another hormonal alteration during the menopause should be considered. We hypothesized that FSH may play a direct role in the onset/progression of AAA in postmenopausal women, potentially through the activation of EC and monocytes/macrophages. In our attempt to unravel which cells within the aorta express the FSHR on their cell surface, we used two different commercial anti-FSHR antibodies. However, we faced an unexpected lack of staining or unspecific staining, which we think is important to share.

Methods

Materials

Human premenopausal ovary, testis, and skin tissue without any abnormalities were obtained from the Department of Pathology [Amsterdam University Medical Centre (Amsterdam UMC)] for the current study. Tissue specimens were retrospectively collected from the Biobank Tissue Archive Pathology (2015_081), which was reviewed and approved by the Committee Review Biobanks of the Amsterdam UMC. All materials were coded and handled in accordance with the national ethical guidelines ("Code of Conduct for Health Research" developed by the Dutch Committee on Regulation of Health Research).

Immunohistochemistry

Of the multiple immunohistochemical (IHC) stainings conducted by the departments Medical Biochemistry and Pathology, the most promising procedure is outlined.

IHC was conducted on ovary and testis tissues that indisputably should express the FSHR (in granulosa and Sertoli cells, respectively) to validate the purchased antibodies. The formalin-fixed paraffin-embedded (FFPE) tissues were cut into 4-µm sections, mounted on coated slides, and dried overnight (37°C). The slides were deparaffinized with xylene (3 x 5min) and rehydrated with ethanol (100%, 100%, 96%, and 70%, 20 dips each). Endogenous peroxidase was quenched with 0.5% H_2O_2 in methanol (15min). Then, we assessed the most optimal antigen retrieval step by rinsing the slides in demineralized water and using three different solutions. Antigen retrieval with citric acid buffer pH 6.0 and Tris-EDTA buffer pH 9.0 were performed in a pressure cooker (20 min, 120°C). The third method was performed in 0.25% pepsin in 0.01 M HCl (10 min, 37°C). Hereafter, the slides were washed in phosphate-buffered saline with Tween (PBST) (1 x 3min). The sections were incubated with either the primary mouse monoclonal antibody directed against the human FSHR (clone FSHR/1400, NSJ Bioreagents; unclear which part of the FSHR it recognizes) or the primary rabbit anti-FSHR polyclonal antibody (MBS178821, MyBioSource; raised against the C18-N187 peptide sequence) in Normal Antibody Diluent (ABD999, Immunologic). After washing with PBST (3x3min), the sections were incubated with the specific polymers Brightvision poly-HRP-anti mouse Ig or Brightvision poly-HRP-anti rabbit Ig (DPVR110HRP, Immunologic), respectively, as a 'secondary antibody'. Bright DAB (BS04-110, Immunologic) was used for visualization (8 min). The ovary tissue was incubated with inhibin-α (IC25-4065, Instruchemie) (1:25, 32min) with the Ventana Benchmark Ultra Instrument and visualized with the Ventana's OptiView DAB IHC detection kit. Skin tissue was pre-treated in Tris-EDTA buffer pH 9.0 and incubated with Cytokeratin17 (Ks.17.E3, NBP2-29421, Novus) (1:100, 60min). Hereafter, the sections were washed in running tap water, rinsed in demineralized water, counterstained with hematoxylin 1:5 (5min), and, for color development, washed in running tap water (5 min) to visualize cellular nuclei. The slides were dried at 59°C, dipped in xylene, and mounted in Pertex (00801, Histolab).

Skin tissue, not known to have FSHR expression, was used as negative control for tissue specificity. As negative control for unexpected staining by the Brightvision polymers as 'secondary antibody', sections of ovary, testis, and skin were incubated as described above, but omitting the primary anti-FSHR antibodies.

Results

Incubation of the ovary tissue with the monoclonal anti-FSHR antibody (1:100, 60 min/overnight, 37°C) revealed no staining of the granulosa cells with any of the three antigen retrieval methods. Subsequently, to enhance the chance of FSHR staining, we used the polyclonal anti-FSHR antibody as it may recognize multiple epitopes (11). From all three antigen retrieval methods, boiling the sections in citric acid buffer pH 6.0 gave the most optimal staining (1:500, overnight, 4°C). Yet, in addition to granulosa cell staining, there was intense non-specific background staining. To diminish this, the antibody was further diluted (1:750, 1:1000, 1:1500), yet this reduced the entire staining instead of enhancing the specific/non-specific ratio. Granulosa cell staining disappeared at a dilution of 1:750 and beyond. We thus performed the FSHR staining on ovary, testis, and skin tissue with the polyclonal anti-FSHR antibody (1:500, citric acid buffer, overnight, 4°C) (Figures 1A2-3, B2-4, C2-3). The granulosa cells stained FSHR positive as expected (asterisk Figure 1A3). However, the severe additional non-specific cellular and extracellular matrix staining makes it difficult to trust the specificity of the antibody, especially when studying the extragonadal tissue, where one does not know which cells should be positive for the FSHR. Ovary tissue staining with an anti-inhibin antibody shows how granulosa cell staining could be when it is specific (Figure 1A4). Similar findings were obtained in testis tissue, where Sertoli cells were probably FSHR positive among additional positive cells in the seminiferous tubules (asterisks Figure 1B3-4). However, since the polyclonal antibody also stained the stroma and Leydig cells, the reliability of this antibody is questioned. Application of solely the secondary antibodies revealed no staining in ovary, testis, and skin tissue sections, revealing that all staining is caused by the anti-FSHR polyclonal antibody (Figures 1A1, B1, C1). In skin tissue, the monoclonal anti-FSHR antibody showed no staining at all; however, the polyclonal anti-FSHR antibody gave positive staining of the stroma, adipocytes, and hair follicles, which indicates abundant non-specific staining (Figure 1C2-3). While adipocytes have been reported to be able to express the FSHR (12),

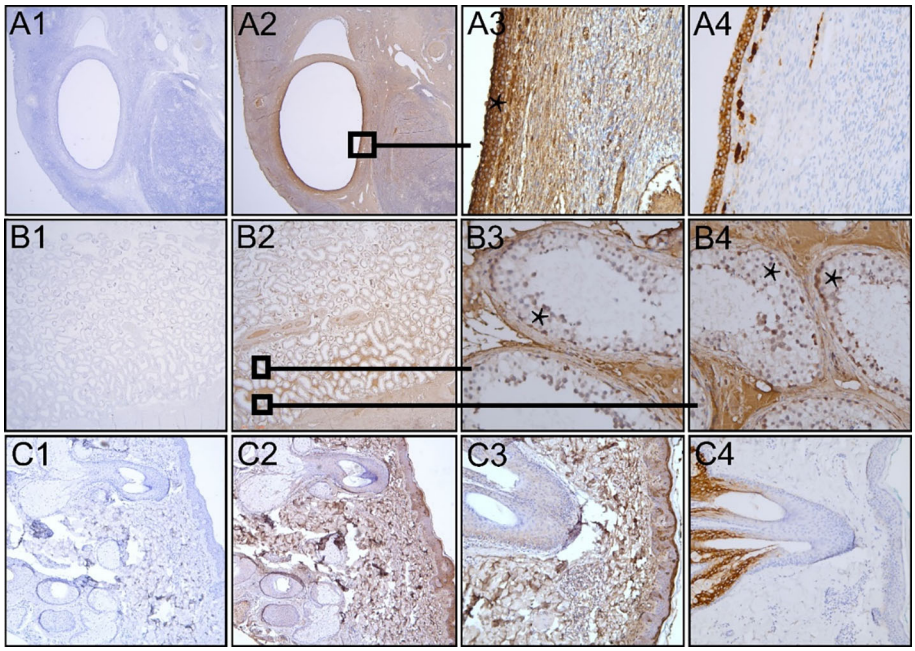

FIGURE 1
Immunohistochemical analysis of FFPE human premenopausal ovary, testis and skin tissue (**A–C**, respectively). Polyclonal anti-FSHR antibody was ommitted (A1, B1 and C1) or the sections were incubated with the antibody (A2-3, B2-4, C2-3 in 1:500 dilution). Sections that were not incubated with the anti-FSHR antibody only showed blue nuclear staining. The asterisks show FSHR positive (red/brown) granulosa cells (A3) and possibly FSHR positive Sertoli cells among other positive cells in the seminiferous tubules of the testis (B3, B4). Staining inhibin in ovary tissue reveals how specific granulosa staining can be (A4). Staining of skin tissue with anti-cytokeratin 17 antibody shows specific staining of a hair follicle with its sebaceous gland (C4), as opposed to the aspecific staining throughout the skin tissue section by the anti-FSHR antibody. Magnification: Panels A1-2, B1-2, and C1-2 12.5x; Panels A3-4, B3-4, and C3-4 200x; Panel C4 100x.

the stroma and hair follicles should not. Specific staining in skin tissue is demonstrated with the anti-cytokeratin 17 antibody, which shows a positive hair follicle and sebaceous gland, as expected (Figure 1C4). In conclusion, the two anti-FSHR antibodies could either not detect the FSHR or recognized more than just the FSHR.

Discussion

We aimed to identify FSHR-bearing cells within the aortic wall, through which FSH may affect AAA onset/progression in postmenopausal women. Exploring this hypothesis, we conducted IHC staining with two anti-FSHR antibodies on positive/negative control tissues for validation. The monoclonal anti-FSHR antibody did not perform in its ability to identify the FSHR in ovary or testis. The polyclonal anti-FSHR antibody stained the granulosa cells and possibly Sertoli cells, yet the additional staining of the other cells/extracellular matrix was equally intense. Since also in the skin tissue, which is devoid of known FSHR expression, staining was observed, we doubt the specificity of the polyclonal antibody. With both antibodies we had observed occasional positive macrophages, EC and smooth muscle cells in our aorta sections (obtained from anonymous donors, data not shown), which is uncertain if this is true FSHR localization and thus relevant. The reason to bring our findings to light is to add accuracy to literature, as the use of non-specific anti-FSHR staining jeopardizes the interpretation of FSHR localization in extragonadal tissues.

Various anti-FSHR antibodies have been used to study extragonadal FSHR protein expression and localization (1–4, 12–17). Chrusciel et al. summarized some commonly (and currently unavailable) used antibodies in extragonadal FSHR research (18). Hybridoma FSH323, validated by positive IHC staining of granulosa and Sertoli cells, is commercially unavailable (13, 14, 17). Interestingly, two groups that used FSH323-derived antibodies showed positive controls in their manuscript but obtained different results. Stilley et al. detected positive staining in human umbilical cord venous EC (14), whereas Stelmaszewska et al. did not and also did not find FSHR mRNA transcripts in EC (17). Another anti-FSHR antibody from Abcam used in extragonadal FSHR research detected the presence of FSHR in human hepatocytes (3) and adipose tissue (12), which was validated using negative/positive IHC controls. However, without stating the catalogue number, it is unclear which antibody was used. Perhaps it was the unavailable rabbit polyclonal antibody ab150557, shown to be specific to FSHR and raised against an unspecified N-terminal peptide, that was expected to identify the canonical FSHR and short variant of FSHR (19), or three other currently available anti-FSHR antibodies by Abcam (1): ab113421 (generated against amino acid sequence 278-327 of the extracellular domain just prior to the transmembrane domain), (2) ab137695 (recognizing the cytoplasmic C-terminal amino acid sequence 631-695), and (3) ab75200 (unclear which part of the FSHR it should recognize). Antibody ab113421 may not recognize the FSHR short variant (lacking exon 9), which is reported in some extragonadal cells (1, 14), because this FSHR isoform misses amino acids 224–285,

which in part overlaps with the peptide that is used to generate these antibodies. Although in a comparison paper between various anti-FSHR antibodies, the sc-13935 anti-FSHR antibody from Santa Cruz Biotechnology does not seem to be specific for the human FSHR (20), the antibody has been shown to be specific in another study (19). However, this antibody seems to be no longer available to repeat the experiments.

A potential explanation for the polyclonal antibody non-specificity may be that it was tested for Western blotting, while not being optimized for IHC in FFPE tissues. Yet, antibodies validated for Western blotting often perform well in IHC (21). The polyclonal anti-FSHR antibody MBS178821 that we used was raised against the C18-N187 amino acid sequence, and should in theory recognize both the full length and short FSHR variant (Figure 2). However, this stretch of amino acids contains multiple beta strands and leucine-rich repeat domains (Figure 2) (22), forming a 3D structure, that is quite common in many other proteins (23), including the receptors for the other gonadotropins (22), and possibly explains the additional staining.

Since the concept of extragonadal FSHR expression is interesting to pursue in light of postmenopausal disease, future FSHR research should include control IHC stainings, information on the part against which the FSHR antibody is raised, and the antibodies' catalogue numbers, which are essential to establish the validity of extragonadal FSHR expression.

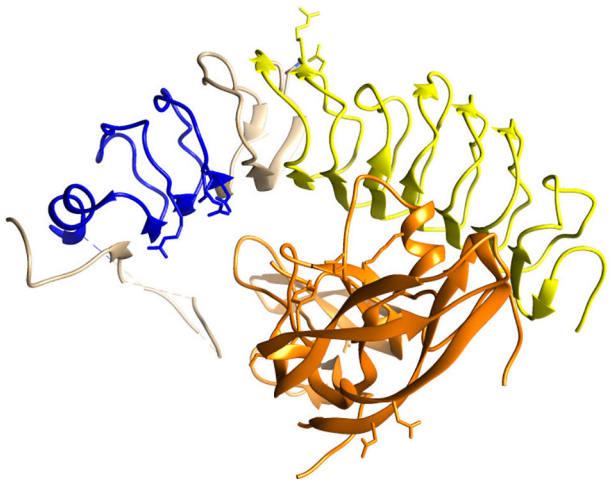

FIGURE 2
Crystallographic image of the extracellular domain of the FSHR (blue, beige, yellow) folding over its ligand FSH (orange), adapted from Jiang et al. (22). In yellow the beta strands/leucine-rich repeat domains in amino acid stretch C18-N187 are highlighted, against which the polyclonal anti-FSHR antibody MBS178821 is raised. The blue ribbon represent the amino acids that exon 9 codes for, which lacks in the short FSHR variant.

Data availability statement

The original contributions presented in the study are included in the article/supplementary material. Further inquiries can be directed to the corresponding author.

Ethics statement

The studies involving human participants were reviewed and approved by Committee Review Biobanks of the Amsterdam University Medical Centre. Written informed consent for participation was not required for this study in accordance with the national legislation and the institutional requirements.

Author contributions

VT and VW contributed to the concept of the work. VT and GH performed the immunohistochemical stainings. GH, CS-H, and VW contributed to the evaluation of the stainings. KK contributed to designing the crystallographic image. VT wrote the first draft of the manuscript and was supported by VW in the writing process. All authors contributed to the article and approved the submitted version.

Funding

This work is financed by the Ministry of Economic Affairs by means of the Private-Public-Partnership Allowance made available by the Top Sector Life Sciences & Health to stimulate public-private Partnerships and by funding of Amsterdam UMC (project NR4Ants). The study was supported by the AMC Foundation.

Conflict of interest

The authors declare that the research was conducted in the absence of any commercial or financial relationships that could be construed as a potential conflict of interest.

Publisher's note

References

1. Robinson LJ, Tourkova I, Wang Y, Sharrow AC, Landau MS, Yaroslavskiy BB, et al. FSH-receptor isoforms and FSH-dependent gene transcription in human monocytes and osteoclasts. *Biochem Biophys Res Commun* (2010) 394(1):12–7. doi: 10.1016/j.bbrc.2010.02.112

2. Sun L, Peng Y, Sharrow AC, Iqbal J, Zhang Z, Papachristou DJ, et al. FSH directly regulates bone mass. *Cell* (2006) 125(2):247–60. doi: 10.1016/j.cell.2006.01.051

3. Song Y, Wang ES, Xing LL, Shi S, Qu F, Zhang D, et al. Follicle-stimulating hormone induces postmenopausal dyslipidemia through inhibiting hepatic cholesterol metabolism. *J Clin Endocrinol Metab* (2016) 101(1):254–63. doi: 10.1210/jc.2015-2724

4. Liu P, Ji Y, Yuen T, Rendina-Ruedy E, DeMambro VE, Dhawan S, et al. Blocking FSH induces thermogenic adipose tissue and reduces body fat. *Nature* (2017) 546 (7656):107–12. doi: 10.1038/nature22342

5. Kuivaniemi H, Ryer EJ, Elmore JR, Tromp G. Understanding the pathogenesis of abdominal aortic aneurysms. *Expert Rev Cardiovasc Ther* (2015) 13(9):975–87. doi: 10.1586/14779072.2015.1074861

6. Villard C, Swedenborg J, Eriksson P, Hultgren R. Reproductive history in women with abdominal aortic aneurysms. *J Vasc Surg* (2011) 54(2):341–5. doi: 10.1016/j.jvs.2010.12.069

7. Makrygiannis G, Courtois A, Drion P, Defraigne JO, Kuivaniemi H, Sakalihasan N. Sex differences in abdominal aortic aneurysm: The role of sex hormones. *Ann Vasc Surg* (2014) 28(8):1946–58. doi: 10.1016/j.avsg.2014.07.008

8. Lederle FA, Larson JC, Margolis KL, Allison MA, Freiberg MS, Cochrane BB, et al. Abdominal aortic aneurysm events in the women's health initiative: Cohort study. *BMJ* (2008) 337:a1724. doi: 10.1136/bmj.a1724

9. Hsia J, Criqui MH, Rodabough RJ, Langer RD, Resnick HE, Phillips LS, et al. Estrogen plus progestin and the risk of peripheral arterial disease: The women's health initiative. *Circulation* (2004) 109(5):620–6. doi: 10.1161/01.CIR.0000115309.63979.92

10. Hsia J, Criqui MH, Herrington DM, Manson JE, Wu L, Heckbert SR, et al. Conjugated equine estrogens and peripheral arterial disease risk: The women's health initiative. *Am Heart J* (2006) 152(1):170–6. doi: 10.1016/j.ahj.2005.09.005

11. Lipman NS, Jackson LR, Trudel LJ, Weis-Garcia F. Monoclonal versus polyclonal antibodies: distinguishing characteristics, applications, and information resources. *ILAR J* (2005) 46(3):258–68. doi: 10.1093/ilar.46.3.258

12. Liu XM, Chan HC, Ding GL, Cai J, Song Y, Wang TT, et al. FSH regulates fat accumulation and redistribution in aging through the Gαi/Ca(2+)/CREB pathway. *Aging Cell* (2015) 14(3):409–20. doi: 10.1111/acel.12331

13. Radu A, Pichon C, Camparo P, Antoine M, Allory Y, Couvelard A, et al. Expression of follicle-stimulating hormone receptor in tumor blood vessels. *N Engl J Med* (2010) 363(17):1621–30. doi: 10.1056/NEJMoa1001283

14. Stilley JA, Guan R, Duffy DM, Segaloff DL. Signaling through FSH receptors on human umbilical vein endothelial cells promotes angiogenesis. *J Clin Endocrinol Metab* (2014) 99(5):E813–20. doi: 10.1210/jc.2013-3186

15. Cui H, Zhao G, Liu R, Zheng M, Chen J, Wen J. FSH stimulates lipid biosynthesis in chicken adipose tissue by upregulating the expression of its receptor FSHR. *J Lipid Res* (2012) 53(5):909–17. doi: 10.1194/jlr.M025403

16. Ji Y, Liu P, Yuen T, Haider S, He J, Romero R, et al. Epitope-specific monoclonal antibodies to FSHβ increase bone mass. *Proc Natl Acad Sci U S A.* (2018) 115(9):2192–7. doi: 10.1073/pnas.1718144115

17. Stelmaszewska J, Chrusciel M, Doroszko M, Akerfelt M, Ponikwicka-Tyszko D, Nees M, et al. Revisiting the expression and function of follicle-stimulation hormone receptor in human umbilical vein endothelial cells. *Sci Rep* (2016) 6:37095. doi: 10.1038/srep37095

18. Chrusciel M, Ponikwicka-Tyszko D, Wolczynski S, Huhtaniemi I, Rahman NA. Extragonadal FSHR expression and function–is it real? *Front Endocrinol (Lausanne).* (2019) 10(32). doi: 10.3389/fendo.2019.00032

19. Patel H, Bhartiya D. Testicular stem cells express follicle-stimulating hormone receptors and are directly modulated by FSH. *Reprod Sci* (2016) 23(11):1493–508. doi: 10.1177/1933719116643593

20. Moeker N, Peters S, Rauchenberger R, Ghinea N, Kunz C. Antibody selection for cancer target validation of FSH-receptor in immunohistochemical settings. *Antibodies* (2017) 6(4):15. doi: 10.3390/antib6040015

21. Lund-Johansen F, Browning MD. Should we ignore western blots when selecting antibodies for other applications? *Nat Methods* (2017) 14(3):215. doi: 10.1038/nmeth.4192

22. Jiang X, Fischer D, Chen X, McKenna SD, Liu H, Sriraman V, et al. Evidence for follicle-stimulating hormone receptor as a functional trimer. *J Biol Chem* (2014) 289 (20):14273–82. doi: 10.1074/jbc.M114.549592

23. Matsushima N, Takatsuka S, Miyashita H, Kretsinger RH. Leucine rich repeat proteins: Sequences, mutations, structures and diseases. *Protein Pept Lett* (2019) 26 (2):108–31. doi: 10.2174/0929866526666181208170027

frontiers | Frontiers in Endocrinology

TYPE Original Research
PUBLISHED 20 February 2023
DOI 10.3389/fendo.2023.1102634

OPEN ACCESS

EDITED BY
Francoise Koumanov,
University of Bath, United Kingdom

REVIEWED BY
Wei Huang,
Dongguan Tungwah Hospital, China
Xinyu Zhang,
Monash University, Australia

*CORRESPONDENCE
Xiangdong Yang
yxd@email.sdu.edu.cn

SPECIALTY SECTION
This article was submitted to Diabetes: Molecular Mechanisms, a section of the journal Frontiers in Endocrinology

RECEIVED 19 November 2022
ACCEPTED 13 January 2023
PUBLISHED 20 February 2023

CITATION
Yu K, Li S, Wang C, Zhang Y, Li L, Fan X, Fang L, Li H, Yang H, Sun J and Yang X (2023) APOC1 as a novel diagnostic biomarker for DN based on machine learning algorithms and experiment. *Front. Endocrinol.* 14:1102634. doi: 10.3389/fendo.2023.1102634

APOC1 as a novel diagnostic biomarker for DN based on machine learning algorithms and experiment

Kuipeng Yu[1,2,3], Shan Li[1], Chunjie Wang[1,3], Yimeng Zhang[1], Luyao Li[1], Xin Fan[1], Lin Fang[1], Haiyun Li[4], Huimin Yang[5], Jintang Sun[3] and Xiangdong Yang[1,2]*

[1]Department of Nephrology, Qilu Hospital of Shandong University, Jinan, Shandong, China, [2]Department of Blood Purification, Qilu Hospital of Shandong University, Jinan, Shandong, China, [3]Laboratory of Basic Medical Sciences, Qilu Hospital of Shandong University, Jinan, Shandong, China, [4]Department of Geriatric Medicine, Qilu Hospital of Shandong University, Jinan, Shandong, China, [5]Department of General Practice, Qilu Hospital of Shandong University, Jinan, Shandong, China

Introduction: Diabetic nephropathy is the leading cause of end-stage renal disease, which imposes a huge economic burden on individuals and society, but effective and reliable diagnostic markers are still not available.

Methods: Differentially expressed genes (DEGs) were characterized and functional enrichment analysis was performed in DN patients. Meanwhile, a weighted gene co-expression network (WGCNA) was also constructed. For further, algorithms Lasso and SVM-RFE were applied to screening the DN core secreted genes. Lastly, WB, IHC, IF, and Elias experiments were applied to demonstrate the hub gene expression in DN, and the research results were confirmed in mouse models and clinical specimens.

Results: 17 hub secretion genes were identified in this research by analyzing the DEGs, the important module genes in WGCNA, and the secretion genes. 6 hub secretory genes (APOC1, CCL21, INHBA, RNASE6, TGFBI, VEGFC) were obtained by Lasso and SVM-RFE algorithms. APOC1 was discovered to exhibit elevated expression in renal tissue of a DN mouse model, and APOC1 is probably a core secretory gene in DN. Clinical data demonstrate that APOC1 expression is associated significantly with proteinuria and GFR in DN patients. APOC1 expression in the serum of DN patients was $1.358\pm0.1292\mu g/ml$, compared to $0.3683\pm0.08119\mu g/ml$ in the healthy population. APOC1 was significantly elevated in the sera of DN patients and the difference was statistical significant ($P > 0.001$). The ROC curve of APOC1 in DN gave an AUC = 92.5%, sensitivity = 95%, and specificity = 97% ($P < 0.001$).

Conclusions: Our research indicates that APOC1 might be a novel diagnostic biomarker for diabetic nephropathy for the first time and suggest that APOC1 may be available as a candidate intervention target for DN.

KEYWORDS

DN, biomarker, diagnostic, machine learning algorithms, APOC1

1 Introduction

Diabetic nephropathy (DN) is one of the most serious complications of diabetes and 45% of DN patients will progress to end-stage renal disease (ESRD) (1), which affects the quality of life and causes a substantial economic burden to society (2). The gold standard for diabetic kidney diagnosis remains renal pathology, but renal puncture biopsy methods are invasive for DN patients. In recent years, some biological signatures have been detected for the diagnosis of DN, such as KIM-1, NGAL, suPAR, YKL-40, and so on (3–5). However, there are no valid and reliable biological markers for the diagnosis of DN.

GEO Database is a database established by the National Centre or Biotechnology Information (NCBI) to determine the critical genes and underlying molecular mechanisms for disease pathogenesis and progression (6). Recently, bioinformatics and machine learning methods extensively employed in biomarker screening by using the GEO database (7–9). What's more, secreted proteins have significance in course of biological activity, specifically in the diagnosis of diseases and future target therapies (10, 11). This provides the opportunity to detect novel plasma markers for the recognition of patients with DN.

The research aims to reveal potential predictor plasma biomarkers of DN by data mining, which will generate novel insights into the mechanisms of DN pathogenesis and provide directions for future research into alternative therapies. If the potential predictor plasma biomarkers accurately predict the probability of DN occurring, the disease may be treated with prevention and intervention at an early stage.

2 Materials and methods

2.1 DEGs data processing

Expression profiles of GSE96804 mRNA were obtained from the GEO database (GPL17586 platform, Affymetrix Human Transcriptome Array 2.0) (12). In total, 61 tissue biopsies, 41 tissue samples from DN tissue samples and 20 from the normal, were obtained from the National Clinical Research Center of Kidney Diseases, Jinling Hospital, Nanjing University School of Medicine. "Limma" packaged (13) in R software was used to process data and the "ggplot2" (14), "Pheatmap" packages for drawing of figures. DEGs were identified with |log Fold Change | ≥1 & adj P Val < 0.05.

2.2 GO and KEGG enrichment analysis

GO analysis was conducted using the 'cluster Profiler' (15), 'GO plot', and 'ggplot2' packages for up- and down-regulated DEGs with altered DN and normal kidney tissue. The KEGG pathway enrichment analysis was completed by DEGs, and the figures were generated with the packages "ggplot2" and "enrich plot".

2.3 WGCNA network construction and data analysis

Gene co-expression networks of DN patients were constructed based on the GSE96804 microarray dataset by the "WGCNA" package (16). The soft-thresholding power was five when 0.9 was used as the correlation coefficient threshold, and 50 was chosen as the minimum number of genes in modules. To merge possible similar modules, we defined 0.25 as the threshold for cutting height. A heatmap between the correlation between modules and DN was drawn, and the ME-brown gene module was the most related to DN.

2.4 Secreted genes download

729 secreted genes are available for the HPA database (https://www.proteinatlas.org). Venn diagram (https://bioinfogp.cnb.csic.es/tools/venny/index.html) demonstrates the genes which are commonly associated with the 3 datasets (DEGs, WCANA, and secreted to blood genes). In the common genes, we further filtered the core secretory genes by using different machine algorithms (Lasso and SVM-RFE algorithm).

2.5 Lasso algorithm and SVM-RFE algorithm data analysis

Lasso logistic regression is a machine learning process that determines covariates by seeking the λ value that minimizes the classification error (17). The "glmnet" package was utilized to structure the LASSO model. Meanwhile, With SVM-RFE, an approach for building machine training on support vector machines, we detect the optimal variables by decimating the feature vectors created by svm (18). Recursive features of differential genes were acquired and erased by running the "e1071 package", and the research was conducted by applying the Lapply function to sort all the features of the training set. Ultimately, the error rate is minimized and the hub gene is eventually obtained.

2.6 Presentation of hub genes

The common genes derived from these two machine algorithms are demonstrated by the Venn diagram, heat maps, line plots, and deviation plots.

2.7 Biomarker expression validation and clinical relevance

As illustrated in our previous research, the expression of biomarkers was confirmed by using the Nephroseq database (https://www.nephroseq.org/resource/main.html) (19). Meanwhile, by using the database, biomarker expression and renal function data were analyzed for correlation.

2.8 Animal experiments

The STZ-induced DN mouse model was elucidated in detail in our previous research (19), and among them, there were 5 mice in the control group (Ctrl) and 5 mice in the diabetic nephropathy group (DN). Following the successful construction of the DN mouse model, we conduct the collection of experimental animals. The research was approved by the Ethics Committee of Qilu Hospital, Shandong University (Approval No: KYLL-2020 (KS)-030).

2.9 Western blot

The experimental operation of Western Blot was as described (20). The main antibodies are described as follows: APOC1(1:2000, Abcam, USA), GAPDH (1:4000; Proteintech Group, China).

2.10 IHC and IF

Immunohistochemistry and immunofluorescence of kidney tissue sections as previously described (21) The main antibodies are described as follows: APOC1(1:200, Abcam, USA), Goat anti-Rabbit IgG Dy-Light 488 (1:500; Abbkine Scientific Company, USA).

2.11 ELISA experiment

We have collected serum specimens from DN patients and healthy. Detection of biomarkers in serum with commercial Elisa kits, ELISA method, in DN patients and healthy. Follow the experimental steps in the Elisa kit instructions to detect the expression level of the marker in the serum (Apolipoprotein CI ELISA kit, Abcam, ab108808, USA).

2.12 ROC

The "PROC" package was used to construct Receiver Operating Characteristic (ROC) curves to characterise hub gene to evaluate the diagnostic value of DN, as previously described (19).

2.13 Statistical analyses

Data are expressed as mean ± SEM. Software R4.1.2 was used to draw the research Figures. GraphPad Prism 6.01 software was used in statistical data analysis. Between the two groups, Student's t-test was used if the data matched the normal distribution, and the Kruskal-Wallis test was used for non-normally distributed data. For statistical analysis of the correlation between the two characters, the Spearman test was applied. Statistical significance was set at $P < 0.05$, $^{*}P < 0.05$, $^{**}P < 0.01$, $^{***}P < 0.001$.

3 Results

3.1 Characterisation of genes for DN using GSE96804 microarray data

The experimental design was illustrated in Figure 1. Compared to transcripts of controls, 504 DEGs were identified by patients, respectively. Our analysis of the results is summarized in the volcano plots, which reflect that 257 genes are up-regulated in DN and 247 genes are down-regulated in DN (Figure 2A). In the illustration, red represents up-regulated and green indicates down-regulated genes. Results demonstrated two clusterings of this data, namely the clusters Control and DN which represents the control group and the DN patients in the heatmap (Figure 2B). Analysis of GO in DEGs determined shared GO terms linked to organic acid catabolic processes, and extracellular matrix organization (Figure 2C). Enrichment pathways to KEGG are

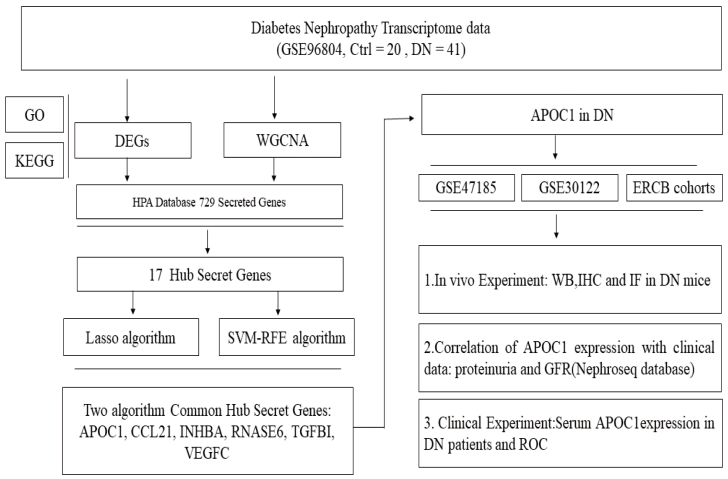

FIGURE 1
Research flow chart.

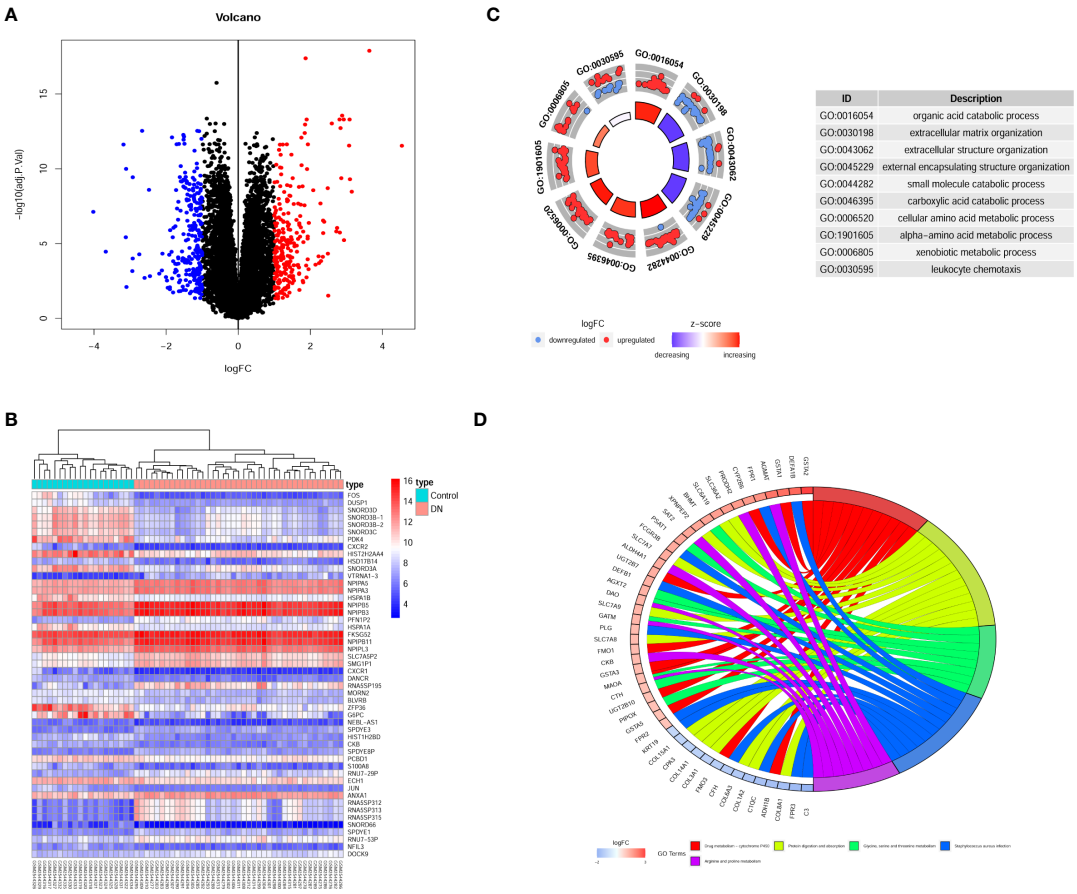

FIGURE 2
Gene recognition and function enrichment of DEGs in GSE96804 database. **(A)** Volcano-map of DEGs (DEGs: |log2FC| > 1, adjusted P<0.05). **(B)** Heatmap of the DEGs. **(C)** Circle map of GO enrichment analysis. **(D)** Circos map of the KEGG enrichment analysis. DEGs, differentially expressed genes; GO, Gene Ontology; KEGG, Kyoto Encyclopedia of Genes and Genomes.

associated with the following: Arginine and proline metabolism, Glycine, serine and threonine metabolism, and Protein digestion and absorption (Figure 2D).

3.2 Hub gene screening for DN by WGCNA

The network topologies for the analysis of various soft threshold powers were identified and the choice of 11 to structure the joint expression network was considered reasonable (Figure 3A). The similarity in gene expression is ascertained by pair-weighting correlation metrics, and clustering is performed using topological overlapping metrics. Gene modules are marked with color at the bottom (Figure 3B). Pearson correlation coefficients for ME and disease were calculated for all modules demonstrating the intimate characteristics of the modules with DN. ME-brown (R = 0.53, P = 1e-05) potentially represented particular features of DN patients (Figure 3C). Furthermore, we observed that the correlation coefficient between the GS of DN and the module members was high in brown modules (R = 0.47, = 3.1e-21, Figure 3D). There was potential biological relevance to heightened co-expression of the genes in the ME-brown module.

3.3 Screening of hub secretory genes for DN by machine algorithms

Venn diagram illustrating common genes across algorithms, filtering for 17 potential secretory genes that may be functionally essential in DN (Figure 4A). By using 2 machine algorithms, Lasso and SVM-RFE, to recognize the characteristic genes of DN. The 17 secreted genes are displayed in Figure 4B. By using 2 machine algorithms, LASSO and SVM-RFE, characteristic genes of the DN were identified again. The Lasso algorithm filtered out 9 potential hub genes (Figures 4C, D), while the SVM algorithm filtered out 7 potential hub genes (Figures 4E, F).

3.4 Expression of 6 secretory genes in DN

The Venn diagram illustrates 2 machine algorithms obtained common 6 hub secretory genes (APOC1, CCL21, INHBA, RNASE6, TGFBI, VEGFC, Figure 5A). Furthermore, the expression of the six genes in the GSE96804 cohort is illustrated by heatmap, line graphs, and deviation plots (Figures 5B–D). The results revealed that 6 secretory gene generators screened for the research were significantly more over-expressed in the diabetic nephropathy population.

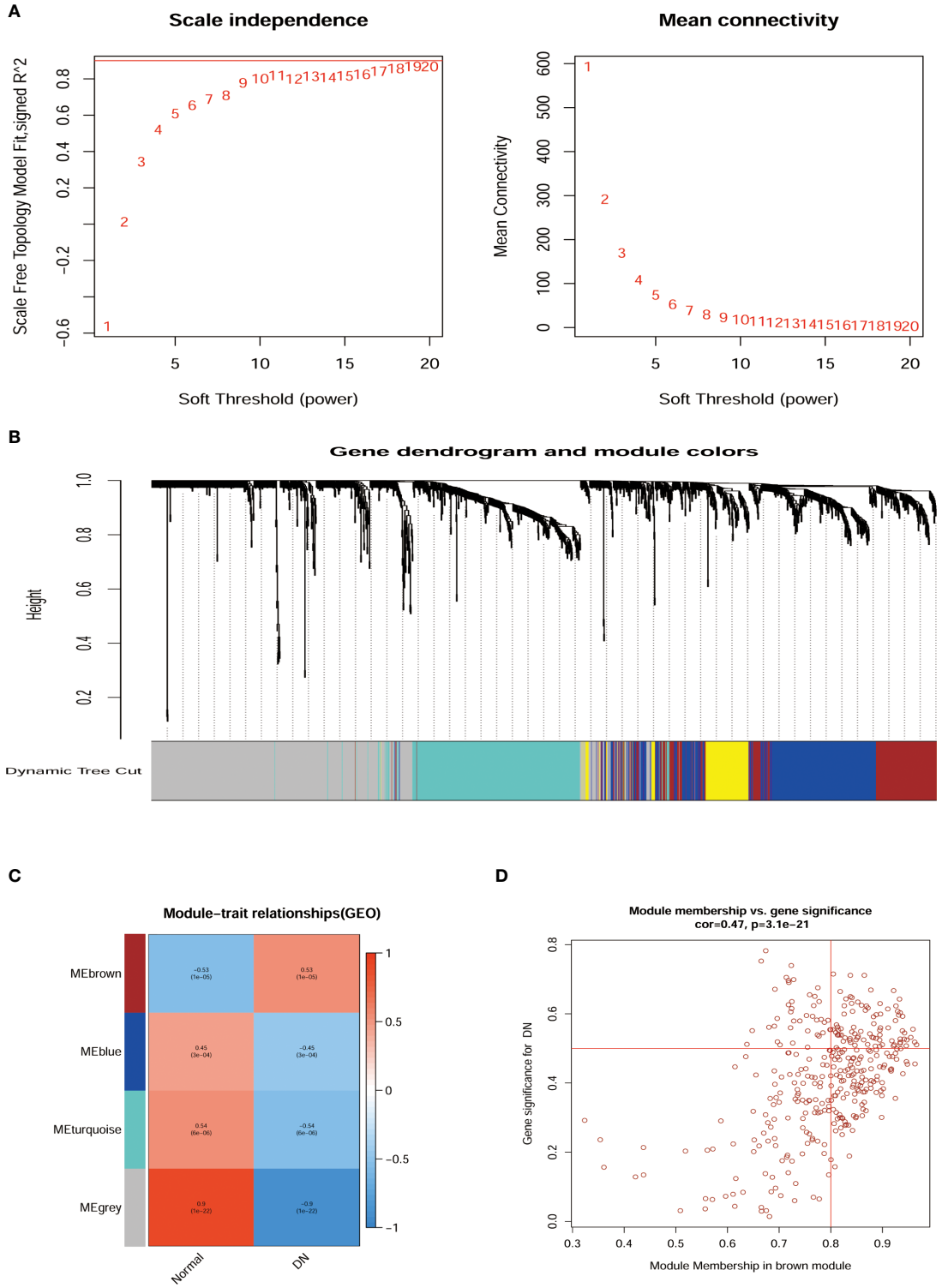

FIGURE 3
Relationship of hub gene modules and DN phenotypes by WGCNA. **(A)** Network topology analysis at different soft threshold powers and network connectivity validation at different weighting factors. **(B)** Cluster Dendrogram of modules colors were constructed with all the differentially expressed genes. **(C)** MEs correlated with diagnosis for DN. **(D)** Scatterplots of gene significance for DN Module membership in brown module. ME, Module eigengenes; WGCNA, weighted gene co-expression network analysis.

3.5 Associated expression of APOC1 in DN

APOC1 expression is elevated in patients with diabetic nephropathy through multiple cohorts of the experimental GEO database (GSE96804, GSE47185, GSE30122, and the ERCB Nephrotic Syndrome Tublnt cohorts in Nephroseq database, Figures 6A–D). ApoC1 expression was elevated in the kidney tissue of mice with DN by Western blot ($P < 0.05$, Figure 6E). What's more, we revealed that APOC1 was expressed predominantly in the glomerulus by immunohistochemistry of mouse kidney tissue

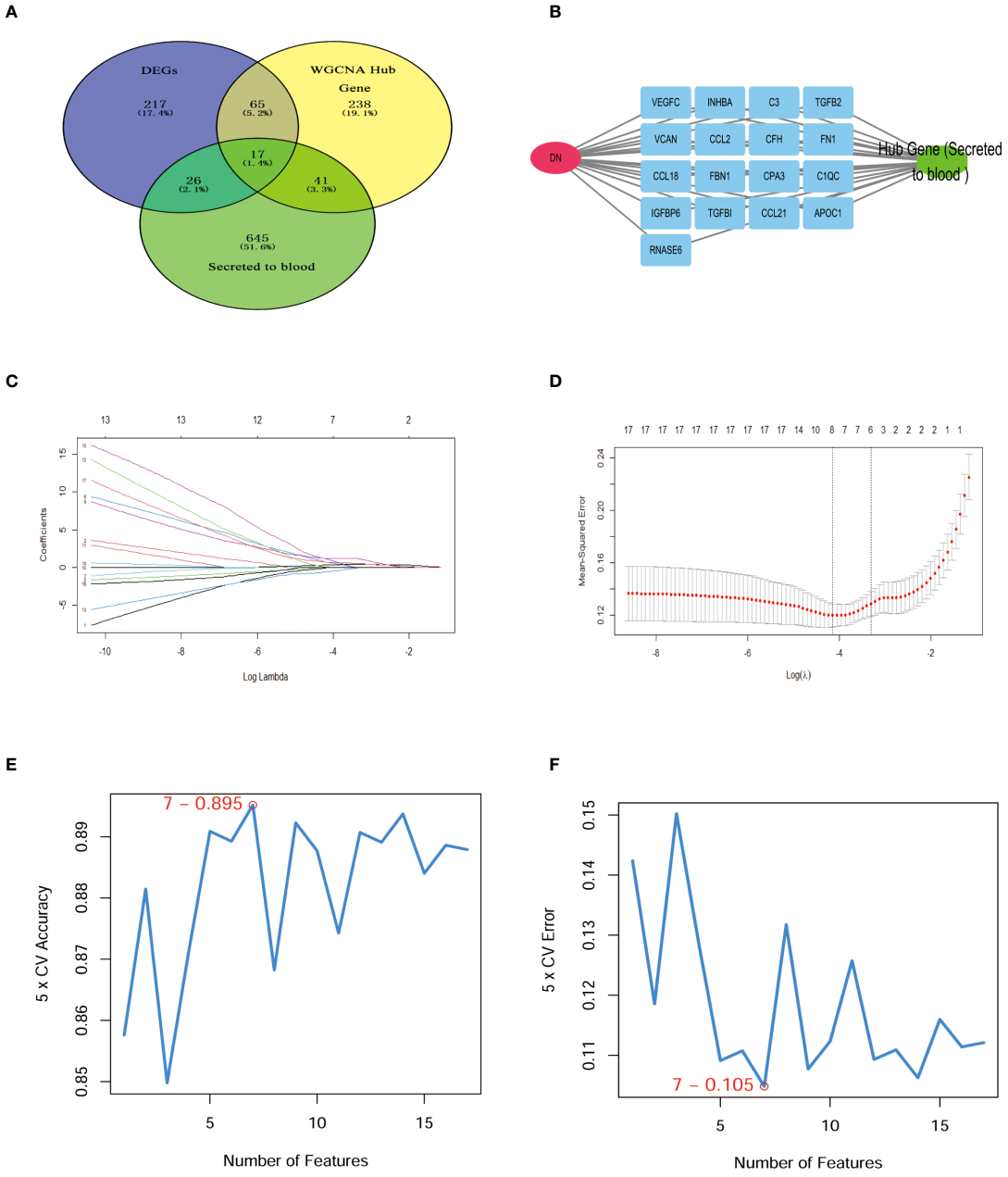

FIGURE 4
Hub secret genes selection in DN. **(A)** Venn diagram demonstrating the hub genes for the different algorithms. (DEGs, WCANA, and secreted to blood genes). **(B)** 17 characteristically secret genes in DN patients. **(C, D)**Biomarker secret genes were selected by Lasso algorithm from the 17 potential hub genes. **(E, F)** Biomarker secret genes were detected for DN by SVM-RFE algorithm from the 17 potential hub genes (the accuracy and the error rate of the SVM model). Lasso, Least absolute shrinkage and selection operator; SVM-RFE, support vector machine recursive feature elimination.

(Figure 6F). These measurements were confirmed by tissue immunofluorescence (Figure 6G).

3.6 Correlation of APOC1 expression with clinical databases

Correlations between APOC1 and the clinical information were validated by employing multiple cohorts from the Nephroseq database. Outcomes demonstrated the APOC1 expression was positively correlated with proteinuria in Schmid diabetes tubint cohorts ($R^2 = 0.515$, $P = 0.013$, Figure 7A). However, associations of APOC1 expression are negatively correlated with GFR in Woroniecka Diabetes Tublnt cohorts ($R^2 = 0.552$, $P = 0.014$, Figure 7B). Additionally, in ERCB Nephrotic Syndrome Tublnt cohorts, APOC1 expression was positively correlated with proteinuria ($R^2 = 0.632$, $P = 0.018$, Figure 7C).

3.7 Plasma expression of APOC1 in DN patients and ROC curve analysis

Altogether 20 healthy and 20 DN patients were enrolled in the research, and the Baseline details were presented in Table 1. Significantly, Elisa results demonstrated that APOC1 expression in

10.3389/fendo.2023.1102634

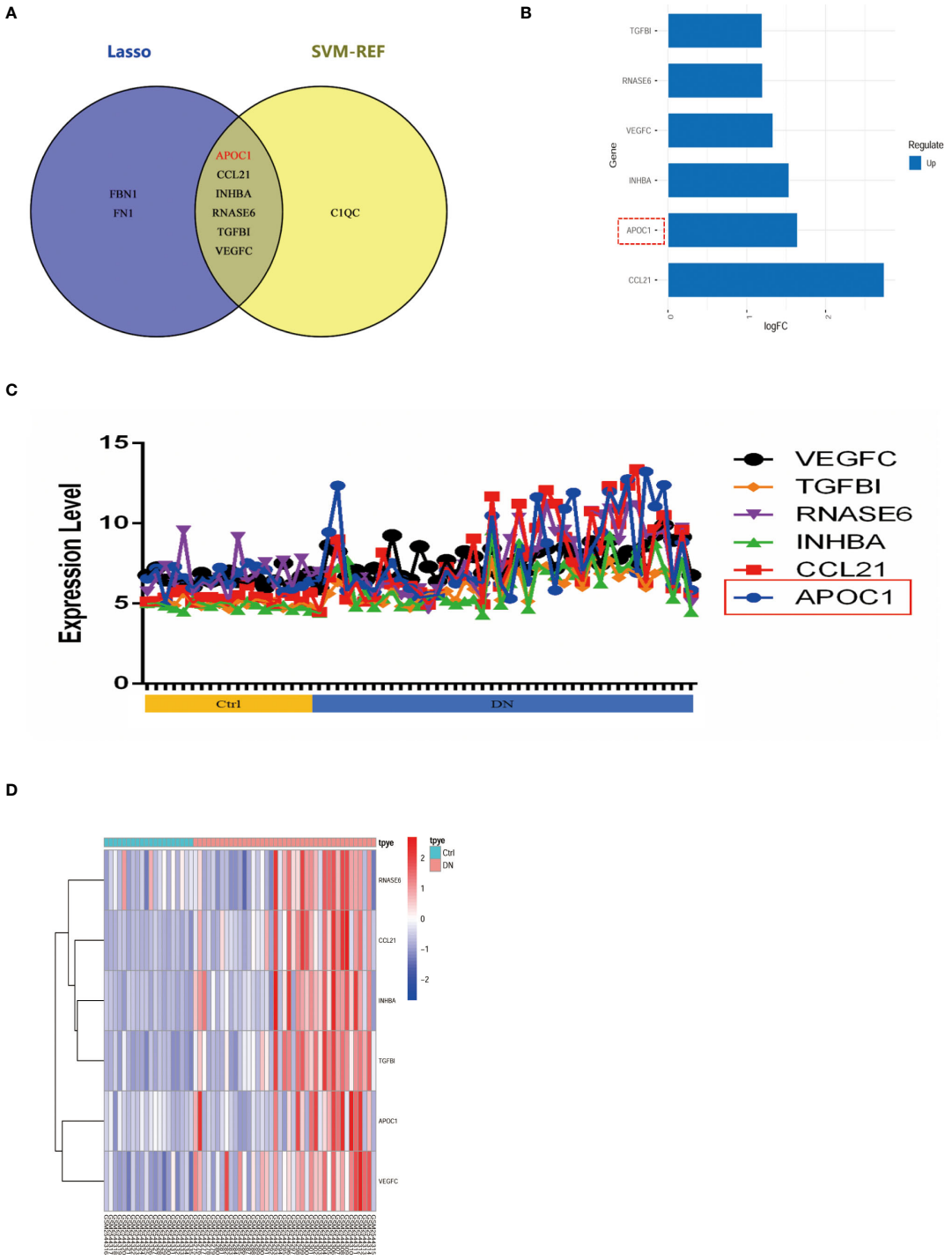

FIGURE 5
6 potential secretory genes were obtained in GSE96804 by machine algorithms. **(A)** The intersection of genes obtained by the two machine algorithms (SVM-RFE and Lasso algorithms). **(B)** Deviation plots showed the expression of six secreted genes in DN. **(C)** Folding line graph illustrates the different expression of 6 hub genes. **(D)** Heat plots revealed elevated expression of six secreted genes in DN.

the serum of DN patients was 1.358±0.1292μg/ml, compared to 0.3683±0.08119μg/ml in the healthy population (Figure 8A). APOC1 was significantly elevated in the sera of DN patients and the difference was statistical significant ($P > 0.001$). Furthermore, APOC1 diagnostic effectiveness for DN as demonstrated by ROC curves (AUC = 92.5%, sensitivity = 95%, and specificity = 97%, $P < 0.001$, Figure 8B).

4 Discussion

DN is considered to the most serious complication of diabetes and imposes a substantial financial burden on individuals and society (22). It is vital to diagnose DN early to improve the prognosis of patients with DN and reduce the financial burden (23). However, the most dominant clinical indicators for the

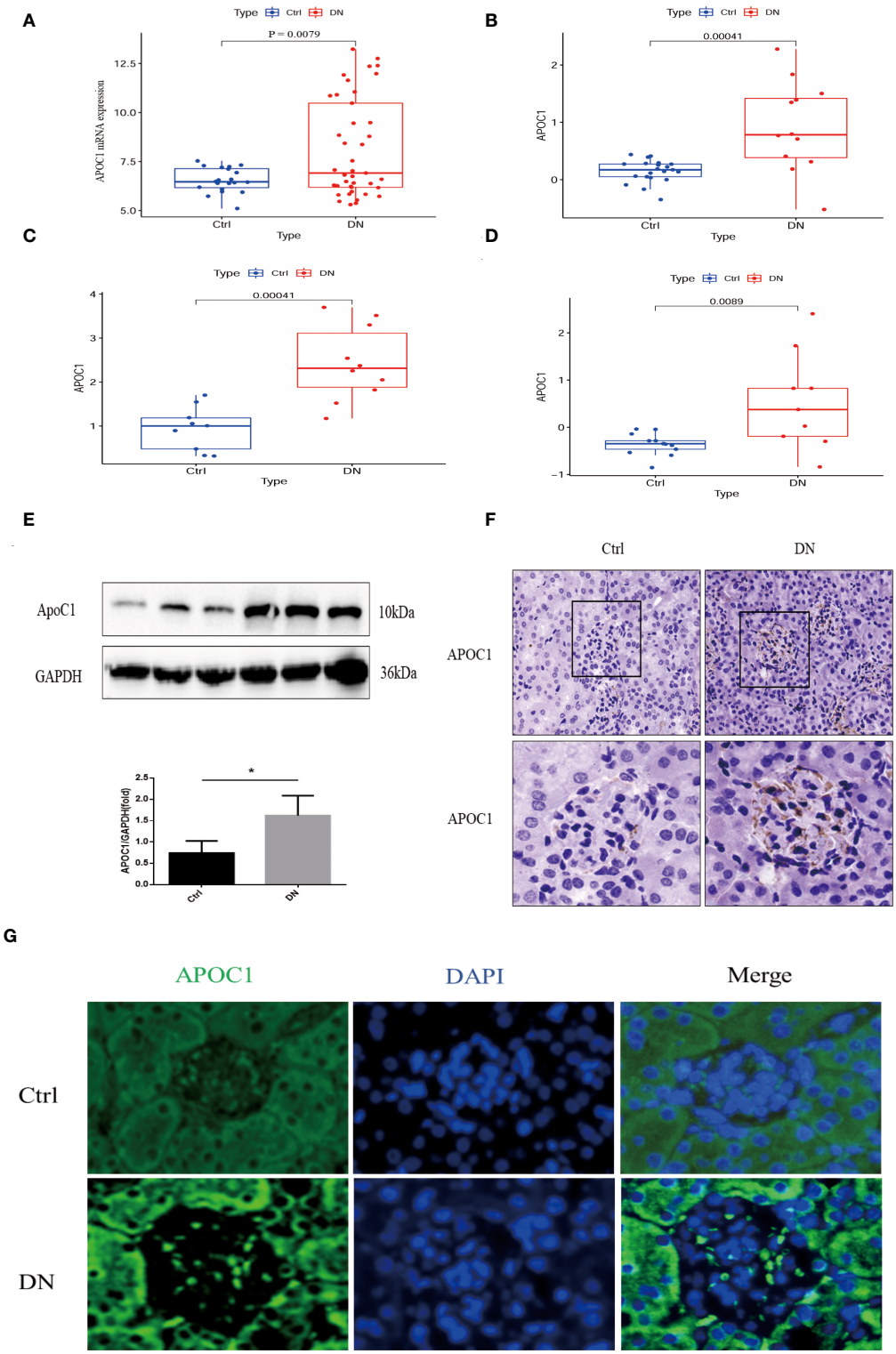

FIGURE 6
Exhibition of the expression of APOC1 in DN. **(A–D)** APOC1 manifested significantly higher expression in different cohorts of DN patients. [**(A)**: GSE96804, Ctrl=20, DN=41, **(B)** GSE47185, Ctrl=21, DN=12, **(C)** ERCB Nephrotic Syndrome Tublnt cohorts in Nephroseq database, Ctrl=9, DN=10, GSE 30122, Ctrl=13, DN=9]. **(E)** Representative Western Blot indicates APOC1 expression to be higher in different mice, Ctrl (n = 4) or DN (n = 4). **(F)** IHC reveals increased expression of APOC1 on glomeruli of mice with DN (Bar = 20 μm). **(G)** Representative protein immunofluorescence of APOC1 in the glomeruli of DN (Bar = 20 μm.). (Data presented as mean ± SEM, *P < 0.05).

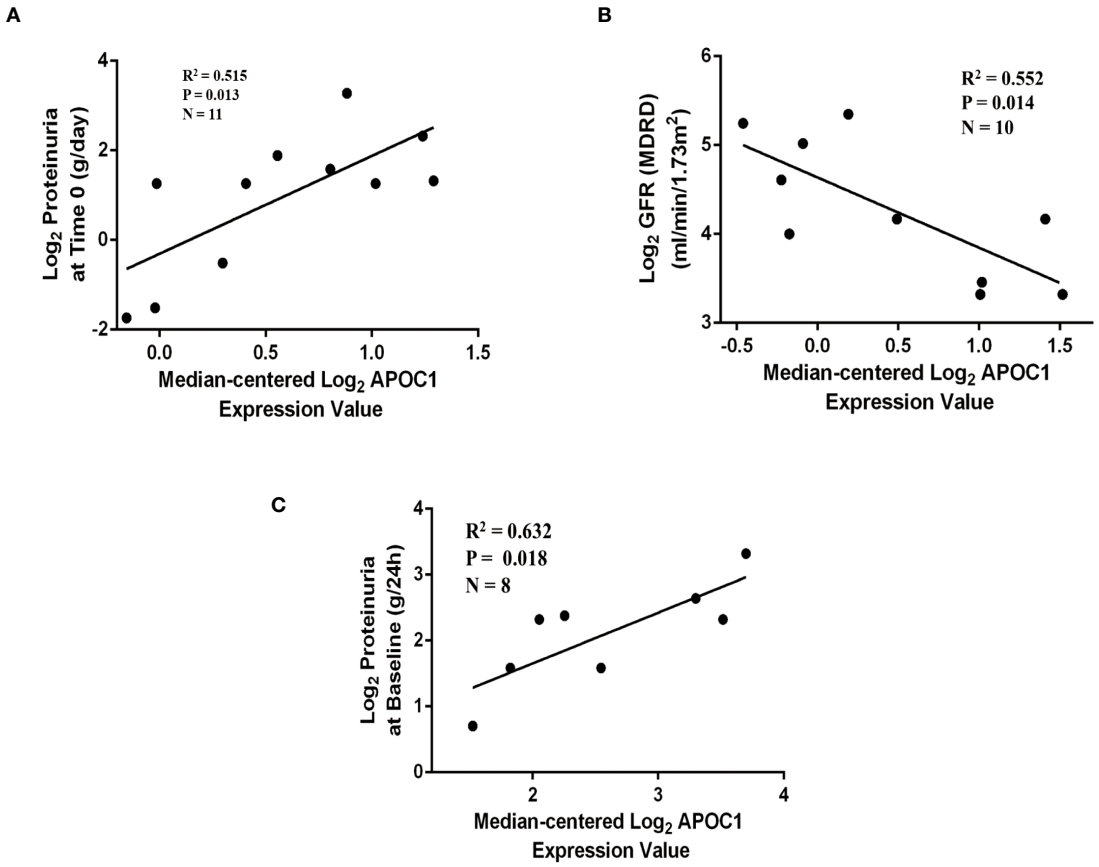

FIGURE 7
Correlation between APOC1 expression and proteinuria and GFR in Nephroseq database. **(A)** Correlation between APOC1 expression and proteinuria in Schmid diabetes tubint cohorts (R^2 = 0.515, P = 0.013). **(B)** Correlation between APOC1 expression and GFE in Woroniecka Diabetes Tublnt cohorts (R^2 = 0.552, P = 0.014). **(C)** Correlation between APOC1 expression and GFE in ERCB Nephrotic Syndrome Tublnt cohorts (R^2 = 0.632, P = 0.018).

diagnosis of DN are still UACR and eGFR, in clinical practice (24). Previous studies have demonstrated that damage to the kidney, such as endothelial damage, tubulointerstitial dilatation, and interstitial fibrosis, has already occurred before the appearance of albuminuria in patients with DN (25). The abnormalities in molecular markers usually precede the clinical symptoms of the disease (26, 27). Therefore, the urgent challenge is to identify suitable, stable, and easily detectable biomarkers for DN diagnosis.

TABLE 1 Baseline characteristics.

Characteristic	Ctrl (n = 20)	DN (n = 20)
Age (year)	46.10 ± 2.625	49.30 ± 3.361
Sex (Female/male)	11/9	7/13
SBP (mmHg)	122.9 ± 1.832	131.8 ± 5.333
DBP (mmHg)	70.70 ± 1.223	75.95 ± 2.300
eGFR (ml/min1.73m^2)	103.0 ± 5.345	106.4 ± 9.705
Cr (μmoI/L)	72.40 ± 3.438	82.80 ± 9.288
ACR	0.0035 ± 0.001313	0.2425 ± 0.1029*
CHO (mmol/l)	5.111 ± 0.2631	4.603 ± 0.3581
TG (mmol/l)	1.459 ± 0.2988	2.018 ± 0.3723
UA (mmol/l)	306.9 ± 13.10	329.9 ± 20.37
APOC1(μg/ml)	0.3683 ± 0.08119	1.358 ± 0.1292***

SBP, Systolic Blood Pressure; Diastolic Blood Pressure; eGFR, Estimated Glomerular Filtration Rate; Cr, Creatinine; ACR, Albumin/Urine Creatinine Ratio; CHO, Cholesterol; TG, Triglyceride; UA, Uric Acid; Ctrl, Healthy population (n = 20); DN, Diabetic nephropathy patients (n = 20). Ctrl vs DN; *P < 0.05; ***P < 0.001.

Microarrays have been extensively implemented in medical research, such as biomarkers for disease diagnosis, and prognosis (28, 29). Consequently, we investigated the differential genes in the kidney tissue of diabetic nephropathy and healthy people by microarray transcriptome analysis (Figure 2). The research demonstrated that 257 up-regulated and 247 down-regulated genes were compared to normal kidney tissue. Furthermore, we also screened for gene modules closely correlated with diabetic nephropathy by the WGCNA method (Figure 3). 17 secretory genes were obtained in the differential and Me-Brown modules (Figure 3, 4), which may have an essential role in DN.

Our investigation further screened for core secretory genes in diabetic nephropathy using the Lasso and SVM-RFE machine learning algorithms, which identified a total of six potential core genes (Figures 4, 5). Among the six secreted genes, APOC1 is newly identified as a member of the lipoprotein family and is closely associated with lipid metabolism and immune inflammation. Our research demonstrated elevated expression of APOC1 in DN. Additionally, APOC1 expression was also confirmed by other

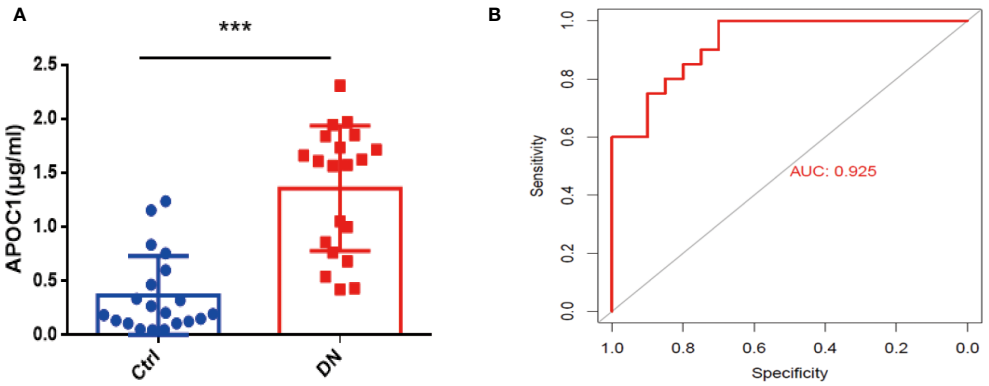

FIGURE 8
Serum APOC1 expression in DN patients and ROC. **(A)** APOC1 expression in serum (Ctrl n = 20, DN n = 20). **(B)** ROC curve of serum APOC1 expression in DN (AUC = 92.5%, sensitivity = 95%, and specificity = 97%, P < 0.001). Ctrl, Healthy population; DN, Diabetic nephropathy patients. ***P < 0.001.

transcriptome microarray data (Figure 6). Lipid metabolism disorders and immunoinflammatory responses are critical in the development and progression of DN patients (30, 31), which means that APOC1 may be also involved in the development of DN.

APOC1 has been implicated in the progress of many diseases such as malignancy (32), atherosclerosis (33), and Alzheimer's disease (34). More importantly, APOC1 is closely associated with cell proliferation, apoptosis, and immune inflammation (35). Recent research also has identified ApoC1 which promotes renal clear cell carcinoma metastasis through activation of the STAT3 pathway (36) and is a potential novel diagnostic and prognostic marker for clear cell renal carcinoma (37). Animal experiments are employed to confirm the results of research. In vivo, we also demonstrated that APOC1 expression was significantly increased in diabetic nephropathy kidney tissues, mainly in the glomerulus, using a mouse model of diabetic nephropathy (Figure 6). Currently, our team are also conducting functional and mechanistic research on the role of APOC1 in DN.

Interestingly, we also conducted a correlation analysis between APOC1 and clinical data. we investigated the correlation of APOC1 expression with urinary protein and eGFR in DN patients through the Nephroseq database (Figure 7). For further evidence, we collected blood samples from 20 patients with DN and 20 healthy. We assayed the expression level of APOC1 in serum by Elisa assay. The outcome showed that APOC1 expression was significantly higher in DN patients and had an excellent diagnostic efficacy for DN (Figure 8). Therefore, we concluded that APOC1 may be a novel biomarker for DN. Nevertheless, many deficiencies remain for our research. The role and mechanism of APOC1 in the development of DN is still unclear. The diagnostic efficacy of APOC1 for DN still needs to be demonstrated in multicentre research. Additionally, APOC1 expression and the prognosis of DN patients still need more prospective investigation.

In conclusion, elevated glomerular and serum expression of APOC1 in DN was identified for the first time through bioinformatics, machine learning, animal model experiments, and clinical data. APOC1 was demonstrated to be a novel and potential biological diagnostic marker for DN, but additional prospective research remains needed to demonstrate its diagnostic value.

Data availability statement

The datasets presented in this study can be found in online repositories. The names of the repository/repositories and accession number(s) can be found in the article/Supplementary Material.

Ethics statement

The studies involving human participants were reviewed and approved by the Ethics Committee of Qilu Hospital, Shandong University (Approval No: KYLL-2020(KS)-030). The patients/participants provided their written informed consent to participate in this study. The animal study was reviewed and approved by the Ethics Committee of Qilu Hospital, Shandong University (Approval No: KYLL-2020(KS)-030).

Author contributions

KY: Original draft and Writing, SL, and CW: Drawing diagrams, LL, XF, L F: Animal experiments and Clinical Data Collection, YZ: Clinical Data Collection, HL, HY, JS: Methodology, XY: Review and editing. All authors contributed to the article and approved the submitted version.

Funding

This research was supported by the National Natural Science Foundation of China (No.82070746), Funded by ECCM Program of Clinical Research Center of Shandong University (No.2021SDUCRCB007), and the National Science Foundation for Young Scientists of China (NO.82000692).

Acknowledgments

Appreciation to all who participated in the article.

Conflict of interest

The authors declare that the research was conducted in the absence of any commercial or financial relationships that could be construed as a potential conflict of interest.

Publisher's note

All claims expressed in this article are solely those of the authors and do not necessarily represent those of their affiliated organizations, or those of the publisher, the editors and the reviewers. Any product that may be evaluated in this article, or claim that may be made by its manufacturer, is not guaranteed or endorsed by the publisher.

Supplementary material

The Supplementary Material for this article can be found online at: https://www.frontiersin.org/articles/10.3389/fendo.2023.1102634/full#supplementary-material

References

1. Ghaderian SB, Hayati F, Shayanpour S, Beladi Mousavi SS. Diabetes and end-stage renal disease; a review article on new concepts. *J Renal Inj Prev* (2015) 4:28–33. doi: 10.12861/jrip.2015.07

2. Cheng HT, Xu X, Lim PS, Hung KY. Worldwide epidemiology of diabetes-related end-stage renal disease, 2000-2015. *Diabetes Care* (2021) 44:89–97. doi: 10.2337/dc20-1913

3. Schrauben SJ, Shou H, Zhang X, Anderson AH, Bonventre JV. Association of multiple plasma biomarker concentrations with progression of prevalent diabetic kidney disease: Findings from the chronic renal insufficiency cohort (CRIC) study. *J Am Soc Nephrol.* (2021) 32:115–26. doi: 10.1681/ASN.2020040487

4. Vasquez-Rios G, Coca SG. Predictors of kidney disease progression in diabetes and precision medicine: Something old, something new, and something borrowed. *J Am Soc Nephrol.* (2021) 32:2108–11. doi: 10.1681/ASN.2021070945

5. Zhang WR, Craven TE, Malhotra R, Cheung AK, Chonchol M, Drawz P, et al. Kidney damage biomarkers and incident chronic kidney disease during blood pressure reduction: A case-control study. *Ann Intern Med* (2018) 169:610–8. doi: 10.7326/M18-1037

6. Barrett T, Wilhite SE, Ledoux P, Evangelista C, Kim IF, Tomashevsky M, et al. NCBI GEO: archive for functional genomics data sets–update. *Nucleic Acids Res* (2012) 41: D991–5. doi: 10.1093/nar/gks1193

7. Huang M, Zhu Z, Nong C, Liang Z, Ma J, Li G. Bioinformatics analysis identifies diagnostic biomarkers and their correlation with immune infiltration in diabetic nephropathy. *Ann Transl Med* (2022) 10:669. doi: 10.21037/atm-22-1682

8. Zhao Z, He S, Yu X, Lai X, Tang S, Mariya MEA, et al. Analysis and experimental validation of rheumatoid arthritis innate immunity gene CYFIP2 and pan-cancer. *Front Immunol* (2022) 13:954848. doi: 10.3389/fimmu.2022.954848

9. Li D, Yu K, Feng F, Zhang Y, Bai F, Zhang Y, et al. Hydroxychloroquine alleviates renal interstitial fibrosis by inhibiting the PI3K/Akt signaling pathway. *Biochem Biophys Res Commun* (2022) 610:154–61. doi: 10.1016/j.bbrc.2022.04.058

10. Huang W, Wang BO, Hou YF, Fu Y, Cui SJ, Zhu JH, et al. JAML promotes acute kidney injury mainly through a macrophage-dependent mechanism. *JCI Insight* (2022) 7:1–19. doi: 10.1172/jci.insight.158571

11. Bullen AL, Katz R, Jotwani V, Garimella PS, Lee AK, Estrella MM, et al. Biomarkers of kidney tubule health, CKD progression, and acute kidney injury in SPRINT (Systolic blood pressure intervention trial) participants. *Am J Kidney Dis* (2021) 78:361–368 e361. doi: 10.1053/j.ajkd.2021.01.021

12. Pan Y, Jiang S, Hou Q, Qiu D, Shi J, Wang L, et al. Dissection of glomerular transcriptional profile in patients with diabetic nephropathy: SRGAP2a protects podocyte structure and function. *Diabetes* (2018) 67:717–30. doi: 10.2337/db17-0755

13. Ritchie ME, Phipson B, Wu D, Hu Y, Law CW, Shi W, et al. Limma powers differential expression analyses for RNA-sequencing and microarray studies. *Nucleic Acids Res* (2015) 43:e47. doi: 10.1093/nar/gkv007

14. Ito K, Murphy D. Application of ggplot2 to pharmacometric graphics. *CPT Pharmacometrics Syst Pharmacol* (2013) 2:e79. doi: 10.1038/psp.2013.56

15. Yu G, Wang LG, Han Y, He QY. clusterProfiler: An r package for comparing biological themes among gene clusters. *OMICS* (2012) 16:284–7. doi: 10.1089/omi.2011.0118

16. Langfelder P, Horvath S. WGCNA: An r package for weighted correlation network analysis. *BMC Bioinf* (2008) 9:559. doi: 10.1186/1471-2105-9-559

17. Antonacci Y, Toppi J, Mattia D, Pietrabissa A, Astolfi L. Single-trial connectivity estimation through the least absolute shrinkage and selection operator. *Annu Int Conf IEEE Eng Med Biol Soc* (2019) 2019:6422–5. doi: 10.1109/EMBC.2019.8857909

18. Zhu YX, Huang JQ, Ming YY, Zhuang Z, Xia H. Screening of key biomarkers of tendinopathy based on bioinformatics and machine learning algorithms. *PloS One* (2021) 16:e0259475. doi: 10.1371/journal.pone.0259475

19. Yu K, Li D, Xu F, Guo H, Feng F, Ding Y, et al. IDO1 as a new immune biomarker for diabetic nephropathy and its correlation with immune cell infiltration. *Int Immunopharmacol.* (2021) 94:107446. doi: 10.1016/j.intimp.2021.107446

20. Yang H, Xie T, Li D, Du X, Wang T, Li C, et al. Tim-3 aggravates podocyte injury in diabetic nephropathy by promoting macrophage activation *via* the NF-kappaB/TNF-alpha pathway. *Mol Metab* (2019) 23:24–36. doi: 10.1016/j.molmet.2019.02.007

21. Liu L, Bai F, Song H, Xiao R, Wang Y, Yang H, et al. Upregulation of TIPE1 in tubular epithelial cell aggravates diabetic nephropathy by disrupting PHB2 mediated mitophagy. *Redox Biol* (2022) 50:102260. doi: 10.1016/j.redox.2022.102260

22. Umanath K, Lewis JB. Update on diabetic nephropathy: Core curriculum 2018. *Am J Kidney Dis* (2018) 71:884–95. doi: 10.1053/j.ajkd.2017.10.026

23. Barrera-Chimal J, Jaisser F. Pathophysiologic mechanisms in diabetic kidney disease: A focus on current and future therapeutic targets. *Diabetes Obes Metab* (2020) 22 Suppl 1:16–31. doi: 10.1111/dom.13969

24. Gross JL, de Azevedo MJ, Silveiro SP, Canani LH, Caramori ML, Zelmanovitz T. Diabetic nephropathy: Diagnosis, prevention, and treatment. *Diabetes Care* (2005) 28:164–76. doi: 10.2337/diacare.28.1.164

25. Slyne J, Slattery C, McMorrow T, Ryan MP. New developments concerning the proximal tubule in diabetic nephropathy: In vitro models and mechanisms. *Nephrol Dial Transplant* (2015) 30 Suppl 4:iv60–67. doi: 10.1093/ndt/gfv264

26. Flyvbjerg A. The role of the complement system in diabetic nephropathy. *Nat Rev Nephrol.* (2017) 13:311–8. doi: 10.1038/nrneph.2017.31

27. Butler AE, Al-Qaissi A, Sathyapalan T, Atkin SL. Angiopoietin-1: An early biomarker of diabetic nephropathy? *J Transl Med* (2021) 19:427. doi: 10.1186/s12967-021-03105-9

28. Yanaoka H, Nagafuchi Y, Hanata N, Takeshima Y, Ota M, Suwa Y, et al. Identifying the most influential gene expression profile in distinguishing ANCA-associated vasculitis from healthy controls. *J Autoimmun* (2021) 119:102617. doi: 10.1016/j.jaut.2021.102617

29. Xu Y, Tan Y, Zhang X, Cheng M, Hu J, Liu J, et al. Comprehensive identification of immuno-related transcriptional signature for active pulmonary tuberculosis by integrated analysis of array and single cell RNA-seq. *J Infect* (2022) 2022:534–544. doi: 10.1016/j.jinf.2022.08.017

30. Lu J, Chen PP, Zhang JX, Li XQ, Wang GH, Yuan BY, et al. GPR43 activation-mediated lipotoxicity contributes to podocyte injury in diabetic nephropathy by modulating the ERK/EGR1 pathway. *Int J Biol Sci* (2022) 18:96–111. doi: 10.7150/ijbs.64665

31. Wu L, Liu C, Chang DY, Zhan R, Zhao M, Man Lam S, et al. The attenuation of diabetic nephropathy by annexin A1 *via* regulation of lipid metabolism through the AMPK/PPARalpha/CPT1b pathway. *Diabetes* (2021) 70:2192–203. doi: 10.2337/db21-0050

32. Zheng XJ, Chen WL, Yi J, Li W, Liu JY, Fu WQ, et al. Apolipoprotein C1 promotes glioblastoma tumorigenesis by reducing KEAP1/NRF2 and CBS-regulated ferroptosis. *Acta Pharmacol Sin* (2022) 2022:2977–2992. doi: 10.1038/s41401-022-00969-5

33. Westerterp M, Berbee JF, Pires NM, van Mierlo GJ, Kleemann R, Romijn JA, et al. Apolipoprotein c-I is crucially involved in lipopolysaccharide-induced atherosclerosis development in apolipoprotein e-knockout mice. *Circulation* (2007) 116:2173–81. doi: 10.1161/CIRCULATIONAHA.107.693382

34. Pathak GA, Zhou Z, Silzer TK, Barber RC, Phillips NR. Two-stage Bayesian GWAS of 9576 individuals identifies SNP regions that are targeted by miRNAs inversely expressed in alzheimer's and cancer. *Alzheimers Dement.* (2020) 16:162–77. doi: 10.1002/alz.12003

35. Fuior EV, Gafencu AV. Apolipoprotein C1: Its pleiotropic effects in lipid metabolism and beyond. *Int J Mol Sci* (2019) 20:1–25. doi: 10.3390/ijms20235939

36. Li YL, Wu LW, Zeng LH, Zhang ZY, Wang W, Zhang C, et al. ApoC1 promotes the metastasis of clear cell renal cell carcinoma *via* activation of STAT3. *Oncogene* (2020) 39:6203–17. doi: 10.1038/s41388-020-01428-3

37. Cui Y, Miao C, Hou C, Wang Z, Liu B. Apolipoprotein C1 (APOC1): A novel diagnostic and prognostic biomarker for clear cell renal cell carcinoma. *Front Oncol* (2020) 10:1436. doi: 10.3389/fonc.2020.01436

frontiers | Frontiers in Endocrinology

TYPE Original Research
PUBLISHED 27 March 2023
DOI 10.3389/fendo.2023.1094689

OPEN ACCESS

EDITED BY
Terry Francis Davies,
Icahn School of Medicine at Mount Sinai, United States

REVIEWED BY
Alessandro Sanguinetti,
Università degli Studi Perugia, Italy
Jacek Gawrychowski,
Department of General and Endocrinological Surgery Silesian Medical University, Poland
Svetlana Mirnaya,
Network of Family Medical Centers LLC, Russia

*CORRESPONDENCE
Wanchun Zhang
zhang_wanchun@126.com

SPECIALTY SECTION
This article was submitted to Thyroid Endocrinology, a section of the journal Frontiers in Endocrinology

RECEIVED 10 November 2022
ACCEPTED 20 February 2023
PUBLISHED 27 March 2023

CITATION
Wang Y, Liu Y, Li N and Zhang W (2023) Comparison of biochemical markers and technetium 99m methoxyisobutylisonitrile imaging in primary and secondary hyperparathyroidism.
Front. Endocrinol. 14:1094689.
doi: 10.3389/fendo.2023.1094689

Comparison of biochemical markers and technetium 99m methoxyisobutylisonitrile imaging in primary and secondary hyperparathyroidism

Yuhua Wang[1,2], Ye Liu[1,2], Na Li[1,2] and Wanchun Zhang[1,2]*

[1]Department of Nuclear Medicine, Shanxi Bethune Hospital, Shanxi Academy of Medical Sciences, Tongji Shanxi Hospital, Third Hospital of Shanxi Medical University, Taiyuan, China, [2]Tongji Hospital, Tongji Medical College, Huazhong University of Science and Technology, Wuhan, China

Objective: To investigate the differences in biochemical marker levels and the extent of lesion visualization on technetium 99m methoxyisobutylisonitrile (^{99m}Tc-MIBI) imaging between primary hyperparathyroidism (PHPT) and secondary hyperparathyroidism (SHPT).

Methods: Nineteen patients with PHPT and 14 patients with SHPT were enrolled in the study, all of whom underwent routine ^{99m}Tc-MIBI dual-phase planar imaging, single-photon emission computed tomography combined with computed tomography (SPECT/CT fusion) imaging, and serum biochemical and hormonal investigations prior to surgery. The target-to-non-target (T/NT) ratios were calculated based on images from the early and delayed phases of ^{99m}Tc-MIBI planar imaging and also based on SPECT/CT fusion imaging. The volume of the parathyroid glands was measured following their excision.

Results: A total of 62 parathyroid glands were removed: 14 parathyroid adenomas and five parathyroid carcinomas in PHPT patients; and 18 parathyroid adenomas, 17 parathyroid hyperplasia lesions, and eight instances of nodular hyperplasia with adenoma in SHPT patients. The median volume of the lesions in PHPT and SHPT was 1.69 cm^3 and 0.52 cm^3 respectively, and the difference between them was statistically significant (P = 0.001). The median T/NT ratios calculated at the early phase of ^{99m}Tc-MIBI planar imaging, the delayed phase of ^{99m}Tc-MIBI planar imaging, and the subsequent SPECT/CT fusion imaging were 1.51, 1.34, and 2.75, respectively, in PHPT, and 1.46, 1.30, and 1.38, in SHPT, respectively. The T/NT ratio difference between PHPT and SHPT on the SPECT/CT fusion imaging was statistically significant (P = 0.002). The histopathology subtypes of the lesions were associated with significant differences in two areas: the T/NT ratios on the SPECT/CT fusion imaging and the volume of the lesions (P=0.002, P<0.001).

Conclusion: The proportion of positive findings on ^{99m}Tc-MIBI dual-phase planar imaging and the T/NT ratios of ^{99m}Tc-MIBI SPECT/CT fusion imaging were higher in PHPT than in SHPT. The volume of parathyroid lesions in SHPT was smaller than in PHPT.

KEYWORDS

parathyroid adenoma, parathyroid hyperplasia, primary hyperparathyroidism, secondary hyperparathyroidism, technetium Tc 99m sestamibi, SPECT/CT fusion imaging

Introduction

Hyperparathyroidism (HPT) is a generalized disturbance of calcium (Ca) and phosphate metabolism that occurs as a result of the oversecretion of parathyroid hormone (PTH), and it can involve many of the organs and systems within the human body. The underlying cause of the hypersecretion allows HPT to be subdivided into primary hyperparathyroidism (PHPT), secondary hyperparathyroidism (SHPT), and tertiary hyperthyroidism (THPT) (1). The majority of PHPT cases (95%) occur sporadically, approximately 85% of PHPT patients is caused by a solitary adenoma, and about 15-20% are caused by multiple gland disease (2, 3). Hyperfunctional parathyroid glands overproduce PTH and leads to hypercalcemia. SHPT is one of the most common serious complications in patients with chronic renal failure on long-term hemodialysis. Parathyroid cell proliferation and PTH secretion increased is due to persistent hyperphosphatemia, hypocalcemia and a lack of VD. Most SHPT patients have multiple enlarged parathyroid glands and frequent parathyroid anatomical variations in location (4).The clinical manifestations of HPT are diverse and include urinary calculi, osteopenia, pathological fractures, and skeletal deformity.

The main treatment for PHPT is parathyroidectomy. In the treatment of SHPT, vitamin D receptor (VDRA) and calcium supplement are first used to regulate the treatment. If the drug treatment is not effective, surgical resection of the parathyroid gland can be chosen (5). Due to less operative time and fewer complications than traditional bilateral exploration, minimally invasive parathyroidectomy (MIP) is recommended in HPT (6). The anatomical location of parathyroid glands has a higher probability of variation (7). Therefore, accurate localization before surgery can improve the success rate of surgery. There are three different options, subtotal parathyroidectomy, total parathyroidectomy with or without auto-transplantation in SHPT patients. If the surgeon does not remove all hyperfunctioning parathyroid tissue, the recurrent SHPT would happen. It has also been reported that relapsing hyperparathyroidism by autografted parathyroid tissue may require extensive demolition of surrounding muscle tissue in addition to excision of hyperactive parathyroid tissue (8). Therefore, identification of hyperactive parathyroid tissue preoperatively is important.

Numerous examination medthods were used preoperatively or intraoperatively in localizing the hyperfunctional parathyroid lesions or predicting the presence of multiglandular disease (3, 9–11). There is widespread used of Technetium 99m methoxyisobutylisonitrile (^{99m}Tc-MIBI) dual-phase planar imaging and single-photon emission computed tomography (SPECT) combined with computed tomography (CT)-SPECT/CT fusion imaging in PHPT and SHPT (12–14). It is used for the localization of hyeperfunction parathyroid glands in PHPT and significantly improved the outcomes of patients undergoing minimally invasive parathyroidectomy in PHPT and can also assist surgeons in selecting the lowest degree of PTG hyperplasia which is appropriate to autotransplantation in SHPT (15). However, there are few articles discussed about the differences between the ^{99m}Tc-MIBI uptake in PHPT and SHPT. This study aims to evaluate the features of PHPT and SHPT, and the differences between them, by examining several biomarkers (PTH, alkaline phosphatase [ALP], phosphorus [P] and Ca), the volume of the tumors, and ^{99m}Tc-MIBI uptake in dual-phase planar and SPECT/CT fusion images.

Materials and methods

Patients

Inclusion criteria: 1.The patient visited our hospital from 2015 to 2019 and had elevated PTH on laboratory examination. 2.The patient has underwent test ^{99m}Tc-MIBI imaging. 3.The patient has underwent test SPECT/CT imaging. 4.The patient underwent parathyroid surgery and was confirmed by postoperative pathology. A total of 33 patients were included. (Figure 1). Chronic kidney disease (CKD) patients with hyperparathyroidism caused by dialysis and unable to be controlled by drug therapy were divided into SHPT group (14 patients in total) and the remaining patients were divided into the PHPT group (19 patients in total). Preoperative PTH, Ca, P and ALP were collected from the two groups. All resected parathyroid glands (PTGs) were measured, and the volume of each PTG was estimated using the following formula: $a \times b \times c \times \pi/6$ cm^3 (where a, b, and c are the dimensions of the gland in centimeters) (5, 6).

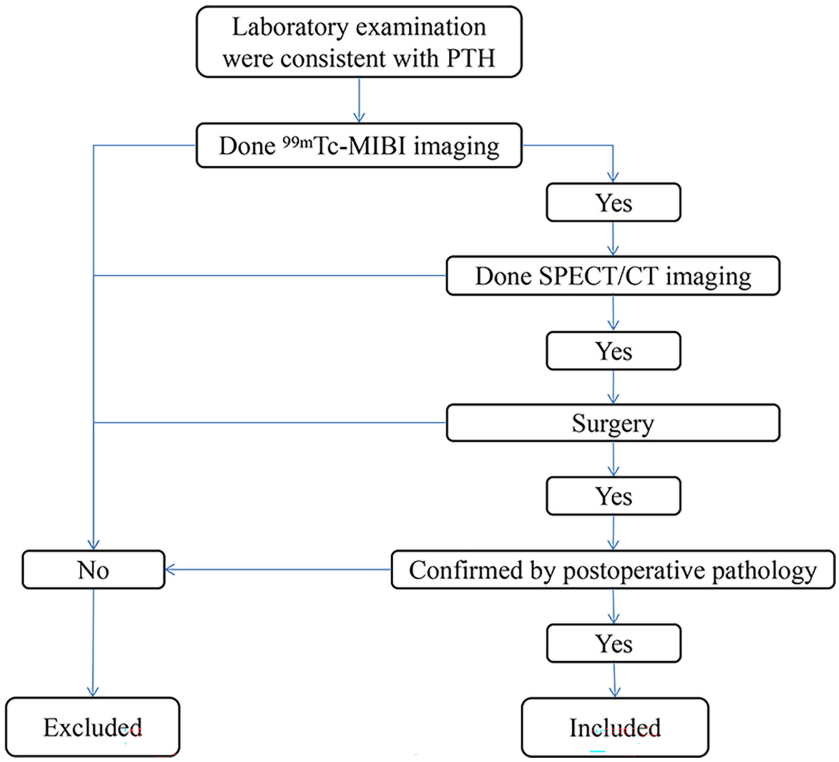

FIGURE 1
Inclusion and exclusion criteria roadmap.

Imaging examinations

Imaging was performed on a double-head gamma-camera equipped with a low-energy, high-resolution collimator (Discovery NM/CT 670, GE Healthcare). The camera was set at a 140 keV photo peak with a 20% energy window. Anterior neck images were obtained in 256 × 256 matrix size, gathering 500k counts per position. The patients received an intravenous injection of 740 MBq of ^{99m}Tc-MIBI. Early-phase planar images were obtained 20 mins after the injection and delayed-phase planar images were obtained 2 h after the injection. Immediately following this, the SPECT/CT fusion images were obtained. The SPECT images included the neck and thorax. A 128 × 128 matrix was used, and images were obtained using 3° per step and 20 s per step over 360°. A CT scan was performed immediately after the SPECT imaging. The main CT parameters were 120 keV, 200 mAs, and a 2.5-mm slice thickness. The SPECT/CT fusion image data were analyzed on a workstation (GE healthcare), which provided transaxial, coronal, and sagittal slices using the SPECT, the CT, and the fused SPECT/CT data.

Imaging analysis

The imaging results were evaluated using visual and semi-quantitative analyses by two experienced nuclear medicine physicians who were blinded both to the surgical results and the histopathology of the lesions. Positive ^{99m}Tc-MIBI scans indicated a fixed concentration in neck or mediastinum on imaging with a parenchymal space-occupying lesion (independent soft tissue mass) in the corresponding position on CT imaging or a soft tissue mass in parathyroid area without ^{99m}Tc-MIBI concentration in SPECT/CT. For semi-quantitative analysis that compared the positive results found on the dual-phase planar imaging and on the SPECT/CT imaging, a region of interest (ROI) was defined manually on the areas of increased ^{99m}Tc-MIBI uptake indicating the presence of lesions in both types of imaging, and an identical ROI was identified on the contralateral side. The target-to-non-target ratio (T/NT) ratio was calculated using the following formula: average lesion count in the ROI/average contralateral tissue counts of ROI.

Statistical analysis

Statistical analysis was performed using SSPS (version 24) software. Continuous data were expressed as mean ± standard deviation or median with interquartile range. The nonparametric Mann–Whitney test was used to compare the T/NT ratios, the levels of biochemical markers, and tumor volumes in the PHPT and SHPT groups. Spearman's rank correlation coefficient was used to calculate the correlation between the T/NT ratio, the biochemical marker levels and the volume of the PTG. The T/NT ratios and tumor volumes were evaluated in relation to the tumors' histopathology using the Kruskal–Wallis analysis of variation (ANOVA). In the case of multiple lesions, the tumor volume was calculated by summing the volumes of all the lesions. Statistical significance was set at $P < 0.05$.

Results

Patient characteristics and preoperative biochemical marker levels

Among the 19 patients with PHPT, there were nine men and 10 women, and the median age was 63 years. In this group, 18 patients had a raised serum PTH level which declined postoperative, and one patient had a normal serum PTH level; 10 patients had a raised serum ALP level, and nine patients had a normal serum ALP level; 17 patients had a raised serum Ca level, and two patients had a normal serum Ca level. All patients had a normal or low serum P level. Among the 14 patients with SHPT, there were 10 men and four women, and the median age was 34 years. The primary diagnosis of the SHPT patients was 5 chronic kidney disease and medicine had ever been used to control PTH level. In this group, all patients had a raised serum PTH level; 10 patients had a raised serum ALP level, and four patients had a normal serum ALP level; four patients had a raised serum Ca level, and 10 patients had a normal serum Ca level; 13 patients had a raised serum P level, and one patient had a normal serum P level. The median or mean serum levels of PTH, ALP, Ca, and P in PHPT and SHPT are shown in Table 1. According to the Mann–Whitney test, the median age in PHPT was higher than SHPT with significance [P=0.001]. The serum levels of both PTH and P were found to be significantly higher in the SHPT patients than in the PHPT patients ($P<0.001$, both). The serum level of Ca was found to be significantly higher in the PHPT patients than in the SHPT patients ($P<0.001$).

Surgical and histopathological results

In total, 62 glands were resected in the 33 patients. In the 19 patients who had PHPT, 16 underwent traditional surgery and 3 underwent minimally invasive approch (MIAVP), 19 PTGs were resected and their histopathology was examined. This confirmed 14 cases of parathyroid adenoma and five cases of parathyroid carcinoma. Among the 14 patients with SHPT, two patients had one excised gland that indicated by preoperative imaging examination, one patient had two excised gland indicated by imaging examination, one patient had three lesions removed intraoperatively but pathological showed two parathyroid lesions, one patient had all three lesions found removed intraoperatively, two patients had four lesions resected intraoperatively but pathological showed three parathyroid lesions, two patients underwent subtotal parathyroidectomy, two patients had total parathyroidectomy with auto-transplantation and the rest three patients had total parathyroidectomy without auto-transplantation. 43 of the glands excised confirmed pathologically origined of the parathyroid gland. A subsequent histopathological examination confirmed the following diagnoses: parathyroid adenoma was found in 17 glands, parathyroid hyperplasia was found in 18 glands, and eight glands had features of both nodular hyperplasia and adenoma. According to the histopathological examination, the median volumes of the PTGs in the PHPT group and the SHPT group were 1.69 cm^3 and 0.52 cm^3, respectively (Table 1). A statistically significant difference was observed between the two groups ($P = 0.001$).

Results from the parathyroid imaging examinations

In all 19 PHPT patients, the ^{99m}Tc-MIBI dual-phase planar imaging yielded positive scintigraphic findings, and 19 lesions were detected in total, all of which were single focal lesions. All of these 19 lesions in planar imaging were also visible upon SPECT/CT fusion imaging. The dual-phase planar imaging detected 23 lesions in 13 out of the 14 patients with SHPT, with nine patients found to have a single focal lesion, and four patients found to have multiple lesions. However, the SPECT/CT fusion imaging in SHPT patients found 26 lesions with an increased uptake of ^{99m}Tc-MIBI and eight lesions with no increased uptake of ^{99m}Tc-MIBI. The results of the SPECT/CT fusion imaging suggested that of the 14 SHPT patients,

TABLE 1 Baseline characteristics of patients included in the study.

Variables	PHPT	N1	SHPT	N2	t/Z/χ^2	P-value
Age (years)	63 (52-73)	19	34 (29-47)	14	-3.190	0.001
Sex (male/female)	10/9	19	4/10	14	1.910	0.167
Preoperative PTH (pg/mL)	334.50 (131.40-564.80)	19	1668.65 (751.67-2763.05)	14	4.025	<0.001
Preoperative ALP (IU/L)	125.00 (103.70-218.20)	19	279.70 (78.27-752.37)	14	0.984	0.341
Preoperative P (mmol/L)	0.82 (0.61-1.02)	19	1.94 (1.74-2.58)	14	4.773	<0.001
Preoperative Ca (mmol/L)	2.82 (2.69-3.35)	19	2.40 (2.15-2.60)	14	-4.408	<0.001
Early T/NT Ratio	1.51 (1.22-1.93)	19	1.46 (1.15-1.58)	23	-1.150	0.25
Delayed T/NT Ratio	1.34 (1.21-1.62)	19	1.30 (1.15-1.54)	23	-1.049	0.294
SPECT/CT T/NT Ratio	2.75 (2.20-3.84)	19	1.38 (1.13-2.61)	26	-3.171	0.002
Volume of PTG (cm^3)	1.69 (0.65-2.93)	19	0.52 (0.16-1.42)	43	-3.306	0.001

PHPT, primary hyperparathyroidism; SHPT, secondary hyperparathyroidism; PTH, parathyroid hormone; P, phosphorus; Ca, calcium; ALP, alkaline phosphatase; BUN, blood urea nitrogen; Scr, creatinine; T/NT, target-to-non-target; PTG, parathyroid gland. N1: the number of PHPT group; N2: the number of SHPT group. Data are represented as median (25–75th percentile).

three had a single lesion, five had two lesions, four had three lesions, and two had four lesions. One SHPT patient had a negative ^{99m}Tc-MIBI dual-phase planar imaging result, but did have visible lesions upon SPECT/CT fusion imaging with no ^{99m}Tc-MIBI uptake.

Semi-quantitative analysis of technetium 99m methoxyisobutylisonitrile imaging

The T/NT ratios calculated based on ^{99m}Tc-MIBI early-phase planar imaging in PHPT and SHPT were 1.51(1.22-1.93) and 1.46 (1.15-1.58), respectively. The T/NT ratios calculated based on ^{99m}Tc-MIBI delayed phase planar imaging in PHPT and SHPT were 1.34(1.21-1.62) and 1.30(1.15-1.54), respectively. The early-phase T/NT ratios were higher than the delayed-phase T/NT ratios for both the PHPT patients and the SHPT patients. When considering both phases, the T/NT ratios were higher in the PHPT patients than in the SHPT patients, but these differences were not statistically significant.

The median T/NT ratio of lesions found upon SPECT/CT fusion imaging in PHPT and SHPT was 2.75 and 1.38, respectively, and the difference between these was statistically significant (P=0.002). The 45 parathyroid lesions with positive SPECT/CT fusion imaging results were classified into five subgroups according to their histopathology: 14 parathyroid adenomas found in 14 PHPT patients (PA in PHPT), five parathyroid carcinomas found in four PHPT patients (PC), nine parathyroid adenomas found in five SHPT patients (PA in SHPT), nine instances of parathyroid hyperplasia found in five SHPT patients (PH), and eight instances of nodular hyperplasia with adenoma found in three SHPT patients (NHA). The Kruskal–Wallis ANOVA test indicated significant differences in the serum PTH, Ca, and P levels between the subgroups (P = 0.001, P<0.001, P<0.001,respectively. There was also a significant difference in the T/NT ratio of the SPECT/CT fusion images and the lesion volume between the subgroups (P =0.002, P<0.001, respectively). The lowest T/NT ratio was found in the NHA subgroup and the highest in PC subgroup. The largest lesion volume was found in the PC subgroup, and the smallest lesion volume was found in the PH subgroup (Figures 2, 3).

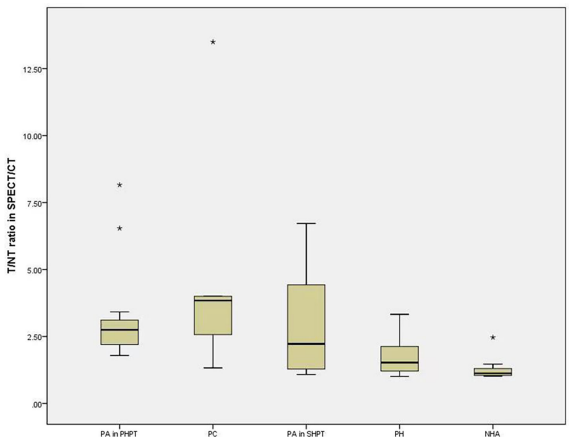

FIGURE 2
The difference of T/NT ratio in SPECT/CT fusion imaging among the subgroups. Boxplots indicate median value (black), first and third quartile range (box). Pairwise comparison by independent sample Kruskal-Wallis test, there was statistical significance between NHA and PA in PHPT (P=0.004). There was statistical difference between NHA and PTC (P=0.14). T/NT, target-to-non-target. PA in PHPT, parathyroid adenomas in primary hyperparathyroidism; PC, parathyroid carcinomas; PA in SHPT, parathyroid adenomas in secondary hyperparathyroidism; PH, parathyroid hyperplasia; NHA, nodular hyperplasia with adenoma. * indicates that the value is an outlier, which is far away from the third quartile line.

Discussion

The radiopharmaceutical ^{99m}Tc-MIBI is liposoluble, intracellular, and cationic, and it accumulates in the mitochondria of viable cells by means of an electrochemical gradient due to the activity of respiratory chain (16). It is a radiopharmaceutical commonly used to perform parathyroid scintigraphy, and it can accumulate in abnormal PTG tissues, especially those that are rich in oxyphil cells (17). The sensitivity of ^{99m}Tc-MIBI scan was 100% in oxyphil cell dominant PHPT patients and was 71.2% in chief cell and mixed cell-dominant PHPT patients (18). The study conducted by Cordes et al. (19) demonstrated that in 82% of ^{99m}Tc-MIBI negative cases oxyphil cells were absent. The absence of oxyphil cells, with their large numbers of mitochondria, in PTGs probably lead to a decrease in the number of radiotracer binding sites resulting in negative ^{99m}Tc-MIBI imaging (19). The PTG in true positive ^{99m}Tc-MIBI imaging consisted predominantly of oxyphil cells and opposite in false negative ^{99m}Tc-MIBI imaging (20). SHPT, a common complication of CRF, is characterized by

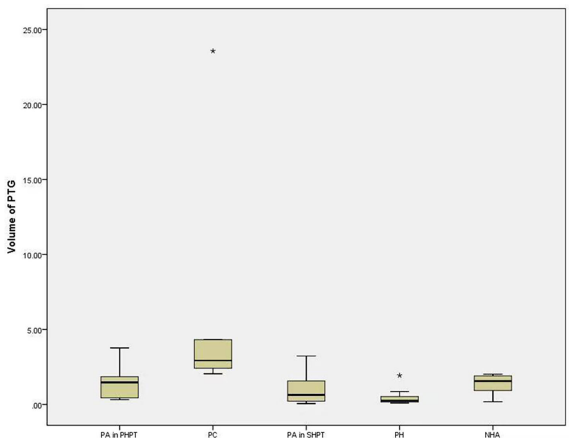

FIGURE 3
The difference of volume of PTG in subgroups. Boxplots indicate median value (black), first and third quartile range (box). Pairwise comparison by independent sample Kruskal-Wallis test, PH and PA in PHPT were statistically significant (P=0.023), PH and PC were statistically significant (P< 0.001), PA in SHPT and PC were statistically significant (P=0.025). PTG, parathyroid gland. PA in PHPT, parathyroid adenomas in primary hyperparathyroidism. PC, parathyroid carcinomas; PA in SHPT, parathyroid adenomas in secondary hyperparathyroidism; PH, parathyroid hyperplasia; NHA, nodular hyperplasia with adenoma. * indicates that the value is an outlier, which is far away from the third quartile line.

parathyroid hyperplasia consisting mainly of chief cells (21). A meta-analysis showed the sensitivity of ^{99m}Tc-MIBI plannar imaging in SHPT patients was 58% (16). In our study, the ^{99m}Tc-MIBI dual-phase planar imaging in SHPT patients was positive in 13 out of 14 patients. The T/NT ratios of the ^{99m}Tc-MIBI dual-phase planar images were lower in the SHPT patients than in the PHPT patients, but not to a statistically significant degree. The T/NT ratios in the SPECT/CT fusion images, eliminating overlapping effects, were significantly lower of the SHPT patients compared to PHPT. Adenomas were primarily present in the PHPT patients, while hyperplasia was primarily present in the SHPT patients. Parathyroid adenomas and parathyroid carcinomas are mainly composed of a mixture of chief and transitional oxyphil cells (22). Chief cells were found in all parathyroid hyperplasia lesions, and oxyphil cells were found in 67.9% of parathyroid hyperplasia lesions (23).

In our study, all the lesions in PHPT which were pathologically confirmed as adenomas and carcinomas were positive both on the dual-phase ^{99m}Tc-MIBI planar imaging and the SPECT/CT fusion imaging. Among the 14 SHPT patients, 12 had multiple lesions, but not all of the lesions in SHPT were positive on the ^{99m}Tc-MIBI dual-phase planar imaging. The SPECT/CT fusion imaging T/NT ratios were lowest in the NHA subgroups, and highest in the PC subgroup. These findings suggest that ^{99m}Tc-MIBI may uptake less in SHPT than PHPT lesions. There are some studies about the oxyphil cells proportion of parathyroid lesions in the PHPT or SHPT (24, 25), but there is little studies directly compared the oxyphil cells proportion between PHPT and SHPT. The predominant cell type found in PHPT and SHPT lesions may account for the differences in the degree of visualization of different lesions on ^{99m}Tc-MIBI dual-phase planar imaging.

Another factor that influences ^{99m}Tc-MIBI accumulation in the parathyroid glands is the parathyroid lesion size (20). Histopathological examination of the resected glands after surgery revealed that the mean volume of the parathyroid lesions was significantly larger in the PHPT group than in the SHPT group in our study. Other studies have also reported the weight and volume of parathyroid lesions. In PHPT, the median weight of an adenoma was found to be 3.0 g-4.1g (26, 27). While the mean mass of lesions in SHPT was found to be 0.91g (28) and the mean volume of a PTG was 838 ± 939 mm^3 in a study with CKD), which is consistent with the present study (29). Elsewhere, in a study of 17 patients, the median weight of parathyroid adenomas gland was larger than of hyperplastic glands with difference (30). The smallest volume in our study was evident in the PH subgroup. Oxyphil cells are larger than chief cells histologically (12–20 and 6–8 μm, respectively) (31). It had a trend towards larger size and weight when the percentage of oxyphil cells >75% in PHPT lesions (25). The volume of lesions decreased as the number of lesions increased (32). Multiple parathyroid lesions are often involved in patients with SHPT. The growth of PTG was stopped by the active form of vitamin D (calcitriol) in chronic renal failure (CRF) patients with comorbid SHPT (33). Most SHPT patients in CKD and SHPT receive vitamin D treatment. Considering the above factors, the difference of volume between PHPT and SHPT is related to oxyphil cells components and disease characteristics.

^{99m}Tc-MIBI SPECT/CT sensitivity is significantly lower in multiple gland disease (MGD) than single-gland disease (SGD) may due to the reason that MGD usually is due to hyperplasia and SGD usually is due to adenoma (32). All the PHPT patients had a single parathyroid lesion identified upon ^{99m}Tc-MIBI dual-phase planar imaging were confirmed by surgery and pathology. Among the 13 SHPT patients with positive ^{99m}Tc-MIBI dual-phase planar imaging result, 11 patients had multiple lesions. In addition, the SPECT/CT fusion imaging found a further eight lesions in these 13 SHPT patients that had no increased ^{99m}Tc-MIBI uptake. Parjeet Kaur et al. (26) suggested that the misdiagnosis of MGD as a single adenoma(SA) on ^{99m}Tc-MIBI scans may be the result of an increased focus on a single enlarged gland, which leads to other small lesions being missed in the context of MGD. The higher rate of negative ^{99m}Tc-MIBI dual-phase planar imaging results in SHPT compared with PHPT may be related to multi-gland hyperplasia.

The study by Min Zhang et al. (34) showed the retention rate of ^{99m}Tc-MIBI in PC lesions was significantly higher than that in benign lesions, and the diameter of PC was larger than adenoma (3). In consist with them, the highest T/NT ratio and the largest volume is both in PC subgroup in our study. Among the pathologic lesions responsible for primary hyperparathyroidism, include adenoma, atypicaladenoma, double adenoma, multigland hyperplasia, and rarely carcinoma, 0.5-2% is parathyroid carcinoma (21). In this study, all 5 cases of parathyroid adenocarcinoma received treatment due to PHPT-related symptoms and were pathologically confirmed as cancer after surgery. We selected ^{99m}Tc-MIBI positive patients with post-operative pathology from suspected HPT patients, so the total number of patients selected was small, leading to selection bias.

There was a significant difference between the mean age of PHPT and SHPT patients in our study. The median age of PHPT patients was 63 year and the median age of SHPT patients was 34 years with significant difference in our study. This result is consistent with the reported mean age of PHPT patients and the group age of SHPT mentioned in the study (2, 35, 36). The age of SHPT patients become younger with the degree of disease (37). With the growth of age or pathological state, the number of eosinophils from the degeneration of the master cells in parathyroid tissues gradually increases (38, 39). In a study of SHPT, the number of focal eosinophilic cells increased with age and the mean age in higher oxyphil cell proportion group was older than in lower group (24). We speculated the difference age between PHPT and SHPT patients may be related to the oxyphil cells.

Our study is limited by its relatively small number of patients and retrospective design which had not analyzed the chief cell and oxphil cell components in the resected lesions. Therefore, future prospective large cohort study needed for analyzing the difference that the uptake of ^{99m}Tc-MIBI and the oxphil content in parathyroid lesions between PHPT and SHPT patients.

In conclusion, the proportion of patients who had a positive result on the ^{99m}Tc-MIBI dual-phase planar imaging was higher in the PHPT group than in the SHPT group, the T/NT ratios on the ^{99m}Tc-MIBI dual-phase planar and SPECT/CT fusion imaging were higher in the former group and the volume of parathyroid lesions involved in SHPT was also smaller than in PHPT. Therefore, it is recommended to combine other technology when ^{99m}Tc-MIBI

imaging is negative in patients with SHPT and it should be aware the possibility of cancer when abnormal concentration and large lesions observed in PHPT patients.

Data availability statement

The original contributions presented in the study are included in the article/supplementary material. Further inquiries can be directed to the corresponding author.

Ethics statement

The studies involving human participants were reviewed and approved by Ethics committee of Shanxi Bethune Hospital, Shanxi Academy of Medical Sciences, Tongji Shanxi Hospital, Third Hospital of Shanxi Medical University.

Author contributions

Conception and design of the research: YW and WZ. Acquisition of data: YL and NL. Analysis and interpretation of the data: YW and NL. Statistical analysis: YL. Writing of the manuscript: YW. Critical revision of the manuscript for intellectual content: WZ. All authors contributed to the article and approved the submitted version.

Acknowledgments

We would like to acknowledge the hard and dedicated work of all the staff that implemented the intervention and evaluation components of the study.

Conflict of interest

The authors declare that the research was conducted in the absence of any commercial or financial relationships that could be construed as a potential conflict of interest.

Publisher's note

All claims expressed in this article are solely those of the authors and do not necessarily represent those of their affiliated organizations, or those of the publisher, the editors and the reviewers. Any product that may be evaluated in this article, or claim that may be made by its manufacturer, is not guaranteed or endorsed by the publisher.

References

1. Ursu H, Ioachim D, Muntianu L. About the guideline for diagnosis and treatment of primary hyperparathyroidism in a country with endemic goiter. *Acta endocrinologica: Int J Romanian Soc Endocrinol* (2010) 6(1):129–38. doi: 10.4183/aeb.2010.129

2. Bilezikian JP, Bandeira L, Khan A, Cusano NE. Hyperparathyroidism. *Lancet* (2018) 391(10116):168–78. doi: 10.1016/S0140-6736(17)31430-7

3. De Pasquale L, Lori E, Bulfamante AM, Felisati G, Castellani L, Saibene AM, et al. Evaluation of Wisconsin and CaPTHUS indices usefulness for predicting monoglandular and multiglandular disease in atients with primary hyperparathyroidism through the analysis of a single-center experience. *Int J Endocrinol* (2021) 2021:2040284. doi: 10.1155/2021/2040284

4. Lau WL, Obi Y, Kalantar-Zadeh K. Parathyroidectomy in the management of secondary hyperparathyroidism. *Clin J Am Soc Nephrol* (2018) 13(6):952–61. doi: 10.2215/CJN.10390917

5. Mizobuchi M, Ogata H, Koiwa F. Secondary hyperparathyroidism: Pathogenesis and latest treatment. *Ther Apher Dial* (2019) 23(4):309–18. doi: 10.1111/1744-9987.12772

6. Noureldine SI, Gooi Z, Tufano RP. Minimally invasive parathyroid surgery. *Gland Surg* (2015) 4(5):410–9. doi: 10.3978/j.issn.2227-684X.2015.03.07

7. Taterra D, Wong LM, Vikse J, Sanna B, Pękala P, Walocha J, et al. The prevalence and anatomy of parathyroid glands: A meta-analysis with implications for parathyroid surgery. *Langenbecks Arch Surg* (2019) 404(1):63–70. doi: 10.1007/s00423-019-01751-8

8. Falvo L, Catania A, Sorrenti S, D'Andrea V, Santulli M, De Antoni E. Relapsing secondary hyperparathyroidism due to multiple nodular formations after total parathyroidectomy with autograft. *Am Surg* (2003) 69(11):998–1002. doi: 10.1177/000313480306901117

9. Sandqvist P, Nilsson IL, Grybäck P, Sanchez-Crespo A, Sundin A. Multiphase iodine contrast-enhanced SPECT/CT outperforms nonenhanced SPECT/CT for preoperative localization of small parathyroid adenomas. *Clin Nucl Med* (2019) 44(12):929–35. doi: 10.1097/RLU.0000000000002778

10. Zhang R, Zhang Z, Huang P, Li Z, Hu R, Zhang J, et al. Diagnostic performance of ultrasonography, dual-phase (99m)Tc-MIBI scintigraphy, early and delayed (99m)Tc-MIBI SPECT/CT in preoperative parathyroid gland localization in secondary hyperparathyroidism. *BMC Med Imaging* (2020) 20(1):91. doi: 10.1186/s12880-020-00490-3

11. Ikuno M, Yamada T, Shinjo Y, Morimoto T, Kumano R, Yagihashi K, et al. Selective venous sampling supports localization of adenoma in primary hyperparathyroidism. *Acta Radiol Open* (2018) 7(2):2058460118760361. doi: 10.1177/2058460118760361

12. Wong KK, Fig LM, Gross MD, Dwamena BA. Parathyroid adenoma localization with 99mTc-sestamibi SPECT/CT: A meta-analysis. *Nucl Med Commun* (2015) 36(4):363–75. doi: 10.1097/MNM.0000000000000262

13. García-Talavera P, Díaz-Soto G, Montes AA, Villanueva JG, Cobo A, Gamazo C, et al. Contribution of early SPECT/CT to (99m)Tc-MIBI double phase scintigraphy in primary hyperparathyroidism: Diagnostic value and correlation between uptake and biological parameters. *Rev Esp Med Nucl Imagen Mol* (2016) 35(6):351–7.

14. Zeng M, Liu W, Zha X, Tang S, Liu J, Yang G, et al. (99m)Tc-MIBI SPECT/CT imaging had high sensitivity in accurate localization of parathyroids before parathyroidectomy for patients with secondary hyperparathyroidism. *Ren Fail* (2019) 41(1):885–92. doi: 10.1080/0886022X.2019.1662804

15. Ma J, Yang J, Chen C, Lu Y, Mao Z, Wang H, et al. Use of (99m)Tc-sestamibi SPECT/CT imaging in predicting the degree of pathological hyperplasia of the parathyroid gland: Semi-quantitative analysis. *Quant Imaging Med Surg* (2021) 11(10):4375–88. doi: 10.21037/qims-21-66

16. Caldarella C, Treglia G, Pontecorvi A, Giordano A. Diagnostic performance of planar scintigraphy using ^{9} ^{9}mTc-MIBI in patients with secondary hyperparathyroidism: A meta-analysis. *Ann Nucl Med* (2012) 26(10):794–803. doi: 10.1007/s12149-012-0643-y

17. Erbil Y, Kapran Y, Işsever H, Barbaros U, Adalet I, Dizdaroğlu F, et al. The positive effect of adenoma weight and oxyphil cell content on preoperative localization with 99mTc-sestamibi scanning for primary hyperparathyroidism. *Am J Surg* (2008) 195(1):34–9. doi: 10.1016/j.amjsurg.2007.01.040

18. Bleier BS, LiVolsi VA, Chalian AA, Gimotty PA, Botbyl JD, Weber RS, et al. Technetium Tc 99m sestamibi sensitivity in oxyphil cell-dominant parathyroid adenomas. *Arch Otolaryngol Head Neck Surg* (2006) 132(7):779–82. doi: 10.1001/archotol.132.7.779

19. Cordes M, Dworak O, Papadopoulos T, Coerper S, Kuwert T. MIBI scintigraphy of parathyroid adenomas: Correlation with biochemical and histological markers. *Endocr Res* (2018) 43(3):141–8. doi: 10.1080/07435800.2018.1437747

20. Stephen AE, Roth SI, Fardo DW, Finkelstein DM, Randolph GW, Gaz RD, et al. Predictors of an accurate preoperative sestamibi scan for single-gland parathyroid adenomas. *Arch Surg* (2007) 142(4):381–6. doi: 10.1001/archsurg.142.4.381

21. Baloch ZW, LiVolsi VA. Pathology of the parathyroid glands in hyperparathyroidism. *Semin Diagn Pathol* (2013) 30(3):165–77. doi: 10.1053/j.semdp.2013.06.003

22. Li J, Chen W, Liu A. Clinicopathologic features of parathyroid carcinoma: A study of 11 cases with review of literature. *Zhonghua Bing Li Xue Za Zhi* (2014) 43 (5):296–300.

23. Howson P, Kruijff S, Aniss A, Pennington T, Gill AJ, Dodds T, et al. Oxyphil Cell Parathyroid Adenomas Causing Primary Hyperparathyroidism: A Clinico-Pathological Correlation. *Endocr Pathol.* (2015) 26(3):250–4. doi: 10.1007/s12022-015-9378-3

24. Ding Y, Zou Q, Jin Y, Zhou J, Wang H. Relationship between parathyroid oxyphil cell proportion and clinical characteristics of patients with chronic kidney disease. *Int Urol Nephrol* (2020) 52(1):155–9. doi: 10.1007/s11255-019-02330-y

25. De la Hoz Rodríguez Á, Muñoz De Nova JL, Muñoz Hernández P, Valdés de Anca Á, Serrano Pardo R, Tovar Pérez R, et al. Oxyphil cells in primary hyperparathyroidism: A clinicopathological study. *Hormones (Athens)* (2021) 20(4):715–21. doi: 10.1007/s42000-021-00305-2

26. Kaur P, Gattani R, Singhal AA, Sarin D, Arora SK, Mithal A, et al. Impact of preoperative imaging on surgical approach for primary hyperparathyroidism: Data from single institution in India. *Indian J Endocrinol Metab* (2016) 20(5):625–30. doi: 10.4103/2230-8210.190540

27. Arya AK, Bhadada SK, Singh P, Sachdeva N, Saikia UN, Dahiya D, et al. Promoter hypermethylation inactivates CDKN2A, CDKN2B and RASSF1A genes in sporadic parathyroid adenomas. *Sci Rep* (2017) 7(1):3123. doi: 10.1038/s41598-017-03143-8

28. Doruyter AG, Hartley T, Ameyo JW, Davids MR, Warwick JM. Hybrid imaging using low-dose, localizing computed tomography enhances lesion localization in renal hyperparathyroidism. *Nucl Med Commun* (2014) 35(8):884–9. doi: 10.1097/MNM.0000000000000131

29. Jäger MD, Serttas M, Beneke J, Müller JA, Schrem H, Kaltenborn A, et al. Risk-factors for nodular hyperplasia of parathyroid glands in sHPT patients. *PloS One* (2017) 12(10):e0186093.

30. Michaud L, Balogova S, Burgess A, Ohnona J, Huchet V, Kerrou K, et al. A pilot comparison of 18F-fluorocholine PET/CT, ultrasonography and 123I/99mTc-sestaMIBI dual-phase dual-isotope scintigraphy in the preoperative localization of hyperfunctioning parathyroid glands in primary or secondary hyperparathyroidism: Influence of thyroid anomalies. *Med (Baltimore)* (2015) 94(41):e1701. doi: 10.1097/MD.0000000000001701

31. Ritter CS, Haughey BH, Miller B, Brown AJ. Differential gene expression by oxyphil and chief cells of human parathyroid glands. *J Clin Endocrinol Metab* (2012) 97 (8):E1499–1505. doi: 10.1210/jc.2011-3366

32. Nichols KJ, Tronco GG, Palestro CJ. Influence of multigland parathyroid disease on 99mTc-sestamibi SPECT/CT. *Clin Nucl Med* (2016) 41(4):282–8. doi: 10.1097/RLU.0000000000001115

33. Paydas S, Acikalim A, Kaya B, Bicer BH, Ulker M, Demircan O, et al. Expression of p53, Ki67, epidermal growth factor receptor, transforming growth-factorα, and p21 in primary and secondary hyperparathyroidism. *Indian J Endocrinol Metab* (2014) 18 (6):826–30. doi: 10.4103/2230-8210.140265

34. Zhang M, Sun L, Rui W, Guo R, He H, Miao Y, et al. Semi-quantitative analysis of (99m)Tc-sestamibi retention level for preoperative differential diagnosis of parathyroid carcinoma [J]. *Quant Imaging Med Surg* (2019) 9(8):1394–401. doi: 10.21037/qims.2019.07.02

35. Bilezikian JP, Cusano NE, Khan AA, Liu JM, Marcocci C, Bandeira F, et al. Primary hyperparathyroidism. *Nat Rev Dis Primers* (2016) 2:16033. doi: 10.1038/nrdp.2016.33

36. El-Sageer EM, Shehata AM, Khalaf M, EI-Heeny A. Neck exploration versus imaging localization of parathyroid in secondary hyperparathyroidism. *Indian J Surg* (2018) 81(5):457–61. doi: 10.1007/s12262-018-1842-0

37. Ritter C, Miller B, Coyne DW, Gupta D, Zheng S, Brown AJ, et al. Paricalcitol and cinacalcet have disparate actions on parathyroid oxyphil cell content in patients with chronic kidney disease [J]. *Kidney Int* (2017) 92(5):1217–22. doi: 10.1016/j.kint.2017.05.003

38. Christie AC. The parathyroid oxyphil cells. *J Clin Pathol* (1967) 20(4):591–602. doi: 10.1136/jcp.20.4.591

39. Lu CL, Yeih DF, Hou YC, Jow GM, Li ZY, Liu WC, et al. The emerging role of nutritional vitamin d in secondary hyperparathyroidism in CKD. *Nutrients* (2018) 10 (12):1890. doi: 10.3390/nu10121890

frontiers | Frontiers in Endocrinology

TYPE Original Research
PUBLISHED 03 May 2023
DOI 10.3389/fendo.2023.1187259

OPEN ACCESS

EDITED BY
Vijaya Kumar Pidugu,
National Cancer Institute (NIH),
United States

REVIEWED BY
Swetha Ramadesikan,
Nationwide Children's Hospital,
United States
Abhishek Kulkarni,
University of Florida, United States
Hima Makala,
National Cancer Institute at Frederick
(NIH), United States

*CORRESPONDENCE
Bassem Refaat
barefaat@uqu.edu.sa
bassem.refaat@yahoo.co.uk

†These authors have contributed
equally to this work and share
senior authorship

SPECIALTY SECTION
This article was submitted to
Cancer Endocrinology,
a section of the journal
Frontiers in Endocrinology

RECEIVED 15 March 2023
ACCEPTED 12 April 2023
PUBLISHED 03 May 2023

CITATION
Refaat B, Aslam A, Idris S, Almalki AH,
Alkhaldi MY, Asiri HA, Almaimani RA,
Mujalli A, Minshawi F, Alamri SA,
AlHussain MI, Baltow BA, Alqasmi MH,
Basfar GT, Alosaimi OM and Muhayya IA
(2023) Profiling estrogen, progesterone,
and androgen receptors in colorectal
cancer in relation to gender, menopausal
status, clinical stage, and
tumour sidedness.
Front. Endocrinol. 14:1187259.
doi: 10.3389/fendo.2023.1187259

Profiling estrogen, progesterone, and androgen receptors in colorectal cancer in relation to gender, menopausal status, clinical stage, and tumour sidedness

Bassem Refaat[1*†], Akhmed Aslam[1†], Shakir Idris[1], Ahmed H. Almalki[1,2], Mofareh Y. Alkhaldi[1,3], Hassan A. Asiri[1,4], Riyad A. Almaimani[5], Abdulrahman Mujalli[1], Faisal Minshawi[1], Sara A. Alamri[6], Mona I. AlHussain[6], Badee A. Baltow[6], Mansour H. Alqasmi[7], Ghaiyda T. Basfar[1,7], Ohoud M. Alosaimi[1,8] and Ibrahim A. Muhayya[3]

[1]Laboratory Medicine Department, Faculty of Applied Medical Sciences, Umm Al-Qura University, Makkah, Saudi Arabia, [2]Regional Laboratory and Central Blood Bank, Ministry of Health, Jizan, Saudi Arabia, [3]Laboratory And Blood Bank Department, Asir Central Hospital, Abha, Saudi Arabia, [4]Forensic Medicine Department, Health Affairs General Directorate in Assir, Abha, Saudi Arabia, [5]Biochemistry Department, Faculty of Medicine, Umm Al-Qura University, Makkah, Saudi Arabia, [6]Histopathology Department, King Abdullah Medical City, Makkah, Saudi Arabia, [7]Clinical Laboratories, Al-Noor Specialist Hospital, Makkah, Saudi Arabia, [8]Clinical Laboratories, Eradah and Mental Health Complex, Ministry of Health, Taif, Saudi Arabia

Background: Although estrogen (ERα/ERβ), progesterone (PGR), and androgen (AR) receptors are pathologically altered in colorectal cancer (CRC), their simultaneous expression within the same cohort of patients was not previously measured.

Methods: ERα/ERβ/PGR/AR proteins were measured in archived paired normal and malignant colon specimens (n =120 patients) by immunohistochemistry, and results were analyzed by gender, age (≤50 vs. ≥60 years), clinical stages (early-stage I/II vs. late-stage III/IV), and anatomical location (right; RSCs vs. left; LSCs). Effects of 17β-estradiol (E2), progesterone (P4), and testosterone alone or combined with the specific blockers of ERα (MPP dihydrochloride), ERβ (PHTPP), PGR (mifepristone), and AR (bicalutamide) on cell cycle and apoptosis were also measured in the SW480 male and HT29 female CRC cell lines.

Results: ERα and AR proteins increased, whilst ERβ and PGR declined markedly in malignant specimens. Moreover, male neoplastic tissues showed highest AR expression, whilst ERβ and PGR weakest alongside ERα strongest expression was seen in cancerous tissues from women aged ≥60 years. Late-stage neoplasms also revealed maximal alterations in the expression of sex steroid receptors. By tumor location, LSCs disclosed significant elevations in ERα with marked declines in PGR compared with RSCs, and ERα strongest alongside PGR weakest expression was detected in advanced LSCs from women aged ≥60 years. Late-

stage LSCs from females aged ≥60 years also showed weakest ERβ and strongest AR expression. In contrast, male RSC and LSC tissues exhibited equal ERβ and AR expression in all clinical stages. ERα and AR proteins also correlated positively, whereas ERβ and PGR inversely, with tumor characteristics. Concomitantly, E2 and P4 monotherapies triggered cell cycle arrest and apoptosis in the SW480 and HT29 cells, and while pre-treatment with ERα-blocker enhanced the effects of E2, ERβ-blocker and PGR-blocker suppressed the E2 and P4 anti-cancer actions, respectively. In contrast, treatment with the AR-blocker induced apoptosis, whilst co-treatment with testosterone hindered the effects.

Conclusions: This study advocates that protein expression of sex steroid receptors in malignant tissues could represent prognostic markers, as well as hormonal therapy could provide an alternative strategy against CRC, and their efficacies could be dependent on gender, clinical stage, and tumor location.

KEYWORDS

testosterone, cell cycle, apoptosis, left-right dichotomy, mifepristone, bicalutamide, estrogen receptor-β (ERβ), estrogen receptor-α (ERα)

1 Introduction

Worldwide, colorectal cancer (CRC) is the most prevalent and fatal gastrointestinal neoplastic disease (1, 2). Several factors increase the risk of CRC, among which tumor location has recently been shown to correlate with tumor characteristics and clinical outcomes. In detail, right-sided cancers (RSCs) are linked with larger tumor size, poor differentiation, mucinous histology, distant metastasis, and worse prognosis compared to left-sided cancers (LSCs) (3–5). Moreover, epidemiological observations have consistently shown lower risk of developing CRC in pre-menopausal women, whilst post-menopausal women using hormonal replacement therapy (HRT) also had markedly lower incidence of CRC relative to nonusers, as well as age-matched men (6–9). Moreover, better prognosis has been noted in CRC female patients aged 18-44 years relative to women > 50 years of age, as well as men of the same age (10). Therefore, it has been suggested that sex steroid hormones could contribute to colon oncogenesis (6–10).

Although the production of sex steroid hormones mainly occurs in the gonads, other peripheral tissues, including colon, express the enzymes required for the biogenesis of sex hormones, including progesterone (P4), testosterone, and the most potent estrogen, 17β-estradiol (E2) (11–13). Colonic mucosa could also respond to sex hormones, since estrogen (ERα & ERβ) (14–16), progesterone (PGR) (17–19), and androgen (AR) (20–22) receptors were detected and showed gender-dependent expression profiles. Moreover, ERβ, PGR and AR in normal colonic tissue are abundant, whilst ERα is weakly expressed (14–22). However, the protein expression of ERα (23–25) and AR (26) increases, whereas ERβ (27–29) and PGR (23, 30–32) decline, markedly in cancerous colonic tissues, and they correlated with the tumor clinicopathological characteristics and/or prognosis. Experimental studies have also shown that E2 induced ERβ-mediated anti-cancer actions, whilst promoting oncogenic effects through ERα in colonic cells, both *in vivo* and *in vitro* (33–36). Moreover, treatment with P4 induced apoptosis and inhibited cancer progression (30, 36), whereas testosterone therapy triggered cell growth and colon carcinogenesis (37–40), *in vitro* and in animal models. Hence, the authors suggested that E2, through ERβ (33–36), and P4 *via* PGR (30, 36) could act as tumor suppressors, whilst activation of ERα by E2 (33–36) and AR by testosterone (37–40) could promote the development and progression of colon neoplasia.

However, none of the earlier studies measured the expression of all the sex steroid hormone receptors within the same cohort of clinical samples or analyzed the results in relation to menopausal status in women. Moreover, little is currently known about the expression of sex steroid receptors with respect to tumor sidedness. Hence, this study investigated the protein expression of ERα, ERβ, PGR, and AR in paired non-cancerous and cancerous tissues collected from patients diagnosed with CRC, and the results were analyzed according to gender, age, clinical stage, and tumor anatomical sites. To support the clinical findings, the SW480 male and HT29 female CRC cell lines were also treated with E2, P4, and testosterone alone or combined with their specific nuclear receptor blockers to measure their effects on cell cycle and apoptosis according to gender. Understanding the roles of sex steroid hormones in colon oncogenesis could provide better prognostic markers and/or alternative hormonal therapies for CRC.

2 Materials and methods

2.1 Clinical study and sample collection

Paired Formalin-Fixed Paraffin-Embedded (FFPE) malignant and their corresponding non-malignant colonic specimens were collected from the archives of Histopathology Department of King

Abdullah Medical City in Makkah (KAMC) following ethical approval (#19-498). The study included 120 Saudi male and female patients between January 2019 and December 2021, aged between ≥ 18 years and ≤ 50 years, or ≥ 60 years and who were diagnosed with primary sporadic CRC. Moreover, all patients did not receive neoadjuvant chemo/radiotherapy prior to their surgery. Patients with a history of inherited or recurrent CRC and/or aged between 51 and 59 years old were excluded to ensure menopausal status.

The final diagnosis with the histopathological staging were based on institutional clinical management guidelines that followed the 8th edition of the American Joint Committee on Cancer tumor-node-metastasis (TNM) staging system. By retrieving the pathology and surgical reports, tumors located from the cecum to the margin of hepatic flexure were categorized as right-sided cancer (RSC), whilst neoplasms located from the splenic flexure to the rectum were considered left-sided cancer (LSC) (4). All the retrieved tissue blocks were examined by consultant histopathologists in KAMC to ensure adequacy.

2.1.1 Immunohistochemistry

Primary mouse monoclonal IgG antibodies (Santa-Cruz Biotechnology Inc.; CA, USA) were used to detect ERα (#sc-8002), ERβ (#sc-53494), PGR (#sc-810), and AR (#sc-7305) in 5-µm sections from each non-malignant and cancerous tissues. Endogenous peroxidases were blocked by using a BLOXALL® Solution (#SP-6000-100; Vector Laboratories Inc., CA, USA) for 15 min. Subsequently, the sections were incubated overnight with the primary antibodies (1:200 concentration for all) at 4°C. After washing, the sections were treated with ImmPRESS® HRP Horse Anti-mouse (#MP-7402) IgG Plus Polymer Peroxidase Kits, as per the manufacturer's protocol (Vector Laboratories Inc.). The same protocol was also used with the negative control sections, but primary isotype mouse (#sc-2025) IgG antibodies (Santa-Cruz Biotechnology Inc.) were used to control for non-specific staining. The sections were studied on a Leica DMi8 microscope (Leica Microsystems, Wetzlar, Germany) and images were acquired from 10 random fields/section with a 20× objective.

The ImageJ software (https://imagej.nih.gov/ij/) was used to measure the protein expression by the IHC Image Analysis Toolbox, as reported elsewhere (4, 41). Briefly, the stained areas (ROI) were identified, and the stain intensity with the percentage of stained areas were measured. The IHC scores were calculated by the following equation, as previously described equation (4, 41):

$$\begin{aligned} &IHC\ stain\ intensity \\ &= [(255 - ROI\ stain\ score) \\ &\quad \times \%\ ROI\ (ROI\ pixels/total\ image\ pixels \times 100)] \end{aligned}$$

The IHC scores for each receptor were then compared between the paired normal and cancerous tissues of each patient (normal *vs.* malignant), as well as between the clinical stages (early [I/II] *vs.* late [III/IV]), both genders (male *vs.* female), tumor sites (RSC *vs.* LSC), and age groups (≤ 50 *vs.* ≥ 60 years).

2.2 *In vitro* experiments

2.2.1 Chemicals and reagents

Ultrapure (>99%) testosterone hormone (#86500) was from Sigma-Aldrich Co. (MO, USA), whilst 17β-Estradiol (E2; #HY-B0141) and progesterone (P4; #HY-N0437) hormones, alongside the specific receptor blockers of ERα (MPP dihydrochloride; #HY-103454), ERβ (PHTPP; #HY-103456), PGR (mifepristone; #HY-13683), and AR (bicalutamide; #HY-14249) were obtained from MedChemExpress LLC (Princeton, NJ, USA). Cell culture media (DMEM & RPMI-1640), fetal bovine serum (FBS), antibiotic-antimycotic solution, and sterile 96-well and 6-well plates were from Thermo Fisher Scientific (MT, USA). The female (HT29) and male (SW480) human colon cancer cell lines were from the American Type Culture Collection (VA, USA).

2.2.2 Cell culture and cell viability assay

The HT29 cells were cultured in RPMI-1640, whilst DMEM was used for the SW480, and all media included 10% FBS and 1% antibiotic-antimycotic solution. All cells were sub-cultured, and growth maintained at 37°C in a humified incubator with 5% CO_2. Following seeding in 96-well plates, both cell lines were treated with each drug alone for 48h to determine the concentrations associated with 50% inhibition (IC50) or 10% increase (EC10) of cell viability using the MTT cytotoxicity assay, as described earlier (42, 43).

2.2.3 Cell cycle analysis

Following determination of IC50 or EC10 concentrations, the cells were seeded in 6-well plates and divided into the following groups: untreated control (CT), E2 (E2), P4 (P4), and testosterone (T) single treatments, alongside the MPP + E2 (E/α), PHTPP + E2 (E/β), mifepristone + P4 (P/M), and bicalutamide + testosterone (T/B) dual therapies. Each receptor blocker was added for a total duration of 48h in the co-therapy protocols, whilst E2, P4, or testosterone therapies were incubated for 24h and were initiated in the single and dual treatment groups 24h after adding their corresponding receptor blockers for 24h.

At the end of experiments, the SW480 and HT29 cells were trypsinised and suspended, washed twice with PBS, and fixed in ice-cold 70% ethanol for 24h at 4°C. Cells were then treated with RNase A (20 µg/ml; Thermo Fisher) for 15 min after washing twice in PBS. Propidium iodide (PI; 2 µg/ml; Thermo Fisher) was used to stain cellular DNA immediately prior to cell cycle analysis with an Acea Novocyte 3000 flow cytometer (Agilent Technologies, CA, USA). The percentage of cells in each phase of cell cycle were determined for 20,000 events (n = 3/group) by the NovoExpress software cell cycle algorithm, as reported earlier (42, 43).

2.2.4 Apoptosis assay

The Annexin V-FITC/PI Apoptosis Assay Kit (Thermo Fisher Scientific) was used to measure the effects of the different therapies on cell death. Briefly, the SW480 and HT29 cells were washed twice with ice cold PBS following the different treatments and re-suspended in 100 µl of 1× Annexin V (AV) binding buffer. Cell suspensions were then incubated in the dark for 15 min at room temperature, after the

addition of AV-FITC (5 µl) and PI (1 µl). Before analysing with the Acea Novocyte 3000 flow cytometer, the samples were kept on ice after adding 400 µl of AV binding buffer. The percentages of live (non-stained), early (AV+/PI-) and late apoptotic (AV+/PI+), and dead (AV-/PI+) cells are shown as mean ± SD (n = 3).

2.3 Statistical analysis

SPSS statistical analysis software version 25 was used for data analysis. Normality and homogeneity of all continuous variables were determined by the Kolmogorov and Smirnov's test and the Levene test, respectively. Ordinal and discontinuous variables are shown as numbers with percentages, and Chi-square (χ^2) test following cross-tabulation were used to measure frequencies. While Student's t or Mann-Whitney U tests were applied to compare between two groups based on normality, one-way analysis of variance (ANOVA) with Tukey's HSD or Games-Howell *post-hoc* tests were used for comparing between several groups based on equality of variance. Continuous variables are shown as mean ± standard deviation (SD) or median with interquartile range (IQR; 25^{th} – 75^{th} percentiles), according to data normality. Correlations were measured by Pearson's or Spearman's tests based on data normality. Significance was considered with P< 0.05.

3 Results

3.1 Clinicopathological characteristics of colonic tumors

Overall, the patients included 64 males (53.3%) and 56 females (46.7%), and the mean of age was comparable between both genders (58.4 ± 13.2 and 58.7 ± 13.1 years, respectively). The T stages were T1 in two (1.7%), T2 in 13 (10.8%), T3 in 72 (60%) and T4 in 33 (27.5%) patients. Regional lymph nodes were positive for malignant cells in 63 (52.5%) patients, whilst distant liver metastasis (stage M1a) was detected in 16 patients (13.3%). The most prevalent histology was Adenocarcinoma (n = 92; 76.7%) whilst the remainder was mucinous carcinoma. Additionally, 20 (16.7%), 72 (60%) and 28 (23.3%) patients had poorly, moderately, and well-differentiated cancers, respectively. Moreover, 42 (35%) and 28 (23.3%) patients were positive for lymphovascular and perineural invasions, respectively. AS per the TNM staging criteria, 50 (41.7%) cases were clinically diagnosed as early (stages I/II) and the remainder (58.3%) as advanced (stages III/IV) malignancies.

According to tumor anatomical sites, RSCs were less frequent (n = 41; 34.2%) and associated with markedly higher rates of mucinous neoplasms, poor differentiation, and distant metastasis relative to LSCs (Supplementary Table 1). However, both the RSC and LSC groups showed comparable average age, as well as distributions of genders, T and N stages, lymphovascular and perineural invasions, and rates of early (I/II) and late (III/IV) cancer stages (Supplementary Table 1). By classifying the patients according to gender and age groups, there were 22 men (18.3%) and 20 women (16.7%) aged ≤ 50 years, whilst patients aged ≥ 60 years included 42 males (35%) and 36 females (30%). All the clinicopathological features were similar between the different groups, except for the rate of T4 stage that was markedly higher in male patients (Table 1).

3.2 Protein expression of sex steroid receptors in clinical samples by IHC.

3.2.1 Estrogen receptors

In non-malignant tissues, the antibodies against ERα (Supplementary Figure 1) and ERβ (Supplementary Figure 2) labelled the cytoplasm and nuclei of colonic epithelia, and the immunostaining of the latter was substantially stronger. Moreover, the expression of ERα was markedly higher in the female right and left non-cancerous tissues compared with male patients (Supplementary Figure 1; P< 0.01 for both). While ERα was equal between the male non-malignant specimens during the different cancer stages, women ≥ 60 years showed significantly higher IHC scores in the left-sided non-neoplastic tissues obtained from the early and late stages relative to women aged ≤ 50 years (Supplementary Figure 1; P< 0.001). On the other hand, female patients aged ≤ 50 years disclosed the highest ERβ expression in the right and left non-malignant specimens compared with both age groups in males, as well as females ≥ 60 years of age (Supplementary Figure 2, P< 0.001 for all). Although ERβ expression in the male non-cancerous tissues was also equal between both age groups, the non-cancerous tissues from the late stages of RSCs and LSCs had markedly lower IHC scores compared with their counterpart early stages (Supplementary Figure 2; P< 0.01 for both). Furthermore, the non-malignant tissues from women aged ≥ 60 years revealed the lowest ERβ protein expression compared with all groups, and the lowest scores were detected in samples obtained from late RSCs (Supplementary Figure 2).

In general, the protein expression of ERα increased significantly (213.4; IQR: 192.9 – 286.3) in cancerous compared with non-cancerous tissues (36.9; IQR: 24.1 – 63.2; P< 0.0001). Moreover, left-side cancers (257.9; IQR: 200.3 – 307.1) had higher ERα expression relative to RSCs (222.5; IQR: 183.3 – 248.7; P< 0.0001). According to clinical stage, late-stage right and left cancers showed markedly higher IHC scores relative to their corresponding early-stage cancerous tissues, and the highest scores were detected in late-stage LSCs (Figure 1; P< 0.0001). However, the ERα IHC scores in late-stage LSCs were comparable between both genders, whilst women aged ≥ 60 years and diagnosed with advanced RSCs displayed the strongest immunostaining relative to men, as well as females aged ≤ 50 years, diagnosed with early-stage RSCs (Figure 1; P< 0.001 for both).

In contrast, ERβ protein declined in cancerous specimens (51.3; IQR: 40.4 – 72.1) compared with their corresponding non-malignant colonic tissues (114.1; IQR: 76.5 – 174.0; P< 0.001; Figure 2). Furthermore, the protein expression of ERβ was equal between right (49.4; IQR: 39.8 – 66.2) and left-sided (50.9; IQR: 36.2 – 75.2) tumors. However, ERβ immunostaining decreased with cancer progression in both genders, and the lowest IHC scores were observed in late-stage

10.3389/fendo.2023.1187259

TABLE 1 The clinicopathological characteristics of CRC according to patients' gender and age groups (n = 120).

	Male patients (n = 64; 53.3%)		Female patients (n = 56; 46.7%)		P-value
	≤ 50 years (n = 22; 18.3%)	≥ 60 Years (n = 42; 35%)	≤ 50 years (n = 20; 16.7%)	≥ 60 Years (n = 36; 30%)	
Tumor sidedness					
Right-sided	8 (6.6%)	13 (10.8%)	7 (5.9%)	13 (10.8%)	0.9
Left-sided	14 (11.7%)	29 (24.2%)	13 (10.8%)	23 (19.2%)	
Tumor infiltration (T stage)					
T1	0 (0%)	0 (0%)	2 (1.7%)	0 (0%)	**0.04**
T2	2 (1.7%)	8 (6.6%)	2 (1.7%)	1 (0.8%)	
T3	12 (10%)	23 (19.2%)	11 (9.1%)	26 (21.7%)	
T4	8 (6.6%)	11 (9.2%)	5 (4.2%)	9 (7.5%)	
Median (IQR) of tumor volume (cm^3)	11.5 (4.8 – 27.5)	8.4 (4.4 – 15.3)	9.5 (4.5 – 18.8)	10.5 (5.5 – 29.5)	0.5
Lymph node (N stage)					
N0	9 (7.5%)	22 (18.4%)	12 (10%)	14 (11.7%)	0.7
N1	8 (6.6%)	11 (9.1%)	5 (4.2%)	14 (11.7%)	
N2	5 (4.2%)	9 (7.5%)	3 (2.5%)	8 (6.6%)	
Distant metastasis (M stage)					
M0	19 (15.8%)	38 (31.7%)	17 (14.2%)	30 (25%)	0.8
M1	3 (2.5%)	4 (3.3%)	3 (2.5%)	6 (5%)	
Histology					
Adenocarcinoma	18 (15%)	33 (27.5%)	16 (13.4%)	25 (20.9%)	0.6
Mucinous	4 (3.3%)	9 (7.5%)	4 (3.3%)	11 (9.1%)	
Differentiation					
Poor	3 (2.5%)	4 (3.3%)	4 (3.3%)	9 (7.5%)	0.5
Moderate	12 (10%)	28 (23.4%)	11 (9.1%)	21 (17.5%)	
Well	7 (5.8%)	10 (8.3%)	5 (4.2%)	6 (5%)	
Lymphovascular invasion					
No	12 (10%)	28 (23.4%)	16 (13.4%)	22 (18.3%)	0.3
Yes	10 (8.3%)	14 (11.7%)	4 (3.3%)	14 (11.7%)	
Perineural invasion					
No	14 (11.7%)	32 (26.7%)	16 (13.4%)	30 (25%)	0.2
Yes	8 (6.6%)	10 (8.3%)	4 (3.3%)	6 (5%)	
AJCC TNM stages					
Stages I/II	8 (6.6%)	19 (15.8%)	12 (10%)	11 (9.1%)	0.1
Stages III/IV	14 (11.7%)	23 (19.2%)	8 (6.6%)	25 (20.9%)	

Bold values indicates statistical significance.

RSCs and LSCs relative to the early-stage specimens (Figure 2, P< 0.01 for all). By further analysis, right and left-sided malignant tissues obtained from women ≥ 60 years of age showed significantly lower ERβ expression than women aged ≤ 50 years, as well as men, and the lowest IHC scores were detected in the late stages of LSCs (Figure 2).

3.2.2 Progesterone receptor

The immunostaining of PGR was visualized in the cytoplasm and nuclei of non-neoplastic colonic specimens from both genders and demonstrated moderate to strong intensities (Supplementary Figure 3). The expression of PGR was also significantly higher in the

10.3389/fendo.2023.1187259

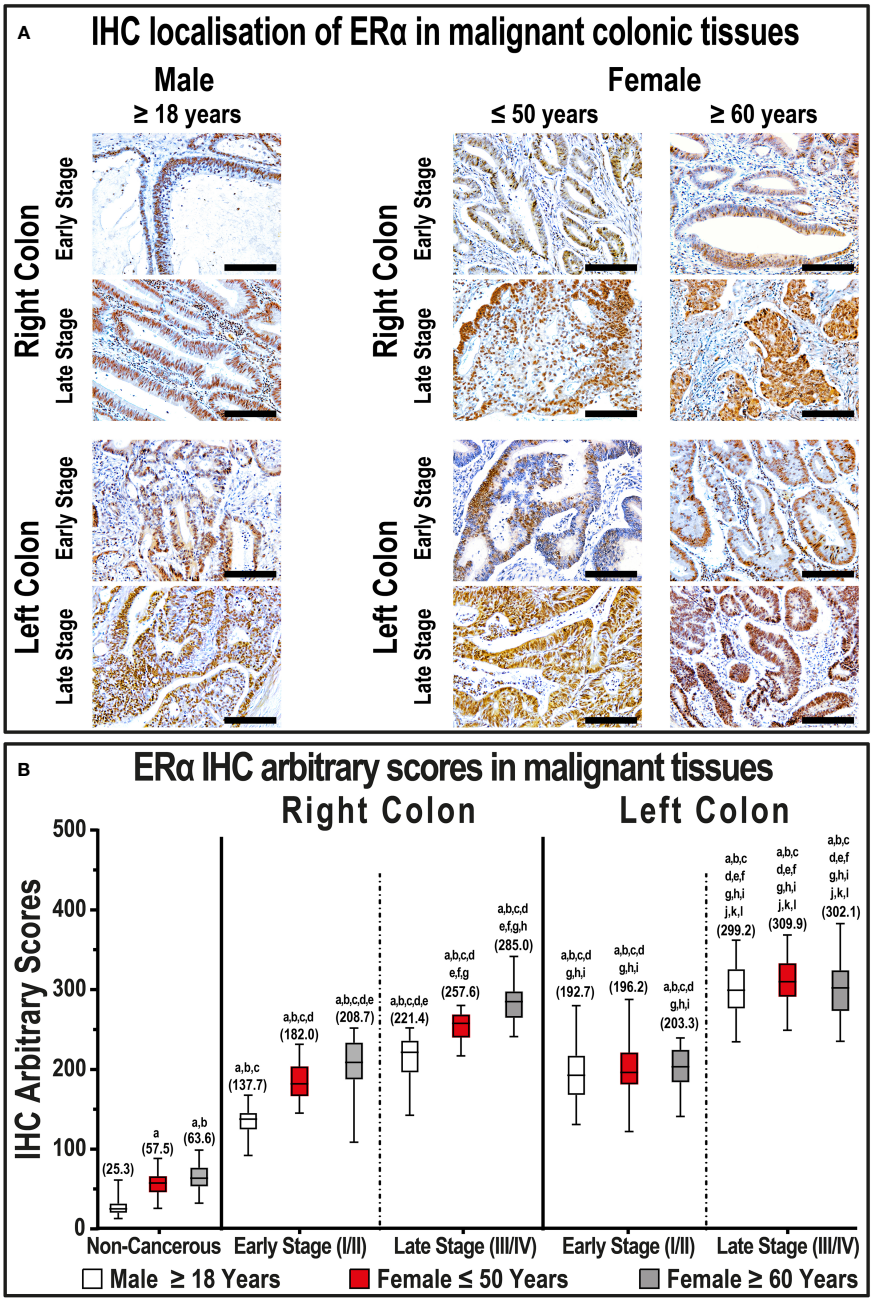

FIGURE 1
(A) Immunohistochemical localization of ERα in malignant colonic tissues (n = 120 patients; 20× objective; Scale bar = 15 µm) alongside **(B)** its IHC arbitrary scores are shown as boxplots according to gender, age, tumor sides and cancer stages. (a = P< 0.05 compared with normal specimens from males ≥ 18 years; b = P< 0.05 compared with normal specimens from females ≤ 50 years; c = P< 0.05 compared with normal specimens from females ≥ 60 years; d = P< 0.05 compared with early-stage right-sided malignant samples from males ≥ 18 years; e = P< 0.05 compared with early-stage right-sided malignant samples from females ≤ 50 years; f = P< 0.05 compared with early-stage right-sided malignant samples from females ≥ 60 years; g = P< 0.05 compared with late-stage right-sided malignant samples from males ≥ 18 years; h = P< 0.05 compared with late-stage right-sided malignant samples from females ≤ 50 years; i = P< 0.05 compared with late-stage right-sided malignant samples from females ≥ 60; j = P< 0.05 compared with early-stage left-sided malignant samples from males ≥ 18 years; k = P< 0.05 compared with early-stage left-sided malignant samples from females ≤ 50 years; l = P< 0.05 compared with early-stage left-sided malignant samples from females ≥ 60 years; m = P< 0.05 compared with late-stage left-sided malignant samples from males ≥ 18 years; n = P< 0.05 compared with late-stage left-sided malignant samples from females ≤ 50 years).

left-sided compared with right-sided non-cancerous tissues obtained from both genders (P< 0.01 for both). Moreover, the strongest PGR expression was observed in right and left non-malignant specimens obtained from females aged ≤ 50 years compared with the different male age groups and women ≥ 60 years (Supplementary Figure 3). Although the expression of PGR in the right-sided non-cancerous samples was equal in females ≥ 60 years and both male age groups, the IHC scores were significantly

10.3389/fendo.2023.1187259

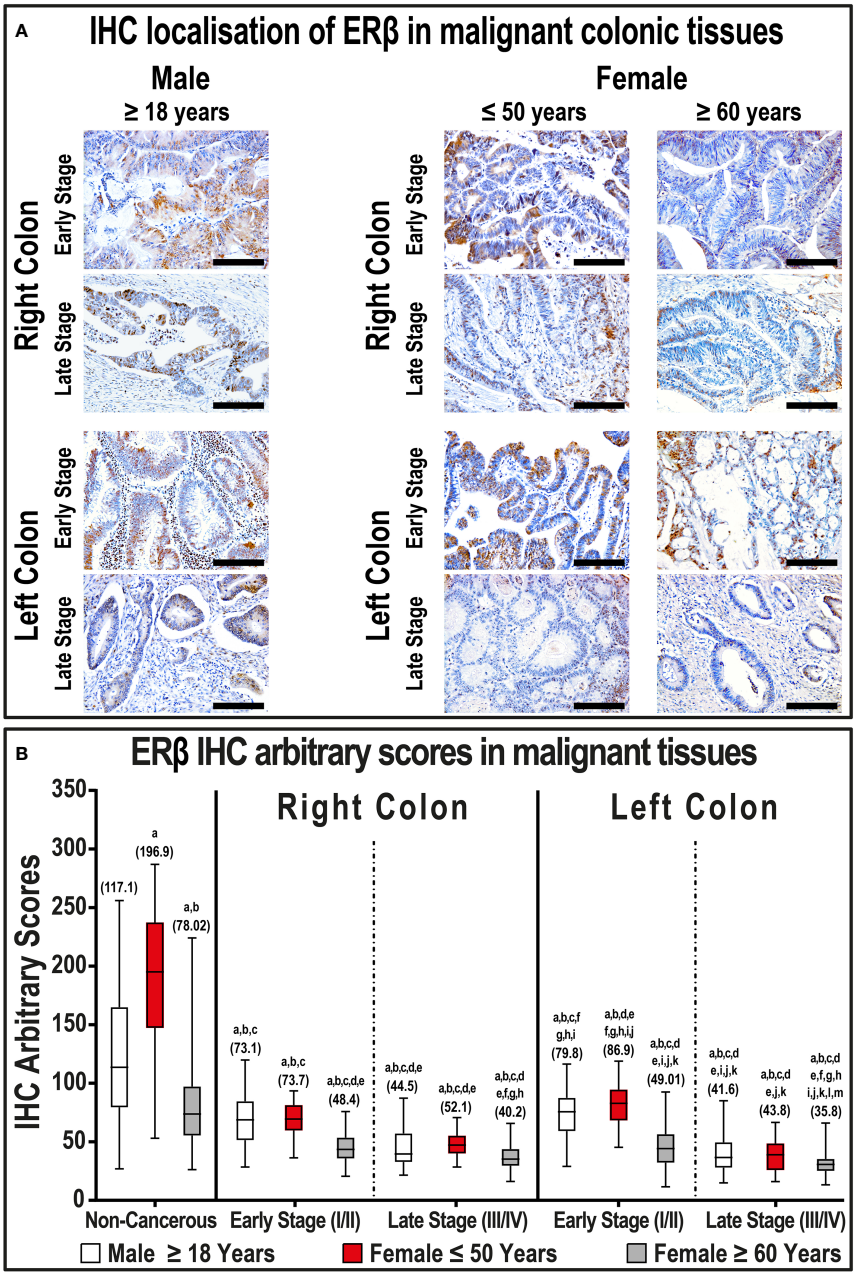

FIGURE 2
(A) Immunohistochemical localization of ERβ in malignant colonic tissues (n = 120 patients; 20× objective; Scale bar = 15 µm) alongside **(B)** its IHC arbitrary scores are shown as boxplots according to gender, age, tumor sides and cancer stages. (a = P< 0.05 compared with normal specimens from males ≥ 18 years; b = P< 0.05 compared with normal specimens from females ≤ 50 years; c = P< 0.05 compared with normal specimens from females ≥ 60 years; d = P< 0.05 compared with early-stage right-sided malignant samples from males ≥ 18 years; e = P< 0.05 compared with early-stage right-sided malignant samples from females ≤ 50 years; f = P< 0.05 compared with early-stage right-sided malignant samples from females ≥ 60 years; g = P< 0.05 compared with late-stage right-sided malignant samples from males ≥ 18 years; h = P< 0.05 compared with late-stage right-sided malignant samples from females ≤ 50 years; i = P< 0.05 compared with late-stage right-sided malignant samples from females ≥ 60; j = P< 0.05 compared with early-stage left-sided malignant samples from males ≥ 18 years; k = P< 0.05 compared with early-stage left-sided malignant samples from females ≤ 50 years; l = P< 0.05 compared with early-stage left-sided malignant samples from females ≥ 60 years; m = P< 0.05 compared with late-stage left-sided malignant samples from males ≥ 18 years; n = P< 0.05 compared with late-stage left-sided malignant samples from females ≤ 50 years).

lower in the former group in the left-sided samples (Supplementary Figure 3).

Generally, the expression of PGR protein declined markedly in malignant tissues (53.0; IQR: 43.2 – 61.8) relative to their corresponding non-malignant colonic samples (187.3; IQR: 169.7 – 216.0; P< 0.001). Left-sided tumors (45.9; IQR: 35.9 – 60.2) also showed markedly lower PGR expression relative to right-sided lesions (62.3; IQR: 51.1 – 81.1; P< 0.001). Furthermore, PGR decreased with cancer progression in both genders, and the lowest IHC scores were detected in women ≥ 60 years of age and diagnosed with early and late-stage LSCs compared with all

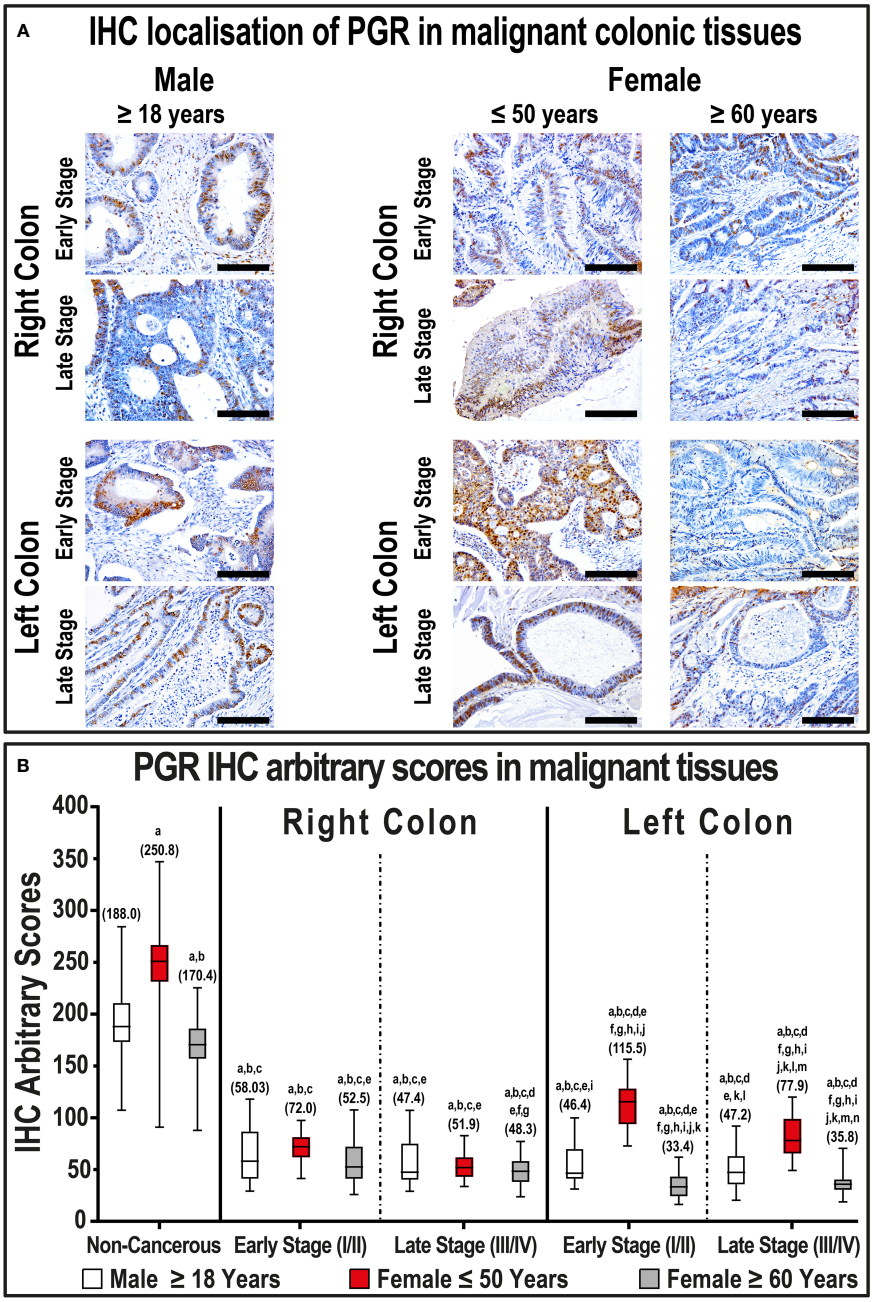

FIGURE 3
(A) Immunohistochemical localization of PGR in malignant colonic tissues (n = 120 patients; 20× objective; Scale bar = 15 µm) alongside **(B)** its IHC arbitrary scores are shown as boxplots according to gender, age, tumor sides and cancer stages. (a = P< 0.05 compared with normal specimens from males ≥ 18 years; b = P< 0.05 compared with normal specimens from females ≤ 50 years; c = P< 0.05 compared with normal specimens from females ≥ 60 years; d = P< 0.05 compared with early-stage right-sided malignant samples from males ≥ 18 years; e = P< 0.05 compared with early-stage right-sided malignant samples from females ≤ 50 years; f = P< 0.05 compared with early-stage right-sided malignant samples from females ≥ 60 years; g = P< 0.05 compared with late-stage right-sided malignant samples from males ≥ 18 years; h = P< 0.05 compared with late-stage right-sided malignant samples from females ≤ 50 years; i = P< 0.05 compared with late-stage right-sided malignant samples from females ≥ 60; j = P< 0.05 compared with early-stage left-sided malignant samples from males ≥ 18 years; k = P< 0.05 compared with early-stage left-sided malignant samples from females ≤ 50 years; l = P< 0.05 compared with early-stage left-sided malignant samples from females ≥ 60 years; m = P< 0.05 compared with late-stage left-sided malignant samples from males ≥ 18 years; n = P< 0.05 compared with late-stage left-sided malignant samples from females ≤ 50 years).

groups (Figure 3, P< 0.01 for all). In contrast, early and late-stage malignant tissues from women aged ≤ 50 years with LSCs, but not RSCs, had markedly stronger PGR immunostain relative to male cancerous tissues (Figure 3).

3.2.3 Androgen receptor

AR showed cytoplasmic and nuclear localization in the non-neoplastic colonic epithelium, and the stain intensity was gender-dependent (Supplementary Figure 4). In more detail, the expression of

AR was significantly higher in the right-sided non-tumorous tissues obtained from males diagnosed with early-stage cancer compared with their corresponding female specimens (P< 0.01). Moreover, all non-malignant specimens from women ≤ 50 years of age disclosed the lowest expression of AR compared with all non-cancerous specimens obtained from males, as well as females aged ≥ 60 years (Supplementary Figure 4). In contrast, non-malignant colonic tissues from women ≥ 60 years of age showed lower AR expression in early-stage, whilst increased significantly in late-stage, RSCs compared with their corresponding male tissues. Moreover, the AR IHC scores in left-sided non-cancerous tissues were equal between both age groups in men, as well as in females ≥ 60 years during the early and late-stage cancers (Supplementary Figure 4).

Overall, AR protein expression increased significantly in the cancerous colonic tissues (364.9; IQR: 268.1 – 388.8) compared with non-cancerous samples (171.6; IQR: 150.1 – 190.9; P< 0.0001). However, the expression of AR was equal between proximal (358.3; IQR: 256.4 – 388.3) and distal (357.5; IQR: 279.4 – 389.8) cancers. There were also no significant differences between the male cancerous specimens according to tumor sidedness and clinical stages (Figure 4), whereas all female right and left-sided malignant samples showed markedly lower AR expression during the different cancer stages compared with their counterpart male malignant tissues (Figure 4). Moreover, the expression of AR was significantly lower in RSC and LSC malignant specimens obtained from women aged ≤ 50 years relative to females aged ≥ 60 years (Figure 4).

3.2.4 Correlations between tumor clinicopathological characteristics and protein expression of sex steroid receptors

Overall, the IHC scores of ERα in cancerous specimens correlated significantly and inversely with those of ERβ (r = -0.533; P< 0.0001) and PGR (r = -0.259; P< 0.0001), whilst directly with AR (r = 0.117; P< 0.0001). On the other hand, ERβ and PGR in malignant tissues correlated positively together (r = 0.648; P< 0.001), whereas they associated negatively with AR (r = -0.159 and r = -0.367, respectively; P< 0.0001 for both). Moreover, the protein expression of ERα and AR in malignant tissues showed significant positive correlations, whereas ERβ and PGR correlated negatively, with older age, tumour size, N stage, numbers of positive lymph nodes, and advanced cancer stage (Table 2).

By further analysis according to gender, ERα protein expression in neoplastic tissues linked indirectly and significantly with ERβ (r = -0.497; P< 0.0001), PGR (r = -0.158; P< 0.0001), and AR (r = -0.309; P< 0.0001). While ERβ in male malignant tissues correlated positively and moderately with PGR (r = 0.588; P< 0.0001), it showed a weak direct association with AR (r = 0.121; P = 0.002). However, there was no associations between PGR and AR in male malignant tissues. In female tissues, ERα IHC scores in cancerous sites associated inversely with ERβ (r = -0.587; P< 0.0001) and PGR (r = -0.351; P< 0.0001), whilst directly with AR (r = 0.726; P< 0.0001). ERβ protein in female cancer specimens also revealed a direct association with PGR (r = 0.765; P< 0.0001), whereas both inversely linked with AR (r = -0.607 and r = -0.537, respectively; P< 0.0001 for both).

Moreover, ERα and AR in malignant colonic samples showed significant direct associations with tumor size, N stage, numbers of positive regional lymph nodes, and late-stage neoplasms in males, as well as female patients (Table 3). In contrast, ERβ and PGR IHC scores in male malignant samples correlated indirectly with N stage, numbers of positive lymph nodes, M stage, lymphovascular invasion and advanced cancer stage, whilst PGR only revealed weak associations with right-sided tumors and poor differentiation (Table 3). In female cancerous specimens, both ERβ and PGR exhibited weak to moderate negative correlations with tumor size, N stage, perineural invasion, and late-stage malignancy. Moreover, PGR, but not ERβ, in female malignant specimens correlated indirectly with older age and T stage (Table 3).

3.3 *In vitro* effects of sex steroid hormones and their specific receptor blockers

3.3.1 Cytotoxicity and dose-response curves

Results of the MTT assay revealed that E2, P4, ERα-blocker (MPP), and AR-blocker (bicalutamide) inhibited proliferation in the SW480 male and HT29 female CRC cell lines (Figure 5). Furthermore, the IC50 concentrations were 10 nM for E2 in both cell lines, 20 nM and 1 nM for P4, 8.6 μM and 17.8 μM for MPP, and 4.5 μM and 9.1 μM for bicalutamide in the SW480 and HT29 cells, respectively (Figure 5). On the other hand, testosterone, ERβ-blocker (PHTPP), and PGR-blocker (mifepristone) monotherapies promoted cell proliferation in the SW480 and HT29 cell lines. While the EC10 concentrations of PHTPP were 30 μM in both cell lines (Figure 5A), they were 26.9 μM and 31.8 μM for mifepristone (Figure 5B), and 20 μM and 30 μM for testosterone (Figure 5C) in the SW480 and HT29 cells, respectively. Hence, the calculated IC50s of E2, P4, MPP, and bicalutamide, alongside the EC10 of PHTPP, mifepristone, and testosterone, were used to measure their effects on cell cycle and apoptosis in the SW480 and HT29 cells.

3.3.2 Cell cycle progression

Single treatments with E2 and P4 hormones significantly increased the numbers of SW480 (3.2-fold & 1.7-fold, respectively) and HT29 (2.2-fold & 10-fold, respectively) cells in the Sub-G1 phase compared with untreated cells (Figure 6). Moreover, ERα-blocker (MPP) markedly increased the percentage of cells relative to non-treated (4.4-fold & 3.3-fold) and E2 monotherapy (1.4-fold & 1.5-fold) in the SW480 and HT29 cell lines, respectively. In contrast, the addition of ERβ-blocker (PHTPP) and PGR-blocker (mifepristone) showed markedly lower numbers of SW480 and HT29 cells in the sub-G1 phase compared with cells treated with E2 and P4 monotherapies (Figure 6). Whilst the percentage of SW480 cells in Sub-G1 phase were equal between testosterone monotherapy and untreated cells, the hormone markedly reduced the percentage of HT29 cells in Sub-G1 phase (2.1-fold; Figure 6). Nonetheless, the use of AR-blocker (bicalutamide) with testosterone significantly elevated the proportions of SW480 and HT29 cells in Sub-G1 phase relative to control (5.9-fold for both cell lines) and testosterone-only (1.8-fold & 12.6-fold, respectively) groups (Figure 6). The scatter and histogram plots, showing the gating strategy used for cell cycle

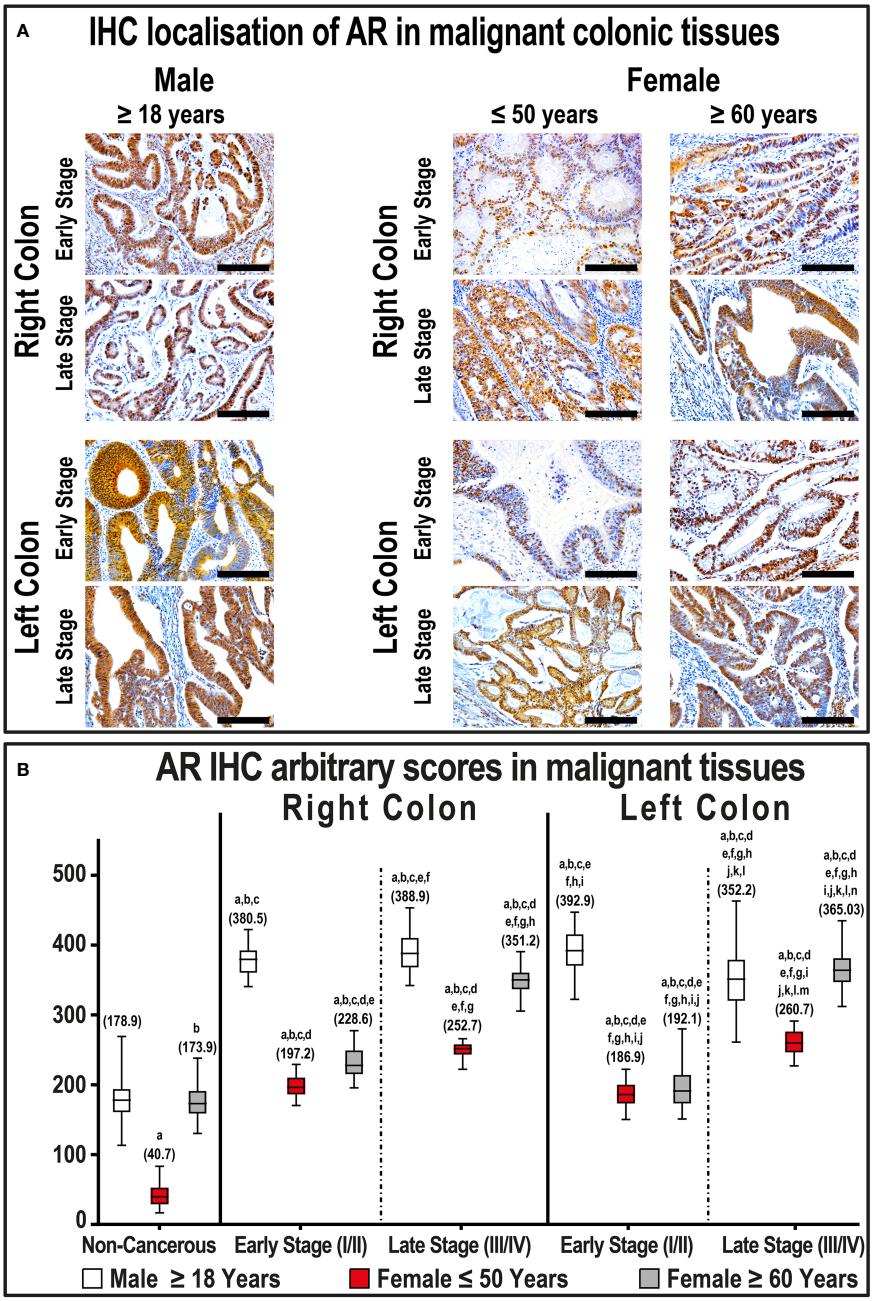

FIGURE 4
(A) Immunohistochemical localization of AR in malignant colonic tissues (n = 120 patients; 20× objective; Scale bar = 15 µm) alongside **(B)** its IHC arbitrary scores are shown as boxplots according to gender, age, tumor sides and cancer stages. (a = P< 0.05 compared with normal specimens from males ≥ 18 years; b = P< 0.05 compared with normal specimens from females ≤ 50 years; c = P< 0.05 compared with normal specimens from females ≥ 60 years; d = P< 0.05 compared with early-stage right-sided malignant samples from males ≥ 18 years; e = P< 0.05 compared with early-stage right-sided malignant samples from females ≤ 50 years; f = P< 0.05 compared with early-stage right-sided malignant samples from females ≥ 60 years; g = P< 0.05 compared with late-stage right-sided malignant samples from males ≥ 18 years; h = P< 0.05 compared with late-stage right-sided malignant samples from females ≤ 50 years; i = P< 0.05 compared with late-stage right-sided malignant samples from females ≥ 60; j = P< 0.05 compared with early-stage left-sided malignant samples from males ≥ 18 years; k = P< 0.05 compared with early-stage left-sided malignant samples from females ≤ 50 years; l = P< 0.05 compared with early-stage left-sided malignant samples from females ≥ 60 years; m = P< 0.05 compared with late-stage left-sided malignant samples from males ≥ 18 years; n = P< 0.05 compared with late-stage left-sided malignant samples from females ≤ 50 years).

analysis in the SW480 and HT29 cell lines, are represented in Supplementary Figures 5, 6, respectively.

E2-alone or combined with ERα-blocker also induced arrest at the S and G2/M phases of cell cycle in the SW480 cells, whilst only promoting G2/M-arrest in the HT29 cells (Figure 6). Moreover, the combination of E2 with its ERβ-blocker was associated with S-phase arrest in the SW480, but not HT29, cells. In contrast, P4, with and without mifepristone, displayed negligible effects on the

TABLE 2 Correlations of tumor clinicopathological characteristics with ERα, ERβ, PGR, and AR protein expression in malignant colonic tissues from all patients (n = 120) by Pearson's correlation test.

	ERα IHC scores	ERβ IHC scores	PGR IHC scores	AR IHC scores
Female gender	0.247**	-0.239**	-0.161	-0.663**
Age	0.351**	-0.254**	-0.291**	0.150
Right-sided cancer	0.143	0.030	-0.136	-0.038
T stage	0.114	-0.230*	-0.084	0.189*
Tumor Size	0.291**	-0.326**	-0.297**	0.105
N Stage	0.617***	-0.579**	-0.208*	0.320**
Numbers of positive lymph nodes	0.604***	-0.591**	-0.259**	0.259**
M Stage	0.206*	-0.295**	-0.104	0.177
Mucinous Carcinoma	0.057	-0.096	-0.144	-0.013
Poor differentiation	0.094	-0.058	0.028	-0.029
Lymphovascular invasion	0.170	-0.263**	-0.162	0.166
Perineural invasion	-0.071	-0.125	-0.092	0.124
Late-stage cancer	0.728***	-0.720***	-0.320**	0.434**

*P< 0.05.
**P< 0.01.
***P< 0.001.

numbers of SW480 and HT29 cells in the different phases of cell cycle (Figure 6). On the other hand, testosterone and bicalutamide co-therapy induced marked increases in the numbers of SW480 and HT29 cells in the S-phase of cell cycle, with concomitant declines in the percentage of cells in the G0/G1 and G2/M phases (Figure 6).

3.3.3 Cell apoptosis

E2 monotherapy significantly reduced the numbers of viable SW480 and HT29 cells that was depicted by marked increases in the percentage of early (2.7-fold & 1.6-fold, respectively) and late (1.9-fold & 4.5-fold, respectively) apoptotic cells relative to untread cells (Figure 7). The addition of ERα-blocker significantly boosted,

TABLE 3 Correlations of tumor clinicopathological characteristics with ERα, ERβ, PGR, and AR protein expression in malignant colonic tissues from male (n = 64) and female (n = 56) patients by Pearson's correlation test.

	Male patients (n = 64)				Female patients (n = 56)			
	ERα	*ERβ*	*PGR*	*AR*	*ERα*	*ERβ*	*PGR*	*AR*
Age	0.407**	-0.031	0.087	0.001	-0.093	0.031	-0.559**	-0.023
Right-sided cancer	0.143	0.080	-0.292*	-0.149	0.109	-0.248	-0.152	0.025
T stage	0.031	-0.087	0.051	0.245*	0.058	-0.191	-0.349**	0.162
Tumor Size	0.275*	-0.196	-0.218	0.242*	0.353*	-0.539**	-0.429**	-0.098
N Stage	0.573***	-0.694**	-0.205	0.360**	0.550**	-0.201	-0.274*	0.654**
Numbers of positive lymph nodes	0.518***	-0.675**	-0.195	0.323**	0.566***	-0.214	-0.180	0.433**
M Stage	0.186	-0.283*	0.024	0.266*	.172	-0.273	-0.167	0.338*
Mucinous Carcinoma	0.039	-0.091	-0.084	0.024	0.096	-0.026	-0.199	0.014
Poor differentiation	-0.015	-0.002	0.288*	0.015	0.099	0.158	-0.133	0.116
Lymphovascular invasion	0.117	-0.304*	-0.101	0.043	0.208	-0.126	-0.214	0.376*
Perineural invasion	-0.084	-0.092	0.044	-0.087	0.222	-0.373*	-0.337*	0.219
Late-stage cancer	0.691***	-0.844***	-0.175	0.478**	0.798***	-0.421**	-0.465**	0.959***

*P< 0.05.
**P< 0.01.
***P< 0.001.

10.3389/fendo.2023.1187259

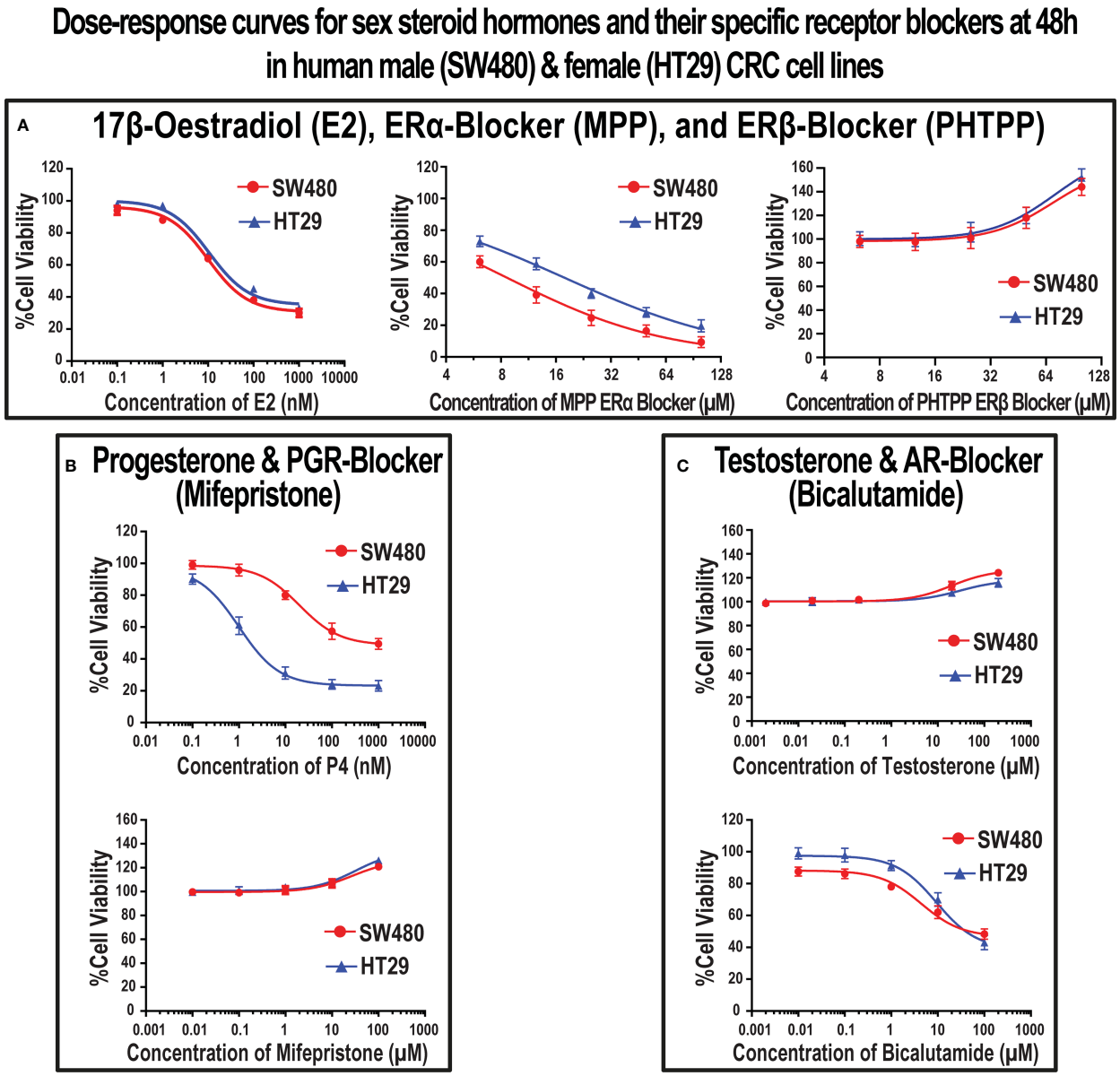

FIGURE 5
Dose-response curves with the IC50 (mean ± SD) and EC10 (mean ± SD) values of **(A)** 17β-estradiol (E2), ERα-blocker (MPP), and ERβ-blocker (PHTPP), **(B)** progesterone (P4) and PGR-blocker (mifepristone), and **(C)** testosterone and AR-blocker (bicalutamide) at 48h in the SW480 male and HT29 female colon cancer cell lines, as determined using the MTT cell viability assay (Data were analyzed by nonlinear regression to determine dose-response; n = 5 replicates/treatment).

whilst ERβ-blocker inhibited, the pro-apoptotic effects of E2 therapy in both cell lines (Figure 7). Similarly, P4 single treatment markedly reduced cell viability by increasing the percentage of early (2.3-fold & 1.2-fold) and late (2.4-fold & 9.6-fold) apoptotic SW480 and HT29 cells, respectively, and the effects were inhibited by the PGR-blocker, mifepristone (Figure 7). In contrast, testosterone monotherapy significantly increased the numbers of viable SW480 and HT29 cells, whilst its combination with bicalutamide showed marked elevations in the percentage of early and late apoptotic SW480 (6.9-fold & 3.3-fold, respectively) and HT29 (2.5-fold & 2.3-fold) cells (Figure 7).

4 Discussion

Herein, we measured ERα, ERβ, PGR, and AR protein expression in archived paired malignant and non-malignant colonic tissues, and the results were analyzed based on gender, age, and tumor sidedness. We also measured the effects of E2, P4, and testosterone, with and without their corresponding specific nuclear receptor blockers, on cell cycle and apoptosis in the SW480 male and HT29 female CRC cell lines. Our results revealed gender-dependent protein expression of the targeted sex steroid receptors in non-cancerous colonic tissues. Moreover, ERα and AR proteins increased, whereas ERβ and PGR

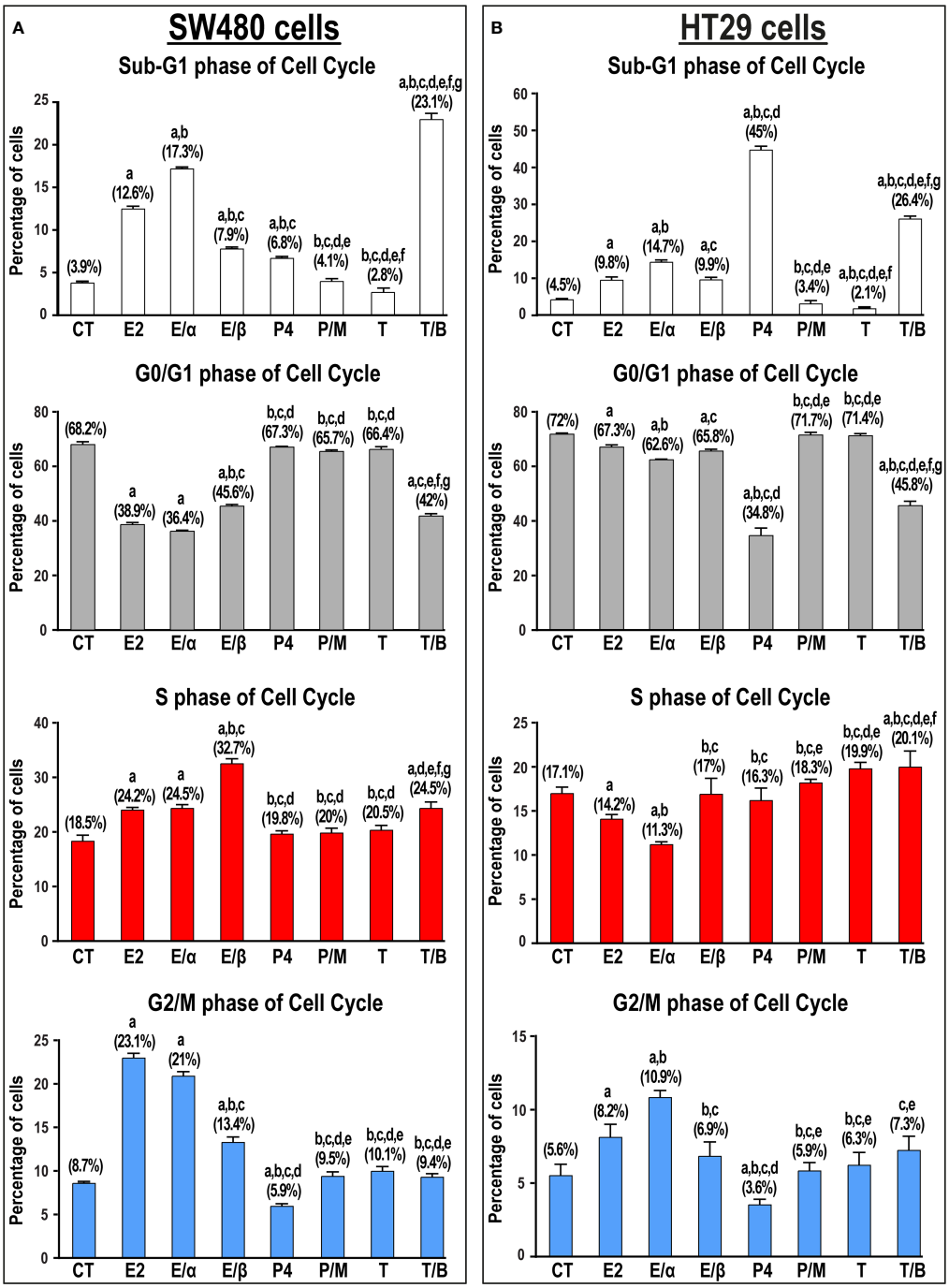

FIGURE 6
Percentage of cells (mean ± SD) in the different phases of cell cycle in non-treated control cells (CT) and following 17β-estradiol (E2), P4 (P4), and testosterone (T) for 24h alongside dual treatments for 48h with MPP ERα-blocker + E2 (E/α), PHTPP ERβ-blocker + E2 (E/β), mifepristone PGR-blocker + P4 (P/M), and bicalutamide AR-blocker + testosterone (T/B) in the **(A)** SW480 male and **(B)** HT29 female colon cancer cell lines (n = 3 biological replicates/group). Treatment with each receptor blocker was for a total duration of 48h in the co-therapy protocols, whilst E2, P4, or T therapies were incubated for 24h and were initiated in the single and dual treatment groups 24h after adding their corresponding receptor blockers for 24h. (Data were analyzed by one-way ANOVA with Tukey's HSD *post-hoc* test; a = P< 0.05 compared with CT; b = P< 0.05 compared with E2 group; c = P< 0.05 compared with E/α group, d = P< 0.05 compared with E/β group; e = P< 0.05 compared with P4 group; f = P< 0.05 compared with P/M group, and g = P< 0.05 compared with T group).

diminished markedly in neoplastic relative to non-neoplastic colonic tissues, and the dysregulations were maximal in late-stage cancers in both genders. ERα and AR proteins also correlated directly, whilst ERβ and PGR negatively, with tumors' histopathological features. Concomitantly, E2 monotherapy induced cell cycle arrest and promoted apoptosis in the SW480 male and HT29 female CRC cell lines, and pre-treating with ERα-blocker enhanced, whereas ERβ-blocker inhibited the anticancer actions. Similarly, P4 induced apoptosis in both cell lines, whilst adding the PGR-blocker impeded the effects. In contrast, testosterone promoted survival in

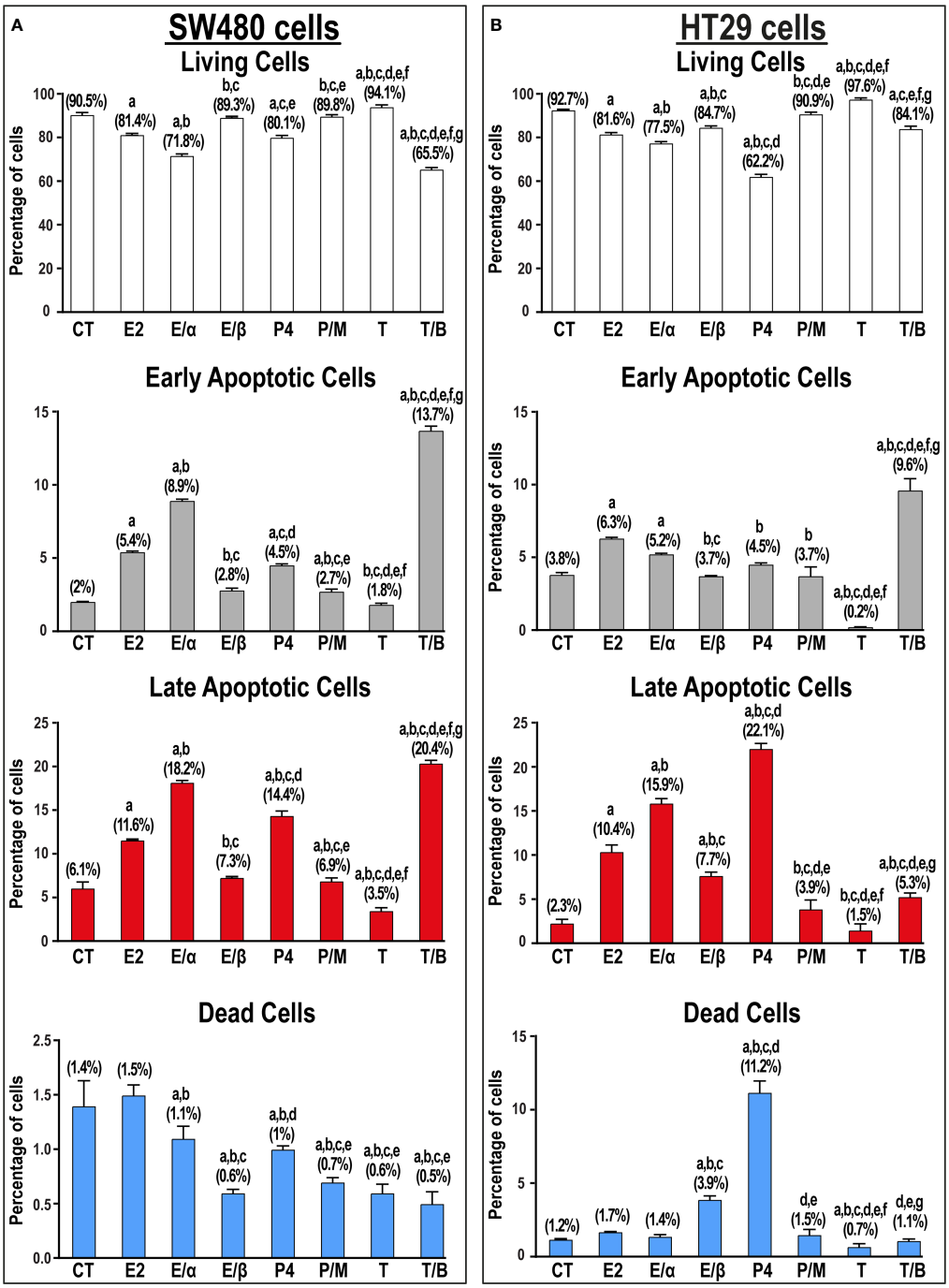

FIGURE 7
Percentage (mean ± SD) of living, early and late apoptotic alongside dead cells in non-treated control cells (CT) and following 17β-estradiol (E2), P4 (P4), and testosterone (T) for 24h alongside dual treatments for 48h with MPP ERα-blocker + E2 (E/α), PHTPP ERβ-blocker + E2 (E/β), mifepristone PGR-blocker + P4 (P/M), and bicalutamide AR-blocker + testosterone (T/B) in the **(A)** SW480 male and **(B)** HT29 female colon cancer cell lines (n = 3 biological replicates/group). Treatment with each receptor blocker was for a total duration of 48h in the co-therapy protocols, whilst E2, P4, or T therapies were incubated for 24h and were initiated in the single and dual treatment groups 24h after adding their corresponding receptor blockers for 24h. (Data were analyzed by one-way ANOVA with Tukey's HSD *post-hoc* test; a = P< 0.05 compared with CT; b = P< 0.05 compared with E2 group; c = P< 0.05 compared with E/α group, d = P< 0.05 compared with E/β group; e = P< 0.05 compared with P4 group; f = P< 0.05 compared with P/M group, and g = P< 0.05 compared with T group).

both cell lines, and the effects were hindered by the specific AR-blocker, bicalutamide. However, the best apoptotic actions in the SW480 male cell line were detected after blocking AR, whilst P4 showed the highest pro-apoptotic effects in the HT29 female cell line.

The importance of sex steroid hormones in colon cancer has gained greater attention, since the rates of CRC in premenopausal, as well as post-menopausal women using HRT, were markedly lower than nonuser post-menopausal women and age-matched

men (6, 8, 9, 44). The risk of CRC also increased significantly in women after oophorectomy (45, 46), and 17β-estradiol treatment *in vivo* and *in vitro* inhibited CRC progression *via* ERβ-mediated actions (33–36), whilst promoted cancer progression through ERα (47–49). Others have likewise reported lower CRC incidence in menopausal women using P4 (50, 51), and the hormone also triggered cell cycle arrest and apoptosis in several human CRC cell lines, including SW480 and HT29 cells (30, 36, 52). Furthermore, ERβ expression declined significantly in malignant relative to non-malignant colonic tissues and coincided with drastically elevated ERα (48, 53–55), and the expression linked with lower survival and higher recurrence rates, advanced stages, and distant metastasis (23–25, 27–29). Although many reports also disclosed marked declines in PGR in cancerous tissues, their results related to its prognostic value in CRC are inconclusive (23, 30–32). In contrast, male rats were more susceptible for developing CRC than females (37, 38), and orchiectomy reduced, whereas testosterone replacement therapy sustained, the numbers of tumors in male animals (38). Similar findings were also reported after chemically inducing CRC in male mice (39), as well as testosterone caused dose-dependent increases in the viability of HT29 cells (40). Moreover, AR increased in malignant clinical samples and correlated directly with tumor size, poor differentiation, lymph node positivity, advanced stage, and poor prognosis (26). However, the authors did not compare the expression between both genders. On the other hand, increased AR in female malignant tissues has been suggested to promote CRC aggressiveness by increasing classes III and V of β-tubulin protein, which are commonly activated in male patients and could underly the observed higher mortality rate in men (56).

Collectively, Our findings correlate with earlier studies reporting gender-dependent expression of ERs (14–16), PGR (17–19), and AR (20–22) in normal colon, which supports the notion that sex steroid hormones contribution to colon biology could, at least in part, be gender-specific. Moreover, our data and prior studies advocate that ERβ (33–36) and PGR (30, 36, 52) mediate tumor suppressive actions, whereas overexpressed ERα (23–25) and AR (37–40) could incite oncogenicity in colon. The present findings also provide additional support for the potential prognostic values of sex steroid receptors in CRC (23–30, 32). Although the current results also reinforce the notion that hormonal therapy could represent an alternative therapy for CRC (36, 38, 39, 50, 51, 57), treatment regimens should be tailored based on gender alongside the expression of sex steroid receptors in malignant tissues to achieve the highest efficacy. In more detail, we suggest that the use of ovarian sex steroid hormones (33–36, 50, 51), as well as blocking androgen receptor (38–40), could inhibit CRC progression by modulating the regulatory molecules of cell cycle and apoptosis. Nonetheless, further studies using the different sex steroid hormones and/or their specific receptor blockers, with and without 5-Fluororacil, are mandatory to measure their therapeutic efficiencies against CRC. Additionally, more studies are needed to elucidate the roles of sex steroid hormones in colon neoplasia by measuring their effects on the expression of oncogenic and tumor suppressive molecules.

Tumor sidedness is another important factor in CRC, and RSCs are linked with older age, poor differentiation, mucinous carcinoma, and worse outcomes (3–5). The oncogenic pathways and molecular features also vary substantially between proximal and distal colonic neoplasms (3–5). Despite this, little is known about the expression of sex steroid receptors in right and left-sided cancers. Herein, there was an overall significant increase in the expression of ERα, whilst PGR declined, in LSCs compared to RSCs. Furthermore, the highest ERα alongside the lowest PGR protein expression were observed in women aged ≥ 60 years and diagnosed with late-stage LSCs. On the other hand, ERβ and AR proteins were in general equal between both anatomical sides. By disseminating the data according to gender, however, late-stage LSCs obtained from females ≥ 60 years of age showed the weakest and strongest protein expression of ERβ and AR, respectively. In contrast, right and left-sided male malignant tissues exhibited equivalent expression of ERβ, as well as AR, in the different clinical stages of CRC.

Taken together, our findings suggest that ERα and PGR protein expression in CRC could be reliant on tumor sidedness alongside gender, age, and clinical stage. Paradoxically, loss of ERβ and AR overexpression in malignant tissues appear to be gender-specific, since in male patients the deregulations were constant between RSCs and LSCs at the different stages, whilst in post-menopausal female patients the alterations were more pronounced in distal colon cancers, especially during the late stages. Hence, we speculate that the rates of CRC are lower in premenopausal women (8, 9, 44) due to higher ERβ (14, 33, 35) and PGR (30, 52) alongside lower ERα (47–49) and AR (56, 58) expression in colonic tissues, whereas their pathological alterations following menopause might trigger CRC. Moreover, future studies should consider gender, age, clinical stage, and tumor sidedness to precisely explore the roles of the targeted sex steroid receptors and/or measure their prognostic values in CRC.

This study has several drawbacks. Firstly, we only measured the protein expression of the targeted receptors, and future studies should also measure their gene expression. Moreover, the patients included had their surgical innervations between January 2019 and December 2021 and, therefore, prognostic data (e.g., 5-year survival rate, disease-free survival rate, etc.), as well as data related to using hormone replacement therapy were not available to correlate them with the expression profiles of the targeted receptors. Hence, additional studies are still needed to measure the prognostic values of sex steroid receptors according to gender, tumor sites, and clinical stages. Furthermore, we only measured the expression of the targeted receptors by IHC, and future prospective studies that include fresh tissues are needed to validate the protein expression by additional techniques (e.g., Western blot). More *in vitro* studies are also required to investigate the molecular pathways underlying the actions of sex steroid hormones and their receptors in CRC (e.g., cell cycle regulatory molecules, apoptosis regulatory molecules, etc.). Moreover, future studies should also measure the genes and proteins of the G-protein coupled membrane (e.g., mER, mPGR, and mAR) and the nuclear receptors, since the membranous receptors were shown to mediate anti-tumorigenic actions in CRC (59, 60).

In conclusion, non-malignant tissues from women ≤ 50 years of age showed markedly lower ERα and AR alongside stronger ERβ and PGR proteins than men and women aged ≥ 60 years, which

could explain the commonly reported lower CRC incidence in premenopausal women. In malignant tissues, the proteins of ERα and AR increased significantly and concurred with decreases in ERβ and PGR, and the tumor clinical characteristics correlated positively with ERα and AR, whilst negatively with ERβ and PGR, supporting the contributions of receptors to colon carcinogenesis. However, the expression profiles of the sex steroid receptors in cancerous tissues varied between genders, clinical stages, and tumor sidedness. Moreover, E2 and P4 monotherapies induced apoptosis, whilst testosterone caused proliferation in the SW480 male and HT29 female CRC cell lines, and the effects were reversed by pre-treating the cells with the specific blockers of ERβ, PGR, and AR receptors, respectively. Collectively, this study advocates the promising prognostic value of the targeted sex steroid receptors, as well as the potential benefits of hormonal therapy in CRC. However, future studies should measure the expression of membranous and nuclear receptors of sex steroid hormones in malignant colonic tissues and the results should be disseminated according to gender, age, clinical stage, and tumor sidedness to accurately determine their prognostic values in CRC. More *in vivo* and *in vitro* studies are also still needed to measure the anti-cancer effects of sex steroid hormones and their receptor blockers, with and without chemotherapy, to precisely tailor hormonal therapeutic regimens against CRC based on gender and the expression of sex steroid receptors.

Data availability statement

The original contributions presented in the study are included in the article/Supplementary Material. Further inquiries can be directed to the corresponding author.

Ethics statement

The studies involving human participants were reviewed and approved by The Institutional Review Board of King Abdullah Medical City in Makkah, Saudi Arabia (KAMC; #19-498). Written informed consent for participation was not required for this study in accordance with the national legislation and the institutional requirements.

Author contributions

Conceptualization: BR, AkA, and SI. Methodology: AkA, SI, AhA, MofA, HA, GB, OA and IM. Investigation: AkA. RA, FM and BR. Visualization: BR, SA, MonA, BB and MaA. Validation: SA, MonA, BB and MaA. Formal analysis: BR, AkA, RA, and FM. Data curation: BR, AkA. and SI. Supervision: BR, AkA, RA and FM. Funding acquisition: BR, AkA, RA and FM. Resources: BR and AkA. Project administration: BR RA and FM. Writing—original draft: BR AhA, MofA and HA. Writing—review and editing: AkA. All authors contributed to the article and approved the submitted version.

Funding

This work was supported by the Deputyship for Research & Innovation, Ministry of Education in Saudi Arabia [Grant Code: IFP22UQU4320045DSR101]. The funding organization was not involved in the design of the study; the collection, analysis, and interpretation of data; writing the report; and did not impose any restrictions regarding the publication of the report.

Conflict of interest

The authors declare that the research was conducted in the absence of any commercial or financial relationships that could be construed as a potential conflict of interest.

Publisher's note

All claims expressed in this article are solely those of the authors and do not necessarily represent those of their affiliated organizations, or those of the publisher, the editors and the reviewers. Any product that may be evaluated in this article, or claim that may be made by its manufacturer, is not guaranteed or endorsed by the publisher.

Supplementary material

The Supplementary Material for this article can be found online at: https://www.frontiersin.org/articles/10.3389/fendo.2023.1187259/full#supplementary-material

SUPPLEMENTARY FIGURE 1
(A) Immunohistochemical localization of ERα in non-malignant colonic tissues collected from patients diagnosed with early-stage (I/II) and late-stage (III/IV) colorectal cancer (20× objective; Scale bar = 15 μm) alongside **(B)** their IHC arbitrary scores are shown as boxplots according to gender, age, tumor sides, and cancer stages. (a = P< 0.05 compared with males ≤ 50 years with right sided early-stage cancer; b = P< 0.05 compared with males ≥ 60 years with right sided early-stage cancer; c = P< 0.05 compared with females ≤ 50 years with right sided early-stage cancer; d = P< 0.05 compared with females ≥ 60 years with right sided early-stage cancer; e = P< 0.05 compared with males ≤ 50 years with right sided late-stage cancer; f = P< 0.05 compared with males ≥ 60 years with right sided late-stage cancer; g = P< 0.05 compared with females ≤ 50 years with right sided late-stage cancer; h = P< 0.05 compared with females ≥ 60 years with right sided late-stage cancer; i = P< 0.05 compared with males ≤ 50 years with left sided early-stage cancer; j = P< 0.05 compared with males ≥ 60 years with left sided early-stage cancer; k = P< 0.05 compared with females ≤ 50 years with left sided early-stage cancer; l = P< 0.05 compared with females ≥ 60 years with left sided early-stage cancer; m = P< 0.05 compared with males ≤ 50 years with left sided late-stage cancer; n = P< 0.05 compared with males ≥ 60 years with left sided late-stage cancer and o = P< 0.05 compared with females ≤ 50 years with left sided late-stage cancer).

SUPPLEMENTARY FIGURE 2
(A) Immunohistochemical localization of ERβ in non-malignant colonic tissues collected from patients diagnosed with early-stage (I/II) and late-stage (III/IV) colorectal cancer (20× objective; Scale bar = 15 μm) alongside **(B)** their IHC arbitrary scores are shown as boxplots according to gender, age, tumor sides, and cancer stages. (a = P< 0.05 compared with males ≤ 50 years with right sided early-stage cancer; b = P< 0.05 compared with males ≥ 60 years with right sided early-stage cancer; c = P< 0.05 compared with females ≤ 50 years with right sided early-stage cancer; d = P< 0.05 compared with females ≥ 60 years with right sided early-

stage cancer; e = P< 0.05 compared with males ≤ 50 years with right sided late-stage cancer; f = P< 0.05 compared with males ≥ 60 years with right sided late-stage cancer; g = P< 0.05 compared with females ≤ 50 years with right sided late-stage cancer; h = P< 0.05 compared with females ≥ 60 years with right sided late-stage cancer; i = P< 0.05 compared with males ≤ 50 years with left sided early-stage cancer; j = P< 0.05 compared with males ≥ 60 years with left sided early-stage cancer; k = P< 0.05 compared with females ≤ 50 years with left sided early-stage cancer; l = P< 0.05 compared with females ≥ 60 years with left sided early-stage cancer; m = P< 0.05 compared with males ≤ 50 years with left sided late-stage cancer; n = P< 0.05 compared with males ≥ 60 years with left sided late-stage cancer and o = P< 0.05 compared with females ≤ 50 years with left sided late-stage cancer).

SUPPLEMENTARY FIGURE 3

(A) Immunohistochemical localization of PGR in non-malignant colonic tissues collected from patients diagnosed with early-stage (I/II) and late-stage (III/IV) colorectal cancer (20× objective; Scale bar = 15 μm) alongside **(B)** their IHC arbitrary scores are shown as boxplots according to gender, age, tumor sides, and cancer stages. (a = P< 0.05 compared with males ≤ 50 years with right sided early-stage cancer; b = P< 0.05 compared with males ≥ 60 years with right sided early-stage cancer; c = P< 0.05 compared with females ≤ 50 years with right sided early-stage cancer; d = P< 0.05 compared with females ≥ 60 years with right sided early-stage cancer; e = P< 0.05 compared with males ≤ 50 years with right sided late-stage cancer; f = P< 0.05 compared with males ≥ 60 years with right sided late-stage cancer; g = P< 0.05 compared with females ≤ 50 years with right sided late-stage cancer; h = P< 0.05 compared with females ≥ 60 years with right sided late-stage cancer; i = P< 0.05 compared with males ≤ 50 years with left sided early-stage cancer; j = P< 0.05 compared with males ≥ 60 years with left sided early-stage cancer; k = P< 0.05 compared with females ≤ 50 years with left sided early-stage cancer; l = P< 0.05 compared with females ≥ 60 years with left sided early-stage cancer; m = P< 0.05 compared with males ≤ 50 years with left sided late-stage cancer; n = P< 0.05 compared with males ≥ 60 years with left sided late-stage cancer and o = P< 0.05 compared with females ≤ 50 years with left sided late-stage cancer).

SUPPLEMENTARY FIGURE 4

(A) Immunohistochemical localization of AR in non-malignant colonic tissues collected from patients diagnosed with early-stage (I/II) and late-stage (III/IV) colorectal cancer (20× objective; Scale bar = 15 μm) alongside **(B)** their IHC arbitrary scores are shown as boxplots according to gender, age, tumor sides, and cancer stages. (a = P< 0.05 compared with males ≤ 50 years with right sided early-stage cancer; b = P< 0.05 compared with males ≥ 60 years with right sided early-stage cancer; c = P< 0.05 compared with females ≤ 50 years with right sided early-stage cancer; d = P< 0.05 compared with females ≥ 60 years with right sided early-stage cancer; e = P< 0.05 compared with males ≤ 50 years with right sided late-stage cancer; f = P< 0.05 compared with males ≥ 60 years with right sided late-stage cancer; g = P< 0.05 compared with females ≤ 50 years with right sided late-stage cancer; h = P< 0.05 compared with females ≥ 60 years with right sided late-stage cancer; i = P< 0.05 compared with males ≤ 50 years with left sided early-stage cancer; j = P< 0.05 compared with males ≥ 60 years with left sided early-stage cancer; k = P< 0.05 compared with females ≤ 50 years with left sided early-stage cancer; l = P< 0.05 compared with females ≥ 60 years with left sided early-stage cancer; m = P< 0.05 compared with males ≤ 50 years with left sided late-stage cancer; n = P< 0.05 compared with males ≥ 60 years with left sided late-stage cancer and o = P< 0.05 compared with females ≤ 50 years with left sided late-stage cancer).

SUPPLEMENTARY FIGURE 5

Cell cycle analysis data for SW480 cells with the gating strategy used for each treatment group. The proportion of each phase of the cell cycle was determined for 20,000 single cell events using the NovoExpress cell cycle algorithm (right panel; histogram), and first gated on the SW480 cell population using forward scatter (FSC) vs side scatter (SSC) scatter plots (left panels), and then using DNA content height (H) *vs.* Area (A) scatter plots (middle panels) to calculate single cell events (pulse processing). The plots shown are representative of one of three similar experiments, and the percentage of each cell cycle phase is shown (mean ± SD; n = 3).

SUPPLEMENTARY FIGURE 6

Cell cycle analysis data for HT29 cells with the gating strategy used for each treatment group. The proportion of each phase of the cell cycle was determined for 20,000 single cell events using the NovoExpress cell cycle algorithm (right panel; histogram), and first gated on the HT29 cell population using forward scatter (FSC) vs side scatter (SSC) scatter plots (left panels), and then using DNA content height (H) *vs.* Area (A) scatter plots (middle panels) to calculate single cell events (pulse processing). The plots shown are representative of one of three similar experiments, and the percentage of each cell cycle phase is shown (mean ± SD; n = 3).

References

1. Bray F, Ferlay J, Soerjomataram I, Siegel RL, Torre LA, Jemal A. Global cancer statistics 2018: GLOBOCAN estimates of incidence and mortality worldwide for 36 cancers in 185 countries. *CA Cancer J Clin* (2018) 68(6):394–424. doi: 10.3322/caac.21492

2. Sung H, Ferlay J, Siegel RL, Laversanne M, Soerjomataram I, Jemal A, et al. Global cancer statistics 2020: GLOBOCAN estimates of incidence and mortality worldwide for 36 cancers in 185 countries. *CA Cancer J Clin* (2021) 71(3):209–49. doi: 10.3322/caac.21660

3. Lee MS, Menter DG, Kopetz S. Right versus left colon cancer biology: integrating the consensus molecular subtypes. *J Natl Compr Canc Netw* (2017) 15(3):411–9. doi: 10.6004/jnccn.2017.0038

4. Refaat B, Zekri J, Aslam A, Ahmad J, Baghdadi MA, Meliti A, et al. Profiling activins and follistatin in colorectal cancer according to clinical stage, tumour sidedness and Smad4 status. *Pathol Oncol Res* (2021) 27(149):1–20. doi: 10.3389/pore.2021.1610032

5. Narayanan S, Gabriel E, Attwood K, Boland P, Nurkin S. Association of clinicopathologic and molecular markers on stage-specific survival of right versus left colon cancer. *Clin Colorectal Cancer* (2018) 17(4):e671–8. doi: 10.1016/j.clcc.2018.07.001

6. Murphy N, Xu L, Zervoudakis A, Xue X, Kabat G, Rohan TE, et al. Reproductive and menstrual factors and colorectal cancer incidence in the women's health initiative observational study. *Br J Cancer* (2017) 116(1):117–25. doi: 10.1038/bjc.2016.345

7. Islami F, Goding Sauer A, Miller KD, Siegel RL, Fedewa SA, Jacobs EJ, et al. Proportion and number of cancer cases and deaths attributable to potentially modifiable risk factors in the united states. *CA Cancer J Clin* (2018) 68(1):31–54. doi: 10.3322/caac.21440

8. Jang YC, Huang HL, Leung CY. Association of hormone replacement therapy with mortality in colorectal cancer survivor: a systematic review and meta-analysis. *BMC Cancer* (2019) 19(1):1199. doi: 10.1186/s12885-019-6428-0

9. Schmuck R, Gerken M, Teegen EM, Krebs I, Klinkhammer-Schalke M, Aigner F, et al. Gender comparison of clinical, histopathological, therapeutic and outcome factors in 185,967 colon cancer patients. *Langenbecks Arch Surg* (2020) 405(1):71–80. doi: 10.1007/s00423-019-01850-6

10. Chen C, Gong X, Yang X, Shang X, Du Q, Liao Q, et al. The roles of estrogen and estrogen receptors in gastrointestinal disease. *Oncol Lett* (2019) 18(6):5673–80. doi: 10.3892/ol.2019.10983

11. Sato R, Suzuki T, Katayose Y, Miura K, Shiiba K, Tateno H, et al. Steroid sulfatase and estrogen sulfotransferase in colon carcinoma: regulators of intratumoral estrogen concentrations and potent prognostic factors. *Cancer Res* (2009) 69(3):914–22. doi: 10.1158/0008-5472.CAN-08-0906

12. Prough RA, Clark BJ, Klinge CM. Novel mechanisms for DHEA action. *J Mol Endocrinol* (2016) 56(3):R139–55. doi: 10.1530/JME-16-0013

13. Diviccaro S, Giatti S, Borgo F, Falvo E, Caruso D, Garcia-Segura LM, et al. Steroidogenic machinery in the adult rat colon. *J Steroid Biochem Mol Biol* (2020) 203:105732. doi: 10.1016/j.jsbmb.2020.105732

14. Papaxoinis K, Triantafyllou K, Sasco AJ, Nicolopoulou-Stamati P, Ladas SD. Subsite-specific differences of estrogen receptor beta expression in the normal colonic epithelium: implications for carcinogenesis and colorectal cancer epidemiology. *Eur J Gastroenterol Hepatol* (2010) 22(5):614–9. doi: 10.1097/MEG.0b013e328335ef50

15. Alzamora R, O'Mahony F, Bustos V, Rapetti-Mauss R, Urbach V, Cid LP, et al. Sexual dimorphism and oestrogen regulation of KCNE3 expression modulates the functional properties of KCNQ1 K+ channels. *J Physiol* (2011) 589(Pt 21):5091–107. doi: 10.1113/jphysiol.2011.215772

16. Hases L, Archer A, Indukuri R, Birgersson M, Savva C, Korach-Andrė M, et al. High-fat diet and estrogen impacts the colon and its transcriptome in a sex-dependent manner. *Sci Rep* (2020) 10(1):16160. doi: 10.1038/s41598-020-73166-1

17. Motylewska E, Stasikowska O, Mełeń-Mucha G. The inhibitory effect of diarylpropionitrile, a selective agonist of estrogen receptor beta, on the growth of

MC38 colon cancer line. *Cancer Lett* (2009) 276(1):68–73. doi: 10.1016/j.canlet.2008.10.050

18. Guarino M, Cheng L, Cicala M, Ripetti V, Biancani P, Behar J. Progesterone receptors and serotonin levels in colon epithelial cells from females with slow transit constipation. *Neurogastroenterol Motil* (2011) 23(6):575–e210. doi: 10.1111/j.1365-2982.2011.01705.x

19. Asavasupreechar T, Saito R, Miki Y, Edwards DP, Boonyaratanakornkit V, Sasano H. Systemic distribution of progesterone receptor subtypes in human tissues. *J Steroid Biochem Mol Biol* (2020) 199:105599. doi: 10.1016/j.jsbmb.2020.105599

20. Stebbings WS, Farthing MJ, Puddefoot JR, Anderson E, Vinson GP, Northover JM, et al. Androgen receptors in colorectal adenomas. *J Cancer Res Clin Oncol* (1988) 114(2):208–11. doi: 10.1007/BF00417839

21. Meggouh F, Lointier P, Saez S. Sex steroid and 1,25-dihydroxyvitamin D3 receptors in human colorectal adenocarcinoma and normal mucosa. *Cancer Res* (1991) 51(4):1227–33.

22. Marugo M, Aste H, Bernasconi D, Fazzuoli L, Conio M, Cuva A, et al. Cytosolic and nuclear androgen receptors in colorectal adenomas. *Anticancer Res* (1992) 12(3):705–8.

23. Ye SB, Cheng YK, Zhang L, Wang XP, Wang L, Lan P. Prognostic value of estrogen receptor-α and progesterone receptor in curatively resected colorectal cancer: a retrospective analysis with independent validations. *BMC Cancer* (2019) 19(1):933. doi: 10.1186/s12885-019-5918-4

24. Ye SB, Cheng YK, Deng R, Deng Y, Li P, Zhang L, et al. The predictive value of estrogen receptor 1 on adjuvant chemotherapy in locally advanced colorectal cancer: a retrospective analysis with independent validation and its potential mechanism. *Front Oncol* (2020) 10:214. doi: 10.3389/fonc.2020.00214

25. Topi G, Ghatak S, Satapathy SR, Ehrnström R, Lydrup ML, Sjölander A. Combined estrogen alpha and beta receptor expression has a prognostic significance for colorectal cancer patients. *Front Med (Lausanne)* (2022) 9:739620. doi: 10.3389/fmed.2022.739620

26. Albasri AM, Elkablawy MA. Clinicopathological and prognostic significance of androgen receptor overexpression in colorectal cancer. experience from Al-madinah Al-munawarah, Saudi Arabia. *Saudi Med J* (2019) 40(9):893–900. doi: 10.15537/smj.2019.9.24204

27. Topi G, Ehrnström R, Jirström K, Palmquist I, Lydrup ML, Sjölander A. Association of the oestrogen receptor beta with hormone status and prognosis in a cohort of female patients with colorectal cancer. *Eur J Cancer* (2017) 83:279–89. doi: 10.1016/j.ejca.2017.06.013

28. Rudolph A, Toth C, Hoffmeister M, Roth W, Herpel E, Jansen L, et al. Expression of oestrogen receptor β and prognosis of colorectal cancer. *Br J Cancer* (2012) 107(5):831–9. doi: 10.1038/bjc.2012.323

29. Babic A, Miladinovic N, Milin Lazovic J, Milenkovic S. Decreased ERβ expression and high cyclin D1 expression may predict early CRC recurrence in high-risk duke's b and duke's c stage. *J buon* (2021) 26(2):536–43.

30. Zhang YL, Wen XD, Guo X, Huang SQ, Wang TT, Zhou PT, et al. Progesterone suppresses the progression of colonic carcinoma by increasing the activity of the GADD45α/JNK/c–Jun signalling pathway. *Oncol Rep* (2021) 45(6):1–13. doi: 10.3892/or.2021.8046

31. Abd ElLateef AAE, Mohamed AES, Elhakeem AA, Ahmed SF. Estrogen and progesterone expression in colorectal carcinoma: a clinicopathological study. *Asian Pac J Cancer Prev* (2020) 21(4):1155–62. doi: 10.31557/APJCP.2020.21.4.1155

32. Salehi Far S, Soltani M, Zardast M, Ghasemian Moghaddam MR. Investigating the factors associated with the level of expression of estrogen and progesterone receptors in patients suffering from colorectal cancer. *J Cancer Epidemiol* (2021) 2021:4478155. doi: 10.1155/2021/4478155

33. Acconcia F, Totta P, Ogawa S, Cardillo I, Inoue S, Leone S, et al. Survival versus apoptotic 17beta-estradiol effect: role of ER alpha and ER beta activated non-genomic signaling. *J Cell Physiol* (2005) 203(1):193–201. doi: 10.1002/jcp.20219

34. Wei Y, Huang C, Wu H, Huang J. Estrogen receptor beta (ERβ) mediated-CyclinD1 degradation via autophagy plays an anti-proliferation role in colon cells. *Int J Biol Sci* (2019) 15(5):942–52. doi: 10.7150/ijbs.30930

35. Topi G, Satapathy SR, Dash P, Fred Mehrabi S, Ehrnström R, Olsson R, et al. Tumour-suppressive effect of oestrogen receptor β in colorectal cancer patients, colon cancer cells, and a zebrafish model. *J Pathol* (2020) 251(3):297–309. doi: 10.1002/path.5453

36. Mahbub AA, Aslam A, Elzubier ME, El-Boshy M, Abdelghany AH, Ahmad J, et al. Enhanced anti-cancer effects of oestrogen and progesterone co-therapy against colorectal cancer in males. *Front Endocrinol (Lausanne)* (2022) 13:941834. doi: 10.3389/fendo.2022.941834

37. Moon RC, Fricks CM. Influence of gonadal hormones and age on 1,2-dimethylhydrazine-induced colon carcinogenesis. *Cancer* (1977) 40(5 Suppl):2502–8. doi: 10.1002/1097-0142(197711)40:5+<2502::AID-CNCR2820400917>3.0.CO;2-7

38. Amos-Landgraf JM, Heijmans J, Wielenga MC, Dunkin E, Krentz KJ, Clipson L, et al. Sex disparity in colonic adenomagenesis involves promotion by male hormones, not protection by female hormones. *Proc Natl Acad Sci U.S.A.* (2014) 111(46):16514–9. doi: 10.1073/pnas.1323064111

39. Song CH, Kim N, Nam RH, Choi SI, Yu JE, Nho H, et al. Testosterone strongly enhances azoxymethane/dextran sulfate sodium-induced colorectal cancer development in C57BL/6 mice. *Am J Cancer Res* (2021) 11(6):3145–62.

40. Farahmandlou N, Oryan S, Ahmadi R, Eidi A. Association of testosterone with colorectal cancer (HT29), human glioblastoma (A172) and human embryonic kidney (HEK293) cells proliferation. *Acta Endocrinol (Buchar)*. (2017) 13(2):144–9. doi: 10.4183/aeb.2017.144

41. Refaat B, Abdelghany AH, BaSalamah MA, El-Boshy M, Ahmad J, Idris S. Acute and chronic iron overloading differentially modulates the expression of cellular iron-homeostatic molecules in normal rat kidney. *J Histochem Cytochem* (2018) 66(11):825–39. doi: 10.1369/0022155418782696

42. Almaimani RA, Aslam A, Ahmad J, El-Readi MZ, El-Boshy ME, Abdelghany AH, et al. In vivo and in vitro enhanced tumoricidal effects of metformin, active vitamin D(3), and 5-fluorouracil triple therapy against colon cancer by modulating the PI3K/Akt/PTEN/mTOR network. *Cancers (Basel)* (2022) 14(6):1–24. doi: 10.3390/cancers14061538

43. Idris S, Refaat B, Almaimani RA, Ahmed HG, Ahmad J, Alhadrami M, et al. Enhanced in vitro tumoricidal effects of 5-fluorouracil, thymoquinone, and active vitamin D3 triple therapy against colon cancer cells by attenuating the PI3K/AKT/mTOR pathway. *Life Sci* (2022) 296:120442. doi: 10.1016/j.lfs.2022.120442

44. Siegel RL, Miller KD, Goding Sauer A, Fedewa SA, Butterly LF, Anderson JC, et al. Colorectal cancer statistics. *CA Cancer J Clin* (2020) 70(3):145–64. doi: 10.3322/caac.21601

45. Luo G, Zhang Y, Wang L, Huang Y, Yu Q, Guo P, et al. Risk of colorectal cancer with hysterectomy and oophorectomy: a systematic review and meta-analysis. *Int J Surg* (2016) 34:88–95. doi: 10.1016/j.ijsu.2016.08.518

46. Koch T, Therming Jørgensen J, Christensen J, Duun-Henriksen AK, Priskorn L, Kildevaeld Simonsen M, et al. Bilateral oophorectomy and rate of colorectal cancer: a prospective cohort study. *Int J Cancer* (2022) 150(1):38–46. doi: 10.1002/ijc.33776

47. Lopez-Calderero I, Carnero A, Astudillo A, Palacios J, Chaves M, Benavent M, et al. Prognostic relevance of estrogen receptor-alpha Ser167 phosphorylation in stage II-III colon cancer patients. *Hum Pathol* (2014) 45(12):2437–46. doi: 10.1016/j.humpath.2014.08.008

48. Liu S, Fan W, Gao X, Huang K, Ding C, Ma G, et al. Estrogen receptor alpha regulates the wnt/β-catenin signaling pathway in colon cancer by targeting the NOD-like receptors. *Cell Signal* (2019) 61:86–92. doi: 10.1016/j.cellsig.2019.05.009

49. Fan W, Gao X, Ding C, Lv Y, Shen T, Ma G, et al. Estrogen receptors participate in carcinogenesis signaling pathways by directly regulating NOD-like receptors. *Biochem Biophys Res Commun* (2019) 511(2):468–75. doi: 10.1016/j.bbrc.2019.02.085

50. Chlebowski RT, Wactawski-Wende J, Ritenbaugh C, Hubbell FA, Ascensao J, Rosenberg CA, et al. Estrogen plus progestin and colorectal cancer in postmenopausal women. *N Engl J Med* (2004) 350(10):991–1004. doi: 10.1056/NEJMoa032071

51. Schindler AE. Long-term use of progestogens: colon adenoma and colon carcinoma. *Gynecol Endocrinol* (2007) 23 Suppl 1:42–4. doi: 10.1080/09513590701584899

52. Meijer BJ, Wielenga MCB, Hoyer PB, Amos-Landgraf JM, Hakvoort TBM, Muncan V, et al. Colorectal tumor prevention by the progestin medroxyprogesterone acetate is critically dependent on postmenopausal status. *Oncotarget* (2018) 9(55):30561–7. doi: 10.18632/oncotarget.25703

53. Armstrong CM, Billimek AR, Allred KF, Sturino JM, Weeks BR, Allred CD. A novel shift in estrogen receptor expression occurs as estradiol suppresses inflammation-associated colon tumor formation. *Endocr Relat Cancer* (2013) 20(4):515–25. doi: 10.1530/ERC-12-0308

54. Principi M, Di Leo A, Pricci M, Scavo MP, Guido R, Tanzi S, et al. Phytoestrogens/insoluble fibers and colonic estrogen receptor β: randomized, double-blind, placebo-controlled study. *World J Gastroenterol* (2013) 19(27):4325–33. doi: 10.3748/wjg.v19.i27.4325

55. López-Calderero I, Carnero A, Astudillo A, Palacios J, Chaves M, Benavent M, et al. Prognostic relevance of estrogen receptor-α Ser167 phosphorylation in stage II-III colon cancer patients. *Hum Pathol* (2014) 45(12):2437–46. doi: 10.1016/j.humpath.2014.08.008

56. Mariani M, Zannoni GF, Sioletic S, Sieber S, Martino C, Martinelli E, et al. Gender influences the class III and V β-tubulin ability to predict poor outcome in colorectal cancer. *Clin Cancer Res* (2012) 18(10):2964–75. doi: 10.1158/1078-0432.CCR-11-2318

57. Sasso CV, Santiano FE, Campo Verde Arboccó F, Zyla LE, Semino SN, Guerrero-Gimenez ME, et al. Estradiol and progesterone regulate proliferation and apoptosis in colon cancer. *Endocr Connect* (2019) 8(3):217–29. doi: 10.1530/EC-18-0374

58. Yu X, Li S, Xu Y, Zhang Y, Ma W, Liang C, et al. Androgen maintains intestinal homeostasis by inhibiting BMP signaling via intestinal stromal cells. *Stem Cell Rep* (2020) 15(4):912–25. doi: 10.1016/j.stemcr.2020.08.001

59. Liu Q, Chen Z, Jiang G, Zhou Y, Yang X, Huang H, et al. Epigenetic down regulation of G protein-coupled estrogen receptor (GPER) functions as a tumor suppressor in colorectal cancer. *Mol Cancer* (2017) 16(1):87. doi: 10.1186/s12943-017-0654-3

60. Gu S, Papadopoulou N, Gehring EM, Nasir O, Dimas K, Bhavsar SK, et al. Functional membrane androgen receptors in colon tumors trigger pro-apoptotic responses in vitro and reduce drastically tumor incidence in vivo. *Mol Cancer* (2009) 8:114. doi: 10.1186/1476-4598-8-114

frontiers | Frontiers in Endocrinology

TYPE Original Research
PUBLISHED 25 May 2023
DOI 10.3389/fendo.2023.1139874

OPEN ACCESS

EDITED BY
Anil Mathew Tharappel,
University of Arizona, United States

REVIEWED BY
Silvana A. Andric,
University of Novi Sad, Serbia
Cheryl A. Frye,
Comprehensive Neuropsychological Services, United States

*CORRESPONDENCE
Huixian Cui
cuihx@hebmu.edu.cn
Sha Li
lisha@hebmu.edu.cn

RECEIVED 07 January 2023
ACCEPTED 15 May 2023
PUBLISHED 25 May 2023

CITATION
Song L, Chen H, Qiao D, Zhang B, Guo F, Zhang Y, Wang C, Li S and Cui H (2023) ZIP9 mediates the effects of DHT on learning, memory and hippocampal synaptic plasticity of male Tfm and APP/PS1 mice. *Front. Endocrinol.* 14:1139874. doi: 10.3389/fendo.2023.1139874

ZIP9 mediates the effects of DHT on learning, memory and hippocampal synaptic plasticity of male Tfm and APP/PS1 mice

Leigang Song[1,2], Huan Chen[1,3,4], Dan Qiao[1], Bohan Zhang[1], Fangzhen Guo[1], Yizhou Zhang[1,3,4], Chang Wang[1,3,4], Sha Li[1,3,4]* and Huixian Cui[1,3,4]*

[1]Department of Human Anatomy, Hebei Medical University, Shijiazhuang, Hebei, China, [2]Department of Sports Human Science, Hebei Sport University, Shijiazhuang, Hebei, China, [3]Neuroscience Research Center, Hebei Medical University, Shijiazhuang, Hebei, China, [4]Hebei Key Laboratory of Neurodegenerative Disease Mechanism, Hebei Medical University, Shijiazhuang, Hebei, China

Androgens are closely associated with functions of hippocampal learning, memory, and synaptic plasticity. The zinc transporter ZIP9 (SLC39A9) regulates androgen effects as a binding site distinct from the androgen receptor (AR). However, it is still unclear whether androgens regulate their functions in hippocampus of mice through ZIP9. Compared with wild-type (WT) male mice, we found that AR-deficient male testicular feminization mutation (Tfm) mice with low androgen levels had learning and memory impairment, decreased expression of hippocampal synaptic proteins PSD95, drebrin, SYP, and dendritic spine density. Dihydrotestosterone (DHT) supplementation significantly improved these conditions in Tfm male mice, although the beneficial effects disappeared after hippocampal ZIP9 knockdown. To explore the underlying mechanism, we first detected the phosphorylation of ERK1/2 and eIF4E in the hippocampus and found that it was lower in Tfm male mice than in WT male mice, it upregulated with DHT supplementation, and it downregulated after hippocampal ZIP9 knockdown. Next, we found that the expression of PSD95, p-ERK1/2, and p-eIF4E increased in DHT-treated mouse hippocampal neuron HT22 cells, and ZIP9 knockdown or overexpression inhibited or further enhanced these effects. Using the ERK1/2 specific inhibitor SCH772984 and eIF4E specific inhibitor eFT508, we found that DHT activated ERK1/2 through ZIP9, resulting in eIF4E phosphorylation, thus promoting PSD95 protein expression in HT22 cells. Finally, we found that ZIP9 mediated the effects of DHT on the expression of synaptic proteins PSD95, drebrin, SYP, and dendritic spine density in the hippocampus of APP/PS1 mice through the ERK1/2-eIF4E pathway and affected learning and memory. This study demonstrated that androgen affected learning and memory in mice through ZIP9, providing new experimental evidence for improvement in learning and memory in Alzheimer's disease with androgen supplementation.

KEYWORDS

androgen, ZIP9, hippocampus, synaptic plasticity, learning and memory

Introduction

Androgens are steroid hormones synthesized in the gonads, adrenal glands, and brain (1) and are important for the development of male sexual organs, secondary sexual characteristics, sexual desire, and normal sexual function. They also regulate learning and memory in the hippocampus by maintaining normal synaptic plasticity and regulating synaptic plasticity-related proteins and dendritic spine density (2–5).

Alzheimer's disease (AD) is a neurodegenerative disease characterized by progressive memory impairment and cognitive impairment (6), with pathological changes that include formation of senile plaques due to excessive deposition of amyloid β (Aβ), neurofibrillary tangles, and extensive neuronal loss (7). There is an increased risk of AD caused by low serum androgen levels (8–11) or anti-androgen therapy (12–14). While androgen supplementation has been found to improve memory impairment (15, 16), the neuroprotective mechanism of androgens on learning and memory in AD remains unclear.

Testicular feminization mutation (Tfm) mice are androgen receptor (AR)-deficient (17) and have decreased circulating androgen (18) due to hereditary single-base deletion of the X chromosome. Surprisingly, learning and memory in Tfm male mice was significantly improved by androgen supplementation. This suggests that there may be androgen-binding sites other than the classical AR that mediate androgen-rescuing learning and memory. The ZIP9 (Zrt-, Irt-like protein family solute carrier family 39 member 9, SLC39A9) is the ninth in a family of 14 ZIP proteins. It has seven transmembrane domains and one intracellular C-terminal domain and is responsible for transmembrane transport of Zn^{2+}. It is also the only ZIP protein that can couple with G-proteins during signal transduction across membranes (19, 20). Recent studies have found that ZIP9 can mediate biological effects of androgens in a variety of cell types. Some of these effects include proliferation of human and mouse melanoma cells (21), migration of human prostate (22) and bladder (23) cancer cells, apoptosis of human breast cancer and prostate cancer cells (20, 24, 25), and the expression of tight junction proteins in mouse (26) and rat (27) Sertoli cells. In a previous study it was found that androgens induced the interaction between ZIP9 and Gnα11, which affected the expression of postsynaptic density protein 95 (PSD95) in mouse hippocampal neuron HT22 cells (28). However, it is not clear whether ZIP9 mediates the effects of androgens on learning and memory in Tfm mice.

In this study, we explored whether androgens induced by ZIP9 affected learning, memory and hippocampal synaptic plasticity in Tfm male mice and investigated the underlying mechanism. Further, we examined whether learning and memory of AD animal model-APP/PS1 mice was mediated through this mechanism.

Materials and methods

Animals

Female Tfm and male C57BL/6J mice were purchased from Jackson Laboratory (Stock #000569, BarHarbor, ME, USA) and Vital River Laboratory Animal Technology Co., Ltd (Beijing, China) respectively. We induced mating of Tfm female with male C57BL/6J mice which produced the following offspring types: wild-type (WT) female, WT male, Tfm female, and Tfm male. All offspring were genotyped using real-time polymerase chain reaction (PCR), and only WT and Tfm male mice were selected for this study. APP/PS1 mice were provided by the Vital River Laboratory Animal Technology Co., Ltd. (Beijing, China). The mice were raised and bred at the Experimental Animal Research and Service Center of Hebei Medical University under conditions of constant temperature (22 ± 2°C), constant humidity (55 ± 5%), lighting (12-h light/dark cycle), and free access to food and water. All animal experiments were carried out according to the National Institutes of Health Guide for Care and Use of Laboratory Animals and approved by Laboratory Animal Ethical and Welfare Committee of Hebei Medical University.

Cell culture

Mouse hippocampal neuron HT22 cells were cultured in phenol red-free DMEM/F12 medium (cat# PM150316, Procell, China) containing 10% fetal bovine serum (FBS) and 1% penicillin-streptomycin under conditions (37 °C, 5% CO_2) in a humidified atmosphere. After digestion with 0.25% trypsin at 85%-90% confluency, the cells were seeded into a 6-well plate, and virus infection experiments were carried out to establish ZIP9 knockdown or overexpression HT22 stable cell lines. Subsequently, the cells were transferred into 6 or 24-well plates for Western blot and immunofluorescence staining. With or without pretreatment with 100 nM ERK1/2 inhibitor SCH772984 (cat#: S7101 Selleck, USA) or 25 nM eIF4E inhibitor eFT508 (eFT, cat#: HY-100022, MCE, USA) for 2 h, the cells in the experimental groups were treated with 10 nM dihydrotestosterone (DHT, cat#: A0462, Tokyo Chemical Industry, Japan) for 24 h, and those in the control group were treated with an equal volume of dimethyl sulfoxide (DMSO).

Establishment of ZIP9 knockdown or overexpression HT22 stable cell lines

ZIP9-knockdown and ZIP9-overexpress lentivirus targeting ZIP9 (5' -ATTGTGTTCGTGGCAATAA-3') and the corresponding negative control lentivirus were provided by Genechem Inc. (Shanghai, China). HT22 cells were infected with the lentivirus for 12 h at 20-30% confluency. The HT22 cells were

then cultured with fresh medium for 72 h until 4.5μg/mL puromycin was added for 48 h to kill uninfected cells. Stable clones were selected using 2.25 μg/mL puromycin after cell passaging, and stable ZIP9 knockdown or overexpression HT22 cell lines were established.

Immunofluorescence staining

HT22 cells were fixed with 4% paraformaldehyde (PFA) for 15 min, blocked with 10% donkey serum for 1 h at room temperature, and incubated overnight at 4°C with the following primary antibodies: rabbit anti-PSD95 (cat#: ab18258, Abcam, USA), rabbit anti-phospho-ERK1/2 (cat#: 9101, cell signaling, USA), and rabbit anti-phospho-eIF4E (cat#: ab76256, Abcam, USA). The next day, the cells were incubated with donkey anti-rabbit fluorescent secondary antibody (cat#: A21207, Invitrogen, USA) for 2 h at room temperature in the dark. They were then counterstained with 4',6-diamidino-2-phenylindole (DAPI) (cat#: C0065, Solarbio, China) for 10 min and sealed with anti-fluorescence quenching sealing tablets (cat#: S2100, Solarbio, China). Images were taken using a laser confocal microscope (Olympus, Japan), and the average optical density was analyzed using Fiji software (National Institutes of Health, USA). Intra and inter-assay coefficients of variation were 2.44%-4.95% and 4.07%-9.81% respectively.

Castration of APP/PS1 mice

After anesthetizing 6-month-old APP/PS1 mice with isoflurane (cat#: R510-22-10, RWD, China), small incisions were made in the scrotums to remove the testes in the experimental group, while the scrotums were cut open and sutured without hurting the testes in the sham operation group.

Adeno-associated virus and microinjection in CA1

Adeno-associated virus (AAV9) and negative control virus with GV478 as a vector were provided by Genechem Inc. (Shanghai, China). The mice were anesthetized with isoflurane and fixed on a brain stereotaxic instrument (StereoDrive, NeuroStar, Germany) lying prone. After the anterior and posterior fontanelle were fully exposed, the CA1 region (left: ML = -2.29 mm, AP = -2.28 mm, DV = 1.62 mm; right: ML = 2.29 mm, AP=-2.28 mm, DV = 1.62 mm) was located by the mouse brain atlas (Watson, 3rd edition). Through the microinjection system, 1μL (1×10^{13} v.g./ml) of virus was injected into the bilateral CA1 region.

Grouping and administration of mice

All our animal experiments followed the 3R principle, that is, replacement, reduction and refinement. According to the experimental design, we calculated the number of animals needed for the experiments in advance, which not only ensured that the sample size met the needs of the experiments, but also avoided unnecessary wastage of resources and mice. Using the formula provided by Charan et al. (29), we determined that the number of mice in each group was 12. Twelve three-month-old WT male mice were in WT+nc-RNAi group, and 36 Tfm male mice were equally divided between Tfm+nc-RNAi, Tfm+nc-RNAi+DHT, and Tfm +ZIP9-RNAi+DHT groups. Four weeks after virus injection, the Tfm+nc-RNAi+DHT and Tfm+ZIP9RNAi+DHT groups were injected intraperitoneally with physiological DHT (1 mg/kg body weight), and the WT+nc-RNAi and Tfm+nc-RNAi groups were injected with an equal volume of vehicle until behavioral tests were completed. Forty-eight 6-month-old APP/PS1 mice were divided equally into Sham+nc-RNAi, Cast+nc-RNAi, Cast+nc-RNAi +DHT, and Cast+ZIP9-RNAi+DHT groups, and then they were castrated or sham operated. Four weeks later, the mice were injected with adeno-associated virus. Four weeks after virus injection, the Cast+nc-RNAi+DHT and Cast+ZIP9-RNAi+DHT groups were injected intraperitoneally with DHT, while the Sham+nc-RNAi and Cast+nc-RNAi groups were injected intraperitoneally with an equal volume of vehicle until the behavioral test was completed. The average weight of mice was 27-30g. All the mice were subjected to behavioral tests, and the behavioral data of 10 mice in each group was used for statistical analysis.

Y-maze

Testing was performed using a Y-shaped maze with arms oriented at 120° angles from each other. Each arm had a size of 30×8×15 cm with markers of different colors and shapes on the inner wall that acted as spatial localization reference for the mice. The three arms were randomly set as the novel arm, start arm, and other arm. During the training session, each mouse was placed in the start arm and allowed to explore the maze freely for 5 min with the novel arm closed off. Four hours later, the novel arm was opened during the test session, and the mouse was placed in the start arm and allowed to freely explore the three arms for 5 min. To avoid smell clues affecting the next mouse, 75% ethanol was used to wipe the bottom and inner walls of the maze after each test. The entire process of the experiment was recorded using a camera and analyzed using the SMART video tracking system. The evaluation indexes were time (%), distance (%) in the novel arm, and the number of entries into the novel arm.

Novel object recognition test

A 3-day new object recognition experiment was performed in an open field box measuring 50×50×40 cm. On day 1, the mice were placed in a box for 5 min of adaptive training with free exploration, facing the sidewall close to the experimenter. On day 2, two identical objects were placed in the left and right corners away from the experimenter and 10 cm from each sidewall. Mice were placed in the box with their backs to the objects and allowed to

explore freely for 10 min. On day 3, one of the original objects was replaced with a novel object of different color and shape, but having the same volume. The exploration time of the mice for the two objects was recorded within 10 min, and the exploration distance was 2-3 cm from the objects. Exploration behavior included placing the front paw on the object, smelling the object, licking the object. Holding a pose or climbing an object without moving is not an exploration of that object. The discrimination index represented by the ratio of exploration time of the novel object to the total exploration time, was calculated.

Morris water maze

The Morris water maze test was used to detect spatial learning and memory in the mice. The circular pool (diameter 120 cm) was divided into four quadrants, and the platform (diameter, 6 cm) was placed in any quadrant 1 cm underwater. In the orientation navigation trial, the mice were placed into the water facing the pool wall from four quadrants, and the time to find the platform was within 60 s, that is, the escape latency. If they could not find the platform in 60 s, the mice were guided to the platform and remained there for 15 s, and the escape latency was recorded as 60 s. The distance before finding the platform and swimming trajectories were recorded. On the 6th day, a spatial probe trial was performed. After the platform was removed, mice were placed in water. The number of mice crossing the position of the platform within 60s and the time spent in the target quadrant were recorded.

Western blot

Radioimmunoprecipitation assay lysate containing phenylmethylsulfonyl fluoride and phosphatase inhibitors was added to the samples, and proteins were extracted for quantitative analysis. After denaturation, 25 μg of protein was loaded onto a 10% sodium dodecyl sulphatepolyacrylamide gel for protein separation and electrotransferred onto polyvinylidene fluoride membranes. The membranes were blocked with 5% non-fat milk at room temperature for 1 h and incubated overnight at 4 °C with the following primary antibodies: rabbit anti-PSD95 (cat#: ab18258, Abcam, USA), rabbit anti-phospho-eIF4E (cat#: ab76256, Abcam, USA), mouse anti-eIF4E (total) (cat#: ab171091, Abcam, USA), rabbit anti-GAPDH (cat#: ab9485, Abcam, USA), rabbit anti-phospho-ERK1/2 (cat#: 9101,cell signaling, USA), mouse anti-Erk1/2 (cat#: 9107, cell signaling, USA), rabbit anti-ZIP9 antibody (cat#: GTX31817,GeneTex, USA), rabbit anti-synaptophysin (SYP cat#: CY5273, Abways, China), and rabbit anti-drebrin (cat#: 10260-1-AP, Proteintech, USA). The membranes were then incubated with goat anti-rabbit fluorescent secondary antibody (cat#611145002, Rockland, USA) or goat anti-mouse secondary antibody (cat#610144002, Rockland, USA) in dark incubation boxes for 2 h. Finally, an Odyssey imaging system (LICOR, USA) was used for visualization and analysis. The relative expression of the target protein was calculated according to the gray value of β-actin or GAPDH as a reference, and the phosphorylation level of the proteins was determined by the ratio of phosphorylated proteins to total proteins. Intra and inter-assay coefficients of variation were 1.86% to 4.73% and 4.28% to 9.77% respectively.

Immunohistochemical staining

After the behavioral study, mice were deeply anesthetized with isoflurane, perfused with PBS, and fixed with 4% PFA. Their brains were removed and fixed in 4% PFA for 24 h. Brains were cut from the superior colliculus to the optic chiasma and separated along the median sagittal plane. The left parts were prepared for Golgi staining, and the right parts were routinely dehydrated, waxed, embedded, and cut into 5 μm-thick sections. After dewaxing, hydration, high pressure antigen repair, and blocking, the sections were incubated at 4 °C overnight with the following primary antibodies: rabbit anti-PSD95 (cat#: ab18258, Abcam, USA), rabbit anti-synaptophysin (cat#: CY5273, Abcam, China), rabbit anti-drebrin (cat#: 10260-1-AP, Proteintech, USA). Subsequently, the sections were incubated with goat anti-rabbit IgG polymer labeled with biotin (cat#: SP-9001, ZSGB-BIO, China) for 30 min, horseradish enzyme-labeled streptomycin for 1 h, and DAB staining. The hippocampal CA1 region was observed and imaged under a 40× light microscope (Leica, Germany), and the average optical density was analyzed using Fiji software (National Institutes of Health, USA). Intra-assay coefficients of variation were 2.03% to 4.89%.

Golgi staining

Golgi staining was performed according to the protocol provided in the Golgi staining kit (cat#: GMS80020.1, GENMED, China). After 24 h of post-fixation, the left brain was immersed in mordant (Reagent A and Reagent B were mixed at 1:1) and stained for 14 days at room temperature in the dark. They were then placed in 30% sucrose solution, dehydrated at 4 °C for 48 h, and cut into 100-μm sections with oscillating tissue slicers. The sections were incubated with staining solution at room temperature for 30 min, followed by incubation with chromogenic solution for 20 min at room temperature in the dark. They were then dehydrated, made transparent, and sealed with neutral resin. The secondary or tertiary dendritic spines of apical dendrites in the hippocampal CA1 region were observed and imaged under a 100× light microscope (Olympus, Japan). Dendritic spine density was analyzed using Fiji software. Three sections were selected from each mouse and three neurons were selected from each section. Intra-assay coefficients of variation were 2.08% to 4.55%.

Statistical analysis

SPSS26.0 statistical software was used for analysis. The results are expressed as mean ± standard deviation (SD). The Shapiro-Wilk test for normality was performed, and the Student's t-test was used for two-sample comparisons of normally distributed data ($P > 0.1$).

Levene's test for homogeneity of variance was conducted on data from multiple groups. One-way analysis of variance (ANOVA) was performed for data with a normal distribution ($P > 0.1$) and homogeneity of variance ($P > 0.1$), and *post hoc* multiple comparisons were performed using the LSD test. The Kruskal-Wallis H test was used to compare multiple groups of quantitative data with non-normal distribution ($P < 0.1$), and *post hoc* multiple comparisons were performed with the independent-samples Kruskal-Wallis Test. The significant differences in escape latency at 1-5 days were assessed using two-way repeated-measures ANOVA. Differences were considered significant at $P < 0.05$. To ensure validity, all the data was analyzed *post-hoc* with G*Power (www.gpower.hhu.de), and the statistical power was set at equal to or greater than to 0.8.

Results

Effects of DHT on learning and memory in Tfm male mice after hippocampal ZIP9 knockdown

Western blot results showed that ZIP9 was expressed in the hippocampi of WT and Tfm male mice, and there was no significant difference between the two groups ($t_{(10)} = -0.084$, $P = 0.935$, Cohen's $d = 0.05$) (Figures 1B, C). To determine whether androgen affects the learning and memory of Tfm male mice through ZIP9, we transfected hippocampal neurons with AAV9-ZIP9-RNAi and control virus (AAV9-nc-RNAi). The expression of hippocampal ZIP9 in the Tfm+ZIP9-RNAi group was significantly lower than that in the Tfm+nc-RNAi group ($t_{(10)} = 6.746$, $P < 0.05$, Cohen's $d = 3.89$) (Figures 1D–F). We tested the effect of DHT induced by ZIP9 on the behavior of WT and Tfm male mice (Figure 1A).

The results of the YM showed that there were significant differences in the percentage of time spent in the novel arm ($F_{(3,36)} = 5.059$, $P < 0.05$, $\eta^2 = 0.297$), the percentage of distance in the novel arm ($F_{(3,36)} = 5.790$, $P < 0.05$, $\eta^2 = 0.325$), and the number of entries into the novel arm ($F_{(3,36)} = 3.614$, $P < 0.05$, $\eta^2 = 0.231$) among all groups. The percentage of time spent in the novel arm, the percentage of distance in the novel arm, and the number of entries into the novel arm of the Tfm+nc-RNAi group were significantly lower than those of the WT+nc-RNAi and Tfm+nc-RNAi+DHT groups, whereas those of the Tfm+nc-RNAi+DHT group were higher than those of the Tfm+ZIP9-RNAi+DHT group (Figures 1G-J, L).

The NOR test showed significant differences in discrimination index (DI) among all groups ($F_{(3,36)} = 12.547$, $P < 0.05$, $\eta^2 = 0.511$). The DI in the Tfm+nc-RNAi group was significantly lower than that in the WT+nc-RNAi group. DHT supplementation increased the DI of Tfm male mice, whereas the increase induced by DHT disappeared after hippocampal ZIP9 knockdown (Figures 1K, M).

In the Morris water navigation task, there were significant differences in the escape latency at 1-5 days ($F_{(3,36)} = 3.502$, $P < 0.05$, $\eta^2 = 0.203$) and the distance to the target on the 5th day ($F_{(3,36)} = 4.657$, $P < 0.05$, $\eta^2 = 0.280$). The values of above parameters for the Tfm+nc-RNAi group were significantly higher than those for the WT+nc-RNAi and the Tfm+nc-RNAi+DHT groups, whereas the values for Tfm+nc-RNAi+DHT group were lower than those for the Tfm+ZIP9-RNAi+DHT group. The subsequent spatial probe trial revealed differences in the number of target crossings ($H = 19.807$, $P < 0.05$) and time in the target zone ($F_{(3,36)} = 7.598$, $P < 0.05$, $\eta^2 = 0.388$). The number of target crossings and time in the target zone of the Tfm+nc-RNAi group were lower than those of the WT+ncRNAi and Tfm+nc-RNAi+DHT groups, whereas those of the Tfm+nc-RNAi+DHT group were higher than those of the Tfm +ZIP9-RNAi+DHT group (Figures 1N-R).

Effects of DHT on hippocampal PSD95, drebrin, SYP protein and dendritic spine density in Tfm male mice after hippocampal ZIP9 knockdown

The IHC staining revealed significant inter group differences in the optical density of synaptic plasticity related proteins, such as PSD95 ($F_{(3,20)} = 17.942$, $P < 0.05$, $\eta^2 = 0.729$), drebrin ($F_{(3,20)} = 77.031$, $P < 0.05$, $\eta^2 = 0.920$), and SYP ($F_{(3,20)} = 16.593$, $P < 0.05$, $\eta^2 = 0.713$). Compared to the WT+nc-RNAi group, the optical density of PSD95, drebrin, and SYP in the Tfm+nc-RNAi group decreased significantly. DHT supplementation increased the optical density of these hippocampal proteins in Tfm male mice, while the increase induced by DHT disappeared after hippocampal ZIP9 knockdown (Figures 2A-D). Western blot revealed non-significant differences in the expression of PSD95 ($F_{(3,20)} = 5.833$, $P < 0.05$, $\eta^2 = 0.467$), drebrin ($F_{(3,20)} = 7.278$, $P < 0.05$, $\eta^2 = 0.552$), and SYP ($F_{(3,20)} = 12.693$, $P < 0.05$, $\eta^2 = 0.656$), as observed by IHC staining (Figures 2E-H).

Golgi staining results showed significant inter-group differences in the density of dendritic spines ($F_{(3,20)} = 33.942$, $P < 0.05$, $\eta^2 = 0.836$). Compared to the WT+nc-RNAi group, the dendritic spine density in the hippocampi of the Tfm+nc-RNAi group decreased significantly. DHT supplementation increased the density of dendritic spines in Tfm male mice, but this increase was not observed after ZIP9 knockdown in the hippocampus (Figures 2I, J).

ZIP9 mediated the effects of DHT on the phosphorylation of ERK1/2 and eIF4E in Tfm male mice hippocampus and HT22 cells

To reveal the underlying mechanism, we studied the effect of DHT induced by ZIP9 on the phosphorylation of ERK1/2 and eIF4E in the hippocampi of Tfm male mice. Western blot revealed significant inter group differences in the phosphorylation of ERK1/2 ($F_{(3,16)} = 143.584$, $P < 0.05$, $\eta^2 = 0.964$) and eIF4E ($F_{(3,16)} = 31.446$, $P < 0.05$, $\eta^2 = 0.855$). Compared to the WT+nc-RNAi group, the phosphorylation of ERK1/2 and eIF4E in the Tfm+nc-RNAi group decreased significantly. DHT supplementation increased the phosphorylation of ERK1/2 and eIF4E in Tfm male mice, but this

10.3389/fendo.2023.1139874

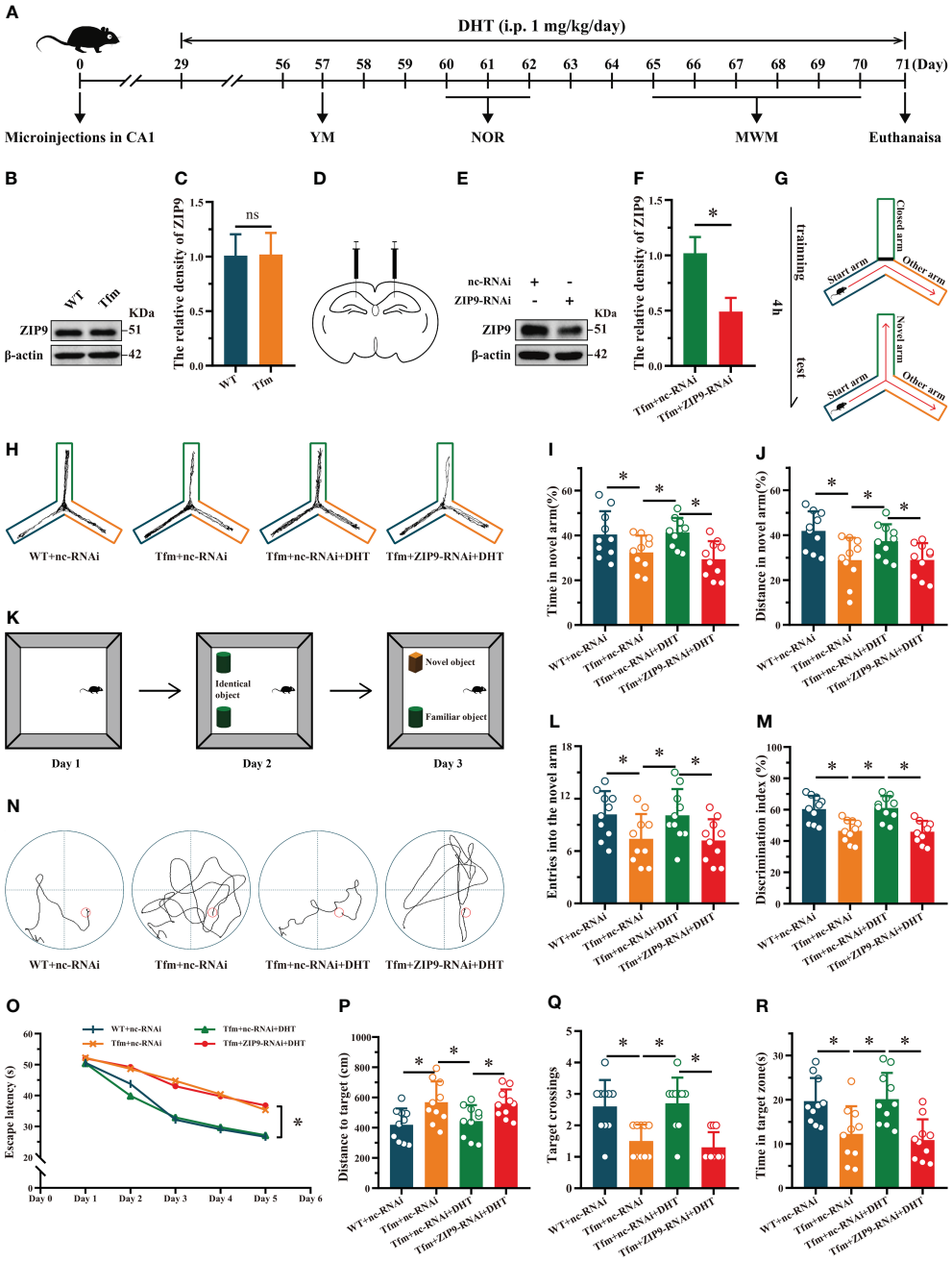

FIGURE 1
Effects of DHT on learning and memory of Tfm male mice after hippocampal ZIP9 knockdown. **(A)** Experimental procedure. Mice treated with microinjections in CA1, DHT (i.p. 1 mg/kg/day), and behavioral tests. **(B, C)** Representative Western blot **(B)** and quantification **(C)** of ZIP9 in the hippocampus of WT and Tfm male mice (*$P > 0.05$, n = 6). **(D)** Schematic diagram of microinjections in the hippocampal CA1 region **(E, F)**. Knockdown efficiency of ZIP9 protein in Tfm male mice hippocampi infected with AAV9-ZIP9-RNAi or AAV9-nc-RNAi (*$P < 0.05$, n = 6). **(G)** Schematic diagram of the YM. **(H)** Trajectories of the YM. **(I, J, L)** YM performed to assess spatial reference memory. **(K)** Schematic diagram of the NOR. **(M)** NOR performed to assess memory retention. **(N)** Trajectories of the MWM (the 5th day). **(O-R)** MWM was used to test spatial learning and memory. DHT, dihydrotestosterone; ZIP9, Zrt-, Irt-like protein 9; Tfm, Testicular feminization mutation; YM, Y-maze test; NOR, novel object recognition test; MWM, Morris water maze. (*$P < 0.05$, n = 10).

increase was not observed after ZIP9 knockdown in the hippocampus (Figures 3A-C).

To study the effects of DHT mediated by ZIP9 on the expression of PSD95 and the phosphorylation of ERK1/2 and eIF4E in HT22 cells, we constructed ZIP9 knockdown or overexpression HT22 stable cell lines by lentivirus infection. The expression of ZIP9 in the ZIP9-shRNA group was significantly lower than that in the nc-shRNA group ($t_{(8)}$ = 17.814, $P < 0.05$, Cohen's d = 25.193) (Figures 3D, E); the expression of PSD95 ($F_{(2,12)}$ = 550.836, $P < 0.05$, η^2 = 0.989), phosphorylation of ERK1/2 ($F_{(2,12)}$ = 402.259, $P < 0.05$, η^2 = 0.985), and eIF4E ($F_{(2,12)}$ = 14.350, $P < 0.05$, η^2 = 0.705) in

10.3389/fendo.2023.1139874

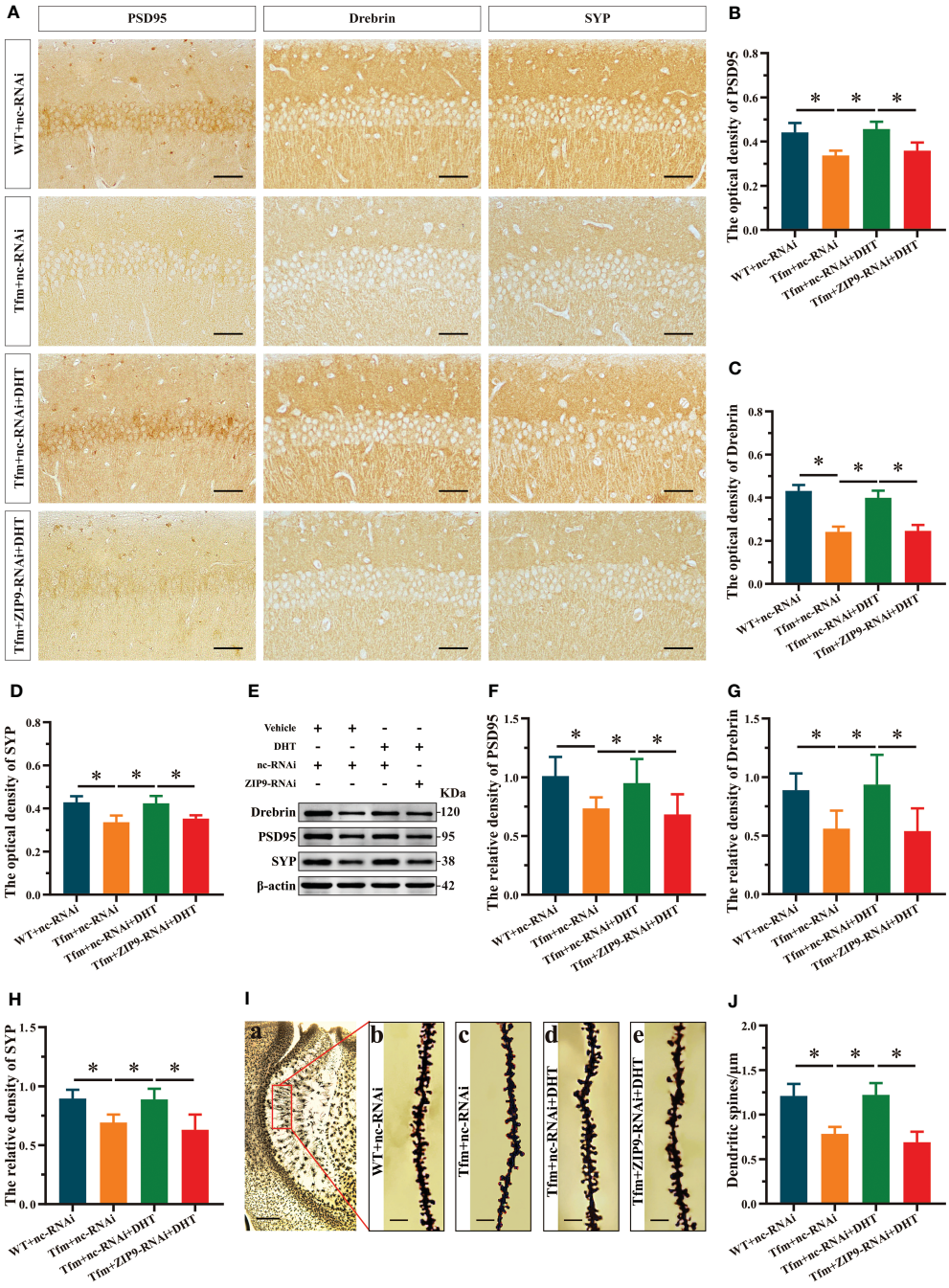

FIGURE 2
Effects of DHT on hippocampal PSD95, drebrin, SYP protein and dendrite spine density of Tfm male mice after hippocampal ZIP9 knockdown. **(A–D)** Representative immunohistochemical staining images **(A)** and quantification **(B-D)** of PSD95 **(B)**, drebrin **(C)**, and SYP **(D)** in the hippocampal CA1 region of the four groups of mice. Scale bars = 50 μm. **(E–H)** Representative Western blot **(E)** and quantification **(F–H)** of PSD95 **(F)**, drebrin **(G)**, and SYP **(H)** in the hippocampus of the four groups of mice. **(I, J)** Representative images **(I)** and quantification **(J)** of Golgi staining in the hippocampus of the four groups of mice. $I_{(a)}$ Scale bars = 200 μm. $I_{(b-e)}$ Scale bars = 5 μm. DHT, dihydrotestosterone; Tfm, Testicular feminization mutation; PSD95, postsynaptic density protein 95; SYP, synaptophysin; ZIP9, Zrt-, Irt-like protein 9. (*$P < 0.05$, n = 6).

the nc-shRNA+DHT group were significantly higher than those in the nc-shRNA and ZIP9-shRNA+DHT groups (Figures 3F-I). IF staining showed that the optical density of PSD95 ($F_{(2,12)} = 39.748$, $P < 0.05$, $\eta^2 = 0.869$), p-ERK1/2 ($F_{(2,12)} = 17.002$, $P < 0.05$, $\eta^2 = 0.739$), and p-eIF4E ($F_{(2,12)} = 33.090$, $P < 0.05$, $\eta^2 = 0.847$) in the nc-shRNA+DHT group were significantly higher than those in nc-shRNA and the ZIP9-shRNA+DHT groups (Figures 3J-O).

We observed the effects of DHT on the expression of PSD95 and phosphorylation of ERK1/2 and eIF4E in ZIP9-overexpression HT22 cells. The results of Western blot showed that the expression of ZIP9 in the ZIP9-oe group was significantly higher than that in the nc-oe group ($t_{(8)} = -6.160$, $P < 0.05$, Cohen's $d = -8.711$, Figures 4A, B); expression of PSD95 ($F_{(2,12)} = 1003.038$, $P < 0.05$, $\eta^2 = 0.994$), phosphorylation of ERK1/2 ($F_{(2,12)} = 385.322$, $P <$

10.3389/fendo.2023.1139874

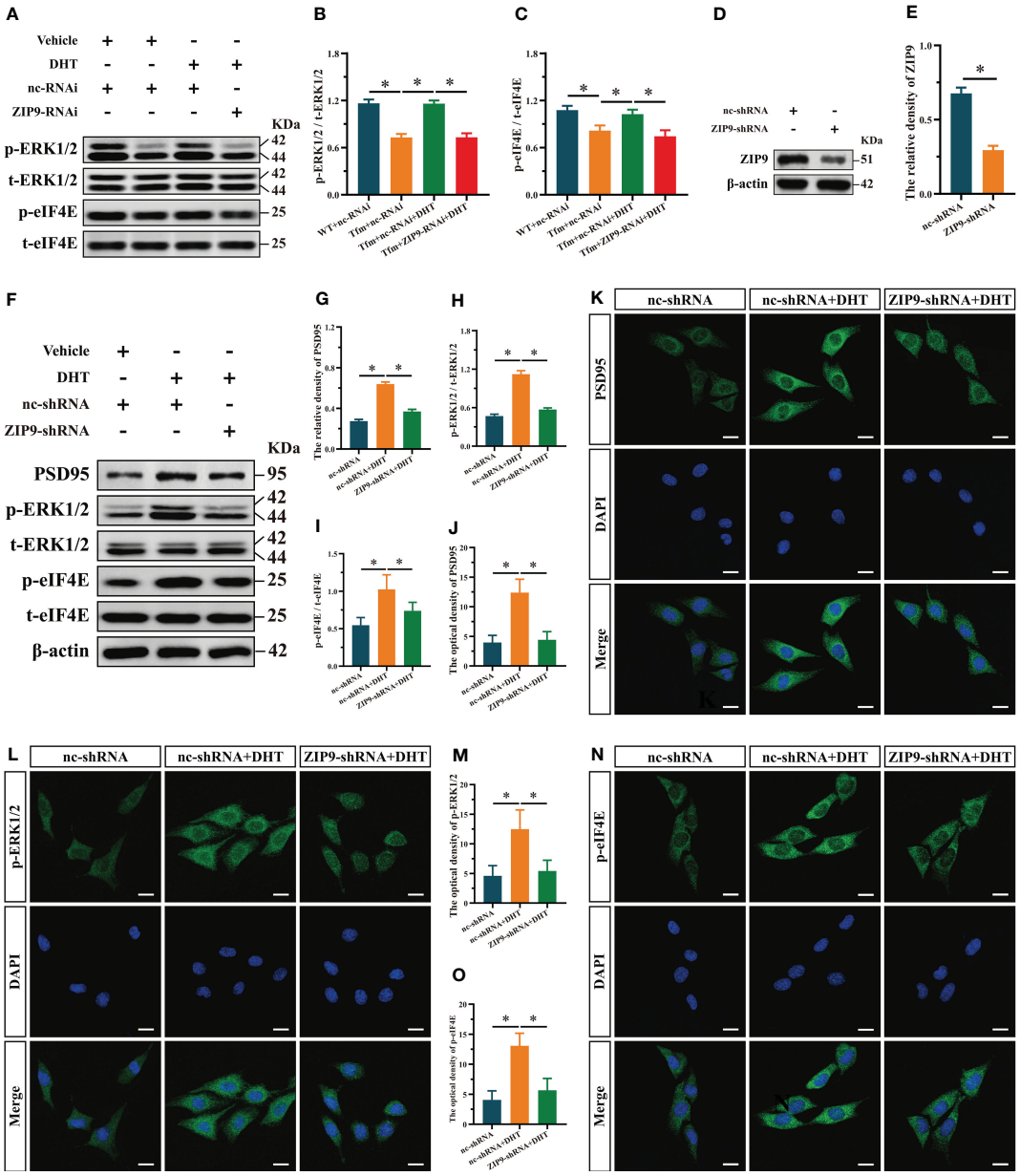

FIGURE 3
Effects of DHT on the phosphorylation of ERK1/2 and eIF4E in Tfm male mice and HT22 cells after ZIP9 knockdown. **(A–C)** Representative Western blot **(A)** and quantification **(B, C)** of the phosphorylation of ERK1/2 **(B)** and eIF4E **(C)** in the hippocampus of the four groups of mice. **(D, E)** The knockdown efficiency of ZIP9 protein in HT22 cells infected with ZIP9-shRNA or nc-RNA. **(F-I)** Representative Western blot **(F)** and quantification **(G-I)** of the expression of PSD95 **(G)**, and the phosphorylation of ERK1/2 **(H)**, eIF4E **(I)** in HT22 cells. **(J, K)** Representative IF staining images **(K)** and quantification **(J)** of PSD95 in HT22 cells. **(L, M)** Representative IF staining images **(L)** and quantification **(M)** of p-ERK1/2 in HT22 cells. **(N, O)** Representative IF staining images **(N)** and quantification **(O)** of p-eIF4E in HT22 cells after ZIP9 knockdown. Scale bars = 20 μm. IF, immunofluorescence; DHT, dihydrotestosterone; Tfm, Testicular feminization mutation; ERK1/2, Extracellular signal-regulated kinase ½; eIF4E, HT22, hippocampal neuron cells; ZIP9, Zrt-, Irt-like protein 9; PSD95, postsynaptic density protein 95. (*$P < 0.05$, n = 5).

0.05, $\eta^2 = 0.985$), and eIF4E ($F_{(2,12)} = 291.648$, $P < 0.05$, $\eta^2 = 0.980$) in the nc-oe+DHT group were significantly higher than those in the nc-oe group, but lower than those in the ZIP9-oe+DHT group (Figures 4C-F). IF staining showed that the optical densities of PSD95 ($F_{(2,12)} = 126.544$, $P < 0.05$, $\eta^2 = 0.955$), p-ERK1/2 ($F_{(2,12)} = 132.102$, $P < 0.05$, $\eta^2 = 0.957$) and p-eIF4E ($F_{(2,12)} = 86.879$, $P < 0.05$, $\eta^2 = 0.935$) in the nc-oe+DHT group were significantly higher than those in the nc-oe group, but lower than those in the ZIP9-oe+DHT group (Figures 4G-L).

ZIP9 mediated the effects of DHT on the phosphorylation of ERK, eIF4E and expression of PSD95 in HT22 cells pretreated with SCH772984

We used SCH772984, a specific inhibitor of ERK1/2, to verify whether ERK1/2 is involved in the expression of PSD95 in HT22 cells induced by DHT through ZIP9. Western blot revealed significant inter group differences in the phosphorylation of

10.3389/fendo.2023.1139874

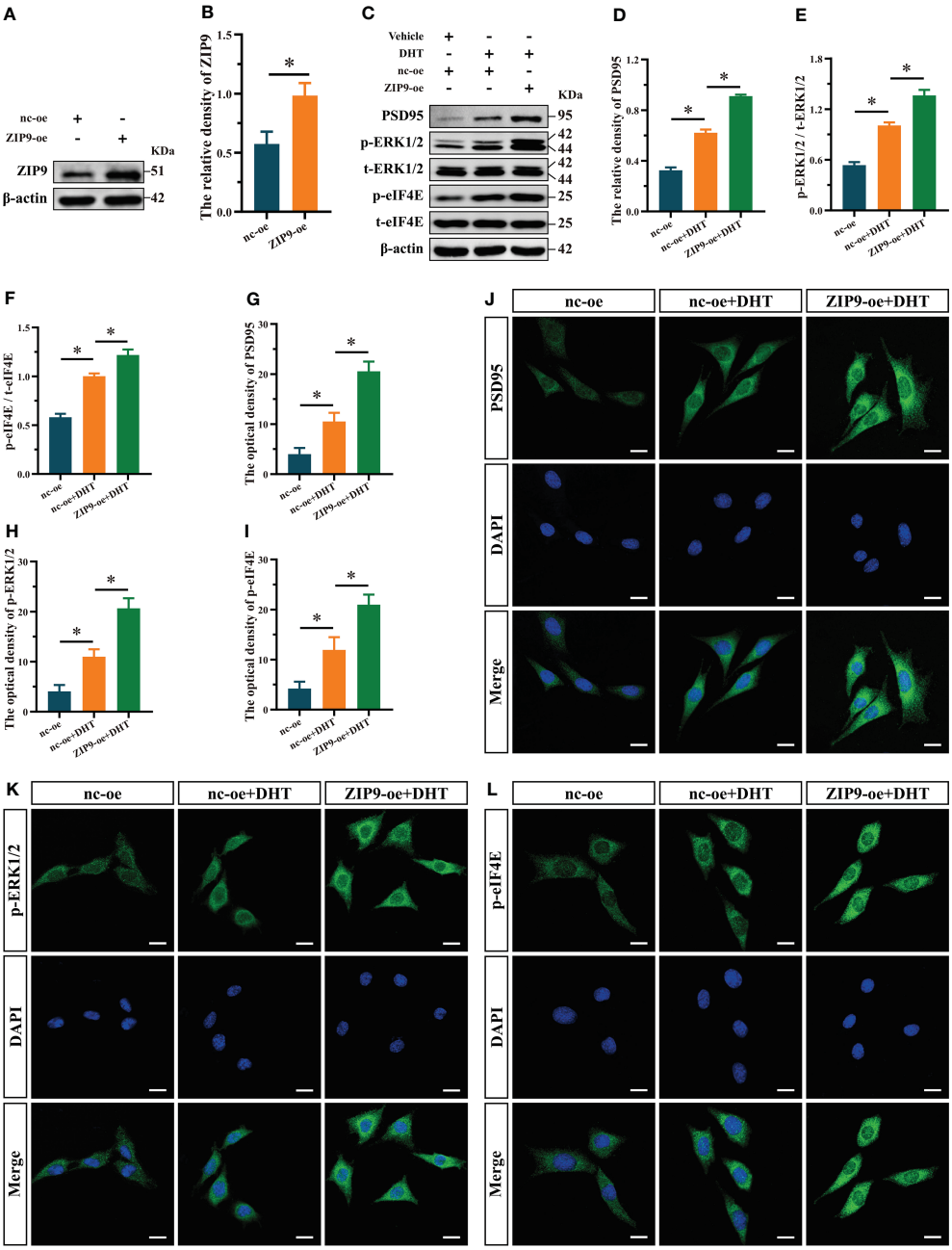

FIGURE 4
Effects of DHT on the expression of PSD95 and the phosphorylation of ERK1/2, eIF4E in HT22 cells after ZIP9 overexpression. **(A, B)** The overexpression efficiency of ZIP9 protein in HT22 cells infected with ZIP9-oe or nc-oe. **(C–F)** Representative Western blot **(C)** and quantification **(D–F)** of PSD95 **(D)**, and the phosphorylation of ERK1/2 **(E)** and eIF4E **(F)** in HT22 cells. **(G, J)** Representative IF staining images **(J)** and quantification **(G)** of PSD95 in HT22 cells. **(H, K)** Representative IF staining images **(K)** and quantification **(H)** of p-ERK1/2 in HT22 cells. **(I, L)** Representative IF staining images **(L)** and quantification **(I)** of p-eIF4E in HT22 cells. Scale bars = 20 μm. DHT, dihydrotestosterone; ERK1/2, Extracellular signal-regulated kinase ½; eIF4E, Eukaryotic translation initiation factor 4E; ZIP9, Zrt-, Irt-like protein 9; PSD95, postsynaptic density protein 95. (*$P < 0.05$, n = 5).

ERK1/2 ($F_{(3,16)}$ = 374.158, $P < 0.05$, η^2 = 0.986), eIF4E ($F_{(3,16)}$ = 124.188, $P < 0.05$, η^2 = 0.959), and the expression of PSD95 ($F_{(3,16)}$ = 274.867, $P < 0.05$, η^2 = 0.981). The phosphorylation of ERK1/2 and eIF4E and the expression of PSD95 in the nc-oe+DHT group were higher than those in the nc-oe group and lower than those in the ZIP9-oe+DHT group, whereas these values for the ZIP9-oe+S +DHT group were lower than those for the ZIP9-oe+DHT group (Figures 5A-D). Consistent with the results of Western blot, IF staining demonstrated that the optical densities of p-ERK1/2 ($F_{(3,16)}$ = 59.122, $P < 0.05$, η^2 = 0.917), p-eIF4E ($F_{(3,16)}$ = 55.533, $P < 0.05$, η^2 = 0.912), and PSD95 ($F_{(3,16)}$ = 48.888, $P < 0.05$, η^2 = 0.902) were significantly different in all groups. The optical densities of p-ERK1/2, p-eIF4E, and PSD95 in the nc-oe+DHT group were higher than those in the nc-oe group and lower than those in the ZIP9-oe+DHT

10.3389/fendo.2023.1139874

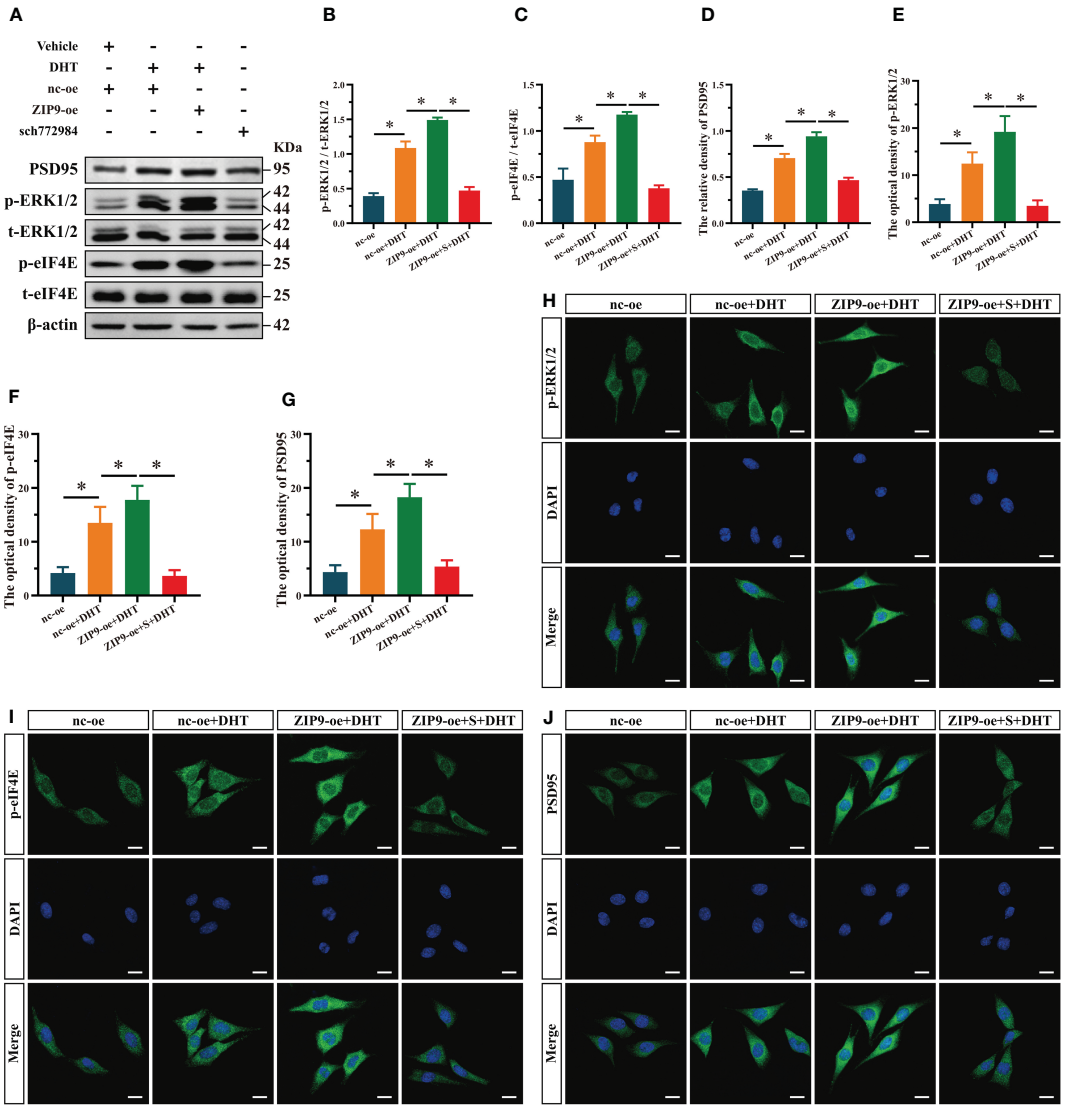

FIGURE 5
ZIP9 mediated the effects of DHT on the phosphorylation of ERK1/2, eIF4E and Expression of PSD95 after ZIP9 overexpression. **(A–D)** Representative Western blot **(A)** and quantification **(B–D)** of the phosphorylation of ERK1/2 **(B)**, eIF4E **(C)** and the expression of PSD95 **(D)** in HT22 cells pretreated with SCH772984. **(E, H)** Representative IF staining images **(H)** and quantification **(E)** of p-ERK1/2 in HT22 cells. **(F, I)** Representative IF staining images **(I)** and quantification **(F)** of p-eIF4E in HT22 cells. **(G, J)** Representative IF staining images **(J)** and quantification **(G)** of PSD95 in HT22 cells. Scale bars = 20 μm. DHT, dihydrotestosterone; ZIP9, Zrt-, Irt-like protein 9; PSD95, postsynaptic density protein 95, ERK1/2, Extracellular signal-regulated kinase ½; eIF4E, Eukaryotic translation initiation factor 4E. S, SCH772984. (*$P < 0.05$, n = 5).

group, whereas those in the ZIP9-oe+S+DHT group were lower than those in the ZIP9-oe+DHT group (Figures 5E-J).

ZIP9 mediated the effects of DHT on the phosphorylation of eIF4E and the Expression of PSD95 in HT22 cells pretreated with eFT508

Finally, we used eFT508, a specific inhibitor of eIF4E, to confirm whether eIF4E was involved in the expression of PSD95 in HT22 cells induced by DHT through ZIP9. Western blot revealed significant inter group differences in the phosphorylation of eIF4E ($F_{(3,16)} = 320.397$, $P < 0.05$, $\eta^2 = 0.984$) and the expression of PSD95 ($F_{(3,16)} = 497.501$, $P < 0.05$, $\eta^2 = 0.989$). The phosphorylation of eIF4E and the expression of PSD95 in the nc-oe+DHT group were higher than those in the nc-oe group and lower than those in the ZIP9-oe +DHT group, whereas those in the ZIP9-oe+eFT+DHT group were lower than those in the ZIP9-oe+DHT group (Figures 6A-C). The IF staining demonstrated significant inter group differences in the optical densities of p-eIF4E ($F_{(3,16)} = 74.668$, $P < 0.05$, $\eta^2 = 0.933$) and PSD95 ($F_{(3,16)} = 59.422$, $P < 0.05$, $\eta^2 = 0.918$. The optical densities of p-eIF4E and PSD95 in the nc-oe+DHT group were higher than those in the nc-oe group and lower than those in the ZIP9-oe+DHT group, whereas these values for the ZIP9-oe+eFT+DHT group were lower than those for the ZIP9-oe +DHT group (Figures 6D-G).

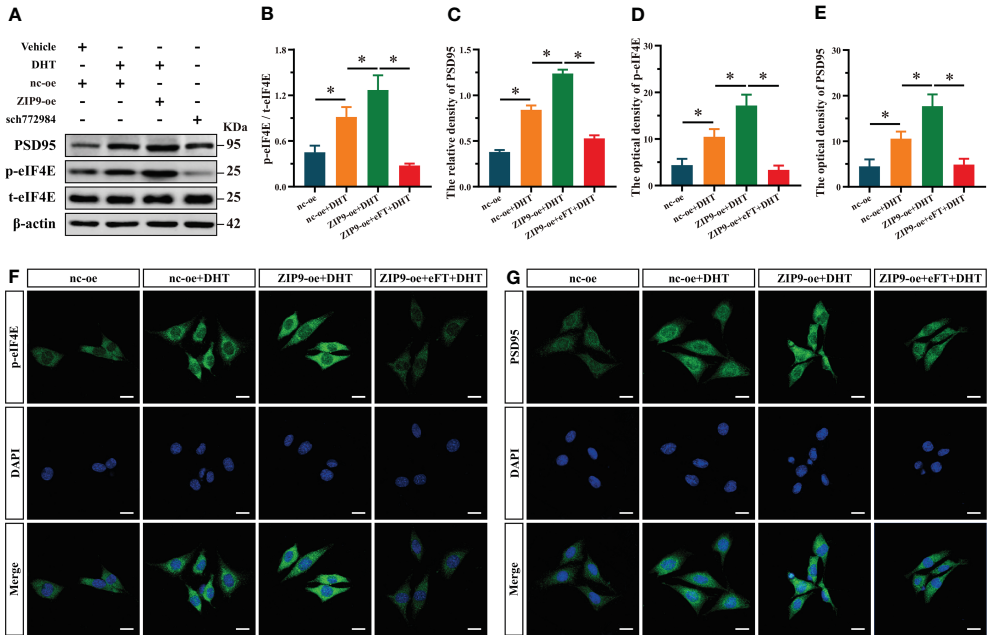

FIGURE 6
ZIP9 mediated the effects of DHT on the phosphorylation of eIF4E and the expression of PSD95 in HT22 cells pretreated with eFT508. **(A-C)** Representative Western blot **(A)** and quantification **(B, C)** of the Phosphorylation of eIF4E **(B)** and expression of PSD95 **(C)** in HT22 cells pretreated with eFT508. **(D, F)** Representative IF staining images **(F)** and quantification **(D)** of p-eIF4E in HT22 cells pretreated with eFT508. **(E, G)** Representative IF staining images **(G)** and quantification **(E)** of PSD95 in HT22 cells pretreated with eFT508. Scale bars = 20 μm. DHT, dihydrotestosterone; ZIP9, Zrt-, Irt-like protein 9; PSD95, postsynaptic density protein 95, ERK1/2, Extracellular signal-regulated kinase ½; eIF4E, Eukaryotic translation initiation factor 4E; eFT, eFT508. (*$P < 0.05$, n = 5).

ZIP9 mediated the effects of DHT on learning and memory of APP/PS1 male mice

We verified the effect of DHT induced by ZIP9 on the behavior of APP/PS1 male mice (Figure 7A). The YM test showed significant inter group differences in the percentage of time spent ($F_{(3,36)}$ = 13.241, $P < 0.05$, $\eta^2 = 0.525$), the percentage of distance travelled ($F_{(3,36)}$ = 7.551, $P < 0.05$, $\eta^2 = 0.386$), and the number of entries ($F_{(3,36)}$ = 7.675, $P < 0.05$, $\eta^2 = 0.390$) in the ovel arm. The values of above parameters for Cast+nc-RNAi group were significantly lower than those for the sham+nc-RNAi and Cast+nc-RNAi+DHT groups, whereas the values for Cast+nc-RNAi+DHT group were higher than those for the Cast+ZIP9-RNAi+DHT group (Figures 7B-E).

The NOR test showed a significant inter group differences in DI ($F_{(3,36)}$ = 11.338, $P < 0.05$, $\eta^2 = 0.486$). The DI of the Cast+nc-RNAi group was significantly lower than that of the sham+nc-RNAi group. DHT supplementation increased the DI of castrated APP/PS1 mice, while this increase disappeared after ZIP9 knockdown in the hippocampus (Figure 7F).

In the Morris water navigation task, there were significant inter group differences in the escape latency at 1-5 days ($F_{(3,36)}$ = 4.307, $P < 0.05$, $\eta^2 = 0.264$) and the distance to the target on the 5th day ($F_{(3,36)}$ = 7.271, $P < 0.05$, $\eta^2 = 0.377$). The values of above parameters for the Cast+nc-RNAi group were significantly higher than those of the Sham +nc-RNAi and Cast+nc-RNAi+DHT groups, whereas the values for the Cast+nc-RNAi+DHT group were lower than those for the Cast +ZIP9-RNAi+DHT group. The subsequent spatial probe trial demonstrated significant differences in the number of target crossings ($F_{(3,36)}$ = 3.803, $P < 0.05$, $\eta^2 = 0.241$) and time in the target zone ($F_{(3,36)}$ = 9.821, $P < 0.05$, $\eta^2 = 0.450$). The number of target crossings and time in the target zone of the Cast+nc-RNAi group were lower than those of the sham+nc-RNAi and Cast+nc-RNAi+DHT groups; however, those of the Cast+nc-RNAi+DHT group were lower than those of the Cast+ZIP9-RNAi+DHT group (Figures 7G-K).

ZIP9 mediated the effects of DHT on hippocampal PSD95, Drebrin, SYP protein and dendritic spine density of APP/PS1 male mice

After the behavioral experiments, we studied the effects of DHT mediated by ZIP9 on the expression of PSD95, drebrin, SYP, and the density of dendritic spines in the hippocampi of APP/PS1 male mice. The IHC staining revealed significant inter group differences in the optical density of PSD95 ($F_{(3,20)}$ = 10.479, $P < 0.05$, $\eta^2 = 0.611$), drebrin ($F_{(3,20)}$ = 12.782, $P < 0.05$, $\eta^2 = 0.657$) and SYP ($F_{(3,20)}$ = 30.519, $P < 0.05$, $\eta^2 = 0.821$). Compared with the Sham+nc-RNAi group, the optical density of PSD95, drebrin, and SYP in the Cast+nc-RNAi group decreased significantly. The DHT supplementation increased the optical density of these proteins in castrated APP/PS1 mice, while the increase vanished after ZIP9 knockdown in the hippocampi (Figures 8A-D). Western blot revealed similar results for the expression of PSD95 ($F_{(3,20)}$ = 27.055, $P < 0.05$, $\eta^2 = 0.802$) and drebrin ($F_{(3,20)}$ = 9.642, $P <$

10.3389/fendo.2023.1139874

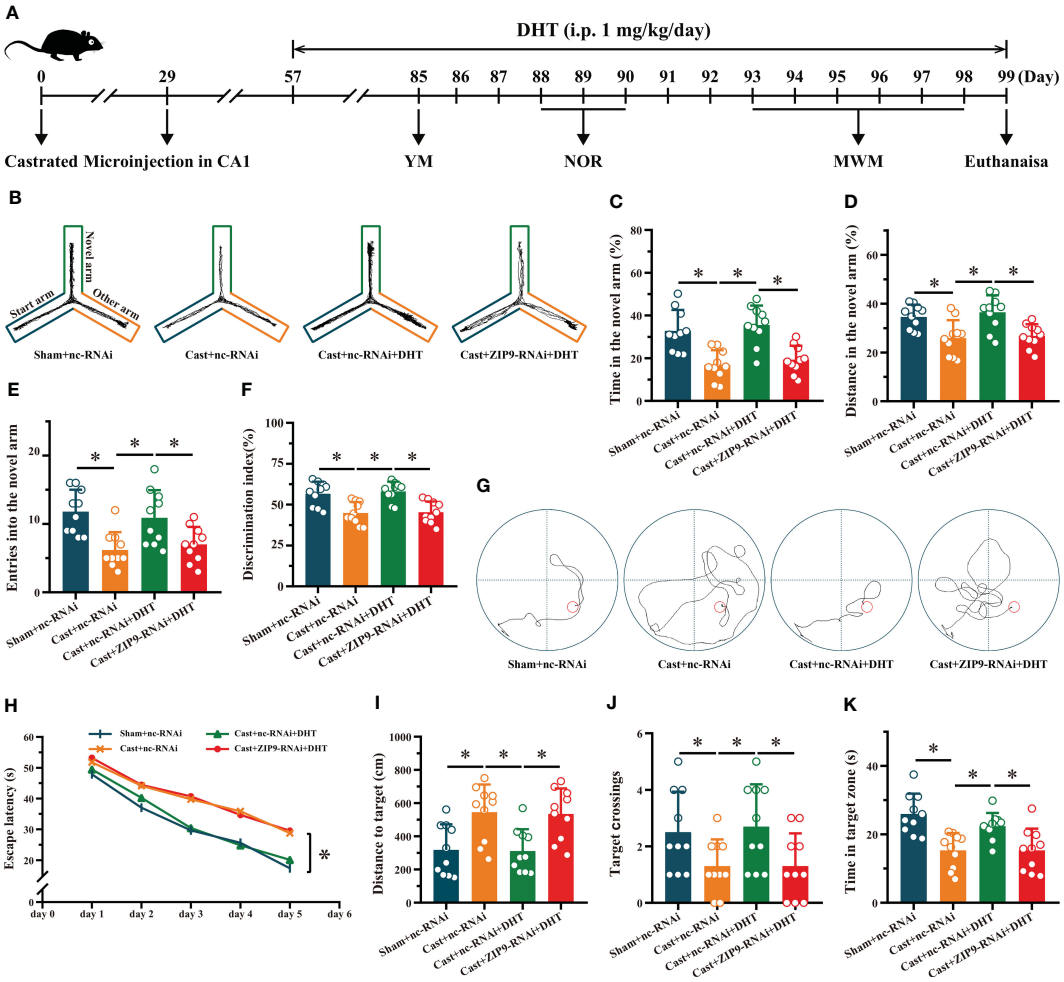

FIGURE 7
ZIP9 mediated the effects of DHT on learning and memory of APP/PS1 male mice. **(A)** Experimental procedure. Mice were treated with castration, microinjections in CA1, DHT (i.p. 1 mg/kg/day), and behavioral tests. **(B)** Representative trajectories of the YM (test). **(C–E)** YM was performed to test for spatial reference memory. **(F)** NOR was performed to assess memory retention. **(G)** Representative trajectories of the MWM (the 5th day). **(H-K)** MWM was used to test spatial memory and long-term memory. DHT, dihydrotestosterone; YM, Y-maze test; NOR, novel object recognition test; MWM, Morris water maze. (*$P < 0.05$, n = 10).

0.05, $\eta^2 = 0.591$) and SYP ($F_{(3,20)} = 6.262$, $P < 0.05$, $\eta^2 = 0.484$) in the hippocampi as observed by IHC staining (Figures 8E-H).

Golgi staining results showed a significant inter group differences in the density of dendritic spines ($F_{(3,20)} = 30.471$, $P < 0.05$, $\eta^2 = 0.820$). Compared to the Sham+nc-RNAi group, the dendritic spine density in the hippocampi of the Cast+nc-RNAi group decreased significantly. DHT supplementation increased dendritic spine density in castrated APP/PS1 mice, but this increase was not observed after ZIP9 knockdown in the hippocampus (Figures 8I, J).

ZIP9 mediated the effects of DHT on the phosphorylation of ERK1/2 and eIF4E in APP/PS1 mice hippocampus

We studied the effect of DHT mediated by ZIP9 on the phosphorylation of ERK1/2 and eIF4E in the hippocampi of APP/PS1 mice. Western blot revealed significant inter group differences in the phosphorylation levels of ERK1/2 ($F_{(3,20)} = 31.214$, $P < 0.05$, $\eta^2 = 824$) and eIF4E ($F_{(3,20)} = 13.242$, $P < 0.05$, $\eta^2 = 0.665$). Compared to the Sham+nc-RNAi group, the phosphorylation of ERK1/2 and eIF4E in the Cast+nc-RNAi group decreased significantly. DHT supplementation improved the phosphorylation of ERK1/2 and eIF4E in castrated APP/PS1 mice, while improvement was not observed after ZIP9 knockdown in the hippocampus (Figures 9A-D).

Discussion

The effect of androgens was previously thought to be mediated by AR. Androgens bind to intracellular AR and form a receptor-ligand complex, which is transferred into the nucleus to regulate target genes and exert biological effects. In addition to the classic AR, recent studies have found that androgen can also exert effects

10.3389/fendo.2023.1139874

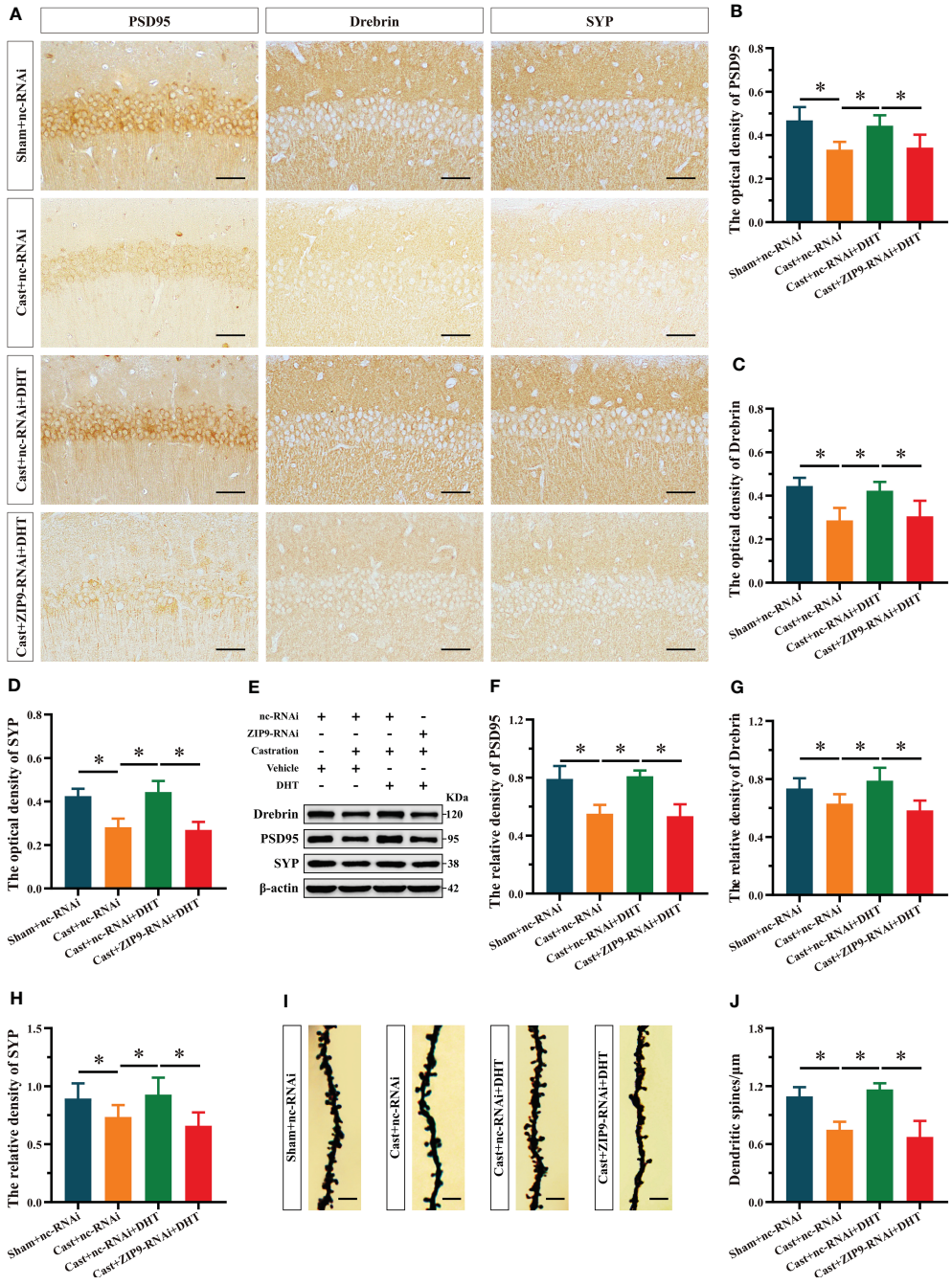

FIGURE 8
ZIP9 mediated the effects of DHT on hippocampal PSD95, drebrin, SYP protein and dendritic spine density in APP/PS1 male mice. **(A-D)** Representative IHC images **(A)** and quantification **(B–D)** of PSD95 **(B)**, drebrin **(C)**, and SYP **(D)** in the hippocampal CA1 region of the four groups of mice. Scale bars = 50 μm. **(E–H)** Representative Western blot **(E)** and quantification **(F–H)** of PSD95 **(F)**, drebrin **(G)**, and SYP **(H)** in the hippocampus of the four groups of mice. **(I, J)** Representative images **(I)** and quantification **(J)** of Golgi staining in the hippocampus of the four groups of mice; Scale bars = 5 μm. DHT, dihydrotestosterone; ZIP9, Zrt-, Irt-like protein 9; PSD95, postsynaptic density protein 95; SYP, synaptophysin. (*$P < 0.05$, n = 6).

through other binding sites, such as GPRC6A (30, 31), TRPM8 (32), OXER1 (33) and ZIP9 (28). As a member of the ZIP family, ZIP9 participates in the transport of Zn^{2+} from extracellular to intracellular matrix (19). It can also bind to androgens and further couple with the G protein to exert biological effects. In cancer studies, androgens have been found to bind to ZIP9 and exert biological effects. Bulldan et al. (22) found that ZIP9 mediates testosterone-induced migratory activity of metastatic prostate cancer cells. Chen et al. (23) suggested that DHT may increase the migration and invasion of AR-negative bladder cancer cells *via* ZIP9, thus promoting the progression of muscle-invasive bladder cancer. Thomas et al. (24) reported that the expression of ZIP9 was upregulated in breast and prostate cancer tissues, and androgen promoted the apoptosis of breast cancer MDAMB-468 cells and

10.3389/fendo.2023.1139874

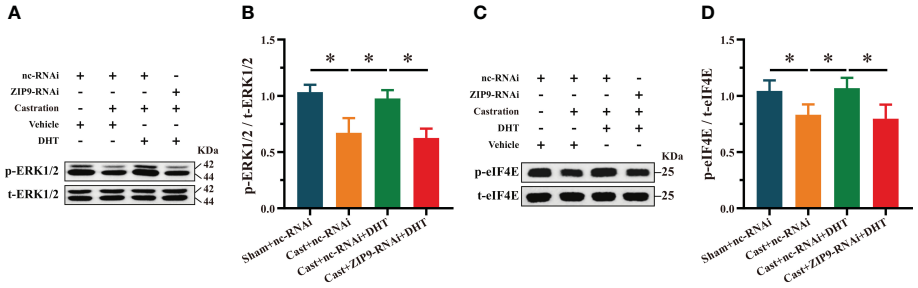

FIGURE 9
ZIP9 mediated the effects of DHT on the phosphorylation of ERK1/2 and eIF4E in APP/PS1 mice hippocampus. **(A, B)** Representative Western blot **(A)** and quantification **(B)** of the phosphorylation of ERK1/2 in the hippocampus of the four groups of mice. **(C, D)** Representative Western blot **(C)** and quantification **(D)** of the phosphorylation of eIF4E in the hippocampus of the four groups of mice. DHT, dihydrotestosterone; ZIP9, Zrt-, Irt-like protein 9; ERK1/2, Extracellular signal-regulated kinase ½; eIF4E, Eukaryotic translation initiation factor 4E. (*$P < 0.05$, n = 6).

prostate cancer PC-3 cells through ZIP9. The authors also noted that ZIP9 was a potential therapeutic target in breast and prostate cancer. ZIP9 is also widely expressed in normal tissues and cells, such as the testis, pancreas, heart, prostate and brain (24). In a study of Sertoli cells, Bulldan et al. (34) found that testosterone can promote the expression of the tight junction protein claudin and the formation of tight junctions through ZIP9, highlighting the importance of this mechanism in male reproductive function. Converse et al. (35) found that androgen regulated stage-dependent pro- and anti-apoptosis in teleost ovaries through ZIP9 by activating different G proteins. They also demonstrated *via* another study (36) that ZIP9 mediated androgen effect in promoting the proliferation of vascular endothelial cells. Malviya et al. (37) suggested that testosterone promotes mineralization in human osteoblastic SAOS-2 cells and myogenesis in mouse myogenic L6 cells through ZIP9. Although our previous studies have shown that T-BSA rapidly increases the expression of PSD95 protein in HT22 cells through ZIP9, it is not yet known whether ZIP9 is involved in learning and memory as an androgen binding site in the hippocampus. The present study used AR-deficient Tfm male mice with learning and memory impairments to study the effects of androgens mediated by ZIP9 on hippocampal learning and memory. The results showed that ZIP9 was expressed in the hippocampus of WT and Tfm male mice with no significant differences between the groups, suggesting that ZIP9 did not directly affect the learning and memory of Tfm mice. However, this did not exclude the possibility that ZIP9, as an androgen-binding site, affects learning and memory in mice.

We used androgen supplementation and hippocampal ZIP9 knockdown models to determine whether androgen affects learning and memory of Tfm male mice through ZIP9. Testosterone can be partially converted by aromatase into estrogen (38, 39), which can affect synaptic plasticity in the hippocampus of mice (40, 41). To avoid this, we used non-aromatized DHT. Behavioral experiments showed that DHT supplementation significantly improved learning and memory in Tfm male mice, but this improvement was inhibited after hippocampal ZIP9 knockdown. This suggests that DHT improved the learning and memory of Tfm male mice through ZIP9. After behavioral experiments, we evaluated hippocampal synaptic plasticity in Tfm male mice since it plays an important role in learning and memory. PSD95 is essential for synaptic plasticity of the nervous system as a scaffold protein in the postsynaptic structure, PSD95-knockout mice showed long-term potentiation, long-term depression impairment, and significant spatial learning and memory impairment in behavioral tests (42). As an important actin-binding protein widely distributed in dendritic spines, drebrin can regulate synaptic plasticity and affect cognitive function by combining with F-actin to promote dendritic spine maturation (36). SYP is important for synaptic plasticity and cognitive function and its content can be used as an index to evaluate the number, density, and transmission efficiency of synapses (43). Dendritic spines are the main sites of synapse formation. Loss of dendritic spines is closely related to a decline in cognitive ability (44, 45). Therefore, we investigated the expression level of synaptic proteins PSD95, drebrin, SYP and the density of dendritic spines to observe the effect of DHT supplementation on synaptic plasticity in Tfm male mice. The results showed that the expression of these components, as well as density of dendritic spines were significantly lower than in WT male mice, with a significant increase after DHT supplementation. To explore how DHT works, we knocked down hippocampal ZIP9 in Tfm male mice and found that the increase in the expression of PSD95, drebrin, and SYP, and the density of dendritic spines induced by DHT disappeared. Combined with the results of the behavioral experiments, we postulate that DHT improves hippocampal synaptic plasticity in Tfm male mice through ZIP9, thereby improving their learning and memory.

The extracellular-signal-regulated kinase (ERK) may be a key downstream signal molecule of ZIP9-mediated androgen effect. Profaska-Szymik et al. (46) found that senescence driven by androgens *via* ZIP9 in regressed vole testes has a functional link with ERK. Other studies (20, 27, 47–51) have also found ZIP9 mediated androgen biological effects through ERK pathway. In the nervous system, ERK plays a vital role in synaptic plasticity, learning, and memory (52–55). The phosphorylation of ERK1/2 can enhance the uncoupling of nNOS-PSD95 in the mouse hippocampus, increase the expression of PSD95 protein, promoting memory retrieval et al. (56). The cap-binding translation initiation factor eIF4E, cooperating with proteins such as helicase eIF4A and scaffolding protein eIF4G binds to mRNA,

allowing the recruitment of ribosomes and translation initiation (57, 58). Gindina et al. (59) found upregulation of eIF4E in dendritic spines during memory formation in adult male Sprague-Dawley rats. These results are consistent with those of our study. The phosphorylation of ERK1/2 and eIF4E in the hippocampus of Tfm male mice was significantly lower than that in WT male mice; DHT supplementation significantly increased these levels, suggesting that there was abnormal phosphorylation of ERK1/2 and eIF4E in Tfm male mice, and that DHT could improve this abnormality. To find out whether ZIP9 mediated this effect of DHT, we knocked down hippocampal ZIP9 in Tfm male mice and found that the beneficial effect of DHT were inhibited. These results were also confirmed at a cellular level. This confirmed that increase in the expression of PSD95 and phosphorylation of ERK1/2 and eIF4E in HT22 cells induced by DHT were inhibited after ZIP9 knockdown and enhanced after ZIP9 overexpression.

Although we found that DHT promoted the phosphorylation of ERK1/2, eIF4E and the expression of PSD95 through ZIP9, the mechanism still required experimental verification. We found that pretreatment with SCH772984, a specific inhibitor of ERK1/2, significantly inhibited the phosphorylation of ERK1/2, eIF4E and expression of PSD95. Pretreatment with eFT508, a specific inhibitor of eIF4E, significantly inhibited the phosphorylation of eIF4E and expression of PSD95 in ZIP9-overexpression HT22 cells. These results are consistent with those of other studies showing that ERK1/2 activation can regulate synaptic protein synthesis by phosphorylating eIF4E, which subsequently affects synaptic plasticity (60, 61). Combined with animal and cell experiments, it was concluded that ZIP9 mediated the effects of DHT on improving the expression of synaptic plasticity-related proteins and dendritic spine density in the hippocampus of Tfm male mice through the ERK1/2-eIF4E pathway, thus improving learning and memory.

The serum level of total or free testosterone in AD patients is significantly lower than that in normal elderly men (62), and the decreased level of testosterone *in vivo* leads to cognitive decline, which was measured by learning and memory (63). Studies have reported that cognitive function of AD patients improved to varying degrees after testosterone replacement therapy (64). This suggests that androgen decline may be a risk factor for AD in older men. Therefore, castration surgery or androgen supplement therapy are often used to intervene in AD animal models to study the pathological mechanism of androgen regulation of AD cognitive impairment (65–68). APP/PS1 is a double-transgenic mouse model that overproduces Aβ and is often used to study the mechanisms of AD neuropathology. Aβ plaques appear in the cerebral cortex at approximately 4 months of age and in the hippocampus at 6 months of age, and increase in size and number with age (69, 70). Obvious learning and memory deficits emerge at 6-10 months old (71, 72). This study found that castration significantly impaired the learning and memory of APP/PS1 mice and decreased the expression of PSD95, drebrin, SYP, and dendritic spine density. Supplementation with DHT ameliorated the adverse effects of castration. To verify whether the improvement induced by DHT in castrated mice depends on ZIP9, we knocked down hippocampal ZIP9 in castrated APP/PS1 mice and found that the improvement of learning and memory, the expression of PSD95, drebrin, SYP, and dendritic spine density induced by DHT were significantly suppressed. Castration significantly decreased the phosphorylation of ERK1/2 and eIF4E in the hippocampus of APP/PS1 mice, and DHT supplementation could improve this deficiency state. To determine the effect of DHT on the phosphorylation of ERK1/2 and eIF4E through ZIP9, we knocked down hippocampal ZIP9 in castrated APP/PS1 mice and found that the phosphorylation of ERK1/2 and eIF4E was significantly downregulated. This suggests that ZIP9 mediates the effects of DHT on the expression of synaptic plasticity-related proteins and dendritic spine density in the hippocampi of APP/PS1 mice through the ERK1/2-eIF4E pathway and affects their learning and memory.

The ZIP9 has been described as a membrane androgen receptor (19, 20, 26, 28, 46, 48, 73–75). Thomas et al. (24) found ZIP9 in the perinuclear and plasma membrane of MDA-MB-468 cells, while some studies also detected it in the reverse Golgi network (76). In addition, since membrane permeable DHT was used in this study, the current data do not support the conclusion that DHT played a role only through ZIP9 located in the cell membrane. However, our experimental results confirmed that DHT could regulate hippocampal synaptic plasticity through ZIP9, thus affecting learning and memory, which was consistent with our research theme.

However the findings of this study have to be seen in light of some limitations. Firstly, considering that the topic of this study is the effects of DHT mediated by ZIP9 on hippocampal synaptic plasticity and learning and memory, we did not detect hippocampal Aβ in APP/PS1 mice, although senile plaque formed by excessive deposition of Aβ is one of the pathological features of AD. Therefore, we are unable to know the effects of DHT mediated by ZIP9 on hippocampal pathology in APP/PS1 mice. Secondly, ZIP9 has both androgen signaling and zinc transport functions, and the mechanism of zinc ion on learning and memory is still unclear. Since this study focused on ZIP9-mediated androgen influence on synaptic plasticity and learning memory in mice, its zinc transport function was not investigated. Finally, only male mice were used in this study, and the results of this study may not be applicable to female animals because of gender differences.

Based on the above experiments, we concluded that ZIP9 mediated the effects of DHT on improving hippocampal synaptic plasticity-related proteins and dendritic spine density in Tfm male mice through the ERK1/2-eIF4E pathway, improving learning and memory. DHT can also affect learning and memory in castrated APP/PS1 mice through this mechanism. This study provides important experimental data for further research into the use of androgen supplementation in Alzheimer's Disease to improve learning and memory.

Data availability statement

The original contributions presented in the study are included in the article/Supplementary Material. Further inquiries can be directed to the corresponding author/s.

Ethics statement

The animal study was reviewed and approved by Hebei Medical University Laboratory Animal Welfare and Ethics Committee.

Author contributions

HXC and SL designed the research, writing-review, editing, project administration. LS and HC performed the experimental phase, methodology, data curation, writing-original draft. DQ, BZ, FG, YZ and CW contributed toward investigation, and visualization. All authors contributed to the article and approved the submitted version.

Funding

This work was supported by project funding from the National Natural Science Foundation of China (91849134 and 82171582).

Conflict of interest

The authors declare that the research was conducted in the absence of any commercial or financial relationships that could be construed as a potential conflict of interest.

Publisher's note

Supplementary material

The Supplementary Material for this article can be found online at: https://www.frontiersin.org/articles/10.3389/fendo.2023.1139874/full#supplementary-material

References

1. Kuwahara N, Nicholson K, Isaacs L and MacLusky NJ. Androgen effects on neural plasticity. *Androg Clin Res Ther* (2021) 2(1):216–30. doi: 10.1089/andro.2021.0022

2. Jacome LF, Barateli K, Buitrago D, Lema F, Frankfurt M and Luine VN. Gonadal hormones rapidly enhance spatial memory and increase hippocampal spine density in Male rats. *Endocrinology* (2016) 157(4):1357–62. doi: 10.1210/en.2015-1959

3. Lumia AR, McGinnis MY. Impact of anabolic androgenic steroids on adolescent males. *Physiol Behav* (2010) 100(3):199–204. doi: 10.1016/j.physbeh.2010.01.007

4. MacLusky NJ, Hajszan T, Johansen JA, Jordan CL and Leranth C. Androgen effects on hippocampal CA1 spine synapse numbers are retained in tfm male rats with defective androgen receptors. *Endocrinology* (2006) 147(5):2392–8. doi: 10.1210/en.2005-0673

5. Mi S, Chen H, Lin P, Kang P, Qiao D, Zhang B, et al. CaMKII is a modulator in neurodegenerative diseases and mediates the effect of androgen on synaptic protein PSD95. *Front Genet* (2022) 13:959360. doi: 10.3389/fgene.2022.959360

6. Goedert M, Spillantini MG. A century of alzheimer's disease. *Science* (2006) 314 (5800):777–81. doi: 10.1126/science.1132814

7. Selkoe DJ. Alzheimer's disease: genes, proteins, and therapy. *Physiol Rev* (2001) 81 (2):741–66. doi: 10.1152/physrev.2001.81.2.741

8. Carroll JC, Rosario ER. The potential use of hormone-based therapeutics for the treatment of alzheimer's disease. *Curr Alzheimer Res* (2012) 9(1):18–34. doi: 10.2174/156720512799015109

9. Paoletti AM, Congia S, Lello S, Tedde D, Orrù M, Pistis M, et al. Low androgenization index in elderly women and elderly men with alzheimer's disease. *Neurology* (2004) 62(2):301–3. doi: 10.1212/01.wnl.0000094199.60829.f5

10. Li Y, Li S, Xu S, Yu H, Tang L, Liu X, et al. Association of androgens and gonadotropins with amnestic mild cognitive impairment and probable alzheimer's disease in Chinese elderly men. *J Alzheimers Dis* (2020) 78(1):277–90. doi: 10.3233/JAD-200233

11. Cai Z, Li H. An updated review: androgens and cognitive impairment in older men. *Front Endocrinol (Lausanne)* (2020) 11:586909. doi: 10.3389/fendo.2020.586909

12. Nead KT, Gaskin G, Chester C, Swisher-McClure S, Dudley JT, Leeper NJ, et al. Androgen deprivation therapy and future alzheimer's disease risk. *J Clin Oncol* (2016) 34(6):566–71. doi: 10.1200/jco.2015.63.6266

13. Nead KT, Gaskin G, Chester C, Swisher-McClure S, Leeper NJ and Shah NH. Association between androgen deprivation therapy and risk of dementia. *JAMA Oncol* (2017) 3(1):49–55. doi: 10.1001/jamaoncol.2016.3662

14. Nead KT, Sinha S and Nguyen PL. Androgen deprivation therapy for prostate cancer and dementia risk: a systematic review and meta-analysis. *Prostate Cancer Prostatic Dis* (2017) 20(3):259–64. doi: 10.1038/pcan.2017.10

15. Cherrier MM, Matsumoto AM, Amory JK, Asthana S, Bremner W, Peskind ER, et al. Testosterone improves spatial memory in men with Alzheimer disease and mild cognitive impairment. *Neurology* (2005) 64(12):2063–8. doi: 10.1212/01.Wnl.0000165995.98986.F1

16. Tan S, Sohrabi HR, Weinborn M, Tegg M, Bucks RS, Taddei K, et al. Effects of testosterone supplementation on separate cognitive domains in cognitively healthy older men: a meta-analysis of current randomized clinical trials. *Am J Geriatr Psychiatry* (2019) 27(11):1232–46. doi: 10.1016/j.jagp.2019.05.008

17. Tejada LD, Rissman EF. Sex differences in social investigation: effects of androgen receptors, hormones and test partner. *J Neuroendocrinol* (2012) 24 (8):1144–53. doi: 10.1111/j.1365-2826.2012.02322.x

18. Zuloaga DG, Morris JA, Jordan CL and Breedlove SM. Mice with the testicular feminization mutation demonstrate a role for androgen receptors in the regulation of anxiety-related behaviors and the hypothalamic-pituitary-adrenal axis. *Horm Behav* (2008) 54(5):758–66. doi: 10.1016/j.yhbeh.2008.08.004

19. Thomas P, Converse A and Berg HA. ZIP9, a novel membrane androgen receptor and zinc transporter protein. *Gen Comp Endocrinol* (2018) 257:130–36. doi: 10.1016/j.ygcen.2017.04.016

20. Thomas P, Pang Y and Dong J. Membrane androgen receptor characteristics of human ZIP9 (SLC39A) zinc transporter in prostate cancer cells: androgen-specific activation and involvement of an inhibitory G protein in zinc and MAP kinase signaling. *Mol Cell Endocrinol* (2017) 447:23–34. doi: 10.1016/j.mce.2017.02.025

21. Aguirre-Portolés C, Payne R, Trautz A, Foskett JK, Natale CA, Seykora JT, et al. ZIP9 is a druggable determinant of sex differences in melanoma. *Cancer Res* (2021) 81 (23):5991–6003. doi: 10.1158/0008-5472.Can-21-0982

22. Bulldan A, Bartsch J-W, Konrad L, Scheiner-Bobis G. ZIP9 but not the androgen receptor mediates testosterone-induced migratory activity of metastatic prostate cancer cells. *Biochim Biophys Acta Mol Cell Res* (2018) 1865(12):1857–68. doi: 10.1016/j.bbamcr.2018.09.004

23. Chen J, Chou F, Yeh S, Ou Z, Shyr C, Huang C, et al. Androgen dihydrotestosterone (DHT) promotes the bladder cancer nuclear AR-negative cell invasion *via* a newly identified membrane androgen receptor (mAR-SLC39A9)-mediated galphai protein/MAPK/MMP9 intracellular signaling. *Oncogene* (2020) 39 (3):574–86. doi: 10.1038/s41388-019-0964-6

24. Thomas P, Pang Y, Dong J and Berg AH. Identification and characterization of membrane androgen receptors in the ZIP9 zinc transporter subfamily: II. role of human ZIP9 in testosterone-induced prostate and breast cancer cell apoptosis. *Endocrinology* (2014) 155(11):4250–65. doi: 10.1210/en.2014-1201

25. Thomas P, Dong J. (-)-Epicatechin acts as a potent agonist of the membrane androgen receptor, ZIP9 (SLC39A9), to promote apoptosis of breast and prostate cancer cells. *J Steroid Biochem Mol Biol* (2021) 211:105906. doi: 10.1016/j.jsbmb.2021.105906

26. Lustofin S, Kaminska A, Brzoskwinia M, Cyran J, Kotula-Balak M, Bilinska B, et al. Nuclear and membrane receptors for sex steroids are involved in the regulation of Delta/Serrate/LAG-2 proteins in rodent sertoli cells. *Int J Mol Sci* (2022) 23(4):2284. doi: 10.3390/ijms23042284

27. Kabbesh H, Bulldan A, Konrad L, Scheiner-Bobis G. The role of ZIP9 and androgen receptor in the establishment of tight junctions between adult rat sertoli cells. *Biol (Basel)* (2022) 11(5):668. doi: 10.3390/biology11050668

28. Berg AH, Rice CD, Rahman MS, Dong J and Thomas P. Identification and characterization of membrane androgen receptors in the ZIP9 zinc transporter subfamily: i. discovery in female atlantic croaker and evidence ZIP9 mediates testosterone-induced apoptosis of ovarian follicle cells. *Endocrinology* (2014) 155 (11):4237–49. doi: 10.1210/en.2014-1198

29. Charan J, Kantharia ND. How to calculate sample size in animal studies? *J Pharmacol Pharmacother* (2013) 4(4):303–6. doi: 10.4103/0976-500x.119726

30. Schuh-Huerta SM, Pera RA. Reproductive biology: bone returns the favour. *Nature* (2011) 472(7341):46–7. doi: 10.1038/472046a

31. Oury F, Ferron M, Huizhen W, Confavreux C, Xu L, Lacombe J, et al. Osteocalcin regulates murine and human fertility through a pancreas-bone-testis axis. *J Clin Invest* (2013) 123(6):2421–33. doi: 10.1172/jci65952

32. Zhang L, Barritt GJ. Evidence that TRPM8 is an androgen-dependent Ca2+ channel required for the survival of prostate cancer cells. *Cancer Res* (2004) 64 (22):8365–73. doi: 10.1158/0008-5472.Can-04-2146

33. Masi M, Garattini E, Bolis M, Di Marino D, Maraccani L, Morelli E, et al. OXER1 and RACK1-associated pathway: a promising drug target for breast cancer progression. *Oncogenesis* (2020) 9(12):105. doi: 10.1038/s41389-020-00291-x

34. Bulldan A, Dietze R, Shihan M, Scheiner-Bobis G. Non-classical testosterone signaling mediated through ZIP9 stimulates claudin expression and tight junction formation in sertoli cells. *Cell Signal* (2016) 28(8):1075–85. doi: 10.1016/j.cellsig.2016.04.015

35. Converse A, Thomas P. Androgens regulate follicle stage-dependent pro- and anti-apoptosis in teleost ovaries through ZIP9 activation of different G proteins†. *Biol Reprod* (2019) 101(2):377–91. doi: 10.1093/biolre/ioz086

36. Koganezawa N, Hanamura K, Sekino Y and Shirao T. The role of drebrin in dendritic spines. *Mol Cell Neurosci* (2017) 84:85–92. doi: 10.1016/j.mcn.2017.01.004

37. Malviya VN, Bulldan A, Wende RC, Kabbesh H, Moller ML, Schreiner PR, et al. The effects of tetrapeptides designed to fit the androgen binding site of ZIP9 on myogenic and osteogenic cells. *Biol (Basel)* (2021) 11(1):19. doi: 10.3390/biology11010019

38. Hojo Y, Hattori TA, Enami T, Furukawa A, Suzuki K, Ishii HT, et al. Adult male rat hippocampus synthesizes estradiol from pregnenolone by cytochromes P45017alpha and P450 aromatase localized in neurons. *Proc Natl Acad Sci USA* (2004) 101(3):865–70. doi: 10.1073/pnas.2630225100

39. Ishii H, Tsurugizawa T, Ogiue-Ikeda M, Asashima M, Mukai H, Murakami G, et al. Local production of sex hormones and their modulation of hippocampal synaptic plasticity. *Neuroscientist* (2007) 13(4):323–34. doi: 10.1177/1073858407301300406O1

40. Gibbs RB. Estrogen therapy and cognition: a review of the cholinergic hypothesis. *Endocr Rev* (2010) 31(2):224–53. doi: 10.1210/er.2009-0036

41. Lu Y, Sareddy GR, Wang J, Wang R, Li Y, Dong Y, et al. Neuron-derived estrogen regulates synaptic plasticity and memory. *J Neurosci* (2019) 39(15):2792–809. doi: 10.1523/jneurosci.1970-18.2019

42. Migaud M, Charlesworth P, Dempster M, Webster LC, Watabe AM, Makhinson M, et al. Enhanced long-term potentiation and impaired learning in mice with mutant postsynaptic density-95 protein. *Nature* (1998) 396(6710):433–39. doi: 10.1038/24790

43. Matosin N, Fernandez-Enright F, Lum JS, Engel M, Andrews JL, Gassen NC, et al. Molecular evidence of synaptic pathology in the CA1 region in schizophrenia. *NPJ Schizophr* (2016) 2:16022. doi: 10.1038/npjschz.2016.22

44. Kandimalla R, Manczak M, Yin X, Wang R and Reddy PH. Hippocampal phosphorylated tau induced cognitive decline, dendritic spine loss and mitochondrial abnormalities in a mouse model of alzheimer's disease. *Hum Mol Genet* (2018) 27 (1):30–40. doi: 10.1093/hmg/ddx381

45. Raven F, van der Zee EA, Meerlo P and Havekes R. The role of sleep in regulating structural plasticity and synaptic strength: implications for memory and cognitive function. *Sleep Med Rev* (2018) 39:3–11. doi: 10.1016/j.smrv.2017.05.002

46. Profaska-Szymik M, Galuszka A, Korzekwa AJ, Hejmej A, Gorowska-Wojtowicz E, Pawlicki P, et al. Implication of membrane androgen receptor (ZIP9) in cell senescence in regressed testes of the bank vole. *Int J Mol Sci* (2020) 21(18):6888. doi: 10.3390/ijms21186888

47. Shihan M, Chan KH, Konrad L, Scheiner-Bobis G. Non-classical testosterone signaling in spermatogenic GC-2 cells is mediated through ZIP9 interacting with Gnα11. *Cell Signal* (2015) 27(10):2077–86. doi: 10.1016/j.cellsig.2015.07.013

48. Converse A, Zhang C and Thomas P. Membrane androgen receptor ZIP9 induces croaker ovarian cell apoptosis *via* stimulatory G protein alpha subunit and MAP kinase signaling. *Endocrinology* (2017) 158(9):3015–29. doi: 10.1210/en.2017-00087

49. Bulldan A, Malviya VN, Upmanyu N, Konrad L, Scheiner-Bobis G. Testosterone/bicalutamide antagonism at the predicted extracellular androgen binding site of ZIP9. *Biochim Biophys Acta Mol Cell Res* (2017) 1864(12):2402–14. doi: 10.1016/j.bbamcr.2017.09.012

50. Converse A, Thomas P. Androgens promote vascular endothelial cell proliferation through activation of a ZIP9-dependent inhibitory G protein/PI3K-Akt/Erk/cyclin D1 pathway. *Mol Cell Endocrinol* (2021) 538:111461. doi: 10.1016/j.mce.2021.111461

51. Möller ML, Bulldan A, Scheiner-Bobis G. Tetrapeptides modelled to the androgen binding site of ZIP9 stimulate expression of tight junction proteins and tight junction formation in sertoli cells. *Biol (Basel)* (2021) 11(1):55. doi: 10.3390/biology11010055

52. Kim EK, Choi EJ. Compromised MAPK signaling in human diseases: an update. *Arch Toxicol* (2015) 89(6):867–82. doi: 10.1007/s00204-015-1472-2

53. Ryu HH, Lee YS. Cell type-specific roles of RAS-MAPK signaling in learning and memory: implications in neurodevelopmental disorders. *Neurobiol Learn Mem* (2016) 135:13–21. doi: 10.1016/j.nlm.2016.06.006

54. Thomas GM, Huganir RL. MAPK cascade signalling and synaptic plasticity. *Nat Rev Neurosci* (2004) 5(3):173–83. doi: 10.1038/nrn1346

55. Stough S, Kopec AM and Carew TJ. Synaptic generation of an intracellular retrograde signal requires activation of the tyrosine kinase and mitogen-activated protein kinase signaling cascades in aplysia. *Neurobiol Learn Mem* (2015) 125:47–54. doi: 10.1016/j.nlm.2015.07.017

56. Li J, Han Z, Cao B, Cai CY, Lin YH, Li F, et al. Disrupting nNOS-PSD-95 coupling in the hippocampal dentate gyrus promotes extinction memory retrieval. *Biochem Biophys Res Commun* (2017) 493(1):862–68. doi: 10.1016/j.bbrc.2017.09.003

57. Amorim IS, Lach G and Gkogkas CG. The role of the eukaryotic translation initiation factor 4E (eIF4E) in neuropsychiatric disorders. *Front Genet* (2018) 9:561. doi: 10.3389/fgene.2018.00561

58. Topisirovic I, Ruiz-Gutierrez M, Borden KL. Phosphorylation of the eukaryotic translation initiation factor eIF4E contributes to its transformation and mRNA transport activities. *Cancer Res* (2004) 64(23):8639–42. doi: 10.1158/0008-5472.Can-04-2677

59. Gindina S, Botsford B, Cowansage K, LeDoux J, Klann E, Hoeffer C, et al. Upregulation of eIF4E, but not other translation initiation factors, in dendritic spines during memory formation. *J Comp Neurol* (2021) 529(11):3112–26. doi: 10.1002/cne.25158

60. Bramham CR, Jensen KB and Proud CG. Tuning specific translation in cancer metastasis and synaptic memory: control at the MNK-eIF4E axis. *Trends Biochem Sci* (2016) 41(10):847–58. doi: 10.1016/j.tibs.2016.07.008

61. Kelleher RJ3rd, Govindarajan A, Jung HY, Kang H, Tonegawa S. Translational control by MAPK signaling in long-term synaptic plasticity and memory. *Cell* (2004) 116(3):467–79. doi: 10.1016/s0092-8674(04)00115-1

62. Rosario ER, Chang L, Stanczyk FZ and Pike CJ. Age-related testosterone depletion and the development of Alzheimer disease. *Jama* (2004) 292(12):1431–2. doi: 10.1001/jama.292.12.1431-b

63. Feldman HA, Longcope C, Derby CA, Johannes CB, Araujo AB, Coviello AD, et al. Age trends in the level of serum testosterone and other hormones in middle-aged men: longitudinal results from the Massachusetts male aging study. *J Clin Endocrinol Metab* (2002) 87(2):589–98. doi: 10.1210/jcem.87.2.8201

64. Lv W, Du N, Liu Y, Fan X, Wang Y, Jia X, et al. Low testosterone level and risk of alzheimer's disease in the elderly men: a systematic review and meta-analysis. *Mol Neurobiol* (2016) 53(4):2679–84. doi: 10.1007/s12035-015-9315-y

65. Yan XS, Yang ZJ, Jia JX, Song W, Fang X, Cai ZP, et al. Protective mechanism of testosterone on cognitive impairment in a rat model of alzheimer's disease. *Neural Regener Res* (2019) 14(4):649–57. doi: 10.4103/1673-5374.245477

66. Hawley WR, Grissom EM, Martin RC, Halmos MB, Bart CL and Dohanich GP. Testosterone modulates spatial recognition memory in male rats. *Horm Behav* (2013) 63(4):559–65. doi: 10.1016/j.yhbeh.2013.02.007

67. Pan W, Han S, Kang L, Li S, Du J and Cui H. Effects of dihydrotestosterone on synaptic plasticity of the hippocampus in mild cognitive impairment male SAMP8 mice. *Exp Ther Med* (2016) 12(3):1455–63. doi: 10.3892/etm.2016.3470

68. Mendell AL, Szigeti-Buck K, MacLusky NJ and Leranth C. Orchidectomy does not significantly affect spine synapse density in the CA3 hippocampal subfield in st. Kitts vervet monkeys (Chlorocebus aethiops sabaeus). *Neurosci Lett* (2014) 559:189–92. doi: 10.1016/j.neulet.2013.10.061

69. Minkeviciene R, Ihalainen J, Malm T, Matilainen O, Keksa-Goldsteine V, Goldsteins G, et al. Age-related decrease in stimulated glutamate release and vesicular glutamate transporters in APP/PS1 transgenic and wild-type mice. *J Neurochem* (2008) 105(3):584–94. doi: 10.1111/j.1471-4159.2007.05147.x

70. Jackson HM, Soto I, Graham LC, Carter GW and Howell GR. Clustering of transcriptional profiles identifies changes to insulin signaling as an early event in a mouse model of alzheimer's disease. *BMC Genomics* (2013) 14:831. doi: 10.1186/1471-2164-14-831

71. Li XY, Men WW, Zhu H, Lei JF, Zuo FX, Wang ZJ, et al. Age- and brain region-specific changes of glucose metabolic disorder, learning, and memory dysfunction in early alzheimer's disease assessed in APP/PS1 transgenic mice using (18)F-FDG-PET. *Int J Mol Sci* (2016) 17(10):1707. doi: 10.3390/ijms17101707

72. Onos KD, Uyar A, Keezer KJ, Jackson HM, Preuss C, Acklin CJ, et al. Enhancing face validity of mouse models of alzheimer's disease with natural genetic variation. *PloS Genet* (2019) 15(5):e1008155. doi: 10.1371/journal.pgen.1008155

73. Pascal LE, Wang Z. Unzipping androgen action through ZIP9: a novel membrane androgen receptor. *Endocrinology* (2014) 155(11):4120–3. doi: 10.1210/en.2014-1749

74. Kalyvianaki K, Panagiotopoulos AA, Malamos P, Moustou E, Tzardi M, Stathopoulos EN, et al. Membrane androgen receptors (OXER1, GPRC6A AND ZIP9) in prostate and breast cancer: a comparative study of their expression. *Steroids* (2019) 142:100–08. doi: 10.1016/j.steroids.2019.01.006

75. Thomas P. Membrane androgen receptors unrelated to nuclear steroid receptors. *Endocrinology* (2019) 160(4):772–81. doi: 10.1210/en.2018-00987

76. Matsuura W, Yamazaki T, Yamaguchi-Iwai Y, Masuda S, Nagao M, Andrews GK, et al. SLC39A9 (ZIP9) regulates zinc homeostasis in the secretory pathway: characterization of the ZIP subfamily I protein in vertebrate cells. *Biosci Biotechnol Biochem* (2009) 73(5):1142–8. doi: 10.1271/bbb.80910

Frontiers in Endocrinology

Explores the endocrine system to find new therapies for key health issues

The second most-cited endocrinology and metabolism journal, which advances our understanding of the endocrine system. It uncovers new therapies for prevalent health issues such as obesity, diabetes, reproduction, and aging.

Discover the latest Research Topics

See more →

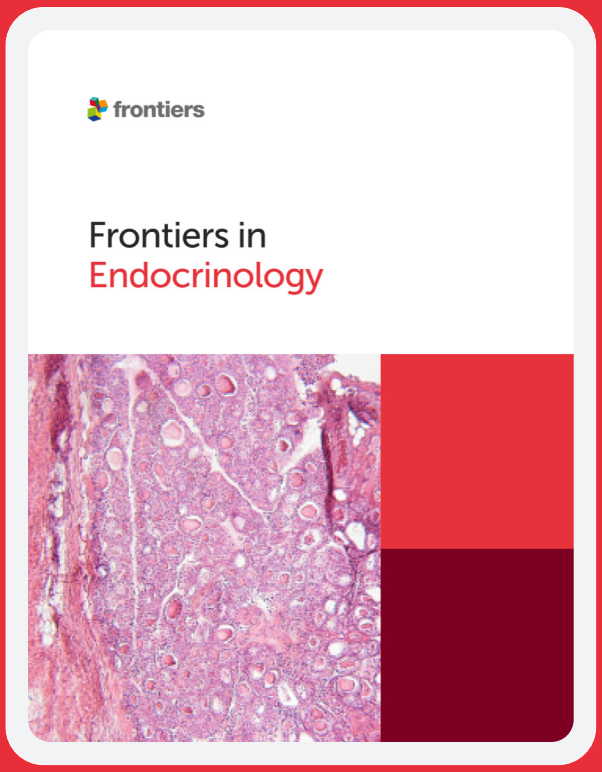

Frontiers

Avenue du Tribunal-Fédéral 34
1005 Lausanne, Switzerland
frontiersin.org

Contact us

+41 (0)21 510 17 00
frontiersin.org/about/contact